Liquid Crystals: From Modified Phases to Applications 2014

Edited by

Ingo Dierking, Joao Luis Figueirinhas and Maria Helena Godinho

Printed Edition of the Special Issue Published in *Materials*

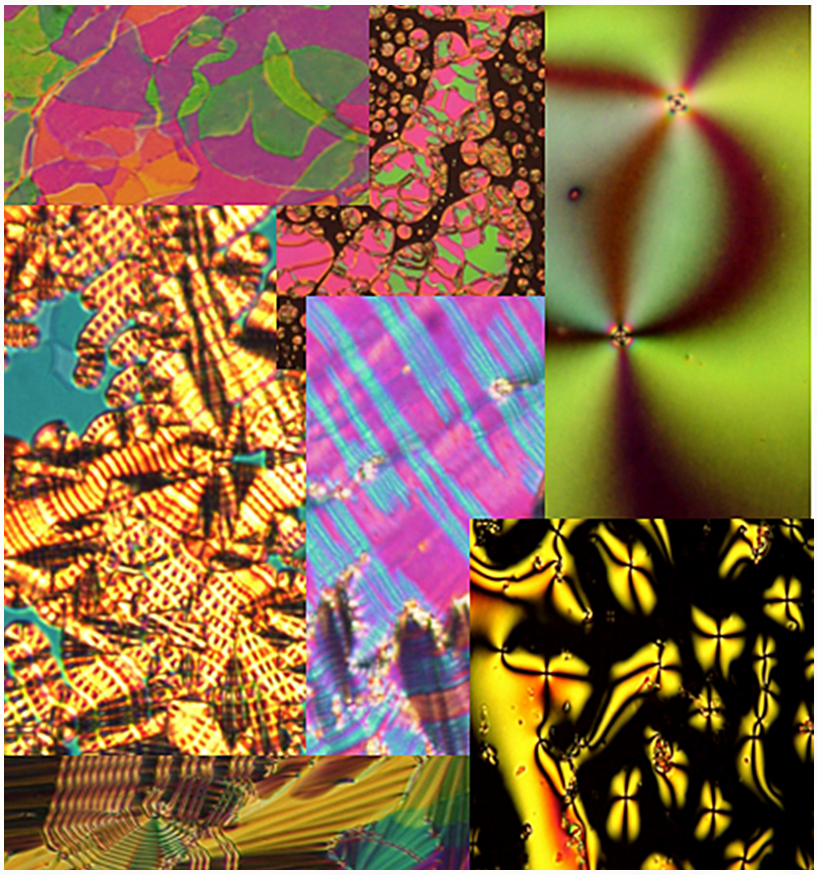

www.mdpi.com/journal/materials

Ingo Dierking, Joao Luis Figueirinhas, Maria Helena Godinho (Eds.)

Liquid Crystals:

From Modified Phases to Applications

2014

MDPI

This book is a reprint of the Special Issue that appeared in the online, open access journal, *Materials* (ISSN 1996-1944) in 2014 (available at: http://www.mdpi.com/journal/materials/special_issues/liquid_crystals).

Guest Editors

Ingo Dierking
School of Physics and Astronomy
University of Manchester
Oxford Road
Manchester, M13 9PL
United Kingdom

Maria Helena Godinho
CENIMAT/I3N
Departamento de Ciência dos Materiais
Faculdade de Ciências e Tecnologia
Universidade Nova de Lisboa
Campus da Caparica
Caparica 2829-516
Portugal

Joao Luis Figueirinhas
CFMC
Technical University of Lisbon
Av. Prof. Gama Pinto 2
1649-003 Lisbon
Portugal

Editorial Office
MDPI AG
Klybeckstrasse 64
Basel, Switzerland

Publisher
Shu-Kun Lin

Production Editor
Martyn Rittman

1. Edition 2014

MDPI • Basel • Beijing • Wuhan

ISBN 978-3-906980-85-0 (Hbk)
ISBN 978-3-906980-86-7 (PDF)

© 2014 by the authors; licensee MDPI AG, Basel, Switzerland. All articles in this volume are Open Access distributed under the Creative Commons license (CC BY), which allows users to download, copy and build upon published articles, even for commercial purposes, as long as the author and publisher are properly credited. This ensures maximum dissemination and a wider impact for our publications. The dissemination and distribution of physical copies of this book as a whole, however, is restricted to MDPI AG, Basel, Switzerland.

Table of Contents

Part II: Polymer-modified Liquid Crystals

Part III: Lyotropic Liquid Crystals

Part IV: Synthesis and Characterization

Part V: Applications of Liquid Crystals

List of Contributors

Erol Akpinar: Department of Chemistry, Arts and Sciences Faculty, Abant Izzet Baysal University, Bolu 14280, Turkey.

José Francisco Algorri: Electronic Technology Department, Carlos III University of Madrid, Butarque 15, E28911, Madrid, Spain.

Pedro Lúcio Almeida: CENIMAT/I3N, Departamento de Ciência dos Materiais, Faculdade de Ciências e Tecnologia, FCT, Universidade Nova de Lisboa, 2829-516 Caparica, Portugal; Área Departamental de Física, Instituto Superior de Engenharia de Lisboa, Instituto Politécnico de Lisboa, R. Conselheiro Emídio Navarro, 1, 1950-062 Lisboa, Portugal.

Angelika Baro: Institut für Organische Chemie, Universität Stuttgart, Pfaffenwaldring 55, Stuttgart D-70569, Germany.

David Barrios: Grupo de Displays y Aplicaciones Fotónicas, Departamento de Tecnología Electrónica, Universidad Carlos III de Madrid, C/Butarque, 15, Leganés E28911, Madrid, Spain.

Noureddine Bennis: Institute of Applied Physics, Military University of Technology, Kaliskiego 2, Warsaw 00-908, Poland.

Germán Cabañero: Centre for Electrochemical Technologies (CIDETEC), Departamento de Nuevos Materiales, Parque Tecnológico de San Sebastián - Paseo Miramón, 196, San Sebastián E20009, Spain.

Michael G. Campbell: Department of Physics, University of Colorado, Boulder, CO 80309, USA.

Seung Nam Cha: Department of Engineering Science, University of Oxford, Oxford OX1 3PJ, UK.

Su Seok Choi: Centre of Molecular Materials for Photonics and Electronics, Department of Engineering, University of Cambridge, Cambridge CB3 0FA, UK.

Harry J. Coles: Centre of Molecular Materials for Photonics and Electronics, Department of Engineering, University of Cambridge, Cambridge CB3 0FA, UK.

Simon Čopar: Faculty of Mathematics and Physics, University of Ljubljana, Jadranska 19, Ljubljana 1000, Slovenia; Jozef Stefan Institute, Jamova 34, Ljubljana 1000, Slovenia.

María Rosario de la Fuente: Departamento de Física Aplicada II, Facultad de Ciencia y Tecnología, Universidad del País Vasco UPV-EHU, Apartado 644, Bilbao E-48080, Spain.

Ingo Dierking: School of Physics and Astronomy, University of Manchester, Schuster Building, Oxford Road, Manchester M13 9PL, UK.

Sergio Diez-Berart: Departamento de Física Aplicada II, Facultad de Ciencia y Tecnología, Universidad del País Vasco UPV-EHU, Apartado 644, Bilbao E-48080, Spain; Grup de Propietas Físiques dels Materials (GRPFM), Departament de Física i Enginyeria Nuclear, E.T.S.E.I.B. Universitat Politècnica de Catalunya, Diagonal 647, Barcelona 08028, Spain.

Julian S. Evans: Department of Physics, University of Colorado, Boulder, CO 80309, USA.

Yeshaiahu Fainman: Department of Electrical and Computer Engineering, University of California San Diego, La Jolla, CA 92037, USA.
Antônio Martins Figueiredo Neto: Instituto de Física, Universidade de São Paulo, Caixa Postal 66318, São Paulo, SP 05314-970, Brazil.
João Luis Figueirinhas: Departamento de Física, Instituto Superior Técnico, Universidade de Lisboa, Av. Rovisco Pais, 1049-001 Lisboa, Portugal; Centro de Física da Matéria Condensada da Universidade de Lisboa, Av. Prof. Gama Pinto 2, 1649-003 Lisboa, Portugal.
Shuji Fujii: Department of Chemistry, Nagaoka University of Technology, Nagaoka 940-2188, Japan; Department of Materials and Interfaces, Weizmann Institute of Science, Rehovot 76100, Israel.
Alejandro García: Departamento de Teoría de la Señal y Comunicaciones, Universidad Carlos III de Madrid, C.\Butarque n° 15, Leganés 28911, Spain.
Braulio García-Cámara: Electronic Technology Department, Carlos III University of Madrid, Butarque 15, E28911, Madrid, Spain.
Maria Helena Godinho: CENIMAT/I3N, Departamento de Ciência dos Materiais, Faculdade de Ciências e Tecnologia, FCT, Universidade Nova de Lisboa, 2829-516 Caparica, Portugal.
Hans Jürgen Grande: Centre for Electrochemical Technologies (CIDETEC), Departamento de Nuevos Materiales, Parque Tecnológico de San Sebastián - Paseo Miramón, 196, San Sebastián E20009, Spain.
Woong-Ki Hong: Jeonju Center, Korea Basic Science Institute, Jeonju, Jeollabuk-do 561-180, Korea.
Yan Ji: Department of Chemistry, Tsinghua University, Beijing 100084, China.
Iam-Choon Khoo: Electrical Engineering Department, Pennsylvania State University, University Park, PA 16802, USA.
Jong Min Kim: Department of Engineering Science, University of Oxford, Oxford OX1 3PJ, UK.
Alexandra Kohlmeier: Department of Chemistry, University of Hull, Hull, HU6 7RX, UK.
Shigeyuki Komura: Department of Chemistry, Tokyo Metropolitan University, Tokyo 192-0397, Japan.
Sabine Laschat: Institut für Organische Chemie, Universität Stuttgart, Pfaffenwaldring 55, Stuttgart D-70569, Germany.
Eunice Sok Ping Leong: Institute of Materials Research and Engineering, 3 Research Link, Singapore 117602, Singapore.
Zhen Li: Department of Chemistry, Tsinghua University, Beijing 100084, China.
Qingkun Liu: Department of Physics, University of Colorado, Boulder, CO 80309, USA.
Yan Jun Liu: Institute of Materials Research and Engineering, 3 Research Link, Singapore 117602, Singapore.
David O. López: Departamento de Física Aplicada II, Facultad de Ciencia y Tecnología, Universidad del País Vasco UPV-EHU, Apartado 644, Bilbao E-48080, Spain; Grup de Propietas Físiques dels Materials (GRPFM), Departament de Física i Enginyeria Nuclear, E.T.S.E.I.B. Universitat Politècnica de Catalunya, Diagonal 647, Barcelona 08028, Spain.

Chun-Yi David Lu: Department of Chemistry, National Taiwan University, Taipei 106, Taiwan.

Georg H. Mehl: Department of Chemistry, University of Hull, Hull, HU6 7RX, UK.

Mayu Miki: Department of Engineering Science, University of Electro-Communications, 1-5-1 Chofugaoka, Chofu, Tokyo 182-8585, Japan.

Ryuichiro Ohira: Department of Engineering Science, University of Electro-Communications, 1-5-1 Chofugaoka, Chofu, Tokyo 182-8585, Japan.

Miguel Ángel Pérez-Jubindo: Departamento de Física Aplicada II, Facultad de Ciencia y Tecnología, Universidad del País Vasco UPV-EHU, Apartado 644, Bilbao E-48080, Spain

Pawel Pieranski: Laboratoire de Physique des Solides, Université Paris-Sud, Bât. 510, Orsay 91405, France.

Joanna Ptasinski: Department of Electrical and Computer Engineering, University of California San Diego, La Jolla, CA 92037, USA; Space and Naval Warfare Systems Center Pacific, San Diego, CA 92152, USA.

Benye Qin: Department of Chemistry, Tsinghua University, Beijing 100084, China.

Miha Ravnik: Faculty of Mathematics and Physics, University of Ljubljana, Jadranska 19, Ljubljana 1000, Slovenia.

Dennys Reis: Instituto de Física, Universidade de São Paulo, Caixa Postal 66318, São Paulo, SP 05314-970, Brazil.

Beatriz Robles-Hernández: Departamento de Física Aplicada II, Facultad de Ciencia y Tecnología, Universidad del País Vasco UPV-EHU, Apartado 644, Bilbao E-48080, Spain; Grup de Propietas Físiques dels Materials (GRPFM), Departament de Física i Enginyeria Nuclear, E.T.S.E.I.B. Universitat Politècnica de Catalunya, Diagonal 647, Barcelona 08028, Spain.

Josep Salud: Grup de Propietas Físiques dels Materials (GRPFM), Departament de Física i Enginyeria Nuclear, E.T.S.E.I.B. Universitat Politècnica de Catalunya, Diagonal 647, Barcelona 08028, Spain.

José Manuel Sánchez-Pena: Departamento de Tecnología Electrónica, Universidad Carlos III de Madrid, C.\Butarque n° 15, Leganés 28911, Spain ; Grupo de Displays y Aplicaciones Fotónicas, Departamento de Tecnología Electrónica, Universidad Carlos III de Madrid, C/Butarque, 15, Leganés E28911, Madrid, Spain.

Aric Sanders: National Institute of Standards and Technology, Boulder, CO 80305, USA.

Nerea Sebastián: Departamento de Física Aplicada II, Facultad de Ciencia y Tecnología, Universidad del País Vasco UPV-EHU, Apartado 644, Bilbao E-48080, Spain.

Christopher P. Schubert: Department of Chemistry, University of Hull, Hull, HU6 7RX, UK.

Daniel Segovia: Departamento de Teoría de la Señal y Comunicaciones, Universidad Carlos III de Madrid, C.\Butarque n° 15, Leganés 28911, Spain.

Guangyuan Si: College of Information Science and Engineering, Northeastern University, Shenyang 110004, Liaoning, China.

Ivan I. Smalyukh: Department of Physics, University of Colorado, Boulder, CO 80309, USA; Department of Electrical, Computer, and Energy Engineering, Materials Science and Engineering Program, and Liquid Crystal Materials Research Center, University of Colorado, Boulder, CO 80309, USA; National Renewable Energy Laboratory, Renewable and Sustainable Energy Institute, University of Colorado, Boulder, CO 80309, USA.
Jung Inn Sohn: Department of Engineering Science, University of Oxford, Oxford OX1 3PJ, UK.
Maria-Gabriela Tamba: Department of Chemistry, University of Hull, Hull, HU6 7RX, UK
Bai Jia Tang: Department of Chemistry, University of Hull, Hull, HU6 7RX, UK
Lei Tao: Department of Chemistry, Tsinghua University, Beijing 100084, China.
Yasuo Tomita: Department of Engineering Science, University of Electro-Communications, 1-5-1 Chofugaoka, Chofu, Tokyo 182-8585, Japan.
Javier Torrecilla: Departamento de Tecnología Electrónica, Universidad Carlos III de Madrid, C.\Butarque n° 15, Leganés 28911, Spain.
Juan C. Torres: Grupo de Displays y Aplicaciones Fotónicas, Departamento de Tecnología Electrónica, Universidad Carlos III de Madrid, C/Butarque, 15, Leganés E28911, Madrid, Spain.
Virginia Urruchi: Departamento de Tecnología Electrónica, Universidad Carlos III de Madrid, C.\Butarque n° 15, Leganés 28911, Spain.
Ricardo Vergaz: Grupo de Displays y Aplicaciones Fotónicas, Departamento de Tecnología Electrónica, Universidad Carlos III de Madrid, C/Butarque, 15, Leganés E28911, Madrid, Spain.
Ana Viñuales: Centre for Electrochemical Technologies (CIDETEC), Departamento de Nuevos Materiales, Parque Tecnológico de San Sebastián - Paseo Miramón, 196, San Sebastián E20009, Spain.
Yen Wei: Department of Chemistry, Tsinghua University, Beijing 100084, China.
Christopher Welch: Department of Chemistry, University of Hull, Hull, HU6 7RX, UK.
Mark E. Welland: Nanoscience Centre, University of Cambridge, Cambridge CB3 0FF, UK.
Tobias Wöhrle: Institut für Organische Chemie, Universität Stuttgart, Pfaffenwaldring 55, Stuttgart D-70569, Germany.
Yang Yang: Department of Chemistry, Tsinghua University, Beijing 100084, China.
Muhammet Yildirim: Department of Chemistry, Arts and Sciences Faculty, Abant Izzet Baysal University, Bolu 14280, Turkey.
Chih Hao Yu: Department of Chemistry, University of Hull, Hull, HU6 7RX, UK.
Xiaoyong Zhang: Department of Chemistry, Tsinghua University, Beijing 100084, China.
Yanhui Zhao: Department of Engineering Science and Mechanics, The Pennsylvania State University, University Park, PA 16802, USA.
Slobodan Žumer: Faculty of Mathematics and Physics, University of Ljubljana, Jadranska 19, Ljubljana 1000, Slovenia; Jozef Stefan Institute, Jamova 34, Ljubljana 1000, Slovenia.

Preface

Liquid crystals are a state of matter which most of the population is aware of through its application in low power, flat panel displays, ranging from simple pocket calculator displays, via their mobile phones and tablets, all the way to the sophisticated screens on lap tops and televisions. Much less so are people aware of the fact that they are surrounded by liquid crystals in the form of washing detergents or cell membranes and the like.

Liquid crystal research is a well established field, which started far more than a century ago, mainly through the synthesis of shape-anisotropic molecules which formed partially ordered states through a process now known as self-assembly. It became a niche topic around the time of the middle of the last century, due to the lack of apparent applications, while solid state and semiconductor devices conquered the world. It was not until the beginning of the 70s, with the invention of the dynamic light scattering and twisted nematic displays, that liquid crystal research boomed.

Today we are looking at a mature field of research, which nevertheless still develops rapidly with the discovery of novel phases, new electro-optic effects, hybrid materials like polymer dispersed and polymer stabilized liquid crystals, or liquid crystal - particle dispersions with added functionality. Liquid crystal research is a field of multidisciplinarity, which brings together physicists, chemists, biologists, and device engineers, experimentalists, theoreticians and computer simulation scientists.

Being anisotropic liquids with elastic properties, liquid crystals fall into the general class of materials known as "soft matter". Two areas of liquid crystal science are broadly distinguished, thermotropic and lyotropic liquid crystals. While the former phases occur simply through a temperature or pressure change, the latter liquid crystal phases appear as a function of concentration of mostly amphiphilic molecules in an isotropic solvent, often water. Both classes of liquid crystals will be covered in this volume.

The present book results from a special issue of the journal "Materials" covering liquid crystals in a broad sense. It is divided into five parts with about four to five peer reviewed contributions each. These can be review papers, which are normally found at the beginning of each part to provide a general introduction. They are followed by a number of original research papers, which are more specific and report recent research results in their category. Part I is related to liquid crystal-nanoparticle dispersions, with a general article about Janus particles by Slobodan Zumer and his group. Part II covers polymer-modified liquid crystals. An introductory review is provided by Ingo Dierking, which is on the subject of polymer-

stabilized ferroelectric liquid crystals. In Part III lyotropic liquid crystals are discussed. Many lyotropic liquid crystals are derived from cellulose, which is reviewed by Maria Helena Godhino, Pedro Lucio Almeida and Joao Luis Figueirinhas. A second review is contributed by Pawel Pieranski on the physics of free-standing lyotropic films. In Part IV the reader is introduced to some aspects of synthesis and characterization, for example discotic liquid crystals, properties of smectic phases and the design of dimers containing gold nanoparticles. At last, applications of liquid crystals are discussed in Part V, especially also non-display applications. Two reviews introduce to the topic: Emerging applications of liquid crystals based on nanotechnology, by Jung Inn Sohn et al. and liquid crystal enabled active plasmonics by Guangyuan Si and co-workers.

As can already be seen from the titles of the various contributions, these are widely covering different aspects of liquid crystal research, and some are in fact interrelated across the Parts organized in this publication. Taken all papers together, we hope that this volume provides an interesting overview of some of the recent research interests of liquid crystals and related materials.

Ingo Dierking
Joao Luis Figueirinhas
Maria Helena Godinho
Guest Editors

Part I: Liquid Crystal—Nanoparticle Dispersions

Janus Nematic Colloids with Designable Valence

Simon Čopar, Miha Ravnik and Slobodan Žumer

Abstract: Generalized Janus nematic colloids based on various morphologies of particle surface patches imposing homeotropic and planar surface anchoring are demonstrated. By using mesoscopic numerical modeling, multiple types of Janus particles are explored, demonstrating a variety of novel complex colloidal structures. We also show binding of Janus particles to a fixed Janus post in the nematic cell, which acts as a seed and a micro-anchor for the colloidal structure. Janus colloidal structures reveal diverse topological defect configurations, which are effectively combinations of surface boojum and bulk defects. Topological analysis is applied to defects, importantly showing that topological charge is not a well determined topological invariant in such patchy nematic Janus colloids. Finally, this work demonstrates colloidal structures with designable valence, which could allow for targeted and valence-conditioned self-assembly at micro- and nano-scale.

Reprinted from *Materials*. Cite as: Čopar, S.; Ravnik, M.; Žumer, S. Janus Nematic Colloids with Designable Valence. *Materials* **2014**, 7, 4272–4281.

1. Introduction

Colloidal dispersions with particles of pre-designed shape, surface, size distribution, or bulk material properties are today one of the prospective routes towards new micro- and nano-functional materials [1,2]. Janus colloids are the type of colloids, where particles have specially designed surfaces, characterized by distinct surface patches of diverse modalities. The classical example of Janus colloids, as proposed by de Gennes [3], are colloidal particles with different chemical makeups on their two hemispheres, for example, one side of the particle being hydrophilic whereas the other hydrophobic. Even such relatively simple Janus colloids exhibit a variety of ordered and disordered structures [4,5]. More generally, Janus particles can be polymeric, inorganic, and polymeric–inorganic, and each kind of Janus particles can be spherical, dumbbell-like, half raspberry-like, cylindrical, disk-like, or any of a variety of other shapes [6,7]. Offering such diverse versatility in the surface functionality, morphology, shape, and chemical composition, the Janus particles indicate a range of possible applications, including as solid surfactants, optical probes for microrheology, self-assembled micro-materials, magnetic and magnetic–fluorescent bifunctional materials, and optical and catalytic materials [6,8].

A new and in many ways unique functionalisation of Janus colloids is achieved by introducing internal orientation—liquid crystalline—order into the Janus dispersions. This can be achieved by either (i) designing macromolecules or particles with internal Janus liquid crystalline order [9,10] or (ii) by dispersing Janus particles into a liquid crystal [11–13]. Under the first approach, the manipulation of the structural fragments of the macromolecules or the topological defects allows for variation of physical properties and thus potential applications, including possibly in the direction of

functional complexity found in living systems. Under the second approach, solid particles with one hemisphere homeotropic (perpendicular) and one hemisphere planar surface anchoring are dispersed in nematic liquid crystals, inducing distortions in the nematic field of Janus-type [11]. These distortions were shown to cause attraction of particle pairs into pairs, with the potential strongly dependent on the relative alignment of the hemispheres. The relative strengths of the anchoring on the two hemispheres was shown to change the stable *orientation* of the Janus particles relative to the far-field nematic director, by affecting the bistability of the two possible orientations of the half-planar-half-homeotropic particles. And finally, by using laser illumination, the Janus particles in nematic were demonstrated to act as rotators when exposed to the laser filed, with the frequency increasing with the increasing intensity of light [12]. Recently, also defect topologies in a nematic liquid crystal near a patchy colloid were explored using isothermal-isobaric Monte Carlo simulations [13].

In this paper, we go beyond the classical two-hemisphere nematic Janus colloids, and demonstrate generalized nematic Janus colloids with multiple and diverse configurations of surface patches with different—*i.e.*, homeotropic and planar—surface anchoring. By using mesoscopic numerical modeling, we explore multiple morphologies of surface patches—*i.e.*, types of Janus particle—and demonstrate a variety of novel complex colloidal structures, based exactly on the multi-valent properties of these designed Janus particles. We show also a combined system of Janus particles and fixed Janus posts (pillars), which act as seeds and micro-anchors for the structures of diverse complexity. The nematic Janus colloidal structures reveal diverse topological defect structures which effectively, prove to be combinations of surface boojum defects and bulk −1/2 disclination lines. Topological analysis is applied to such defects, importantly showing that topological charge is not a well determined topological invariant in such patchy nematic Janus colloids, acquiring various values for same particle type.

2. Results and Discussion

The simplest design of a particle with heterogeneous anchoring separates the particle's surface into two hemispheres with different anchoring conditions, *i.e.*, one homeotropic and one with planar degenerate surface anchoring (see Figure 1a, Type 1). Typically, this type of particle surface morphology is easiest to manufacture and was already reported in liquid crystals [11–13]. To extend this idea further, and really explore the role of surface morphology, we increased the number of distinct patches on the particle surface and used numerical simulations to probe the orientation dependence of particle's interaction with homogeneous nematic field (for more on modeling and theory, see Section (3). In nematics, the elastic interaction is complemented and sometimes superseded by topological interactions, mediated by topological defects—lines and points of undetermined molecular orientation. This makes the interaction not only anisotropic, but creates hysteresis and multiple metastable states. The capability of particles forming "covalent" bonds via entangled defects, explored before for not-Janus homeotropic-anchoring-only particles with great success [14–16], can be exploited for stabilization of designed particle aggregates.

We used two surface types: homeotropic and planar degenerate in our construction of higher-valence particles (Figure 1a). The standard two-hemisphere capped Janus particle in different orientation to the far-field is shown in (Figure 1b). Snapshots of the director profile (in black) and

corresponding defects (in red) are presented for angles 0°, 30°, 60°, and 90° of the symmetry axis with respect to the far-field director. The particle induces a single boojum when aligned along the symmetry axis, but when rotated beyond 60°, obtains a −1/2 defect line arc, tethered to the surface at the line separating the two Janus hemispheres. The free energy varies with rotating the particle, inducing a torque that restores the particle to the equilibrium state. Interestingly, two rotational minima are observed: the global stable minimum at 0° and a metastable minimum at 90° giving bistability of the two possible particle orientations. By changing the planar and homeotropic anchoring strengths and their relative ratio one can control the relative stability or metastability of the two minima.

Figure 1. Janus particle in nematic liquid crystal with diverse morphologies of surface anchoring. (**a**) Janus Particles with various configurations of surface patches (Type 1–4) of homeotropic and degenerate planar surface anchoring; (**b**–**e**) Type 1–4 particles in homogeneously aligned planar nematic cell at various angles with respect to the far-field nematic direction. The red isosurfaces denote regions of decreased nematic order, *i.e.*, boojums, seams between patches, and defect arcs through the bulk; (**f**) Total free energy of various-type Janus particles for different particle orientations shown in (**b**–**e**). Particles of types 1 and 2 align with the symmetry axis parallel to the far-field.

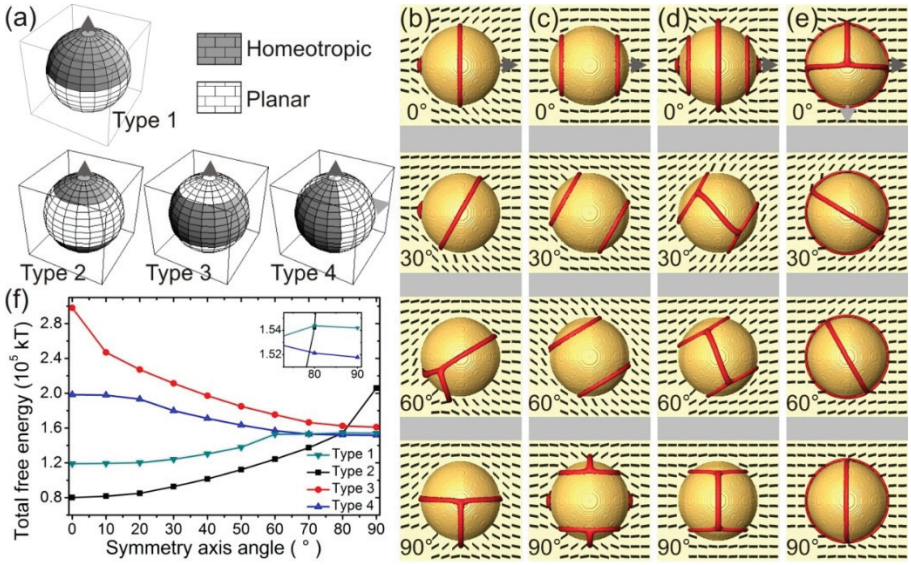

Figure 1c–e shows results for generalized Janus particles with more complex morphologies of the surface patches. Type 2 particles have caps with homeotropic surface anchoring and a waist with degenerate planar anchoring, Type 3 has planar caps and a homeotropic waist, and Type 4 have planar and homeotropic stripes alternating in meridional wedges. When rotating the particles, the defect configurations vary by typically either opening the defect cores or generating −1/2 defect arcs. From the total free energy rotation profiles (Figure 1f) one can see that all three configurations have their free energies in a roughly similar range, but with different equilibrium orientations. The equilibrium particle orientations are sensitive to relative strengths of the homeotropic and planar anchoring which could be used for optimization of desired particle orientations. To generalize the behavior of colloidal particles with patterned surfaces, one can consider them as superpositions of

homeotropic-only and planar-only anchoring particles. Bulk pieces of the director field bordering to proper surface regions of the "single-anchoring particle" are to be glued together to tile in the surface of a patterned particle in order to build the director profile around a given patterned particle.

These generalized Janus nematic colloids show a variety of complex topological defect structures in the nematic, which are typically generalized by considering a topological invariant called topological charge [17,18], or the geometry-aware generalization called the defect rank [19]. The conservation of the topological charge ascribed to the particle generally—in non-Janus nematic colloids—governs the creation of all defects accompanying the particle, such as point defects, Saturn rings and boojums. However, around Janus particles the line defects do not generally form closed loops, as seen in Figure 1 where defect arcs are observed. At the seams between patches of different surface anchoring, the elastic free energy density is typically increased, turning the seams into effective surface defects. Moreover, these defect seams naturally attract point defects, boojums and act as a natural tethering spots for the defect lines or loops which then form defect arcs. As a consequence, the particle itself no longer has a fixed topological charge and in the case of tethering, no topological charge can be assigned at all because the director field has singularities at the tethering points. Such particles have degrees of freedom available to minimize the elastic stress surrounding it, as they are not bound by strict topological constraints. The freedom comes from the choice of interpolation of the director field at the seams. The ambiguity of topological charge in Janus nematic colloids is demonstrated in Figure 2. For instance, the particle with planar caps at the poles, can assume three states with different topological charges (Figure 2). The seams can be thought to carry a quarter winding number in two-dimensional the cross section, as the director makes a quarter of a full turn there. However, this turn can be either clockwise or counter-clockwise (−1/4 or +1/4) and the nematic director surrounding the particle as a whole can be in either of the two configurations. The particle can be in a state with topological charge +1 with surrounding Saturn ring (Figure 2a), a charge-neutral state (Figure 2b) or a state with topological charge −1 with an anti-Saturn ring (Figure 2c). Generally, the charge neutral state will expectedly have lowest free energy, because it minimizes elastic stress and the cost of the defect core, and is therefore most likely to be observed in experiments. The states with +1 and −1 topological charge are either metastable or entirely unstable. If the particle is allowed to rotate, states with defect arcs and ill-defined topological charge are also observed (as in Figure 1d). This mechanism is universal and the more patches a particle has, the less elastic deformation it imparts to its surroundings. In the limit of many patches, the particle can be considered having a "rough" surface with effectively no anchoring. The only thing that remains is the reduced degree of order at the surface, which could give rise to wetting and depletion forces.

Morphology of the surface patches could be related to the "valence" of the particle for forming structures, by imparting a desired symmetry in the arrangement of the patches. Figure 3 demonstrates the stability of a cluster containing a Janus "core" with two homeotropic caps and a planar waist and two homeotropic-only "satellite" particles. The seams of the Janus particle provide tethering points that bind the Saturn rings of the satellite particles to the core if the caps of the Janus particle are facing the satellites (Figure 3b). The particles are confined to a thin homeotropic cell, which prevents them from arranging into a chain along the direction of the field, which is a preferred arrangement in the bulk. However, the orientation with caps toward the satellite particles is unstable. The caps

tend to orient along the uniform bulk director set by the homeotropic cell boundaries (see Figure 3). In our broader testing of different Janus configurations, we discovered this instability is universal, because the homeotropic "pull" of the uniform ambient field overpowers the binding to the satellite particles, except in the configuration of the chain along the uniform field, when these two interactions are parallel.

Figure 2. Ambiguity of topological charge in Janus nematic colloids. A simple composite particle with planar degenerate poles and homeotropic equator can select from three director configurations at the seams, causing the resulting defect charge (rank, [19]) to be either (**a**) +1; (**b**) 0; or (**c**) −1. The ±1 structures require a defect ring defect which is energetically unfavorable and makes these structures metastable or unstable relative to the 0 charge structure. The seams between the patches can be considered as surface defect lines with a quarter winding number.

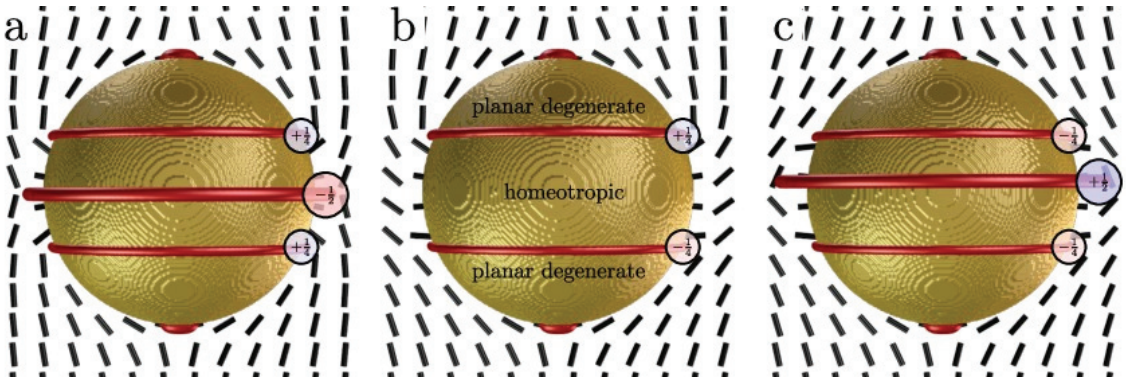

The orientation instability becomes irrelevant if a Janus particle is replaced with a fixed vertical Janus post which then serves as a micro-anchor for the colloidal structure. Indeed, recent experiments with microfabricated arrays of microposts provide a promising starting ground for physical realization of such Janus posts [20]. We simulated a "Janus" micropost with four patches of alternating homeotropic and planar degenerate anchoring (Figure 4). Just like with the spherical Janus particle, we observe strong preference of the satellite particles to bind to the homeotropic patches on the post's surface, and because the post cannot tilt, we obtain a stable state. The particle binds strongly to the middle of the homeotropic patch with a partial Saturn-ring arc, tethered to the seams between homeotropic and planar patches, while its free energy is the highest in the vicinity of the planar denegerate patch. The free energy profile (Figure 4b) reveals a torque that forces the particle into the stable configuration. Both the seams between the planar and homeotropic anchoring and the corner between the post and the cell walls are a high free-energy regions that traps defects. We observe a hysteresis effect when rotating the particle around the post: the tethered disclination line latches on to the lower or upper corner, creating a high-energy metastable state that can decay via thermal fluctuations or minute vertical movement of the particle, which we ignored in our simulations (Figure 4a).

Figure 3. Designing colloidal superstructures with Janus particles. The bivalent Janus particle binds two non-Janus homeotropic particles by tethering their Saturn ring defects to the seams around the caps. The Janus particle in the desired orientation with the symmetry axis in the *x* direction is stable under rotations around the vertical (*z*) axis, but unstable under rotations about the horizontal axis (*y*). Its lowest energy state aligns the caps with the external director along the *z* axis (**b**). The stable configuration of the superstructure is shown in (**a**, bottom right).

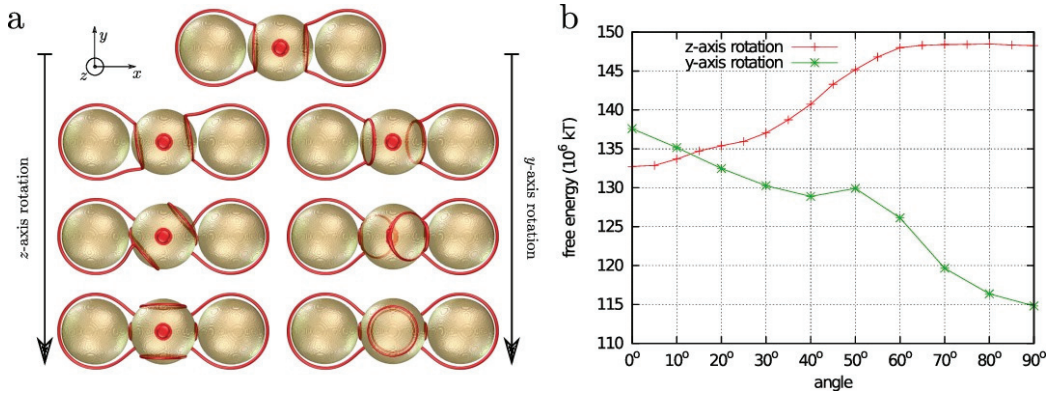

Figure 4. A homeotropic non-Janus particle bound to a Janus post within a nematic cell. The Janus post is segmented into 4 alternating patches of homeotropic (shaded) and planar degenerate anchoring. (**a**) We observe two bound states (one stable, one metastable) when the particle is centred next to the homeotropic patch. The metastable state (upper panel) has the defect line tethered to the bottom corner of the post, whereas in the stable state the defect line tethers to the Janus seams of the post; (**b**) Free energy study of the particle binding shows that the maximum or minimum of the free energy are found when the particle is positioned exactly symmetrically at the homeotropic or planar patch, respectively.

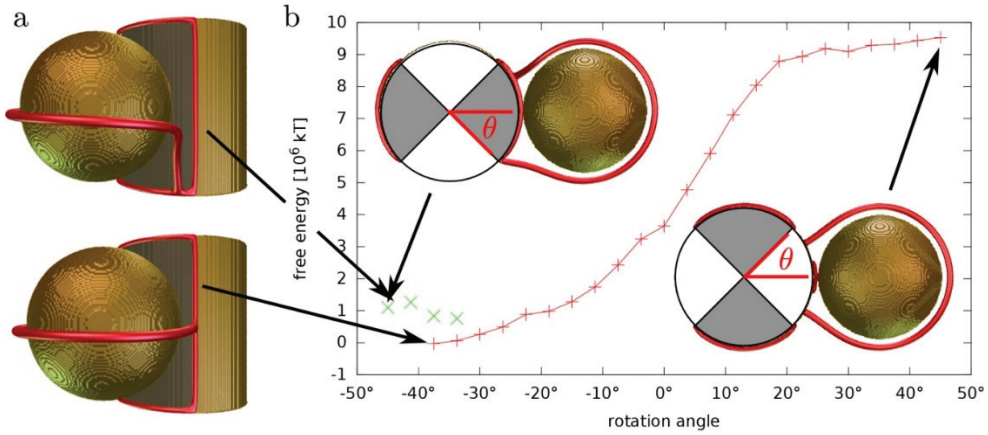

3. Perspectives for Future Studies

Because the shape and stability of the disclinations are topologically protected, the choice of particle size, confinement, liquid crystal elastic anisotropy and strength of surface anchoring has little effect on the qualitative behavior of the Janus nematic coolids, but does affect the free energy

landscape and thus interaction strength and kinetics of assembly. We explored this extensive phase (material) space only in a very narrow region; therefore, one could improve and fine-tune the desired phenomena. The conformation in the stable state depends more strongly on the surface morphology, relative distribution and size of the Janus patches. Further studies could reveal other interesting and potentially useful states with diminished symmetry and possibly a randomized lattice. For example, using particle types with three caps could prevent formation of straight homogeneous chains by breaking the symmetry. Larger clusters of such particles could still form complex structures of lower symmetry even if highly symmetric valence states were unstable. Such frustration and symmetry breaking could potentially lead to glassy states or quasi-crystals, which were already observed with colloidal platelets [21]. The proposed mixing of Janus particles with different surface patterns opens a combinatorial variety of possibilities for particle arrangement.

Using a fixed Janus post in the homeotropic cell (far field director is along z direction) to trap and bind particles via horizontal disclination arcs which we propose here, could be used on one hand as a structural seed and on the other hand as a micro-anchor for the colloidal aggregation. The surface pattern can be engineered to set the valence that promotes desired lattice geometry. A fixed lattice could provide a long-range order, while the satellite particles are still movable to provide switching. Alternatively, free-floating cylinders, confined to prevent turning, could provide translational freedom to build lattices, but without instability to rotation around a horizontal axis, providing the best of both worlds.

4. Modeling and Theory Section

Numerical modeling based on minimization of the phenomenological Landau-de Gennes free energy was uses as the central approach for modeling the described Janus nematic colloids. This approach was in recent years demonstrated to give qualitative and quantitative results when compared to experiments and in details described in the reference [22]. The approach is based on the free energy functional written in terms of the nematic order parameter tensor (Q-tensor), approximated on a discrete finite difference mesh. The free energy is minimized by using a quasi-time-step relaxation scheme that mimics real orientational dynamics in the absence of material flow. For homeotropic surface patches, the Rapini-Papoular type uniform surface anchoring free energy is assumed, whereas for degenerate planar anchoring patches the surface energy formulated by Fournier and Galatola [23] is used. In order to model the Janus particles with various surface morphologies surface patterned particles, logical conditions are set to discriminate between planar and homeotropic surface regions. Despite their spherical shape, beads with patterned surfaces are anisotropic with the anisotropy arising from the patterning. Their orientation with respect to the undisturbed (far-field) director is in general characterized by two angles or by just one if the surface patterning is rotationally symmetric.

In the simulations, the following material parameters, $A = -1.72 \times 10^6$ J/m^3, $B = -2.12 \times 10^6$ J/m^3, $C = 1.73 \times 10^6$ J/m^3, $L = 40$ pN, characteristic for a typical (5CB) nematic liquid crystal described in the single-elastic constant approximation were used in the free energy of the form described in [22]. The surface anchoring strengths on both homeotropic and planar degenerate parts characterized by $W = 10^{-2}$ J/m^2 are in the limit of strong anchoring. The chosen value has been used in simulations of liquid crystal colloids before, with excellent agreement with experiments [14]. The particle diameters

are 1 μm in Figures 1–3 and 0.9 μm in Figure 4. The choice of parameters ensure the regime of the disclination loops that are stable against a collapse into point defects and the strong anchoring that keeps the disclinations away from the surface. Variations of particle size, anisotropy of elastic constants, and anchoring strength have only a minor effect on the general behavior of defects and interactions of the Janus particles, as long as the parameters allow for the realization of the same regime.

5. Conclusions

To conclude, the generalized Janus nematic colloids could be used as a novel route towards particle functionalized structures in nematic liquid crystal colloids. By designing the morphology or surface patches with homeotropic or planar surface anchoring, the elastic distortion of the nematic orientation field and inter-particle interaction potentials can be varied and engineered to high-complexity and spatial anisotropy. As a possible platform for valence-determined assembly of colloidal structures, a colloidal superstructure is shown, where two non-Janus particles bind to the bivalent Janus colloidal particle, by pinning their (Saturn-ring) defect loops to the tethering spots generated at the contact lines between the surface patches at the Janus particle. The capacity to control the valence and stability of free-floating spherical particles is hindered by a multitude of topological states. We avoid this problem by suggesting binding of colloidal particles to a fixed Janus post in a nematic cell, which forms a micro-seed and micro-anchor for the colloidal particles in such hybrid confined structures.

The nematic profiles of multi-valent Janus colloids are shown to be dominated by the emergence of topological defects, which are effective combinations of surface boojums, possibly spread into lines of reduced order, and bulk segments of +1/2 or −1/2 defect line, which typically form defect arcs. The topological analysis also demonstrated the ambiguity of the topological charge as a topological invariant in Janus nematic colloids, as it can acquire multiple values for one given particle type.

Finally, the basic motivation for this research originates in assembling novel functional micro- and sub-micro-materials with unusual and possibly unique properties that could be used in a range of fields, from complex optics, photonics, metamaterials, to plasmonics and biotechnology.

Acknowledgments

We acknowledge funding from the Slovenian Research Agency: Grant No. Z1-5441 and Programme P1-0099. Miha Ravnik acknowledges support from EU FP7 Marie Curie Integration Grant FREEFLUID Channel-free liquid crystal microfluidics.

Author Contributions

Simon Čopar and Miha Ravnik performed the numerical modeling and analyzed the results. Simon Čopar developed the topological description. Slobodan Žumer supervised the research. All authors co-wrote the manuscript.

Conflicts of Interest

The authors declare no conflict of interest.

References

1. Wensink, H.H.; Löwen, H.; Marechal, M.; Härtel, A.; Wittkowski, R.; Zimmermann, U.; Kaiser, A.; Menzel, A.M. Differently shaped hard body colloids in confinement: From passive to active particles. *Eur. Phys. J.* **2013**, *222*, 3023–3037.
2. Yi, G.-R.; Pine, D.J.; Sacanna, S. Recent progress on patchy colloids and their self-assembly. *J. Phys. Condens. Matter* **2013**, *25*, doi:10.1088/0953-8984/25/19/193101.
3. De Gennes, P.G. Soft matter. *Rev. Mod. Phys.* **1992**, *64*, 645–648.
4. Vissers, T.; Preisler, Z.; Smallenburg, F.; Dijkstra, M.; Sciortino, F. Predicting crystals of Janus colloids. *J. Chem. Phys.* **2013**, *138*, doi:10.1063/1.4801438.
5. Iwashita, Y.; Kimura, Y. Stable cluster phase of Janus particles in two dimensions. *Soft Matter* **2013**, *9*, 10694–10698.
6. Hu, J.; Zhou, S.; Sun, Y.; Fanga, X.; Wu, L. Fabrication, properties and applications of Janus particles. *Chem. Soc. Rev.* **2012**, *41*, 4356–4378.
7. Percec, V.; Wilson, D.A.; Leowanawat, P.; Wilson, C.J.; Hughes, A.D.; Kaucher, M.S.; Hammer, D.A.; Levine, D.H.; Kim, A.J.; Bates, F.S.; *et al*. Self-assembly of Janus dendrimers into uniform dendrimersomes and other complex architectures. *Science* **2010**, *328*, 1009–1014.
8. Jiang, S.; Chen, Q.; Tripathy, M.; Luijten, E.; Schweizer, K.S.; Granick, S. Janus particle synthesis and assembly. *Adv. Mater.* **2010**, *22*, 1060–1071.
9. Saez, I.M.; Goodby, J.W. "Janus" supermolecular liquid crystals—giant molecules with hemispherical architectures. *Chem. Eur. J.* **2003**, *9*, 4869–4877.
10. Mondiot, F.; Wang, X.; de Pablo, J.J.; Abbott, N.L. Liquid crystal-based emulsions for synthesis of spherical and non-spherical particles with chemical patches. *J. Am. Chem. Soc.* **2013**, *135*, 9972–9975.
11. Conradi, M.; Ravnik, M.; Bele, M.; Zorko, M.; Žumer, S.; Muševič, I. Janus nematic colloids. *Soft Matter* **2009**, *5*, 3905–3912.
12. Conradi, M.; Zorko, M.; Muševič, I. Janus nematic colloids driven by light. *Opt. Exp.* **2010**, *18*, 500–506.
13. Melle, M.; Schlotthauer, S.; Mazza, M.G.; Klapp, S.H.L.; Schoen, M. Defect topologies in a nematic liquid crystal near a patchy colloid. *J. Chem. Phys.* **2012**, *136*, doi:10.1063/1.4717619.
14. Ravnik, M.; Škarabot, M.; Žumer, S.; Tkalec, U.; Poberaj, I.; Babič, D.; Osterman, N.; Muševič, I. Entangled nematic colloidal dimers and wires. *Phys. Rev. Lett.* **2007**, *99*, doi:10.1103/PhysRevLett.99.247801.
15. Tkalec, U.; Ravnik, M.; Čopar, S.; Žumer, S.; Muševič, I. Two-dimensional nematic colloidal crystals self-assembled by topological defects. *Science* **2011**, *333*, 62–65.
16. Tkalec, U.; Muševič, I. Interaction of micro-rods in a thin layer of a nematic liquid crystal. *Soft Matter* **2013**, *9*, 8140–8150.
17. Mermin, N.D. The topological theory of defects in ordered media. *Rev. Mod. Phys.* **1979**, *51*, 591–648.

18. Alexander, G.P.; Chen, B.G.; Matsumoto, E.A.; Kamien, R.D. Disclination loops, point defects, and all that in nematic liquid crystals. *Rev. Mod. Phys.* **2012**, *84*, 497–514.
19. Čopar, S.; Žumer, S. Topological and geometric decomposition of nematic textures. *Phys. Rev. E* **2012**, *85*, doi:10.1103/PhysRevE.85.031701.
20. Cavallaro, M.; Gharbi, M.A.; Beller, D.A.; Čopar, S.; Shi, Z.; Baumgart, T.; Yang, S.; Kamien, R.D.; Stebe, K.J. Exploiting imperfections in the bulk to direct assembly of surface colloids. *Proc. Nat. Acad. Sci. USA* **2013**, *110*, 18804–18808.
21. Dontabhaktuni, J.; Ravnik, M.; Žumer, S. Quasicrystalline tilings with nematic colloidal platelets. *Proc. Nat. Acad. Sci. USA* **2014**, *111*, 2464–2469.
22. Ravnik, M.; Žumer, S. Landau-de Gennes modeling of nematic liquid crystal colloids. *Liq. Cryst.* **2009**, *36*, 1201–1214.
23. Fournier, J.B.; Galatola, P. Modeling planar degenerate wetting and anchoring in nematic liquid crystals. *Europhys. Lett.* **2005**, *72*, 403–409.

Preparation of Nanocomposite Plasmonic Films Made from Cellulose Nanocrystals or Mesoporous Silica Decorated with Unidirectionally Aligned Gold Nanorods

Michael G. Campbell, Qingkun Liu, Aric Sanders, Julian S. Evans and Ivan I. Smalyukh

Abstract: Using liquid crystalline self-assembly of cellulose nanocrystals, we achieve long-range alignment of anisotropic metal nanoparticles in colloidal nanocrystal dispersions that are then used to deposit thin structured films with ordering features highly dependent on the deposition method. These hybrid films are comprised of gold nanorods unidirectionally aligned in a matrix that can be made of ordered cellulose nanocrystals or silica nanostructures obtained by using cellulose-based nanostructures as a replica. The ensuing long-range alignment of gold nanorods in both cellulose-based and nanoporous silica films results in a polarization-sensitive surface plasmon resonance. The demonstrated device-scale bulk nanoparticle alignment may enable engineering of new material properties arising from combining the orientational ordering of host nanostructures and properties of the anisotropic plasmonic metal nanoparticles. Our approach may also allow for scalable fabrication of plasmonic polarizers and nanoporous silica structures with orientationally ordered anisotropic plasmonic nanoinclusions.

Reprinted from *Materials*. Cite as: Campbell, M.G.; Liu, Q.; Sanders, A.; Evans, J.S.; Smalyukh, I.I. Preparation of Nanocomposite Plasmonic Films Made from Cellulose Nanocrystals or Mesoporous Silica Decorated with Unidirectionally Aligned Gold Nanorods. *Materials* **2014**, 7, 3021–3033.

1. Introduction

Nanostructured materials are poised to revolutionize scientific instruments, technologies, and consumer devices. Liquid crystalline intermediate phases confer long-range orientational order that has been previously used to improve the properties of fibers and deposited films for biomedical [1], optical [2], and electronic [3,4] applications. Liquid crystals (LCs) can act as smart hosts that align anisotropic nanoparticle inclusions and leverage nanoscale anisotropy into device scale polarization sensitivity [5]. Self-assembly of plasmonic nanoparticles in LCs has been extensively studied recently [6–8]. Gold nanorods (GNRs) have two surface plasmon resonance (SPR) modes, the transverse mode at 525 nm and red-shifted longitudinal mode dependent on the aspect ratio, associated with short and long axes of the rod, respectively [9]. Aligning GNRs allows one to produce so-called "plasmonic polarizers", which have been previously realized in stretched polyvinyl alcohol films [10] and magnetically tunable LC systems [11]. Here we report the first plasmonic polarizers in a cellulose-based LCs derived from natural materials and in a silica system that potentially confers greater device stability than its organic alternatives.

Scalability of nanofabrication is an important consideration for massive industrial production of solar energy photo-conversion and optical devices. Gold nanoparticles can be produced through numerous scalable syntheses [12] and are currently widely commercially available. Cellulose, the most abundant biopolymer on earth, is naturally found in wood and cotton as a blend of amorphous regions and rod-like crystallites with diameters of ~3–10 nm and lengths of 100–300 nm [13]. Facile

sulfuric acid hydrolysis dissolves the amorphous regions leaving a charge stabilized colloidal suspension of rod-like crystallites that act as the building blocks of LC phases. Cellulose nanocrystals (CNCs) and mesoporous silica have been utilized as templates to assemble and synthesize nanoparticles [14–16], but the alignment of rod-like nanoparticles in these hosts has not been achieved. In this work, we first use these colloidal dispersions of CNCs to align co-dispersed GNRs of much shorter aspect ratio, with a longitudinal SPR peak within the visible optical spectrum, and then use the ensuing cellulose-gold colloidal nano-dispersion to obtain thin solid films with orientationally ordered organization of both cellulose and gold nano-colloids. Furthermore, we demonstrate that these structured films can be converted into mesoporous silica films decorated with aligned GNRs. Because of the combination of ordered plasmonic nanostructures, relatively large surface areas, and easy surface functionalization, the new composite mesoporous silica films may potentially offer many applications in optics, nanophotonics, biodetection, *etc*.

2. Results and Discussion

2.1. Cellulose Films with Aligned GNRs

The quality of alignment in films thicker than the size of nanorods is commonly characterized by the three-dimensional (3D) orientational scalar order parameter:

$$S = \frac{\langle 3\cos^2\theta - 1\rangle}{2} \tag{1}$$

where θ is the angle between the long axes of rods and the director **n** (describing local average orientation of these constituent rods). In our system, S is equal to the scalar order parameter corresponding to the longitudinal transition dipole moment. Therefore, the order parameter of GNRs can be deduced from the polarized optical transmission data by first determining the absorbance $A^{\parallel}$ and $A^{\perp}$ at the longitudinal SPR peak for polarizer orientations parallel and perpendicular to **n**, respectively and then using the expression

$$S = \frac{A^{\parallel} - A^{\perp}}{A^{\parallel} + 2A^{\perp}} \tag{2}$$

We found that the simple by-hand shearing of CNC-GNR co-dispersions produced films of variable quality with some relatively large areas of uniform alignment (Figure 1a,b) with the GNRs having scalar order parameter $S = 0.49$, as determined from the optical extinction data (Figure 1c,d). This is comparable to the order parameter of ~0.35–0.65 for shear-oriented pure CNCs [17]. Previous studies, which optimized the mechanical shearing conditions, reported achieving films of highly aligned CNCs [18]. Therefore, one can expect that by controlling the shearing speed and concentration, it may be possible to reproducibly create even more highly aligned thin films with GNRs. If the shearing method is further optimized, it could potentially allow for large-scale production of uniform thin films composed of CNCs and GNRs on various thin substrates.

Figure 1. Cellulose films decorated with Gold nanorods (GNRs) produced by use of shear alignment of Cellulose nanocrystal (CNC)-GNR co-dispersions. (**a**,**b**) Bright field polarized microscopy images with analyzer aligned perpendicular (**a**) and parallel (**b**) to the director **n** show that nanorods are generally aligned along **n**, with absorption due to the transverse and longitudinal SPRs yielding pink and blue colors, respectively. (**c**,**d**) The extinction spectra of a thin dried film of CNCs and GNRs for linear polarizations perpendicular (**c**) and parallel (**d**) to **n**, confirming that the transverse and longitudinal SPRs with peaks at 525 nm and 680 nm, respectively, are significantly stronger in the perpendicular and parallel orientations, respectively.

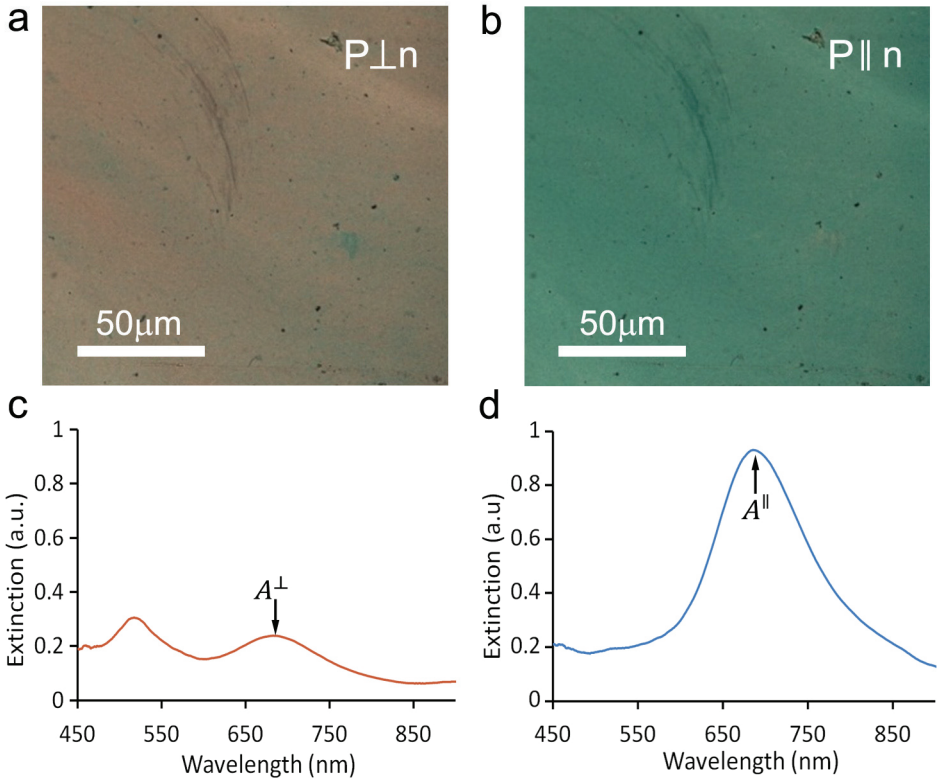

However, we also find that the gravity-assisted alignment method could consistently produce higher quality aligned films without the need for any mechanization. This alignment is accomplished with a CNC-GNR liquid crystalline co-dispersion droplet stretched along the flow direction, becoming roughly semi-cylindrically-shaped with the contact lines parallel to the gravity-induced flow direction and the droplet's thickness gradient perpendicular to it. Due to evaporation, the concentration of CNCs within a droplet is the highest along the edges, which causes a LC phase to first emerge at the boundary [19]. In the process of gravity-assisted alignment, there are flow forces, which tend to align **n** along the direction of flow [18], and LC elastic forces, which tend to align the liquid crystalline dispersion at the edges with **n** parallel to the contact line and orthogonal to the thickness gradient in the meniscus to avoid elastic-energy-costly director distortions [20]. Thus, in such an experimental deposition geometry, these two forces act in the same direction and augment each other in producing the desired unidirectional alignment of the LC. Consequently, the films tended to have the most uniform alignment parallel to both the contact line and the direction of flow, with the alignment quality being the best near the edges where both forces were present. Slow water

evaporation retains this alignment relatively intact while producing orientationally-ordered solid films of CNCs. Bright field polarizing optical microscopy (POM) images shows that GNRs are generally aligned along **n** (Figure 2a,b). The dried films possess two well-defined extinction peaks, which were maximized when the incident light has linear polarization parallel or perpendicular to the uniformly aligned director **n**. The observed peaks in the obtained spectra correspond to longitudinal and transverse SPR effect, respectively, indicating a high degree of orientational ordering of plasmonic GNRs in the matrix of an aligned CNC-based thin film. Two-photon luminescence (TPL) images with the polarization parallel (Figure 2e) and perpendicular (Figure 2f) to **n** indicate that the GNRs are well aligned along the LC director of the CNC matrix. A cross sectional TPL image (Figure 2g) shows that this signal is strong over a vertical distance of ~2 μm, which indicates that the thickness of the film is on the order of 1 μm, since the vertical resolution is ~500 nm. The typical extinction spectra for a film with a 3D orientational order parameter of $S = 0.67$ are shown in Figure 2h, in which the longitudinal SPR wavelength (680 nm) is the same as that of GNRs in CNCs by shearing alignment. The scalar order parameter varied somewhat, depending on exact details of the thin film preparation, but was typically found to be as high as $S = 0.67$.

Figure 2. Aligned CNC films with aligned GNRs obtained by the gravity-assisted method. (**a**,**b**) Bright-field polarizing optical microscopy (POM) images with polarizations parallel (**a**), and perpendicular (**b**), to the director **n** show different colors associated with the two SPRs, respectively. POM images of a film between crossed polarizers (**c**) and with an inserted 530 nm retardation plate (**d**) with one polarizer parallel to **n**, allowing us to visualize imperfections in the alignment. (**e**,**f**) Two-photon luminescence (TPL) micrographs for polarization parallel (**e**) and perpendicular (**f**) to **n** demonstrate that GNRs are well dispersed within the film (no big aggregates observed within the uniform background due to the TPL signal from nanorods) align along **n**, with a stronger signal seen in (**e**). (**g**) The corresponding vertical cross-section for linear polarization of excitation light parallel to **n**. (**h**) Extinction spectra measured for polarization parallel and perpendicular to **n**.

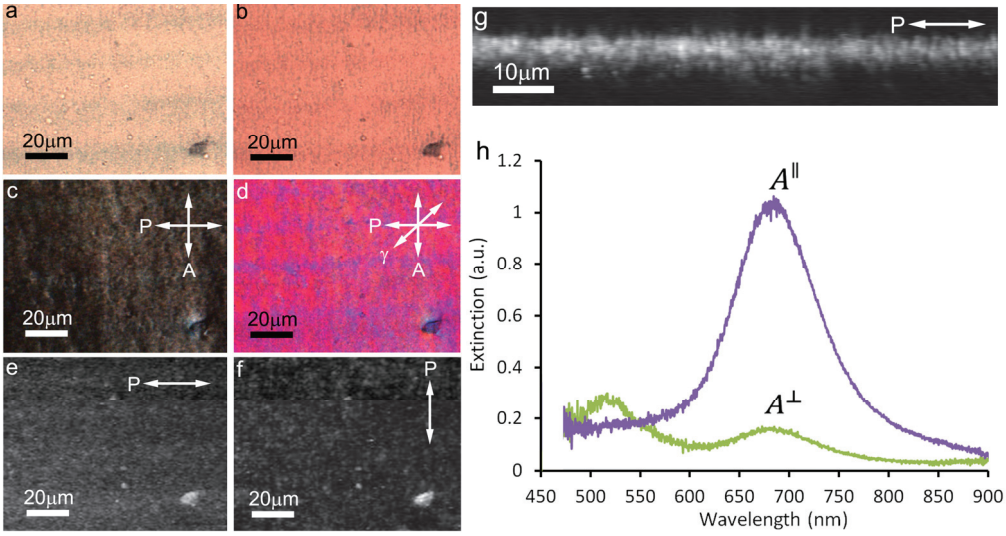

To elucidate the nanoscale morphology of films, we used a combination of focused ion beam (FIB) milling and scanning electron microscopy (SEM) to probe the structural organization of CNCs and GNRs within the thin films. The images using the in-lens (IL) detector allow us to reveal the alignment of the CNCs (Figure 3a) while the energy selective in-lens backscattered detector (ESB) image emphasize the GNRs, which are aligned with the cellulose LC director field (Figure 3b). The interior structure of the film was revealed in an extended region where the conductive coating had collapsed due to nearby FIB milling. The interior structure of the CNC film can be understood as a nanoporous network-like arrangement with GNRs distributed throughout the bulk while exhibiting no positional but long-range nematic-like orientational ordering (Figure 3c,d). Furthermore, we used FIB to remove the top layer from a cross-sectional area to determine the thickness of the films, which was determined to be approximately 300–500 nm (Figure 3e). In the studied thin films, the unidirectional alignment could be seen extending over large distances over which the nanorods were uniformly dispersed (Figure 3f) and unidirectionally aligned (inset of Figure 3f).

Figure 3. SEM imaging of thin films of CNCs with embedded GNRs (with a thin carbon coat to improve conductivity). (**a,b**) Co-located images obtained with (**a**) in-lens (IL), and (**b**) energy selective in-lens backscattered detector (ESB), detectors at 5 kV, allowing for simultaneous visualization of the unaligned CNC orientation field and the orientation of GNRs embedded in the film. (**c**) Everhart-Thornley (ET) imaging at low resolution and (**d**) IL imaging at high resolution reveal an interior network-like structure of the film at the site of a carbon film collapse induced by focused ion beam (FIB) in a nearby region. FIB allows for visualization of the cross-section of the film. ET imaging at 5 kV. (**e**) Tilt corrected for the 54° angle of the FIB milling, shows that the GNRs are distributed inside the bulk of the ~300 nm thick GNR film. The underlying glass substrate is visible in the bottom of the panel. (**f**) Low resolution ET imaging at 500 V demonstrates the long-range order of the film (no carbon layer is present). The inset shows the local orientation of GNRs.

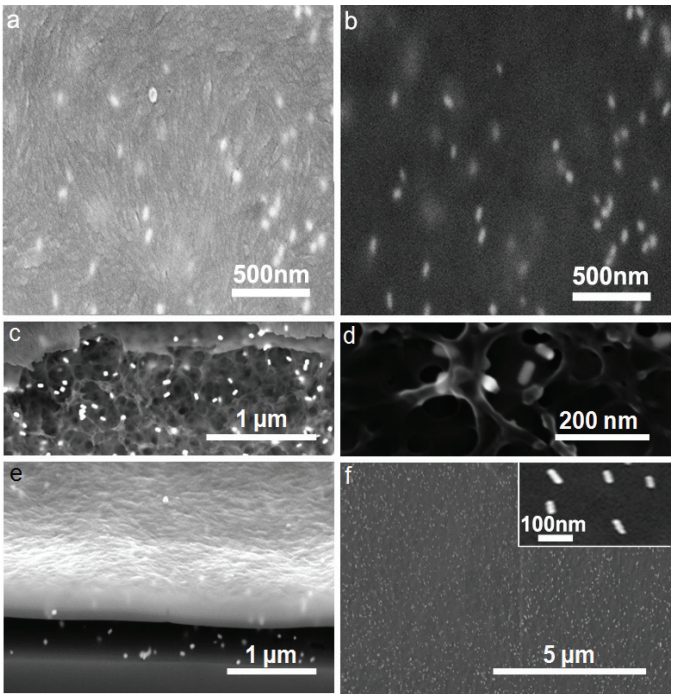

2.2. Free-Standing Mesoporous Silica Films with Aligned GNRs

We also created thin free-standing films which consisted of only silica and GNRs by using a method previously reported in the literature [21], with certain modifications described below in the methods section. To obtain nematic-like ordering within the film we placed a drop of the solution on aluminum foil, where at the meniscus, the CNC LC experiences elastic forces which align it parallel to the receding contact line (in order to minimize elastic distortions and their free energy cost) [20]. Once the CNC-GNR films with nematic-like ordering were used as a replica for patterning nanoscale morphology of silica films, as described in the materials section, we found that the orientational ordering of GNRs persisted in the silica matrix upon removal of CNCs via the high-temperature treatment (Figure 4). Previous work [22] has shown that PVP capped GNRs are not stable at high temperatures and will transform into spheres in less than an hour at a temperature of 250 °C. However, we found that by using silica capped rods, the resultant films still possessed a well defined polarization-dependent SPR effect, indicating that silica capped GNRs maintained their rod-like structure. Using low-voltage SEM, we observed that the films had a mesoporous structure, which was consistent with what was previously observed for such films without GNRs [21]. GNRs tended to be evenly dispersed throughout the film, with a lower degree of alignment than in the cellulose films. The estimated scalar order parameter of GNRs that we could achieve by polarization-dependent extinction spectra in this case was $S = 0.25$. The reduced value of the orientational order parameter may be partially due to the high-temperature treatment known to affect gold nanoparticles [22]. The longitudinal plasmonic peak shifted from 680 nm (Figure 1d, 2h) to 630 nm (Figure 3c) due to a combination of two effects, the nanorods being deformed by heating and the silica having different dielectric properties than the cellulose. However, it is interesting that the alignment persisted upon removal of CNCs, providing a potentially useful approach for scalable fabrication of composite mesostructured films with orientationally ordered plasmonic nanoparticles in a silica matrix. These obtained hybrid thin films can be practically useful. The mesoporous silica surface, which encloses the GNRs, can be functionalized with various chemicals, and the unique absorption properties of the film could be used to study chemical reactions, or to create a catalyst for chemical reactions. The presence of orientationally-ordered plasmonic nanostructures in such films may provide the means of efficient use of light for controlling and guiding reactions and processes in various applications.

Figure 4. Mesoporous silica films containing aligned GNRs. (**a**,**b**) Bright field polarizing microscopy images with the polarization parallel (**a**) and perpendicular (**b**) to the director. (**c**) Absorption spectra of the film as measured with polarization parallel (red) and perpendicular (blue) to the director. (**d**,**e**) TPL images of GNRs taken with polarization parallel (**d**) and perpendicular (**e**) to the director, confirming alignment of the gold nanoparticles with their long axes on-average parallel to the director. The homogeneous TPL signal in the images confirms uniform distribution of GNRs. (**f**,**g**) SEM images of the mesoporous film showing (**f**) alignment of GNRs and (**g**) the porous morphology. To minimize charging, images (**f**) and (**g**) were acquired using ET at 1 kV and 2 kV primary beam acceleration voltage, respectively.

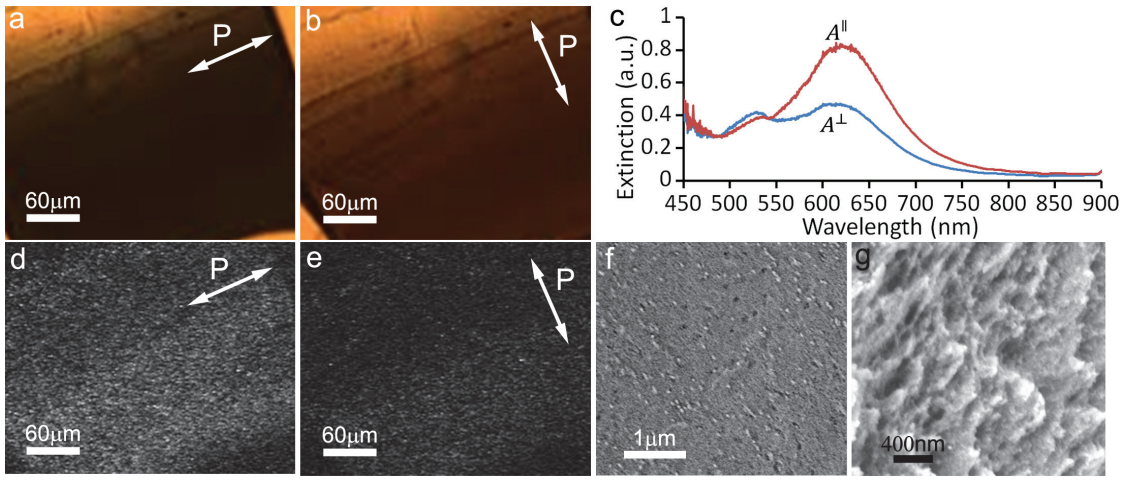

2.3. Discussion

Unlike their dichroic dye based counterparts, plasmonic polarizers allow for very precise control over the operational spectrum of a polarizer as well as the ability to polarize light of different wavelengths, including the ultraviolet and infrared parts of an optical spectrum [23]. The transverse plasmonic absorption is generally a function of the material used for the rod-like nanoparticles, with nickel having an absorption peak at 380 nm, silver absorbing at 420 nm, gold at 525 nm and copper at ~580 nm [23]. The longitudinal SPR is red shifted by an amount determined by the aspect ratio of the nanoparticle. Thus, a plasmonic polarizer potentially offers precise control of both the transverse and longitudinal device scale absorption across the electromagnetic spectrum, ranging from the ultraviolet through the visible and into the infrared [23]. Although plasmonic polarizers can be achieved by a number of different methods, such as stretching of polymer films with incorporated anisotropic plasmonic nanoparticles, our approach offers benefits of utilizing abundant cellulose-based nanomaterials and scalable self-assembly-based fabrication. The deposition of structured films from co-dispersions of anisotropic nanoparticles demonstrated with the example of metal nanorods and CNCs can be potentially extended to a variety of other technologically interesting nanoparticles, such as semiconductor-based quantum rods and discs as well as upconversion nanoparticles. Thus, a broad range of hybrid materials with different functionality can be potentially obtained using this approach.

Mesoporous silica films decorated with GNRs provide a more permanent structure that can potentially be incorporated into optical glasses. Furthermore, the mesoporous structure of these films allows for infiltration of solutions so that one can potentially use them in different forms of chemical and biological detection, exploring how exciting either the longitudinal or transverse plasmonic mode of a nanoparticle changes the catalytic activity. The pore size can be somewhat tunable by changing the source material of the cellulose, depending on the need of particular applications.

3. Experimental Section

3.1. Synthesis of Cellulose Nanocrystals

CNCs were synthesized using a known acid hydrolysis method [13,21]. Ten grams of bleached cotton was hydrolyzed in 150 mL of 65 wt.% sulfuric acid under continuous stirring in a 45 °C water bath. Every hour the mixture was sonicated for 5 min and a small amount of the solution was extracted and observed using POM to determine if the hydrolysis was complete. About 700 mL of *deionized (DI)* water was added to the completed reaction to quench the acid hydrolysis. Within a 24 hour period of time, the more concentrated dispersion of CNCs sedimented to a bottom layer, which constituted about 1/3 of the total volume, and the supernatant was removed. The cellulose was washed several times via redispersing in DI water, centrifugation, and removing the supernatant, which resulted in an increase of the pH to ~1. To further reduce the sulfuric acid content, the solution was placed inside of a dialysis tube (MWCO 12000–14000, Thermo Fisher Scientific Inc.) and dialyzed against DI water. The DI water was occasionally replaced, and the dialysis continued until the DI water maintained a constant pH, which normally took 2–3 days. After this, suspensions were filtered through Millipore filter with 3 μm holes. At this stage, the concentration of CNCs was normally 2–3 wt.% and was used in our experiments as described below.

3.2. Functionalization of GNRs

Cetyltrimethylammonium bromide capped GNRs with mean diameters and lengths of 20 nm and 50 nm respectively were synthesized in aqueous solution using a well-known method [24]. In order to protect against the acidic environment of the cellulose solution, the rods were recapped with methoxypolyethyleneglycol thiol (mPEG-SH, JemKem Technology) by a method described in [25]. Briefly, 300 μL of aqueous GNRs with optical density of ~100 and 300 μL of an aqueous 10 wt.% mPEG-SH solution were added to 10 mL of water. The solution was left at room temperature for 12 h to ensure that the mPEG-SH had bonded to the surface of GNRs. The solution was centrifuged for 10 min at 10,000 rpm, and the supernatant was decanted. After this, the GNRs solution was re-dispersed using sonication. The capping procedure was repeated to ensure a complete coating of mPEG on the nanorods.

To incorporate the nanorods in mesoporous silica films using approaches that we will discuss below, the mPEG-capped GNRs were recapped with silica as described in [26]; 26 μL ammonium hydroxide (27% NH_3 by weight) in 400 μL of H_2O were mixed with 2 mL of ethanol. GNRs were then added until the solution had a slightly opaque blue color. After this, 0.24 μL of tetramethyl orthosilicate (TMOS) was added to the mixture. The mixture was then left overnight to react and,

afterwards, the silica-capped GNRs were transferred into an aqueous solution by centrifugation and redispersion.

3.3. Shearing of Liquid Crystalline Co-Dispersions of CNCs and GNRs

The mPEG-capped GNRs dispersion was mixed with CNCs dispersed in water with a concentration ~3 wt.%, which was close to the critical concentration at which a chiral-nematic phase spontaneously forms (and was readily observed at drop edges and as water evaporated). To ensure that the nanorods were well dispersed, the sample was sonicated for at least 30 min. To shear the solution, a razor blade or pipet tip was held close a glass slide. A small amount of co-dispersed aqueous CNCs and GNRs was pipetted so that it formed a meniscus between the substrate and the glass slide. The razor blade or pipet tip was then moved back and forth at a slow speed. Each time it was moved back and forth, a thin coating of cellulose nanocrystals and gold nanorods was deposited. After water evaporation, the procedure was repeated again with another small amount of the solution. This was continued until approximately 50–150 microliters of solution had been deposited on a substrate with about one square centimeter area.

3.4. Gravity-Assisted Alignment of CNCs and GNRs

A glass substrate was placed at an oblique angle of 70–80° from the horizontal. A small drop of concentrated solution of mPEG capped GNRs and 3 wt.% CNCs co-dispersed in water was placed at the top of the slide and allowed to flow down under the action of gravity. After the solution reached the bottom, it was recovered with a pipet and again placed at the same location at the top of the slide. This process continued until the film reached a desired thickness, which was typically between 200 nm and 1 μm. The length of these aligned films is typically several inches long. We characterized the resultant film by use of a combination of focused ion milling and scanning electron microscopy techniques.

3.5. Free-Standing Mesoporous Films with Aligned GNRs

To create mesoporous silica films, we used a method developed by Shopowitz *et al*. [21], which we modified to achieve nematic-ordering by drying more quickly. 5 vol.% TMOS was added to an aqueous solution of 3 wt.% CNCs and dissolved by use of 30 min of sonication. Then an aqueous dispersion of silica capped GNRs was added slowly until the solution had a dark purple appearance. The solution was heated in an aluminum foil bowl on a hotplate with occasional agitation to prevent formation of a film of dried cellulose on top of the liquid. After the solution had dried, the ensuing dry films were peeled off the aluminum foil. To remove the cellulose from the films, the free-standing films were heated to 100 °C at a rate of 120 °C per hour and maintained at 100 °C for two hours. Then, the samples were baked at 540 °C for eight hours, and subsequently ambient-air-cooled down to the room temperature. This thermal treatment assured that all CNCs were eliminated from the mesoporous films obtained through the above-described preparation procedure. The size of these silica mesoporous films with aligned GNRs is on the scale of millimeters.

3.6. Nonlinear Optical Luminescence Imaging

TPL imaging was performed on an inverted IX-81 Olympus microscope using 850 nm excitation light from a tunable Ti:Sapphire oscillator (Chameleon Ultra II, Coherent) with 140 fs pulse width and 80 MHz repetition rate at an average power < 1 mW in the sample plane. A 60× oil objective with NA = 1.42 was used for epi-detection of TPL within a 400–700 nm range (selected by an appropriate interference filter) by a photomultiplier tube (H5784-20, Hamamatsu). To probe spatial patterns of orientation, the linear polarization direction of the excitation light was controlled using a half-wave retardation plate placed immediately before the objective. The experimental setup and technique are described in details elsewhere [2].

3.7. Focused Ion Beam Milling and Scanning Electron Microscopy

The nano-scale structure and morphology of the resultant films of CNCs and silica with GNRs were characterized using a combination of FIB milling and SEM by means of a FIB-SEM (Auriga, Carl Zeiss). The studied films were poor electrical conductors and, therefore, a variety of charge reduction techniques were employed to create images of sufficient resolution without distortion and artifacts. In the case of mesoporous silica, the imaging was performed for free-standing films, and low resolution imaging of long range order in CNC films was obtained as deposited on glass slides. To eliminate the effects of charge accumulation for these samples, an acceleration voltage close to the secondary emission crossover point was chosen [27]. However in the case of high resolution and bulk characterization of CNCs with GNRs, a charge dissipation layer of carbon (~50 nm in thickness) was sputtered over the film and glass coverslip. To clearly identify the GNRs, CNCs or mesoporous silica, the energy of secondary electrons collected was controlled by choice of detector. Three detectors were used: an IL, a standard Everhart-Thornley (ET), and ESB to choose from low energy-high angle, mixed energy-angle insensitive, and high energy-high angle secondary electrons, respectively. Low energy-high angle secondary electrons reveal the surface structure of films, whereas higher energy secondary electrons provide material contrast emphasizing GNRs. The interior structure of the film was revealed by milling the sample with the FIB, and imaged either at the site of the milling or at a location where the sputtered carbon film had collapsed.

4. Conclusions

We have demonstrated that rod-like cellulose nanocrystals forming liquid crystalline phases can confer alignment to gold nanorods within thin solid films prepared by several different deposition methods. We have also demonstrated scalable fabrication of thin mesoporous films of silica decorated by orientationally ordered anisotropic gold nanoparticles. These simple, reproducible methods for fabrication of plasmonic nanostructured thin films with orientational ordering and polarization sensitivity of optical properties demonstrate the power of self-assembly to create unique optical characteristics in thin composite films. The achieved combination of ordered nanoscale morphology in both silica and organic cellulose-based films, along with the long-range oriented metal nanostructures, are of great interest for renewable energy, optical, catalytic and anti-counterfeiting technologies.

Acknowledgments

We thank P. J. Ackerman, J. Kuehlen, T. Lee, B. Senyuk, and J. van de Lagemaat for discussions. This research was supported by the DOE grant ER46921.

Author Contributions

Michael G. Campbell, Qingkun Liu and Julian S. Evans did sample preparation and characterization. Aric Sanders performed nanoscale imaging. Ivan I. Smalyukh designed and directed the project. All authors analyzed data and wrote the manuscript.

Conflicts of Interest

The authors declare no conflict of interest.

Disclaimer

Contribution of the U.S. Department of Commerce is not subject to copyright in the U.S; licensee MDPI, Basel, Switzerland. Certain commercial equipment, instruments or materials are identified in this document. Such identification does not imply recommendation or endorsement by the National Institute of Standards and Technology.

References

1. Chung, W.J.; Oh, J.W.; Kwak, K; Lee, B.Y.; Meyer, J.; Wang, E.; Hexemer, A.; Lee, S.W. Biomimetic self-templating supramolecular structures. *Nature* **2011**, *478*, 364–368.
2. Liu, Q.; Senyuk, B.; Tang, J.; Lee, T.; Qian, J.; Smalyukh, I.I. Plasmonic complex fluids of nematic-like and helicoidal self-assemblies of gold nanorods with negative order parameter. *Phys. Rev. Lett.* **2012**, *109*, 088301.
3. Xu, Z.; Gao, C. Graphene chiral liquid crystals and macroscopic assembled fibres. *Nat. Commun.* **2011**, *2*, 571.
4. Behabtu, N.; Young, C.C.; Tsentalovich, D.E.; Kleinerman, O.; Wang, X.; Anson, W.M.; Bengio, E.A.; Waarbeek, R.F.; Jong, J.J.; Hoogerwerf, R.E.; *et al*. Strong, light, multifunctional fibers of carbon nanotubes with ultrahigh conductivity. *Science* **2013**, *339*, 182–186.
5. Evans, J.S.; Beier, C.; Smalyukh, I.I. Alignment of high-aspect ratio colloidal gold nanoplatelets in nematic liquid crsytals. *J. Appl. Phys.* **2011**, *110*, 033535.
6. Qi, H.; Hegmann, T. Formation of periodic stripe patterns in nematic liquid crystals doped with functionalized gold nanoparticles. *J. Mater. Chem*. **2006**, *16*, 4197.
7. Umadevi, S.; Feng, X.; Hegmann, T. Large area self-assembly of nematic liquid-crystal-functionalized gold nanorods. *Adv. Funct. Mater.* **2013**, *23*, 1393–1403.
8. Jones, M.R.; Osberg, K.D.; Macfarlane, R.J.; Langille, M.R.; Mirkin, C.A. Templated techniques for the synthesis and assembly of plasmonic nanostructures. *Chem. Rev.* **2011**, *111*, 3736–3827.

9. Gardner, D.F.; Evans, J.S.; Smalyukh, I.I. Towards reconfigurable optical metamaterials: Colloidal nanoparticle self-assembly and self-alignment in liquid crystals. *Mol. Cryst. Liq. Cryst.* **2011**, *545*, 1227.
10. Murphy, C.J.; Orendorff, C.J. Alignment of gold nanorods in polymer composites and on polymer surfaces. *Adv. Mater.* **2005**, *17*, 2173–2177.
11. Liu, Q.; Cui, Y.; Gardner, D.; Li, X.; He, S.; Smalyukh, I.I. Self-alignment of plasmonic gold nanorods in reconfigurable anisotropic fluids for tunable bulk metamaterial applications. *Nano Lett.* **2010**, *10*, 1347–1353.
12. Jana, N.R.; Gearheart, L.; Murphy. C.J. Seeding growth for size control of 5–40 nm diameter gold nanoparticles. *Langmuir* **2001**, *17*, 6782–6786.
13. Peng, B.L.; Dhar, N.; Liu, H.L.; Tam, K.C. Chemistry and applications of nanocrystalline cellulose and its derivatives: a nanotechnology perspective. *Can. J. Chem. Eng.* **2011**, *9999*, 1–16.
14. Qi, H.; Shopsowitz, K.E.; Hamad, W.Y.; MacLachlan, M.J. Chiral nematic assemblies of silver nanoparticles in mesoporous silica thin films. *J. Am. Chem. Soc.* **2011**, *133*, 3728–3731.
15. Kelly, J.A.; Shopsowitz, K.E.; Ahn, J.M.; Hamad, W.Y.; MacLachlan, M.J. Chiral nematic stained glass: Controlling the optical properties of nanocrystalline cellulose-templated materials. *Langmuir* **2012**, *28*, 17256–17262.
16. Lokanathan, A.R.; Uddin, K.M.A.; Rojas, O.J.; Laine, J. Cellulose nanocrystal-mediated synthesis of silver nanoparticles: Role of sulfate groups in nucleation phenomena. *Biomacromolecules* **2014**, *15*, 373–379.
17. Diaz, J.A.; Wu, X.; Martini, A.; Youngblood, J.P.; Moon, R.J. Thermal expansion of self-organized and shear-oriented cellulose nanocrystal films. *Biomacromolecules* **2013**, *14*, 2900–2908.
18. Hoeger, I.; Rojas, O.J.; Efimenko, K.; Velev, O.D.; Kelley, S.S. Ultrathin film coatings of aligned cellulose nanocrystals from a convective-shear assembly system and their surface mechanical properties. *Soft Matter* **2011**, *7*, 1957–1967.
19. Uetani, K.; Yano, H. Semiquantitative structural analysis of highly anisotropic cellulose nanocolloids. *ACS Macro Lett.* **2012**, *1*, 651–655.
20. Smalyukh, I.I.; Zribi, O.V.; Butler, J.C.; Lavrentovich, O.D.; Wong, G.C.L. Structure and dynamics of liquid crystalline pattern formation in drying droplets of DNA. *Phys. Rev. Lett.* **2006**, *96*, 177801.
21. Shopsowitz, K.E.; Qi, H.; Hamad, W.Y.; MacLachlan, M.J. Free-standing mesoporous silica films with tunable chiral nematic structures. *Nature* **2010**, *468*, 422–425.
22. Petrova, H.; Juste, J.P.; Pastoriza-Santos, I.; Hartland, G.V.; Liz-Marzan, L.M.; Mulvaney, P. On the temperature stability of gold nanorods: comparison between thermal and ultrafast laser-induced heating. *Phys. Chem. Chem. Phys.* **2005**, *8*, 814–821.
23. Maier, S.A. *Plasmonics: Fundamentals and Applications*; Springer: Berlin, Germany, 2007.
24. Perez-Juste, J.; Liz-Marzan, L.M.; Carnie, S.; Chan, D.Y.C.; Mulvaney, P. Electric-field-directed growth of gold nanorods in aqueous surfactant solutions. *Adv. Funct. Mater.* **2004**, *14*, 571–579.

25. Von Maltzahn, G.; Centrone, A.; Park, J.H.; Ramanathan, R.; Sailor, M.J.; Hatton, T.A.; Bhatia, S.N. SERS coded gold nanorods as a multifunctional platform for densely multiplexed near-infrared imaging and photothermal heating. *Adv. Mater.* **2009**, *21*, 3175–3180.
26. Fernandez-Lopez, C.; Mateo-Mateo, C.; Alvarez-Puebla, R.A.; Perez-Juste, J.; Pastoriza-Santos, I.; Liz-Marzan, L.M. Highly controlled silica capping of PEG-capped metal nanoparticles and preperation of SERS-encoded particles. *Langmuir* **2009**, *25*, 13894–13899.
27. Pawley, J. Low voltage scanning electron microscopy. *J. Microsc.* **1984**, *136*, 45–68.

Directional Scattering of Semiconductor Nanoparticles Embedded in a Liquid Crystal

Braulio García-Cámara, José Francisco Algorri, Virginia Urruchi and José Manuel Sánchez-Pena

Abstract: Light scattering by semiconductor nanoparticles has been shown to be more complex than was believed until now. Both electric and magnetic responses emerge in the visible range. In addition, directional effects on light scattering of these nanoparticles were recently obtained. In particular, zero backward and minimum-forward scattering are observed. These phenomena are very interesting for several applications such as, for instance, optical switches or modulators. The strong dependence of these phenomena on the properties of both the particle and the surrounding medium can be used to tune them. The electrical control on the optical properties of liquid crystals could be used to control the directional effects of embedded semiconductor nanoparticles. In this work, we theoretically analyze the effects on the directional distribution of light scattering by these particles when the refractive index of a surrounded liquid crystal changes from the ordinary to the extraordinary configuration. Several semiconductor materials and liquid crystals are studied in order to optimize the contrast between the two states.

Reprinted from *Materials*. Cite as: García-Cámara, B.; Algorri, J.F.; Urruchi, V.; Sánchez-Pena, J.M. Directional Scattering of Semiconductor Nanoparticles Embedded in a Liquid Crystal. *Materials* **2014**, *7*, 2784–2794.

1. Introduction

Active plasmonics has recently appears as an emergent research field [1]. The active tuning of plasmonic phenomena could be determinant for the design and development of all-optical devices for manipulating light at the nanoscale. Plasmon resonances could be modified through the variation of the size, shape or composition of the nanoparticle or by changing the refractive index of the surrounding medium. While any change in the geometrical and structural properties of the particle introduces static modifications, the variation of the effective refractive index of the host medium can be dynamic, reversible, and controllable [2]. Liquid crystals are probably one of the most important active dielectric media, due to their small elastic constant and high birefringence [3], thus their refractive index can be easily modified. In addition, there are several ways to control it. Electrically-controlled [4], light-controlled [5] and also thermal-controlled [6] techniques have been reported to modify both the refractive index of a liquid crystal and then the plasmon resonance of nanoparticles embedded on it. This has led to the emergence of active devices based on complex metamaterials composed of plasmonic nanostructures embedded in LC [7]. For instance, optical switches [8,9], modulators [10,11] or filters [12], among others.

Recent works have shown that semiconductor nanoparticles, e.g., silicon, germanium, *etc.*, present Mie resonances in light scattering with a similar behavior to plasmon polaritons [13,14]. The interest on these phenomena has grown rapidly due to important advantages respect with plasmonic

nanoparticles. This first one is that semiconductor nanoparticles has lower absorption in the visible range than metallic ones; thus, thermal effects on them are less important. Although these effects are interesting for some applications such as photothermal therapies, the heating suffering the nanostructures produce degradation. The second one is the CMOS compatibility of semiconductors and then, the easy integration of this kind of devices on chips. In addition, these nanoparticles have a magnetodielectric response in the visible range, never observed before. They present both electric and magnetic response in this range [13]. This effect has certainly been a wake-up call in the nanoscience field. Coherent effects between electric and magnetic contribution, producing certain control over the spatial distribution of the scattered light, were suggested more than 30 years ago [15]. However, they were unable to be experimentally demonstrated until now. Both zero-backward and minimum-forward scattering has been finally observed in the laboratory [16–18]. The control of directionality of light scattering can be very useful for applications ranging from biosensors [19] to all-optical devices for computing [20,21] or renewable energies [22].

Herein, we numerically study the possibility to control the directionality of light scattering of semiconductor nanoparticles embedded in a liquid crystal through controlling the optical anisotropy of this active medium via an external electric field. For this task, we have considered semiconductor nanoparticles for which the directionality conditions proposed by Kerker and coworkers [15] are satisfied in the visible range. In order to maximize the change in the scattered energy at certain directions, several materials and liquid crystals have been considered.

2. Theoretical Background

The electromagnetic scattering by a homogeneous and isotropic sphere of radius r illuminated by a linearly polarized plane wave of wavelength λ is properly explained in the Lorentz-Mie theory [23,24]. The different dependences of light scattering on the properties of both the particle and the surrounding medium are quite interesting for a great range of applications. These dependences are usually studied through the extinction and scattering efficiencies. These parameters can be expressed as a multipolar expansion given by [24]:

$$Q_{sca} = \frac{2}{x^2}\sum_{n=1}^{\infty}(2n+1)\left(|a_n|^2 + |b_n|^2\right)$$
$$Q_{ext} = \frac{2}{x^2}\sum_{n=1}^{\infty}(2n+1)\Re\left(a_n + b_n\right) \quad (3)$$

where a_n and b_n are, respectively, the electric and magnetic n-polar Mie coefficients; and x is the size parameters, defined as $x = k \cdot r$; k being the light wavenumber. Extinction refers to the part of the incident beam that is extinguished due to the two main light-matter interaction phenomena: scattering and absorption. Unlike metals, considered semiconductors present dominant scattering in the visible range. Thus, scattering and extinction are mainly equal in the present case. However, hereinafter, we will still consider the extinction efficiency as a representative parameter of light-matter interaction.

In addition, the spatial distribution of the scattered energy by the particle is also quite interesting due to its use as antennas [25]. The angular dependence of this energy is usually described via the differential scattering efficiency (Q_{diff}) [24]:

$$Q_{diff} = \frac{1}{x^2}\left\{\left|\sum_n \frac{(2n+1)}{n(n+1)}(a_n\pi_n + b_n\tau_n)\right|^2 + \left|\sum_n \frac{(2n+1)}{n(n+1)}(a_n\tau_n + b_n\pi_n)\right|^2\right\} \tag{4}$$

where π_n and τ_n introduce the angular dependence through the Legendre functions of first kind. The particular cases of the differential scattering efficiencies at the forward and backward directions are described via the forward scattering (Q_{FS}) and the radar backscattering (Q_{RBS}) efficiencies, and are given by [20]:

$$\begin{aligned} Q_{RBS} &= \frac{1}{x^2}\left|\sum_n (2n+1)(-1)^n(a_n - b_n)\right|^2 \\ Q_{FS} &= \frac{1}{x^2}\left|\sum_n (2n+1)(a_n + b_n)\right|^2 \end{aligned} \tag{5}$$

For subwavelength particles, this is nanoparticles in the visible range; the multipolar expansion can be well approximated by the first two electric and magnetic terms (a_1, a_2, b_1 and b_2). Under this approximation, previous expression can be reduced in the following way. The extinction efficiency of the nanoparticle is given by:

$$Q_{ext} = \frac{2}{x^2}[3\mathrm{Re}(a_1 + b_1) + 5\mathrm{Re}(a_2 + b_2)] \tag{6}$$

whereas the Q_{diff} is described by

$$Q_{diff} = \frac{1}{x^2}\left\{\begin{array}{l}\left|\frac{3}{2}(a_1 + b_1\cos\theta) + \frac{5}{6}(3a_2\cos\theta + 6b_2\cos^2\theta - 3b_2)\right|^2 \\ \quad + \left|\frac{3}{2}(a_1\cos\theta + b_1) + \frac{5}{6}(6a_2\cos^2\theta - 3a_2 + 3b_2\cos\theta)\right|^2\end{array}\right\} \tag{7}$$

Finally, the Q_{RBS} and Q_{FS} for such small particle have the following expressions [24]:

$$\begin{aligned} Q_{RBS} &= \frac{1}{x^2}\left|-3(a_1 - b_1) + 5(a_2 - b_2)\right|^2 \\ Q_{FS} &= \frac{1}{x^2}\left|3(a_1 + b_1) + 5(a_2 + b_2)\right|^2 \end{aligned} \tag{8}$$

Coherent effects can occur between different dipolar and quadrupolar terms in the forward and backward directions. In particular, previous works showed that the electric and the magnetic dipoles can interfere constructively or destructively producing minima in either the backward or the forward scattered intensity at certain light frequencies [15]. The relationships between the first two Mie coefficients to achieve the zero-backward or a minimum forward scattering are denoted as generalized Kerker's conditions. These are easily predicted from Equation (6) and are described as [15,26]:

$$\begin{gathered} a_1 = b_1 \\ \Re(a_1) = \Re(b_1) \quad and \quad \Im(a_1) = -\Im(b_1) \end{gathered} \tag{9}$$

These conditions were unachievable for several years, because conventional materials did not present both electric and magnetic response in the visible range. However, very recently these phenomena are observed in semiconductor particles [16–18].

On the other hand, nematic LC is a complex medium composed of long helical rods or organic molecules producing a certain order in the direction of the components, labeled by a unit vector, or the director n. This anisotropic structure involves a uniaxial optical symmetry with two principal refractive indexes, the ordinary refractive index (n_o) and the extraordinary refractive index (n_e). While n_o it is seen for electromagnetic radiation with the electric field perpendicular to the director, n_e is related to polarized radiation with the electric field parallel to the director [3]. This optical anisotropy is usually characterized through the birefringence parameter, which is defined as $\Delta n = n_e - n_o$. The variation of the refractive index seeing by an incident beam can be controlled by the polarization of light, but also by electric-field driven methods [2,4] or heat-driven methods [2,6], among others. In particular, we have considered the nematic LC E7 that is widely used. This is a mixture composed of 4-cyano-4'-n-pentyl-biphenyl (5CB), 4-cyano-4'-nheptyl-biphenyl (7CB), 4-cyano-4'-n-octyloxy-biphenyl and 4-cyano-4''-n-pentyl-p-terphenyl. It has a birefringence of 0.2 in the visible range and works in the nematic phase in a wide temperature range, from −10 to 59 °C [27]. In addition, its dielectric anisotropy is positive ($\Delta\varepsilon$ = 13.8) and it is commercially available [4].

3. Results and Discussion

Light scattering by high-refractive-index semiconductor nanoparticles (e.g., silicon, germanium) with radius of few hundreds of nanometers presents Mie resonances for incident wavelengths in the visible range, as was commented above. In contrast with plasmonic nanoparticles, the spectrum of the scattered radiation by semiconductor nanoparticles is more complex, showing both electric and magnetic resonances [13,14]. However, the spectral behavior is similar and they depend on both the size and shape of the nanoparticles, and the refractive index of the surrounding medium. This allows the use of active mediums, such as liquid crystals, to tune the scattering properties of semiconductor nanoparticles. Figure 1a shows the extinction efficiency, Q_{ext}, of a silicon nanoparticle with a radius of R = 100 nm embedded in a nematic LC, in particular, in an E7 LC. Both ordinary and extraordinary states of the LC are considered. Experimental refractive indexes have been used for these and other semiconductor materials and liquid crystals. They were obtained from references [28,29], respectively. As can be seen, the shift from the ordinary to the extraordinary state, meaning a change of the refractive index of the LC from 1.52 to 1.73 at room temperature [29], produces a slight modification of the extinction spectrum. In order to obtain a deep knowledge of the variations as well as the origin of each resonant peak, the spectral evolution of the first four dipolar contributions of the extinction efficiency (see Equation (4)) are plotted in Figure 1b. The magnetic modes, related to Mie coefficients b_1 and b_2 are predominant and the change from the ordinary to the extraordinary state only produces on them a small decrease of the maximum value. Any spectral shift is negligible. Electric modes, related to a_1 and a_2, suffer both a slight spectral shift and a decrement of the maximum Q_{ext}. As was commented above, these resonances are mainly presented in light scattering, unlike metals whose resonances are mainly related to the absorption.

Figure 1. (**a**) Extinction efficiency of a silicon nanoparticle (R = 100 nm) embedded in an E7 LC when either n_e or n_o is considered; (**b**) four first multipolar contributions of the extinction efficiency when either the ordinary or extraordinary state of E7 LC is considered.

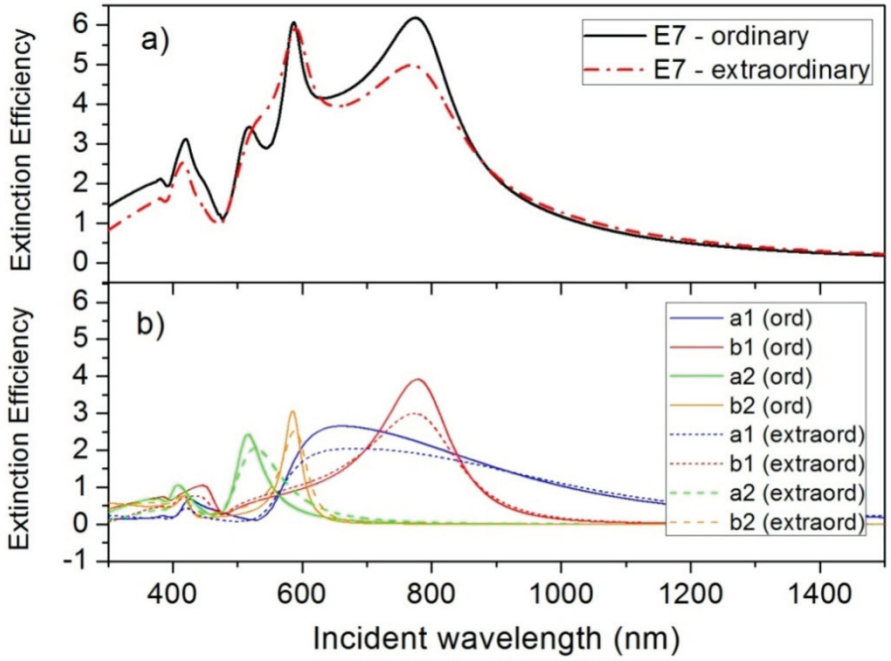

The existence of both electric and magnetic resonances in light scattering of semiconductor nanoparticles allows the appearance of coherent effects. As was previously cited, interferential phenomena between the dipolar electric and magnetic contributions produce anisotropy in the angular distribution of the scattered radiation. In particular, almost null backward and minimum forward scattering can be obtained when the dipolar Mie coefficients satisfy the expressions of Equation (7), respectively [15,26]. From Figure 1b, it seems that these conditions could be fulfilled at these wavelengths for which a_1 and b_1 contributions cross each other. Although the changes in the Q_{ext} spectrum, when the surrounding refractive index changes from n_o to n_e, are not remarkable, the slight shifts could affect the satisfaction of these conditions. Checking the scattering patterns at these wavelengths, we can observe that Kerker's conditions are satisfied at 840.9 nm and 719.7 nm, respectively, when the incident light sees the ordinary refractive index of E7 LC. If the state of the LC is modified such that the incident light sees its extraordinary index, wavelengths of Kerker's conditions shift to 840.8 nm and 700.7 nm, respectively. As can be seen, while the zero-backward condition is quite steady, the minimum-forward condition is much more dependent on the boundary conditions [30]. Figure 2 attempts to show how these variations affect the angular distribution of the scattered light. Figure 2a shows Q_{diff} of the silicon nanoparticles at λ = 840.9 nm when the surrounding refractive index corresponds with either n_o (solid blue line) or n_e (dashed red line) of E7 LC. Figure 2b shows Q_{diff} when the incident wave fulfills the second Kerker's condition, λ = 719.7 nm, under both refractive indices of E7 LC. While the zero-backward condition (Figure 2a) is almost unalterable with a deep decrease of light scattering in the backward direction (θ = 180°) at both considered scenarios, the distribution of the scattered radiation under the minimum-forward

condition (Figure 2b) slightly changes, in particular in the backward hemisphere (θ = 90°–270°). As it was related in several works [16,30], the forward condition is hard to obtain. Moreover, its observance strongly depends on the refractive index of the surrounding medium [19]. For this reason, as the refractive index of E7 LC ranges from 1.5 to 1.7, a proper minimum-forward scattering cannot be observed.

Figure 2. Differential efficiency (Q_{diff}) of a single silicon nanoparticle (R = 100 nm) embedded in an E7 nematic LC when the incident wavelength satisfies (**a**) the first Kerker's condition and (**b**) the second Kerker's condition. The ordinary (solid blue lines) and the extraordinary (dashed red line) index of E7 LC are considered.

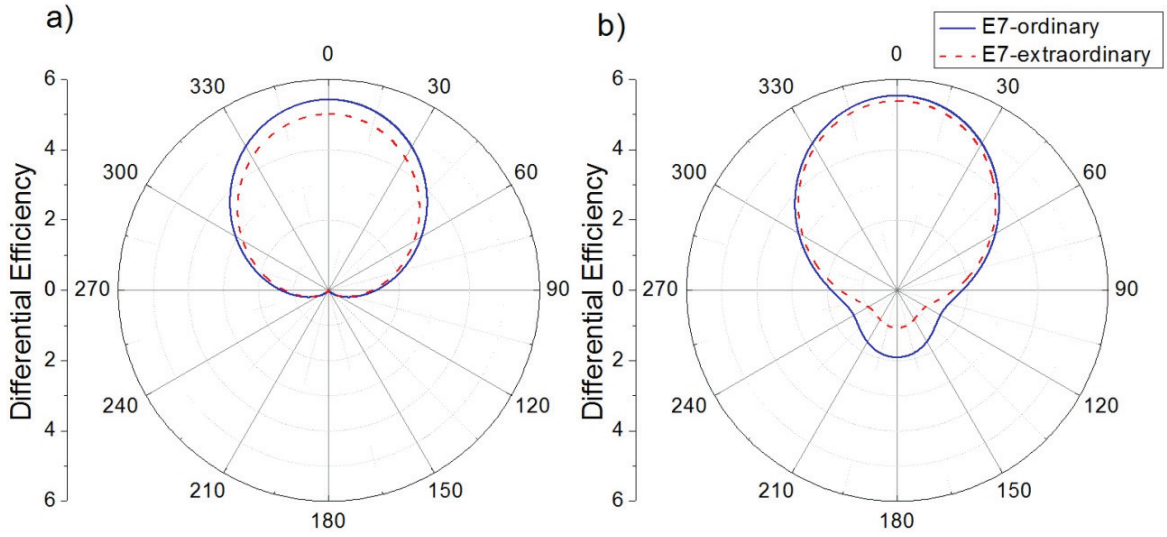

Previous polar plots do not show remarkable changes in the scattered radiation at the forward and backward directions when the state of the LC changes. Similar results are obtained for other semiconductor nanoparticles embedded in different LC. However, a more precise observance of these phenomena can be made through the analysis of the forward scattering (Q_{FS}) and the radar backscattering (Q_{RBS}) efficiencies. These parameters give us information about light scattering at these certain directions, and they can be expressed as a function of Mie theory, as can be seen in Equations (3) and (6) for a complete or approximated situation, respectively. As we are interested in the modification of these parameters when the refractive index of the LC changes by means of an electric control, variations of both efficiencies from the ordinary to the extraordinary configuration are considered. Figure 3a shows the variation of Q_{RBS} of a particle with a radius of 100 nm and made of different semiconductors, expressed in dB, and as a function of the surrounding LC when the refractive index of the LC changes from the ordinary to the extraordinary one. The incident wavelength is such that the first Kerker's condition is satisfied in the ordinary state. On the other hand, Figure 3b represents the change of Q_{FS} when the incident wavelength satisfies the second Kerker's condition in the ordinary state. As can be seen, larger variations are obtained in the backward scattering (Figure 3a). In particular, *AlSb* nanoparticles seem optimum for these tasks, presenting a maximum variation of −3.5 dB when they are embedded in *E44* LC. However, silicon nanoparticles also present large variations. Among the considered liquid crystals, *E7* and *E44* produce the maximum variations.

Figure 3. Variation of (**a**) the radar backscattering efficiency (Q_{RBS}) and (**b**) the forward scattering efficiency, in dB, of a spherical particle of R = 100 nm embedded in a LC that changes its refractive index from the ordinary to the extraordinary value *versus* the surrounding LC. The incident wavelength satisfies the first and second Kerker's conditions, respectively, when the LC presents the n_o. Several semiconductor materials are considered.

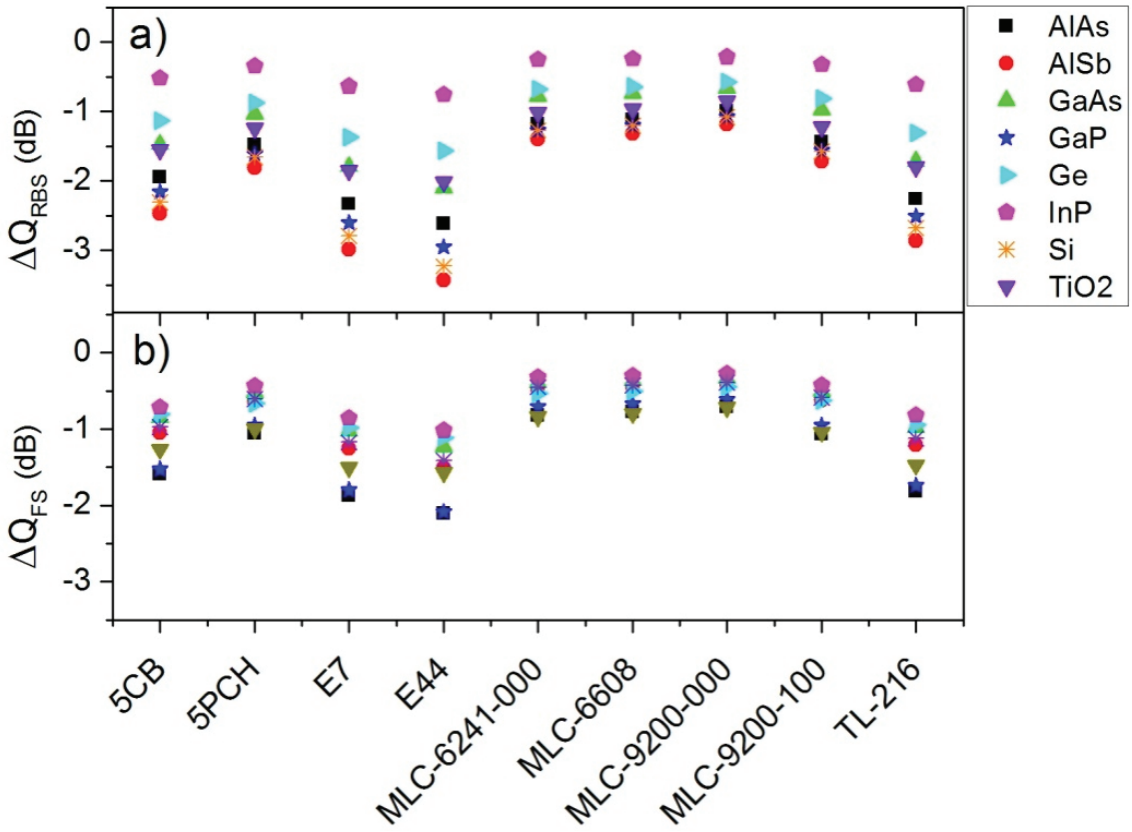

From Figure 2b it can be seen that the larger variation of light scattering when the minimum-forward scattering condition is fulfilled does not occur in the forward direction (θ = 0°), if not in the backward direction (θ = 180°). For this reason, Figure 4 shows the variation of the Q_{RBS} when the incident wavelength satisfies the second Kerker's condition. In this case, the variation is positive and the differences between different LC and semiconductor materials are larger. In this sense, TiO_2 nanoparticles present maximum values when they are embedded in 5CH, E7 or E44.

Figure 4. Variation of the radar backscattering efficiency (Q_{RBS}), in dB, of a spherical particle of R = 100 nm embedded in a LC that changes its refractive index from the ordinary to the extraordinary value *versus* the surrounding LC. The incident wavelength satisfies the minimum-forward scattering condition when the LC presents the n_o. Several semiconductor materials are considered.

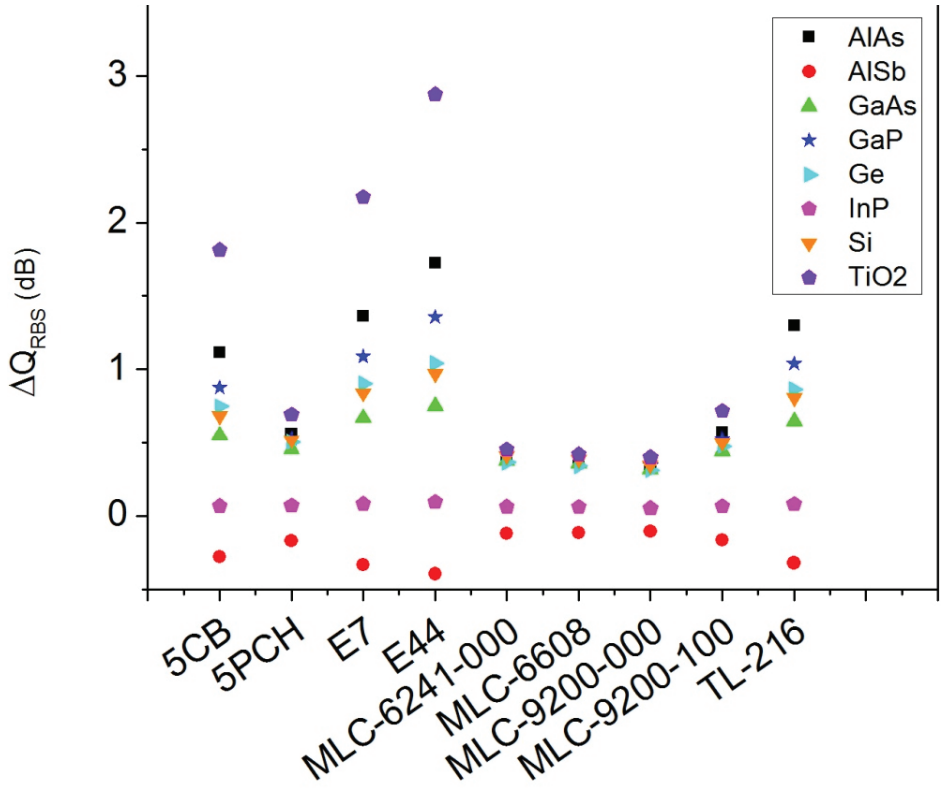

4. Conclusions

Active plasmonic devices have arisen for several applications. These devices usually considered plasmon structures, e.g., metallic nanoparticles or structures, embedded in electrically and optically active media, for instance liquid crystals. The recent discover of resonant behaviors in light scattering of semiconductor nanospheres have been appeared as an important stimulus for Plasmonics. In particular, the presence of both electric and magnetic allows the appearance of coherent effects and thus a certain control over the spatial distribution of the scattered energy by these particles. In this work, we have analyzed the possibility to vary these directional behaviors of light scattering by embedding these semiconductor nanoparticles in a LC. We have observed that the influence of the refractive index of the LC when it changes from its ordinary to the extraordinary value is weak for the considered LC. Maximum values of −3.5 dB are observed. In addition, the relative high refractive index of LC frustrates a minimum-forward scattering compared with other scattering directions. For these reasons, the analysis of backward scattering is more appropriate. Present results could be optimized through the use of high-birefringence and low-refractive-index liquid crystals. The electric control over the spatial distribution of light scattering could be useful for several applications, e.g., optical switches; therefore, its analysis is interesting.

Acknowledgments

This work has been supported by the Spanish Ministry of Science and Innovation (Grant No. TEC2009-13991-C02-01) and Comunidad de Madrid (Grant No. FACTOTEM2 S2009/ESP-1781). B.G.-C. thanks Carlos III University of Madrid for his postdoctoral grant.

Author Contributions

Braulio García-Cámara conceived this work, carried out numerical simulations, analyzed data and wrote the manuscript. José Francisco Algorri and Virginia Urruchi analyzed data and wrote the manuscript. José Manuel Sánchez-Pena supervised the study. All authors contributed to scientific discussion and critical revision of the article.

Conflicts of Interest

The authors declare no conflict of interest.

References

1. Zayats, A.V.; Maier, S. *Active Plasmonics and Tunable Plasmonic Metamaterials*; John Wiley & Sons: New York, NY, USA, 2013.
2. Si, G.; Zhao, Y.; Leong, E.S.P.; Liu, Y.J. Liquid-crystals-enabled active plasmonics: A Review. *Materials* **2014**, *7*, 1296–1317.
3. De Gennes, P.G. *The Physics of Liquid Crystals*; Oxford University Press: London, UK, 1974.
4. Kossyrev, P.; Yin, A.; Cloutier, S.G.; Cardimona, D.A.; Huang, D.; Alsing, P.M.; Xu, J.M. Electric field tuning of plasmonic response of nanodot array in liquid crystal matrix. *Nano Lett.* **2005**, *5*, 1978–1981.
5. De Sio, L.; Klein, G.; Serak, S.; Tabiryan, N.; Cunningham, A.; Tone, C.M.; Ciuchi, F.; Bürgi, T.; Umeton, C.; Bunning, T. All-optical control of localized plasmonic resonance realized by photoalignment of liquid crystal. *J. Mater. Chem. C* **2013**, *1*, 7483–7487.
6. De Sio, L.; Placido, T.; Serak, S.; Camparelli, R.; Tamborra, M.; Tabiryan, N.; Curri, M.L.; Bartolino, R.; Umeton, C.; Bunning, T. Nano-localized heating source for photonics and plasmonics. *Adv. Opt. Mater.* **2013**, *1*, 899–904.
7. Abdulhalim, I. Liquid crystal active nanophotonic and plasmonics: From science to devices. *J. Nanophoton* **2012**, *6*, doi:10.1117/1.JNP.6.061001.
8. Liu, Y.J.; Hao, Q.; Smalley, S.T.; Liou, J.; Khoo, I.C.; Huang, T.J. A frequency-addressed plasmonic switch based on dual-frequency liquid crystals. *Appl. Phys. Lett.* **2010**, *97*, 091101:1–091101:3.
9. Zografopoulos, D.C.; Beccherelli, R. Long-range plasmonic directional coupler switches controlled by nematic liquid crystals. *Opt. Express* **2013**, *21*, 8240–8250.
10. Smalley, J.S.T.; Zhao, Y.; Nawaz, A.A.; Hao, Q.; Ma, Y.; Khoo, I-C.; Huang, T.J. High contrast modulation of plasmonic signals using nanoscale dual-frequency liquid crystals. *Opt. Express* **2011**, *19*, 15265–15274.

11. Buchnev, O.; Ou, J.Y.; Kaczmarek, M.; Zheludev, N.I.; Fedotov, V.A. Electro-optical control in a plasmonic metamaterial hybrised with a liquid-crystal cell. *Opt. Express* **2013**, *21*, 1633–1638.
12. Liu, Y.J.; Si, G.Y.; Leong, E.S.P.; Xiang, N.; Danner, A.J.; Teng, J.H. Light-driven plasmonic color filter by overlaying photoresponsive liquid crystals on gold annular aperture arrays. *Adv. Mater.* **2012**, *24*, OP131–OP135.
13. García-Etxarri, A.; Gómez-Medina, R.; Froufe-Pérez, L.S.; López, C.; Chantada, L.; Scheffold, F.; Aizpurua, F.J.; Nieto-Vesperinas, M.; Sáenz, J.J. Strong magnetic response of submicron silicon particles in the infrared. *Opt. Express* **2011**, *19*, 4815–4820.
14. Gómez-Medina, R.; García-Cámara, B.; Suárez-Lacalle, I.; González, F.; Moreno, F.; Nieto-Vesperinas, M.; Sáenz, J.J. Electric and magnetic dipolar response of germanium nanospheres: Interference effects, scattering anisotropy and optical forces. *J. Nanophoton* **2011**, *5*, 053512:1–053512:10.
15. Kerker, M.; Wang, D.S.; Giles, L. Electromagnetic scattering by magnetic spheres. *J. Opt. Soc. Am.* **1983**, *73*, 765–767.
16. Geffrin, J.M.; García-Cámara, B.; Gómez-Medina, R.; Albella, P.; Froufe-Pérez, L.S.; Eyraud, C.; Litman, A.; Vaillon, R.; González, F.; Nieto-Vesperinas, M.; *et al.* Magnetic and electric coherence in forward- and backward scattered electromagnetic waves by a single dielectric subwavelength sphere. *Nat. Commun.* **2012**, *3*, doi:10.1038/ncomms2167.
17. Fu, Y.H.; Kuznetsov, A.I.; Miroshnichenko, A.E.; Yu, Y.F.; Luk'yanchuk, B. Directional visible light scattering by silicon nanoparticles. *Nat. Commun.* **2013**, *4*, 1527:1–1527:24.
18. Person, S.; Jain, M.; Lapin, Z.; Sáenz, J.J.; Wicks, G.; Novotny, L. Demonstration of zero optical backscattering from single nanoparticles. *Nano Lett.* **2013**, *13*, 1806–1809.
19. García-Cámara, B.; Gómez-Medina, R.; Sáenz, J.J.; Sepúlveda, B. Sensing with magnetic dipolar resonances in semiconductor nanospheres. *Opt. Express* **2013**, *21*, 23007–23020.
20. Wei, H.; Wang, Z.; Tian, X.; Käll, M.; Xu, H. Cascade logic gates in nanophotonic plasmon networks. *Nat. Commun.* **2011**, *2*, doi:10.1038/ncomms1388.
21. García-Cámara, B. Intra-/inter-chip optical communications. In *Communication Architectures for Systems-on-Chip*; Ayala, J.L. Ed.; CRC Press: Boca Raton, FL, USA, 2011; pp. 249–322.
22. Atwater, H.A.; Polman, A. Plasmonics for improved photovoltaic devices. *Nat. Mater.* **2010**, *9*, 205–213.
23. Kerker, M. *The Scattering of Light and other Electromagnetic Radiation*; Academic Press: New York, NY, USA, 1969.
24. Bohren, C.F.; Huffman, D.R. *Absorption and Scattering of Light by Small Particles*; John Wiley & Sons: New York, NY, USA, 1983.
25. Munárriz, J.; Malyshev, A.V.; Malyshev, V.A.; Knoester, J. Optical nanoantennas with tunable radiation patterns. *Nano Lett.* **2013**, *13*, 444–450.
26. García-Cámara, B.; Alcaraz de la Osa, R.; Saiz, J.M.; González, F.; Moreno, F. Directionality in scattering by nanoparticles: Kerker's null-scattering conditions revisited. *Opt. Lett.* **2011**, *36*, 728–730.

27. Yang, C.-S.; Lin, C.-J.; Pan, R.-P.; Que, C.T.; Yamamoto, K.; Tani M.; Pan, C.-L. The complex refractive indices of the liquid cristal mixture E7 in the terahertz frequency range. *J. Soc. Am. B* **2010**, *27*, 1866–1873.
28. Palik, E.D. *Handbook of Optical Constants of Solid*; Academic Press: Orlando, FL, USA, 1985.
29. Li, J.; Wen, C.-H.; Gauza, S.; Lu, R.; Wu, S.-T. Refractive indices of liquid crystals for display applications. *J. Disp. Technol.* **2005**, *1*, 51–61.
30. García-Cámara, B.; Saiz, J.M.; González, F.; Moreno, F. Distance limit of the directionality conditions for the scattering of nanoparticles. *Metamaterials* **2010**, *4*, 15–23.

Dispersion of γ-Alumina Nano-Sized Spherical Particles in a Calamitic Liquid Crystal. Study and Optimization of the Confinement Effects

Sergio Diez-Berart, David O. López, Nerea Sebastián, María Rosario de la Fuente, Josep Salud, Beatriz Robles-Hernández and Miguel Ángel Pérez-Jubindo

Abstract: We report an experimental study on confined systems formed by butyloxybenzylidene octylaniline liquid crystal (4O.8) + γ-alumina nanoparticles. The effects of the confinement in the thermal and dielectric properties of the liquid crystal under different densities of nanoparticles is analyzed by means of high resolution Modulated Differential Scanning Calorimetry (MDSC) and broadband dielectric spectroscopy. First, a drastic depression of the N-I and SmA-N transition temperatures is observed with confinement, the more concentration of nanoparticles the deeper this depression is, driving the nematic range closer to the room temperature. An interesting experimental law is found for both transition temperatures. Second, the change in shape of the heat capacity peaks is quantified by means of the full width half maximum (FWHM). Third, the confinement does not noticeably affect the molecular dynamics. Finally, the combination of nanoparticles and the external applied electric field tends to favor the alignment of the molecules in metallic cells. All these results indicate that the confinement of liquid crystals by means of γ-alumina nanoparticles could be optimum for liquid crystal-based electrooptic devices.

Reprinted from *Materials*. Cite as: Diez-Berart, S.; López, D.O.; Sebastián, N.; de la Fuente, M.R.; Salud, J.; Robles-Hernández, B.; Pérez-Jubindo, M.Á. Dispersion of γ-Alumina Nano-Sized Spherical Particles in a Calamitic Liquid Crystal. Study and Optimization of the Confinement Effects. *Materials* **2014**, *7*, 1502–1519.

1. Introduction

The importance of liquid crystals in the field of materials science is enormous, from theoretical and experimental reasons and, also, from the point of view of applications. Liquid crystal research covers many disciplines, from chemistry (design and synthesis), physics (fundamentals, models, characterization...), biology and medicine (many lyotropic liquid crystals are biocompatible and many biomolecules and macromolecules are mesogens), food and soap industries, thermal, mechanical, electronic and optical engineering (thermometers, biomechanic robots, displays, wave guides, lasers...) [1,2], *etc*.

Among all these industrial applications, liquid crystal-based electro-optical devices are largely spread and very well known. The duality of liquid-like fluidity and crystal-like anisotropy makes these materials ideal for such applications. On the one hand, the intrinsic dielectric and optical anisotropies imply a great variety of technical possibilities, as the compounds can be used in the construction of polarisers, filters, modulators, displays, *etc*. On the other hand, the fluidity of mesophases like the nematic (N) or smectic A (SmA) phases, among others, makes the molecules of the liquid crystal likely to orient *ad lib* by the application of small perturbations to the material

(in form of electric or magnetic fields, simple chemical surfactants...). Putting these properties of liquid crystals together, the utility of such compounds in this field of technology is pretty obvious.

In order to design any electro-optical device based on liquid crystalline properties, optimizing not just the electrical and optical, but also the thermal properties of the mesogens, is one of the priorities. The importance of the thermal behavior lies in the fact that the device must be designed to work in a particular temperature range, the so called temperature window, depending on the application itself.

One simple way to tune the thermal, optical and electrical properties, improving some effects and reducing some others non-desired, is by means of confinement [3–37]. Quenched random disorder on liquid crystals may induce smooth and/or drastic variations in their physical properties and, therefore, an exhaustive study of these systems is of great importance. Furthermore, liquid crystals in a device are strongly perturbed by confining interfaces, which means that under adequate confinement techniques, we are able to study how the properties will behave in actual micro- or nano-sized devices, and we may, indeed, be hitting two targets with one shot.

In this work, we are studying the influence on the thermal, dielectric and dielectric properties of calamitic liquid crystals affected by the random disorder induced by the dispersion of nano-sizedγ-alumina particles, which are used for the first time for confining purposes. As shown recently [35], this kind of nanoparticles noticeably reduces the undesired ionic effects on liquid crystals, which goes in the good direction when the optimization of electrical properties is pursued. Furthermore, as we are about to demonstrate, they shift the phase transition temperatures down, in a very much drastic way as compared to other structures used for confinement purposes like, for example, Anopore membranes or Aerosil silica particles.

The material object of the present research is the butyloxybenzylidene octylaniline, hereafter refered as 4O.8, a smecto-nematogenic compound whose thermal properties in bulk [38,39], confined in silica aerogel matrices [12] and confined under the dispersion of Aerosil particles [13,14] have been analyzed earlier. This is, however, the first time their dielectric properties, in bulk as well as under confinement, are reported, as it was claimed to be non-polar so far [13,38]. We show in this work that the molecule has a small (compared to common cyanobiphenyls) but measurable dipolar transversal moment, which induces a negative dielectric anisotropy.

The results presented in this manuscript, all for bulk and confined samples, are addressed in two parts, one for each of the studied properties: (1) We start with the calorimetric data, in which we can observe the deep depression in phase transition temperatures and the change in the shape of the heat capacity (C_p) peaks in the confined samples. Both effects are higher as the concentration of nanoparticles in the liquid crystal increases. A comparison between dispersions of γ-alumina and Aerosil nanoparticles is performed; (2) The behavior of the static and the complex dielectric permittivities, which allow us to interpret the molecular dynamics, is presented and discussed.

2. Results and Discussion

In order to check the influence of the random confinement on the analysed physical properties of the 4O.8 compound, we have prepared ten different samples: one bulk 4O.8 sample ($\rho_S = 0$), seven more with different concentrations of γ-alumina nanoparticles ($\rho_S = 0.01$ g·cm^{-3}, $\rho_S = 0.05$ g·cm^{-3}, $\rho_S = 0.13$ g·cm^{-3}, $\rho_S = 0.17$ g·cm^{-3}, $\rho_S = 0.19$ g·cm^{-3}, $\rho_S = 0.23$ g·cm^{-3} and $\rho_S = 0.28$ g·cm^{-3}, where

ρ_S accounts for density in grams of γ-alumina per cm^3 of 4O.8) and the last two with hydrophilic Aerosil dispersions ($\rho_{S,AS}$ = 0.05 $g \cdot cm^{-3}$ and $\rho_{S,AS}$ = 0.23 $g \cdot cm^{-3}$). The main difference between the hydrophilic silica Aerosil and γ-alumina nanoparticles is that the formers are surrounded by OH radicals, whereas the latters are radical-free. In the case of hydrophilic Aerosil, when the weight concentration, $\rho_{S,AS}$, of these particles exceeds a certain threshold ($\rho_{S,AS}$~0.01 $g \cdot cm^{-3}$), the OH groups tend to get attached forming hydrogen bonds, which induce the formation of thixotropic gelly structures. Depending on the concentration, these gels can be soft (0.01 $g \cdot cm^{-3} < \rho_{S,AS} < 0.1\ g \cdot cm^{-3}$) or stiff ($\rho_{S,AS} > 0.1\ g \cdot cm^{-3}$), and the quenching of the mesogenic material becomes more pronounced as the concentration increases. Alumina nanoparticles, however, are not able to form these hydrogen bonds, as they are not coated with any functional group. They are spherical and have diameter lengths ranging between 3 and 30 nm, as can be observed from the transmission electronic microscopy (TEM) photo in Figure 1, being the average diameter about 15 nm.

Figure 1. Transmition Electronic Microscopy picture of the γ-alumina nanoparticles.

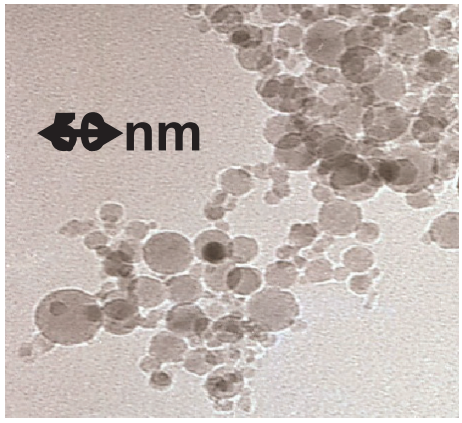

2.1. Thermal Analysis

The first issue to check is how the mesophases are affected by the dispersion of the nanoparticles. As mentioned above, 4O.8 is a smecto-nematogenic liquid crystal, and presents the following phase sequence on heating from room temperature: Crystal-Plastic Crystal-SmA-N-I. For the thermal analysis, we are focusing on the SmA-N and N-I phase transitions.

Figure 2 shows the excess heat capacity, ΔC_p, behavior as a function of temperature, for bulk 4O.8 and two of the γ-alumina dispersed samples (ρ_S = 0.05 $g \cdot cm^{-3}$ and ρ_S = 0.23 $g \cdot cm^{-3}$), around the N-I phase transition. The SmA-N phase transition ΔC_p peaks of the same three samples are displayed in the inset of Figure 2.

It can be observed that neither of the mesophases, SmA nor N, is suppressed by confinement. Furthermore, the more the concentration of nanoparticles, the more the transition temperatures are shifted down. It should be stressed that we are proving that the depression in transition temperatures is much more pronounced for confinement via γ-alumina than via Aerosil for the same concentration of nanoparticles, as shown in the values listed in Table 1. It can be seen how our data (in Aerosil) are quite in accordance with those from the work by Haga and Garland [13]. As it can be observed, and as a very interesting first result, moderate concentrations of γ-alumina nanoparticles are capable of shifting the SmA-N and N-I transition temperatures down to values around ten degrees below the

bulk, and even more, while similar concentrations of Aerosil just make them decrease about two or three degrees.

Figure 2. Heat capacity data as a function of temperature near the N-I phase transition (and near the SmA-N phase transition in the inset) of the system 4O.8 + γ-alumina, for the samples with concentrations $\rho_S = 0$ (bulk, blue circles), $\rho_S = 0.05$ g·cm^{-3} (green circles) and $\rho_S = 0.23$ g·cm^{-3} (red circles). Dashed lines indicate the N-I (and SmA-N in the inset) transition temperatures for each of the samples.

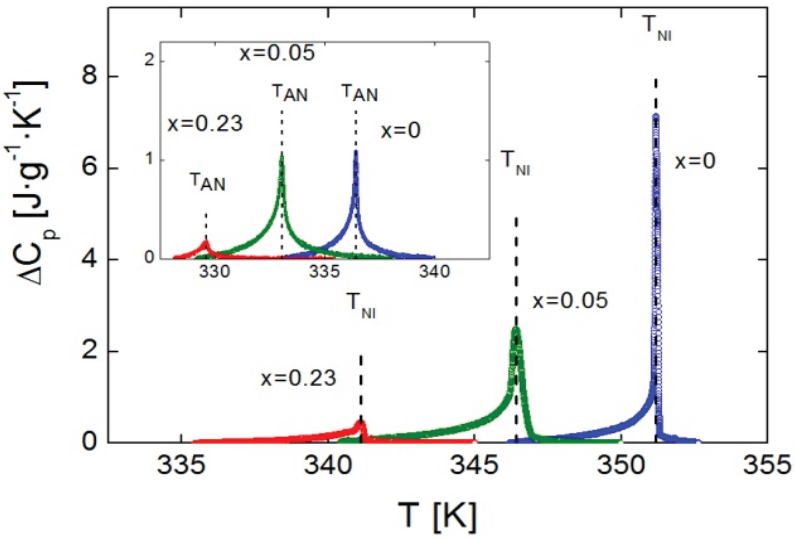

Table 1. N-I and SmA-N phase transition temperatures and nematic range (NR) for the studied samples.

ρ_S (g·cm^{-3})	T_{NI} (K)	T_{AN} (K)	NR (K)
0 (bulk 4O.8)	351.19	336.42	14.77
0.01	349.35 (−1.84)	334.86 (−1.56)	14.49
0.05	346.43 (−4.76)	333.34 (−3.08)	13.09
0.13	343.64 (−7.55)	331.34 (−5.08)	12.30
0.17	342.93 (−8.26)	330.95 (−5.47)	11.98
0.19	342.44 (−8.75)	330.34 (−6.08)	12.10
0.23	341.32 (−9.87)	329.86 (−6.53)	11.46
0.28	340.88 (−10.31)	329.26 (−7.16)	11.62
$\rho_{S,AS} = 0.05$	349.54 (−1.65)	334.64 (−1.78)	14.90
$\rho_{S,AS} = 0.23$	348.48 (−2.71)	333.89 (−2.53)	14.59

Figure 3 shows the dependence with concentration of the absolute value of the depression of the transition temperatures divided by the bulk transition temperature for the N-I (full circles) and SmA-N (empty circles) phase transitions. The experimental points for the studied concentrations can be fitted using the following equation (lines in Figure 3):

$$1 - \frac{T_{NI,\rho_S}}{T_{NI,bulk}} = \sqrt{a_{NI}\rho_S} \qquad (1a)$$

$$1 - \frac{T_{AN,\rho_S}}{T_{AN,bulk}} = \sqrt{a_{AN}\rho_S} \qquad (1b)$$

being $T_{NI,\rho s}$ the N-I phase transition temperature at the considered concentration, ρ_s; $T_{NI,bulk}$ the N-I phase transition temperature for the bulk, and a_{NI} the fitting parameter for the N-I phase transition, while $T_{AN,\rho s}$, $T_{AN,bulk}$ and a_{AN} are corresponding parameters for the SmA-N phase transition. In the inset of Figure 3, we can see how the corresponding linear fittings are quite good. This result suggest that the depression of transition temperatures with concentration follows a monotonous behavior. However, when trying to obtain similar relationships with the Aerosil data this is not possible, as they clearly present a change of behaviour when passing from the soft-gel regime to the stiff-gel regime (~0.1 g·cm^{-3}). These results seem to indicate that with γ-alumina nanoparticles there is not such a distinction between soft and stiff-gel regimes as with Aerosil, which is in accordance with the fact that the former do not have functional groups in the surface.

Another important outcome of this research is that the values of the fitting parameter a are 3.2 × 10^{-3} cm^3·g^{-1} for the N-I phase transition and 1.6 × 10^{-3} cm^3·g^{-1} for the SmA-N phase transition. There is a factor of about 2 between both transitions. The fact that the N-I transition temperatures become more affected than those of the SmA-N one, may indicate that, even if both transitions are weakly first order in nature, the latter is more continuous (more directed to second order). What is really impressive is the ratio of about 2 between both a_{NI} and a_{AN} parameters, which shall be object of further research.

Figure 3. Absolute value of the depression of the transition temperatures divided by the bulk transition temperature for the N-I (full circles) and SmA-N (empty circles) phase transitions. Straight and dashed lines indicate the fittings to Equations (1a,b), respectively. The inset shows the corresponding linear relationships coming from squaring Equations (1a,b).

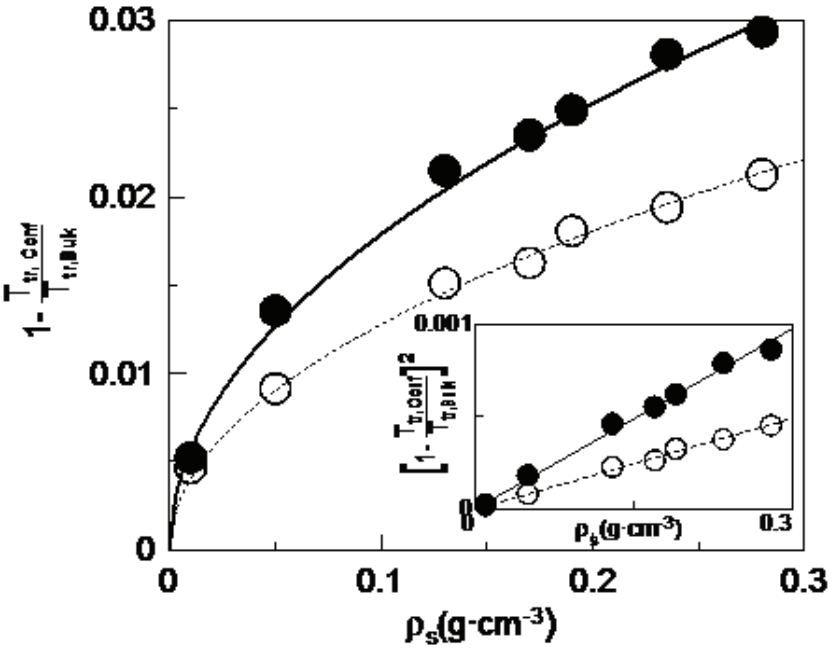

In addition to the change in transition temperatures, the influence of the confinement is remarkable in the shape and height of the C_p peaks in both the SmA-N and N-I phase transitions. As the concentration of nanoparticles increases, the C_p peaks become broader, rounded and shorter in height. This effect, that can be observed for the samples with ρ_S = 0, 0.05 and 0.23 g·cm^{-3} in Figure 4a (N-I phase transition) and 4b (SmA-N phase transition), is qualitatively similar to what occurs in other types of liquid crystals under confinement [4,10,11,13,16,24,28,31,33]. A quantitative measure of the broadening of the peaks is done by means of their full width at half maximum (FWHM). The values of the FWHM in the N-I C_p peaks increase from 0.1 K in the bulk sample to ~0.3 K in the ρ_S = 0.01–0.19 g·cm^{-3} samples, arriving up to ~0.5 K in the ρ_S = 0.23 g·cm^{-3}, 0.28 g·cm^{-3} samples. For the SmA-N peaks, FWHM goes from 0.2 K in the bulk to ~0.5 K in the confined samples. These values are similar to those corresponding to the dispersion of Aerosil nanoparticles in the same liquid crystal for small concentrations (soft-gel regime), as confirmed by the $\rho_{S,AS}$ = 0.05 g·cm^{-3} sample, where the FWHM is 0.3 K for the N-I peak and 0.5 K for the SmA-N one. Nevertheless, such values are much smaller than those for high concentrations (stiff-gel regime) of Aerosil in 4O.8, as for the $\rho_{S,AS}$ = 0.23 g·cm^{-3} sample, the FWHM of the N-I and SmA-N peaks are 0.8 K and 1.4 K, respectively. This confirms the fact that, at least, the γ-alumina particles do not form stiff-gels, as the Aerosil particles do. But the FWHM values are close to those samples comparable in concentration with Aerosil soft-gel regime ones, which means that FWHM measurements do not rule out the formation of soft-gels with γ-alumina nanoparticles. The question is, therefore, if γ-alumina nanoparticles can form any kind of soft-gel or similar, even if they cannot form hydrogen bonding networks.

Regarding the experimental results about the drastic shifting down of transition temperatures together to the lower (compared to Aerosil) effect in the C_p peak-shapes for the confinement by means of γ-alumina nanoparticles, we may propose a possible explanation: Might be that when Aerosil particles form thixotropic gel structures small "islands" of liquid crystal are embedded inside the gel hollows. Such structures are much more uniform and homogeneous than the combination of the liquid crystal with dispersing γ-alumina particles, which might just act like "simple" impurities. The homogeneity of the LC + Aerosil structures could induce local anisotropic disordering, implying a drastic change with respect to the nature of the bulk liquid crystal, which is reflected in a marked variation in the nature of the phase transitions and, so, in the shape of the C_p peaks at the transitions. In the other hand, the LC + γ-alumina system simply lowers the transition temperatures but, at the same time, it just slightly changes the transitions' nature. The γ-alumina nanoparticles do not considerably alter the liquid crystalline structure, but they do introduce an isotropic disorder that just shifts the mesophases down in temperature. Such a distinction between gel structures and LC + impurities becomes clearer when particle concentration is high, which could explain why at low concentrations (soft-gel regime for Aerosil) the C_p peak shapes in both N-I and SmA-N phase transitions are similar for both kinds of confinements. Anyhow, this remains an open question and more experiments must be performed in order to clarify and understand the behaviour of such confinements. Following this argument, we are now carrying on studies with γ-alumina nanoparticles dispersed in other kinds of liquid crystals [40].

Besides, the broadening of the C_p peaks means that the weakly first order phase transitions become even weaker with confinement and, eventually, might be driven to second order in nature [28,33]. Further exhaustive studies should be done in order to determine the critical behavior of these phase transitions, and see how it evolves with changing the concentration of nanoparticles, but such an analysis is beyond the scope of the present work.

Figure 4. Comparison of the excess heat capacity peak shapes near the (**a**) N-I and (**b**) SmA-N phase transitions for different concentrations of the 4O.8 + γ-alumina system: $\rho_S = 0$ (blue circles), $\rho_S = 0.05$ g·cm^{-3} (green circles) and $\rho_S = 0.23$ g·cm^{-3} (red circles). Dashed lines indicate the phase transitions.

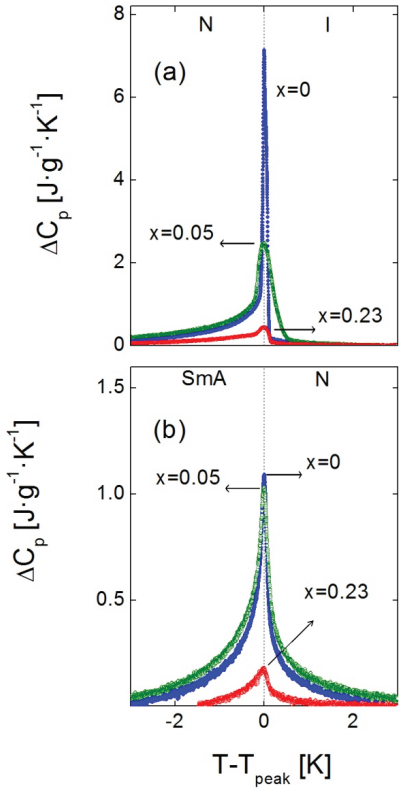

2.2. Dielectric Analysis

First of all, it must be said that, in the dielectric measurements, the depressions in phase transition temperatures are not as pronounced as in the calorimetric ones. The difference in the samples themselves as well as the added interaction of the applied electric field, drastically change the transition temperatures behaviour with respect to the high resolution calorimetry experiments. Anyway, in this section we will just focus on the dielectric properties of the bulk 4O.8 and the influence of confinement in these properties alone. It should be stressed that such kind of studies are being performed for the first time in bulk 4O.8.

Several studies have claimed for the non-polarity of 4O.8 [13,38]. Nevertheless, the 4O.8 molecule has a mainly transverse dipole moment due to the imine group, as can be seen in Scheme 1.

There is another transverse dipole due to the oxygen atom, that can be ruled out, in comparison with that of the imine group. Therefore, 4O.8 should present a negative dielectric anisotropy due to the mainly transverse dipole moment. In order to measure this response, measurements of the static

and the complex dynamic dielectric permittivitty in the I, N and SmA phases have been performed, for bulk 4O.8 and for confined samples.

Scheme 1. Butyloxybenzylidene octylaniline (4O.8) molecule.

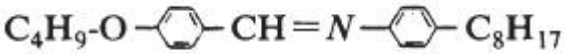

2.2.1. Static Dielectric Permittivity

As the perpendicular component of the static dielectric permittivity, $\varepsilon_{\perp}$, is higher than the parallel component, $\varepsilon_{||}$, the dielectric anisotropy of the molecules is negative ($\Delta\varepsilon = \varepsilon_{||} - \varepsilon_{\perp}$). This can be checked in Figure 5, were both components are presented *versus* $T\text{-}T_{NI}$, for two of the bulk, along with the static dielectric permittivity value in the isotropic phase. These measurements have been performed at 10 kHz, a frequency high enough to rule out the conductivity and ionic contributions and, at the same time, lower than that of the orientational contributions. The behavior of $\varepsilon_{||}$ and $\varepsilon_{\perp}$, for bulk as well as for confined samples, is the typical of calamitic liquid crystals with negative dielectric anisotropy [41]. Comparing to the bulk, the confined samples have a smaller dielectric anisotropy (in absolute value) in the N mesophase, which is nearly zero close to the N-I phase transition.

Figure 5. Static dielectric permittivity *vs*. temperature for the $\rho_S = 0$ (bulk) and $\rho_S = 0.28$ g·cm^{-3} samples of the 4O.8 + γ-alumina system: Empty circles correspond to the isotropic phase; triangles correspond to the perpendicular component of the static dielectric permittivity in the mesophases, empty triangles for the $\rho_S = 0$ sample and full triangles for the $\rho_S = 0.28$ g·cm^{-3} sample; squares represent the parallel component of the static dielectric permittivity in the mesophases, empty squares for $\rho_S = 0$ and full squares for $\rho_S = 0.28$ g·cm^{-3}. The dashed line marks the N-I phase transition.

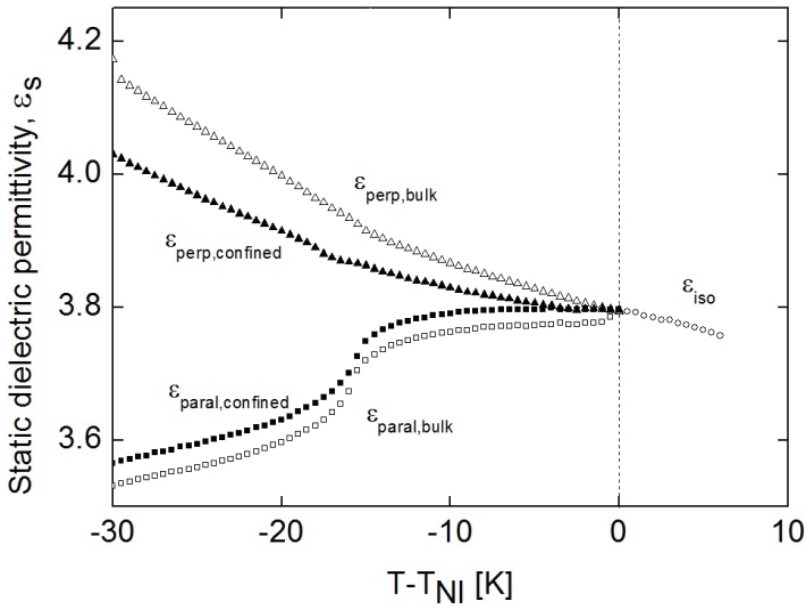

2.2.2. Molecular Dynamics: Relaxation Modes

Bulk Sample

Figure 6 shows both the real and imaginary parts of the complex dielectric permittivitty for bulk 4O.8, in both the I and N phases, the latter in a likely-planar alignment (molecules mainly parallel to the cell surfaces and perpendicular to the probing electric field). Spontaneously, the sample adopts a mixed alignment when placed into the metallic cell. When a bias DC field of 35 V is applied, the compound adopts a likely-planar alignment, as the material has a negative dielectric anisotropy. Any attempts to get the homeotropic alignment (molecules perpendicular to the cell surfaces and parallel to the probing electric field) was unfruitful. It can be observed the existence of two relaxation processes in both the I and N phases, the one at higher frequencies (around 1–10 GHz) with higher amplitude (about 3–5 times, depending on temperature) than the one at lower frequencies (1–10 MHz). Such a ratio in the strength of the modes is coherent with the fact that the dipolar moment is almost transverse (negative dielectric anisotropy). The low frequency mode (denoted as ω_1, from now on [42]) is due to the end-over-end rotations of the molecules around their short axis and the high frequency one (denoted as ω_2, from now on [42]) is due to the coupling of two types of molecular motions: rotations around their long axes and precessions around the nematic director. When cooling down to the SmA phase from the N, the behavior of the modes does not change significantly, being the spectra similar in both mesophases.

Figure 6. Frequency dependence of the real (full circles) and imaginary (empty circles) parts of the complex dielectric permittivity of the bulk 4O.8 (**a**) in the isotropic phase (T = 353 K) and (**b**) in the nematic phase (T = 343 K) in a likely-planar alignment. Black solid lines are fittings according to Equation (2). Red and blue lines represent deconvolution into the imaginary parts of the ω_1 and ω_2 modes, respectively. For simplicity, the direct current conductivity contribution (σ_{dc}) is not drawn, but is considered in the fitting procedure.

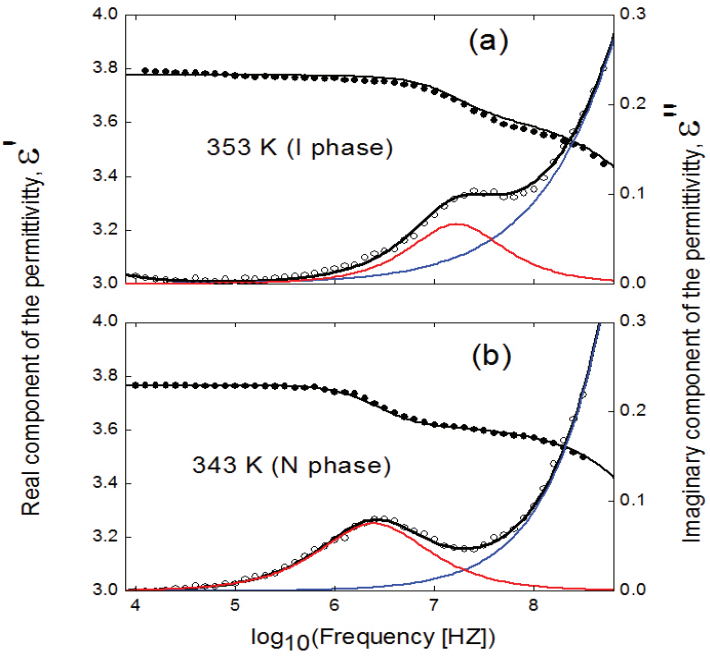

The experimental results of the complex dielectric permittivity, ε(ω), have been fitted through the empirical function:

$$\varepsilon(\omega) = \sum_k \frac{\Delta\varepsilon_k}{[1 + (i\omega\tau_k)^{\alpha_k}]^{\beta_k}} + \varepsilon_\infty - i\frac{\sigma_{DC}}{\omega\varepsilon_0} \quad (2)$$

where the summation is extended over the two relaxation modes, and each one is fitted according to the Havriliak-Negami function; k = 1, 2 are the different relaxation processs; $\Delta\varepsilon_k$ and τ_k are the dielectric strength and a relaxation time related to the frequency of maximum dielectric loss, respectively, of each relaxation mode; α_k and β_k are the parameters that describe the shape (width and symmetry) of the relaxation spectra; ε_∞ is the dielectric permittivity at high frequencies (but lower than those corresponding to atomic and electronic resonance phenomena) and σ_{DC} is the electric conductivity. According to the fits, ω_1 is a Debye relaxation mode ($\alpha = \beta = 1$). The high frequency mode (ω_2) lays in the brink of the frequency window and, therefore, the values coming from the fitting of such a mode must be taken with extreme caution. Although in Figure 6 the ω_2 mode is in the brink of the frequency window, it can be characterized at sufficiently low temperatures. This way, we have been able to fit the parameters of such a mode through Equation (2) at high temperatures, coming from lower temperatures and following a coherent behavior in their temperature dependences. Anyway, these fitting values must be taken with extreme caution, and we can temptativously say that ω_2 is a Cole-Davidson mode ($\alpha = 1 \neq \beta$), with β ranging from 0.8 at high temperatures to 0.9 near the SmA-N phase transition.

Figure 7. Arrhenius plot of the relaxation frequencies of the ω_1 (circles) and ω_2 (triangles) modes for the bulk 4O.8 (empty symbols) and $\rho_S = 0.28$ g·cm^{-3} (full symbols) samples of the 4O.8 + γ-alumina system. Dashed lines indicate the N-I phase transitions for both samples.

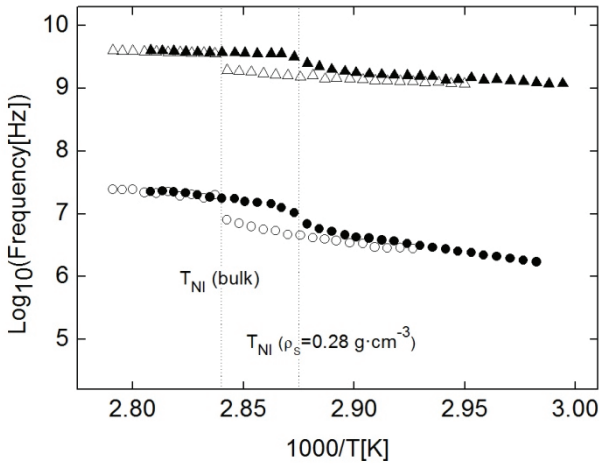

The frequency dependence on temperature for both modes can be seen in the Arrhenius plot in Figure 7 (empty symbols). The presence of two relaxation modes in the isotropic phase is typical of materials with an anisotropic rotational diffusion tensor. The behavior of both modes is as expected for these kinds of molecular reorientations. The frequency jump for the ω_2 mode at the N-I phase transition is very smooth, and the activation energy of this relaxation is quite low, as expected for

this kind of reorientations. On the other hand, ω_1 jumps down clearly in frequency when going from I to N and its activation energy is higher than that corresponding to the ω_2 mode. The validity of the fitting of ω_2, although limited, can be taken as optimal as its tendency is typical of these kind of relaxation modes in rod-like molecules [25,26,28,43], as can be seen from the Arrenius plot in Figure 7.

Confined Samples

The results of the confined samples (4O.8 + γ-alumina as well as 4O.8 + Aerosil) do not show noticeable differences with respect to the bulk ones, nor in amplitudes, neither in frequencies of the relaxation modes, but only the fact that they spontaneously adopt a planar alignment without a DC bias. In some cases, the spontaneous arrangement of calamitics in untreated metallic cells tends to be planar or nearly planar [43,44], though this is not always true and, sometimes, the cell surfaces must be treated with some surfactant in order to achieve the desired planar alignment of the molecules [25]. Fluidity of the nematic phase induces an average disorder of the molecules and, therefore, of the global nematic director, which translates in an inhomogeneous alignment of the sample, as is the case of the bulk 4O.8 sample. Nevertheless, the introduction of nanoparticles (γ-alumina as well as Aerosil) produces a decrease in fluidity and. Intriguingly, even if it induces random disorder, when combined with the applied electric field, it seems to increase the orientational order in a molecular planar alignment. Hence, the inhomegeneity within the metallic cell diminishes and the molecular arrangement is more planar-like. If this were the case, it should induce the homeotropic molecular alignment in samples of liquid crystals with positive dielectric anisotropy confined by the dispersion of hydrophilic (polar) nanoparticles. We are currently trying to study this phenomenon with some liquid crystals with longitudinal net dipole moments.

With respect to the relaxation modes, the behavior is similar to that of the bulk sample, with the same ω_1 and ω_2 modes. As in the bulk, ω_1 is Debye-like and ω_2 is, temptatively, Cole-Davidson, with β ranging from 0.6 to 0.8 as temperature decreases. Full symbols in Figure 7 show the frequency dependence on temperature of both modes for the $\rho_S = 0.28$ g·cm^{-3} sample. As it can be observed from this figure, the values are similar to those from the bulk sample, and this result can be reproduced for each of the studied samples. Such results mean that not only qualitatively, but also quantitatively, the dielectric behaviour of the planar samples is the same, irrespective of the given concentration (from $\rho_S = 0$ to $\rho_S = 0.28$ g·cm^{-3}) and the nature (γ-alumina or Aerosil) of nanoparticles. As can be deduced from these results, fluidity differences between bulk and confined samples do not influence at all molecular reorientations.

3. Experimental Section

3.1. Preparation of the Materials

The pure 4O.8 compound was synthesized and purified at the Institute of Chemistry, Military University of Technology, Warsaw, Poland. Its purity was stated to be 99.6% and no further purification was made.

The alumina nanoparticles, in the γ-phase, were commercially obtained from Tecnan (Los Arcos, Spain) and their purity was claimed to be 99.995%. The density of the nanoparticles is about

3.65 $g \cdot cm^{-3}$ and they have a surface area of about 110 $m^2 \cdot g^{-1}$. The particles, which are not coated with any functional group, are spherical and have diameter lengths ranging between 3 and 30 nm, as can be observed from the transmission electronic microscopy (TEM) photo in Figure 1, being the average diameter about 15 nm.

The silica spherical particles, of the type Aerosil 300, were commercially obtained by Degussa (Frankfurt, Germany). They are hydrophilic, with OH radicals in the surface and an average diameter of 7 nm. The quoted values of density and surface area are 2.6 $g \cdot cm^{-3}$ and 300 $m^2 \cdot g^{-1}$, respectively. TEM measurements confirm that, as the γ-alumina particles, Aerosil particles present a polydispersive nature.

The dispersion of the nanoparticles in the pure compound was made mechanically, in an ultrasound bath in the isotropic phase (I) at temperatures slightly above the N-I transition temperature for the pure compound. The homogeneity of the mixtures was stated by the high resolution heat capacity measurements and the methodology of preparation was validated by comparison with bibliographical data for the Aerosil dispersions of the same liquid crystal [13].

3.2. Transmission Electronic Microscopy

A field transmission electronic microscope JEOL JSM-7001F was used. The sample was metallized with Pt-Pd, and the photo of Figure 1 was obtained at 200 K and 120 keV.

3.3. Heat Capacity Measurements

Static heat capacity data at constant pressure were obtained through the Modulated Differential Scanning Calorimetry (MDSC) technique via a commercial TA instruments Q-2000 (New Castle, DE, USA), for which extensive details can be found elsewhere [45]. Similar to an AC calorimeter, the MDSC technique, in addition to heat capacity data, simultaneously provides phase shift data (δ) that allow determining the phase coexistence region in weakly first order transitions. The experimental conditions were adjusted in such a way that the phase delay (δ) between the modulated heat flow (the response to the perturbation) and the induced temperature oscillations (perturbation) was nearly zero out of the phase transition, and the imaginary part of the complex heat capacity data vanished.

Typically, measurements were performed on heating from the crystal phase up to the isotropic phase; the temperature rate was 0.01 $K \cdot min^{-1}$ with a modulation temperature amplitude (temperature oscillations) of ±0.07 K and a period of 23 s.

3.4. Dielectric Measurements

Measurements of the static dielectric permittivity, ε_S, were performed using the HP 4192A impedance analyzer. We have used two different kind of square glass cells, depending on the desired alignment of the molecules with respect to the probing electric field. For measuring the parallel component of the static dielectric permittivity homeotropic alignment (molecules perpendicular to the cell surfaces) is required. Otherwise, for the study of the perpendicular component of the static dielectric permittivity, molecules must be in planar alignment (parallel to the cell surfaces). Both

types of cells are from Instec (Boulder, CO, US), with an electrode surface of 1 cm^2 and thicknesses of 9 μm (homeotropic cells) and 8 μm (planar cells). The temperature control was made by a Linkam THMSG-600 hot stage and a Linkam TMS-94 temperature controller (Waterfield, Surrey, UK).

Measurements of the complex dielectric permittivitty were performed by means of two different equipments, depending on the analyzed frequency range. For radio frequencies (1 MHz to 1.8 GHz) the measurements were made by means of a HP 4291A impedance analyzer. For audio frequencies (1 kHz to 10 MHz) the HP 4192A impedance analyzer was used. The cell consists of two gold-plated brass electrodes (diameter 5 mm) separated by silica spacers, making a plane capacitor of about 50 μm thick. A modified HP 16091A coaxial test fixture was used as the sample holder. It was held in a cryostat made by Novocontrol (Hundsangen, Germany), and both temperature and dielectric measurements were computer controlled. Additional details of the experimental technique can be found somewhere else [43,45,46]. Dielectric measurements were performed on cooling with stabilization at different temperature steps and a temperature control on the order of 20 mK.

4. Conclusions

In the present work, we have presented a high resolution calorimetric and dielectric study both in 4O.8 bulk and in confined samples of γ-alumina nanoparticles dispersed in 4O.8.

The dispersion of γ-alumina nanoparticles in 4O.8 shifts downwards both N-I and SmA-N phase transition temperatures. The higher the concentration of nanoparticles, the lower the transition temperatures are with respect to the bulk. This effect is typical of confined systems, but in this case the decrease of the phase transition temperatures is much more pronounced than with any other type of confinement studied so far. For comparable concentrations of nanoparticles (γ-alumina and Aerosil), the T_{NI} shifts down three times more (low concentrations) and four times more (high concentrations) in the case of γ-alumina than in the case of Aerosil. Regarding the T_{AN}, the shifting down from the bulk is about twice more (low concentrations) and three times more (high concentrations).

An important experimental result to compare confinement by means of γ-alumina or Aerosil is the possibility of fitting data with γ-alumina to Equations (1a,b), which cannot be done for Aerosil data, in which there is a clear change of behavior. This suggests that γ-alumina nanoparticles, unlike Aerosil, do not present two different regimes, *i.e.*, a soft-gel regime below concentrations of about 0.1 $g \cdot cm^{-3}$ and a stiff-gel regime above. The relationship of these fittings between both N-I and SmA-N phase transitions is really intriguing as there is a correspondence of about 2:1 between the a_{NI} and the a_{AN} fitting parameters. Additional studies should be undertaken.

The other thermal effect caused by the confinement is the change in the shape and height of the heat capacity peaks at phase transitions. In the studied case, this change of shape (reflected as a brodening) is not as noticeable as for the confinement by means of Aerosil. The values of the FWHM of the C_p peaks of the 4O.8 + γ-alumina are similar than those of Aerosil dispersions for the so-called soft-gel regime ($\rho_S < 0.1$ $g \cdot cm^{-3}$), but are much smaller for the stiff-gel regime ($\rho_S > 0.1$ $g \cdot cm^{-3}$). In summary, γ-alumina nanoparticles introduces a disorder in the compound, *i.e.*, it favours the more disordered phases with respect to the more ordered ones, as observed by a notable lowering of both N-I and SmA-N transition temperatures. Althoug this also happens by means of Aerosil dispersion, with the γ-alumina it is much more pronounced. At the same time, confinement by means of γ-alumina does not affect the nature of the phase transitions as much as Aerosil particles do for high

concentrations ($\rho_S > 0.1$ g·cm^{-3}). This seems to indicate that the γ-alumina nanoparticles, at least do not form stiff-gels, like the Aerosil does.

The most noticeable change in the dielectric results consequence of the confinement is that the dielectric anisotropy is less negative than in the bulk. The dynamic dielectric properties are similar for bulk and confined samples, presenting two relaxation modes (reorientations around short and long molecular axes) whose frequencies do not depend on nanoparticles concentration whatsoever. There is, nevertheless, one interesting influence of the γ-alumina (and Aerosil also) particles, which is the induced ordering of the molecules facilitating planar configurations in metallic samples, when bulk 4O.8 adopts an inhomogenous fashion.

Finally, we would like to say that the 4O.8 + γ-alumina system could be an optimal candidate for electro-optical applications, for the following reasons: (1) the nematic range can get closer to room temperature with concentration of nanoparticles and, so, more accessible for device applications; (2) dielectric properties do not suffer significant changes due to confinement, which is interesting in the meaning that molecular dynamics is not slowed down and electro-optical response is, therefore, fast enough for switching applications; (3) it seems that γ-alumina nanoparticles improve the molecular orientational ordering with the dipolar moment parallel to the applied electric field.

Acknowledgments

The authors are grateful for financial support from the MICINN projects MAT2009-14636-C03-02,03 and MAT2012-38538-C03-02,03. The authors also thank the recognition from the Generalitat de Catalunya of GRPFM as Emergent Research Group (2009-SGR-1243) and from the Gobierno Vasco (GI/IT-449-10). One of us, NS, would like to thank the Universidad del País Vasco for a post-doctoral grant.

Author Contributions

Sergio Diez Berart and David O. López have planned the work. SDB and Josep Salud have made the confined samples. DOL and JS have performed high resolution calorimetric measurements. María Rosario de la Fuente and Miguel Ángel Pérez Jubindo planned the dielectric measurements. SDB, Nerea Sebastián and Beatriz Robles Hernández performed and analyzed dielectric measurements. SDB has written the paper.

Conflicts of Interest

The authors declare no conflict of interest.

References

31. Sage, I.C.; Crossland, W.A.; Wilkinson, T.D.; Gleeson, H.F.; Leigh, W.J.; Workentin, M.S. Applications. In *Handbook of Liquid Crystals*, 1st ed.; Demus, D., Goodby, J.W., Gray, G.W., Spiess, H.W., Eds.; Wiley-VCH: Weinheim, Germany, 1998; Volume 1, pp. 731–895.

32. Blunk, D.; Praefcke, K.; Vill, V.; Fairhurst, C.; Fuller, S.; Gray, J.; Holmes, M.C.; Tiddy, G.J.T.; Hoffmann, S.; Zugenmaier, P. Amphiphilic Liquid Crystals. In *Handbook of Liquid Crystals*, 1st ed.; Demus, D., Goodby, J.W., Gray, G.W., Spiess, H.W., Eds.; Wiley-VCH: Weinheim, Germany, 1998; Volume 3, pp. 303–482.
33. Bellini, T.; Clark, N.A.; Muzny, C.D.; Wu, L.; Garland, C.W.; Shaefer, D.W.; Oliver, B.J. Phase-behavior of the liquid-crystal 8CB in a silica aerogel. *Phys*. *Rev*. *Lett*. **1992**, *69*, 788–791.
34. Iannacchione, G.S.; Finotello, D. Calorimetric study of phase transitions in confined liquid crystals. *Phys*. *Rev*. *Lett*. **1992**, *69*, 2094–2097.
35. Iannacchione, G.S.; Crawford, G.P.; Zumer, S.; Doane, J.W.; Finotello, D. Randomly constrained orientational order in porous glass. *Phys*. *Rev*. *Lett*. **1993**, *71*, 2595–2598.
36. Iannacchione, G.S.; Mang, J.T.; Kumar, S.; Finotello, D. Surface-induced discrete smectic order in the isotropic phase of 12CB in cylindrical pores. *Phys*. *Rev*. *Lett*. **1994**, *73*, 2708–2711.
37. Wu, L.; Zhou, B.; Garland, C.W.; Bellini, T.; Shaefer, D.W. Heat-capacity study of nematic-isotropic and nematic-smectic-A transitions for octylcyanobiphenyl in silica aerogels. *Phys*. *Rev*. *E* **1995**, *51*, 2157–2165.
38. Iannacchione, G.S.; Crawford, G.P.; Qian, S.; Doane, J.W.; Finotello, D.; Zumer, S. Nematic ordering in highly restrictive Vycor glass. *Phys*. *Rev*. *E* **1996**, *53*, 2402–2411.
39. Qian, S.; Iannacchione, G.S.; Finotello, D. Critical behavior at the smectic-A to nematic transition confined to a random network. *Phys*. *Rev*. *E* **1996**, *53*, R4291–R4294.
40. Zhou, B.; Iannachionne, G.S.; Garland, C.W.; Bellini, T. Random-field effects on the nematic-smectic A phase transition due to silica aerosil particles. *Phys*. *Rev*. *E* **1997**, *55*, 2962–2968.
41. Kutnjak, Z.; Garland, C.W. Calorimetric study of phase transitions for butyloxybenzylidene octylaniline in silica aerogels: Static and dynamic behavior. *Phys*. *Rev*. *E* **1997**, *55*, 488–495.
42. Haga, H.; Garland, C.W. Calorimetric study of heptyloxybenzylidene butylaniline in silica aerogels. *Liq*. *Cryst*. **1997**, *22*, 275–277.
43. Haga, H.; Garland, C.W. Effect of silica aerosil particles on liquid-crystal phase transitions. *Phys*. *Rev*. *E* **1997**, *56*, 3044–3052.
44. Haga, H.; Garland, C.W. Thermal study of the influence of aerosils on the phase transitions of heptyloxybenzylidene butylaniline. *Liq*. *Cryst*. **1997**, *23*, 644–652.
45. Qian, S.; Iannacchione, G.S.; Finotello, D. Critical behavior of a smectic-A to nematic phase transition imbedded in a random network of voids. *Phy*. *Rev*. *E* **1998**, *57*, 4305–4315.
46. Iannacchione, G.S.; Garland, C.W.; Mang, J.T.; Rieker, T.P. Calorimetric and small angle X-ray scattering study of phase transitions in octylcyanobiphenyl-aerosil dispersions. *Phy*. *Rev*. *E* **1998**, *58*, 5966–5981.
47. Busch, K.; John, S. Liquid-crystal photonic-band-gap materials: The tunable electromagnetic vacuum. *Phys*. *Rev*. *Lett*. **1999**, *83*, 967–970.
48. Yablonovitch, E. Liquid *vs*. photonic crystals. *Nature* **1999**, *401*, 539–541.
49. Wiersma, D.S.; Cavalieri, S. Light emission-A temperature-tunable random laser. *Nature* **2001**, *414*, 708–709.
50. Gottardo, S.; Wiersma, D.S.; Vos, W.L. Liquid crystal infiltration of complex dielectrics. *Phys*. *B* **2003**, *338*, 143–148.

51. Caggioni, M.; Roshi, A.; Barjani, S.; Mantegazza, F.; Iannacchione, G.S.; Bellini, T. Isotropic to nematic transition os aerosil-disordered liquid crystals. *Phys*. *Rev*. *Lett*. **2004**, *93*, 127801:1–127801:4.
52. Cordoyiannis, G.; Nounesis, G.; Bobnar, V.; Kralj, S.; Kutnjak, Z. Confinement-induced orientational order in a ferroelectric liquid crystal containing dispersed aerosils. *Phys*. *Rev*. *Lett*. **2005**, *94*, 027801:1–027801:4.
53. Mercuri, F.; Paolini, S.; Zammit, U.; Marinelli, M. Dynamics at the nematic-isotropic phase transition in aerosil dispersed liquid crystal. *Phys*. *Rev*. *Lett*. **2005**, *95*, 247801:1–247801:4.
54. Diez, S.; López, D.O.; de la Fuente, M.R.; Pérez-Jubindo, M.A.; Salud, J.; Tamarit, J.L. Thermodynamic and dielectric studies concerning the influence of cylindrical submicrometer confinement on heptyloxycyanobiphenyl. *J*. *Phys*. *Chem*. *B* **2005**, *109*, 23209–23217.
55. Diez, S.; Pérez-Jubindo, M.A.; de la Fuente, M.R.; López, D.O.; Salud, J.; Tamarit, J.L. On the influence of cylindrical sub-micrometer confinement on heptyloxycyanobiphenyl (7OCB). A dynamic dielectric study. *Chem*. *Phys*. *Lett*. **2006**, *423*, 463–469.
56. Diez, S.; Pérez-Jubindo, M.A.; de la Fuente, M.R.; López, D.O.; Salud, J.; Tamarit, J.L. Dielectric relaxation in bulk and cylindrically confined octylcyanobiphenyl (8CB). *Liq*. *Cryst*. **2006**, *33*, 1083–1091.
57. Kralj, S.; Cordoyiannis, G.; Zidansek, A.; Lahajnar, G.; Amenitsch, H.; Zumer, S.; Kutnjak, Z. Presmectic wetting and supercritical-like phase behavior of octylcyanobiphenyl liquid crystal confined to controlled-pore glass matrices. *J*. *Chem*. *Phys*. **2007**, *127*, 154905:1–154905:9.
58. Perez-Jubindo, M.A.; de la Fuente, M.R.; Diez-Berart, S.; Lopez, D.O.; Salud, J. Influence of cylindrical submicrometer confinement on the static and dynamic properties in nonyloxycyanobiphenyl (9OCB). *J*. *Phys*. *Chem*. *B* **2008**, *112*, 6567–6577.
59. Cordoyiannis, G.; Kurihara, L.K.; Martinez-Miranda, L.J.; Glorieux, C.; Thoen, J. Effects of magnetic nanoparticles with different surface coating on the phase transitions of octylcyanobiphenyl liquid crystal. *Phys*. *Rev*. *E* **2009**, *79*, 011702:1–011702:5.
60. De Luca, A.; Barna, V.; Ferjani, S.; Caputo, R.; Versace, C.; Scaramuzza, N.; Bartolino, R.; Umeton, C.; Strangi, G. Laser action in dye doped liquid crystals: From periodic structures to random media. *J*. *Nonlinear Opt*. *Phys*. **2009**, *18*, 349–365.
61. De la Fuente, M.R.; Lopez, D.O.; Perez-Jubindo, M.A.; Dunmur, D.A.; Diez-Berart, S.; Salud, J. Cylindrical sub-micrometer confinement results for the odd-symmetric dimer α,ω-bis[(4-cyanobiphenyl)-4′yloxy]undecane (BCB.O11). *J*. *Phys*. *Chem*. *B* **2010**, *114*, 7864–7873.
62. Karatairi, E.; Rozic, B.; Kutnjak, Z.; Tzitzios, V.; Nounesis, G.; Cordoyiannis, G.; Thoen, J.; Glorieux, C.; Kralj, S. Nanoparticle-induced widening of the temperature range of liquid-crystalline blue phases. *Phys*. *Rev*. *E* **2010**, *81*, 041703:1–041703:5.
63. Diez-Berart, S.; Lopez, D.O.; de la Fuente, M.R.; Salud, J.; Perez-Jubindo, M.A.; Finotello, D. Critical behaviour in liquid-crystalline phase transitions: A comparative study of 9OCB in bulk and Anopore membranes. *Liq*. *Cryst*. **2010**, *37*, 893–901.
64. Grigoriadis, C.; Duran, H.; Steinhart, M.; Kappl, M.; Butt, H.J.; Floudas, G. Suppression of phase transitions in a confined rodlike liquid crystal. *ACS Nano* **2011**, *5*, 9208–9215.

65. Joshi, T.; Prakash, J.; Kumar, A.; Gangwar, J.; Srivastava, A.K.; Singh, S.; Biradar, A.M. Alumina nanoparticles find an application to reduce the ionic effects of ferroelectric liquid crystal. *J. Phys. D* **2011**, *44*, 315404:1–315404:7.
66. Kralj, S.; Cordoyiannis, G.; Jesenek, D.; Zidansek, A.; Lahajnar, G.; Novak, N.; Amenitsch, H.; Kutnjak, Z. Dimensional crossover and scaling behavior of a smectic liquid crystal confined to controlled-pore glass matrices. *Soft Matter* **2012**, *8*, 2460–2470.
67. Zupancic, B.; Diez-Berart, S.; Finotello, D.; Lavrentovich, O.D.; Zalar, B. Photoisomerization-controlled phase segregation in a submicron confined azonematic liquid crystal. *Phys. Rev. Lett.* **2012**, *108*, 257801:1–257801:5.
68. Stine, K.J.; Garland, C.W. Calorimetric study of nematic to smectic-A tricritical behavior. *Phys. Rev. A* **1989**, *39*, 3148–3156.
69. Salud, J.; Lopez, D.O.; Diez-Berart, S.; de la Fuente, M.R. Tests of the tricritical point in the SmA-to-N phase transition of binary mixtures of butyloxybenzylidene octylaniline and hexyloxybenzylidene octylaniline. *Liq. Cryst.* **2013**, *40*, 293–304.
70. Diez-Berart, S.[1]; López, D.O.[1]; Salud, J.[1]; Sebastián, N.[2]; Robles-Hernández, B.[2]; De la Fuente, M.R.[2]; Diego, J.A.[3]; Sellarés, J.[3]; Ros, M.B[4]. [1]GRPFM, Departament de Física i Enginyeria Nuclear, E.T.S.E.I.B., Universitat Politècnica de Catalunya, Barcelona, Spain; [2]Departamento de Física Aplicada II, Facultad de Ciencia y Tecnología, Universidad del País Vasco (UPV/EHU), Bilbao, Spain; [3]DILAB, Departament de Física i Enginyeria Nuclear, E.T.S.E.I.B., Universitat Politècnica de Catalunya, Barcelona, Spain; [4]Departamento de Química Orgánica, Universidad de Zaragoza, Instituto de Ciencia de Materiales de Aragón (ICMA-CSIC), Zaragoza, Spain. Unpublished work, 2014.
71. Dunmur, D.A.; Toriyama, K. Dielectric Properties. In *Physical Properties of Liquid Crystals*, 1st ed.; Demus, D., Goodby, J.W., Gray, G.W., Spiess, H.W., Eds.; Wiley-VCH: Weinheim, Germany, 1999; pp. 129–150.
72. Nordio, P.L.; Rigatti, G.; Segre, U. Dielectric relaxation theory in nematic liquids. *Mol. Phys.* **1973**, *25*, 129–136.
73. Cusmin, P.; de la Fuente, M.R.; Salud, J.; Pérez-Jubindo, M.A.; Diez-Berart, S.; López, D.O. Critical behavior and scaling relationships at ehe SmA_d-N and N-I transitions in nonyloxycyanobiphenyl (9OCB). *J. Phys. Chem. B* **2007**, *111*, 8974–8984.
74. Salud, J.; Cusmin, P.; de la Fuente, M.R.; Pérez-Jubindo, M.A.; López, D.O.; Diez-Berart, S. Study of the critical behavior and scaling relationships at the N-to-I phase transition in hexyloxycyanobiphenyl. *J. Phys. Chem. B* **2009**, *113*, 15967–15974.
75. Puertas, R.; Rute, M.A.; Salud, J.; López, D.O.; Diez, S.; van Miltenburg, J.C.; Pardo, L.C.; Tamarit, J.L.; Barrio, M.; Pérez-Jubindo, M.A.; de la Fuente, M.R. Thermodynamic, crystallographic and dielectric study of the nature of glass transitions in cyclo-octanol. *Phys. Rev. B* **2004**, *69*, 224202:1–224202:9.
76. Sebastián, N.; de la Fuente, M.R.; Lopez, D.O.; Perez-Jubindo, M.A.; Salud, J.; Diez-Berart, S.; Ros, M.B. Dielectric and thermodynamic study on the liquid crystal dimer α-(4-cyanobiphenyl)-4′-oxy)-ω-(1-pyreniminebenzylidene-4′-oxy)undecane (CBO11O.Py). *J. Phys. Chem. B* **2011**, *115*, 9766–9775.

Part II: Polymer-Modified Liquid Crystals

A Review of Polymer-Stabilized Ferroelectric Liquid Crystals

Ingo Dierking

Abstract: The polymer stabilized state of ferroelectric liquid crystals (FLC) is reviewed; and the effect of a dispersed polymer network in an FLC outlined and discussed. All fundamental material aspects are demonstrated; such as director tilt angle; spontaneous polarization; response time and viscosity; as well as the dielectric modes. It was found that the data can largely be explained by assuming an elastic interaction between the polymer network strands and the liquid crystal molecules. The elastic interaction parameter was determined; and increases linearly with increasing polymer concentration.

Reprinted from *Materials*. Cite as: Dierking, I. A Review of Polymer-Stabilized Ferroelectric Liquid Crystals. *Materials* **2014**, 7, 3568–3587.

1. Introduction

1.1. Liquid Crystals [1–3]

Liquid crystals are anisotropic fluids, which are thermodynamically located between the isotropic liquid and the three-dimensional crystal. Two broad classes of liquid crystals are distinguished, lyotropic phases [4,5], which are formed by variation of the concentration of amphiphilic molecules in a suitable solvent, and thermotropic phases, which are observed by temperature variation. The former class of liquid crystals will be disregarded in this review, while the latter is further distinguished by the molecular shape of the constituent molecules. Calamitic phases are formed by cylinder-like mesogens, discotic phases by disk-shaped molecules, and bent-core phases [6,7] by so called banana liquid crystals.

Numerous liquid crystal phases can be observed, depending on the order of the constituent mesogens [8]. The simplest of the phases is the nematic phase, which solely exhibits an average orientational order of the long axes of the molecules (called the director **n**), while their centres of mass are isotropically distributed (Figure 1a). The nematic phase is also the one observed at the highest temperature. On cooling, fluid smectic phases are formed, which in addition to orientational order also exhibit a one-dimensional positional ordering, *i.e.*, a layered structure. Within a smectic layer the centres of mass of the mesogens is again isotropically distributed. For the smectic A (SmA) phase the layer normal **k** is parallel to the director **n**, while in the smectic C (SmC) phase it is inclined by a temperature dependent angle called the tilt angle, θ (Figure 1b,c, respectively). Further liquid crystal phases are the hexatic phases, which exhibit short and long range two-dimensional positional order, *i.e.*, an additional feature of order within individual smectic layers.

Figure 1. Schematic representation of the (**a**) nematic; (**b**) smectic A (SmA) and (**c**) smectic C (SmC) phase of calamitic (rod-like) mesogens. Molecular order increases on cooling from the left to the right side of the diagram.

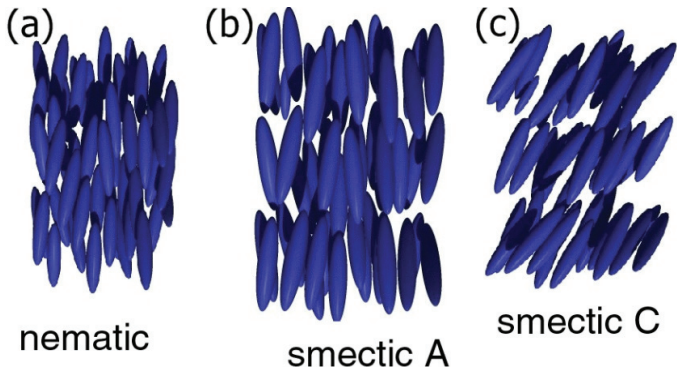

In order to identify different liquid crystalline phases, a variety of experimental techniques is generally employed, among them differential scanning calorimetry (DSC), small angle and wide angle X-ray diffraction (SAXS, WAXS), and texture observation by polarizing optical microscopy (POM) [8]. An example of the latter is shown in Figure 2, where the characteristic defects allow a verification of the phase under investigation, in this case point singularities of a nematic phase (Figure 2a, Schlieren texture), Dupin cyclides of a fluid smectic A phase (Figure 2b, focal conic texture), and the broken fan-shaped texture of SmC (Figure 2c).

Figure 2. Characteristic polarizing microscopic defect textures of (**a**) the nematic Schlieren texture; (**b**) SmA focal conic and (**c**) broken focal conic texture of the SmC phase. (Reproduced with permission from [8]. Copyright 2003 Wiley-VCH Verlag GmbH&Co. KGaA).

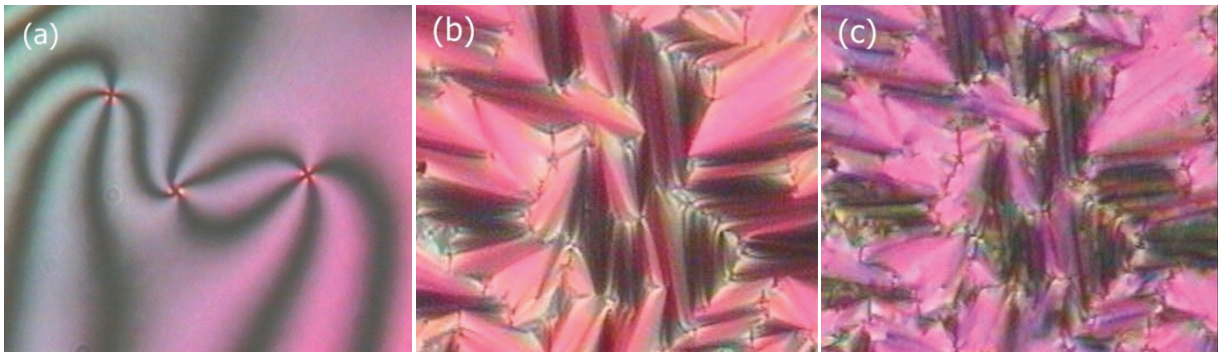

1.2. Ferroelectric Liquid Crystals [9,10]

Introduction of chirality or "handedness" to liquid crystalline materials leads to exciting changes of the phases. Novel structures are observed, like helical superstructures, novel phases, the so called frustrated phases (Blue Phases [11], Twist Grain Boundary phases [12]), which only occur in chiral systems, are formed, and novel effects can be seen. The latter are, for example, selective reflection leading to photonic bandgaps [13], or extremely fast electro-optic modulation via the electroclinic effect [14,15]. However, the most pronounced observation is that of ferroelectricity

in fluid systems [16,17]. Indeed, ferroelectric liquid crystals (FLC) are the only fluid ferroelectrics known to man.

The occurrence of a spontaneous polarization in the SmC* phase can easily be understood by following the symmetry arguments of Meyer [16]. He deduced that all chiral titled smectic phases exhibit a local spontaneous polarization and are thus pyroelectric. In the SmC* phase, as in some others, this polarization is switchable between two stable states, thus ferroelectric. As depicted in Figure 3a, the structure of the achiral SmC phase contains three symmetry elements, namely a two-fold rotation axis, a mirror plane and therefore a resultant inversion centre. Application of those local symmetry elements to a molecular dipole moment $\mu = (\mu_x, \mu_y, \mu_z)$ gives $\mu_i = (-\mu_x, -\mu_y, -\mu_z)$, giving a net dipole moment of the achiral SmC phase of $\mu_{SmC} = (0, 0, 0)$, a vanishing spontaneous polarization. For chiral molecules the mirror plane and the inversion centre are lacking and a dipole moment $\mu = (\mu_x, \mu_y, \mu_z)$, which is subjected to the only remaining symmetry element, the two-fold rotation axis, becomes $\mu_{rot} = (-\mu_x, -\mu_y, -\mu_z)$ and the resultant dipole moment of the chiral SmC* phase is $\mu_{SmC}^* = (0, \mu_y, 0)$. The spontaneous polarization is the sum of the non-vanishing lateral dipole moment components per unit volume. Reversal of an applied electric field switches the spontaneous polarization between two stable states, and the smectic C* structure is ferroelectric.

Figure 3. (**a**) Symmetry elements of the achiral SmC phase, explaining the absence of a spontaneous polarization; (**b**) schematic helical superstructure of the chiral SmC* phase (**left**) and associated polarized microscopic image of the equidistant line pattern (**right**). (Reproduced with permission from [8]. Copyright 2003, Wiley-VCH Verlag GmbH&Co. KGaA).

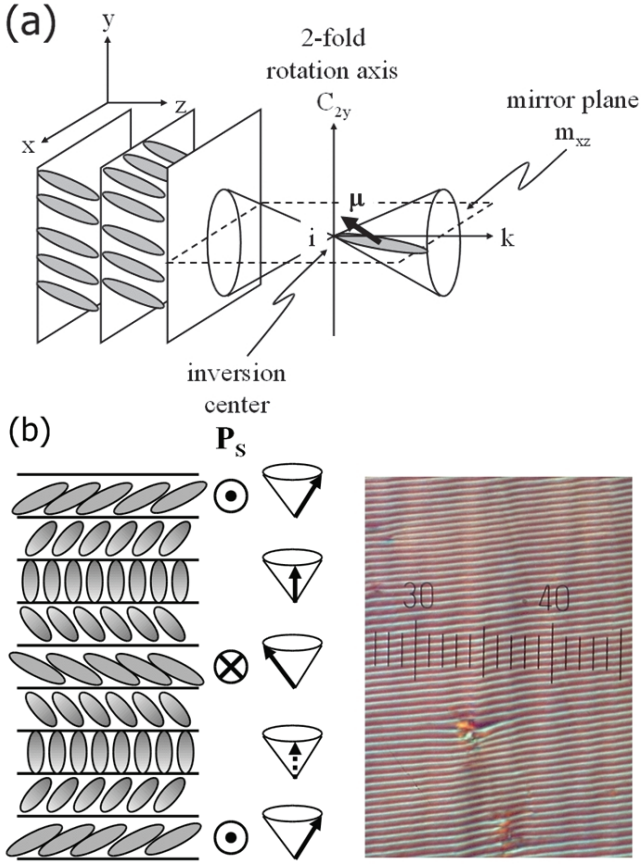

This is not the whole truth though. For a bulk sample the spontaneous polarization compensates by forming a helical superstructure, and the SmC* phase is more correctly called helielectric. The helical structure of SmC* manifests itself in polarizing microscopy through the appearance of an equidistant line pattern, as shown in the inset of Figure 3b Subjecting the SmC* phase to thin cells with strong surface interactions and suppressing the helical superstructure leads to the so called surface stabilized ferroelectric liquid crystal (SSFLC) [17]. This state is indeed ferroelectric and from a virgin sample a domain structure is observed, which represents the two ferroelectric domains of polarization up and polarization down. The latter is shown in Figure 3b.

1.3. Polymer Stabilization [18,19]

Polymer stabilisation of liquid crystals refers to a method first used on nematic and cholesteric phases [20–24] in the development of reflective displays, or electronic paper [25–31]. It is now widely used also for other liquid crystal phases and purposes. A small amount, generally less than 10% by weight, of a photoreactive monomer is mixed into the liquid crystalline phase, while care has to be taken to stay below the solubility limit of the monomer. These photoreactive monomers can be liquid crystalline by themselves, but do not need to be, as long as they exhibit a similar elongated shape and form anisotropy as the liquid crystal host molecules. A minute amount of a photoinitiator, often benzoin methyl ether (BME) is also added to the mixture. The latter will not be incorporated into the actual structure, but is simply present as a catalyst to facilitate the chemical reaction, which will take place when the mixture is subjected to UV illumination.

The mixture is filled into suitable cells, which promote a certain desired zero electric field alignment. Since the monomers exhibit the same shape anisotropy as the liquid crystal molecules, they will align along the local director of the liquid crystal. UV illumination then causes an open polymer network to be formed by the photoreactive monomers. This polymer network will follow the local director field in which it was formed, thus acting as a template of the liquid crystal structure [32,33] (Figure 4). The network is phase separated from the liquid crystal, and the interaction between both is thus of elastic nature. The liquid crystal may then be forced out of its equilibrium orientation for example by electric or magnetic fields, and on turning the outside stimuli off, the polymer network drives the liquid crystal back to its original director configuration. Other scenarios may be envisioned. The liquid crystal can be washed out by a suitable solvent and be replaced by a different material. A left handed helical polymer network structure may be filled with a right handed cholesteric material of the same or a different pitch [34]. Polymerisation can be carried out in the orthogonal SmA phase, and the transition into the tilted SmC phase can be investigated, a scenario which we will come back to below. In all cases the fundamental idea is the same: a polymer network is formed which stabilises the liquid crystal director configuration in which it was formed. Elastic interactions between the large surface of the polymer network and the liquid crystal will aim to drive the system back into its equilibrium orientation.

Figure 4. Schematic of a polymer stabilized liquid crystal. The polymer network acts as a template of the self-organised liquid crystalline phase that it was formed in.

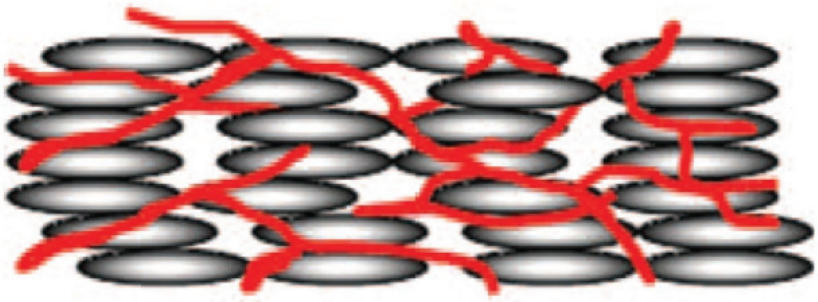

A few examples of polymer networks formed in different liquid crystals are presented in Figure 5 [33,35–37]. The images are taken by scanning electron microscopy, after coating the polymer network with a thin layer of gold. In part (a) a s = +1 point defect is shown (left), which clearly represents the expected director field from a defect of a Schlieren texture [35] (right) as introduced in Figure 2a. Figure 5b demonstrates the helical superstructure of the cholesteric or chiral nematic phase by an oblique cut through the helix from the top to the bottom substrate plates. The pitch was adjusted to 10 μm so that three half turns of the helix are visible in the 15 μm thick cell [33] (left). The imaged structure is equivalent to a so called Bouligand cut (right), which is used to demonstrate helical superstructures in biological systems. Similarly, the individual smectic blocks of a twist grain boundary (TGB) phase can be imaged [36] (Figure 5c left), including the discontinuous twist which is mediated via boundaries of screw dislocations (right). Also such structures can be found in biological systems. In the SmA phase the polymer network is well oriented along the director of a uniform sample (Figure 5d left) [36]. It can be seen that the individual features of the polymer strands are on average about 0.1 μm in size (Figure 5d right). The size of the voids depends on various preparation conditions, such as monomer concentration, polymerisation temperature, and UV dose [29]. In general, the polymer network formation process is completed within about 10–15 min.

2. Effects on SmC* Material Parameters

The first polymer stabilized ferroelectric liquid crystal (PSFLC) was made by Hikmet and Lub [38] from Philips in 1995, in an effort to overcome the mechanical problems of surface stabilized ferroelectric liquid crystals. Samples were polymerized in the SmC* phase and an oriented polymer network along the smectic layer normal was observed. It was found [39] that polymer network stabilization has a considerable influence on the electro-optic performance of FLCs and the physical parameters as compared to the non-stabilized sample.

Figure 5. Exemplary scanning electron microscopy (SEM) images of polymer networks formed in different liquid crystalline phases: (**a**) nematic s = ±1 defect pair (**top**) and schematic director field (**bottom**); image side length ~50 µm (Reproduced with permission from [35]. Copyright 2013 Royal Society of Chemistry); (**b**) helical superstructure of the chiral nematic, N* phase (**top**), which can be illustrated by an oblique cut called a Bouligand cut (**bottom**); image side length ~50 µm (Reproduced with permission from [33]. Copyright 1997 American Physical Society); (**c**) different director orientation in SmA* twist grain boundary (TGB) blocks (**top**) and schematic representation (**bottom**); image side length ~5 µm. (Reproduced with permission from [36]. Copyright 2009 Royal Society of Chemistry) and (**d**) well oriented SmA phase (**left**) and close-up (**right**); image side length ~5 µm. The material used is the well known RM257 from Merck, and the liquid crystal has been removed by a suitable solvent after polymerization. For the SEM investigations the polymer network was then coated with a very thin layer of gold.

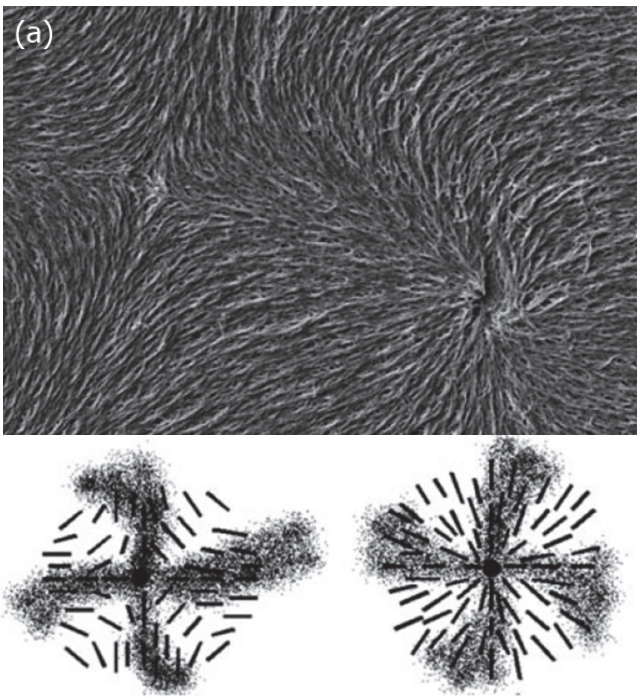

Figure 5. *Cont.*

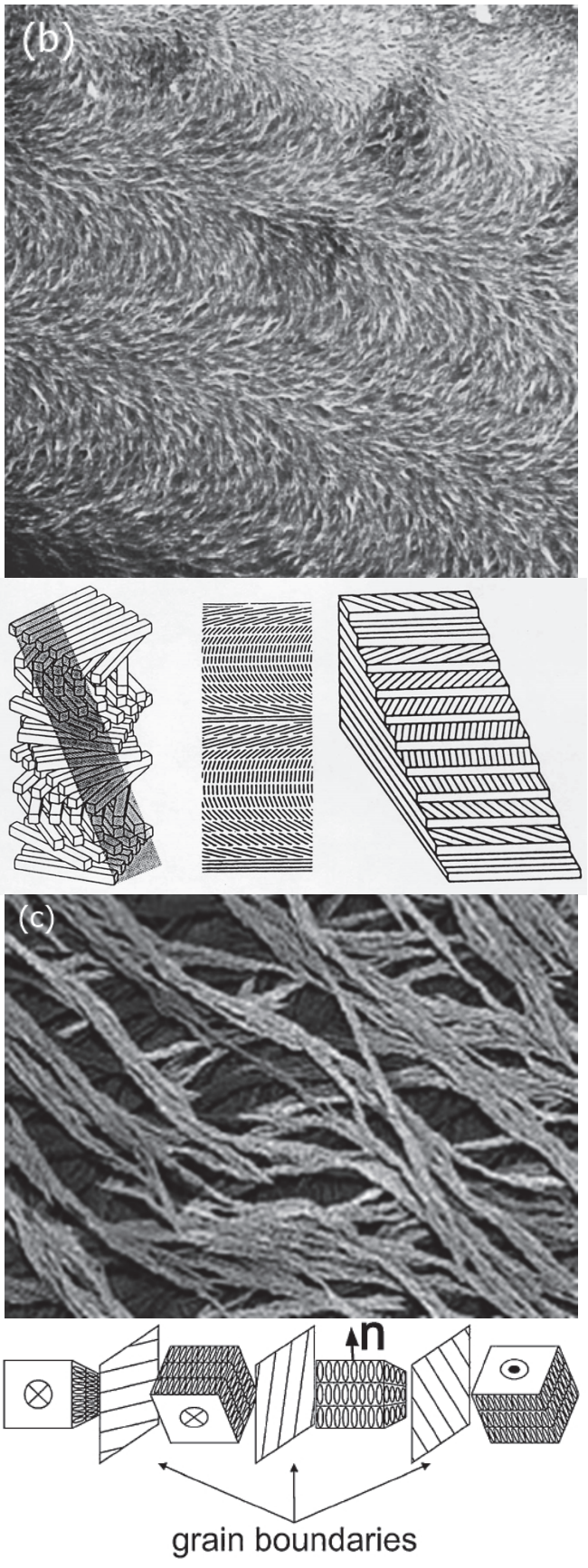

Figure 5. *Cont.*

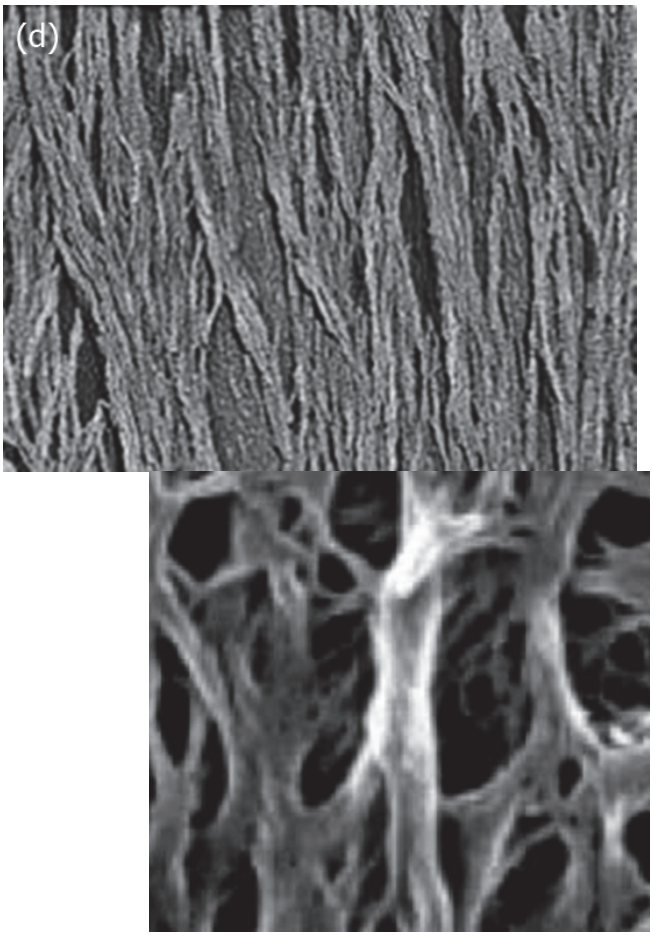

2.1. Tilt Angle and Spontaneous Polarization

The two most fundamental parameters of the SmC* phase are the tilt angle and the spontaneous polarization. The former is the primary order parameter for the transition between the non-tilted, paraelectric SmA* and the tilted, ferroelectric SmC* phase, while the spontaneous polarization represents the secondary order parameter of the transition, as it is coupled to the tilt angle. While maintaining their general temperature dependence of increasing values for decreasing temperatures, both the tilt angle and the polarization decrease for increasing polymer concentration [40–42]. This is demonstrated in Figure 6a,b, respectively. The reason for this behaviour can be found in regions in the vicinity of the network that are strongly dominated by the polymer, thus not switching at all, or at least only partially, in contrast to the saturated switching of the bulk regions. There is thus a decrease of the effective tilt angle and the polarization. The polymer dominated regions become more and more pronounced with increasing polymer concentration, and the two prime parameters of the SmC* phase decrease for increasing polymer content. The electroclinic effect, describing an induced tilt angle in the very close vicinity of the SmA*–SmC* transition is in our case practically not affected by the process of polymer stabilization, most likely due to the fact that it is very small and only observed over a narrow temperature regime. The situation appears to be different for large electroclinic effect materials, as shown by Petit *et al.* [43] in Figure 7. Here the increase in polymer network density causes a decrease of the electroclinically induced tilt angle, as would be expected. The fact that the respective investigations were carried out on short-pitch FLCs in contrast to the

normally investigated surface stabilized FLCs may also play a role for the interpretation of these results.

Figure 6. Effect of the polymer network on the principle order parameters of the SmA*–SmC* transition, (**a**) tilt angle (Reproduced with permission from [42]. Copyright 2008, Institute of Physics); and (**b**) spontaneous polarization (Reproduced with permission from [44]. Copyright 2009 Institute of Physics). Both quantities decrease for increasing polymer network concentration.

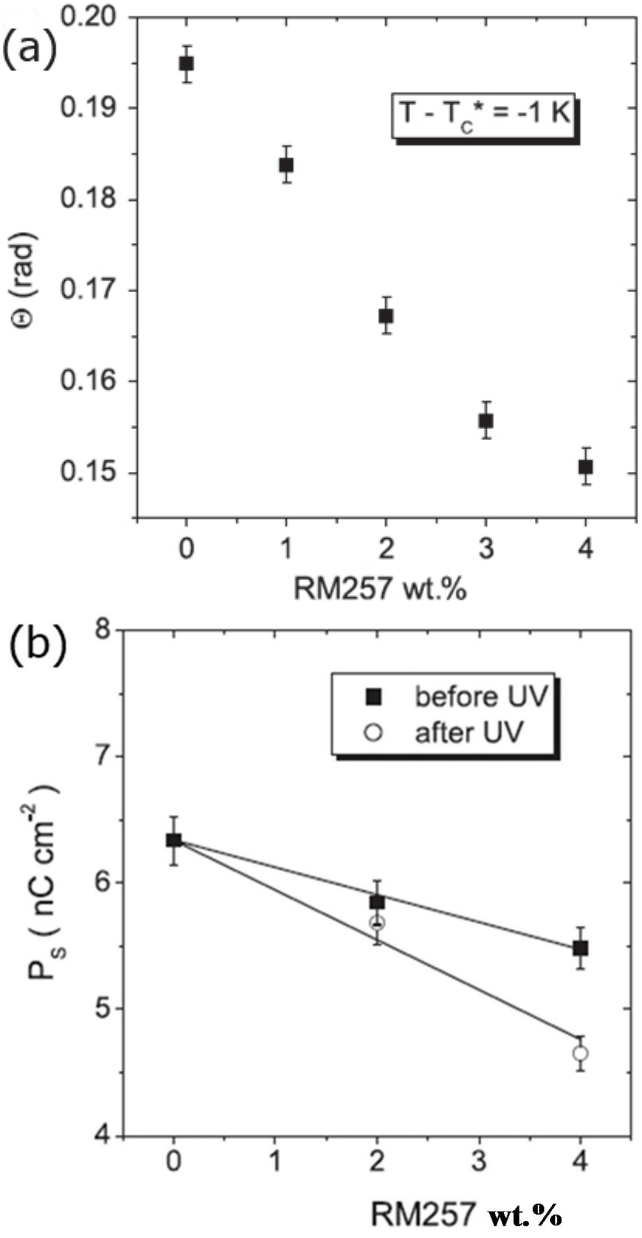

Figure 7. Effect of the polymer network on the electroclinically induced tilt angle in the vicinity of the SmA*–SmC* transition. The electroclinic effect is reduced for increasing polymer content. (Reproduced with permission from [43]. Copyright 2008 Taylor & Francis).

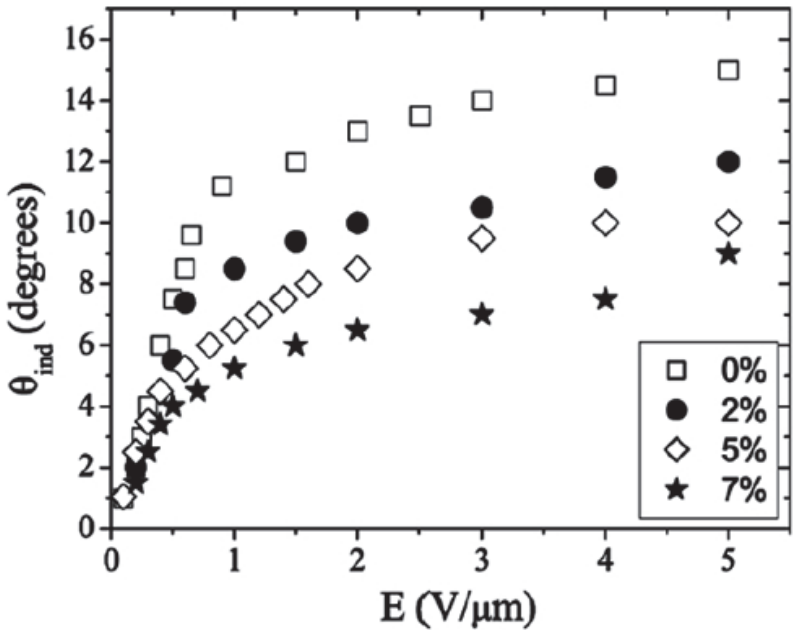

2.2. Landau Coefficients and Interaction Parameter

In physical terms, this behaviour can be described by a generalized Landau model of the SmA* to SmC* transition [45,46], which is extended by an additional factor, describing the interaction between the liquid crystal and the polymer network. In a non-helical FLC device subjected to an electric field, E, the difference in the free energy density between the SmA* and SmC* phase, $g–g_0$, is given by:

$$g - g_0 = \frac{1}{2}\alpha(T - T_C)\Theta^2 + \frac{1}{4}b\Theta^4 + \frac{1}{6}c\Theta^6 + \frac{P^2}{2\varepsilon_0\chi_0} - C\Theta P - \frac{\Omega P^2\Theta^2}{2} - PE \qquad (10)$$

where Θ is the tilt angle, P is the total polarisation, $a = \alpha(T\text{-}T_C)$, b and c are the first three Landau expansion coefficients, C is the bilinear coupling coefficient, χ_0 is the high frequency dielectric susceptibility in the direction of the electric field, Ω is the biquadratic coupling coefficient and T_C is the transition temperature of the related achiral SmA to SmC transition. It should be noted that the Landau description is only valid in the vicinity of the phase transition. Nevertheless, this is the region where the significant changes are observed. For PSFLC systems an additional term is required in the generalised Landau model to take into account the interaction between the polymer network and the liquid crystal. Employing the simple model of Li *et al.* [47] the interaction between the polymer network and the liquid crystal acts to restore the local liquid crystal director to the orientation of the polymer network. They introduced an elastic coupling interaction term, $\frac{1}{2}W_P \sin^2\Theta \approx \frac{1}{2}W_P\Theta^2$, where W_P is the interaction coefficient between the polymer network and the liquid crystal. The free energy density then reads as:

$$g - g_0 = \frac{1}{2}\alpha(T - T_C)\Theta^2 + \frac{1}{2}W_P\Theta^2 + \frac{1}{4}b\Theta^4 + \frac{1}{6}c\Theta^6 + \frac{P^2}{2\varepsilon_0\chi_0} - C\Theta P - \frac{\Omega P^2\Theta^2}{2} - PE \tag{11}$$

Minimisation of the free energy density (Equation (2)) with respect to the total polarisation P leads to the relation [48,49]:

$$P = \frac{C\Theta + E}{\frac{1}{\varepsilon_0\chi_0} - \Omega\Theta^2} \tag{12}$$

Simultaneous fitting of the total polarisation as a function of tilt angle with respect to varying applied electric field amplitude allows the determination of *C*, χ_0 and Ω. Minimisation of Equation (2) with respect to Θ and resubstitution of Equation (3) leads to a temperature-tilt relationship of:

$$T(\Theta, E) = T_C - \frac{1}{\alpha}\left[W_P + b\Theta^2 + c\Theta^4 - \frac{(C\Theta + E)\left(\frac{C}{\varepsilon_0\chi_0} + \Omega\Theta E\right)}{\Theta\left(\frac{1}{\varepsilon_0\chi_0} - \Omega\Theta^2\right)^2}\right] \tag{13}$$

For $T_C \approx T_C^*$ Equation (4) can be directly employed to determine α, b, c and W_P via a second set of simultaneously fitted curves T(Θ,E), using the previously determined parameters C, χ_0 and Ω. One finds that the Landau coefficients are largely unaffected by the introduction of the polymer network, while the elastic coupling coefficient linearly increases for increasing polymer concentration [42,50] (Figure 8). A more thorough analysis, taking into account the physical dimensions of the network shows, that the elastic coupling coefficient depends on polymer concentration and the penetration depth of the elastic forces into the bulk of the liquid crystal. A linear increase of the elastic coupling coefficient with values of the same order of magnitude was also reported by Petit *et al.* [51].

Figure 8. For small concentrations the elastic coupling coefficient between polymer network and liquid crystal increases linearly with increasing network density. (Reproduced with permission from [50]. Copyright 2008 American Physical Society).

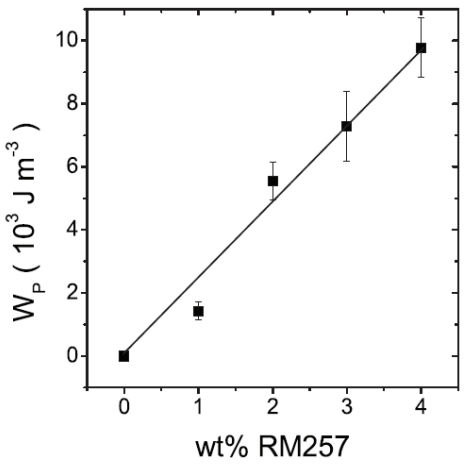

2.3. Response Times and Effective Viscosity

In the ferroelectric SmC* phase the response times exponentially increase for decreasing temperature, which is a plain viscosity effect when observed at equal applied voltages. This behaviour is not changed for PSFLCs. It is generally found that mixing the monomer into the FLC material increases the response times the more monomer is added. This effect is most likely due to the relatively large size of the monomers, despite themselves being liquid crystalline over a certain range of temperature, with the monomer increasing the viscosity of the FLC-monomer mixtures. Subsequent UV polymerization of the monomers and formation of the polymer networks then reduces the effective viscosity and the response times of the PSFLC become shorter, even shorter than those observed for the neat FLC material [44]. It is further found that after polymerization the response times decrease for increasing polymer network concentration, as depicted in Figure 9a. Since the response time τ is directly proportional to the effective viscosity η via $\tau = \eta/P_S E$, the equivalent trend is also observed for the viscosity as a function of polymer network content (Figure 9b). Such behaviour has been reported by several authors [52–55], but it should be pointed out, that results of the opposite behaviour have also been published, *i.e.*, an increase in viscosity with increasing polymer concentration [56].

Figure 9. (**a**) The response time after formation of the polymer network decreases for increasing network density and (**b**) for the effective viscosity a comparable trend is observed. (Reproduced with permission from [44]. Copyright 2009 Institute of Physics).

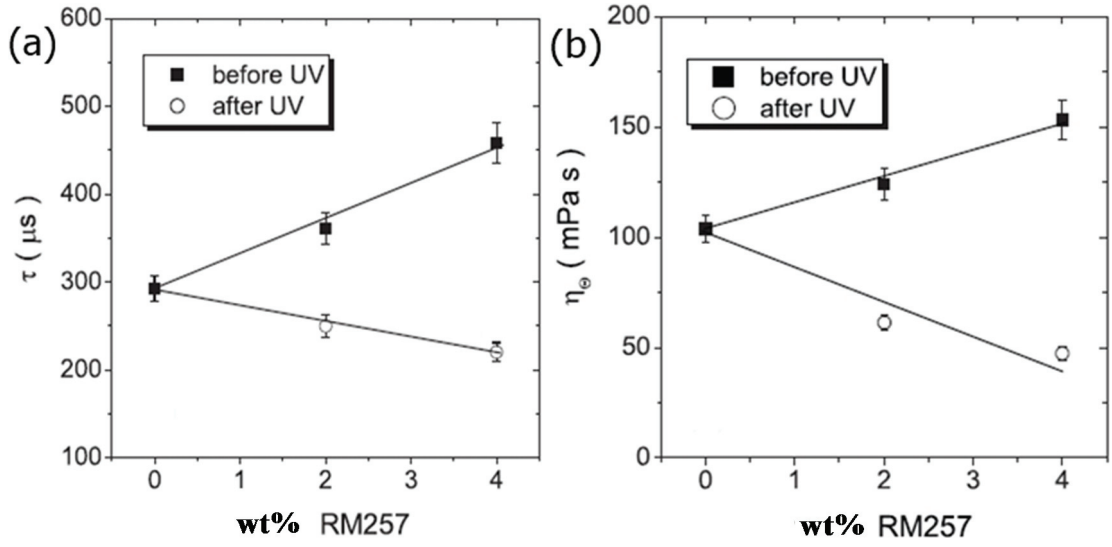

2.4. Dielectric Spectroscopy

The ferroelectric SmC* phase exhibits two major collective dielectric modes, the Goldstone mode and the softmode. The former is related to tilt fluctuations on the cone, while the latter is due to tilt fluctuations changing the value of the tilt angle. It should be noted that the effect of a polymer network on the softmode is in general relatively small [57], while pronounced effects are observed on the Goldstone mode. We will thus focus our discussion on the Goldstone mode, and the collective fluctuations of the director on the tilt cone [58]. Dielectric spectroscopic data is often illustrated in a frequency independent plot of the dielectric absorption ε'' as a function of the dielectric permittivity

ε′, the so called Cole-Cole plot, as it is shown in Figure 10 for different polymer network concentrations. Already here it can be seen that an increase of polymer network density suppresses the Goldstone mode, or more precisely, it decreases the dielectric strength ($\Delta\varepsilon = \varepsilon_0 - \varepsilon_\infty$) for all temperatures in the SmC* phase (Figure 11a), while the relaxation frequency ν_R is increased (Figure 11b). This general behaviour has been reported by numerous authors [53,57–60] and seems to be noncontroversial. It can be explained by the reduction of collective fluctuations due to an increasing density of polymer network, and thus an increase of elastic interactions between liquid crystal and network. The effect of the polymer network is equivalent to that of an application of an electric bias field [58]. The dielectric strength decreases for increasing polymer concentration, because more and more liquid crystal molecules are elastically coupled to the polymer, reducing their collective fluctuations. The relaxation frequency is proportional to the effective elastic constant K_{eff} and inversely proportional to the effective viscosity, $\nu_R \sim K_{eff}/\eta_{eff}$, and thus displays a behaviour as expected with increasing network content.

As mentioned above, the effect of the polymer network on the softmode of a ferroelectric liquid crystal appears to be much less pronounced [57]. The softmode appears at frequencies above the Goldstone mode, and also here a slight decrease of the dielectric strength is observed for increasing network density at equal reduced temperatures, as depicted in Figure 12a, while the relaxation frequency slightly increases (Figure 12b).

Figure 10. Cole-Cole plot, ε″ *versus* ε′, of the dielectric properties for varying polymer network concentration. (Reproduced with permission from [58]. Copyright 2009 EDP Sciences).

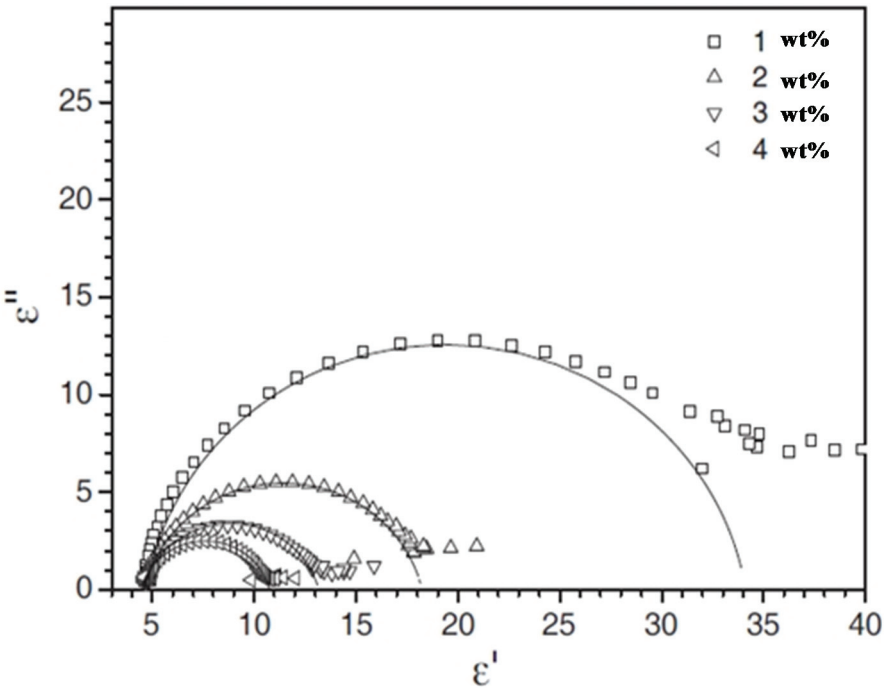

Figure 11. (**a**) The dielectric strength of the Goldstone mode is suppressed for increasing polymer concentration; while (**b**) the relaxation frequency increases with increasing network density. (Reproduced with permission from [58]. Copyright 2009 EDP Sciences).

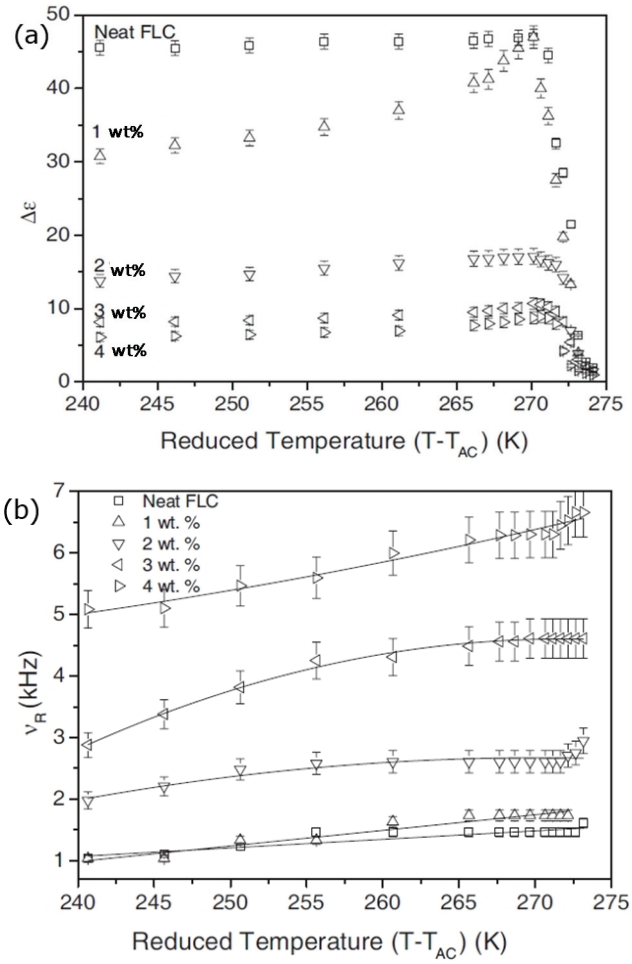

Figure 12. (**a**) Also the softmode dielectric strength is slightly suppressed for increasing polymer concentration; while (**b**) the softmode relaxation frequency slightly increases. (Reproduced with permission from [57]. Copyright 2009 American Physical Society).

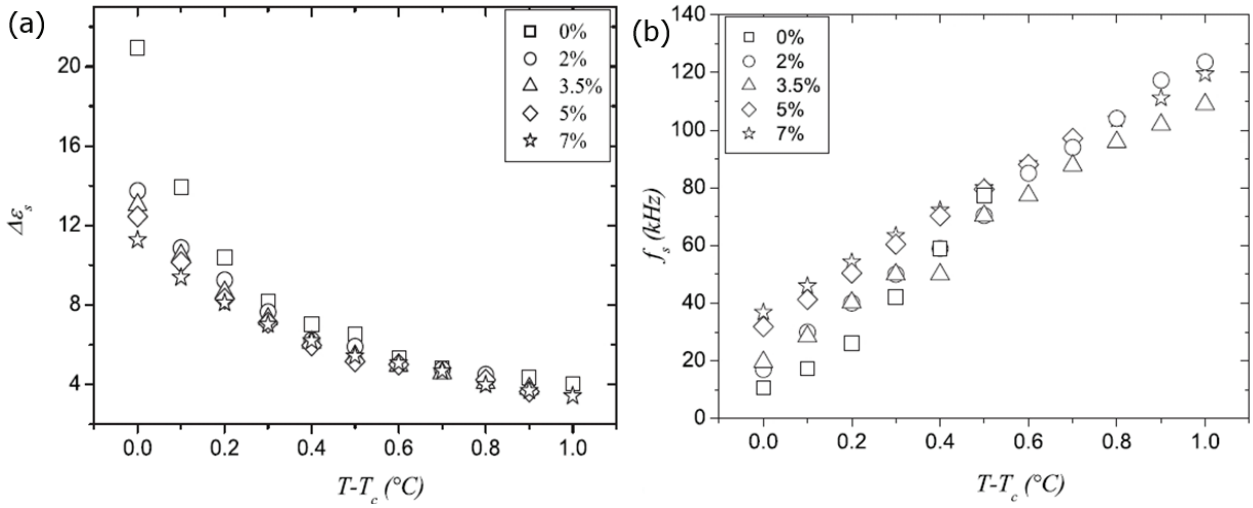

In the context of display applications of FLCs, also the stabilization of the so called V-shaped switching mode, which basically exhibits a thresholdless, linear, hysteresis-free electro-optic response to an applied electric field, is of much interest [61,62]. Stabilizing the texture and electro-optic response of such V-shaped switching has been the focus of numerous papers [47,63–66] on polymer stabilized antiferroelectric liquid crystals. Hysteresis may be observed in certain PSFLC materials, especially for low monomer concentrations, which limits application aspects of these materials. Nevertheless, quite often the hysteresis is small and not of significant relevance.

3. Antiferroelectric Materials

SmC* liquid crystals can not only exhibit a ferroelectric structure with all molecules tilted in the same direction (synclinic), but also an antiferroelectric modification, where molecules of adjacent smectic layers are tilted in the opposite direction (anticlinic, disregarding any helical superstructure in a simplified view). The electro-optic switching of these systems is monostable, as compared to the bistable switching of the ferroelectric phase. The antiferroelectric phase switches from the stable E = 0 V state to either one of the ferroelectric states, depending on the polarity of the applied voltage.

3.1. Calamitic Antiferroelectrics

Antiferroelectricity in liquid crystals is attributed to have been discovered first for rod-like, elongated molecules [67–70]. The director configuration in its simple form is depicted in Figure 13a, together with the standard electro-optic response (Figure 13b). Introduction of a polymer network makes the switching transition between antiferroelectric to ferroelectric states more continuous, which allows for easy gray scale generation [71,72] (see Figure 14), an advantage of the antiferroelectric SmC*$_A$ phase over the ferroelectric SmC* phase, when display applications are considered. Of special interest for display applications are the orthoconic antiferroelectric liquid crystal materials, systems with a tilt angle of 45°, or very close to that value [73,74]. These systems exhibit a very good dark state due to the zero birefringence at these tilt angles. Also in this case, polymer stabilization was used to improve the mechanical stability [75].

Figure 13. (**a**) Schematic structural drawing of an antiferroelectric liquid crystal, without the helical superstructure (Reproduced with permission from [8]. Copyright 2003 Wiley-VCH) and (**b**) standard electro-optic response of the SmC$_A$* phase ((Reproduced with permission from [71]. Copyright 2001 American Chemical Society).

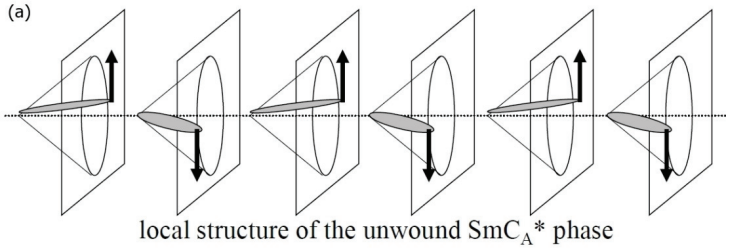

Figure 13. *Cont.*

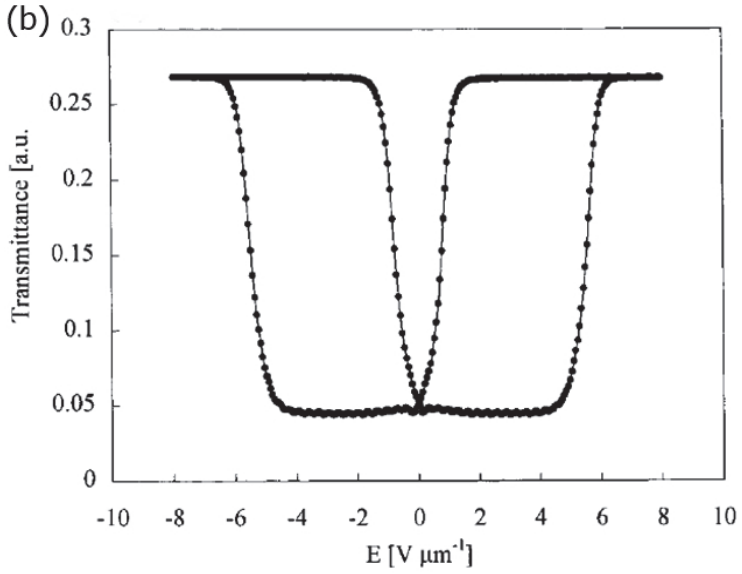

Figure 14. Electro-optic response of a polymer stabilized antiferroelectric liquid crystal, which allows for easier gray scale generation. (Reproduced with permission from [70]. Copyright 1996 American Institute of Physics).

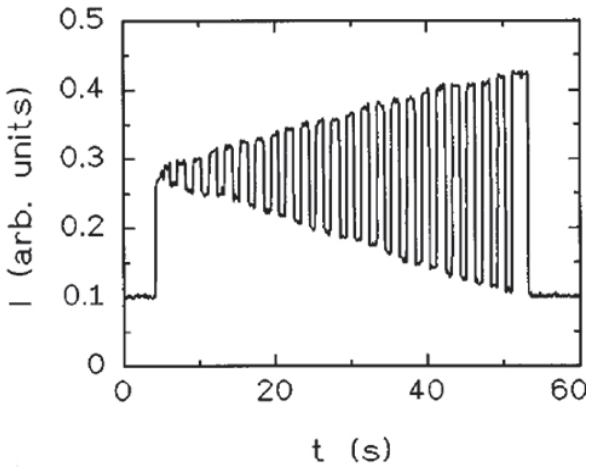

In general, like for ferroelectric liquid crystals, also in antiferroelectric phases the polymer network has an influence on the fundamental material parameters. The contrast of the switching process reduces for increasing polymer concentration, as does the spontaneous polarization. This is due to an effective tilt angle, which is smaller than that observed for the neat liquid crystal, as an increasing amount of molecules contributes less and less to the switching process for increasing network content, due to elastic interactions between liquid crystal and polymer network.

3.2. Bent-Core Antiferroelectrics

Bent-core mesogens form quite remarkable liquid crystal phases [6,7], in so far as structural chirality and chiral effects can be observed from achiral molecules [76]. Alternatively, addition of an achiral bent-core material to a chiral matrix has been shown to increase chirality, for example through the decrease of the cholesteric pitch [77], the occurrence [78] or widening [79] of a Blue

phase, and the increase of the chiral bilinear tilt-polarization coupling coefficient [80,81]. As neat materials, bent-core phases mostly exhibit antiferroelectric properties. One of the largest obstacles in their use for applications is the fact that bent-core phases are notoriously difficult to orient uniformly, thus diminishing their electro-optic response quality. A recent study [82] of the switching performance of polymer stabilized antiferroelectric bent-core phases has revealed a large temperature region, improved alignment ability, and enhanced contrast for such systems. In addition, it was found that the response times decrease for increasing polymer network content, in agreement with results on polymer stabilized ferroelectric liquid crystals.

4. Summary

The basic principles of polymer stabilization of ferroelectric liquid crystals were outlined, and their influence on the most important physical parameters characterized. It was shown that both the tilt angle and the spontaneous polarization effectively decrease with increasing polymer concentration. This was explained by the liquid crystal being partially dominated by the network, not contributing to the switching process, due to elastic binding to the polymer. A Landau analysis provides evidence for this interpretation, because an introduced interaction parameter between liquid crystal molecules and stabilizing polymer network increases linearly with increasing network density at small polymer concentrations. The response times of the polymer stabilized systems are found to be shorter than those of the neat liquid crystal, and decrease with increasing network concentration. This also implies that the effective viscosity of the stabilized system decreases. While the process of polymer stabilization does not exhibit a pronounced effect on the softmode dielectric relaxation, it is clearly observable in the lower frequency Goldstone mode relaxation. The Goldstone mode in general gets suppressed and the dielectric strength reduces with increasing polymer concentration, while the relaxation frequency increases. This behaviour conforms with the interpretation above: elastic binding of the molecules to the network reduces director fluctuations, while it enhances their relaxation frequency. A similar effect of the polymer network as on the parameters of the ferroelectric SmC* phase, can be observed for the antiferroelectric state, independent of whether this state is formed by calamitic or by bent-core mesogens.

Conflicts of Interest

The author declares no conflict of interest.

References

1. Collings, P.J.; Hird, M. *Introduction to Liquid Crystals: Chemistry and Physics*; Taylor & Francis: London, UK, 1997.
2. Chandrasekhar, S. *Liquid Crystals*, 2nd ed.; Cambridge University Press: Cambridge, UK, 1992.
3. De Gennes, P.G.; Prost, J. *The Physics of Liquid Crystals*, 2nd ed.; Clarendon Press: Oxford, UK, 1993.
4. Figueiredo Neto, A.M.; Salinas, S.R.A. *The Physics of Lyotropic Liquid Crystals*; Oxford University Press: Oxford, UK, 2005.

5. Petrov, A.G. *The Lyotropic State of Matter*; Gordon and Breach: New York, NY, USA, 1999.
6. Pelzl, G.; Diele, S.; Weissflog, W. Banana-shaped compounds—A new field of liquid crystals. *Adv. Mater.* **1999**, *11*, 707–724.
7. Takezoe, H.; Takanishi, Y. Bent-core liquid crystals: Their mysterious and attractive world. *Jpn. J. Appl. Phys.* **2006**, *45*, 597–625.
8. Dierking, I. *Textures of Liquid Crystals*; Wiley-VCH: Weinheim, Germany, 2003.
9. Lagerwall, S.T. *Ferroelectric and Antiferroelectric Liquid Crystals*; Wiley-VCH: Weinheim, Germany, 1999.
10. Musevic, I.; Blinc, R.; Zeks, B. *The Physics of Ferroelectric and Antiferroelectric Liquid Crystals*; World Scientific: Singapore, 2000.
11. Crooker, P.P. Chapter 7. Blue Phases. *Chirality in Liquid Crystals*; Kitzerow, H.-S., Bahr, C., Eds.; Springer Verlag: Berlin, Germany, 2001.
12. Kitzerow, H.-S. Chapter 10. Twist Grain Boundary Phases. *Chirality in Liquid Crystals*; Kitzerow, H.-S., Bahr, C., Eds.; Springer Verlag: Berlin, Germany, 2001.
13. De Vries, H. Rotatory power and other optical properties of certain liquid crystals. *Acta Crystallogr.* **1951**, *4*, 219–226.
14. Garoff, S.; Meyer, R.B. Electroclinic effect at the ac phase change in a chiral smectic liquid crystal. *Phys. Rev. Lett.* **1977**, *38*, doi:10.1103/PhysRevLett.38.848.
15. Garoff, S.; Meyer, R.B. Electroclinic effect at the ac phase change in a chiral smectic liquid crystal. *Phys. Rev. A* **1979**, *19*, doi:10.1103/PhysRevA.19.33.
16. Meyer, R.B.; Liebert, L.; Strzelecki, L.; Keller, P. Ferroelectric liquid crystals. *J. Phys. Lett.* **1975**, *36*, 69–71.
17. Clark, N.A.; Lagerwall, S.T. Submicrosecond bistable electro-optic switching in liquid crystals. *Appl. Phys. Lett.* **1980**, *36*, 899–901.
18. Crawford, G.P.; Zumer, S. Liquid Crystals in Complex Geometries: Formed by Polymer and Porous Networks; Taylor & Francis: London, UK, 1996.
19. Broer, D.J.; Crawford, G.P.; Zumer, S. *Cross-Linked Liquid Crystalline Systems*; CRC Press: Boca Raton, FL, USA, 2011.
20. Hikmet, R.A.M. Electrically induced light scattering from anisotropic gels. *J. Appl. Phys.* **1990**, *68*, 4406–4414.
21. Fung, Y.K.; Yang, D.-K.; Ying, S.; Chien, L.-C.; Zumer, S.; Doane, J.W. Polymer networks formed in liquid crystals. *Liq. Cryst.* **1995**, *19*, 797–801.
22. Hikmet, R.A.M. Anisotropic gels and plasticized networks formed by liquid crystal molecules. *Liq. Cryst.* **1991**, *9*, 405–416.
23. Hikmet, R.A.M. Anisotropic gels in liquid crystal devices. *Adv. Mater.* **1992**, *4*, 679–683.
24. Fung, Y.K.; Borstnik, A. Zumer, S.; Yang, D.-K.; Doane, J.W. Pretransitional nematic ordering in liquid crystals with dispersed polymer networks. *Phys. Rev. E* **1997**, *55*, 1637–1645.
25. Yang, D.-K.; Chien, L.-C.; Doane, J.W. Cholesteric liquid crystal/polymer dispersion for haze-free light shutters. *Appl. Phys. Lett.* **1992**, *60*, 3102.
26. Dierking, I. Polymer network—Stabilized liquid crystals. *Adv. Mater.* **2000**, *12*, 167–181.
27. Rajaram, C.V.; Hudson, S.D.; Chien, L.-C. Morphology of polymer-stabilized liquid crystals. *Chem. Mater.* **1995**, *7*, 2300–2308.

28. Dierking, I.; Kosbar, L.L.; Afazali-Ardakani, A.; Lowe, A.C.; Held, G.A. Network morphology of polymer stabilized liquid crystals. *Appl. Phys. Lett.* **1997**, *71*, 2454–2456.
29. Dierking, I.; Kosbar, L.L.; Lowe, A.C.; Held, G.A. Polymer network structure and electro-optic performance of polymer stabilized cholesteric textures. I. The influence of curing temperature. *Liq. Cryst.* **1998**, *24*, 387–395.
30. Held, G.A.; Kosbar, L.L.; Dierking, I.; Lowe, A.C., Grinstein, G.; Lee, V.; Miller, R.D. Confocal microscopy study of texture transitions in a polymer stabilized cholesteric liquid crystal. *Phys. Rev. Lett.* **1997**, *79*, 3443–3446.
31. Dierking, I.; Kosbar, L.L.; Lowe, A.C.; Held, G.A. Polymer network structure and electro-optic performance of polymer stabilized cholesteric textures II. The effect of UV curing conditions. *Liq. Cryst.* **1998**, *24*, 397–406.
32. Fuh, A.Y.-G.; Tsai, M.-S.; Huang, C.-Y. Polymer network formed in liquid crystals: Polymer-network-induced birefringence in liquid crystals. *Jpn. J. Appl. Phys.* **1996**, *35*, 3960–3963.
33. Dierking, I.; Kosbar, L.L.; Afzali-Ardakani, A.; Lowe, A.C.; Held, G.A. Two-stage switching behavior of polymer stabilized cholesteric textures. *J. Appl. Phys.* **1997**, *81*, 3007–3014.
34. Mitov, M.; Dessaud, N. Going beyond the reflectance limit of cholesteric liquid crystals. *Nat. Mater.* **2006**, *5*, 361–364.
35. Dierking, I. Recent developments in polymer stabilised liquid crystals. *Polym. Chem.* **2010**, *1*, 1153–1159.
36. Archer, P.; Dierking, I. Polymer stabilisation of twisted smectic liquid crystal defect states. *Soft Matter* **2009**, *5*, 835–841.
37. Dierking, I.; Archer, P. Imaging liquid crystal defects. *RSC Advances* **2013**, *3*, 26433.
38. Hikmet, R.A.M.; Lub, J. Anisotropic networks with stable dipole orientation obtained by photopolymerization in the ferroelectric state. *J. Appl. Phys.* **1995**, *77*, 6234–6238.
39. Hikmet, R.A.M.; Michielsen, M. Anisotropic network stabilized ferroelectric gels. *Adv. Mater.* **1995**, *7*, 300–304.
40. Hikmet, R.A.M.; Boots, H.M.J.; Michielsen, M. Ferroelectric liquid crystal gels Network stabilized ferroelectric display. *Liq. Cryst.* **1995**, *19*, 65–76.
41. Guymon, C.A.; Hoggan, E.N.; Walba, D.M.; Clark, N.A.; Bowman, C.N. Phase behaviour and electro-optic characteristics of a polymer stabilized ferroelectric liquid crystal. *Liq. Cryst.* **1995**, *19*, 719–727.
42. Archer, P.; Dierking, I. Elastic coupling in polymer stabilized ferroelectric liquid crystals. *J. Phys. D* **2008**, *41*, doi:10.1088/0022-3727/41/15/155422.
43. Petit, M.; Daoudi, A.; Ismaili, M.; Buisine, J.M.; Da Costa, A. Effect of the polymer network density formed in short pitch ferroelectric liquid crystal on the electroclinic effect. *Mol. Cryst. Liq. Cryst.* **2008**, *487*, 61–73.
44. Archer, P.; Dierking, I. Electro-optic properties of polymer-stabilized ferroelectric liquid crystals before, during and after photo-polymerization. *J. Opt. A* **2009**, *11*, doi:10.1088/1464-4258/11/2/024022.

45. Zeks, B. Landau free energy expansion for chiral ferroelectric smectic liquid crystals. *Mol. Cryst. Liq. Cryst.* **1984**, *114*, 259–270.
46. Carlsson, T.; Zeks, B.; Levstik, A.; Filipic, C.; Levstik, I.; Blinc, R. Generalized Landau model of ferroelectric liquid crystals. *Phys. Rev. A* **1987**, *36*, 1484–1487.
47. Li, J.; Zhu, X.; Xuan, L.; Huan, X. "V-Shaped" electro-optic characteristics in FLC gels. *Ferroelectrics* **2002**, *277*, 85–105.
48. Gieβelmann, F.; Zugenmaier, P. Mean-field coefficients and the electroclinic effect of a ferroelectric liquid crystal. *Phys. Rev. E* **1995**, *52*, 1762–1772.
49. Gieβelmann, F.; Heimann, A.; Zugenmaier, P. Experimental determination of Landau-expansion coefficients in ferroelectric liquid crystals. *Ferroelectrics* **1997**, *200*, 237–256.
50. Archer, P.; Dierking, I.; Osipov, M.A. Landau model for polymer-stabilized ferroelectric liquid crystals: Experiment and theory. *Phys. Rev. E* **2008**, *78*, doi:10.1103/PhysRevE.78.051703.
51. Petit, M.; Daoudi, A.; Ismaili, M.; Buisine, J.M. Distortion and unwinding of the helical structure in polymer-stabilized short-pitch ferroelectric liquid crystal. *Eur. Phys. J. E* **2006**, *20*, 327–333.
52. Pirs, J.; Bos, P.; Petkovšek, R.; Kralj, S.; Pirš, S.; Zumer, S.; Matuszczyk, T. Influence of the polymer network on the switching behaviors in the polymer stabilized ferroelectric liquid crystals. *Jpn. J. Appl. Phys.* **2002**, *41*, 6011–6015.
53. Manohar, R.; Yadav, S.P.; Pandey, K.K.; Srivastava, A.K.; Misra, A.K. Comparative study of dielectric and electro-optical properties of pure and polymer ferroelectric liquid crystal composites. *J. Polym. Res.* **2011**, *18*, 435–441.
54. Zheng, W.J. Article title. *Mol. Cryst. Liq. Cryst.* **2007**, *475*, 173–181.
55. Beckel, E.R.; Cramer, N.B.; Harant, A.W.; Bowman, C.N. Electro-optic properties of thiol-ene polymer stabilized ferroelectric liquid crystals. *Liq. Cryst.* **2003**, *30*, 1343–1350.
56. Guymon, C.A.; Dougan, L.A.; Martens, P.J.; Clark, N.A.; Walba, D.M.; Bowman, C.N. Polymerization conditions and electrooptic properties of polymer-stabilized ferroelectric liquid crystals. *Chem. Mater.* **1998**, *10*, 2378–2388.
57. Petit, M.; Hemine, J.; Daoudi, A.; Ismaili, M.; Buisine, J.M.; Da Costa, A. Effect of the network density on dynamics of the soft and the Goldstone modes in short-pitch ferroelectric liquid crystals stabilized by an anisotropic polymer network. *Phys. Rev. E* **2009**, *79*, doi:10.1103/PhysRevE.79.031705.
58. Kaur, S.; Dierking, I.; Gleeson, H.F. Dielectric spectroscopy of polymer stabilised ferroelectric liquid crystals. *Eur. Phys. J. E* **2009**, *30*, 265–274.
59. Cherfi, Y.; Hemine, J.; Douali, R.; Beldjoudi, N.; Ismaili, M.; Leblond, J.; Legrand, C.; Daoudi, A. Linear and non-linear dielectric properties of a short-pitch ferroelectric liquid crystal stabilized by a polymer network. *Eur. Phys. J. E* **2010**, *33*, 335–342.
60. Kundu, S.; Nayek, P.; Ray, T.; Majumder, T.P.; Roy, S.K.; Kobayashi, S. Influence of network stabilization on the dielectric and electrooptical properties of ferroelectric liquid crystal FELIX-M4851/100. *Jpn. J. Appl. Phys.* **2009**, *48*, doi:10.1143/JJAP.48.061501.

61. Rudquist, P.; Lagerwall, J.P.F.; Buivydas, M.; Gouda, F.; Lagerwall, S.T.; Clark, N.A.; Maclennan, J.E.; Shao, R.; Coleman, D.A.; Bardon, S.; *et al*. The case of thresholdless antiferroelectricity: Polarization-stabilized twisted SmC* liquid crystals give V-shaped electro-optic response. *J. Mater. Chem.* **1999**, *9*, 1257–1261.
62. Blinov, L.M.; Pozhidaev, E.P.; Podgornov, F.V.; Pikin, S.A.; Palto, S.P.; Sinha, A.; Yasuda, A.; Hashimoto, S.; Haase, W. "Thresholdless" hysteresis-free switching as an apparent phenomenon of surface stabilized ferroelectric liquid crystal cells. *Phys. Rev. E* **2002**, *66*, doi:10.1103/PhysRevE.66.021701.
63. Li, J.; Wang, Z.; Cai, Y.; Huang, X. Study of EO properties of polymer network stabilized ferroelectric liquid crystal in smectic C* phase. *Ferroelectrics* **1998**, *213*, 91–99.
64. Shikada, M.; Tanaka, Y.; Xu, J.; Furuichi, K.; Hasebe, H.; Takatsu, H.; Kobayashi, S. Novel mesogenic polymer stabilized ferroelectric liquid crystal display device exhibiting V-shaped electrooptic characteristics. *Jpn. J. Appl. Phys.* **2001**, *40*, 5008–5010.
65. Furue, H.; Koizumi, Y.; Hatano, J.; Yokoyama, H. Molecular alignment structure and switching of a ferroelectric liquid crystal stabilized by a polymer network created in the SmA phase. *Mol. Cryst. Liq. Cryst.* **2005**, *437*, 1439–1446.
66. Pozhidaev, E.; Chgrinov, V.; Hegde, G.; Xu, P.Z. Multistable electro-optical modes in ferroelectric liquid crystals. *J. Soc. Inf. Disp.* **2009**, *17*, 53–59.
67. Beresnev, L.A.; Blinov, L.M.; Baikalov, V.A.; Pozhidayev, E.P.; Purvanetskas, G.V.; Pavluchenko, A.I. Ferroelectricity in tilted smectics doped with optically active additives. *Mol. Cryst. Liq. Cryst.* **1982**, *89*, 327–338.
68. Levelut, A.M.; Germain, C.; Keller, P.; Liebert, L.; Billard, J. Two new mesophases in a chiral compound. *J. Phys. Fr.* **1983**, *44*, 623–629.
69. Galerne, Y.; Liebert, L. Antiferroelectric chiral smectic-O* liquid crystal. *Phys. Rev. Lett.* **1991**, *66*, 2891–2895.
70. Chandani, A.D.L.; Hagiwara, T.; Suzuki, Y.; Ouchi, Y.; Takezoe, H.; Fukuda, A. Tristable switching in surface stabilized ferroelectric liquid crystals with a large spontaneous polarization. Article title. *Jpn. J. Appl. Phys. Lett.* **1988**, *27*, L729–L732.
71. Strauss, J.; Kitzerow, H.-S. Gray-scale in polymer-stabilized antiferroelectric liquid crystal displays. *Appl. Phys. Lett.* **1996**, *69*, doi:10.1063/1.117871.
72. Artal, M.C.; Ros, M.B.; Serrano, J.L. Antiferroelectric liquid-crystal gels. *Chem. Mater.* **2001**, *13*, 2056–2067.
73. Lagerwall, S.T.; Dahlgren, A.; Jagemalm, P.; Rudquist, P.; D'have, K.; Pauwels, H.; Dabrowski, R.; Drzewinski, W. Unique electro-optical properties of liquid crystals designed for molecular optics. *Adv. Funct. Mater.* **2001**, *11*, 87–94.
74. Rudquist, P. Orthoconic antiferroelectric liquid crystals. *Liq. Cryst.* **2013**, *40*, 1678–1697.
75. Rudquist, P.; Elfstrom, D.; Lagerwall, S.T.; Dabrovski, R. Polymer-Stabilized orthoconic anti-ferroelectric liquid crystals. *Ferroelectrics* **2006**, *344*, 177–188.
76. Link, D.R.; Natale, G.; Shao, R.; Maclennan, J.E.; Clark, N.A.; Korblova, E.; Walba, D.M. Spontaneous formation of macroscopic chiral domains in a fluid smectic phase of achiral molecules. *Science* **1997**, *278*, 1924–1927.

77. Gorecka, E.; Cepic, M.; Mieczkowski, J.; Nakata, M.; Takezoe, H.; Zeks, B. Enhanced chirality by adding achiral molecules into the chiral system. *Phys. Rev. E* **2003**, *67*, doi:10.1103/PhysRevE.67.061704.
78. Nakata, M.; Takanishi, Y.; Watanabe, J.; Takezoe, H. Blue phases induced by doping chiral nematic liquid crystals with nonchiral molecules. *Phys. Rev. E* **2003**, *68*, doi:10.1103/PhysRevE.68.041710.
79. Dierking, I.; Blenkhorn, W.; Credland, E.; Drake, W.; Kociuruba, R.; Kayser, B.; Michael, T. Stabilising liquid crystalline blue phases. *Soft Matter* **2012**, *8*, 4355–4362.
80. Archer, P.; Dierking, I. Experimental determination of the full Landau potential of bent-core doped ferroelectric liquid crystals. *Phys. Rev. E* **2005**, *72*, doi:10.1103/PhysRevE.72.041713.
81. Archer, P.; Dierking, I. Chirality enhancement through addition of achiral molecules. *Chem. Commun.* **2010**, *46*, 1467–1469.
82. Atorf, B.; Hoischen, A.; Ros, M.B.; Gimeno, N.; Tschierske, C.; Dantlgraber, G.; Kitzerow, H. Switching performance of a polymer-stabilized antiferroelectric liquid crystal based on bent-core molecules. *Appl. Phys. Lett.* **2012**, *100*, 223301:1–223301:4.

Optical Properties of Electrically Tunable Two-Dimensional Photonic Lattice Structures Formed in a Holographic Polymer-Dispersed Liquid Crystal Film: Analysis and Experiment †

Mayu Miki, Ryuichiro Ohira and Yasuo Tomita

Abstract: We report on theoretical and experimental investigations of optical wave propagations in two-dimensional photonic lattice structures formed in a holographic polymer-dispersed liquid crystal (HPDLC) film. In the theoretical analysis we employed the 2×2 matrix formulation and the statistical thermodynamics model to analyze the formation of anisotropic photonic lattice structures by holographic polymerization. The influence of multiple reflections inside an HPDLC film on the formed refractive index distribution was taken into account in the analysis. In the experiment we fabricated two-dimensional photonic lattice structures in an HPDLC film under three-beam interference holographic polymerization and performed optical measurements of spectral transmittances and wavelength dispersion. We also demonstrated the electrical control capability of the fabricated photonic lattice structure and its dependence on incident wave polarization. These measured results were compared with the calculated ones by means of photonic band and beam propagation calculations.

Reprinted from *Materials*. Cite as: Miki, M.; Ohira, R.; Tomita, Y. Optical Properties of Electrically Tunable Two-Dimensional Photonic Lattice Structures Formed in a Holographic Polymer-Dispersed Liquid Crystal Film: Analysis and Experiment †. *Materials* **2014**, *7*, 74–95.

1. Introduction

Electro-optic photopolymer-liquid crystal (LC) composites known as holographic polymer-dispersed liquid crystals (HPDLCs) consist of LCs doped into photopolymer followed by holographic polymerization that represents a fast and relatively simple way of fabricating Bragg grating structures [1–4]. Because of the extremely large electro-optic response and the large optical anisotropy of LCs, HPDLCs have shown promises for electrically switchable Bragg grating devices including optical beam switching/control devices, lasers, optical memory and photonic crystals (PhCs) [5–9]. A different type of HPDLCs, polymer liquid-crystal polymer slices (POLICRYPS) or polymer liquid crystal polymer holograms electrically manageable (POLIPHEM) structures that can be fabricated above the LC nematic-isotropic transition temperature, has also been developed [10,11]. Because of their low light scattering properties as compared with HPDLCs possessing LC droplets they have also been used for various photonic applications [12–14]. Among reported device applications PhCs [15–18] possessing dielectric periodic structures in 2D and 3D space have been of great interest since they exhibit photonic band gaps (PBGs) in the optical spectrum. Such PBGs provide the strong control of light propagation in such a way that optical

waves at certain wavelengths are either inhibited or confined in PhCs. The fabrication of PhCs using inorganic materials has already reached a mature state of evolution [17,19–22]. Inorganic semiconductor materials particularly possess high refractive indices and low absorption in the near-infrared spectral region, potentially exhibiting full PBGs. However, they typically lack the ease of active modification of PBGs for electrical or optical control of propagating light in PhCs, which are prerequisites for many photonic device elements. On the other hand, PhCs with LC-doped organic materials such as HPDLCs and POLICRYPS/POLIPHEM have the possibility of electrically tuning PBGs and therefore are interesting and viable candidates for tunable PhCs, although they do not possess a full potential PBGs owing to their much lower refractive index contrast than those with inorganic materials. So far, various organic PhC structures with HPDLCs have been realized by holographic polymerization [3,4] for electrical switching and lasing actions [23–32]. Moreover, interesting observations of strong wavelength dispersion and unusual refraction from a 2D honeycomb PhC fabricated by three-beam interference holographic polymerization in HPDLCs have been reported [33,34]. It was found that refraction angles due to the wavelength dispersion were strongly dependent on incident light wavelengths and angles. However, the electrical control capability with such a 2D honeycomb PhC has not been fully explored yet. In addition, it is an open question how PhC structures and their optical properties are altered with holographic polymerization when non-absorptive but reflective indium-tin oxide (ITO) electrodes on both sides of an HPDLC film exist for the electrical control. The 2D honeycomb photonic lattice structure is also interesting from a viewpoint of an optical analogue of graphene, a monolayer of graphite, in solid-state physics [35,36], by which new optical phenomena have been reported [37–42].

In this paper we describe theoretical and experimental investigations of the optical properties of electrically controllable 2D honeycomb (graphene)-type PhCs with HPDLCs. We employ the 2×2 matrix formulation [43] and the statistical thermodynamic model [44,45] to calculate light-intensity interference distributions and the corresponding anisotropic refractive index distributions in an HPDLC film under three-beam interference holographic exposure. The effect of multiple reflections recorded in an HPDLC film sandwiched between ITO-electrode loaded glass substrates on the formed interference pattern and the refractive index distribution is taken into account in the theoretical analysis. Experimental results of strong polarization-dependent spectral transmittances and wavelength-dependent refraction as well as their electrical control are also presented and are compared with the theoretical calculation.

2. Theoretical

2.1. Transfer Matrix Formulation

Let us consider holographic polymerization of a photosensitive film in a sample cell by mutually coherent three plane-wave beams at co-polarizations as shown in Figure 1. In our case the sample cell contains a thin film of HPDLC mixture sandwiched between two coplanar glass substrates on which non-absorptive but reflective ITO electrodes are deposited for an electric field application to the HPDLC film. In order to take the effect of multiple reflections between two ITO electrodes on

the light-intensity interference distribution into account, we employ the 2×2 matrix formulation for isotropic layered media [43]. For the sake of simplicity we assume that nematic LCs mixed with host monomer were randomly oriented (*i.e.*, optically isotropic) before and during curing. This assumption may not be exactly correct in the LC-rich regions where LCs may undergo the nematic ordering along a preferred direction so that the HPDLC film becomes optically anisotropic. This happens when the volume fraction of LCs diffusing into the dark illuminated regions exceeds 0.8∼0.9 during curing [46]. However, it would be legitimate to use the 2×2 matrix formulation in our analysis since the nematic reorientation process substantively occurs in the last half of the whole curing period where the conversion of monomer to polymer has substantively exceeded 50% [46].

Figure 1. (**a**) Configuration of three-beam interference holographic polymerization and (**b**) its wave number (**k**-space) representation.

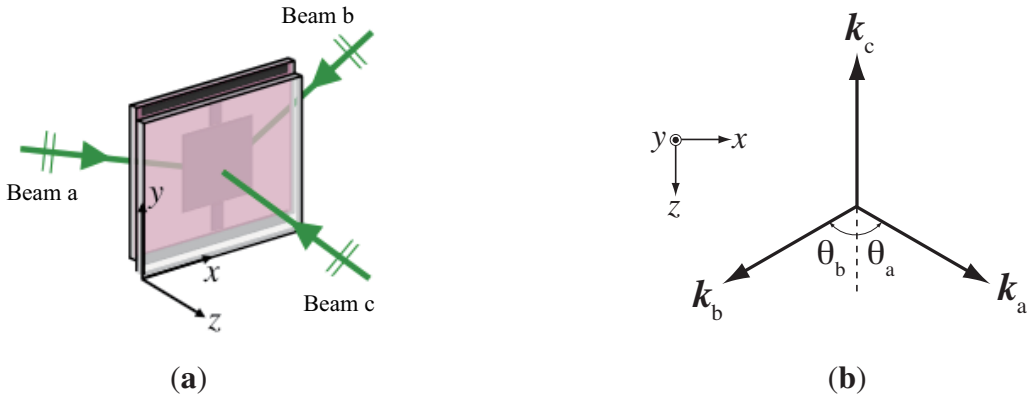

(**a**) (**b**)

Figure 2 shows a three-layer system sandwiched between two glass substrates that are treated as semi-infinite layers, where the x-z plane forms the plane of incidence as shown in Figure 1. In Figure 2 $A(z)$ and $B(z)$ correspond to amplitudes of right- and left-traveling waves, respectively, along the z direction in each layer.

Figure 2. Three-layer system for the analysis.

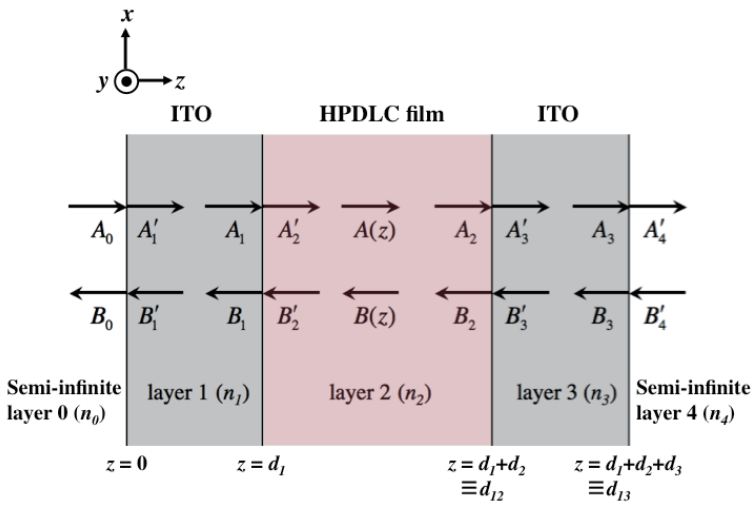

Also, $A_{\ell-1}$ and B'_ℓ (A'_ℓ and $B_{\ell-1}$) of right- and left-traveling waves denote amplitudes incident on (transmitted through) the interface between the $(\ell-1)$th and the ℓth layers, respectively. Therefore, the following boundary conditions are given:

$$\begin{aligned}
&A_0 = A(0^-), \quad B_0 = B(0^-), \quad A'_1 = A(0^+), \quad B'_1 = B(0^+),\\
&A_1 = A(d_1^-), \quad B_1 = B(d_1^-), \quad A'_2 = A(d_1^+), \quad B'_2 = B(d_1^+),\\
&A_2 = A(d_{12}^-), \quad B_2 = B(d_{12}^-), \quad A'_3 = A(d_{12}^+), \quad B'_3 = B(d_{12}^+),\\
&A_3 = A(d_{13}^-), \quad B_3 = B(d_{13}^-), \quad A'_4 = A(d_{13}^+), \quad B'_4 = B(d_{13}^+),
\end{aligned} \tag{1}$$

where z^- (z^+) denotes the left (right) side of the interface at z, and d_{12} and d_{13} stand for $d_1 + d_2$ and $d_1 + d_2 + d_3$, respectively. Using the 2×2 matrix formulation, we can relate the amplitudes A_0 and B_0 to the amplitudes A'_4 and B'_4 as

$$\begin{bmatrix} A_0 \\ B_0 \end{bmatrix} = M_1 P_2 M_3 \begin{bmatrix} A'_4 \\ B'_4 \end{bmatrix}. \tag{2}$$

In Equation (2) P_2 is a propagation matrix that accounts for the propagation through the bulk of the 2nd layer (*i.e.*, the HPDLC film). Its general form for the lth layer $(l = 1, 2, 3)$ is given by

$$P_l = \begin{bmatrix} e^{i\phi_l} & 0 \\ 0 & e^{-i\phi_l} \end{bmatrix}, \tag{3}$$

where ϕ_l is a phase shift for the lth layer of thickness d_l and is given by $k_{lz} d_l$. Here k_{lz} is the z component of the wavenumber k_l given by

$$k_{lz} = n_l \frac{2\pi}{\lambda} \cos\theta_l, \tag{4}$$

where n_l is the refractive index of the lth layer, λ is a wavelength in vacuum, and θ_l is the ray angle with respect to the z axis in the lth layer. In Equation (2) a 2×2 transfer matrix M_l for the lth layer $(l = 1, 3)$ is given by [43]

$$M_l = \begin{bmatrix} (m_l)_{11} & (m_l)_{12} \\ (m_l)_{21} & (m_l)_{22} \end{bmatrix} \tag{5}$$

for s waves with

$$\begin{aligned}
(m_l)_{11} &= \frac{1}{2}\left(1 + \frac{n_{l+1}\cos\theta_{l+1}}{n_{l-1}\cos\theta_{l-1}}\right)\cos\phi_l + \frac{i}{2}\left(\frac{n_l\cos\theta_l}{n_{l-1}\cos\theta_{l-1}} + \frac{n_{l+1}\cos\theta_{l+1}}{n_l\cos\theta_l}\right)\sin\phi_l,\\
(m_l)_{12} &= \frac{1}{2}\left(1 - \frac{n_{l+1}\cos\theta_{l+1}}{n_{l-1}\cos\theta_{l-1}}\right)\cos\phi_l + \frac{i}{2}\left(\frac{n_l\cos\theta_l}{n_{l-1}\cos\theta_{l-1}} - \frac{n_{l+1}\cos\theta_{l+1}}{n_l\cos\theta_l}\right)\sin\phi_l,\\
(m_l)_{21} &= \frac{1}{2}\left(1 - \frac{n_{l+1}\cos\theta_{l+1}}{n_{l-1}\cos\theta_{l-1}}\right)\cos\phi_l - \frac{i}{2}\left(\frac{n_l\cos\theta_l}{n_{l-1}\cos\theta_{l-1}} - \frac{n_{l+1}\cos\theta_{l+1}}{n_l\cos\theta_l}\right)\sin\phi_l,\\
(m_l)_{22} &= \frac{1}{2}\left(1 + \frac{n_{l+1}\cos\theta_{l+1}}{n_{l-1}\cos\theta_{l-1}}\right)\cos\phi_l - \frac{i}{2}\left(\frac{n_l\cos\theta_l}{n_{l-1}\cos\theta_{l-1}} + \frac{n_{l+1}\cos\theta_{l+1}}{n_l\cos\theta_l}\right)\sin\phi_l,
\end{aligned} \tag{6}$$

and for p waves with

$$
\begin{aligned}
(m_l)_{11} &= \frac{1}{2}\left(\frac{\cos\theta_{l+1}}{\cos\theta_{l-1}} + \frac{n_{l+1}}{n_{l-1}}\right)\cos\phi_l + \frac{i}{2}\left(\frac{n_l\cos\theta_{l+1}}{n_{l-1}\cos\theta_l} + \frac{n_{l+1}\cos\theta_l}{n_l\cos\theta_{l-1}}\right)\sin\phi_l,\\
(m_l)_{12} &= \frac{1}{2}\left(\frac{\cos\theta_{l+1}}{\cos\theta_{l-1}} - \frac{n_{l+1}}{n_{l-1}}\right)\cos\phi_l + \frac{i}{2}\left(\frac{n_l\cos\theta_{l+1}}{n_{l-1}\cos\theta_l} - \frac{n_{l+1}\cos\theta_l}{n_l\cos\theta_{l-1}}\right)\sin\phi_l,\\
(m_l)_{21} &= \frac{1}{2}\left(\frac{\cos\theta_{l+1}}{\cos\theta_{l-1}} - \frac{n_{l+1}}{n_{l-1}}\right)\cos\phi_l - \frac{i}{2}\left(\frac{n_l\cos\theta_{l+1}}{n_{l-1}\cos\theta_l} - \frac{n_{l+1}\cos\theta_l}{n_l\cos\theta_{l-1}}\right)\sin\phi_l,\\
(m_l)_{22} &= \frac{1}{2}\left(\frac{\cos\theta_{l+1}}{\cos\theta_{l-1}} + \frac{n_{l+1}}{n_{l-1}}\right)\cos\phi_l - \frac{i}{2}\left(\frac{n_l\cos\theta_{l+1}}{n_{l-1}\cos\theta_l} + \frac{n_l\cos\theta_l}{n_{l-1}\cos\theta_{l-1}}\right)\sin\phi_l. \qquad (7)
\end{aligned}
$$

The amplitudes $A(z)$ and $B(z)$ in $d_1 \le z \le d_{12}$ and the amplitudes A'_4 and B'_4 are related as

$$
\begin{bmatrix} A(z) \\ B(z) \end{bmatrix} = \begin{bmatrix} \exp[ik_{2z}(d_{12}-z)] & 0 \\ 0 & \exp[-ik_{2z}(d_{12}-z)] \end{bmatrix} M_3 \begin{bmatrix} A'_4 \\ B'_4 \end{bmatrix}. \qquad (8)
$$

Note that one can put $B'_4 = 0$ for a right-traveling incident wave with the amplitude A_0 (*i.e.*, there is no reflection in the semi-infinite 4th layer) since the glass substrate-air boundaries (the glass substrate-prism boundaries in our experiment as shown later) are assumed to be index matched. Then, we find from Equation (2) that the amplitude A'_4 is given by

$$
A'_4 = \frac{1}{m_{11}} A_0, \qquad (9)
$$

where m_{ij} $(i, j = 1, 2)$ is a matrix element of the 2×2 transfer matrix M for the three-layer system as defined by

$$
M = M_1 P_2 M_3. \qquad (10)
$$

Substituting either Equation (6) or Equation (7) with $B'_4 = 0$ into Equation (5) and using Equation (3), we obtain

$$
A(z) = \frac{(m_3)_{11}}{m_{11}} \exp[ik_{2z}(-z + d_{12})] A_0 \qquad (11)
$$

and

$$
B(z) = \frac{(m_3)_{21}}{m_{11}} \exp[-ik_{2z}(-z + d_{12})] A_0. \qquad (12)
$$

Thus, the resultant amplitude $E_{A_0}(x, z)$ in $d_1 \le z \le d_{12}$ for an obliquely incident right-traveling plane wave having the amplitude $A_0(x)$ from the semi-infinite 0th layer is given by

$$
E_{A_0}(x, z) = \frac{1}{m_{11}}\Big[(m_3)_{11}\exp[ik_{2z}(-z + d_{12})] + (m_3)_{21}\exp[-ik_{2z}(-z + d_{12})]\Big] A_0(x). \qquad (13)
$$

In the same way the resultant amplitude at z, $E_{B'_4}(x, z)$ in $d_1 \le z \le d_{12}$ for an obliquely incident left-traveling plane wave having the amplitude $B'_4(x)$ from the semi-infinite 4th layer is given by

$$
\begin{aligned}
E_{B'_4}(x, z) = \frac{1}{m_{11}}\Big\{ &[-(m_3)_{11}m_{12} + (m_3)_{12}m_{11}]\exp[ik_{2z}(-z + d_{12})] \\
&+ [-(m_3)_{21}m_{12} + (m_3)_{22}m_{11}]\exp[-ik_{2z}(-z + d_{12})]\Big\} B'_4(x).
\end{aligned} \qquad (14)
$$

Finally, we can calculate the 2D intensity distribution $I(x,z)$ in $d_1 \leq z \leq d_{12}$ as a result of the interference between three incident plane waves (two from the 0th layer and the other from the 4th layer), as given by

$$I(x,z) = |[E_{A_0}(x,z)]_a + [E_{A_0}(x,z)]_b + E_{B_4'}(z)|^2, \tag{15}$$

where $[A_0(x)]_a$ and $[A_0(x)]_b$ are obliquely incident right-traveling plane waves at their incident ray angles θ_a and θ_b, respectively, in the 0th layer, and B_4' is one normally incident left-traveling plane wave (see Figure 1 and the experimental setup shown in Figure 7, in which amplitudes of the three incident plane waves with a unit amplitude are given by

$$\begin{aligned} [A_0(x)]_a &= \exp(-ikn_0 \sin\theta_a x), \\ [A_0(x)]_b &= \exp(-ikn_0 \sin\theta_b x), \\ B_4' &= 1. \end{aligned} \tag{16}$$

2.2. Light-Intensity Interference Distributions

In order to numerically evaluate the 2D intensity distribution $I(x,z)$ given by Equation (15), we use the following numerical data: the refractive indices of glass substrates (the semi-infinite 0th and 4th layers) and non-absorptive but reflective ITO electrodes (the 1st and 3rd layers) are given by n_0 = n_4 = 1.52 and n_1 = n_3 = 1.95, respectively. The refractive index of the HPDLC film (an LC-monomer blend) is calculated in the following way: since LCs are assumed to be randomly distributed on average in a host material, its average refractive index n_{LC} is given by $\sqrt{(2n_o^2 + n_e^2)/3}$, where n_o and n_e are ordinary and extraordinary refractive indices of LC, respectively. For a nematic LC used in our experiment (see subsection 3.1) n_{LC} is calculated to be 1.599 with n_o = 1.529 and n_e = 1.730. Using the Lorentz-Lorenz formula [47] with the HPDLC mixture of 40.8 vol.% nematic LC and 59.2 vol.% photopolymer blend ($n_{polymer}$= 1.545), we found n_2, the average refractive index of the HPDLC film (the 2nd layer, see Figure 2), to be 1.567.

Figure 3a shows the calculated intensity distribution in the free space (*i.e.*, we set n_0 = n_2 = n_4 = 1.567 and d_1 = d_3 = 0) by three s-polarized plane-wave interference polymerization at $\theta_a = -\theta_b = 60^\circ$ and at a wavelength of 532 nm. It can be seen that, as reported for a simple three-beam interference configuration [28,33], the intensity distribution exhibits the triangular lattice symmetry [17]. Figure 3b and Figure 3c show the calculated intensity distributions in the HPDLC film (d_2 = 10 μm) without (*i.e.*, d_1 = d_3 = 0) [Figure 3b] and with (*i.e.*, d_1 = d_3 = 25 nm) [Figure 3c] ITO electrodes by three s-polarized plane-wave interference polymerization. It can be seen that the intensity distributions are strongly influenced by multiple reflections between two ITO electrodes and that the perfect triangular lattice symmetry seen in the free space is broken as multiple reflections is stronger. Figure 4 shows the calculated intensity distributions in the free space [Figure 4a] and in the HPDLC film (d_2 = 10 μm) without [Figure 4b] and with [Figure 4c] ITO electrodes by three p-polarized plane-wave interference polymerization. It can be seen in [Figure 4a] that the 2D intensity distribution in the free space exhibits the same triangular lattice symmetry as the case of s waves but its contrast is lower and reversed. In order to explain this change, we consider the 2D

intensity distribution $I(x,z)[\equiv I(\mathbf{r})]$ in the free space for the configuration of three-beam interference holographic polymerization (see Figure 1 with $a=1$, $b=2$ and $c=3$) with their unit amplitudes as given by

$$I(\mathbf{r}) = \sum_{m=1}^{3}\sum_{n=1}^{3} \mathbf{e}_m \cdot \mathbf{e}_n^* \exp\left[-i(\mathbf{G}_{mn}\cdot\mathbf{r} + \phi_{mn})\right], \tag{17}$$

where $\mathbf{e}_m$ is a complex eigen polarization vector for beam m, $\mathbf{G}_{mn}(\equiv \mathbf{k}_m - \mathbf{k}_n)$ is the reciprocal wave vector and $\phi_{mn}(\equiv \phi_m - \phi_n)$ is the relative phase between the constant phases of ϕ_m and ϕ_n for beams m and n, respectively. It is straightforward to show that for three s or p polarized beams at $\theta_1 = -\theta_2 = 60^\circ$ $I(\mathbf{r})$ is given by

$$I(\mathbf{r}) = \begin{cases} 3 + 2[\cos(\mathbf{G}_{12}\cdot\mathbf{r} + \phi_{12}) + \cos(\mathbf{G}_{13}\cdot\mathbf{r} + \phi_{13}) + \cos(\mathbf{G}_{23}\cdot\mathbf{r} + \phi_{23})], & \text{for s waves;} \\ 3 - [\cos(\mathbf{G}_{12}\cdot\mathbf{r} + \phi_{12}) + \cos(\mathbf{G}_{13}\cdot\mathbf{r} + \phi_{13}) + \cos(\mathbf{G}_{23}\cdot\mathbf{r} + \phi_{23})], & \text{for p waves.} \end{cases} \tag{18}$$

Equation (18) shows that the 2D intensity distribution in the free space for p waves exhibits the same symmetry as the case of s waves but its contrast is lower and reversed, independently of relative phases between three beams. It can also be seen in Figure 4(b) and Figure 4(c) that multiple reflections tends to break the triangular lattice symmetry with different unit cell patterns from the case of s waves. Therefore, we expect that loading of non-absorptive but reflective ITO electrodes (for the electrical control purpose) strongly influences on the symmetry of PhC structures. In order to avoid this effect, one may need to form a dielectric matching layer on ITO electrodes.

Figure 3. Calculated intensity distributions under s-polarized three-beam interference holographic exposure at a wavelength of 532 nm (**a**) in the free space and in the HPDLC film (**b**) without and (**c**) with ITO electrodes.

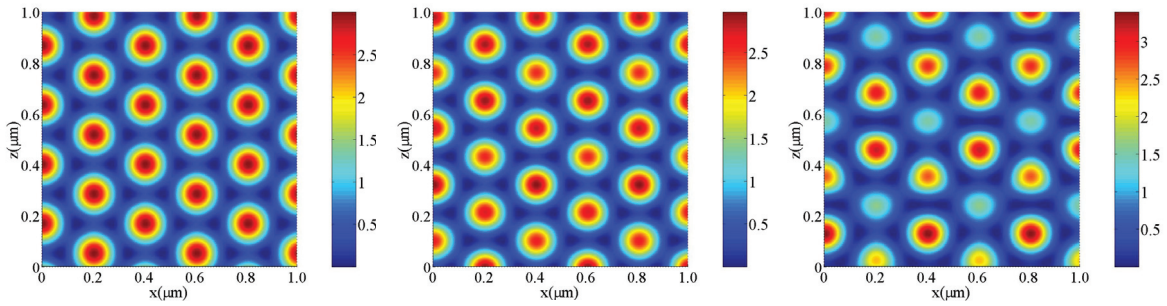

(**a**) (**b**) (**c**)

Figure 4. Calculated intensity distributions under p-polarized three-beam interference holographic exposure at a wavelength of 532 nm (**a**) in the free space and in the HPDLC film (**b**) without and (**c**) with ITO electrodes.

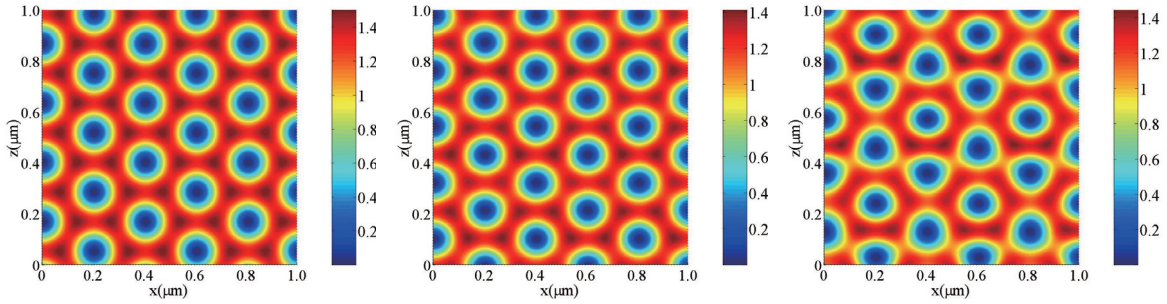

(**a**) (**b**) (**c**)

2.3. Refractive Index Distributions and Numerical Method

We are now in a position to calculate 2D refractive index distributions in the HPDLC film with ITO electrodes by using the statistical thermodynamics model [44] with the help of the calculated 2D intensity distributions. The model employs the Flory-Huggins chemical potential, together with the photopolymerization-diffusion equation, for a three-component system (monomer, polymer and LC) to obtain 2D concentration distributions of the three components during and after photopolymerization. In this case we set the polymerization rate of LCs to be zero. We also assume the diffusion-dominant polymerization process and the same size of an LC molecule as that of monomer. Furthermore, we introduce the threshold LC volume fraction $\phi_{LC}|_{th}$ (=0.8∼0.9) that determines whether LCs are either randomly oriented at the volume fraction of LCs $\phi_{LC} < \phi_{LC}|_{th}$ or aligned by the nematic ordering along the y direction in high ϕ_{LC} regions forming the cylinder-like LC channels (cavities) [25] at $\phi_{LC} \geq \phi_{LC}|_{th}$. This assumption is approximately justified by our experiments as described in subsection 4.2. Under this assumption the position-dependent refractive index of LCs for s (p) waves is given by the formula $\sqrt{(2n_o^2 + n_e^2)/3}$ $\left(\sqrt{(2n_o^2 + n_e^2)/3}\right)$ at $\phi_{LC} < \phi_{LC}|_{th}$ and is given by n_e (n_o) at $\phi_{LC} \geq \phi_{LC}|_{th}$. We also assume that when an external electric field E_{ex} (being higher than the threshold voltage [48]) is applied along the z direction, all LCs reorient along the z direction. In this way we can calculate 2D anisotropic refractive index distributions for s and p waves via the Lorentz-Lorenz formula with calculated concentrations and refractive indices of the formed polymer and LCs.

Figure 5 shows calculated 2D refractive index distributions by three s-polarized plane-wave interference polymerization when no E_{ex} is applied for s [Figure 5a] and p [Figure 5b] waves, and when E_{ex} is applied for any polarized wave [Figure 5c]. In this calculation we set $\phi_{LC}|_{th}$ to be 0.8. It can be seen that LC is rich in the dark illuminated regions as a result of the mutual diffusion of monomer and photo-insensitive species (*i.e.,* LCs) [4,45,49,50]. The refractive index of the HPDLC film is higher (lower) in the LC-rich regions than in the formed polymer-rich regions for s (p) waves since the refractive index of LCs is equal to n_e (n_o) at $\phi_{LC} \geq \phi_{LC}|_{th}$. It can also be seen that

the formed 2D refractive index distributions for s and p wave readout exhibit complementary 2D honeycomb-like PhC structures each other although s wave readout probes higher contrast structure than p wave readout. The contrast reversal of the PhC structures between s and p wave readout is understandable because the refractive index at the lattice sites (*i.e.*, the lowest intensity regions) is n_e (n_o) for s (p) wave. When E_{ex} is on, LCs reorient along the z direction. In this case both s and p waves sense only a difference in refractive index between n_o (=1.53) and $n_{polymer}$ (=1.545), resulting in very low contrast PhC structure as shown in Figure 5(c).

Figure 5. Calculated refractive index distributions by s-polarized three-beam interference holographic polymerization when no E_{ex} is applied for (**a**) s (TM) and (**b**) p (TE) wave readout, and (**c**) when E_{ex} is applied for any polarized wave. Note that the minimum and maximum values for the color bar levels in (**a**) are different from those in (**b**) and (**c**).

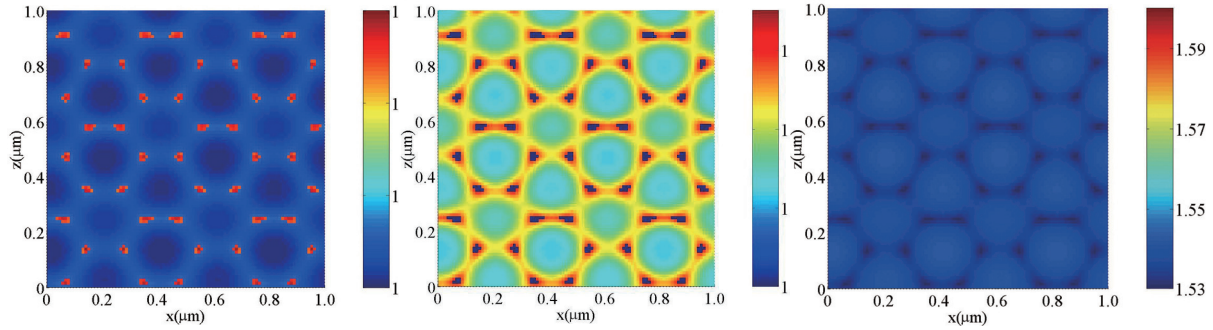

(**a**) (**b**) (**c**)

Figure 6 shows calculated 2D refractive index distributions by three p-polarized plane-wave interference polymerization when no E_{ex} is applied for s [Figure 6a] and p [Figure 6b] waves, and when E_{ex} is applied for any polarized wave [Figure 6c].

It can be seen that the 2D refractive index distributions for s [Figure 6(a)] and p [Figure 6(b)] waves exhibit complementary 2D triangular-like PhC structures since LCs migrates toward lower intensity regions that form a 2D triangular-like PhC structure as seen in Figure 4(c). When E_{ex} is on, both s and p waves sense only a difference in refractive index between n_o (=1.53) and $n_{polymer}$ (=1.545), resulting in very low contrast PhC structure as shown in Figure 6(c).

Our method of numerical analyses is as follows: numerical data of the calculated 2D refractive index distributions obtained by the method described so far were used with a commercially available numerical software package (CrystalWave, Photon Design) by which the PhC properties (*i.e.*, photonic band structures, anisotropic spectral transmittances and wavelength dispersion) were numerically analyzed with the built-in programs using the finite difference time domain (FDTD) method and the plane-wave expansion method [51].

Figure 6. Calculated refractive index distributions by p-polarized three-beam interference holographic polymerization when no E_{ex} is applied for (**a**) s (TM) and (**b**) p (TE) wave readout, and (**c**) when E_{ex} is applied for any polarized wave. Note that the minimum and maximum values for the color bar levels in (**a**) are different from those in (**b**) and (**c**).

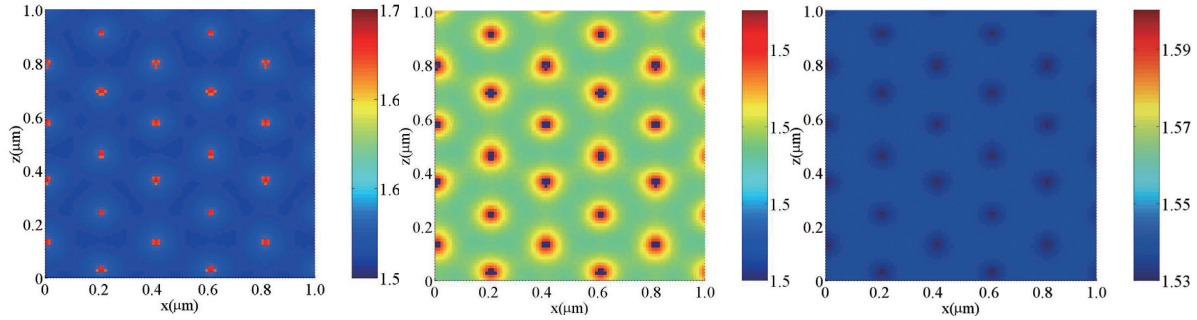

(**a**) (**b**) (**c**)

3. Experimental

3.1. Sample Preparation and Three-Beam Interference Holographic Polymerization

We prepared HPDLC syrup consisting of the 30 wt.% mixture of a nematic LC (TL203, Merck) with a monomer blend of 34 wt.% of multifunctional acrylate monomer (Ebecryl8301, Cytec), 11.5 wt.% of thiol-ene-based monomer (NOA65, Norland) and 18.3 wt.% *N*-vinyl pyrrolidone (Tokyo Chemical Industry). We also used 4 wt.% of octanoic acid (Tokyo Chemical Industry) that acted as surfactant. To sensitize in the green (532 nm), we employed 0.7 wt.% of Rose Bengal (Tokyo Chemical Industry) and 1.5 wt.% of *N*-phenyl-glycine (Tokyo Chemical Industry). The HPDLC syrup was injected by the capillary action into a sample cell consisting of two glass substrates with a 10 μm-thick spacer. We note that the commercially available thiol-ene prepolymer NOA65 contains a trifunctional thiol and a tetrafunctional urethane allyl ether ene, exhibiting free radical mediated step-growth polymerizations [52,53]. It was reported that HPDLCs based on thiol-ene monomers gave smaller LC droplets and much lower light scattering than HPDLCs based on acrylate-based monomers capable of free radical mediated chain-growth polymerizations [53–55]. Indeed, we did not observe noticeable light scattering from our HPDLC samples during and after curing. Such a low light scattering property would come from the fact that the average size of the formed LC droplets was much smaller than a wavelength of recording beams (532 nm) in the microscopic morphology of our 10-μm-thick HPDLC film samples as shown in the next section. Measured refractive indices of LC were n_e = 1.730 and n_o = 1.529 at extraordinary and ordinary polarizations, respectively, while those of the photopolymer blend were 1.503 and 1.545 in the liquid and solid phases, respectively. All these refractive indices were measured by an Abbe refractometer (DR-M2, ATAGO) at a wavelength of 546 nm. ITO electrodes were deposited on two glass substrates for an application of an electric field between the two glass substrates as shown in Figure 1. An experimental

setup for holographic polymerization and transmission measurements is shown in Figure 7. A coherent, linearly polarized and expanded beams from a diode pumped frequency-doubled Nd:YVO_4 laser operating at a wavelength of 532 nm was divided into two mutually coherent beams with equal intensities by a half mirror. One of the two beams was normally incident onto the sample through a neutral density (ND) filter and a trapezoidal BK7 prism (n = 1.52), whereas the other beam was divided into two equal-intensity beams that were incident onto the sample at the bisector angle of 120° via an equilateral triangular BK7 prism (n = 1.52). Index matching oil (n = 1.52) was filled in between these prisms and the sample cell to avoid unwanted refraction and multiple reflections of incident beams between the prisms and the HPDLC film sample cell. The three coplanar beams at equal intensities (67 mW/cm^2) and at co-polarizations (three s or p waves) interfered with one another, giving a 2D light-intensity distribution in the x-z plane. Such holographic exposure created a 2D refractive index distribution in the HPDLC film as described in Subsection 2.3. After 20-minutes holographic exposure the HPDLC film was post-cured with an ultraviolet LED light source operating at a wavelength of 365 nm for 30 minutes to ensure that remaining monomer, if any, was consumed completely. Although we employed a conventional three-beam holographic setup [56,57] without any particular phase stabilization control [58,59], any nonlinear effect such as wave mixing between interfering beams during curing [60] would not play a role in our fabrication process. This is so because good agreement is seen between the morphology of our fabricated PhC structures and the calculated ones as will be seen in Subsection 4.1.

Figure 7. Experimental setup for three-beam interference holographic polymerization.

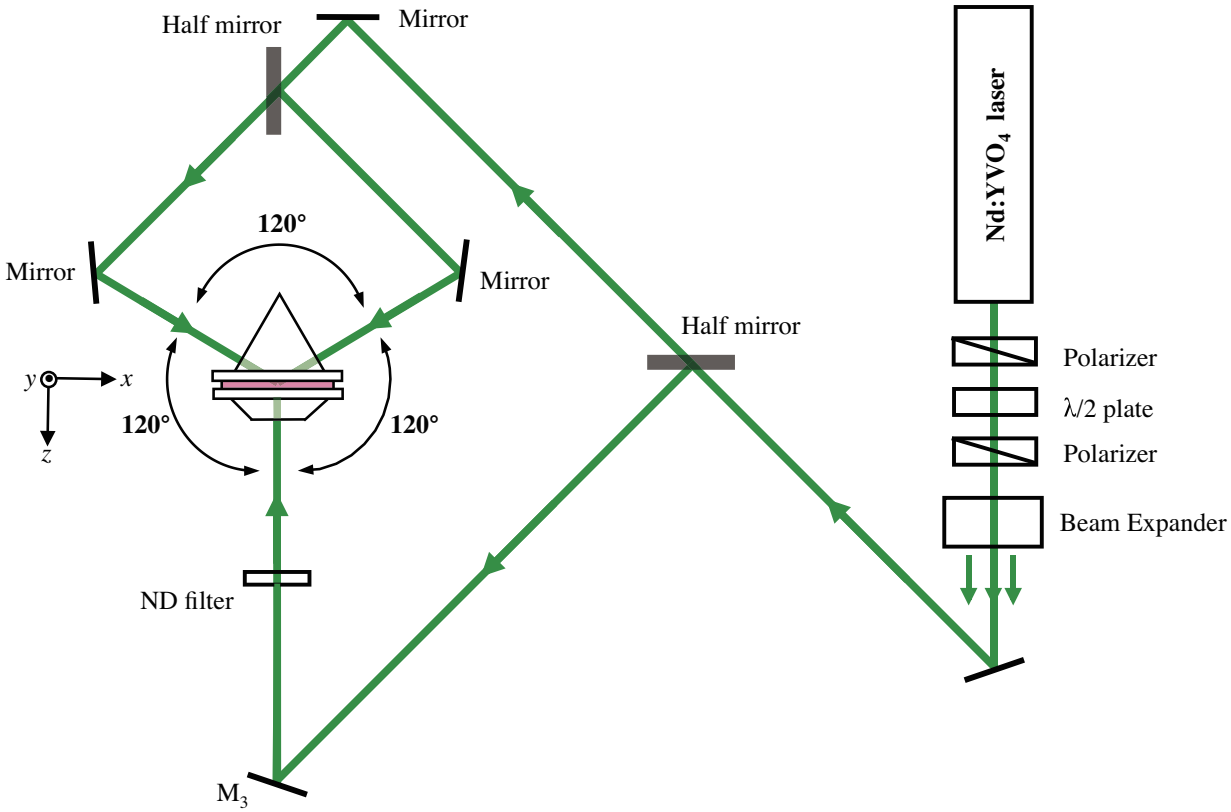

3.2. Measurements of Spectral Transmittance and Wavelength Dispersion

Spectral transmittances of the recorded HPDLC film were measured by use of a white light source (LS-11-LL, Ocean Optics) and a fiber-coupled spectrometer (ORIEL FICS, ORIEL). The collimated and linearly polarized white light was normally incident on the patterned HPDLC film along the z direction. We also employed linearly polarized laser beams operating at various wavelengths (404 nm, 532 nm and 632.8 nm) to examine the wavelength dispersion characteristics of the patterned HPDLC film at various incident angles. In these measurements two semi-spherical BK7 prisms (n = 1.52) contacted to both surfaces of the recorded HPDLC film sample cell with the index-matching oil to avoid unwanted reflections and refraction at the glass substrate-air boundaries. In order to investigate a dependence of spectral transmittances on an externally applied electric field and the wavelength dispersion characteristics, we employed a bipolar 2 kHz square-wave voltage applied to the two ITO electrodes.

4. Results and Discussion

4.1. Morphology of Fabricated Photonic Crystal Structures

We examined the morphology of holographically patterned PhC structures in HPDLC films by removing LC compound from PhC lattice sites. This was done by dipping cured HPDLC films into methanol and by observing the polymer structures in various cross sectional planes by means of a scanning electron microscopy (SEM). Figure 8 shows cross sectional SEM images of the polymer structures in the y-z, x-y and x-z planes for HPDLC films under three-beam interference polymerization by using three s-polarized [Figure 8(a)] and p-polarized [Figure 8(b)] plane waves. The calculated 3D polymer concentration distributions in volume fraction are also shown at the leftmost positions of Figure 8(a) and Figure 8(b), where bright portions correspond the polymer-rich (LC-poor) regions and dark portions correspond to polymer-poor (LC-rich) regions in which LCs were washed away after the methanol treatment. It can be seen that the observed SEM images are in good agreement with the calculated polymer structures in terms of their morphology and sizes when polymerization shrinkage predominantly taken place along the thickness (z) direction is taken into account. More specifically, calculated and measured periods of the polymer structures along the z direction are (0.220 and 0.660 μm) and ($\sim$0.20 and $\sim$0.60 μm), and these differences are of the order of polymerization shrinkage (approximately a few %, typical for multifunctional acrylates and our monomer blend).

We also note that the observed 3D polymer structure created by s-polarized three-beam interference polymerization [Figure 8(b)] possess the grating period of $\sim$0.20 μm along the x direction in the x-y plane, which is shorter than the calculated one of 0.404 μm at z = 0. This discrepancy can be understood by examining the calculated polymer structure in the x-y plane at z = 0.078 μm, as shown in Figure 9. It can be seen that the adjacent spacing between low and high concentration modulations [see the cross section along the x direction 0.078 at z = 0.078 μm in Figure 6(b)] is 0.202 μm, in good agreement with the measured value. In what follows we consider

the case of s-polarized three-beam interference holographic polymerization since, as shown later, no noticeable wavelength dispersion was observed with three p waves.

Figure 8. 3D polymer structures for HPDLC films under three-beam interference holographic polymerization by using three (**a**) s- and (**b**) p-polarized plane waves. Calculated 3D polymer distributions in volume fraction, cross sectional SEM images in the y-z, x-y and x-z planes are shown in order from the left in (**a**) and (**b**).

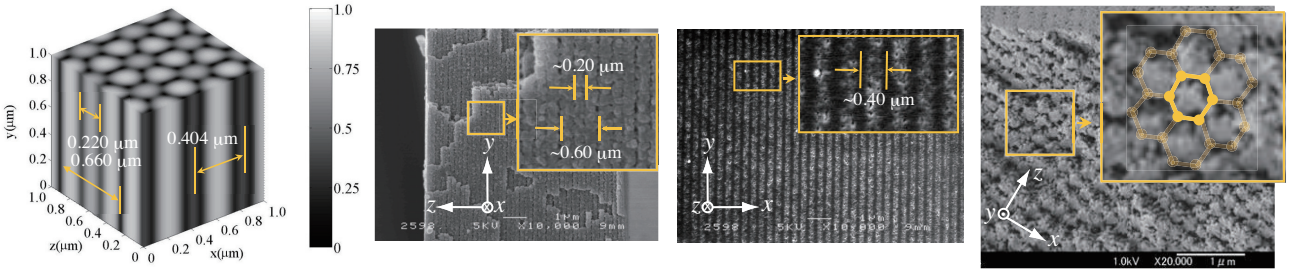

(**a**)

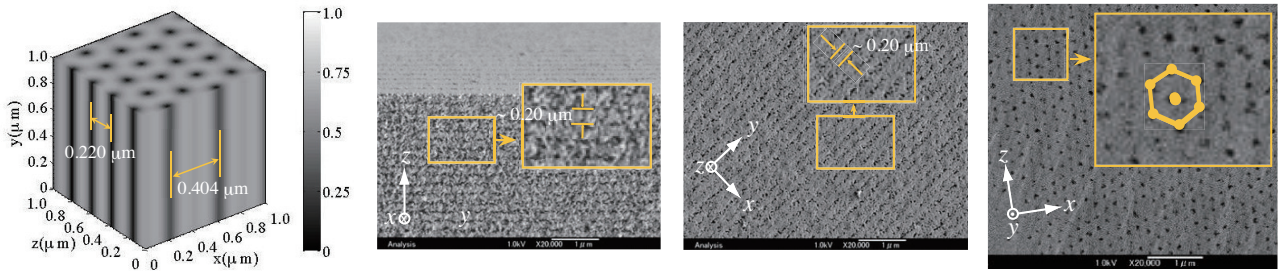

(**b**)

Figure 9. Calculated cross section of the polymer concentration distribution in the x-y plane at z = 0.078 μm prepared by p-polarized three-beam interference holographic polymerization.

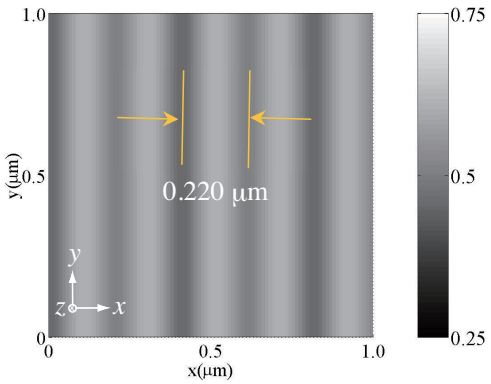

4.2. Spectral Transmittance

Figure 10 shows measured spectral transmittances of an HPDLC film recorded by three s-polarized plane-wave interference holographic polymerization and readout by normally incident s [Figure 10a] and p [Figure 10b] waves for different values of E_{ex}. It can be seen that the transmittance spectra have a strong readout-polarization dependence. The observed Bragg reflection (*i.e.*, the transmittance minimum) for s waves is much significant than that for p waves in the absence of E_{ex}. This result indicates that, as is consistent with our assumption made in our theoretical analysis, nematically ordered LCs in the regions above $\phi_{LC}|_{th}$ predominantly orient along the y direction in the absence of E_{ex}, giving the high contrast PhC structure for s wave readout as seen in Figure 5a. The observed Bragg reflection for p wave readout would have contribution from the x-direction component of LC directors due to the statistical distributions of LCs in x-z plane as a result of their thermal fluctuations [61]. It can also be seen that the observed Bragg reflections for both s and p wave readout in the absence of E_{ex} take place at the Bragg wavelengths λ_{Bragg} of 528 and 525 nm, respectively, that are shorter than the recording wavelength of 532 nm. We speculate that such blue shifts are caused by polymerization shrinkage of the order of a few % as mentioned earlier. The asymmetry in the spectral transmittance profiles, prominent for s wave readout, may also be caused by the distortion of the recorded 2D PhC structure due to the polymerization shrinkage and to the residual background absorption from Rose Bengal dyes that tend to orient along LC directors. We also see that the application of E_{ex} higher than 9 V/μm diminishes Bragg reflection for s wave readout. This is so because most of nematically ordered LCs reorient along the z direction at E_{ex} higher than 9 V/μm so that the PhC structure tends to disappear as seen in Figure 5c. The decreasing trend of λ_{Bragg} for s wave readout with an increase in E_{ex} can also be explained by the reorientation of LCs so that the average refractive index of the recorded 2D PhC structure decreases. On the other hand, it can be seen in Figure 10b that the application of E_{ex} higher than 9 V/μm does not sufficiently diminishes the PBG structure for p wave readout. We speculate that while most of nematically ordered LCs reorient under E_{ex} along the z direction, randomly oriented LCs embedded in the polymer-rich regions are not completely reorient along the z direction. This trend would result in non-negligible refractive index modulation unlike our theoretical model that assumes the complete reorientation of all LCs under E_{ex} along the z direction. The increasing trend of λ_{Bragg} for p wave readout with an increase in E_{ex} suggests an increase in the average refractive index of the recorded 2D PhC structure, which may be explained by an increase in the statistically distributed x component of nematically ordered LCs with increasing E_{ex}.

Figure 11 shows calculated spectral transmittances of HPDLC films recorded by three p-polarized plane-wave interference holographic polymerization and readout by normally incident s [Figure 10(a)] and p [Figure 10(b)] waves without and with E_{ex}. We chose $\phi_{LC}|_{th}$ = 0.9 that reproduced similar Bragg minimum transmittances without E_{ex} for s and p wave readout to the measured ones shown in Figure 10.

Figure 10. Measured spectral transmittances of of an HPDLC film recorded by three s-polarized plane-wave interference holographic polymerization and readout by normally incident (**a**) s and (**b**) p waves for different values of E_{ex}.

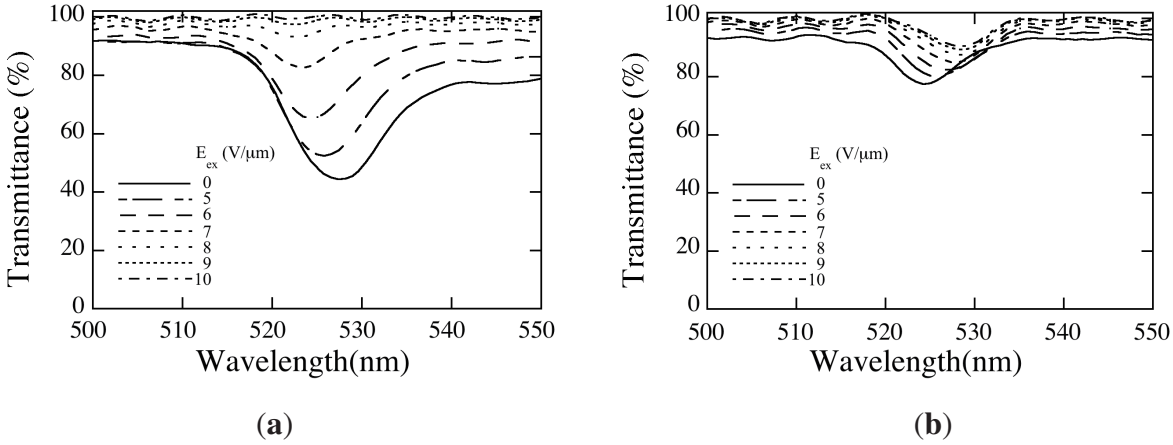

Figure 11. Calculated spectral transmittances of an HPDLC film recorded by three p-polarized plane-wave interference holographic polymerization and readout by normally incident (**a**) s and (**b**) p waves without and with E_{ex}.

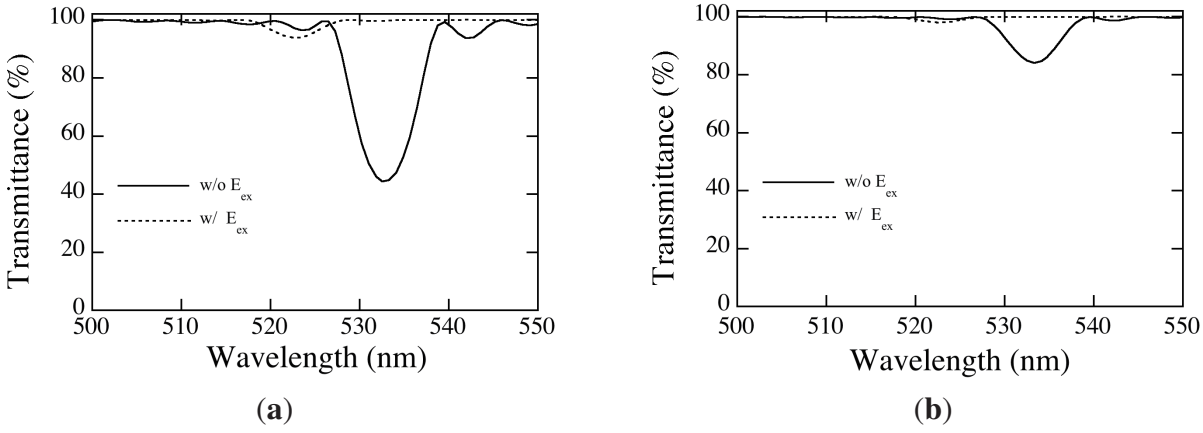

The calculated Bragg transmittance without E_{ex} for p wave readout is much higher than that for s wave readout, consistent with the measured results. The decreasing trend of λ_{Bragg} in the presence of E_{ex} for s wave readout due to a decrease in the average refractive index is also consistent with the measured result as mentioned above. Therefore, we consider that our simplified assumption of the director orientation of nematically ordered LCs above $\phi_{LC}|_{th}$ along the y direction in the absence of E_{ex} is adequate. The disappearance of Bragg transmittance in the presence of E_{ex} for p wave, as seen in Figure 11b, results from the assumption of our theoretical model that all LCs reorient along the z direction as described in Subsection 2.3. The discrepancy in an E_{ex}-induced transmittance change between theoretical and experimental results may be explained by, as described above, the insufficient reorientation of randomly oriented LCs embedded in the polymer-rich regions under E_{ex} along the z direction, which maintains the refractive index contrast of the 2D PhC structure to some extent. The discrepancy in the E_{ex}-induced shift of λ_{Bragg} for p wave readout between theoretical and

experimental results may be explained by an increase in the statistically distributed x component of nematically ordered LCs with increasing E_{ex}, as mentioned above. Further investigation is necessary to clarify the discrepancy.

4.3. Wavelength Dispersion Characteristics

We examined the wavelength dispersion characteristics of our 2D honeycomb-like PhC and its electrical control. Figure 12 illustrates the result for an HPDLC film recorded by three s-polarized plane-wave interference holographic polymerization and readout by normally incident s-polarized white light in the absence of E_{ex}. We observed the symmetric wavelength dispersion from the blue to the red with the full dispersion-angle width of approximately 25°. The observed refraction angles in the green were found to be approximately ±60° measured from the normal to the HPDLC film surface. Such wavelength dispersion diminished when E_{ex} was larger than 9 V/μm, confirming the electrical control of the 2D honeycomb-like PhC using an HPDLC. We note that the wavelength dispersion as shown in Figure 12 was observed neither by normally incident p-polarized white light nor from a 2D honeycomb-like PhC fabricated by three p-polarized plane-wave interference holographic polymerization. It is also interesting to note that no wavelength dispersion was observed when a similar 2D PhC structure was made without ITO electrodes.

Figure 12. Observed wavelength dispersion pattern from an HPDLC film recorded by three s-polarized plane-wave interference holographic polymerization and readout by normally incident s-polarized white light in the absence of E_{ex}.

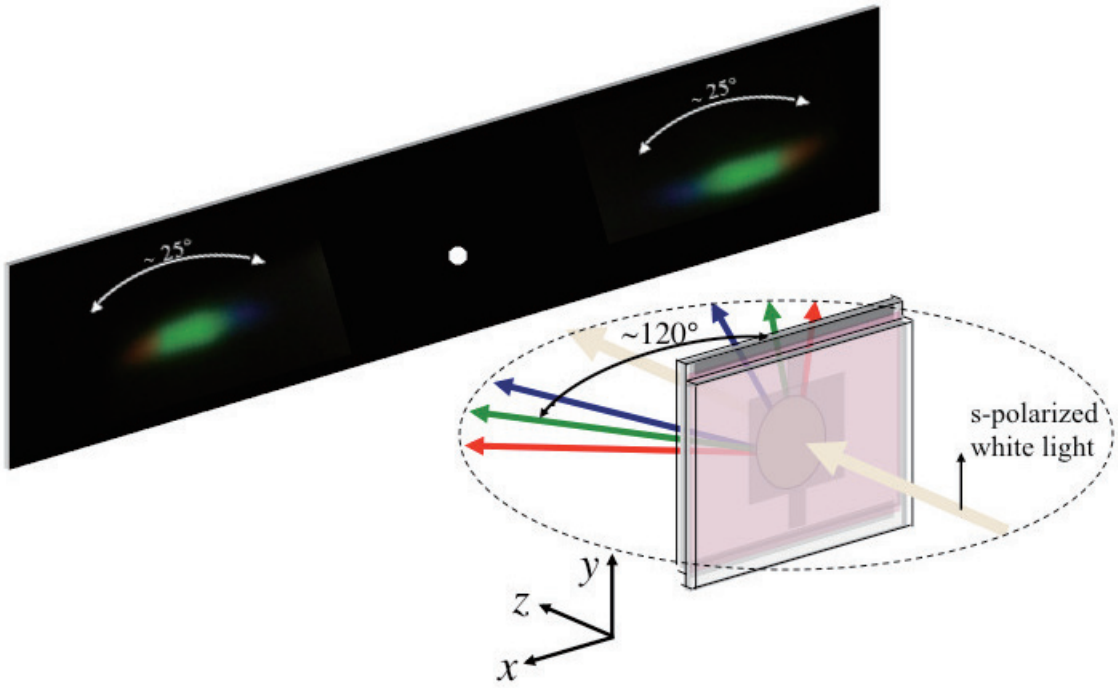

In order to quantitatively investigate effects of the observed wavelength dispersion phenomenon on incident ray angle and wavelength, we measured dependences of refraction ray angle on incident

ray angle at different s-polarized laser wavelengths (404, 532 and 633 nm) for the same HPDLC film as used in Figure 12. The result is shown in Figure 13, where the incident ray angle θ_{in} (the refraction ray angle θ_r) is defined as an angle between the surface normal of the HPDLC film's substrate and the incident (refracted) ray in the counter-clockwise direction. Both incident and refraction angles have the same (opposite) signs when the positive (negative) refraction takes place. Calculated results by the FDTD analysis are also plotted in Figure 13. It can be seen that, as similar to the observation by Li *et al.* [34], strong wavelength dispersion occurs at three wavelengths. While only the positive refraction was observed at 404 nm in our experiment, the calculation predicted the peculiar negative refraction at $\theta_{in} = \pm 2^\circ$ (see two open triangle symbols in the hatched areas in Figure 13). We also observed both positive and negative refraction at 532 nm in the incident angle range of $-6^\circ \leq \theta_{in} \leq +6^\circ$ and also at 633 nm with $\theta_{in} = 0^\circ$. Furthermore, we only observed the negative refraction at 532 nm in the incident angle range of $|\theta_{in}| \geq 6^\circ$ and at 633 nm with $\theta_{in} \neq 0^\circ$. Although these observations could be explained partly by our numerical analysis, further investigation is necessary to clarify the discrepancy between measured and calculated results.

Figure 13. Refraction angles as a function of incident angle at different wavelengths and at s polarization. Measured and calculated data points are denoted by (▲, ■, ●) and (△, □, ○) at (404 nm, 532 nm, 633 nm), respectively. The white and gray regions denote positive and negative refraction, respectively.

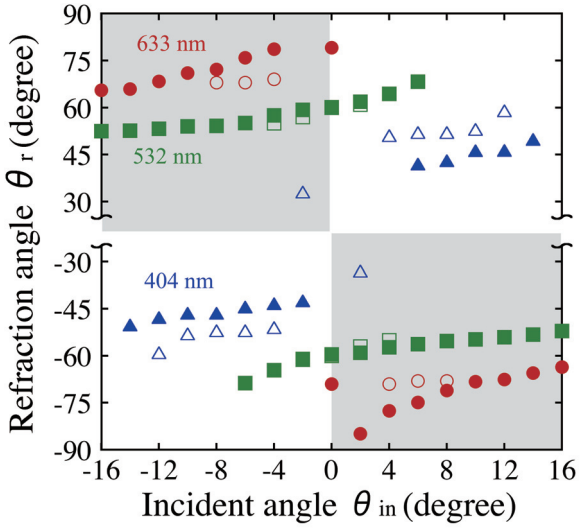

5. Conclusions

We have studied the holographic fabrication of 2D PhC structures in HPDLC films and their electrically controllable optical properties both theoretically and experimentally. We have employed the 2×2 matrix formulation and the statistical thermodynamic model to calculate the refractive index distributions in HPDLC films by three-beam holographic polymerization. We have shown that refractive index distributions are strongly influenced by the polarization state of three waves and by multiple reflections between two transparent ITO electrodes that are used for electrical

tuning of PhC structures. It has been found that while a 2D honeycomb-like PhC structure forms by three s-polarized plane-wave interference holographic polymerization, a triangular-like photonic lattice structure forms by three p-polarized plane-wave interference holographic polymerization. Their local lattice structures are significantly altered by the multiple interference effect. We have confirmed such a difference in PhC symmetry by the examination of SEM images of recorded HPDLC films. We have also observed a strong polarization dependence of the optical properties including spectral transmittance and wavelength dispersion. It has been found that an incident s wave propagating in the 2D honeycomb-like PhC structure exhibits the broadband wavelength dispersion from the blue to the red with the dispersion angle of $\sim$25°. We has also shown that such a wavelength dispersion phenomenon gives the negative refraction under limited incident conditions. We have demonstrated that the observed wavelength dispersion can be completely suppressed by externally applied electric fields higher than 9 Vμm. Since our theoretical analysis relies on the statistical thermodynamic model that considers a single phase mixture of LC and the formed polymer for the photopolymerization-diffusion kinetics, more realistic and exact statistical thermodynamic models [62,63] that take the LC droplet formation and the nematic ordering process in the phase separation dynamics into account may explain our experimental results more accurately and answer to our unsolved questions on anisotropic spectral transmittances and negative refraction. Moreover, it would also be interesting to investigate possibilities of novel optical phenomena and their electrical control of 2D HPDLC honeycomb (graphene)-type photonic lattices in linear and nonlinear optical regimes.

Author Contributions

Mayu Miki conducted the theoretical analysis and numerical calculations, designed and performed experiments, analyzed data and wrote the manuscript; Ryuichiro Ohira performed numerical calculations, analyzed data and wrote the manuscript; Yasuo Tomita supervised the project, designed experiments and edited the manuscript.

Conflicts of Interest

The authors declare no conflicts of interest.

References

1. Sutherland, R.L.; Natarajan, L.V.; Tondiglia, Y.P. Bragg gratings in an acrylate polymer consisting of periodic polymer-dispersed liquid-crystal planes. *Chem. Mater.* **1993**, *5*, 1553–1538.
2. Bunning, T.J.; Natarajan, L.V.; Tondiglia, V.P.; Sutherland, R. L. Holographic polymer-dispersed liquid crystals (H-PDLCs). *Annu. Rev. Mater. Sci.* **2000**, *30*, 83–115.
3. Liu, Y.J.; Sun, X.W. Holographic Polymer-Dispersed Liquid Crystals: Materials, Formation, and Applications. *Adv. OptoElectron.* **2008**, *2008*, 684349:1–684349:52.

4. Smith, D.M.; Li, C.Y.; Bunning, T.J. Light-directed mesoscale phase separation via holographic polymerization. *J. Poly. Sci. B Polym. Phys.* **2014**, *52*, 232–250.
5. Crawford, G.P. Electrically switchable Bragg gratings. *Opt. Photonics News* **2003**, *April*, 54–59.
6. Criante, L.; Lucchetta, D.E.; Vita, F.; Castagna, R.; Simoni, F. Distributed feedback all-organic microlaser based on holographic polymer dispersed liquid crystals. *Appl. Phys. Lett.* **2009**, *94*, 111114-1–111114-3.
7. Lucchetta, D.E.; Vita, F.; Simoni, F. All-optical switching of diffraction gratings infiltrated with dye-doped liquid crystals. *Appl. Phys. Lett.* **2010**, *97*, 231112-1–231112-3.
8. Riquelme, M.; Ortuno, M.; Marquez, A.; Gallego, S.; Pascual, I.; Belendez, A. A dynamic beam splitter using polymer dispersed liquid crystals materials. *Proc. SPIE* **2012**, *8498*, 8498-1–8498-11.
9. Ogiwara, A.; Watanabe, M.; Moriwaki, R. Formation of temperature dependable holographic memory using holographic polymer-dispersed liquid crystal. *Opt. Lett.* **2013**, *38*, 1158–1160.
10. Caputo, R.; De Sio, L.; Veltri, A.; Umeton, C.; Sukhov, A.V. Development of a new kind of switchable holographic grating made of liquid-crystal films separated by slices of polymeric material. *Opt. Lett.* **2004**, *29*, 1261–1263.
11. Sakhno, O.; Slussarenko, S.; Stumpe, J. POLIPHEM: new type of nanoscale polymer-LC-switchable photonic devices. *Proc. SPIE* **2004**, *5521*, 38–45.
12. Caputo, R.; De Luca, A.; De Sio, L.; Pezzi, L.; Strangi, G.; Umeton, C.; Veltri, A.; Asquini, R.; d'Alessandro, A.; Donisi, D.; Beccherelli, R.; Sukhov, A.V.; Tabiryan, N.V. POLISCRYPS: a liquid crystal composed nano/microstructure with a wide range of optical and electro-optical applications. *J. Opt. Pure Appl. Opt.* **2009**, *11*, 024017.
13. Vasnetsov, M.V.; Slussarenko, S.S., Jr.; Stumpe, J.; Sakhono, O.; Slussarenko, S.S.; Abbate, G. Lasing by second-order Bragg diffraction in dye-doped POLIPHEM gratings. *Mol. Cryst. Liq. Cryst.* **2010**, *516*, 159–166.
14. De Sio, L.; Umeton, C. Dual-mode control of light by two-dimensional periodic structures realized in liquid-crystalline composite materials. *Opt. Lett.* **2010**, *35*, 2759–2761.
15. Yablonovitch, E. Inhibited spontaneous emission in solid-state physics and electronics. *Phys. Rev. Lett.* **1987**, *58*, 2059–2062.
16. Joannopoulos, J.D.; Meade, R.D.; Winn, J.N. *Photonic Crystals*; Princeton University Press: Princeton, NJ, USA, 1995.
17. Lourtioz, J.-M.; Benisty, H.; Berger, V.; Gérard, J.-M.; Maystre, D.; Tchelnokov, A. *Photonic Crystals Towards Nanoscale Photonic Devices*; Springer-Verlag: Berlin, Germany, 2005.
18. Prather, D.W.; Shi, S.; Sharkawy, A.; Murakowski, J.; Schneider, G.J. *Photonic Crystals*; Wiley: Hoboken, NJ, USA, 2009.
19. Baba, T. Photonic crystals and microdisk cavities based on GaInAsP-InP system. *IEEE J. Select. Topics Quantum Electron.* **1997**, *3*, 808–829.
20. Kawakami, S.; Kawashima, T.; Satomi, T. Mechanism of shape formation of three-dimensional periodic nanostructures by bias sputtering. *Appl. Phys. Lett.* **1999**, *74*, 463–465.

21. John, S.; Busch, K. Photonic band gap formation in certain self-organizing systems. *Phys. Rev. E* **1998**, *58*, 3896–3908.
22. Noda, S.; Tomida, K.; Yamamoto, N.; Chutinan, A. Full three-dimensional photonic bandgap crystals at near-infrared wavelengths. *Science* **2000**, *289*, 604–606.
23. Tondiglia, V.P.; Natarajan, L.V.; Sutherland, R.L.; Tomlin, D.; Bunning, T.J. Holographic formation of electro-optical polymer-liquid crystal photonic crystals. *Adv. Mater.* **2002**, *14*, 187–191.
24. Jakubiak, R.; Bunning, T.J.; Vaia, R.A.; Natarajan L.V.; Tondiglia, V.P. Electrically switchable, one-dimensional polymeric resonators from holographic photopolymerization: A new approach for active photonic bandgap materials. *Adv. Mater.* **2003**, *15*, 241–244.
25. Escuti, M.J.; Qi, J.; Crawford, G.P. Two-dimensional tunable photonic crystal formed in a liquid-crystal/polymer composite: Threshold behavior and morphology. *Appl. Phys. Lett.* **2003**, *83* 1331–1333.
26. Escuti, M.J.; Qi, J.; Crawford, G.P. Tunable face-centered-cubic photonic crystal formed in holographic polymer dispersed liquid crystals. *Opt. Lett.* **2003**, *28*, 522–524.
27. Escuti, M.J.; Crawford, G.P. Mesoscale three dimensional lattices formed in polymer dispersed liquid crystals: A diamond-like face centered cubic. *Mol. Cryst. Liq. Cryst.* **2004**, *421*, 23–36.
28. Liu, Y.J.; Sun, X.W. Electrically tunable two-dimensional holographic photonic crystal fabricated by a single diffractive element. *Appl. Phys. Lett.* **2006**, *89*, 171101-1–171101-3.
29. Liu, Y.J.; Sun, X.W. Electrically tunable three-dimensional holographic photonic crystal made of polymer-dispersed liquid crystals using a single prism. *Jpn. J. Appl. Phys.* **2007**, *46*, 6634–6638.
30. Sun, X.H.; Tao, X.M.; Ye, T.J.; Xue, P.; Szeto, Y.-S. Optics design and fabrication of 3D electrically switchable hexagonal photonic crystal. *Appl. Phys. B* **2007**, *87*, 65–69.
31. Luo, D.; Sun, X.W.; Dai, H.T.; Demir, H.V.; Yang, H.Z.; Ji, W. Electrically tunable lasing from a dye-doped two-dimensional hexagonal photonic crystal made of holographic polymer-dispersed liquid crystals. *Appl. Phys. Lett.* **2010**, *97*, 081101-1–081101-3.
32. Luo, D.; Dai, H.T.; Demir, H.V.; Sun, X.W.; Yang, H.Z.; Ji, W. Spatial angle dependent lasing from a dye-doped two-dimensional hexagonal photonic crystal made of holographic polymer-dispersed liquid crystals. *Opt. Express* **2012**, *20*, 9058–9063.
33. Li, M.S.; Wu, S.-T.; Fuh, A.Y.-G. Superprism phenomenon based on holographic polymer dispersed liquid crystal film. *Appl. Phys. Lett.* **2006**, *88*, 091109-1–091109-3.
34. Wu, S.-T.; Li, M.S.; Fuh, A.Y.-G. Unusual refractions in photonic crystals based on polymer-dispersed liquid crystal films. *Appl. Phys. Lett.* **2007**, *91*, 251117-1–251117-3.
35. Wallance, P.R. The band theory of graphite. *Phys. Rev.* **1947**, *71*, 622–634.
36. Novoselov, K.S.; Geim, A.K.; Morozov, S.V.; Jiang, D.; Katsnelson, M.I.; Grigorieva, I.V.; Dubonos, S.V.; Firsov, A.A. Two-dimensional gas of massless Dirac fermions in graphene. *Nature* **2005**, *438*, 197–200.
37. Peleg, O.; Bartal, F.; Manela, O.; Segev, M.; Christodoulides, D.N. Conical diffraction and gap solitons in honeycomb photonic lattices. *Phys. Rev. Lett.* **2007**, *98*, 103901-1–103901-4.

38. Bahat-Treidel, O.; Peleg, O.; Segev, M. Symmetry breaking in honeycomb photonic lattices. *Opt. Lett.* **2008**, *33*, 2251–2253.
39. Bahat-Treidel, O.; Peleg, O.; Segev, M.; Buljan, H. Breakdown of Dirac dynamics in honeycomb lattices due to nonlinear interactions. *Phys. Rev. A* **2010**, *82*, 013830-1–013830-6.
40. Ablowitz, M.J.; Zhu, Y. Nonlinear diffraction in photonic graphene. *Opt. Lett.* **2011**, *36*, 3762–3764.
41. Zeuner, J.M.; Rechtsman, M.C.; Nolte, S.; Szameit, A. Edge states in disordered photonic graphene. *Opt. Lett.* **2014**, *39*, 602–605.
42. Chern, R.-L.; Han, D. Nonlocal optical properties in periodic lattice of graphene layers. *Opt. Express* **2014**, *22*, 4817–4829.
43. Yeh, P. Matrix formulation for isotropic layered media. In Optical Waves in Layered Media; Wiley: New York, NY, USA, 1988; Chapter 5.
44. Leewis, C.M.; de Jong, A.M.; van IJzendoorn, L.J. Reaction-diffusion model for the preparation of polymer gratings by patterned ultraviolet illumination. *J. Appl. Phys.* **2004**, *95*, 4125–4139.
45. Tomita, Y.; Suzuki, N.; Endoh, Y.; Kurozumi, S.; Miki, M.; Chikama, K. Holographic assembly of nanoparticles in polymers for 3D recording and patterning. *Proc. SPIE* **2007**, *6657*, 665702-1–665702-7.
46. Sutherland, R.L.; Tondiglia, V.P.; Natarajan, L.V.; Bunning, T.J. Phenomenological model of anisotropic volume hologram formation in liquid-crystal-photopolymer mixtures. *J. Appl. Phys.* **2004**, *96*, 951–965.
47. Aubrecht, I.; Miler, M.; Koudela, I. Recording of holographic diffraction gratings in photopolymers: Theoretical modelling and real-time monitoring of grating growth. *J. Mod. Opt.* **1998**, *45*, 1465–1477.
48. Wu, B.-G.; Erdmann, J.H.; Doane, J.W. Response times and voltages for PDLC light shutters. *Liquid Crystals* **1989**, *5*, 1453–1465.
49. Tomita, Y.; Suzuki, N.; Chikama, K. Holographic manipulation of nanoparticle distribution morphology in nanoparticle-dispersed photopolymers. *Opt. Lett.* **2005**, *30*, 839–841.
50. Tomita, Y.; Chikama, K.; Nohara, Y.; Suzuki, N.; Furushima, K.; Endoh, Y. Two-dimensional imaging of atomic distribution morphology created by holographically induced mass transfer of monomer molecules and naoparticles in a silica-nanoparticle-dispersed photopolymer film. *Opt. Lett.* **2006**, *31*, 1402–1404.
51. Sakoda, K. *Optical Properties of Photonic Crystals*; Springer: Berlin, Germany, 2001.
52. Pinto-Iguanero, P.; Olivares-Pérez, A.; Fuentes-Tapia, I. Holographic material film composed by Norland Noa 65 adhesive. *Opt. Mater.* **2002**, *20*, 225–232.
53. Natarajan, L.V.; Shepherd, C.K.; Brandelik, D.M.; Sutherland, R.L.; Chandra, S.; Tondiglia, V.P.; Tomlin, D.; Bunning, T.J. Switchable holographic polymer-dispersed liquid crystal reflection gratings based on thol-ene photopolymerization. *Chem. Mater.* **2003**, *15*, 2477–2484.

54. Natarajan, L.V.; Brown, D.P.; Wofford, J.M.; Tondiglia, V.P.; Sutherland, R.L.; Lloyd, P.F.; Bunning, T.J. Holographic polymer dispersed liquid crystal reflection gratings formed by visible light initiated thiol-ene photopolymerization. *Polymer* **2006**, *47*, 4411–4420.
55. White, T.J.; Natarajan, L.V.; Tondiglia, V.P.; Bunning, T.J.; Guymon, C.A. Polymerization kinetics and monomer functionality effects in thiol-ene polymer dispersed liquid crystals. *Macromolecules* **2007**, *40*, 1112–1120.
56. Escuti, M.J.; Crawford, G.P. Holographic photonic crystals. *Opt. Eng.* **2004**, *43*, 1973–1987.
57. Vita, F.; Lucchetta, D.E.; Castagna, R.; Criante, L.; Simoni, F. Large-area photonic structures in freestanding films. *Appl. Phys. Lett.* **2007**, *91*, 103114-1–103114-3.
58. De Sio, L.; Caputo, R.; De Luca, A.; Veltri, A.; Umeton, C.; Sukhov, A.V. *In situ* optical control and stabilization of the curing process of holographic gratings with a nematic film-polymer-slice sequence structure. *Appl. Opt.* **2006**, *45*, 3721–3727.
59. De Sio, L.; Veltri, A.; Tedesco, A.; Caputo, R.; Umeton, C.; Sukhov, A.V. Charcterization of an active control system for holographic setup stabilization. *Appl. Opt.* **2008**, *47*, 1363–1367.
60. Caputo, R.; De Sio, L.; Veltri, A.; Umeton, C.; Sukhov, A.V. Observation of two-wave coupling during the formation of POLICRYPS diffraction gratings. *Opt. Lett.* **2005**, *30*, 1840–1842.
61. Sutherland, R.L. Polarization and switching properties of holographic polymer-dispersed liquid-crystal gratings. I. Theoretical model. *J. Opt. Soc. Am. B* **2002**, *19*, 2995–3003.
62. Meng, S.; Kyu, T.; Natarajan, L.V.; Tondiglia, V.P.; Sutherland, R.L.; Bunning, T.J. Holographic photopolymerization-induced phase separation in reference to the phase diagram of a mixture of photocurable monomer and nematic liquid crystal. *Macromolecules* **2005**, *38*, 4844–4854.
63. Meng, S.; Duran, H.; Hu, J.; Kyu, T.; Natarajan, L.V.; Tondiglia, V.P.; Sutherland, R.L.; Bunning, T.J. Influence of photopolymerization reaction kinetics on diffraction efficiency of H-PDLC undergoing photopatterning reaction in mixtures of acrylic monomer/nematic liquid crystals. *Macromolecules* **2007**, *40*, 3190–3197.

Frequency and Temperature Dependence of Fabrication Parameters in Polymer Dispersed Liquid Crystal Devices

Juan C. Torres, Ricardo Vergaz, David Barrios, José Manuel Sánchez-Pena, Ana Viñuales, Hans Jürgen Grande and Germán Cabañero

Abstract: A series of polymer dispersed liquid crystal devices using glass substrates have been fabricated and investigated focusing on their electrical properties. The devices have been studied in terms of impedance as a function of frequency. An electric equivalent circuit has been proposed, including the influence of the temperature on the elements into it. In addition, a relevant effect of temperature on electrical measurements has been observed.

Reprinted from *Materials*. Cite as: Torres, J.C.; Vergaz, R.; Barrios, D.; Sánchez-Pena, J.M.; Viñuales, A.; Grande, H.J.; Cabañero, G. Frequency and Temperature Dependence of Fabrication Parameters in Polymer Dispersed Liquid Crystal Devices. *Materials* **2014**, *7*, 3512–3521.

1. Introduction

Polymer dispersed liquid crystals (PDLC) devices consist of a thin film of a polymer matrix containing micro-sized droplets of a liquid crystal. In order to fabricate PDLC devices, the mixture is usually laid between two transparent substrates coated with a conductive layer, usually of indium tin oxide (ITO) [1]. These PDLC devices can be used in eletro-optic applications such as: smart windows [2], variable optical attenuators (VOAs) [3] and projection displays [4].

In order to use PDLC devices as an optical switcher, the refractive index of the isotropic polymer and the ordinary refractive index of the liquid crystal should be similar [5]. In the absence of an electric field, the directors of the microdroplets are randomly distributed and strongly scatter the light so the device appears opaque. When an AC electrical field is applied, the liquid crystal dipoles are re-oriented parallel to the field and the ordinary refractive index of the liquid crystal matches with the polymer refractive index, and the material becomes transparent [6]. The transmission of light through the device, therefore, can be controlled by applying an electrical field. Furthermore, unlike with other electro-optic devices like twisted-nematic LC (TNLC) or surface-stabilized ferroelectric liquid crystal (SSFLC), the transparent state can be highly transmissive because no polarizers are required to achieve the switching effect.

PDLC has a great number of advantages in comparison with the other liquid crystal technologies used in displays, such as: high brightness (because of its high transparency), wide view angle, fast response (in the order of milliseconds), absence of surface treatment and the possibility of intermediate transmission levels electrically controllable. The scattering properties of PDLC devices can be used in “smart” windows that regulate the light intensity inside buildings. The shift with temperature of the electrooptic response curve of the PDLC is well known [6]. When using these devices with intermediate transparency levels rather than in ON/OFF mode, the knowledge of the temperature variation is mandatory in a double way: to optimize the contrast and to estabilize the transparency level [2].

Therefore, in order to ensure a determinate transmission level, it is necessary to change the electrical field applied to the PDLC according to the ambient temperature. The most practical way to mitigate the temperature influence in an effective way is to control the electrical field, as the optical properties are mainly related to it.

On the other hand, an electrical equivalent circuit (EEC) associated to electrical properties (frequency, impedance and voltage) that also varies with temperature is of great practical interest, because it can be used to develop new driving circuits and signals in order to reduce power consumption and increase optical contrast.

In this work, the electrical properties of a series of PDLCs have been analyzed. This behavior can be represented through an adequate combination of passive elements which responses are associated to physical parameters. An electrical equivalent circuit describing such behavior has been proposed. The component values of the circuit have been obtained from complex impedance measurements. Experimental results and simulation have been compared in order to validate the EEC. The aim of the work is to explore the temperature dependence of the equivalent circuit electrical parameters of the device. This knowledge allows, then, a practical way to control the optical performance of the device regardless of the temperature.

2. Experimental Setup

The PDLCs devices were manufactured from an homogeneous mixture of 20 wt% of a UV curable matrix (Bisphenol A glycerolate diacrylate from Aldrich) and 80 wt% of an eutectic nematic liquid crystal mixture (E7 from Merck) consisting mostly of 4-pentyl-4'-cyanobiphenyl, with positive dielectric anisotropy. Glass cells with ITO coated inner surfaces with an effective area of 1.3×1.3 cm^2 and a 20.5 μm internal gap, were filled by capillarity with the mixtures at 65 °C. PDLC was formed by polymerization induced phase separation (PIPS) method, exposing the cell to a 365 nm light for 10 min. The UV flux was 350 mW/cm^2 at a distance of 15 cm (Vilber Lourmat VL4LC, Marne La Vallee, France).

The key to obtain the orientation is the observation of the device by polarization microscopy, observing the pattern of the droplets with the sample located between two crossed polarizers [6]. The morphology of the PDLC composites was studied at 20× magnification using a Leica DM400M microscope (Leica Microsystems, Wetzlar, Germany), a Leica camera DFC420C (Leica Microsystems) and placing the devices between crossed polarizers (Figure 1, the scale bar corresponds to 100 μm). Unfortunately, the droplets are too small to be resolved. The small size can be associated to a fast polymerization and phase separation process because of UV curing at high temperature (65 °C) as it is reported elsewhere [7,8].

Afterwards, the measurement of complex impedance (magnitude and phase) was carried out using an impedance analyzer (SOLARTRON 1260, Solartron Analytical, Farnborough, UK), in a wide frequency range, 0.1 to 10 MHz. PDLC devices have been placed in a programmable hot-stage (Linkham plate LTS-E350, Linkam Corp., Surrey, UK) in order to guarantee a stable temperature during a whole measurement process. The sample temperature range was measured from 25 to 40 °C with a change of 5 °C per measurement.

Figure 1. Micro-textures of the droplets morphologies of the polymer dispersed liquid crystals (PDLC) films under cross polarizers at 20× magnification and PDLC devices in the OFF and ON state: (**a**) V_{RMS} = 0 V; (**b**) V_{RMS} = 24 V.

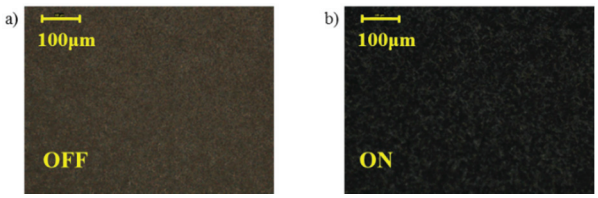

3. Impedance Behavior

The complex impedance was measured using a sinusoidal voltage signal with 100 mV_{RMS} and frequency sweeping in the range from 10^{-1} to 10^{7} Hz. The modulus and phase measurements corresponding to the PDLC device can be represented in a Bode plot, where the trend of the impedance magnitude and phase can be analyzed. Figure 2 shows the experimental data of the magnitude and phase of impedance as a function of frequency, measured in the temperature range between 25 and 40 °C. Impedance results in all devices are similar and the small discrepancy should be due to differences in the preparation of the PDLC composites. Selecting the suitable frequency range for the operation of the devices is a matter of simplifying the PDLC response, and Figure 2 can contribute to making this choice. Low frequencies are discarded because a low frequency electric field can induce degradation of the LC material due to the adsorption of ion charges and generation of strong electric field on the electrode layers [9,10], and a strong dependence with the temperature is also observed in Figure 2 at those frequencies. Moreover, the suitable frequency range should be selected by choosing the range where the device shows a purely capacitive behavior, simplifying its response. In that range, there is a linear decay in magnitude and a phase close to −90 degrees [2].

Figure 2. Experimental complex impedance as a function of frequency in the temperature range between 25 °C and 40 °C.

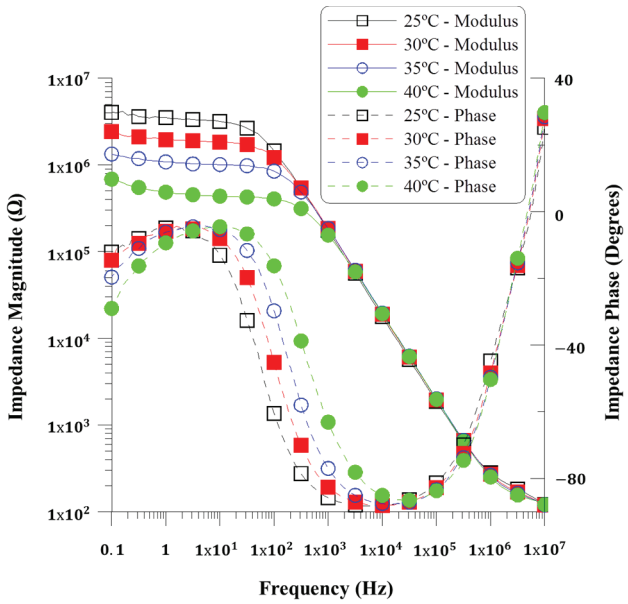

Complex impedance measurements displayed in the Figure 2 reveal that there is a capacitive behavior displacement when increasing the temperature, but also that the working frequency range of 10^4 to 10^5 Hz should be the optimal one, since the temperature dependence is null both in the impedance value and in the electrical response, which is purely capacitive.

4. Electrical Equivalent Circuit Proposal

An equivalent electric circuit has been obtained in order to study the dependence of electrical components on frequency, voltage and temperature. Figure 3 shows a Nyquist plot of experimental impedance, where its real part is plotted on the X axis and its imaginary part on the Y axis, the shape of which shape suggests that there are two different regions with a distinct behavior [11].

The semicircle portion, due to impedance on frequencies from 10 to 10^7 Hz, is usually related to the effect of charges stored in a capacitor which is discharging through a resistor. This discharge is produced with an exponential decay in time, being the diameter related to a time constant dependent on the resistor and capacitor values. Semicircle appearance means that there is only one time constant involved. This effect can be closely modeled by a Randles equivalent circuit.

Figure 3. Impedance spectrum (Nyquist plot) for PDLC.

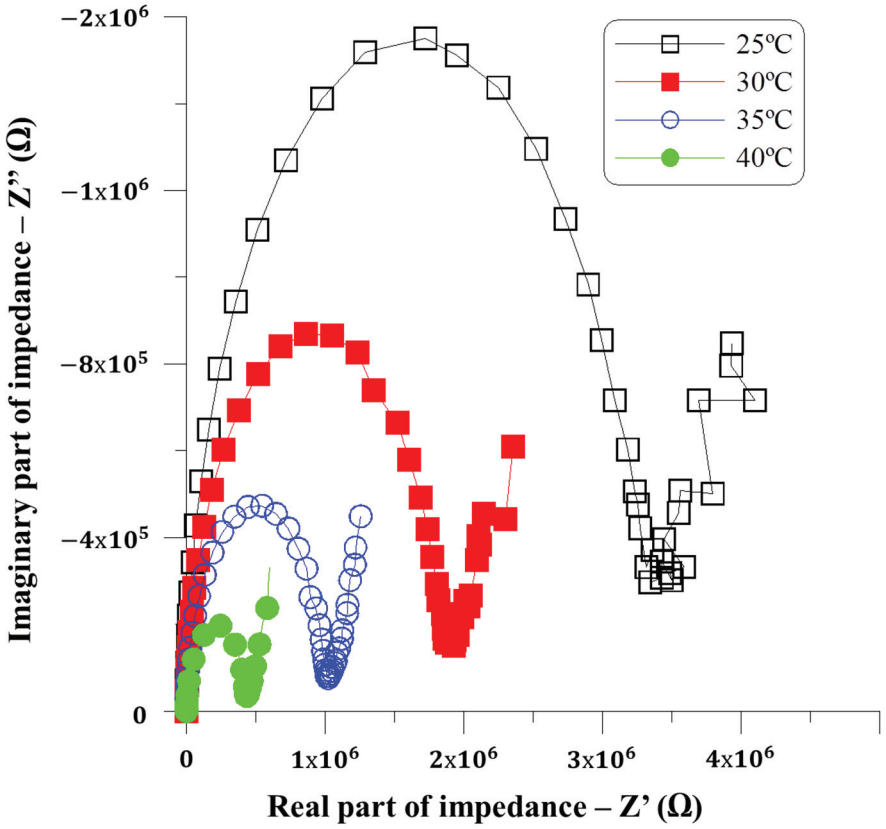

The equivalent circuit for the Randles cell is shown in Figure 4a. This circuit includes a resistor R_s, which represents the influence of electrodes, a double layer capacitor C_{dl} due to dipolar polarization and the symmetry of the device, which is composed of several layers, and a resistor R_{ct} standing for the mobility of free charges and dipolar displacement inside the device.

Figure 4. (**a**) Equivalent electric circuit for a frequency range from 10 to 10^7 Hz; (**b**) equivalent electric circuit for a frequency range from 10^{-1} to 10 Hz.

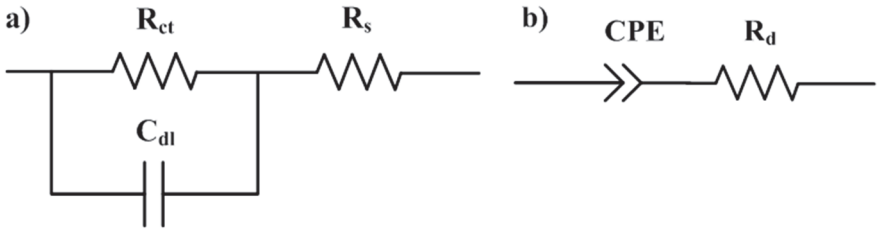

At high frequencies, C_{dl} impedance is as low as it behaves as a short circuit, and all of the impedance is coming from R_s. As it is a resistance due to electrodes, no apparent dependence with temperature is found at highest frequencies.

At low frequencies, C_{dl} impedance is as high as it behaves as an open circuit, and the main influence is R_{ct}, which value is thus related with the diameter of the semicircle of Figure 3. As a resistance due to charge transfer or movement, it depends clearly on temperature.

Nyquist plots show also a straight tail with a certain slope which appears at low frequencies in the range of 10^{-1} Hz to 10 Hz. As it is shown in Figure 3, during this frequency range, the phase of the impedance, *i.e.*, the slope on the Nyquist plot, remains almost constant. These results are in good agreement with those showed in Figure 2, at low frequencies. Several researches have reported a similar behavior [9,10,12–14], where the constant phase is explained by the creation of a strong electric field on the alignment layers. Therefore, a constant phase element (CPE) has been included to model the phenomenon.

CPE is a simple distributed element which tends to behave as a capacitor and has a constant phase angle in the impedance. The electric equivalent circuit proposed for such situation is represented in Figure 4b. The model includes an association CPE in series with a resistance R_d due to dipolar displacement.

Based on the fact that each frequency range presents a different behavior, a combination of the two proposed different equivalent circuits must cover the whole range. The complex impedance Z for these equivalent circuits can be described by Equation (1) for higher frequencies and Equation (2) for lower ones:

$$Z|_{10<f<10^7} = R_s + \frac{R_{ct}}{1 + \mathrm{s} \cdot \mathrm{C_{dl}} \cdot R_{ct}} \quad (1)$$

$$\mathrm{Z}|_{10^{-1}<f<10} = R_d + \frac{1}{\mathrm{T} \cdot \mathrm{s}^{-\mathrm{P}}} \quad (2)$$

The coefficient T and the exponent P are the parameters of the CPE. Generally, 0 < P < 1; however, CPE tends to a response of a capacitor of capacitance T when P is equal to 1. As the frequency ranges could be separated in the electrical circuit effects, both electric circuits can be simplified in a single circuit when the low frequencies parameters (CPE and R_d) are embedded in the R_{ct} element. This proposal is shown in Figure 5, valid for the whole frequency range between 10^{-1} and 10^7 Hz. The influence of each element will depend on the frequency range.

Figure 5. Equivalent electric circuit for a frequency range of 10^{-1} to 10^{7} Hz.

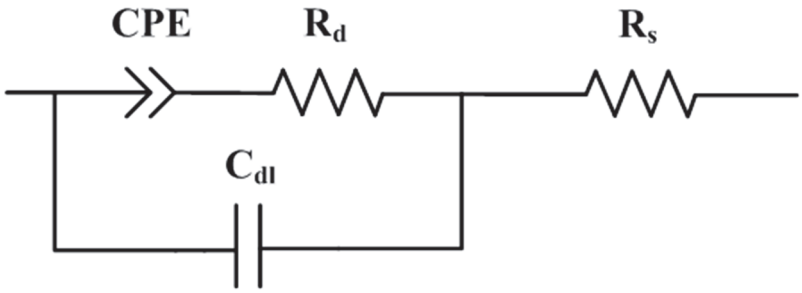

The following fit is done for the measurements at 25 °C. For high frequencies, the capacitive elements act as short circuit. Thus, the value of R_s is equivalent to the impedance magnitude at highest frequency. This impedance has a value of 178 Ω (see Figure 2). On the other hand, the capacitance C_{dl} can be estimated using the impedance magnitude plot of Figure 1. At frequencies into the selected 10 to 100 kHz range, when the device has a purely capacitive behavior because the phase is close to −90°, C_{dl} should be the main contribution, and could be calculated using the following expression (derived from the one of a capacitor impedance):

$$C_{dl} = \frac{1}{2 \cdot \pi \cdot f_{-90°} \cdot |Z|_{-90}} \tag{3}$$

Therefore, the capacitances C_{dl} are 0.89 nF. Complex non-linear least squares (CNLS) was used to obtain the value of R_d and the parameters of CPE, fitting the rest of the equivalent circuit parameters of Figure 5 with the impedance measurements, and using the Levenberg Marquardt nonlinear interpolation method [15]. The elements of the equivalent circuits are given in Table 1.

Table 1. Results of fitting presented in the Figure 5.

Parameter	Value	Error (%)
R_d (MΩ)	3.01	1.7
CPE-T	9.06×10^{-7}	4.7
CPE-P	0.37	8.8

The experimental magnitude and phase impedance were compared with the simulated data to validate the proposed equivalent electric circuit. This comparison is shown in Figure 6 as Bode plots. It can be inferred that the electric equivalent circuit proposed in Figure 5 satisfactorily reproduces the performance of impedance complex behavior for the PDLC devices under study in a wide frequency range. A slight discrepancy appears in the high frequency region, probably due to the inductance of the PDLC wires.

Figure 6. Experimental modulus and phase (squares-line) and simulated data (triangles-dashed line) for a frequency range from 10^{-1} Hz to 10^{7} Hz in the PDLCs devices.

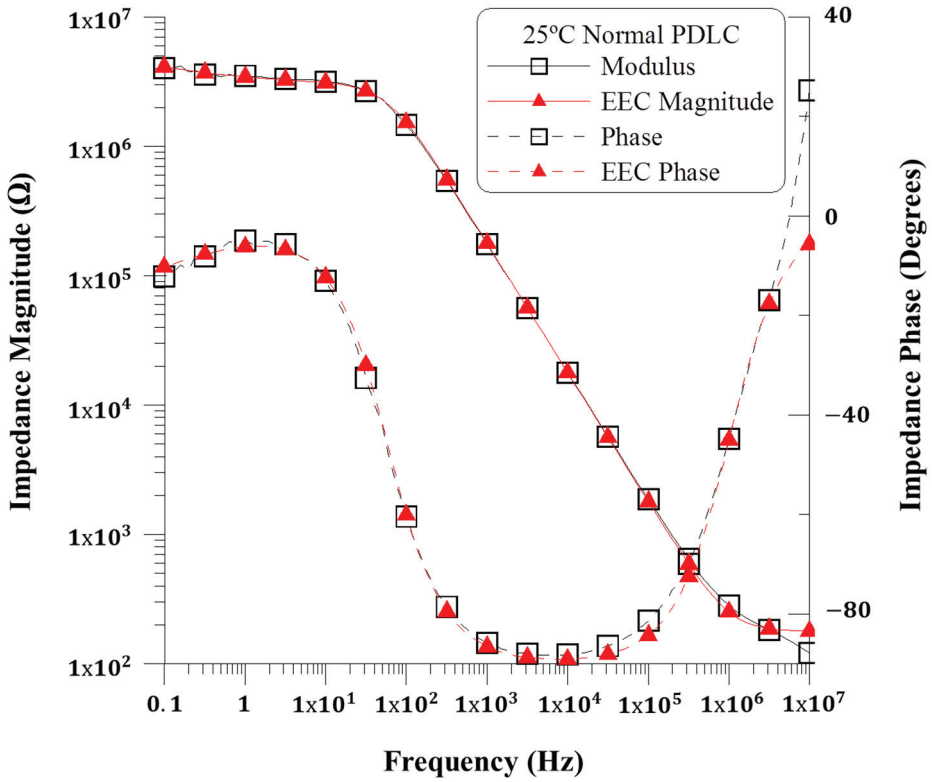

Once the equivalent circuit has been fitted with the impedance measurement for a given temperature, the evolution of the electrical response as the temperature increases has also been analyzed. The previous fitting is repeated for the measurements at every temperature. At high frequencies, the R_s element is the main influence in the electric circuit. At these frequencies the temperature dependence is null and does not lead to a change in the complex impedance; therefore, the evolution of the R_s is independent of temperature. Moreover, in order to analyze the influence with temperature, the C_{dl} parameter has been added in the fitting.

Table 2 shows the evolution of the retrieved fitted elements of the equivalent circuit with the temperature. These results are in good agreement with those reported previously in the diagram showing the experimental complex impedance as a function of frequency (Figure 2).

The influence of C_{dl} related to dipolar polarization is independent with temperature, whereas CPE-P and CPE-T parameters related to ion accumulation, increase with temperature. Therefore, as it is expected from the above discussion, PDLC has a less capacitive behavior when the temperature is increased. The exception is observed in R_d parameter related to dipolar displacement.

On the other hand, the resistance R_d value is now the one related to the diameter of the semicircle in the Nyquist plot. The Figure 3 shows that when temperature increases, the diameter of the semicircle decreases, and also the value of R_d and thus the dipolar displacement. The C_{dl} element at the whole frequency range (10^{-1}–10^{7} Hz) slightly changes with temperature, as the constant shape of the semicircle predicts. The straight tails of Nyquist plots at Figure 3 are related with the component

CPE, and the slope depends on the parameter CPE-P. The slope increases with the temperature. This behavior can be reflected in the values of the CPE-P parameter in Table 2. Further characterizations must be done to explain this effect.

Table 2. Results of fitting in the temperature range of 25 to 40 °C.

Parameter	Parameter@25 °C	Value	Error%
@25 °C	R_d (MΩ)	3.00	1.72
	C_{dl} (nF)	0.89	0.45
	CPE-T	9.15×10^{-7}	5.26
	CPE-P	0.37	8.89
@30 °C	R_d (MΩ)	1.73	1.08
	C_{dl} (nF)	0.83	0.40
	CPE-T	1.51×10^{-6}	3.82
	CPE-P	0.43	5.91
@35 °C	R_d (MΩ)	0.96	0.71
	C_{dl} (nF)	0.82	0.40
	CPE-T	2.38×10^{-6}	3.01
	CPE-P	0.55	3.69
@40 °C	R_d (MΩ)	0.41	0.95
	C_{dl} (nF)	0.84	0.64
	CPE-T	3.39×10^{-6}	3.07
	CPE-P	0.58	3.41

5. Conclusions

In this work, electrical properties of PDLCs have been studied as a function of temperature and frequency of the applied voltage. An electrical model is suggested and validated. Using the proposed model, many physical processes can be simulated, such as influence of electrodes, dipole movements contribution, ion charge accumulates and the effects of the temperature. Future research will focus on the simulation of optimized driving circuits and signals in order to reduce power consumption using this equivalent circuit.

Acknowledgments

This work was supported by the Ministerio de Ciencia e Innovación of Spain (grant No. TEC2009-13991-C02-01) and Comunidad de Madrid (grant No. FACTOTEM2 S2009/ESP-1781).

Author Contributions

All the authors contributed equally to the manuscript.

Conflicts of Interest

The authors declare no conflict of interest.

References

1. Yang, D.-K.; Wu, S.-T. *Liquid Crystal Materials, in Fundamentals of Liquid Crystal Devices*; John Wiley and Sons, Ltd.: Chichester, UK, 2006.
2. Sanchez, J.M.; Vazquez, C.; Perez, I.; Otón, J.M.; Rodriguez, I. Electro-optic system for online light transmission control of polymer-dispersed liquid crystal windows. *Opt. Eng.* **2002**, *41*, 1608–1611.
3. Pontes, M.A.J.; Vázquez, C.; Pena, J.M.S.; Lallana, P.C.; Montero, D.S. Variable Optical Attenuator for Perfluorinated Gradual Index Polymer Optical Fiber Using a Polymer Dispersed Liquid Crystal Cell. In Proceedings of the SPIE, Liquid Crystals: Optics and Applications, Warsaw, Poland, 30 August–1 September 2005.
4. Crooker, P.P.; Yang, D.K. Polymer-dispersed chiral liquid crystal color display. *Appl. Phys. Lett.* **1990**, *57*, 2529–2531.
5. Ramsey, R.A.; Sharma, S.C.; Henry, R.M.; Atman, J.B. Electro-optical properties and interfacial charges in polymer-dispersed liquid crystal devices. *Mat. Res. Soc. Proc.* **2003**, *771*, 339–344.
6. Drzaic, P.S. *Liquid Crystal Dispersions*; World Scientific Publishing Co.: Singapore, Singapore, 1995.
7. Han, J.-W.; Kang, T.J.; Park, G. Effects of composition, curing-time, and temperature on the electro-optical characteristics of polymer-dispersed liquid crystal films. *J. Korean Phys. Soc.* **2000**, *36*, 156–163.
8. Fuh, A.Y.G.; Huang, K.L.; Lin, C.H.; Lin, I.-I.C.; Jiang, I.M. Studies of the dependence of the electra-optical characteristics of polymer dispersed liquid crystal films on curing temperature. *Chin J. Phys.* **1990**, *28*, 551–557.
9. Thurston, R.N.; Chengm, J.; Meyer, R.B.; Boyd, G.D. Physical mechanisms of DC switching in a liquid-crystal bistable boundary layer display. *J. Appl. Phys.* **1984**, *56*, doi:10.1063/1.333956.
10. Perlmutter, S.H.; Doroski, D.; Moddel, G. Degradation of liquid crystal device performance due to selective adsorption of ions. *Appl. Phys. Lett.* **1996**, *69*, doi:10.1063/1.117404.
11. Barsoukov, E.; Macdonald, J.R. *Impedance Spectroscopy: Theory, Experiment, and Applications*, 2nd ed.; John Wiley & Sons, Inc.: New York, NY, USA, 2005.
12. Bisquert, J.; Garcia-Belmonte, G.; Bueno, P.; Longo, E.; Buñhoes, L.O.S. Impedance of constant phase element CPE-blocked diffusion in film electrodes. *J. Electroanal. Chem.* **1998**, *452*, 229–234.
13. Biswas, K.; Sen, S.; Dutta, P.K. Realization of a constant phase element and its performance study in a differentiator circuit. *IEEE Trans. Circuits Syst. II Exp. Briefs* **2006**, *53*, 802–806.
14. Szypłowska, A.; Nakonieczna, A.; Wilczek, A.; Paszkowski, B.; Solecki, G.; Skierucha, W. Application of a coaxial-like sensor for impedance spectroscopy measurements of selected low-conductivity liquids. *Sensors* **2013**, *13*, 13301–13317.
15. Marquardt, D.M. An algorithm for least-squares estimation of nonlinear parameters. *SIAM J. Appl. Math.* **1963**, *11*, 431–441.

Liquid Crystalline Network Composites Reinforced by Silica Nanoparticles

Zhen Li, Yang Yang, Benye Qin, Xiaoyong Zhang, Lei Tao, Yen Wei and Yan Ji

Abstract: Liquid crystalline networks (LCNs) are a class of polymers, which are able to produce mechanical actuation in response to external stimuli. Recent creation of LCNs with exchangeable links (xLCNs) makes LCNs easy moldable. As the xLCNs need to be shaped at a high temperature, it is important to enhance their thermal and mechanical properties. In this paper, a series of xLCNs/SiO_2 composites containing 1%–7% SiO_2 nanoparitcles (SNP) were prepared and their thermal and mechanical properties were examined. The results show that xLCNs/SNP composites have lower liquid crystalline-isotropic phase transition temperature and higher decomposition temperature than pure LCN. The tensile strength and the elongation at break of xLCNs at high temperatures were also enhanced due to the addition of SNPs.

Reprinted from *Materials*. Cite as: Li, Z.; Yang, Y.; Qin, B.; Zhang, X.; Tao, L.; Wei, Y.; Ji, Y. Liquid Crystalline Network Composites Reinforced by Silica Nanoparticles. *Materials* **2014**, *7*, 5356–5365.

1. Introduction

Liquid crystalline networks (LCNs) are a type of smart materials which have the ability to convert external stimuli into mechanical response [1–3]. Due to such a capability and other remarkable physical characteristics, such as softness, lightweight, and so on [4], LCNs have been proposed as a promising candidate for many applications, such as muscle mimics [5–7], motors [8], contact lenses [9], microgrippers [10], microvalves [11], haptic devices [12], and tunable lasing media [13]. Usually the macroscopic orientation of liquid crystal order is hard to achieve, which has greatly limited their application in practice. Recently, the permanent network crosslinks were replaced by exchangeable links, resulting in the xLCNs [14]. Not only can the xLCNs be molded and remolded into various shapes, but also they can be aligned conveniently. As the xLCNs materials need to be processed at high temperatures, it is desirable to enhance their thermal and mechanical properties.

The incorporation of nanoparticles into LCNs is a commonly way to improve the LCN's performance. For examples, as carbon nanotubes (CNTs) are capable of converting light into heat efficiently, the LCNs became sensitive to light after the addition of CNTs [15,16]. The silica coated nanoparticles can also act as light absorber [17]. Schmidt's group reported the incorporation of superparamagnetic Fe_3O_4 nanoparticles into LCN. Due to hysteresis, the materials exhibited actuation upon the application of an alternating magnetic field [18]. Anisotropic magnetic nanoparticles were also incorporated into the LCN [19]. Other nanoparticles, such as $PbTiO_3$ [20], Molybdenumoxide [21], were also reported. There are investigations on the mechanical and thermal properties of the LCN and nano particles (NPs) composites [22]. In general, the presence of nanoparticles lowers liquid crystalline-isotropic phase transition temperature (Ti) and glass transition temperature (Tg) slightly, while increasing the stiffness of the materials. However, the corporation

of SiO_2 nanoparticles into LCN, especially "xLCN" with the exchangeable links, has not been investigated.

In many cases, SiO_2 nanoparticles were incorporated to reinforce polymeric materials. Chengfang Ou [23] reported three series of epoxy/SiO_2 composites. Compared to pure epoxy, these composites had higher Tg and decomposition temperature (Td). Alzina *et al.* modified the SiO_2 with epoxide functional groups and examined the thermal properties of the composite. In this system, the Tg and Td decreased in the presence of SiO_2 [24].

In this paper, a series of xLCNs/SiO_2 composites (xLCN/SNPs), which contained 1–7 wt% SiO_2 nanoparticles (SNP) were obtained. The thermal and mechanical tests show that xLCNs/SNP composites have lower Ti and higher Td than the pure xLCN. There is also an improvement on the tensile strength and the elongation at break due to the addition of SNP.

2. Results and Discussion

2.1. The Glass and Isotropic Transition Temperatures

DSC was utilized to determine the Tg and Ti of these composites. Figure 1 shows the DSC thermograms of the xLCN/SNP composites and the blank xLCN. Two thermal transitions appeared in each sample: a Tg and a Ti. An apparent difference of the Ti location can be seen from the curves. To obtain accurate value of Ti, the DSC measurements at different heating/cooling rate were taken and the Ti value was calculated by extrapolating the values to zero rate (Figure S1). As shown in Table 1, every Ti of the xLCN/SNP samples was lower than that of the blank xLCN. This is probably because nanoparticles act like impurities, disturbing the liquid crystal orientation [17,25,26]. Meanwhile, as the nanoparticles content increased, the Ti increased too. A possible explanation is that the SNPs also restrict the motion of the molecules. Similar to Ti, such phenomenon was observed for Tg.

Figure 1. DSC thermograms of xLCNs/SiO_2 composites (xLCN/SNP) and blank xLCN.

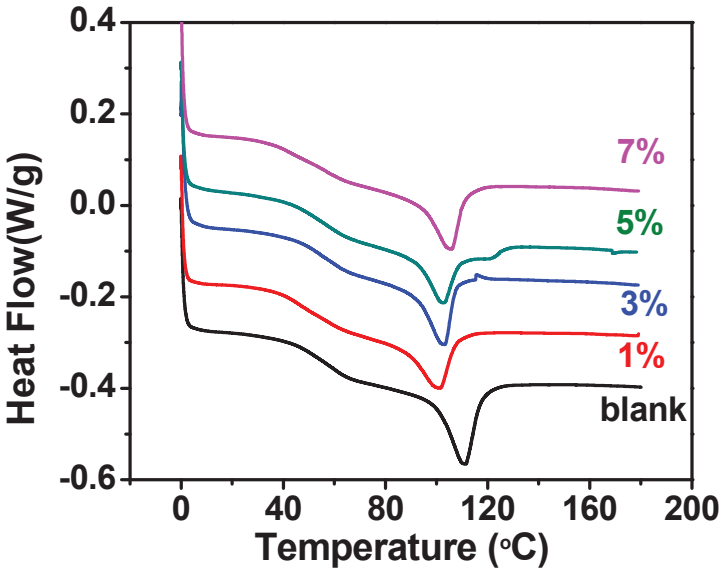

Table 1. Thermal data of xLCNs/SiO_2 composites (xLCN/SNP) and blank xLCN sample.

Sample	Tg (°C)	Ti (°C)	Td (°C)	Ti enthalpy (J/g)	Weight at 800 °C (%)
blank	60.2	114.3	329.5	7.93	0
SNP 1%	46.1	104.1	360.1	6.05	1.49
SNP 3%	54.4	105.2	340.4	6.64	3.12
SNP 5%	57.4	108.2	357.3	7.20	3.87
SNP 7%	56.8	107.9	356.2	7.06	5.92

2.2. Thermal Stability

Thermogravimetric analyses of thermoset nanocomposites are presented in Figure 2. The degradation of pure xLCN started at about 275 °C. When silica nanoparticles were added, the material degraded at higher temperatures. As can be seen from Figure 2, the Td of xLCN with 1% SNP was about 30 °C higher than that of the blank one. All the samples doped with silica nanoparticles were more stable than the blank sample. The weight percent at 800 °C of all samples were listed in Table 2, these values largely depended on the SNP content, and as the SNP increased, the weigh value at 800 °C increased too. Although there was not much relevance observed between Td and SNP contents, it still could be concluded that the overall thermal stability was improved by the addition of SiO_2 nanoparticles.

Figure 2. TGA curves of xLCNs/SiO_2 composites (xLCN/SNP) and blank xLCN sample.

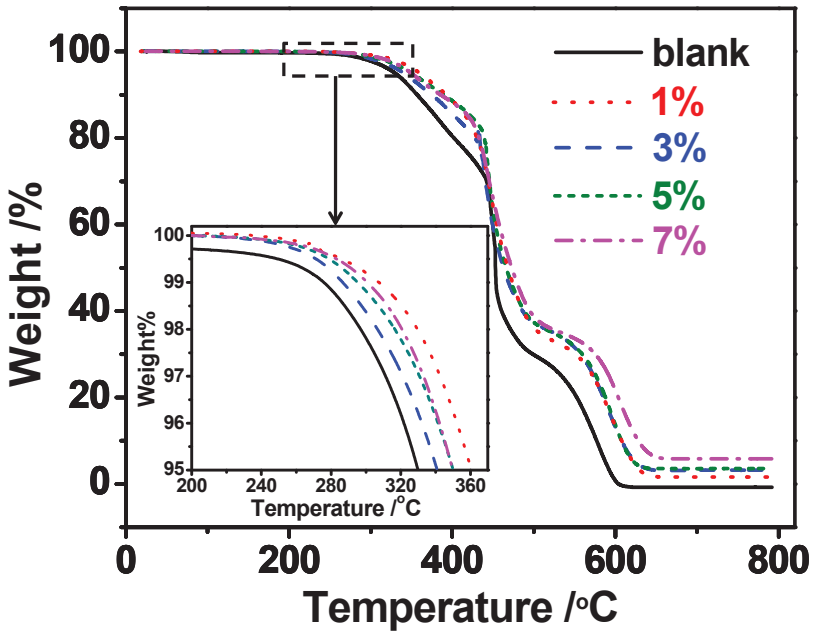

Table 2. Young's modulus of xLCNs/SiO_2 composites (xLCN/SNP) and blank xLCN sample at different temperatures.

Temperature (°C)	Blank	SNP 1%	SNP 3%	SNP 5%	SNP 7%
30	3.636	2.674	3.063	3.208	2.494
90	0.0454	0.0608	0.0557	0.0501	0.0447
160	0.0151	0.0182	0.0143	0.0199	0.0178

2.3. Dynamic Mechanical Properties of the Composites

The mechanical properties of the composites were investigated by a tensile test with the force increased by a rate of 0.1 N/min from 0.1 N to 18 N at different temperatures. Figure 3a shows the stress-strain curves of xLCN/SNP and blank xLCN samples at 30 °C. At this temperature, pure LCN always had higher Young's modulus. As shown in the picture, the blank sample had smaller strain than the xLCN/SNP composites under the same stress. However, as shown in Figure 3b, compared to the xLCN/SNP composites, the blank sample broke easily at lower strain. When silica nanoparticles were added, the modulus of the material reduced a bit but a bigger elongation at break was achieved for most samples.

Figure 3. Stress-Strain curves and breaking stress/strain plot of xLCNs/SiO_2 composites (xLCN/SNP) and blank xLCN samples at 30 °C.

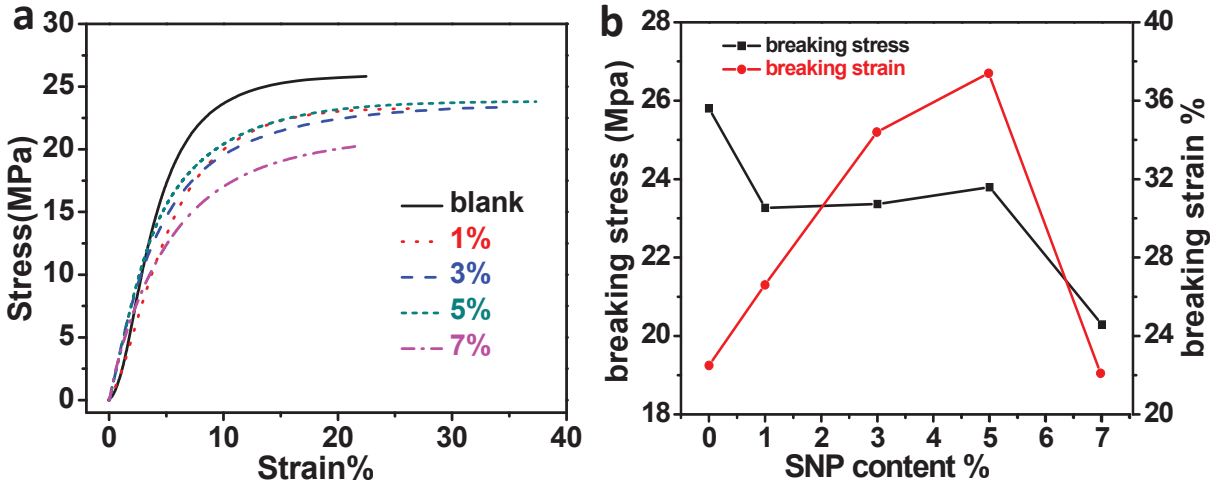

Since xLCNs need to be reshaped at a temperature above Tg to get a temporary shape and above 160 °C for a permanent shape, it is important to evaluate the mechanical properties of those composites at those high temperatures. As can be seen in Figure 4a, all the xLCN/SNP composites can stand larger stress than the pure xLCNs sample at the same strain, but the sample with excessive nanoparticles (>5%) would break more easily. As presented in Figure 4c, the mechanical properties of xLCN/SNP composites were all better than the blank sample at 160 °C. At this temperature, the sample with SNP content can stand bigger stress and larger strain before break, which can be seen in Figure 4d. As shown in Table 2, compared to the blank sample, most of the xLCN/SNP composites have bigger Young's modulus. One possible explanation for this phenomenon is that as the temperature rises over Tg or Ti, the interaction between polymer chains get weaker, and the interaction between SNP and polymer become to play a more important role [27].

Figure 4. Stress-Strain curves and breaking stress/strain plot of xLCNs/SiO_2 composites (xLCN/SNP) and blank xLCN sample at (**a**,**b**) 90 °C and (**c**,**d**) 160 °C.

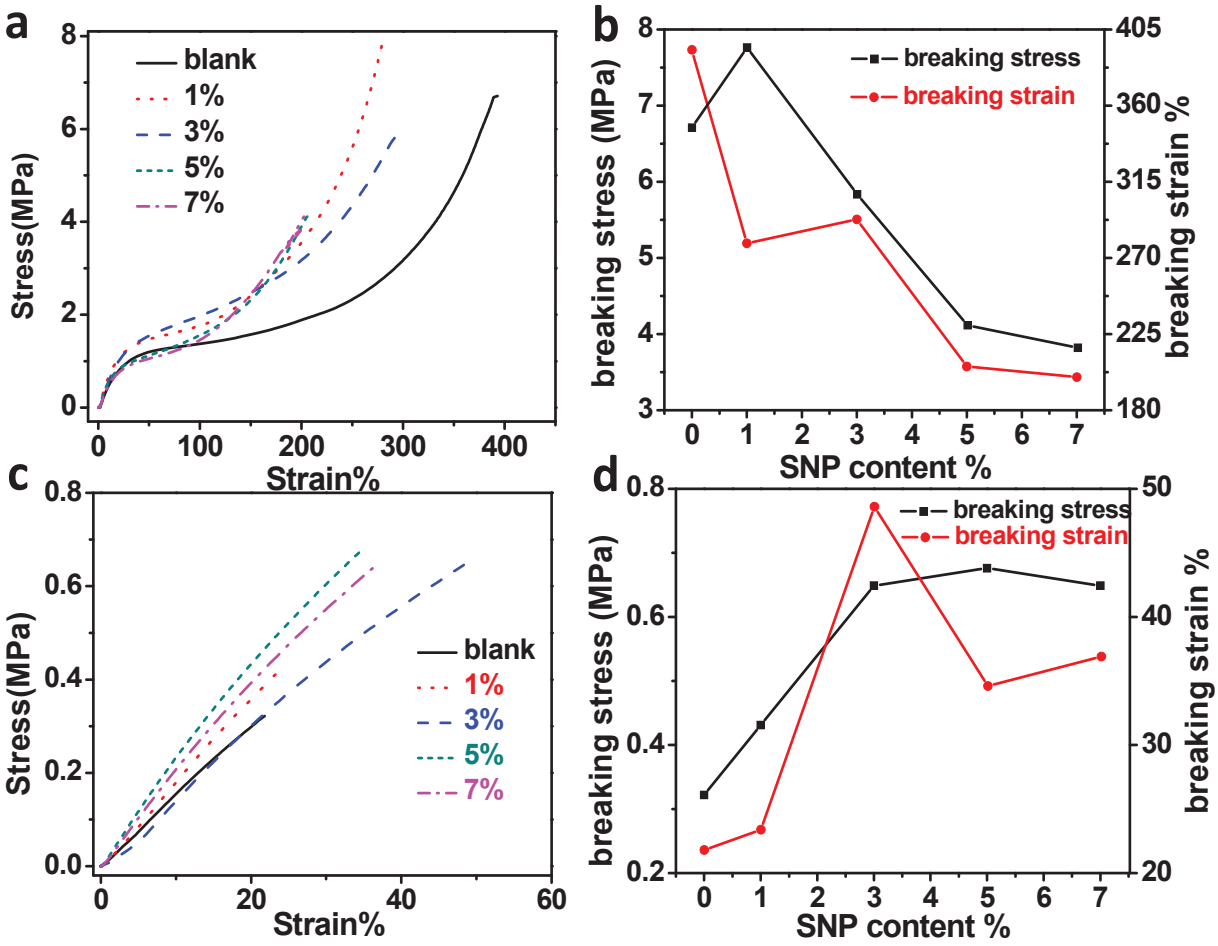

2.4. Morphology Investigation of Fractured Surface

SEM micrographs were recorded to investigate the agglomeration of the SiO_2 nanoparticles in polymer matrix, which has an important influence on the mechanical properties [28]. As presented in Figure 5a, the silica nanoparticles are narrowly dispersed with a polydispersity of 0.06 (Figure S2). A SEM image of the nanoparticles at a magnification of 30,000 was presented in Figure S3. Figure 5b–f shows SEM micrographs of the fracture surfaces of samples which were prepared in liquid nitrogen. The cross section of blank sample seems clean and homogeneous. As shown in Figure 5c,d, for the sample with lower content of SNP, the cross section was similar like the blank sample and agglomeration can be hardly observed by the small white dots. As the content of SNP increased, the fracture surface gets rough and small cluster can be observed, indicating the agglomeration. However, the clusters are far smaller than 1 μm and many isolated SiO_2 nanoparticle dots can be observed, which indicates a good dispersion.

Figure 5. SEM micrographs of (**a**) silica nanoparticles and the fracture surfaces of (**b**) blank samples and the xLCNs/SiO_2 composites (xLCN/SNP) composites with (**c**) 1%; (**d**) 3%; (**e**) 5%; (**f**) 7% content.

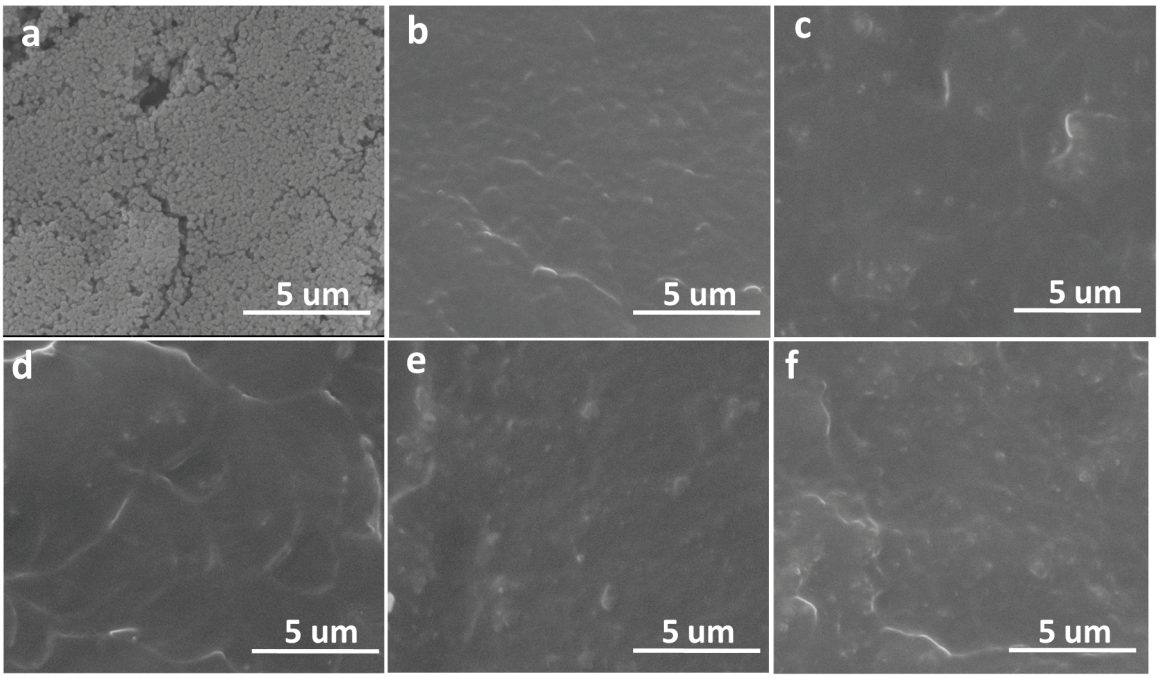

2.5. Thermal Actuation and Shape Memory

Like the blank sample, all the monodomain SiO_2 dispersed xLCNs can show the similar thermal reversible actuation and the polydomain samples exhibit the irreversible triple shape memory effect. For example, a free-standing monodomain xLCN/SNP (5%) sample was prepared by the method reported before [14]. Figure 6a shows the change of natural length of the monodomain xLCN/SNP (5%) film at different temperatures. At the temperature (115 °C) above Ti, the sample strip was in isotropic phase. When it cooled down to room temperature (30 °C), the sample elongated to an uniaxially aligned strip. The triple shape-memory of the polydomain xLCN/SNP (5%) was demonstrated in Figure 6b. The sample with a flat shape (A) was deformed into a V-shape (B) at 130 °C. After cooling down to 75 °C, this shape was fixed temporarily. Then the sample was further deformed at 75 °C into a new shape (C), which was then fixed by cooling below Tg. During the heating process, the sample recovered the shape B (above Tg) and then the original shape A (above Ti) successively. As shown in this experiment, xLCN still have the triple shape memory effect and the corresponding monodomain maintains the properties with the absence of SNPs.

Figure 6. (**a**) The change of natural length of a free-standing monodomain xLCNs/SiO_2 composites (xLCN/SNP) (5 wt%) between the liquid-crystal phase (30 °C) and the isotropic phase (115 °C); (**b**) Triple shape memory of a polydomain xLCNs/SiO_2 composites (xLCN/SNP) (5 wt%) sample.

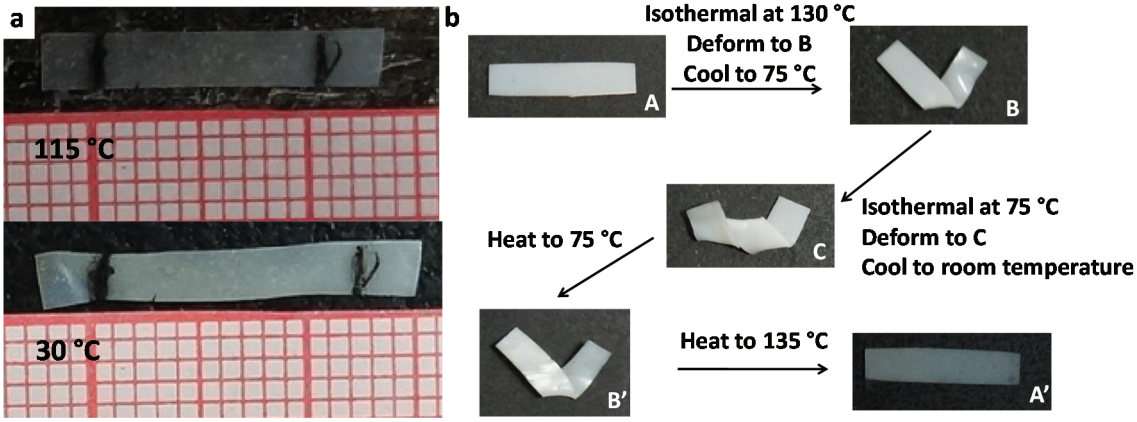

3. Experimental Section

3.1. Preparation of SiO_2 Nanoparticles

Silica nanoparticles (SNP) were synthesized using the classic Stober method [29]. Catalyzed by ammonia, tetraethyl orthosilicate (TEOS) were hydrolyzed in ethanol. An amount of 1.9 g aqueous ammonia solution containing 28% NH_4OH was diluted in technical ethanol (96%) to 20 mL. An amount of 8.33 g TEOS was dissolved in technical ethanol to 20 mL and was slowly added to the NH_4OH solution. Then the mixture was stirred overnight at room temperature. The product was separated by centrifugation at 8000 rpm and dried in vacuum at 60 °C. Dynamic light scattering (DLS) showed the nanoparticles have a size of 250 nm.

3.2. Preparation of xLCNs/SNP Film

The process for the synthesis of the LCN/SNP composites is presented in Scheme 1. An amount of 0.298 g 4,4'-dihydroxybiphenyl, 0.202 g sebacic acid, and various SNP content (1%–7%) were dispersed in chloroform and sonicated for 5 min. Then the mixture was evaporated and melt at 160 °C before a triazabicyclodecene catalyst (5 mol% to the COOH groups) was introduced and stirred manually until homogeneous. Then the mixture was cured at 180 °C for 4 h between two glass slides covered with polytetrafluoroethylene tape. The monodomain preparation procedure is exactly the same as that used in former paper [14], which has given all the detailed information.

Scheme 1. Sketch of the chemical process to obtain xLCNs/SiO_2 composites (xLCN/SNP).

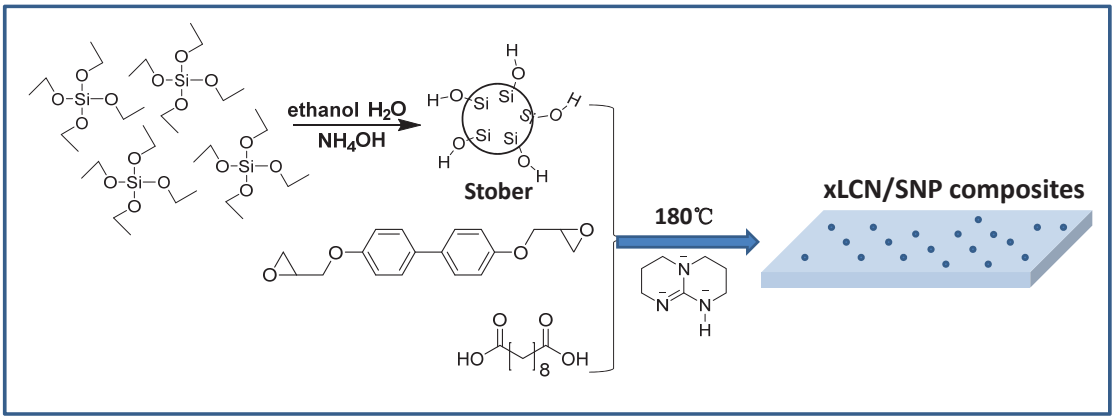

3.3. Characterization

DSC measurements were performed on TA 2000 analyzer (TA Instruments, New Castle, PA, USA). Appropriate amount of samples were heated from 20 °C to 180 °C at a temperature scanning rate of 10 °C/min under dry nitrogen atmosphere. The DSC measurements at different heating/cooling rate of 5 °C/min, 10 °C/min, 15 °C/min, 20 °C/min, 25 °C/min were taken and the Ti value was calculated by extrapolating the values to zero rate (Figure S1). Thermogravimetric analyses (TGA) were performed on a TA-Q50 (TA Instruments, New Castle, PA, USA), under air atmosphere with a heating rate of 20 °C/min from 30 °C to 800 °C.The morphology of the xLCN/SNP film was obtained by scanning electron microscopic (SEM) (FEI, Hillsboro, TX, USA).The tensile tests were measured by a dynamic mechanical analyzer (DMA) (TA Instruments, New Castle, PA, USA). For every sample, the force increased from 0.1 N to 18 N by a rate of 0.1 N/min at 30 °C, 90 °C, and 160 °C.

4. Conclusions

In this paper, a series of xLCNs/SiO_2 composites with 1–7 wt% SiO_2 nanoparitcles (SNP) were obtained. According to DSC, the Tg and Ti of the all xLCN/SNP samples were lower than that of pure LCN. Determined by TGA, the Td of the xLCN/SNP composites was always higher than that of pure LCN and exhibited a maximum increment of 35 °C by the addition of 1 wt% SiO_2. Morphology investigation proved that the SiO_2 nanoparticles were well dispersed. The stress-strain results showed that at a temperature above Tg or even above Ti, xLCN/SNP composites demonstrated higher tensile strength and the elongation at break. In summary, by incorporation the SiO_2 nanoparticles into xLCN materials, xLCN/SNP composites with better thermal stability and mechanical property were achieved, which may improve the performance of the xLCNs during molding and reshaping process.

Acknowledgments

This research was supported by the National Science Foundation of China (No. 21274075 and No. 51203086) and the National 973 Project of China (No. 2011CB935700).

Author Contributions

Yan Ji developed the concept, Lei Tao, Yan Ji and Yen Wei arranged the funding and infrastructure for the project, Zhen Li performed the experiments, Yang Yang, Benye Qin, and Xiaoyong Zhang participated in the preparation of xLCNs samples, and Zhen Li, Yan Ji and Yen Wei contributed to writing the paper.

Conflicts of Interest

The authors declare no conflict of interest.

References

1. Warner, M.; Terentjev, E.M. *Liquid Crystal Elastomers*; Oxford University Press: Oxford, UK, 2003; Volume 120.
2. Küpfer, J.; Finkelmann, H. Liquid crystal elastomers: Influence of the orientational distribution of the crosslinks on the phase behaviour and reorientation processes. *Macromol. Chem. Phys.* **1994**, *195*, 1353–1367.
3. Hogan, P.; Tajbakhsh, A.; Terentjev, E. Uv manipulation of order and macroscopic shape in nematic elastomers. *Phys. Rev. E* **2002**, *65*, 041720.
4. Ji, Y.; Marshall, J.E.; Terentjev, E.M. Nanoparticle-liquid crystalline elastomer composites. *Polymers* **2012**, *4*, 316–340.
5. Marshall, J.E.; Gallagher, S.; Terentjev, E.M.; Smoukov, S.K. Anisotropic colloidal micromuscles from liquid crystal elastomers. *J. Am. Chem. Soc.* **2013**, *136*, 474–479.
6. Thomsen, D.L.; Keller, P.; Naciri, J.; Pink, R.; Jeon, H.; Shenoy, D.; Ratna, B.R. Liquid crystal elastomers with mechanical properties of a muscle. *Macromolecules* **2001**, *34*, 5868–5875.
7. Tajbakhsh, A.; Terentjev, E. Spontaneous thermal expansion of nematic elastomers. *Eur. Phys. J. E* **2001**, *6*, 181–188.
8. Yamada, M.; Kondo, M.; Mamiya, J.-i.; Yu, Y.; Kinoshita, M.; Barrett, C.J.; Ikeda, T. Photomobile polymer materials: Towards light-driven plastic motors. *Angew. Chem. Int. Ed.* **2008**, *47*, 4986–4988.
9. Amigó-Melchior, A.; Finkelmann, H. A concept for bifocal contact—or intraocular lenses: Liquid single crystal hydrogels ("LSCH"). *Polym. Adv. Technol.* **2002**, *13*, 363–369.
10. Sánchez-Ferrer, A.; Fischl, T.; Stubenrauch, M.; Wurmus, H.; Hoffmann, M.; Finkelmann, H. Photo-crosslinked side-chain liquid-crystalline elastomers for microsystems. *Macromol. Chem. Phys.* **2009**, *210*, 1671–1677.
11. Sánchez-Ferrer, A.; Fischl, T.; Stubenrauch, M.; Albrecht, A.; Wurmus, H.; Hoffmann, M.; Finkelmann, H. Liquid-crystalline elastomer microvalve for microfluidics. *Adv. Mater.* **2011**, *23*, 4526–4530.

12. Torras, N.; Zinoviev, K.E.; Esteve, J.; Sánchez-Ferrer, A. Liquid-crystalline elastomer micropillar array for haptic actuation. *J. Mater. Chem. C* **2013**, *1*, 5183–5190.
13. Finkelmann, H.; Kim, S.T.; Palffy-Muhoray, P.; Taheri, B. Tunable mirrorless lasing in cholesteric liquid crystalline elastomers. *Adv. Mater.* **2001**, *13*, 1069–1072.
14. Pei, Z.; Yang, Y.; Chen, Q.; Terentjev, E.M.; Wei, Y.; Ji, Y. Mouldable liquid-crystalline elastomer actuators with exchangeable covalent bonds. *Nat. Mater.* **2014**, *13*, 36–41.
15. Ji, Y.; Huang, Y.Y.; Terentjev, E.M. Dissolving and aligning carbon nanotubes in thermotropic liquid crystals. *Langmuir* **2011**, *27*, 13254–13260.
16. Ji, Y.; Huang, Y.Y.; Rungsawang, R.; Terentjev, E.M. Dispersion and alignment of carbon nanotubes in liquid crystalline polymers and elastomers. *Adv. Mater.* **2010**, *22*, 3436–3440.
17. Mukherjee, P.K. Influence of non-mesogenic impurities on a nematic to isotropic phase transition. *Liq. Cryst.* **1997**, *22*, 239–243.
18. Kaiser, A.; Winkler, M.; Krause, S.; Finkelmann, H.; Schmidt, A.M. Magnetoactive liquid crystal elastomer nanocomposites. *J. Mater. Chem.* **2009**, *19*, 538–543.
19. Haberl, J.M.; Sánchez-Ferrer, A.; Mihut, A.M.; Dietsch, H.; Hirt, A.M.; Mezzenga, R. Liquid-crystalline elastomer-nanoparticle hybrids with reversible switch of magnetic memory. *Adv. Mater.* **2013**, *25*, 1787–1791.
20. Domenici, V.; Zupančič, B.; Laguta, V.V.; Belous, A.G.; V'yunov, O.I.; Remškar, M.; Zalar, B. $PbTiO_3$ nanoparticles embedded in a liquid crystalline elastomer matrix: Structural and ordering properties. *J. Phys. Chem. C* **2010**, *114*, 10782–10789.
21. Domenici, V.; Conradi, M.; Remškar, M.; Viršek, M.; Zupančič, B.; Mrzel, A.; Chambers, M.; Zalar, B. New composite films based on MoO_{3-x} nanowires aligned in a liquid single crystal elastomer matrix. *J. Mater. Sci.* **2011**, *46*, 3639–3645.
22. Haberl, J.M.; Sánchez-Ferrer, A.; Mihut, A.M.; Dietsch, H.; Hirt, A.M.; Mezzenga, R. Strain-induced macroscopic magnetic anisotropy from smectic liquid-crystalline elastomer-maghemite nanoparticle hybrid nanocomposites. *Nanoscale* **2013**, *5*, 5539–5548.
23. Ou, C.-F.; Shiu, M.-C. Epoxy composites reinforced by different size silica nanoparticles. *J. Appl. Polym. Sci.* **2010**, *115*, 2648–2653.
24. Alzina, C.; Sbirrazzuoli, N.; Mija, A. Epoxy-amine based nanocomposites reinforced by silica nanoparticles. Relationships between morphologic aspects, cure kinetics, and thermal properties. *J. Phys. Chem. C* **2011**, *115*, 22789–22795.
25. Poulin, P.; Raghunathan, V.; Richetti, P.; Roux, D. On the dispersion of latex particles in a nematic solution. I. Experimental evidence and a simple model. *J. Phys. II* **1994**, *4*, 1557–1569.
26. Anderson, V.; Terentjev, E. Cellular solid behaviour of liquid crystal colloids 2. Mechanical properties. *Eur. Phys. J. E* **2001**, *4*, 21–28.
27. Halder, S.; Ghosh, P.K.; Goyat, M.S.; Ray, S. Ultrasonic dual mode mixing and its effect on tensile properties of SiO_2-epoxy nanocomposite. *J. Adhes. Sci. Technol.* **2013**, *27*, 111–124.
28. Lai, Y.-H.; Kuo, M.; Huang, J.; Chen, M. On the peek composites reinforced by surface-modified nano-silica. *Mater. Sci. Eng.: A* **2007**, *458*, 158–169.
29. Stöber, W.; Fink, A.; Bohn, E. Controlled growth of monodisperse silica spheres in the micron size range. *J. Colloid Interface Sci.* **1968**, *26*, 62–69.

Part III: Lyotropic Liquid Crystals

From Cellulosic Based Liquid Crystalline Sheared Solutions to 1D and 2D Soft Materials

Maria Helena Godinho, Pedro Lúcio Almeida and João Luis Figueirinhas

Abstract: Liquid crystalline cellulosic-based solutions described by distinctive properties are at the origin of different kinds of multifunctional materials with unique characteristics. These solutions can form chiral nematic phases at rest, with tuneable photonic behavior, and exhibit a complex behavior associated with the onset of a network of director field defects under shear. Techniques, such as Nuclear Magnetic Resonance (NMR), Rheology coupled with NMR (Rheo-NMR), rheology, optical methods, Magnetic Resonance Imaging (MRI), Wide Angle X-rays Scattering (WAXS), were extensively used to enlighten the liquid crystalline characteristics of these cellulosic solutions. Cellulosic films produced by shear casting and fibers by electrospinning, from these liquid crystalline solutions, have regained wider attention due to recognition of their innovative properties associated to their biocompatibility. Electrospun membranes composed by helical and spiral shape fibers allow the achievement of large surface areas, leading to the improvement of the performance of this kind of systems. The moisture response, light modulated, wettability and the capability of orienting protein and cellulose crystals, opened a wide range of new applications to the shear casted films. Characterization by NMR, X-rays, tensile tests, AFM, and optical methods allowed detailed characterization of those soft cellulosic materials. In this work, special attention will be given to recent developments, including, among others, a moisture driven cellulosic motor and electro-optical devices.

Reprinted from *Materials*. Cite as: Godinho, M.H.; Almeida, P.L.; Figueirinhas, J.L. From Cellulosic Based Liquid Crystalline Sheared Solutions to 1D and 2D Soft Materials. *Materials* **2014**, *7*, 4601–4627.

1. Introduction

Cellulose, the main constituent of plant cell walls, is a linear polysaccharide (Figure 1), which is mainly used to produce paper. However, in this work we are more interested in soft materials obtained from converted cellulose, not only into nano rods, but also in cellulose derivatives. In 1976, Gray reported that concentrated solutions of cellulose derivatives could self-assemble into ordered phases [1]. Those liquid crystalline phases displayed colors that changed with concentration and viewing angle, which were attributed to a cholesteric structure. The maximum peak wavelength (λ_0) reflected by the samples for incident light normal to the surface may be expressed as, $\lambda_0 = n_e P \cos\theta$, where n_e is the average refractive index; P the helical pitch; and θ the angle between the light propagation direction and the helix axis [2]. The values of λ_0 may, therefore, be tuned by altering the helical pitch or the average refractive index of the chiral nematic material. Some theories were proposed to interpret the variation of the pitch with polymer concentration. For example, the theory

proposed by Kimura *et al*. [3] predicts a linear dependence of the reciprocal pitch against $\phi(1 - \phi/3)/(1 - \phi)^2$, where ϕ is the polymer concentration, which is in fairly good agreement with the experiments [4]. Due to cellulose relatively stiff cellulose backbone, which forces a parallel orientation of the chains, a wide range of cellulose derivatives was found to form both lyotropic and thermotropic chiral nematic liquid crystals [5]. The selective light reflection, as well as the optical turbidity of the liquid crystalline cellulose derivatives solutions can be tuned, not only by the application of external fields [6,7], but also by the addition of aqueous salt solvents [8] and by playing with solvent/cellulose derivative systems [9–11]. The dynamic control of the cholesteric coloration and optical clarity of lyotropic aqueous cellulose derivatives was more recently achieved by using various N-alkyl-substituted methylimidazolium salts and a weak electric field [12,13]. The electro-optical behavior of the system was interpreted in terms of the salt-containing liquid-crystalline system and the medium viscous electrolytic and high resistance characteristics [12]. In order to improve the optical characteristics of the solutions the treatment of surfaces, as well as the use of solvents that decrease the viscosity of the liquid crystalline cellulose solutions was investigated [14]. Many efforts were done to trap the chiral nematic structure into iridescent solid films. Principal attempts refer the use of solvents that can undergo polymerization and also the use of UV sensitive substituents [15–18]. Lasing in solid cross-linked cholesteric cellulose based films with high reflectivity doped with fluorescent dyes was also recently evidenced in literature [19]. The fabrication of cellulosic spheres by microfluidics, with iridescence was also described in literature [20]. addition to cellulose derivatives liquid crystalline phases it was also found that Nano crystalline cellulose (NCC) films were capable of reflecting colored light if prepared from liquid-crystalline cellulose suspensions. NCC liquid crystal templates were used to generate new photonic materials, which can combine mesoporosity with long-range chiral ordering [21,22]. Moreover the incorporation of NCC rods into composite materials results into systems with enhanced mechanical properties, which have been investigated systematically in literature [23]. NCC rods seemed the perfect material to incorporate in cellulosic water-soluble matrices because of their intrinsic hydrophilic character [24]. Many studies were performed and described in literature that concerns the preparation of films from NCC/polymer mixtures in aqueous media [25], more recently nano cellulose paper was applied as substrate and gate dielectric to produce flexible field effect transistors [26] and also electro-optical sensors [27].

Figure 1. Chemical structure of the repeating unit of cellulose (dimer cellobiose).

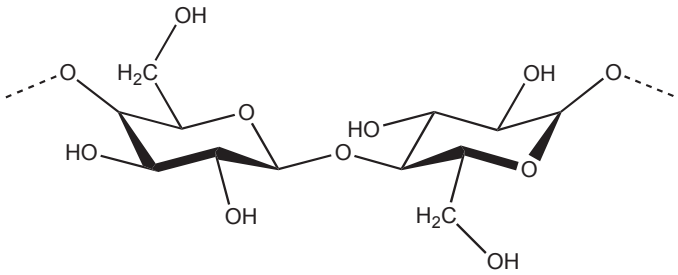

In addition to that, sheared cellulose derivatives casted solid films, with a complex network of defects, which are easily identified by polarizing optical microscopy (POM), under cross polars, were also obtained and studied [28]. Various reports were published in order to correlate the defects

appearance and the rheological behavior of the precursor solutions but some fundamental questions are not yet answered (Figure 2). X-rays results showed that the cholesteric order can be destroyed in sheared films and that a bundle of warped helicoidal fiber-like structures where the cellobiose block spins around the axis of the fiber can develop. The bundles should have fibers with both the levogyre and dextrogyre arrangements, with equal probabilities, and have a residual orientation along the shear direction [29].

Figure 2. Scanning electron microscopy micrograph of a free-standing cellulosic film prepared from a sheared liquid crystalline solution.

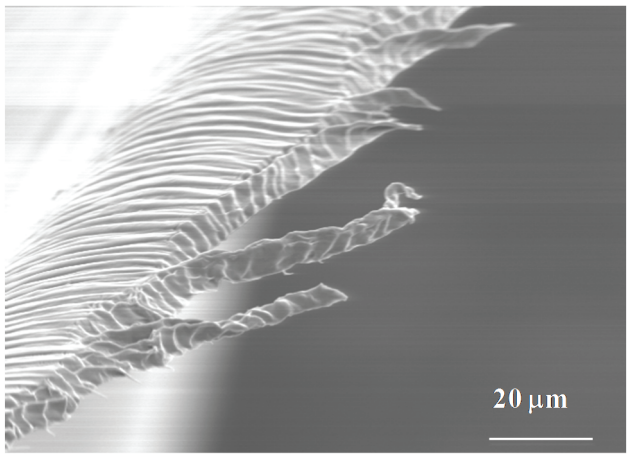

Atomic force microscopy (AFM) measurements revealed that sheared films topographical features could be affined by playing with the films processing conditions [28]. It was demonstrated that the films prepared from liquid crystalline solutions can show two periodic structures, primary and secondary set bands. The former consisting of bands perpendicular to the shear direction while the latter has the bands slightly tilted from that direction. An out-of-plane angle variation of the sinusoidal molecular orientation was also reported [29,30]. The anisotropic nature of cellulosic solutions give them also unique characteristics that has impact, for example, in the way the viscosity changes with polymer concentration. For low polymer concentrations, while in the isotropic phase, the viscosity of the solutions increases with the increase of polymer fraction. However, for higher polymer concentrations, corresponding to the formation of the liquid crystalline phase, the increase in concentration results in a decrease of the viscosity. This was attributed to the spontaneous orientation of the mesogenic cellulose segments above the critical concentration [31]. The viscosity drop, associated to the liquid crystalline phase appearance, is an important effect that one can take profit from when working with relatively high concentrated cellulose based solutions. The characteristics of the solutions make them suitable for preparing shear-casting films with unique characteristics that allowed the preparation of alignment layers to liquid crystals, as well as refractive gratings [24,27].

Electrospinning as well as cellulose acid hydrolysis (Figure 3) can be used to produce fibers from cellulose based liquid crystalline solutions, with diameters ranging from few nanometers to hundreds of microns, which can be at the origin of mats with very high surface areas [32]. The most interesting result obtained from cellulosic liquid crystals by using the electrospinning technique, was the

generation of jets and fibers with intrinsic curvature, which arise from stiff line defects (disclinations) that develop during processing. Due to the intrinsic curvature of the system micro-jets swinging as well as micro/nano fibers winding and overwinding, self-motions could be observed and controlled by adjusting temperature and electrospun experimental parameters. These cellulose-based materials not only mimic at the micro/nano scale the helical shapes observed, for example, in tendrils but also their motion and mechanical adaptability could be reproduced. The same mechanism was in action for all these systems providing that the same physical model, proposed for elastic filaments with intrinsic curvature, could be applicable. The cellulose-based non-woven mats produced were expected to play a significant role in the generation of nano- and microdevices, because of their capacities as separation media, actuators, and host materials for drug delivery [31–33].

Figure 3. Scanning electron microscopy micrographs of a nanocellulose fibers network mat obtained from cotton after acid hydrolysis.

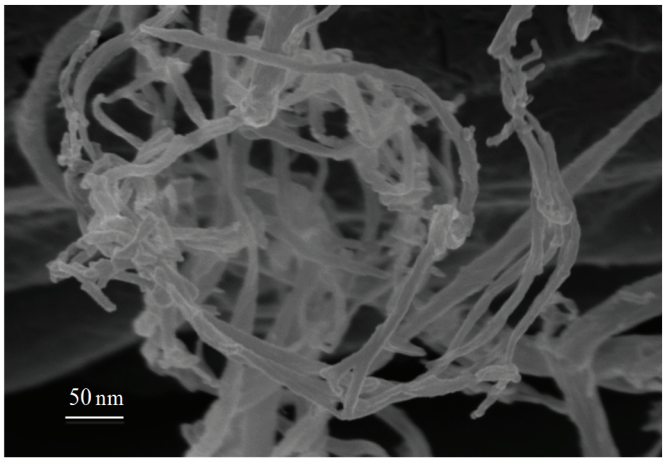

In this work, we aim to review snapshots of research carried out on cellulosic-based liquid crystalline systems, which give insights into the relation between structure/properties on sheared casted films and fibers and networks of cellulose nanorods (not organized in an iridescent cholesteric structure)/Liquid crystal systems. In particular we will focus on the use of several techniques, which include solid state NMR, Rheo-NMR, MRI, X-rays, AFM, and mechanical essays. To illustrate the potential applications of the fibers and films produced from liquid crystalline cellulose networks we refer their use to build a soft sensitive moisture motor and electro-optical devices.

2. Liquid Crystalline Solutions Studied by Nuclear Magnetic Resonance (NMR) Methods

2.1. Liquid Crystalline Cellulose Solutions Flow in Capillaries

In order to understand the origin of the intrinsic curvature observed for cellulosic liquid crystalline materials, Magnetic Resonance Imaging (MRI) experiments were performed on different acetoxypropylcellulose (APC) dimethylacetamide (DMac) solutions. The synthesis of APC was performed according to the procedure previously described in [34]. The MRI data were taken on a vertical wide bore 7.05 T Bruker 300 AVANCE III NMR spectrometer (Rheinstetten, Germany) according to [33]. The studies were performed on cellulosic solutions that were sheared in capillaries

with different diameters. The flow inside the capillaries and the jet at the end of them were observed. Depending on the shear rate and on the anisotropic characteristics of cellulosic solutions, the jet showed spontaneous curvature and torsion. MRI analysis allowed imaging of characteristic structure at chosen filament cross-sections along the capillary tube as can be observed in Figure 4.

Figure 4. Cellulosic solutions in a straight glass capillary. (**A**–**C**) are MRI images of the cross-section of a capillary filled with: (**A**) an isotropic cellulosic solution (20% w/w, APC/DMac); (**B**,**C**) a liquid crystalline solution (60% w/w, APC/DMac) in subsequent cross-sections. Solutions were continuously sheared for 10 min ($\dot{\gamma} = 20\ s^{-1}$) and frozen before MRI measurements. (**A1**), (**B1**) and (**C1**) show the time sequence illustrating the jet escaping of the free capillary end generated by different shear rates (in all three cases for the liquid crystalline solution). Reproduced from [33] with permission from The Royal Society of Chemistry.

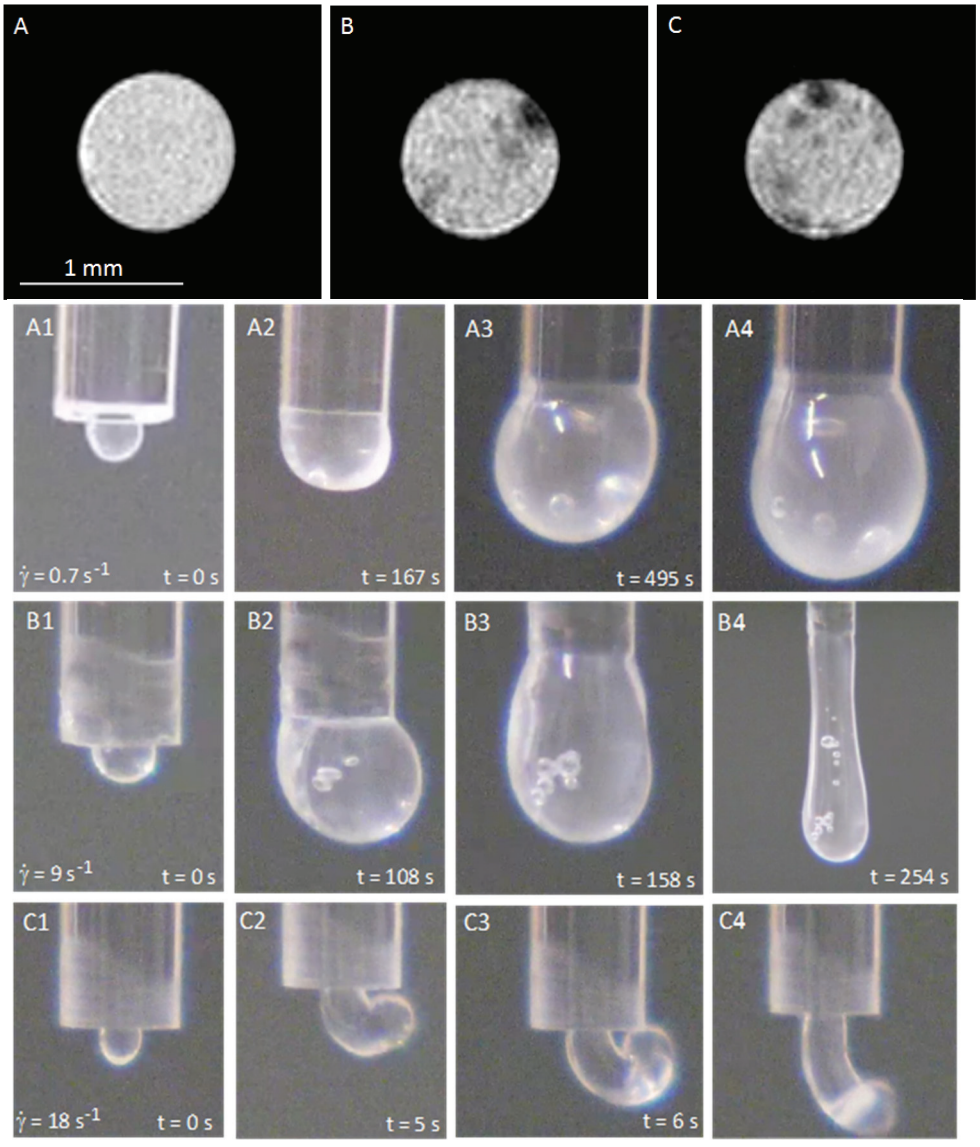

Isotropic solutions confined in the capillary, which generate straight fibers on extrusion, showed a homogeneous symmetric cross-section structure (Figure 4A), implying that the averaging of

differing structural features would maintain a straight fiber conformation. Confined solutions of cellulose in the cholesteric liquid-crystal phase, which generate curved fibers, showed a heterogeneous structure in cross-section with the hard "island" predominantly located closest to the tube walls and never in the middle of the tube. The off-axis position of the hard "islands" varies along the tube (Figure 4B,C). POM confirmed that the hard "islands" correspond to the core of a linear topological defect (disclination) that can be observed in anisotropic pre- sheared solutions above a certain critical shear rate (Figure 5). POM images show that the defects lines are forming a helix along the capillary tube. This observation is supported by the MRI measurements indicates that from one layer to the following the hard objects rotate (in Figure 4 an anticlockwise rotation can be seen). The MRI image contrast reflects the local mechanical stiffness of the material, so that dark regions represent hard "islands" on each cross-section, with the average diameter from 25 to 50 μm, which is much lower than the capillary diameter (R^*) and similar to the average diameter of the helices measured in POM images.

The present results show that liquid crystalline disclinations are at the origin of the intrinsic curvature observed for jets and electrospun fibers obtained from cellulosic mesophases. The intrinsic curvature of the fibers, responsible for their curl and twist, arises from an off-axis core line defect disclination which is present when the fibers were prepared from liquid crystalline solutions. The consequence of the intrinsic curvature of the system was also observed during thinning and break-up of jets produced by continuous motion of anisotropic solutions. The spirals and helices found at micro/nano scale mimic the shapes observed, for example, in hair [35] and tendrils [36] due to a similar intrinsic curvature dominated mechanism, providing that, for all these systems, the physical model proposed for elastic rods with intrinsic curvature could be applicable. The fine-tuning of temperature will allow us to control the non-woven self-winding mats' ability adjusting their surface-to-volume ratio, due to the intrinsic curvature of constituent fibers, which opens horizons for fabricating new natural scaffolds for tissue engineering [33].

Figure 5. A representative POM image, under cross polarizers, of an APC/dimethylacetamide helical liquid crystalline precursor solution inside a glass capillary (600 μm). The sample was frozen after being sheared (shear rate; $\dot{\gamma} = 18\ s^{-1}$) for 10 min. The axis of the tube is parallel to one of the polarizers. The helix radius, R, pitch $P = 2\ \pi R/\tan\theta$ and the helical angle θ are marked on the image. The natural curvature and twist parameters are set by $k = 1/R$ and $\tau = P/2\ \pi R^2$, respectively. Reproduced with permission from [33]. Copyright 2010, The Royal Society of Chemistry.

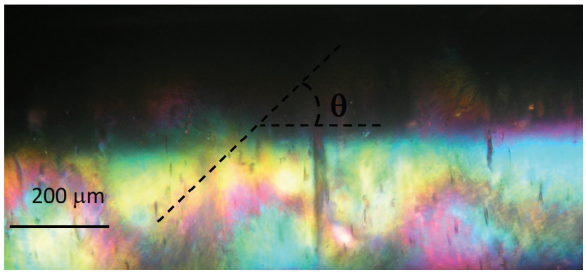

2.2. Rheo-NMR Studies of Precursor Cellulosic Solutions

The characterization of precursor cellulosic solutions was found to be crucial to understand the relation between properties and structure. In order to perform this goal, Rheo-NMR techniques have been used in the study of liquid crystalline cellulosic solutions under shear [37] and relaxation [38] while NMR spectroscopy was applied to the study of the corresponding films and fibers [39]. These studies allowed for the characterization of the molecular order and structure in these systems, yielding information not directly accessible to other techniques as light scattering [40] or Xray diffraction [41].

A Rheo-NMR study [42,43] on the model system hydroxypropylcellulose + deuterium oxide (HPC + D_2O) at 50% by weight concentration showed a rich and complex behavior both under shear and in relaxation as can be observed from the deuterium spectra recorded in both processes and shown in Figure 6 for selected shear rates.

Figure 6. NMR spectra evolution of HPC in D_2O. (**a**) During the shearing process with shear rates of 0.1 and 1 s^{-1}; (**b**) after the cessation of shear. Reprinted with permission from [42]. Copyright 2013, American Chemical Society.

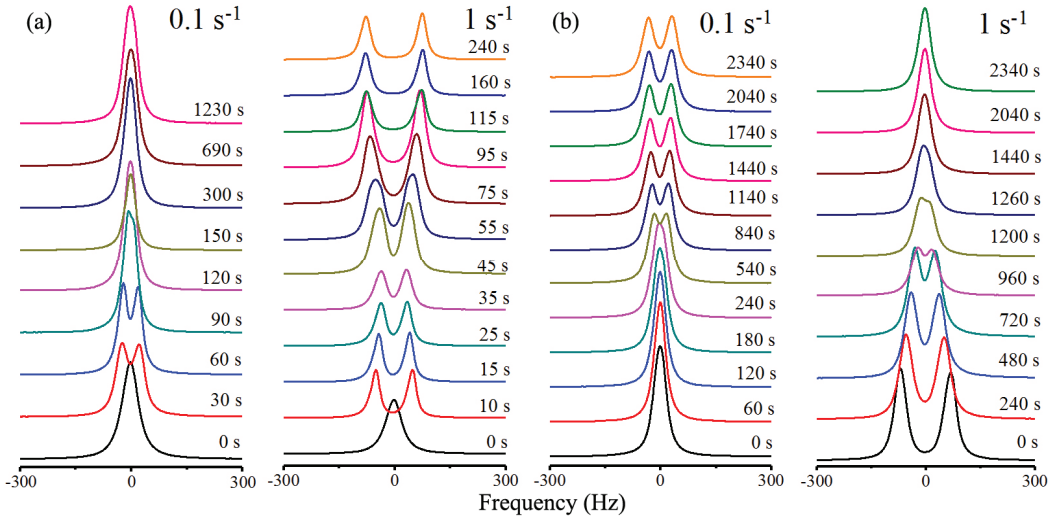

It was found under shear that depending upon the shear rate the system goes from a regime of tumbling cholesteric domains [44,45] observed at low shear rates $\dot{\gamma} = 0.1\ s^{-1}$ where the system order is low, to a regime of director flow alignment with partial or total helix suppression for shear rates $\dot{\gamma}$ of the order of 1 s^{-1} or above. The three distinct flow regimes introduced by Onogi and Asada [46] in the context of shear flow of LC polymers were directly identified in the Rheo-NMR [47] results and were ascribed to the tumbling of cholesteric domains, the partial flow alignment of the director and helix deformation and the director flow alignment with partial or total helix suppression. Relaxation data in the different regimes show that the system moves towards the reformation of the cholesteric domains and depending upon the starting point where the system is left in to relax this process may be more or less involved. When relaxation initiates from the tumbling cholesteric domains regime the cholesteric domains grow and possibly accrete giving rise to an immediate increase in order. When relaxation initiates from the flow director aligning regime, cholesteric helices

start to form from the aligned director state, producing a significant decrease in order that only reverts when the reformed cholesteric domains start to accrete and grow, a process that takes significantly longer times to develop.

This study was carried out through the analysis of the deuterium spectra arising from the D_2O molecules and shown in part in Figure 6. The spectra showed the presence of a single population of D_2O molecules experiencing a large motional averaging. The deuterium spectra were analysed and simulated considering the presence of water rich regions (WRR) imbedded with the polymer chains and the presence of fast molecular diffusion within these WRR that allow the D_2O molecules to sample the order of the neighbouring polymer chains. Based on those results, and the accumulated knowledge on this system [37], it was possible to identify five different mesoscopic states reached by the HPC/water system during shear and relaxation as shown in Figure 7. State I is the partially aligned cholesteric polydomain state obtained after relaxation from shearing with low shear rates. State II is the cholesteric polydomain state attained after relaxation from shearing with high shear rates. State III is the tumbling regime of the cholesteric domains obtained with low shear rates, state IV is the partial flow alignment state associated with the intermediate shear rates, and state V is the flow aligned nematic obtained at high shear rates. The up arrows indicate the relaxation path while the down arrows indicate the path under shear starting from the polydomain cholesteric reached in the preparation state. This picture is in direct correspondence with the three regions of steady shear flow introduced by Onogi and Asada [46], state III appears at low shear rates and corresponds to the tumbling regime, the intermediate region corresponds to state IV and state V is associated with the high shear rate region.

Figure 7. Mesoscopic states reached by the HPC/water system during shear and relaxation. Reprinted with permission from [42]. Copyright 2013, American Chemical Society.

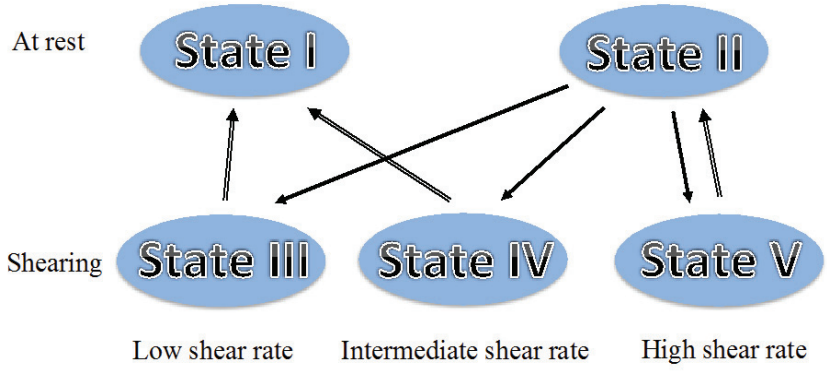

3. Liquid Crystalline Cellulose Networks Characterized by Different Experimental Techniques

3.1. Solid State NMR Spectroscopy of APC Networks With Nematic 5CB Inclusions

In a recent NMR study [39], bulk samples, thin films and electro spun fibers of the cellulosic composite formed by liquid crystalline acetoxypropylcellulose (APC) and deuterated nematic

40-pentyl-4-cyanobiphenyl (5CB-αd2) with the percentage of 85% APC by weight were characterized by deuterium spectroscopy in terms of molecular orientational order. Deuterium spectra obtained in thin films and bulk samples show similar temperature dependences as the one found in spun fibers and shown in Figure 8.

Figure 8. Deuterium spectra obtained in spun fibers at different temperatures starting within the isotropic phase (**left**) and going deeply inside the nematic range (**right**) (blue line, data; red line, model fit). Reprinted with permission from [39]. Copyright 2010, American Chemical Society.

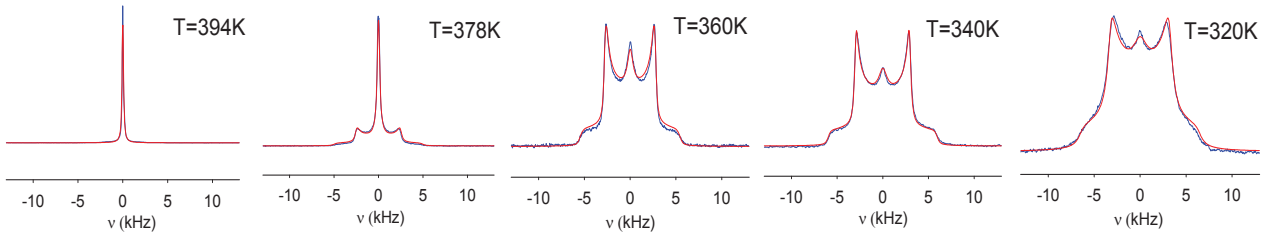

It was found that the low molecular weight liquid crystal is phase separated from the APC and concentrates on submicron droplets in the three types of samples. These droplets are seen to develop a nematic wetting layer at the APC-5CBαd2 interface that experiences an order-disorder transition driven by the polymer network N-I transition. Simulation of the deuterium powder patterns as a function of temperature has shown that the APC network I-N transition exhibits a pronounced subcritical behavior within a heterogeneity scenario.

This study relied on the analysis of the deuterium spectra arising from the 5CBαd2 molecules as they diffuse inside the submicron size droplets, sampling both their isotropic core, as well as the polymer surface induced nematic layer. A Landau-de Gennes modelling of this induced order allowed the order profile inside the droplets to be determined as a function of the surface order S_S imposed by the polymer chains, enabling the simulation of the ordered part of the deuterium spectra shown in Figure 7. At the network I-N transition a significant coexistence of both isotropic and ordered components in the deuterium spectra indicates the presence of heterogeneity in the network. To model the network order parameter temperature dependence and the network heterogeneity, a Landau de Gennes modeling of the network order was considered with a Gaussian distribution in the isotropic phase super cooling limit temperature T^* [39]. This modeling allowed the full fitting of the spectra shown in Figure 8 and the determination of the S_S temperature dependence shown in Figure 9.

The S_S temperature dependence shows that the network is subcritical and the spread in transition temperatures of around 7 K for each of the three samples studied indicates the presence of heterogeneity in the APC + 5CBαd2 system [39].

Figure 9. Temperature dependence of the order parameter S_S for $T_{Ci} = \langle T_C \rangle$ for the three distinct samples studied. Triangles refer to the fiber sample, squares to the bulk sample and circles to the film sample. Reprinted with permission from [39]. Copyright 2010, American Chemical Society.

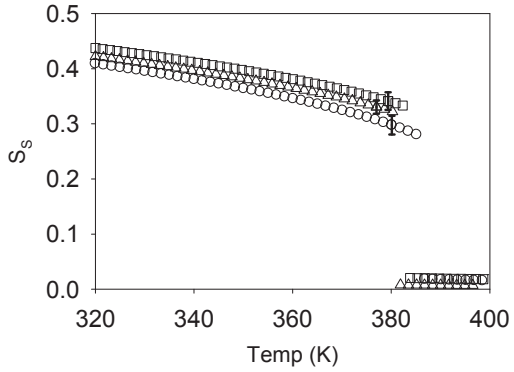

3.2. Wide Angle X-ray Scattering and Polarized Optical Microscopy of Crosslinked APC Films under Strain

Cellulosic liquid crystalline networks obtained from the previous studied systems can be at the origin of promising soft matter devices [24]. In order to characterize these type of networks, Wide Angle X-ray Scattering (WAXS) studies were performed [48] namely of crosslinked APC films produced from chiral nematic solutions [29]. The studies were carried on films subjected or not to a uniaxial stress. The results indicate that the films are constituted by a bundle of helicoidal fiber-like structures, where the cellobiose block spins around the axis of the fiber. Without the stretch, these bundles are warped, only with a residual orientation along the casting direction. The stretch orients the bundles along it, increasing the nematic-like ordering of the fibers. Under stress, the network of molecules that connects the cellobiose blocks and forms the cellulosic matrix tends to organize their links in a hexagonal-like structure. The X-ray diffraction patterns of the free standing, unstretched, cellulose films present three diffraction peaks, anisotropically disposed around the z-axis, as shown in Figure 10. In Figure 11a,b, the diffracted intensity is plotted as a function of q (scattering vector), along the x and y axes directions. The diffraction peaks in the curves Ixq were fitted with Lorentzian functions to find the characteristic distances (d) and full-widths at half- height (W).

The characteristic distances associated to the peaks are $d_1 = (1.13 \pm 0.02)$ nm; $d_2 = (0.44 \pm 0.01)$ nm; and $d_3 = (0.50 \pm 0.01)$ nm. In a previous work [30] only peak 1 was observed due to the limited range of scattering wave vectors investigated. The correlation lengths $D = \lambda_x/(W \cdot \cos\theta)$ calculated are $D_1 \approx 3$ nm; $D_2 \approx 2$ nm; and $D_3 \approx 14$ nm.

Figure 10. X-ray diffraction pattern of the unstretched cellulose film. The single arrow represents the casting direction. Peaks 1, 2, and 3 are identified. Reprinted with permission from [29]. Copyright 2011, Springer.

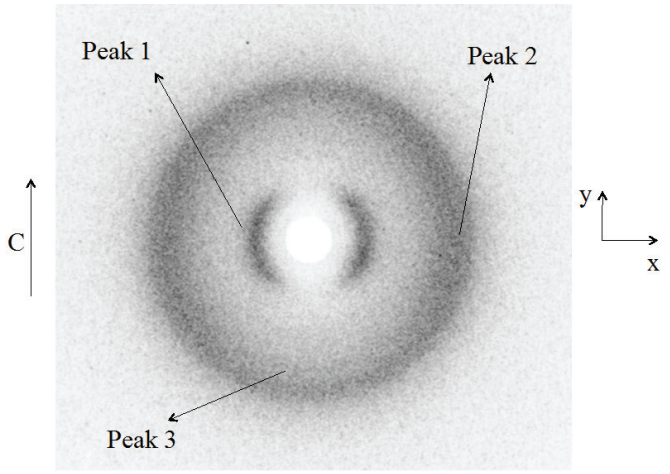

Figure 11. X-ray diffracted intensity of unstretched cellulose film. (**a**) As a function of q, along the x-axis; (**b**) as a function of q, along the y-axis. The insert refers to a zoom around q ≈ 13 nm^{-1}. Reprinted with permission from [29]. Copyright 2011, Springer.

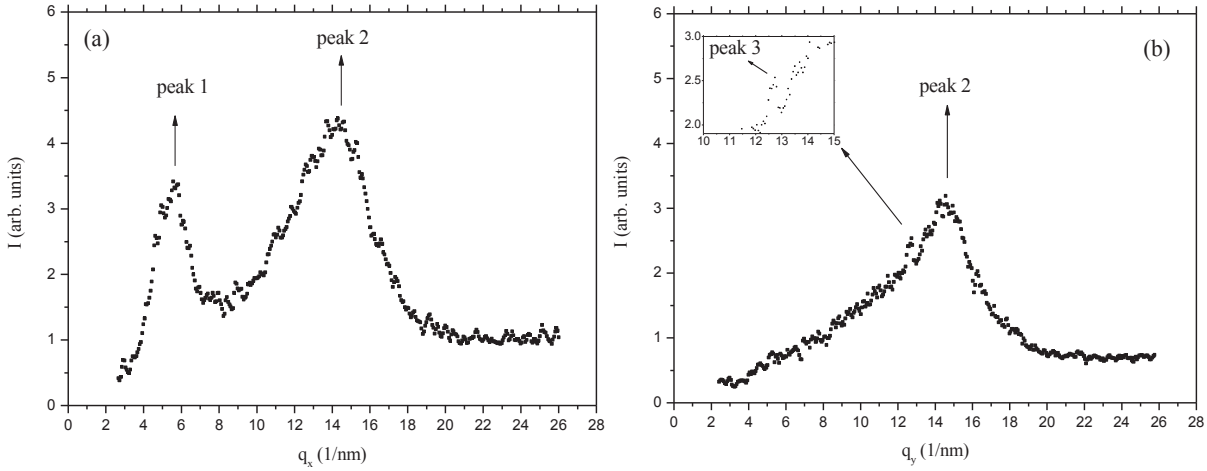

The analysis of the diffraction peaks in the x–y plane indicates that peaks 1 and 2 are more intense along the x direction, which corresponds to the direction perpendicular to the casting. On the other hand, we could not fully verify if peak 3 is also anisotropic with respect to the z-axis since the presence of peak 2, particularly along the x-axis direction, prevents a reliable azimuthal analysis of it. Nevertheless, visual inspection of Figure 10 seems to indicate that this peak is preferentially located in the direction perpendicular to the casting direction. The azimuthal angle analysis of the diffracted intensity (angle φ, measured in the xy plane, starting from the x-axis, in the counter clockwise direction) of the peaks allowed us to obtain the orientational order parameters (OP) [29].

Concerning the case where the film is subjected to a uniaxial stress parallel to the casting direction (Figure 12). We did not observe significant differences in the patterns obtained in the different film locations of the X-ray exposures, indicating, at least, in our experimental conditions, homogeneity of the film.

As the stress increases, the order parameters of the three peaks increase, reaching values at the maximum stress applied (ε_y = 0.40) of OP_1 = (0.85 ± 0.03); OP_2 = (0.43 ± 0.02); and OP_3 = (0.82 ± 0.01). This increase in the orientational order parameter of peak 1 is consistent with the results obtained in [30]. Figure 13 shows the diffracted intensity as a function of q along the x (Figure 13a) and y (Figure 13b) axis directions. As the stretch is increased, peak 3 become more and more defined in the diffracted intensity *versus* q curves (Figure 13b). The positions of the peaks were not modified by the stress. An intriguing result was obtained when we analyzed peak 2 profile as a function of the azimuthal angle φ (Figure 13c).

A hexagonal distribution of diffraction maxima could be identified in the peak 2 position, which provided a hexagonal lattice parameter $d_H \approx 0.5$ nm about the same of the characteristic distance d_3. The value of d_H was obtained assuming that the diffraction peaks of hexagonal symmetry observed in the position of peak 2 ($d \approx 0.44$ nm) correspond to the (100) diffraction plane of the two-dimensional hexagonal packing, *i.e.*, $d_H = d_{100}/(\cos(\pi/6))$. The typical dimension of an extended glucose molecule is of the order of 0.5 nm and the cellobiose, composed by two glucose molecules, is the repeating building-block in the cellulosic sample. The structure proposed for the cellulosic film has to take into account the diffraction characteristic distances observed, the dimension of the cellobiose building block, and the information that, before the casting, the system presents a cholesteric structure. We propose that in the film there is a bundle of helicoidal fiber-like structures where the cellobiose block spins around the axis of the fiber. The distance between the fibers should be of the order 1.1 nm, corresponding to peak 1 of the diffraction pattern. Since there is no evidence of chiral activity in the cellulosic films in the macroscopic scale, these bundles should have fibers with both the levogyre and dextrogyre arrangements, with equal probabilities. Without the stretch, these bundles of fibers may be warped, only with a residual orientation along the casting direction. The stretch orients the bundles along it, increasing the nematic-like ordering of the fibers. Under stress, the network of molecules that connects the cellobiose blocs and forms the cellulosic matrix tends to organize their links in a hexagonal- like structure.

Figure 12. Cellulose film at maximum stretch with ε_y = 0.40. (**a**) Sketch of the cellulose film under stretch and indication from where the X-ray diffraction patterns were taken. The single arrow indicates the casting direction and the double arrow the stretching direction; (**b**) diffraction patterns obtained at the different film location. Reprinted with permission from [29]. Copyright 2011, Springer.

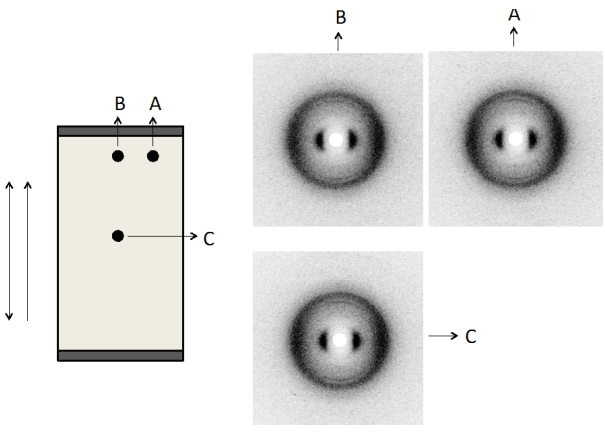

Figure 13. X-ray diffracted intensity of stretched cellulose film at maximum stretch with $\varepsilon_y = 0.40$. (**a**) As a function of q, along the x-axis; (**b**) as a function of q, along the y-axis. The insert refers to a zoom around $q \approx 13$ nm^{-1}; (**c**) as a function of the azimuthal angle φ, referring to peak 2. The sinusoidal curve is only a guide for the eyes. Reprinted with permission from [29]. Copyright 2011, Springer.

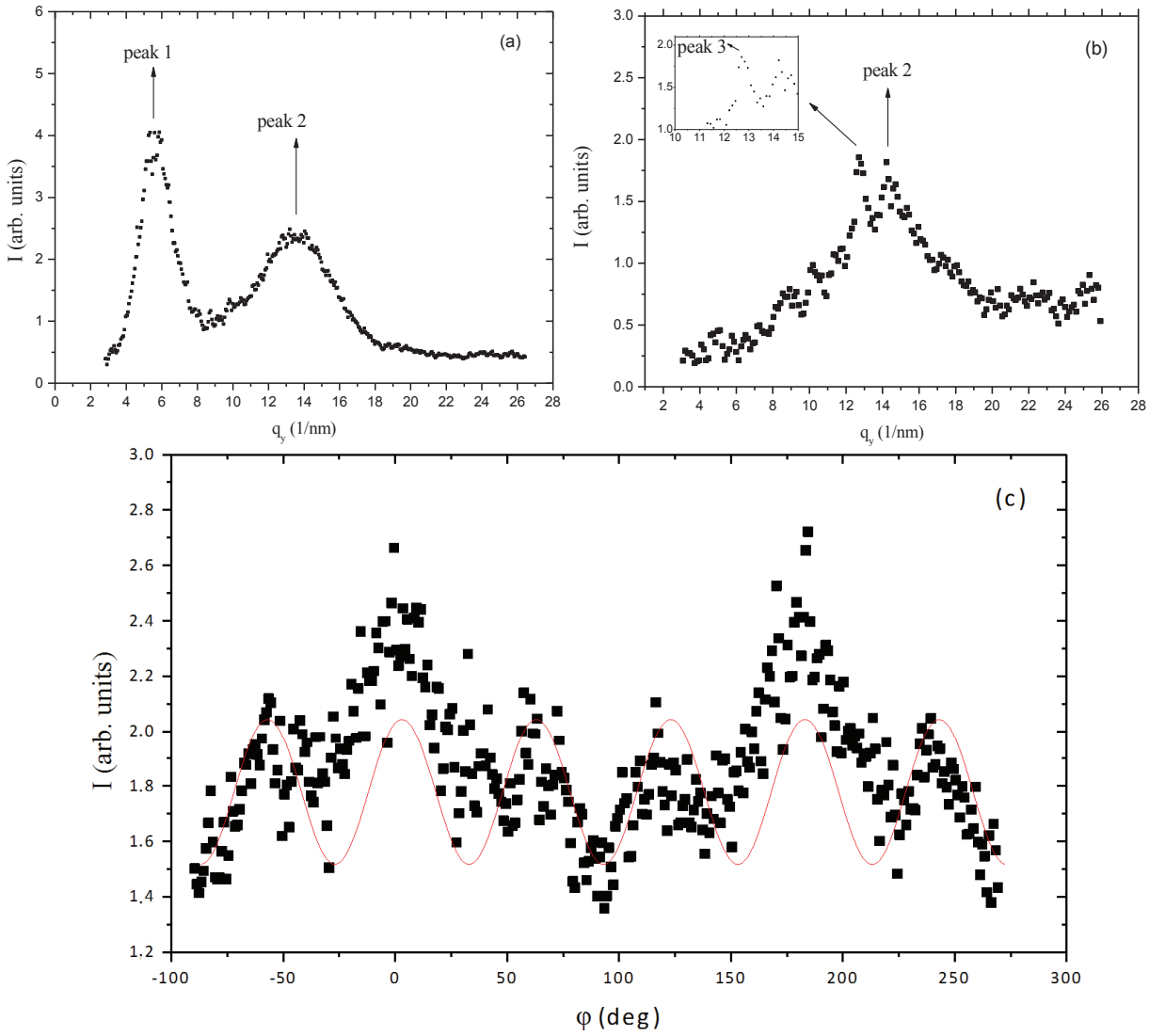

The same samples used to perform the WAXS essays were used to perform POM essays. The optical microscopy texture of the sample under crossed polarizers (casting direction parallel to the analyser) revealed that the film is birefringent, but with a non-uniform texture (Figure 14a).

The analysis of the texture under crossed polarizers leads to the macroscopic arrangement of the director sketched in Figure 14b. There are light and dark regions that form a pattern with stripes, with a periodicity of ≈ 4.4 μm (distance between three light regions), perpendicular to the direction of the casting. This periodic structure is originated by the shear-casting procedure. After the cast the molecular chains have a collective relaxation that results in the formation of that pattern. This morphology has been observed in other cellulose derivative films and was found to be influenced by the precursor solution composition, solvent evaporation rate, film thickness, and rate and duration of shear [28,49]. The application of successive stretches in the direction of the casting

(*i.e.*, in this experimental configuration, parallel to the analyser direction) showed that the texture of the film becomes increasingly dark. This is because the direction of the optical axis, previously created by the casting, is parallel to the analyser direction. If the optical axis of the sample is rotated by 45° in the plane of the microscope plate, the texture became bright. This result is consistent with the nanoscopic structure proposed in the previous X-ray scattering section. The fiber-like structure where the cellobiose block spins around the axis of the fiber defines the director direction, parallel to the casting direction. As the X-ray beam probes a large portion of the sample (typical beam diameter of about 1 mm) the diffraction pattern reveals the mean orientation direction of the director. Upon relaxation (initially at $\varepsilon = 0.29$ and after $t_R = 5$ min) the film did not recover the initial texture, in accordance with the X-ray results already discussed.

Figure 14. Optical microscopic textures under crossed polarizers (OMP) of (**a,e**) the film unstretched; (**b**) and sketch of the director orientation; (**c**) OMP of the film under stretch parallel to the casting direction; and (**d**) upon relaxation; (**f**) OMP of the film under stretch perpendicular to the casting direction; and (**g**) upon relaxation. The single arrow indicates the casting direction and the double arrow the stretching direction. Reprinted with permission from [29]. Copyright 2011, Springer.

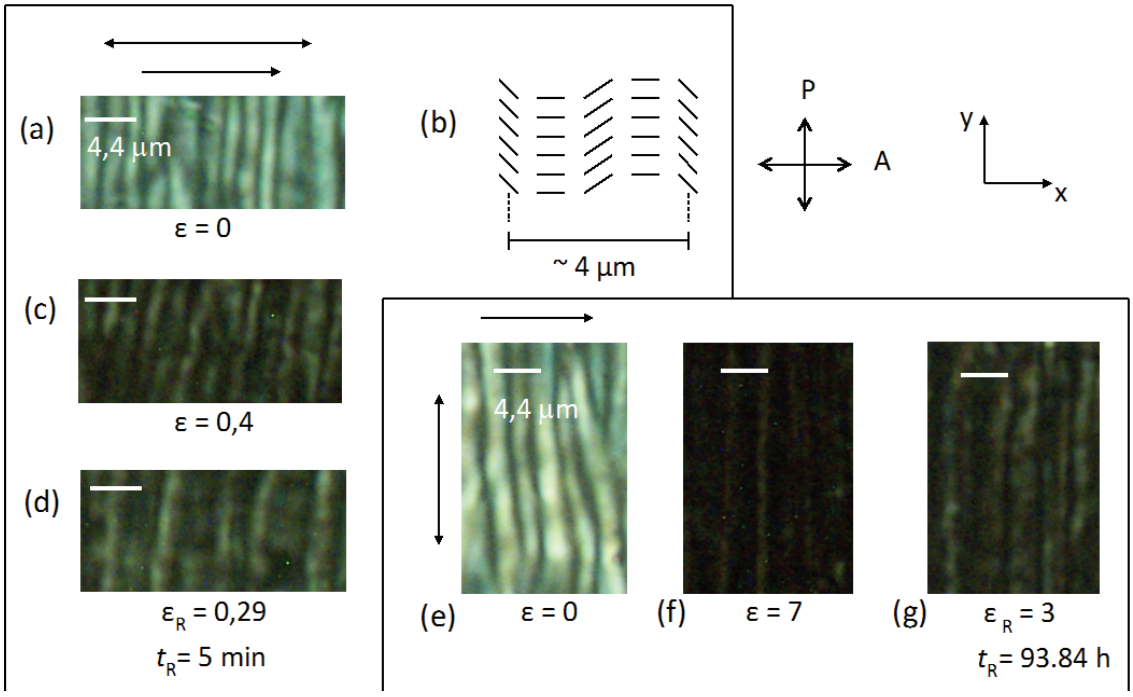

When the stretch is applied perpendicular to the casting direction the texture of the sample under crossed polarizers (Figure 14e,f) becomes increasingly darker with increasing stretch, and then clearer after its relaxation (Figure 14g). Assuming the structure depicted in Figure 14b, the stretch along the direction perpendicular to the casting will impose a tendency of reorientation of the fiber-like arrangement parallel to the stretching direction. This reorientation may in principle proceed either in the clockwise or the anticlockwise direction but due to the initial oscillatory form of the director around the casting direction due to the band structure, different regions will rotate in opposite sense depending on the initial director orientation at each point. Depending on the location of the

film analyzed and the boundary conditions imposed by the borders of the film, the fibers will tend to reorient to their local environment. This fact can explain the different X-ray patterns obtained in different film positions (Figure 15). At the border of the film (positions A and B in Figure 15) the director, that was initially oriented on average parallel to the casting direction (x-axis), is now primarily oriented at ± π/4 with respect to the x-axis due to the boundary conditions that prevent a complete rotation of the director to the stretching direction. In the center of the film (position C in Figure 15), the director is oriented primarily along the y-axis (stretching direction). Let us look in more detail at the appearance of the film under stress, without the crossed polarizers. The film initially had 2 mm in length (L_0), 5 mm in width and 21 μm in thick and was stretched every 6 min until 16 mm in length, and then relaxed.

Figure 16 shows the sequence of stretches of the film from ε = 0.71 (Figure 16b) until ε = 7 (Figure 16d), with the stress applied perpendicular to the casting direction. It is clearly observed an additional periodicity in the direction perpendicular to the casting direction.

Figure 15. Sketch of the cellulose film under stretch (ε = 7.00) and indication from where the X-ray diffraction patterns were taken. The single arrow indicates the casting direction and the double arrow the stretching direction. Diffraction patterns obtained at the different film locations. Reprinted with permission from [29]. Copyright 2011, Springer.

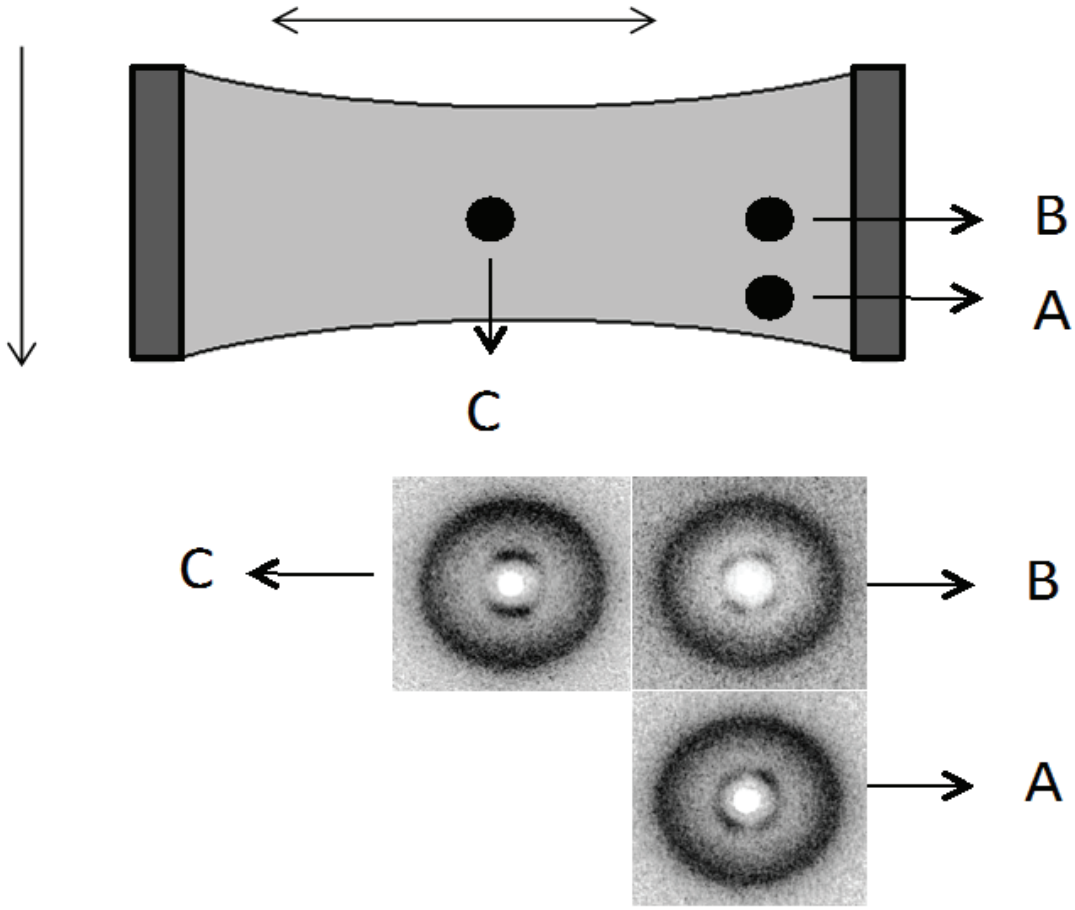

The distance (along the x-axis) between two successive stripes increases linearly with ε (Figure 17). Under crossed polarizers these stripes are also birefringent (Figure 18). This result

indicates that the effect of the casting in the macroscopic structure of the cellulosic film is not only to impose a periodic bend organization of the local director, as sketched in Figure 14b in its direction, but also bends this super structure in the direction perpendicular to it in a larger length scale. Upon relaxation, the film takes a long time to recover its original length (Figure 16e,f). However, its shape is strongly modified, in particular its width (direction perpendicular to the stretch), indicating the plastic behavior of the deformation.

Figure 16. Textures from optical microscopy without crossed polarizers (OM) of the film unstretched (**a**); under successive stretches (**b**,**c**,**d**); and under relaxation (**e**,**f**). Stretch perpendicular to the casting direction. The single arrow indicates the casting direction and the double arrow the stretching direction. Reprinted with permission from [29]. Copyright 2011, Springer.

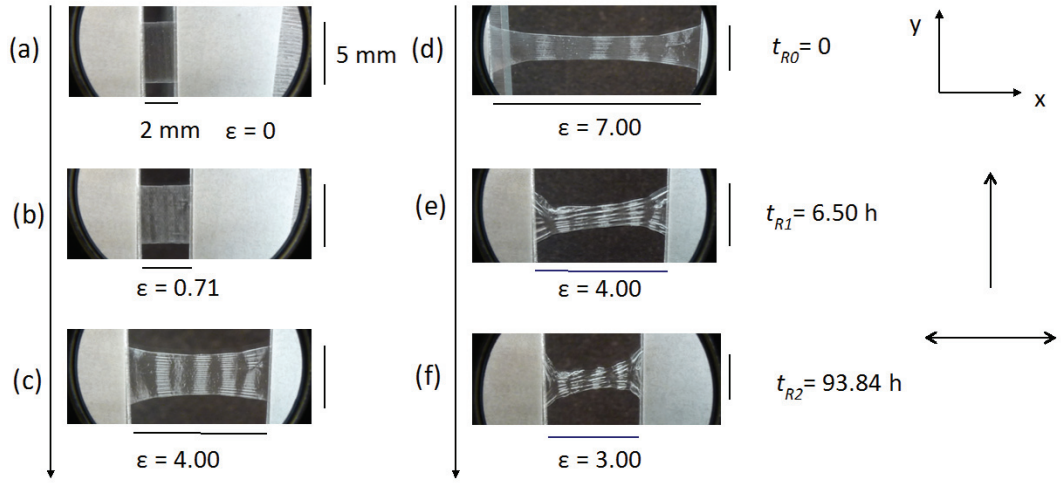

Figure 17. Distance between two consecutive stripes along the x-axis, as a function of ε. Data corresponding to the experimental situation of Figure 16. Reprinted with permission from [29]. Copyright 2011, Springer.

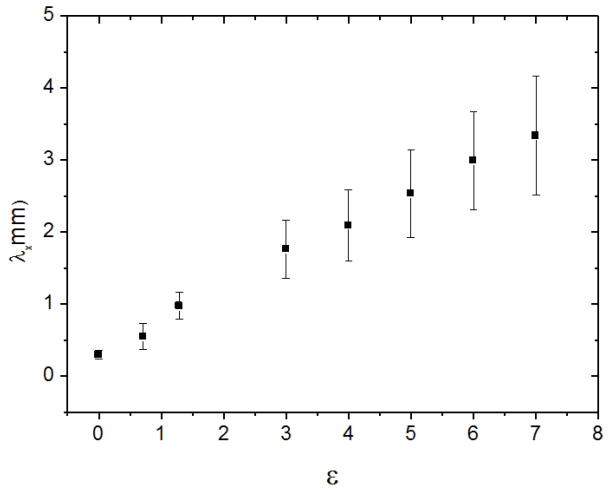

When the film is stretched in the direction parallel to the casting direction this additional periodicity is not observed.

3.3. Atomic Force Microscopy of HPC Films

To perform the Atomic Force Microscopy (AFM) experiments, solutions of cellulose derivatives at several concentrations, ranging from the isotropic to the anisotropic phase region, were prepared.

Figure 18 shows the 3D topography image (20 × 20 μm^2 scan) of the free surface of a sheared HPC film prepared from a 60% w/w solution at a shear rate v_1 = 5 mm/s. The image shows two different scale ranges: a primary set of "large" bands, perpendicular to the shear direction, and a smoother texture characterized by a secondary periodic structure containing "small" bands.

Figure 19 shows a top view image of the height scan of the surface shown in Figure 18 and the analysis of the height profile at two cross sections: AA' and BB'. Cross section AA' was taken along the shear direction. The periodicity of the "large" bands, Δl_1, and the average peak-to-valley height for these bands, h_1, were determined from the AA' height profile plot, as indicated. Cross section BB' was taken along the direction of the secondary periodic "small" bands. The periodicity of the "small" bands, Δl_2, and their peak-to-valley height, h_2, were measured from the BB′ height profile plot, as indicated. The arrows on the top of the view image along AA' and BB' lines mark the points used for the measurements performed in the height profile plots.

Figure 18. 3D topography image (20 × 20 μm^2 scan) of the free surface of a sheared HPC film prepared from a 60% w/w solution at a shear rate v_1 = 5 mm/s. Reprinted with permission from [28]. Copyright 2002, American Chemical Society.

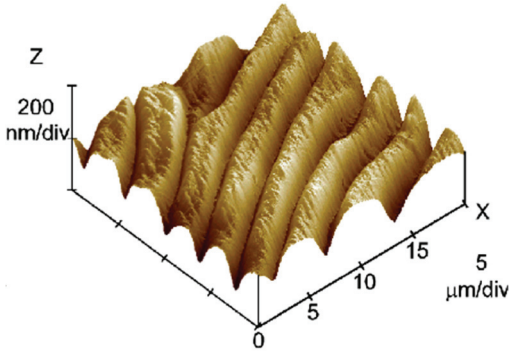

Figure 20 shows the top view image of the amplitude scan of the free surface of three sheared HPC films prepared at a shear rate of v_1 = 5 mm/s from solutions of different concentrations: (a) 30% (w/w), (b) 50% (w/w); and (c) 65% (w/w). The surface of the film prepared from 30% (w/w) does not possess any periodicity. A primary and a secondary set of bands were observed only on the films prepared from anisotropic solutions, *i.e.*, 50%–65% (w/w). Moreover, the films prepared from the solutions of the same concentration, using a higher shear rate v_2 = 10 mm/s), exhibit similar topographies, but they are characterized by different parameters. At a constant concentration, for example at 65% (w/w), the periodicity of the bands (Δl_1) shows a tendency to decrease when the shear rate increases ($\Delta l_1(v_1)$ = 2.97 μm and $\Delta l_1(v_2)$ = 1.97 μm). At a constant shear rate, as the concentration of the polymer increases, the periodicity of the bands decreases (for v_1, at 50% and 65% (w/w), Δl_1 = 4.68 μm and Δl_1 = 2.97 μm, respectively).

Figure 19. Top view image of the height scan of the surface shown in Figure 20 and the height profile analysis at the two cross sections: AA' and BB'. The arrows on the top of a view image along AA' and BB' lines mark the points used for the measurements of the height profile. Reprinted with permission from [28]. Copyright 2002, American Chemical Society.

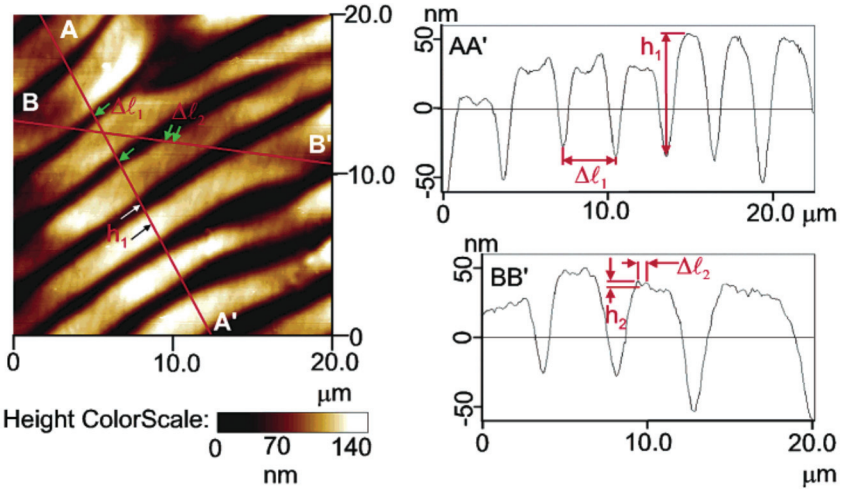

Figure 20. Top view image of the amplitude scan of the free surface of three sheared HPC films prepared at a shear rate of v_1 = 5 mm/s from solutions with HPC/water ratios: (**a**) 30% (w/w); (**b**) 50% (w/w); and (**c**) 65% (w/w). Reprinted with permission from [28]. Copyright 2002, American Chemical Society.

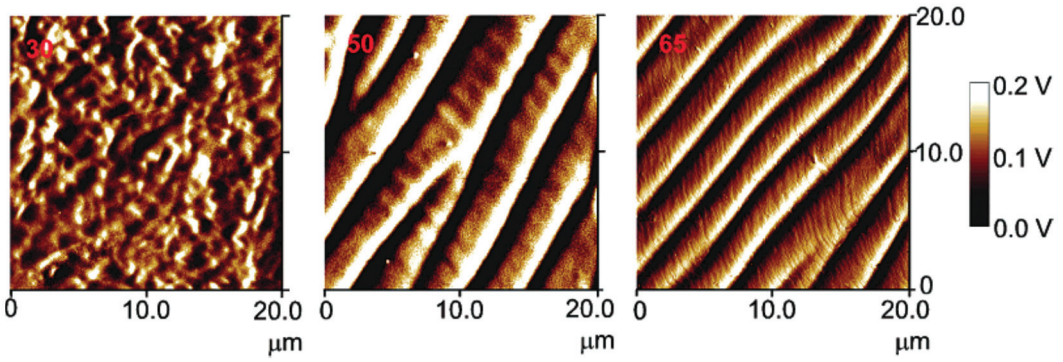

A tuneable topographic system may be obtained from HPC aqueous liquid crystalline solutions [50]. The results point out that two kinds of periodicities may be locked and adjusted in these systems as a function of the processing conditions. The set of "large" bands, which develops perpendicular to the shear direction, can be described as a relaxation process, which occurs immediately after the end of a shear applied to polymer liquid-crystalline solutions and attributed to contraction strains of the sheared sample induced by stress relaxation after cessation of flow. The secondary bands periodicities show a net tendency to decrease with polymer content, which seems an indication that the development of the "small" bands are mainly ruled by the cholesteric liquid crystal characteristics imposed by the initial precursor solutions. The pitch of the precursor chiral nematic solution and the related values of the liquid crystal elastic constants of the material can therefore be mainly responsible for the variation in size of the secondary bands, observed

experimentally [24]. The films are found to be self-affine between 300 nm and 4 μm but not for higher scales. In general, the fractal dimension is found to increase with both polymer concentration and shear rate. This trend reflects the increasing complexity of the surface topography when the films are prepared with higher polymer concentrations or with higher shear rates [28].

3.4. Mechanical Behavior of Solid Cellulose Derivatives Films

Anisotropic solid films were fabricated by spreading the HPC anisotropic solutions, 60% (w/w), with the help of a calibrated shear casting knife, at room temperature, in an appropriate Teflon mould, this procedure allows the precise control of the shear casting flow speed (v) (1 mm·s^{-1}) and enables the ready removal of the films without damaging at room temperature, other methods to obtain sheared HPC solid films involved higher processing temperatures [51]. After solvent controlled evaporation, the solid cast shear films had an average thickness between 14 and 30 μm. As evaporation continues, the density of rod-like fragments increases near the free top surface, giving rise to increased orientational order. This in turn causes elongation at the top of the film in the direction parallel to the director, and since the dimensions of the bottom surface in contact with the glass substrate are fixed, the top surface buckles, forming a set of grooves shown previously [52–54].

Figure 21. Stress-strain relations. Squares correspond to strain parallel to the shear direction and the nematic director. Circles correspond to strain perpendicular to the shear direction and the nematic director. For this geometry, above a threshold, the stress is nearly independent of strain. This indicates "semi-soft" elasticity, characteristic of nematic elastomers. The negative slope at higher strains corresponds to failure due to tearing of the films. Reprinted with permission from [55]. Copyright 2013, Nature Publishing Group.

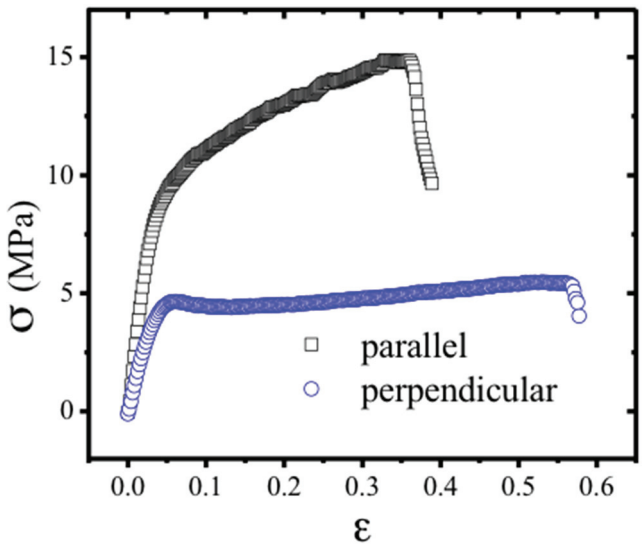

The modulus of the cellulose network has been measured for strain along the director, as well as perpendicular to it. Results are shown in Figure 21; for small strains, Young's modulus is 263 ± 39 MPa for shear parallel and 140 ± 9 MPa perpendicular to the director. Above a threshold

of 4 MPa, the stress in the perpendicular direction is nearly independent of the strain. This "semi-soft" elastic response is characteristic of liquid crystal elastomers [56] and has been associated to a director reorientation. However, as already highlighted [57], a reset of order can also be the underlying mechanism for this process as observed in sheared anisotropic cellulosic films [30]. The film rupture is preceded of a plastic regime when stretching is imposed parallel to the casting direction while it is preceded of significant necking during the "semi-soft" elastic response when stretching is imposed perpendicular to the casting direction.

When exposed to water vapor, free standing films prepared from a 60% (w/w) solution bend, as shown in Figure 22. When water vapor penetrates the free surface of the film, the sample bends around an axis parallel to the shear direction, with the free surface on the outside (Figure 22a). This is consistent with expansion of the free surface of the film in the direction perpendicular to the director. Such an expansion is expected, since the order parameter is reduced by the presence of the solvent water, and furthermore the presence of water molecules between the cellulose chains in the rigid segments is expected to cause the thickness of the rod-like fragments to increase.

Figure 22. Bending of freestanding films. (**a**) The film free top surface; and (**b**) the film glass bottom surface exposed to water vapour. Sheared films were prepared from liquid crystalline HPC/water solution, the arrows indicate shear direction. Reprinted with permission from [55]. Copyright 2013, Nature Publishing Group.

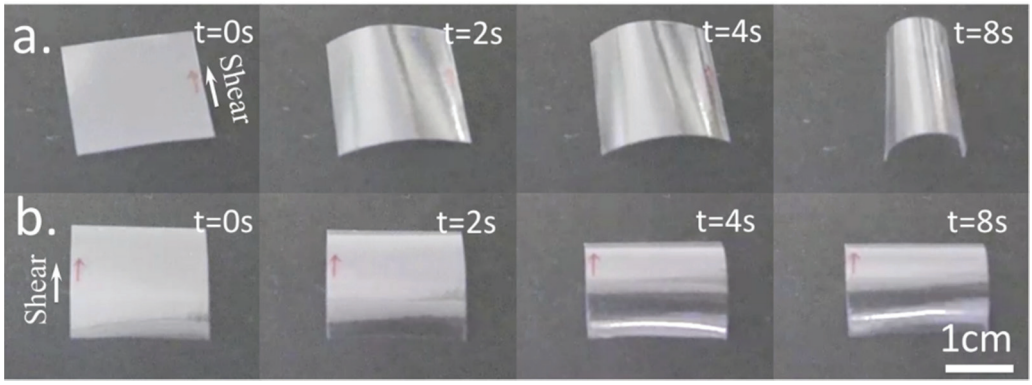

The shear stress associated with such bend has been measured, as a function of time (Figure 23), in a 20 mm × 20 mm × 32 μm planar sample at 24 °C with free surface exposed to humidity. Measurements were taken with Mettler Toledo AG204 load sensor. The maximum stress measured was 383 Pa.

When the film is allowed to dry, either by heating or by being placed in a low-humidity environment, the film unbends, reversibly assuming its original shape. The bending is relatively fast, on the scale of ≈1 s.

Figure 23. Dynamics of stress evolution. Shear stress in a 20 mm × 20 mm × 32 μm planar sample at 24 °C with free surface exposed to humidity as function of time, measured with a Mettler Toledo AG204 load sensor. The maximum stress measured was 383 Pa. Reprinted with permission from [55]. Copyright 2013, Nature Publishing Group.

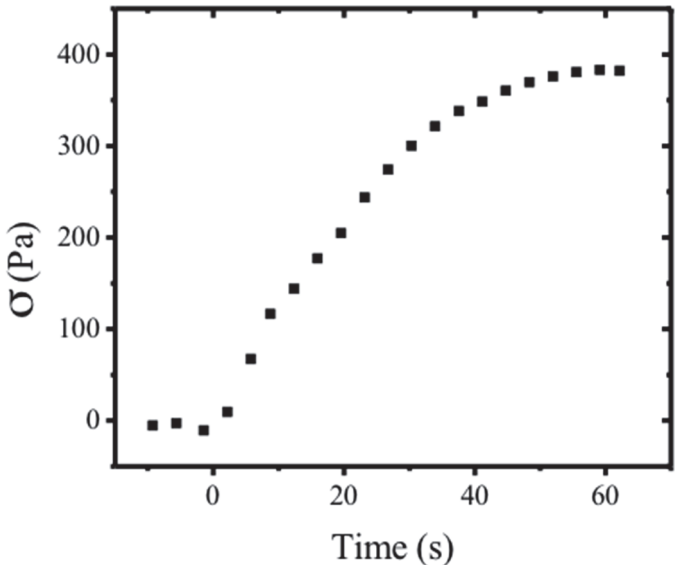

Interestingly, when the glass side of the film is exposed to water vapor, it bends around an axis perpendicular to the shear direction, with the glass side being convex (Figure 22b). This is consistent with a nearly isotropic expansion of the glass side surface due to the presence of moisture. Since corrugations on the free surface give rise to a smaller effective modulus for bend in this direction, as has been confirmed by independent measurements, bend occurs around an axis perpendicular to the shear direction. The bend produced by exposing the glass side to water vapor is considerably smaller than that of the free surface. Taking advantage to the bending moisture effect a soft cellulosic motor was built (Figure 24) [55].

Figure 24. Moisture-driven liquid crystal cellulose engine. (**a**) Schematic of the motor, showing location of moist air and rotation direction. The alignment direction is parallel to the axes of the wheels. The free surface of the film is on the outer side; (**b**) series of video frames showing rotation. The motor is housed in a dry environment. Momentum transfer from the moist air is small, and opposes the observed motion. Belt dimensions are: 1.0 cm × 8.0 cm × 30 μm; wheel diameter is 14 mm. The direction of rotation is indicated by a black arrow, and of moist air flow by a white arrow (**a**). In (**b**), t = 2 s/frame. Reprinted with permission from [55]. Copyright 2013, Nature Publishing Group.

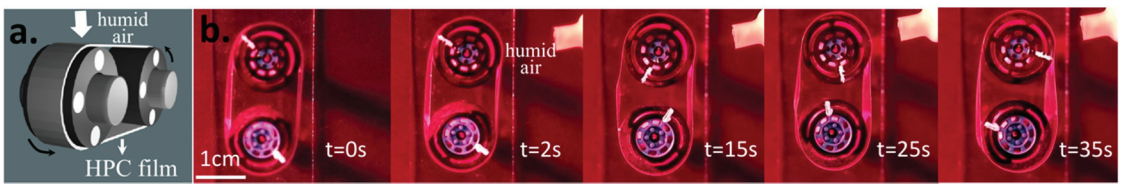

Nano crystalline cellulose rods can be incorporated into composite materials, enhancing their mechanical properties [58]. NCC filler was used as a probe, which can influence the mechanical properties of the films but does not destroy the liquid crystalline characteristics of the composite material. In fact, adding 0.1% of NCC rods implies that the Young's modulus of the films, as well as the tensile strength, measured in perpendicular (Per) and parallel (Par) directions to the casting, were increased by a factor of 2.5 and 3.2 for Par and 3.0 and 2.2 for Per, respectively, when compared with films prepared from HPC anisotropic solutions [24]. Because of the high degree of molecular orientation, the HPC and the HPC/NCC films exhibit high modulus and strength along the shear direction and the mechanical strength in the transverse direction is low. These anisotropic mechanical properties are consistent with the molecular orientation, which results from the flow of the liquid crystalline solution under shear stress. The fact that the Young's modulus and strength is much higher for HPC/NCC compared with HPC films, along the shear direction, is an indication that NCC rods align along this direction when the films are prepared. NCC rods enhanced the brittle behavior along this direction, as well as in the Per direction and act as a stiffener to the anisotropic cellulose matrix, which is also reflected in the strength deformation values for Par and Per directions.

The features (not the values) of the stress/strain curves obtained were similar to those from other APC and HPC already reported in the literature for isotropic and anisotropic cellulose derivatives [59–61].

3.5. Cellulose Derivatives Composites in Electro-Optical Applications

Cellulose derivatives composites for electro-optical (EO) applications were introduced in 1982 by Craighead *et al*. [62], followed a few years later by a different type of cellulose derivative EO cell, named cellulose-based polymer dispersed liquid crystal (CPDLC) [63,64]. Due to the good match between the ordinary refractive index of the nematic liquid crystal (NLC) E7 (1.510) and the refractive indexes of HPC (1.49), a very clear ON state is achieved when an electric field E_{on} is applied to the devices as can be seen in Figure 25.

The CPDLC cell was composed of a rough cellulose derivative polymeric film surrounded by two NLC layers and the set placed in between two transparent conducting rigid or flexible substrates. These thin solid films were prepared from cellulose derivatives solutions, casted, and sheared simultaneously by moving a calibrated Gardner knife at 1.25 $mm \cdot s^{-1}$. The films were allowed to dry at room temperature and kept in a controlled relative humidity (20%) chamber until further use. To evaluate the EO properties of these devices, the EO characterization was carried out using a laser-equipped optical bench in association with a function generator, a voltage amplifier, and a diode detector. The laser light was perpendicular to each sample and upon crossing it was collected at the diode detector whose output was fed to an amplifier and later recorded with a digital storage scope. All measurements were performed at room temperature. These cells showed very challenging properties, presenting high transmission coefficients values (around 0.8) in the ON state, but exhibiting turn-ON fields around 1.5 V/μm, giving rise to rather high turn-on voltages [65]. Later on, a light scattering EO device where layers of two different cellulose derivatives were deposited as nonwoven nano and microfiber mats onto the conductive substrates by electrospinning, were presented [66]. These devices can be used as high efficiency light shutters or as privacy windows

since they can be electrically controlled to scatter light (OFF state) or to transmit it (on state) [67]. These last devices presented an innovative method of preparing cellulose-based light scattering devices, which led to a major improvement in their EO properties and also their production cost. Using cellulose-based nano and microfibers mats as a network, EO light-scattering devices were produced as polymer-stabilized liquid crystal-type devices. In these devices, the cellulose derivatives were deposited as nonwoven nano- and microfiber mats onto the conductive substrates by electrospinning, and the cell was filled up by capillarity with a NLC. In these optical shutters, the LC is embedded with the fibers as a continuous phase, maximizing the LC/polymer surface contact and thus promoting improved EO properties. An increase in the on transparency and a marked decrease in the operating voltage of these devices were observed as the consequences of the improved interaction of the NLC with the nano and microfibers. More recently, a new type of EO device with improved EO properties was presented taking advantage of the high surface area of nanoscale cellulose whiskers [27].

On this later technology, cellulose-based LC EO devices were prepared by stacking between two transparent conductive oxide–coated glasses, two layers of a nematic LC having in between a thin film composed of nano crystalline cellulose rods. The major step forward in the EO properties of this type of device is the significant reduction of the turn ON electric field and the decrease in the response time to reach the ON state as can be seen in Figure 26.

Figure 25. Macroscopic effect of the (**a**) ON; and (**b**) OFF states. Reprinted with permission from [66]. Copyright 2009, AIP Publishing.

(**a**) (**b**)

Figure 26. Curves of the applied electric field dependence of the light transmission coefficient of these devices compared with electrospun cellulose fiber devices (HPC and CA). Reprinted with permission from [27]. Copyright 2013, Taylor and Francis.

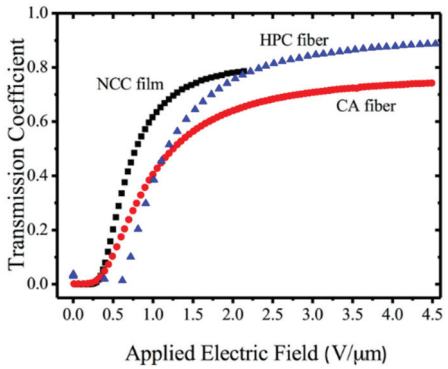

4. Summary

The cholesteric nature of the cellulose derivatives liquid crystalline solutions gives rise to a complex rheological behavior and consequently has a fundamental impact on the properties of the films and fibers produced from these anisotropic solutions by different methods where different levels of shear are involved. Formation of helices in electro-spun fibers and the curling of cast planar films stem from the complex nature of the molecular packing imposed by the preparation induce shear on the precursor solutions. These features impart specific mechanical and optical properties to the cellulose derivatives fibers and films that make them high interest materials for photonics, microelectronics and related applications, as well as for build soft stimuli responsive devices.

Acknowledgments

The authors acknowledge financial support from Portuguese Science and Technology Foundation through grants: PTDC/CTM-Pol/1484/2012, PTDC/FIS/110132/2009, PEst-OE/FIS/UI0261/2011, PEst-C/CTM/LA0025/2013-14.

Conflicts of Interest

The authors declare no conflict of interest.

Author Contributions

Maria Helena Godinho, Pedro Lúcio Almeida and João Luis Figueirinhas planned, wrote the manuscript and contributed equally to this work.

References

1. Werbowyj, R.S.; Gray, D.G. Liquid crystalline structure in aqueous hydroxypropyl cellulose solutions. *Mol. Cryst. Liq. Cryst.* **1976**, *34*, 97–103.
2. Werbowyj, R.S.; Gray, D.G. Optical-properties of (hydroxypropyl) cellulose liquid-crystals—Cholesteric pitch and polymer concentration. *Macromolecules* **1984**, *17*, 1512–1520.
3. Kimura, H.; Hosino, M.; Nakano, H. Temperature dependent pitch in cholesteric. *J. Phys. Soc. Jpn.* **1982**, *51*, 1584–1590.
4. Werbowyj, R.S.; Gray, D.G. Ordered phase formation in concentrated hydroxypropylcellulose solutions. *Macromolecules* **1980**, *13*, 69–73.
5. Charlet, G.; Gray, D.G. Solid cholesteric films cast from aqueous (hydroxypropy1). *Cellulose* **1987**, *20*, 33–38.
6. Nishio, Y.; Kai, T.; Kimura, N.; Oshima, K.; Suzuki, H. Controlling the selective light reflection of a cholesteric liquid crystal of (hydroxypropyl)cellulose by electrical stimulation. *Macromolecules* **1998**, *31*, 2384–2386.
7. Chiba, R.; Nishio, Y.; Miyashita, Y. Electrooptical behavior of liquid-crystalline (hydroxypropyl)cellulose/inorganic salt aqueous solutions. *Macromolecules* **2003**, *36*, 1706–1712.

8. Nishio, Y.; Chiba, R.; Miyashita, Y.; Oshima, K.; Miyajima, T.; Kimura, N.; Suzuki, H. Salt addition effects on mesophase structure and optical properties of aqueous hydroxypropyl cellulose solutions. *Polym. J.* **2002**, *34*, 149–157.
9. Shimamoto, S.; Uraki, Y.; Sano, Y. Optical properties and photopolymerization of liquid crystalline (acetyl) (ethyl) cellulose/acrylic acid system. *Cellulose* **2000**, *7*, 247–358.
10. Guo, J.X.; Gray, D.G. Effect of degree of acetylation and solvent on the chiroptical properties of lyotropic (acetyl)(ethyl) cellulose solutions. *J. Polym. Sci. Part B Polym. Phys.* **1994**, *32*, 2529–2537.
11. Gray, D.G. Chiral nematic ordering of polysaccharides. *Carbohydr. Polym.* **1994**, *25*, 277–284.
12. Ito, M.; Teramoto, Y.; Nishio, Y. Electrooptical behavior of aqueous (hydroxypropyl)cellulose liquid crystals containing imidazolium salts. *Biomacromolecules* **2012**, *13*, 565–569.
13. Chiba, R.; Ito, M.; Nishio, Y. Addition effects of imidazolium salts on mesophase structure and optical properties of concentrated hydroxypropylcellulose aqueous solutions. *Polym. J.* **2010**, *42*, 232–241.
14. Muller, M.; Zentel, R. Cholesteric phases and films from cellulose derivatives. *Macromol. Chem. Phys.* **2000**, *201*, 2055–2063.
15. Wenzlik, D.; Zentel, R. High optical quality films of liquid crystalline cellulose derivatives in acrylates. *Macromol. Chem. Phys.* **2013**, *214*, 2405–2414.
16. Bhadani, S.N.; Gray, D.G. Crosslinked cholesteric network from the acrylic-acid ester of (hydroxypropyl) cellulose. *Mol. Cryst. Liq. Cryst.* **1984**, *102*, 255–260.
17. Muller, M.; Zentel, R.; Keller, H. Solid opalescent films originating from urethanes of cellulose. *Adv. Mater.* **1997**, *9*, 159–162.
18. Zhao, C.T.; Cai, B.L. UV-Initiated solidification of liquid crystalline ethylcellulose/acrylic acid films and bands formed in this process. *Macromol. Rapid Commun.* **1995**, *16*, 323–328.
19. Wenzlik, D.; Varanytsia, A.; Munoz, A.; Kosa, T.; Taheri, B.; Zentel, R.; Palffy-Muhoray, P. Distributed feedback lasing in cellulose films. *Opt. Mater. Express* **2014**, *4*, 162–171.
20. Wenzlik, D.; Ohm, C.; Serra, C.; Zentel, R. Preparation of cholesteric particles from cellulose derivatives in a microfluidic setup. *Soft Matter* **2011**, *7*, 2340–2344.
21. Shopsowitz, K.E.; Qi, H.; Hamad, W.Y.; MacLachlan, M.J. Free-standing mesoporous silica with tunable chiral nematic structures. *Nature* **2010**, *468*, 422–425.
22. Mostofa, K.; Hamad, W.Y.; MacLachlan, M.J. Tunable mesoporous bilayer photonic resins with chiral nematic structures and actuator properties. *Adv. Mater.* **2014**, *26*, 2323–2328.
23. Klemm, D.; Friederike, K.; Moritz, S.; Lindstrom, T.; Ankerfors, M.; Gray, D.; Dorris, A. Nanocelluloses: A new family of nature-based materials. *Angew. Chem. Int. Ed.* **2011**, *50*, 5438–5466.
24. Fernandes, S.N.; Geng, Y.; Vignolini, S.; Glover, B.J.; Trindade, A.C.; Canejo, J.P.; Almeida, P.L.; Brogueira, P.; Godinho, M.H. Structural color and iridescence in transparent sheared cellulosic films. *Macromol. Chem. Phys.* **2013**, *214*, 25–32.
25. Habibi, Y. Key advances in the chemical modification of nanocelluloses. *Chem. Soc. Rev.* **2014**, *43*, 1519–1542.

26. Gaspar, D.; Fernandes, S.N.; de Oliveira, A.G.; Fernandes, F.G.; Grey, P.; Pontes, R.V.; Pereira, L.; Martins, R.; Godinho, M.H.; Fortunato, E. Nanocrystalline cellulose applied simultaneously as the gate dielectric and the substrate in flexible field effect transistors. *Nanotechnology* **2014**, *25*, 094008:1–094008:11.
27. Geng, Y.; Brogueira, P.; Figueirinhas, J.L.; Godinho, M.H.; Almeida, P.L. Light shutters from nanocrystalline cellulose rods in a nematic liquid crystal. *Liq. Cryst.* **2013**, *40*, 769–773.
28. Godinho, M.H.; Fonseca, J.G.; Ribeiro, A.C.; Melo, L.V.; Brogueira, P. Atomic force microscopy study of hydroxypropylcellulose films prepared from liquid crystalline aqueous solutions. *Macromolecules* **2002**, *35*, 5932–5936.
29. Sena, C.; Godinho, M.H.; Oliveira, C.L.P.; Neto, A.M.F. Liquid crystalline cellulosic elastomers: Free standing anisotropic films under stretching. *Cellulose* **2011**, *18*, 1151–1163.
30. Godinho, M.H.; Filip, D.; Costa, I.; Carvalho, A.-L.; Figueirinhas, J.L.; Terentjev, E.M. Liquid crystalline cellulose derivative elastomer films under uniaxial strain. *Cellulose* **2009**, *16*, 199–205.
31. Canejo, J.P.; Borges, J.P.; Godinho, M.H.; Brogueira, P.; Teixeira, P.I.C.; Terentjev, E.M. Helical twisting of electrospun liquid crystalline cellulose micro- and nanofibres. *Adv. Mater.* **2008**, *20*, 4821–4825.
32. Canejo, J.P.; Godinho M.H. Cellulose perversions. *Materials* **2013**, *6*, 1377–1390.
33. Godinho, M.H.; Canejo, J.P.; Feio, G.; Terentjev, E.M. Self-winding of helices in plant tendrils and cellulose liquid crystal fibres. *Soft Matter* **2010**, *6*, 5965–5970.
34. Guo, J.X.; Gray, D.G. Preparation and liquid-crystalline properties of (acetyl)(ethyl) cellulose. *Macromolecules* **1989**, *22*, 2082–2086.
35. Bertails, F.; Audoly, B.; Cani, M.-P.; Querleux, B.; Leroy, F.; Leveque, J.-L. Super-helices for predicting the dynamics of natural hair. *ACM Trans. Graph.* **2006**, *25*, 1180–1187.
36. Goriely, A.; Tabor, M. Spontaneous helix hand reversal and tendril perversion in climbing plants. *Phys. Rev. Lett.* **1998**, *80*, 1564–1567.
37. Hongladarom, K.; Secakusuma, V.; Burghardt, W.R. Relation between molecular orientation and rheology in lyotropic hydroxypropylcellulose solutions. *J. Rheol.* **1994**, *38*, 1505–1523.
38. Riti, J.B.; Navard, P. Textures during recoil of anisotropic hydroxypropylcellulose solutions. *J. Rheol.* **1998**, *42*, 225–237.
39. Kundu, S.; Feio, G.; Pinto, L.F.V.; Almeida, P.L.; Figueirinhas, J.L.; Godinho, M.H. Deuterium NMR study of orientational order in cellulosic network microfibres. *Macromolecules* **2010**, *43*, 5749–5755.
40. Hongladarom, K.; Ugaz, V.M.; Cinader, D.K.; Burghardt, W.R.; Quintana, J.P.; Hsiao, B.S.; Dadmun, M.D.; Hamilton, W.A.; Butler, P.D. Birefringence, X-ray scattering, and neutron scattering measurements of molecular orientation in sheared liquid crystal polymer solutions. *Macromolecules* **1996**, *29*, 5346–5355.
41. Keates, P.; Mitchell, G.R.; Peuvrel, D.E.; Navard, P. Insitu X-ray-scattering study of anisotropic solutions of hydroxypropylcellulose subjected to shear-flow. *Polymer* **1993**, *34*, 1316–1319.
42. Geng, Y.; Almeida, P.L.; Feio, G.M.; Figueirinhas, J.L.; Godinho, M.H. Water-Based Cellulose Liquid Crystal System Investigated by Rheo-NMR. *Macromolecules* **2013**, *46*, 4296–4302.

43. Godinho, M.H.; van der Klink, J.J.; Martins, A.F. Shear-history dependent "equilibrium" states of liquid-crystalline hydroxypropylcellulose solutions detected by rheo-nuclear magnetic resonance. *J. Phys.-Condensed Matter* **2003**, *15*, 5461–5468.
44. Burghardt, W.R.; Fuller, G.G. Role of director tumbling in the rheology of polymer liquid crystal solutions. *Macromolecules* **1991**, *24*, 2546–2555.
45. Marrucci, G. Tumbling regime of liquid-crystalline polymers. *Macromolecules* **1991**, *24*, 4176–4182.
46. Onogi, S.; Asada, T. Rheology and rheoptics of polymer liquid crystals. *Rheology* **1980**, *1*, 127–147.
47. Grabowski, D.A.; Schmidt, C. Simultaneous measurement of shear viscosity and director orientation of a side-chain liquid-crystalline polymer by Rheo-NMR. *Macromolecules* **1994**, *27*, 2632–2634.
48. Samuels, R.J. Solid-state characterization of the structure and deformation behavior of water-soluble hydroxypropylcellulose. *J. Polym. Sci. Part A 2 Polym. Phys.* **1969**, *7*, 1197–1258.
49. Evmenenko, G.; Yu, C.J.; Kewalramani, S.; Dutta, P. Structural characterization of thin hydroxypropylcellulose films. X-ray reflectivity studies. *Langmuir* **2004**, *20*, 1698–1703.
50. Patnaik, S.S.; Bunning, T.J.; Adams, W.W.; Wang, J.; Labes, M.M. Atomic-force microscopy and high-resolution scanning electron-microscopy study of the banded surface-morphology of hydroxypropylcellulose thin-films. *Macromolecules* **1995**, *28*, 393–395.
51. Nishio, Y.; Takahashi, T. Morphological study of hydroxypropyl cellulose films prepared from thermotropic melt under shear. *J. Macromol. Sci. Phys.* **1984**, *B23*, 483–495.
52. Mori, N.; Morimoto, M.; Nakamura, K. Hydroxypropylcellulose films as alignment layers for liquid crystals. *Macromolecules* **1999**, *32*, 1488–1492.
53. Wang, J.; Labes, M.M. Control of the anisotropic mechanical-properties of liquid-crystal polymer-films by variations in their banded texture. *Macromolecules* **1992**, *25*, 5790–5793.
54. Wang, J.; Bhattacharya, S.; Labes, M.M. Solvent evaporation induced torsad texture of sheared liquid-crystalline polymers. *Macromolecules* **1991**, *24*, 4942–4947.
55. Geng, Y.; Almeida, P.L.; Fernandes, S.N.; Cheng, C.; Palffy-Muhoray, P.; Godinho, M.H. A cellulose liquid crystal motor: A steam engine of the second kind. *Sci. Rep.* **2013**, *3*, 1028.
56. Bladon, P.; Warner, M.; Terentjev, E.M. Orientational order in strained nematic networks. *Macromolecules* **1994**, *27*, 7067–7075.
57. Andresen, E.M.; Mitchell, G.R. Orientational behaviour of thermotropic and lyotropic liquid crystal polymer systems under shear flow. *Europhys. Lett.* **1998**, *43*, 296–301.
58. Favier, V.; Canova, G.R.; Cavaille, J.Y.; Chanzy, H.; Dufresne, A.; Gauthier, C. Nanocomposite materials from latex and cellulose whiskers. *Polym. Adv. Technol.* **1995**, *6*, 351–355.
59. Almeida, P.L.; Kundu, S.; Beja, D.; Fonseca, J.; Figueirinhas, J.L.; Godinho, M.H. Deformation of isotropic and anisotropic liquid droplets dispersed in a cellulose liquid crystalline derivative. *Cellulose* **2009**, *16*, 427–434.
60. Borges, J.P.; Godinho, M.H.; Martins, A.F.; Trindade, A.C.; Belgacem, M.N. Cellulose based composite films. *Mech. Compos. Mater.* **2001**, *37*, 257–264.

61. Borges, J.P.; Godinho, M.H.; Belgacem, M.N.; Martins, A.F. New bio-composites based on short fibre reinforced hydroxypropylcellulose films. *Compos. Interfaces* **2001**, *8*, 233–241.
62. Craighead, H.V.; Cheng, J.; Hackwood, S. New display based on electrically induced index matching in an inhomogeneous medium. *Appl. Phys. Lett.* **1982**, *40*, 22–24.
63. Godinho, M.H.; Figueirinhas, J.L.; Martins, A.F. Novel PDLC type display based on cellulose derivatives. *Liq. Cryst.* **1996**, *20*, 373–376.
64. Godinho, M.H.; Martins, A.F.; Figueirinhas, J.L. Composite systems for display applications from cellulose elastomers and nematic liquid crystals. *Opt. Mater.* **1998**, *9*, 226–229.
65. Almeida, P.L.; Godinho, M.H.; Cidade, M.T.; Figueirinhas, J.L. Electro-optical properties of cellulose based PDLC type cells: Dependence on the type of diisocyanate cross-linking agent used. *Mol. Cryst. Liq. Cryst.* **2001**, *368*, 121–128.
66. Almeida, P.L.; Kundu, S.; Borges, J.P.; Godinho, M.H.; Figueirinhas, J.L. Electro-optical light scattering shutter using electrospun cellulose-based nano- and microfibers. *Appl. Phys. Lett.* **2009**, *95*, doi:10.1063/1.3186640.
67. Kato, T. Self-assembly of phase-segregated liquid crystal structures. *Science* **2002**, *295*, 2414–2418.

Physics of Free-Standing Lyotropic Films

Pawel Pieranski

Abstract: We explore the structures and properties of stable, free-standing films of lyotropic mesophases drawn on apertures of various shapes in an atmosphere of controlled humidity. New phenomena are uncovered and interpreted.

Reprinted from *Materials*. Cite as: Pawel Pieranski Physics of Free-Standing Lyotropic Films. *Materials* **2014**, *7*, 143–160.

1. Introduction

Free-standing thermotropic smectic films (FSTSF) have been widely studied in the past, and their fascinating properties have been thoroughly reviewed [1,2]. Their first and most remarkable property is the huge disproportion between their lateral dimensions L and their thickness d. Indeed, the first ones are macroscopic and determined by the size (typically of a few millimeters) and shape of the frames, flat or not, on which smectic films are suspended. In contradistinction with that, the thickness, d, of FSTSF is rather nanometric, because, in smectic phases, such films are stacks of N molecular layers having thicknesses of a few nanometers. The typical aspect ratio is therefore:

$$AR = \frac{lateral\ dimensions}{thickness} = 10\ mm/10\ nm \approx 10^6 \quad (1)$$

Moreover, this number, N, of layers can be known and controlled with the absolute accuracy of $\Delta N = 1$. The second remarkably property of FSTSF is their surprising robustness. Unlike ephemeral soap bubbles, whose fragility is proverbial, the life-time of FSTSF becomes unlimited, once they are protected (for example, in vacuum; see Section 2.2) against dust particles and other impurities. In such conditions: (1) they can be pierced by fibers; (2) one can make them vibrate like drumheads; (3) flows can be induced in them; (4) they resist the deformation of their frames and (5) their structure can be changed as a function of temperature and other parameters, such as the thickness, N.

Let us stress that the structure of FSTSF is especially interesting to study in materials displaying the SmCphase in which FSTSF are equipped with the 2D vectorial director field, $\vec{c}$, resulting from the tilt of molecules with respect to the layers' normal. The field, $\vec{c}$, is very sensitive to perturbations, such as flows and/or solid or liquid inclusions. An exhaustive and well-documented review on this topic can be found in the recent work [3].

Thanks to their robustness, FSTSF can be not only drawn on solid frames, but also, other shapes can be given to them. For example, when drawn between two coaxial circular frames, they take the shape of a catenoid, or when inflated like soap bubbles using a glass tube, they are spherical. Freely floating smectic bubbles can be produced also, for example, by stretching of the catenoid beyond its stability limit. The dynamical behavior of such freely floating smectic bubbles is fascinating and unusual [4].

Free-standing lyotropic films (FSLF) have also been studied in the past, but much less than the thermotropic ones, because they are more difficult to handle. Indeed, being, by definition, made

from mixtures of surfactants with water, they must be protected against drying. This apparent difficulty, once overtaken through an appropriate control of the humidity, RH, of the surrounding atmosphere, becomes an advantage, because the concentration, c_{H_2O}, of water in lyotropic films can be changed continuously by this means. For example, in pioneering experiments performed with the phospholipid, DMPC (dimyristoylphosphatidylcholine) [5–8], X-ray diffraction and optical reflectivity experiments on FSLF have been performed, and the phase behavior of the DMPC/water binary system has been explored as a function of temperature T and humidity H. The most spectacular result of these experiments was the discovery of three distinct two-dimensional variants, $L_{\beta F}$, $L_{\beta L}$ and $L_{\beta I}$, of the phase labeled previously as L_β (see Figure 1b).

Figure 1. X-ray diffraction and optical reflectivity experiments with lyotropic films: (**a**) Experimental setup used in [5–8]; (**b**) temperature *vs.* humidity phase diagram of dimyristoylphosphatidylcholine (DMPC).

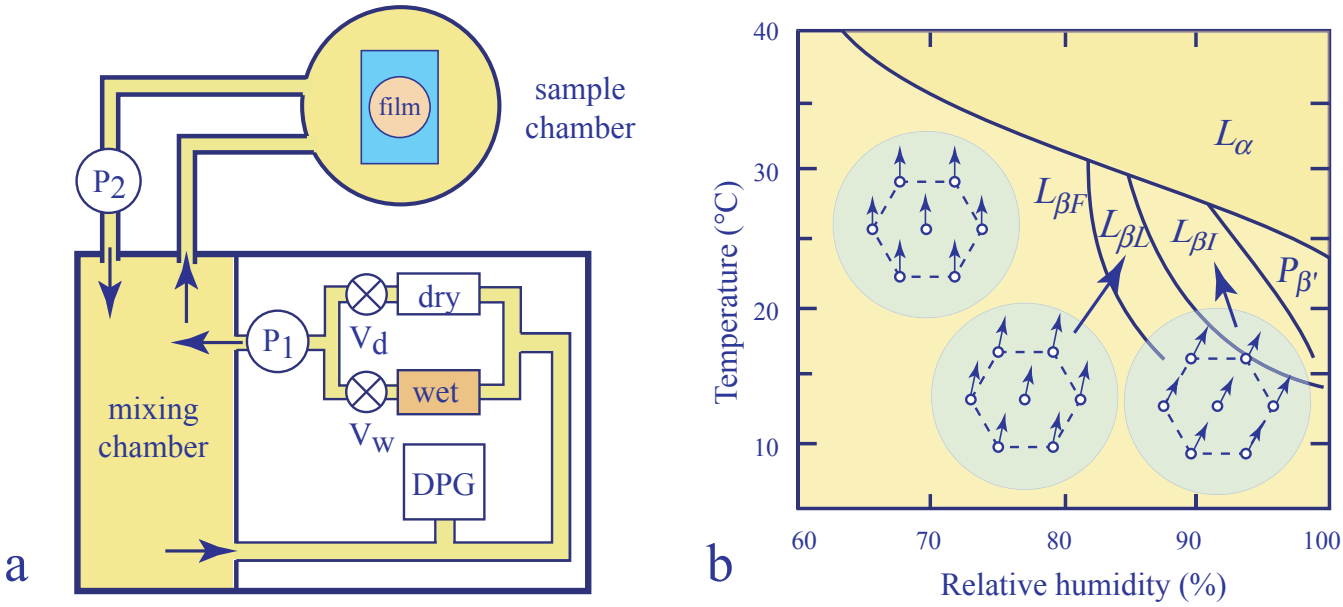

Let us stress that soap films or soap bubbles, which have been and still are widely studied, can be considered as a special case of FSLF drawn from diluted surfactant/water solutions in the micellar phase. In particular, buoyancy and Marangoni effect-driven flows, discussed in Section 4.3, exist obviously in soap films, too. In the context of the present paper, the recent review paper of Langevin and Monroy [9] is certainly very useful.

In the present paper, we will first describe a new setup tailored for experiments with FSLF and operating under a different principle than the one in setups used previously [5–8]. Subsequently, we will outline the most striking properties of FSLF and the new phenomena unveiled in them by means of this new setup. Each of these properties and phenomena would deserve much more detailed experiments and discussions. Here, we provide the first bird's-eye view with the aim of stimulating the work that remains to be done.

2. Control of Humidity

2.1. Mixing Wet and Dry Fluxes

In experiments reported in [5–8], the relative humidity of air in the sample chamber was controlled by the system shown schematically in Figure 1a.

The operating principle of this system consists in mixing, in different proportions, fluxes of air passing through humidifying and drying chambers labeled in Figure 1, respectively, as wet and dry. The less or more humid air produced by this means is sent to the mixing chamber and recirculated through the feedback loop (driven by the pump, P_1) in which its relative humidity is first measured by the dew point gauge (DPG) and readjusted by means of the valves, V_d and V_w, controlling the dry and wet fluxes. The second passive loop (driven by the pump, P_2) recirculates the air of known humidity through the sample chamber.

A similar, but simpler, system has been used in experiments described in [2] (see the Section C.VIII.1.b "Temperature and humidity control" of this reference) where electronic valves coupled with flow meters were used to set precisely the fluxes of perfectly dry and wet nitrogen. These two fluxes were merged by means of a Y-shaped connector and sent directly (without the feedback loop) through a long enough flexible pipe into the sample chamber.

2.2. Water Vapor Injected to Vacuum

In experiments described in the present paper for the first time, a new setup operating by virtue of a different principle has been used. It stems from former experiments with thermotropic smectic films considered as perfect drums [10]. As shown in Figure 2, it consists of a large aluminum sample chamber made of two parts equipped with glass windows.

The upper "cover" part is removable and allows full access to the sample and other equipment contained in the lower "pan" part. An O-ring located between the cover and pan parts make the whole system vacuum-tight. The sample chamber is connected by the intermediate of valves V1 and V2, respectively, to a primary vacuum pump and to a glass reservoir partially filled with water. A pressure gauge measures the pressure of the water vapor inside the sample chamber with an accuracy of 0.1 mbar.

The operating principle of this setup is the following. At the beginning of the experiments, both valves V1 and V2 are open, so that air is evacuated from the sample chamber, as well as from the reservoir containing water. After closing the connection with the vacuum pump (valve V1), the pressure, p_{wv}, of water vapor increases slowly in the sample chamber. Once p_{wv} reaches a suitable value, the valve V2 is closed.

Figure 2. The experimental setup used in the experiments described here. This stems from former the studies of Even [10,11].

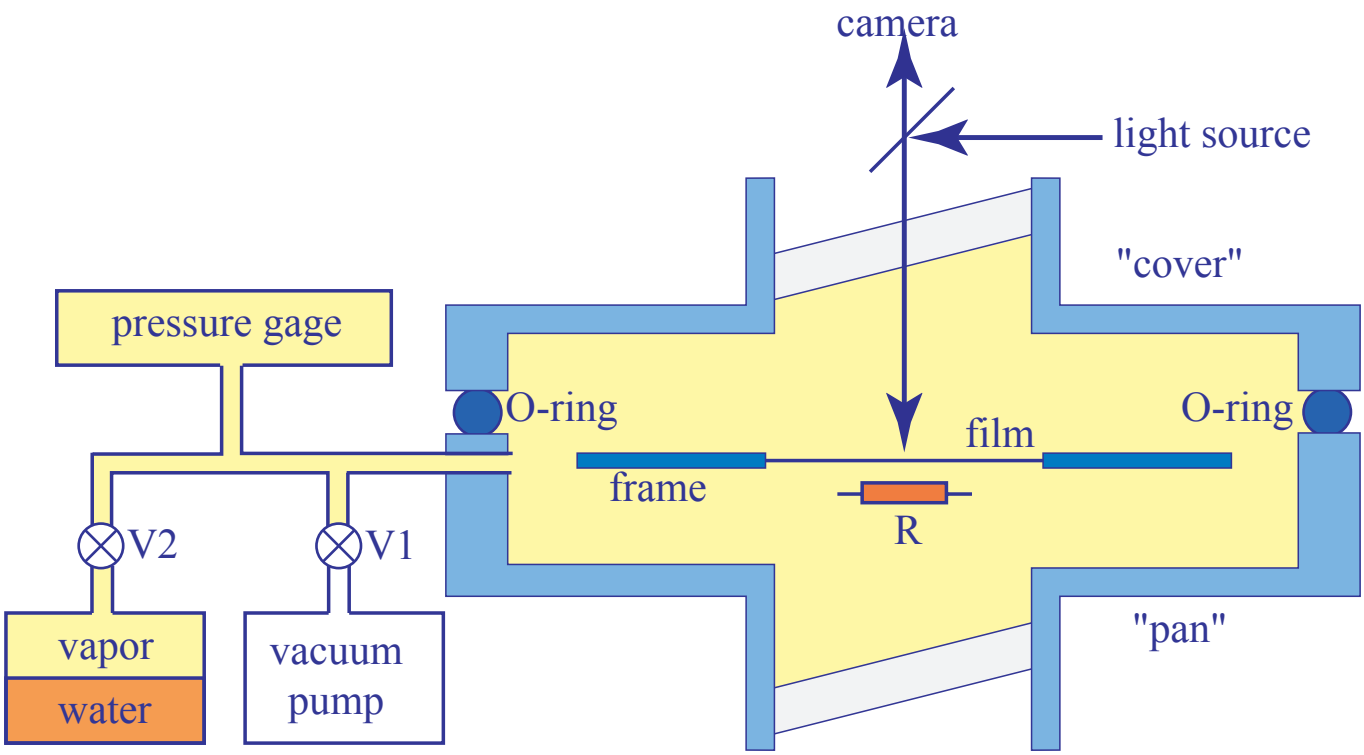

3. Drawing Lyotropic Films

3.1. Choice of the Relative Humidity

It is the easiest to draw lyotropic free-standing films in the lamellar phase. Therefore, for a given temperature, T, the suitable pressure, p_{wv}, of the water vapor should be such that the relative humidity:

$$RH = \frac{p_{wv}}{p_{sat}(T)} \times 100\% \tag{2}$$

(where p_{sat} is the pressure of saturated vapor) would be located in the domain of the lamellar phase on the T *vs.* RH phase diagram.

Let us stress that this kind of phase diagram is known only for a very few surfactants (e.g., DMPC, monoolein, phytantriol, $C_{12}EO_6$), because, traditionally, the phase behavior of surfactant/water mixtures is known from isoplethal studies in which, by definition, a finite number of samples with a fixed concentrations is used. Such studies lead to classical T *vs.* *concentration* phase diagrams.

Fortunately, in the case of the non-ionic surfactant, $C_{12}EO_6$, used in the experiments described below, the T *vs.* RH phase diagram is known from previous studies of the faceting of cubic phases. It is shown in Figure 3b beside the classical T *vs.* c one (Figure 3a). Typically, at a room temperature of $T = 22$ °C and a relative humidity of $RH = 87\%$, the corresponding point, $P(RH, T)$, is located inside the domain of the lamellar phase.

Figure 3. Phase diagrams of the binary mixture, $C_{12}EO_6$/water: (**a**) the classical one; (**b**) the T *vs.* RH phase diagram pertinent for studies of free-standing lyotropic films.

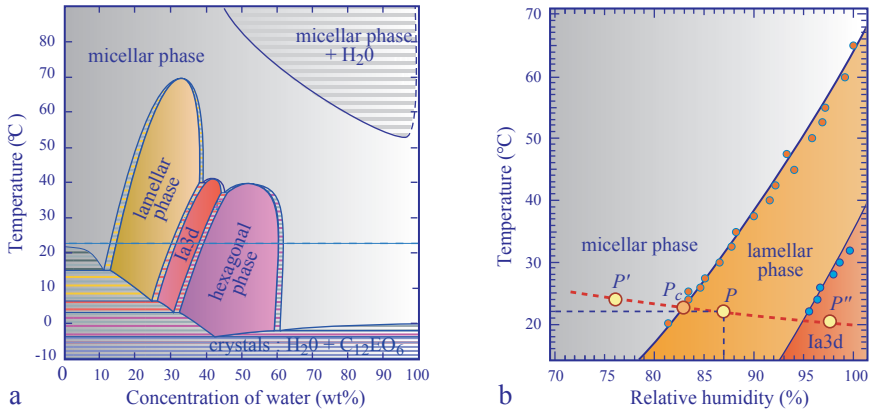

3.2. Drawing Method

Knowing that at room temperature $T = 22$ °C, the pressure of the saturated water vapor is $p_{sat} = 26.43$ mbar, the pressure of the water vapor in the sample chamber should be set to $p_{wv} = 23$ mbar.

The setup shown in Figure 2, as well as the frames (f in Figure 4) used for studies of lyotropic films stem from the former experiments with thermotropic smectic films considered as perfect drums [10]. They are made from thin stainless plates in which apertures of suitable shapes have been cut off. The frame, f, in Figure 4 contains two such apertures. By comparing the two pictures of Figure 4, one remarks on the motion of the spreader, s, passing over the circular aperture. The spreader is actually stretching an FSLF on the circular aperture and, at the same time, wets the surface of the frame, f, with a thin layer of the surfactant. Obviously, in this demonstration made with the open sample chamber, the FSLF drawn on the circular aperture is unstable. Nevertheless, such a preliminary manipulation is suitable, because pre-wetting of the frame with the surfactant is a necessary condition for the successful drawing of a stable lyotropic film.

Figure 4. System used for the drawing of free-standing films. The two pictures (**a**) and (**b**) illustrate the motion of the spreader, s.

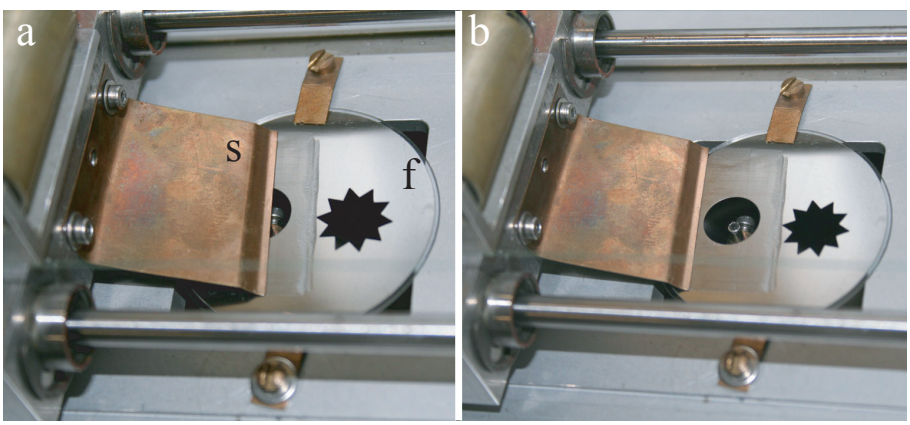

The second necessary condition for the successful drawing of a film is a smooth and slow enough motion of the spreader. As the drawing of the film must be done inside the closed sample chamber, the spreader is moved by a motorized translation stage visible in Figure 4. The drawing process itself is shown in a series of pictures in Figure 5.

Figure 5. Drawing a free-standing lyotropic film on a triangular frame. The side length of the triangle is 20 mm. The film is made of the lamellar phase of the $C_{12}EO_6$/water mixture. The process of the film drawing is illustrated by the series of six pictures (**a**)–(**f**) taken at intervals of about 30 s.

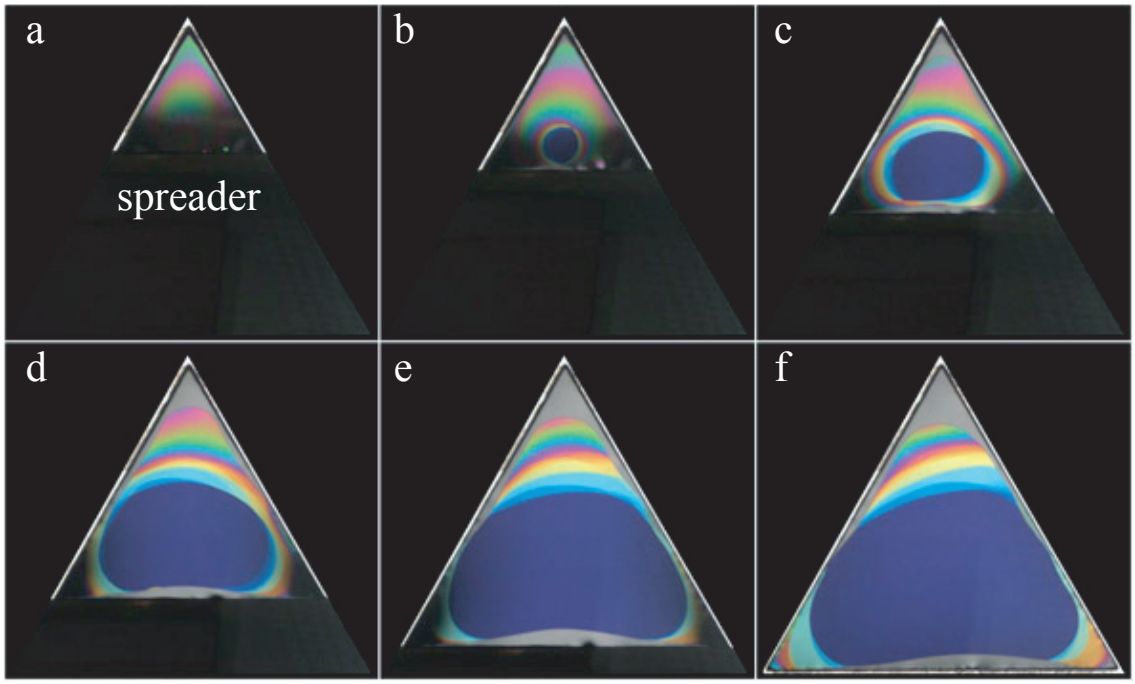

Here, instead of the circular aperture shown in Figure 4, an equilateral triangular aperture has been used, because the triangular shape has an advantage over the circular one for the drawing process. During the film drawing, its surface area $S(t)$ increases at the rate, dS/dt. If d is the film thickness, the volume, V, of the film increases with the rate $dV/dt = (dS/dt) \times d$, which means that this volume of the lamellar phase is pulled out from the meniscus per unit time. The rate of transfer of matter from the meniscus to the film per unit length of the meniscus (whose total length is L) is driven by a transient increase in the film tension:

$$\Delta\tau \propto \frac{1}{L}\frac{dS}{dt} \tag{3}$$

From simple geometrical considerations made with the triangular frame, it is easy to show that:

$$\frac{1}{L} \times \frac{dS}{dt} = \frac{1}{3}v_s \tag{4}$$

where v_s is the velocity of the spreader. Therefore, for a constant velocity, v_s, of the spreader, the transient increase of the film tension, $\Delta\tau$, remains constant during the drawing process. Thanks to this feature, the main cause of the film break-up—the opening of pores due to excessive film tension—can be avoided.

3.3. Evolution toward a Constant Thickness

As shown in the series of pictures in Figure 5, the thickness of the film is not uniform during the drawing process. This non-uniform, out of equilibrium state evolves very slowly toward the equilibrium state of uniform thickness (see Figure 6). How and why this evolution occurs has been described and explained in [2] (see, also, Section 4.3). An example of this slow evolution is shown in the series of pictures taken during 24 h at intervals of 3 h.

Figure 6. Evolution of a film in the lamellar phase of the $C_{12}EO_6$/water mixture. Pictures (**a**)–(**i**) were taken at intervals of 3 h.

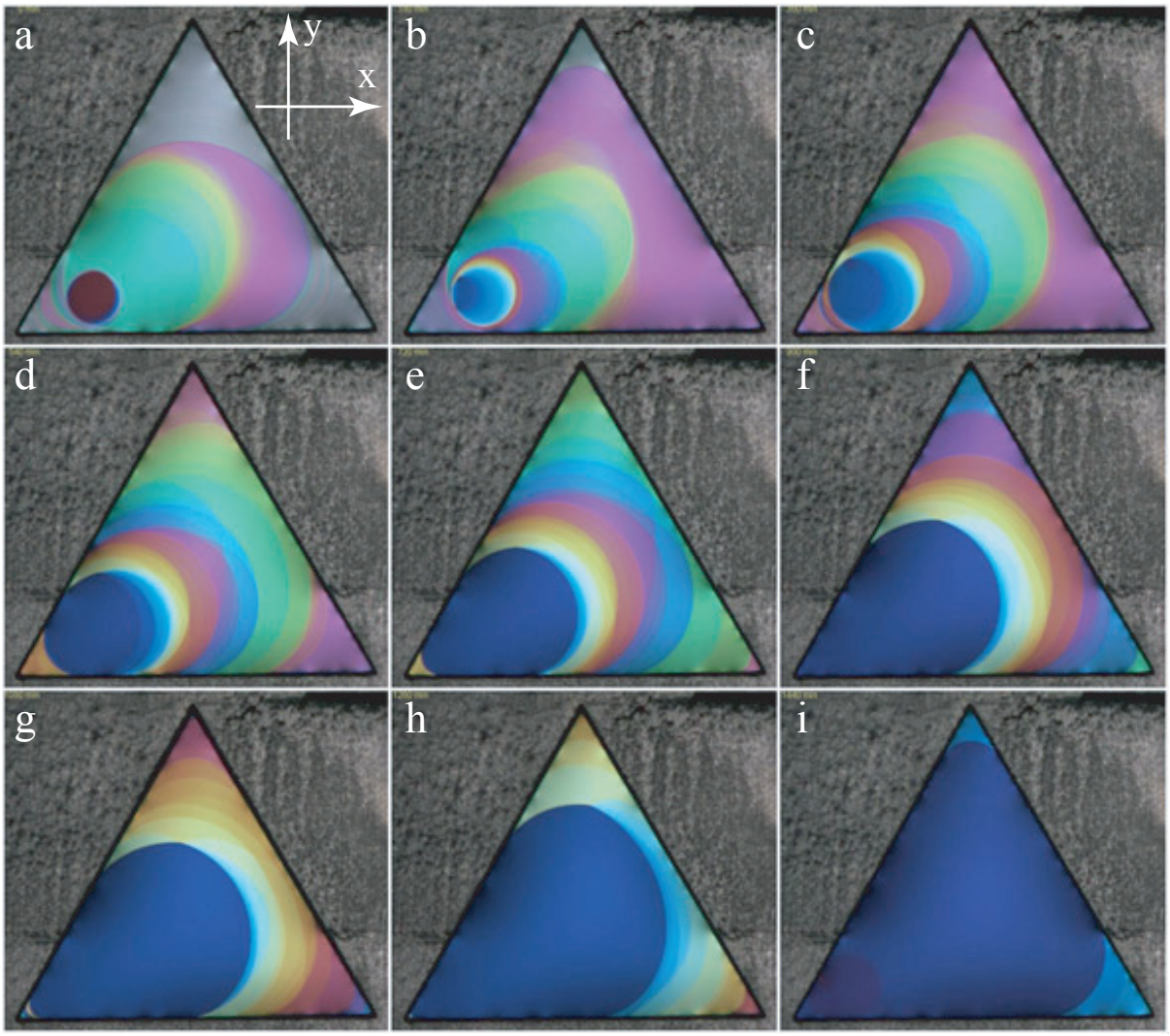

Thanks to this property of the lyotropic films, experiments with films of a non-uniform thickness can be easily performed, as we will see in the next section.

4. Phenomena Occurring in Free-Standing Lyotropic Films

4.1. Buoyancy Forces in Tiled Films

When a film of non-uniform thickness is intentionally tilted out from its horizontal position (by tilting the whole sample chamber), one observes that the thinnest field of the film always raises the steepest slope. For a film of shape $z = z(x, y)$, the direction of motion is given by $\vec{\nabla} z$. This effect is obviously due to buoyancy forces similar to those that occur in a three-dimensional liquid. In films, the mass per unit area is proportional to the film thickness, d (or N), so that the thinnest field of the film is pushed by a force proportional to $\Delta N \vec{\nabla} z$. This force should vanish for a perfectly horizontal position of the film. Unfortunately, such a perfectly horizontal position exists only in theory. In practice, the thinnest part of the film never stays in the center of the frame.

4.2. Centrophobic Behavior

There is another reason for such a centrophobic behavior of the thinnest field in films. Let us remind ourselves that films are drawn on an aperture made in a stainless steel plate. Such a plate cannot be either perfectly horizontal or perfectly flat. When the frame, on which a film is spanned, is not flat, then the film itself must have a global saddle shape. As a result, the buoyancy force is unavoidable, and the thinnest part of the film cannot stay in the center of the frame.

4.3. Marangoni-Type Effect

The series of pictures in Figure 7 shows how the thinnest (brownish) field moves in a film of non-uniform thickness. This motion could be driven, as discussed above, by the tilt $\Delta N \vec{\nabla} z$ of the triangular frame, which is indicated in pictures (a) and (c) by arrows.

However, the cause of the motion visible in Figure 7 is a different one. In this experiment, the film remains horizontal, and the thinnest field of the film follows the motion of a small heating element—small resistor—whose shape and (x,y) position is indicated by the dashed rectangle. As this resistor is located below the film, it is invisible in the reflecting microscope: it is masked by the light reflected by the film.

Such behavior could be called thermophilic, because in this experiment, the film is locally heated by the resistor. In the first approximation, the corresponding distribution of temperature has the symmetry of revolution around the point, HS (hot spot in Figure 8), located above the center of the resistor:

$$T = T(r) \tag{5}$$

where r is the distance from HS. In Figure 8, $T(r)$ is represented by shades of red. At a constant pressure, p_{wv}, of water vapor in the sample chamber, the relative humidity decreases with temperature, because $p_s(T)$ grows with T . Therefore, the relative humidity, $RH(r)$, is lower in the vicinity of the resistor. For this reason, the behavior of the film could also by termed hygrophilic, because its thicker parts are attracted to areas where the relative humidity is larger.

Figure 7. Hygrophilic behavior of lyotropic films. The dashed-line rectangle indicates the (x,y) position of a heating resistor located below the film (see Figure 2). Pictures (**a**)–(**c**) were taken at intervals of 5 s. Obviously, the thinnest part of the film follows the motion of the resistor.

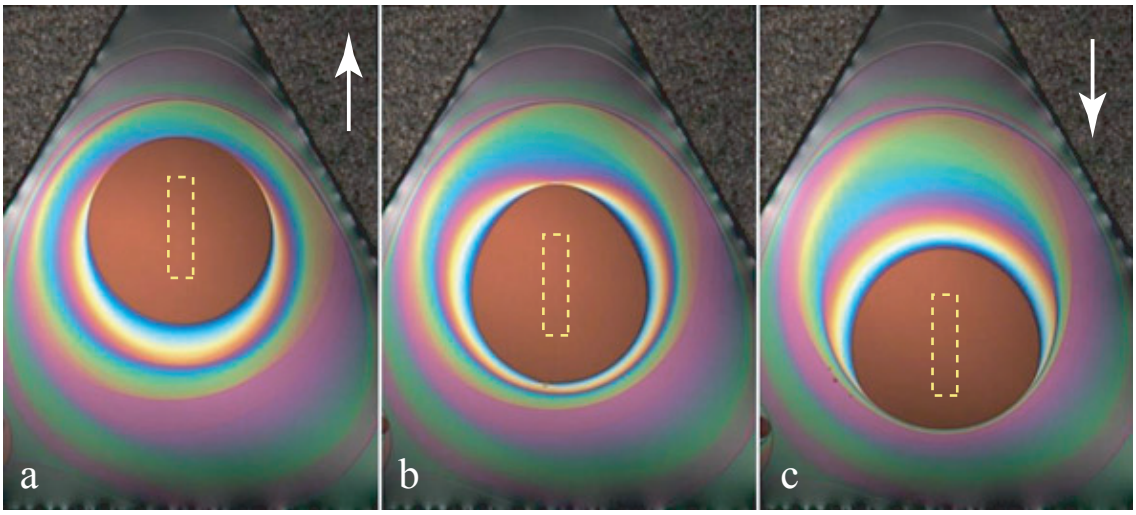

Figure 8. Marangoni-type effect in lyotropic films: (**a**) the distribution of temperature has the symmetry of revolution around the point, HS (hot spot), which coincides with the center, O, of a concentric system of steps; (**b**) the temperature distribution is shifted by l with respect to the system of steps. The temperature varies now as a function of φ along steps. The resulting gradient of steps tensions drives flows represented here in the reference frame of the system of steps.

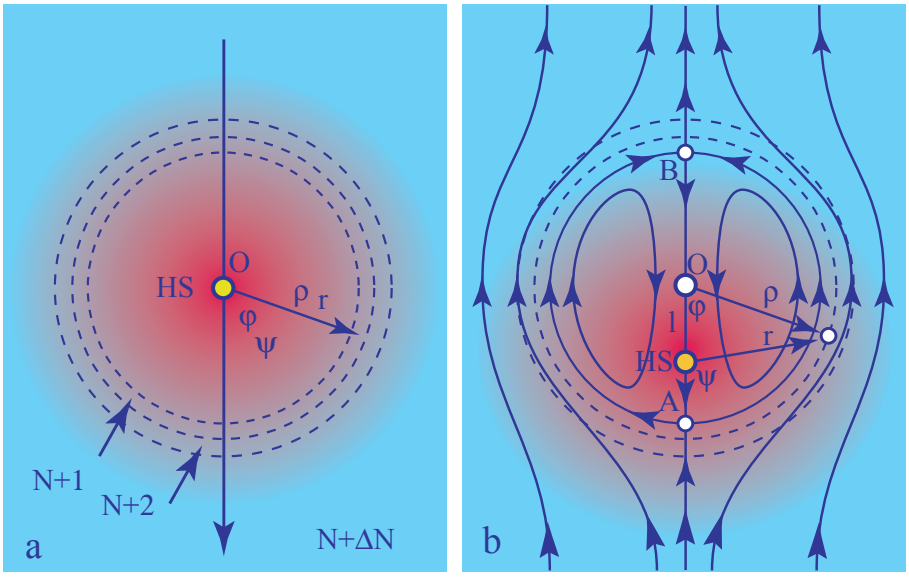

In the search for an explanation of this behavior, it is convenient to introduce two systems of polar coordinates. The first one, (r, ψ), with the origin HS (hot spot), has been already used for the description of the temperature distribution $T = T(r, \psi)$. The second system of polar coordinates,

(ρ, φ), with the origin zero, is related to the system of concentric steps surrounding the circular field of thickness, N , centered at zero. As shown in Figure 8 (for the purpose of simplicity, only two steps are shown), this central field is surrounded by a system of concentric circular fields of growing thickness: $N + 1, N + 2, ...$; so that one can write:

$$N = N(\rho) \tag{6}$$

The effective tension in the film depends both on the thickness, N, and the temperature, T:

$$\gamma = \gamma(N, T) \tag{7}$$

when the center HS of the temperature distribution coincides with the center, O, of the distribution of steps (see Figure 8a), the tension of the film depends only on ρ:

$$\gamma = \gamma(N, \rho) \tag{8}$$

so that, inside each field of thickness N, the variation of the surface tension with ρ can be compensated for by an opposite variation of the 2D pressure inside bilayers forming the film. By this means, the mechanical equilibrium inside each field is restored. As discussed in [2], this effective tension has a discontinuity at each step. The resulting force is orthogonal to steps and pulls them toward the meniscus. This is the explanation of the thinning behavior shown in Figure 6. Let us stress that this motion of steps, which is similar to the climbing of dislocations, is so slow, that it can be neglected on the time scale of the thermophilic phenomenon.

What happens when the center HS of the temperature distribution is shifted with respect to the center, O, of the distribution of steps, as shown in Figure 8b? The most evident feature of this configuration is that steps separating adjacent fields are no longer isothermal as they were previously. It is easy to find that if l is the distance, O–HS (see Figure 8b), then the distance, r, from the hot spot, HS, is given by:

$$r = \sqrt{(\rho \cos \varphi - l)^2 + (\rho \sin \varphi)^2} \tag{9}$$

by substituting this expression into Equation (5), one obtains the variation of the temperature as a function of the polar coordinates (ρ, φ). In conclusion, along the step of radius ρ, the temperature varies with the angle, φ.

Steps in free-standing films can be considered as interfaces between two-dimensional phases; fields of thickness N. When the temperature varies along a step, its tension, τ, varies as a function of φ, too, and:

$$\sigma_\varphi = \frac{1}{\varrho} \times \frac{\partial \tau}{\partial \varphi} \tag{10}$$

is the force per unit length tangent to the step. This force can be balanced only by viscous stresses, so that it drives flows in the film. The resulting flow field is represented in Figure 8b in the reference frame (ρ, φ) of the thinnest field, N.

4.4. From-Step-to-Step, Motion of Inclusions

The picture in Figure 9a shows a film in the lamellar phase of non-uniform thickness containing an inclusion. This inclusion is moving in the direction, $\vec{x}$, indicated by the arrow orthogonal to the steps. The series of 15 pictures in Figure 9b shows that this motion is not smooth, but rather "jerky": the trajectory, x(t), is stairs-like; x remains constant in segments AB, CD and EF, while the motion from-step-to-step occurs in segments BC and DE. The second remarkable feature of this motion is that the inclusion "is climbing" the staircase; it moves in the direction of growing thickness N.

The explanation of this behavior is quite simple. The inclusion floating in the film-containing steps is surrounded by a meniscus made of steps. In Figure 9c–e, steps are drawn with lines of different colors ranging from yellow to red. For example, in Figure 9c, there are two orange steps $N/N+1$: one belongs to the system of steps of the whole film, while the second one belongs to the circular meniscus surrounding the inclusion. These two steps can coalesce, as shown in FIugre 9d, and as a result, the inclusion moves from the field, N, to $N+1$. This process is obviously recurrent.

Figure 9. From-step-to-step motion of an inclusion: (**a**) general view of the film of non-uniform thickness containing an inclusion; (**b**) series of 15 successive images taken at an interval of 0.5 s; (**c**–**e**) evolution of the systems of steps driving the motion of the inclusion.

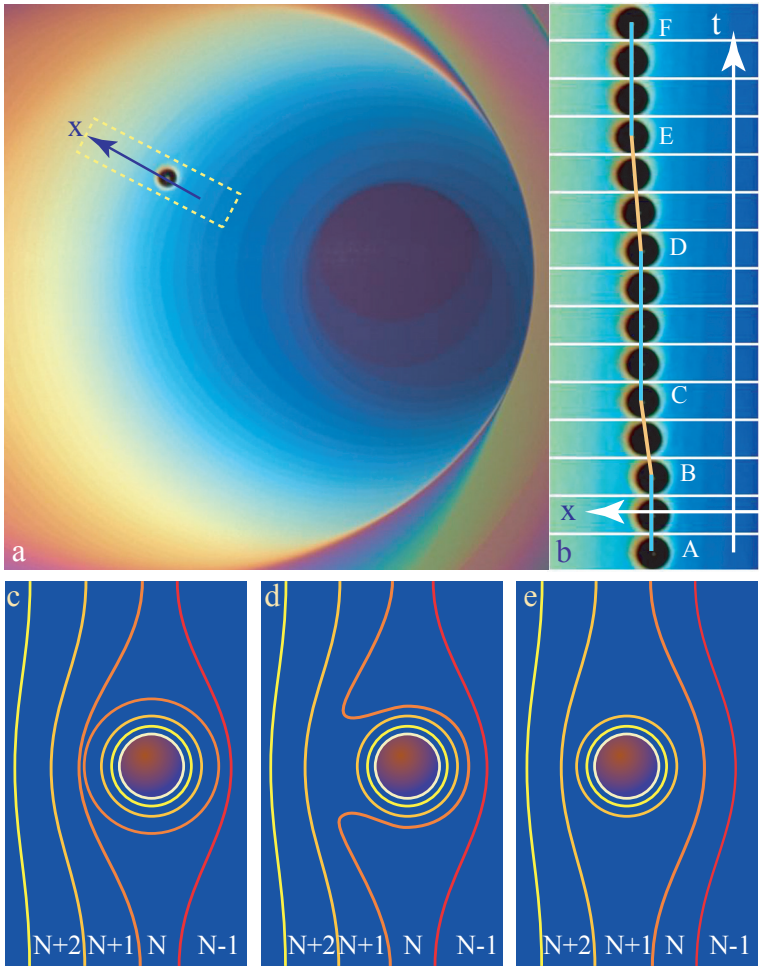

4.5. Deformation of the Meniscus

The phenomenon of the from-step-to-step motion described above unveils the microscopic structure of the meniscus surrounding the inclusion at its junction with the film: it is made of a system of circular steps. A similar structure should exist at the edge of the linear meniscus connecting a film of uniform thickness (resulting from the processes described in Section 3.3) with the edge of the frame. However, when the frame is very thin, this meniscus is so small, that it is itself difficult to see at low magnification, so that these steps cannot be resolved (see Figure 10b).

Figure 10. Instability of the meniscus driven by a steep rise in humidity from 88% to 95%. The series of pictures (**b**)–(**e**) was taken in the time interval labeled "water reservoir" in the plot, $p_{wv}(t)$, shown in (**a**).

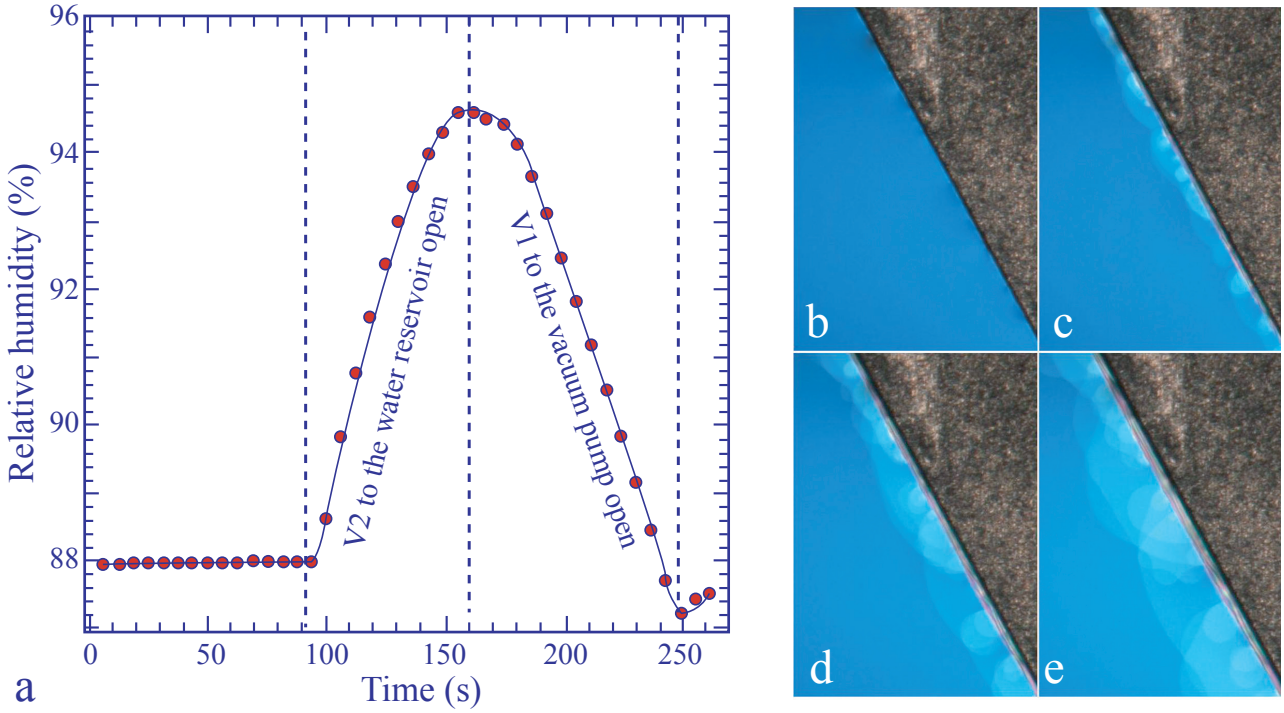

We have found that upon a steep increase, Δp_{wv}, of the water vapor pressure, p_{wv} (see the plot, $p_{wv}(t)$, in Figure 10a), the meniscus is so strongly deformed, that the steps composing its thinnest part become apparent, as is shown in Figure 10c–e.

Experiments showed also that this deformation of the meniscus is transient: when p_{wv} is kept at its new value, the processes described in Section 3.3 restore the initial narrow shape of the meniscus. From this, one can infer that the deformation of the meniscus is transient and must be due to the gradient of the water concentration, which appears in the meniscus during the change of water concentration in it.

5. Phase Transitions

5.1. Lamellar to Micellar Transition, Nucleation and Growth

The small resistor, R, located below the lyotropic film (see Figure 2) allows the local heating of it. As discussed previously in Section 4.2, the relative humidity is modified by the local heating of the film, because for a given pressure, p_{wv}, of the water vapor contained in the sample chamber, the relative humidity defined by Equation (2) depends on the temperature of the film. As an example, we show in Figure 3b the isobaric trajectory $RH = RH(T)$ defined by Equation (2) in which p_{wv} = $const$. This trajectory passes through the point, $P(87\%, 22\ ^\circ\text{C})$, in the domain of the lamellar phase. When the film and the water vapor surrounding it are heated by the resistor and the temperature increases, for example, from 22 °C to 24 °C, the relative humidity is lowered from 87% to 76%, and the corresponding point, $P'(76\%, 24\ ^\circ\text{C})$, on the phase diagram in Figure 3b is now located inside the domain of the inverted micellar phase, L2. The trajectory, PP', crosses the lamellar/micellar transition line at the point, $P_c(RH_c, T_c)$.

When the resistor, R, is very close to the film, the isotherms $T(x, y) = const$ and the isoaquilents (*i.e.*, lines of constant humidity) $RH[T(x, y)] = const$ in its vicinity have elliptical shapes, such as the one drawn with a dashed line in Figure 11a.

Let us suppose that this isotherm shown in Figure 11a is the critical one, that is to say, it is defined by the condition $T(x, y) = T_c$. As a consequence, inside it, the lamellar phase should be replaced by the micellar phase. The lamellar/micellar transition being of the first order, it starts by the nucleation of the micellar phase on the defect indicated by the arrow in Figure 11a. Subsequently, the micellar domain grows as shown in the next three pictures Figure 11b–d.

Figure 11. Lamellar ⇒ micellar L2 transition driven by the local heating by means of the resistor, R, located below the film. (**a**–**d**) Nucleation and growth of the micellar domain; (**e**) flow pattern driven by temperature gradients.

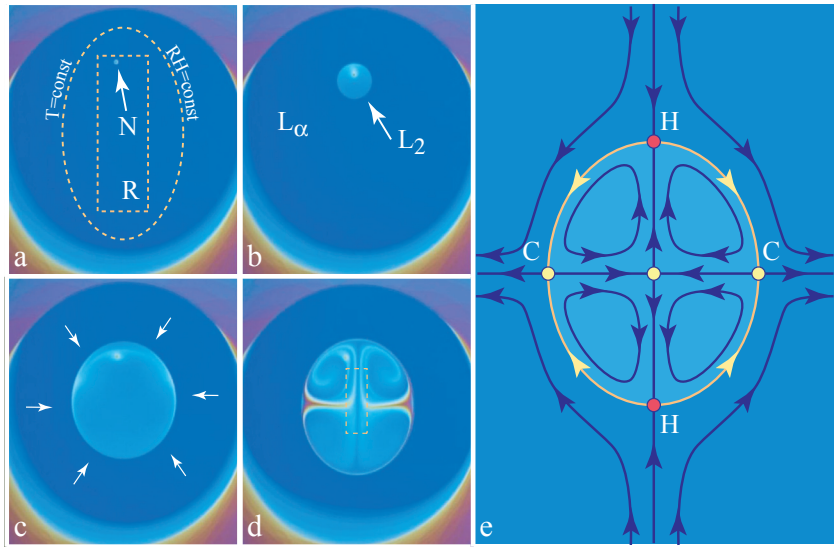

The same transition is illustrated by the series of pictures in Figure 12. Here, two micellar domains nucleate simultaneously in the lamellar film. They grow and coalesce into one domain that continues to grow.

From interference colors in these pictures, one can infer that:

1. The micellar domain is thicker than the lamellar one, so that the flux of surfactant across the lamellar/micellar interface must be larger than the one that would result from the motion of the interface alone. This means that the micellar domains acts as a sink, so that in the lamellar phase surrounding the micellar domain, there is a flow, $\vec{v}$, converging toward the micellar domain (see the arrows in Figure 11c).
2. This additional flow persists when the micellar domain reaches its stationary size, so that the thickness and the volume of the micellar phase continues to increase.
3. The persistent flow of the surfactant across the interface drives vortex-like flows depicted in Figure 11e).

Figure 12. Lamellar ⇒ L1 transition. The time, counted in seconds from the beginning of the heating, at which pictures (**a**)–(**h**) have been taken, is indicated in their upper left corners.

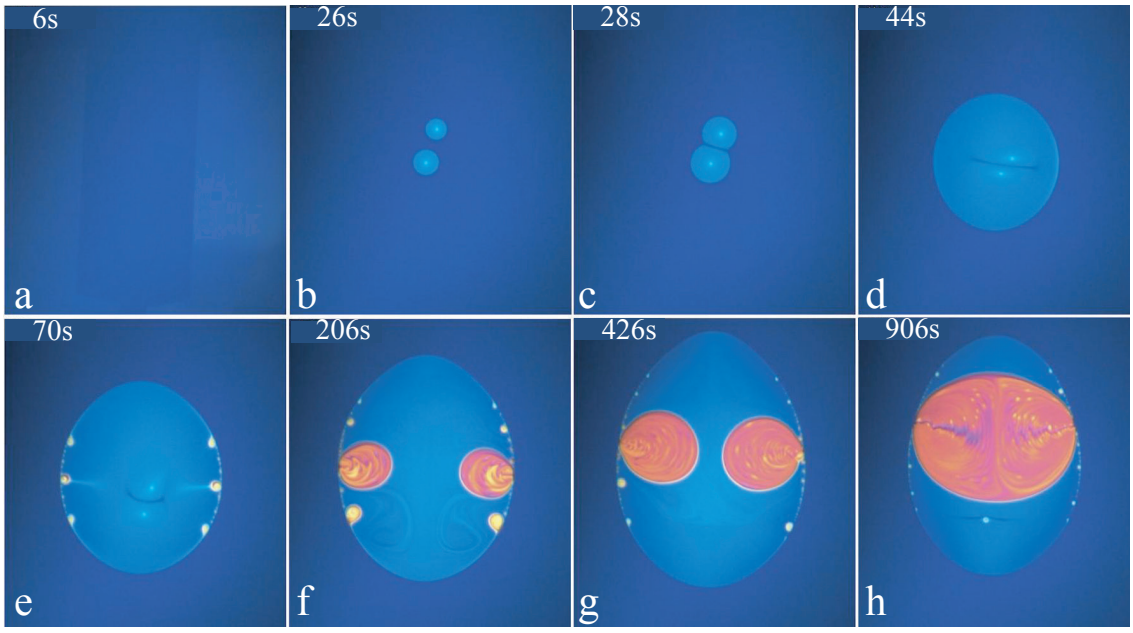

None of the above three observations had been explained, so far. We will attempt to do this below.

5.2. The Role of the Tension of the Lamellar/Micellar Interface

In the search for such explanations, one must certainly take into account the tension of the lamellar/micellar interface seen as a line in a two-dimensional film. In three dimensions, the Laplace pressure created by the tension of a curved lamellar/micellar interface would be equilibrated by an

adequate static pressure difference, Δp, across the interface: the pressure inside the micellar domain would be larger than in the surrounding lamellar phase. In a free-standing film, it is impossible to create such a static pressure difference across the lamellar/micellar interface, because the micellar phase cannot be compressed. Indeed, if one would try to compress it by decreasing its surface area, S, the thickness, d, would increase in such proportions that the volume $V = Sd$ would stay constant.

The Laplace force (per unit length of the interface) can nevertheless be equilibrated by viscous stresses created by the extensional flow at the entrance to the micellar phase (see Figure 13), where the thickness has to increase from d to $d + \Delta d$ on the time scale of the order of $t \approx l/v$, where l is the width of the interface and v the velocity of the flow across it. The extension rate is then:

$$\dot{\varepsilon} \approx \frac{1}{d}\frac{\Delta d}{l/v} \tag{11}$$

and the viscous stress due to it is:

$$\sigma_{xx} = \eta\dot{\varepsilon} \tag{12}$$

where η is the extensional viscosity of the micellar phase. If τ is the tension of the interface and R its radius of curvature in the (x,y) plane, then the following balance of forces should be satisfied:

$$\eta d\frac{1}{d}\frac{\Delta d}{l/v} \approx \frac{\tau}{R} \tag{13}$$

Finally:

$$\Delta d \approx \frac{\tau}{R}\frac{l/v}{\eta} \tag{14}$$

Figure 13. Flow across the lamellar/micellar interface as seen in the reference frame of the interface.

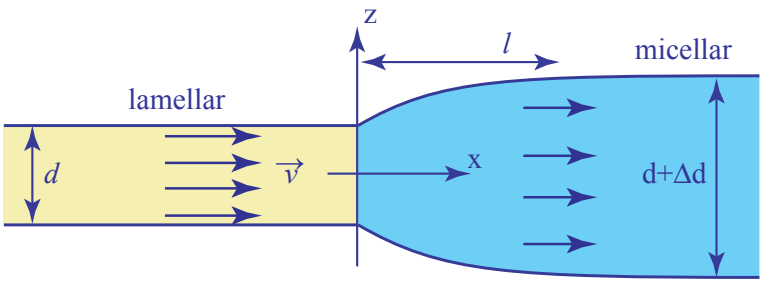

.

The tension at the lamellar→micellar interface can be estimated from experiments in which the micellar phase nucleates at steps of the film. The lens-shaped micellar domains in the two pictures of Figure 14 result from the equilibrium of tensions of three interfaces meeting at triple points, TP. Obviously, the tensions, τ_1 and τ_2, are of the same magnitude as the tension, τ_3, of the step $N/N+1$ in the lamellar phase.

Figure 14. Nucleation of the micellar phase on steps of the film in the lamellar phase: (**a**) general of the film; (**b**) detailed view of one micellar domain, TP are triple point.

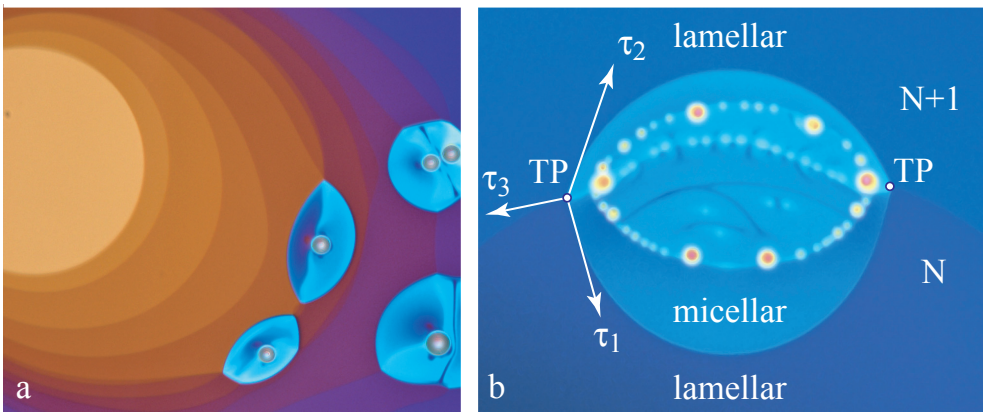

5.3. Lamellar to Ia3d Transition

When at $T = 22$ °C, the relative humidity is larger than 97%, the lamellar/Ia3d boundary on the phase diagram in Figure 3 is crossed, and the cubic Ia3d phase grows, as shown in Figure 15. Let us emphasize that the Ia3d crystals were nucleated at the frame surface and are growing from the meniscus. For this reason, they are are much thicker than the film. It should be possible by an adequate local cooling to nucleate and to make Ia3d crystals grow inside the film.

Figure 15. Growth of Ia3d crystals in the film in the lamellar phase. Nucleation of crystals occurs at the edge of the aperture. Pictures (**a**)–(**c**) have been taken at intervals of about 15 s.

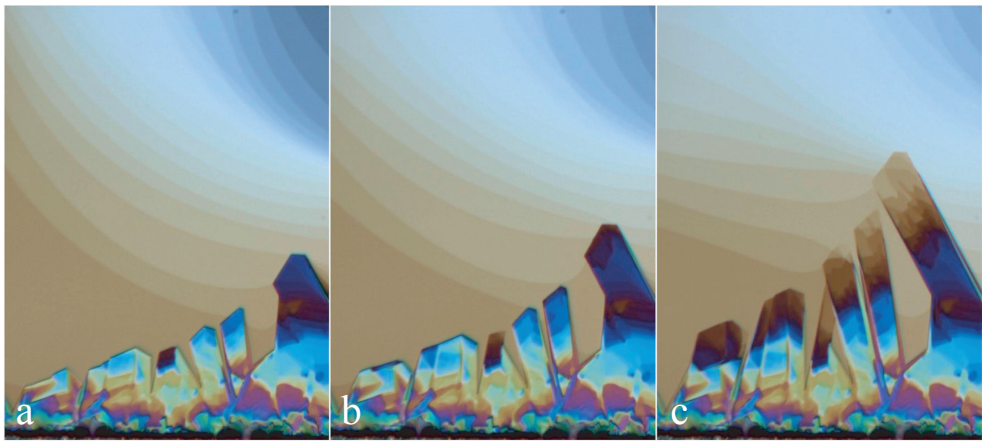

6. Conclusions

As mentioned in the Introduction, free-standing lyotropic films deserve to be studied for at least two reasons.

First of all, on flat frames, their structure—stacks of perfectly aligned layers—is very favorable for structural X-ray or optical studies. Moreover, their composition can be varied *in situ* continuously

and precisely through the control of the relative humidity of the surrounding atmosphere. Thanks to these two features, new phases of the DMPC/water system have been discovered in the pioneering work presented in [5–8].

The second reason is that free-standing lyotropic films are very interesting on their own, because their properties and the phenomena occurring in them are unusual. A few of them have been described in the previous section, but our conviction is that many other phenomena remain to be discovered.

As, on the other hand, free-standing films are rather difficult to handle, we focused in Sections 2.2 and 3 on the process of drawing films in an atmosphere of controlled humidity. We hope that all these technical details and comments will be useful and stimulating for experimentalists.

The theoretical interpretation of the equilibrium and out of equilibrium properties of free-standing lyotropic films is challenging, because it involves thermal and molecular exchanges with the surrounding humid atmosphere. In the simplest case of isothermal experiments with films of uniform thickness, the surrounding atmosphere acts as a reservoir of water molecules, whose chemical potential is set by the pressure of the water vapor. However, in the presence of thermal gradients, films are out of equilibrium, and thermal diffusion must be taken into account. This difficulty is amplified by the presence of steps and flows that can be driven by gradients of step tensions. Even more challenging is the issue of phase transitions in lyotropic films. The simplest case of the lamellar to micellar L2 transition tackled in Section 5 is far from being understood.

We hope that for all these reasons, the present paper can be stimulating also for theorists.

Acknowledgments

The present work benefited from collaboration with Catherine Even and from the technical help of Vincent Klein, Sambath Saranga, André Bialek, Jean-Louis Signoret and Bernard Le Bourhis.

Conflicts of Interest

The author declares no conflict of interest.

References

1. Sonin, A.A. *Freely Suspended Liquid Crystalline Films*; Wiley-VCH: Weinheim, Germany, 1995.
2. Oswald, P.; Pieranski, P. Smectic free films. In *Smectic and Columnar Liquid Crystals*; Taylor & Francis: Boca Raton, FL, USA, 2006.
3. Bohley, H.; Stannarius, R. Inclusions in free standing smectic liquid crystal films. *Soft Matter* **2008**, *4*, 683–702.
4. May, K.; Harth, K.; Trittel, T.; Stannarius, R. Freely floating smectic films. *ChemPhysChem* **2014**, doi:10.1002/cphc.201301183.
5. Young, C.Y.; Clark, N.A. Dynamics of freely suspended lyotropic films. I. An inelastic light scattering study of thermal surface fluctuations. *J. Chem. Phys.* **1981**, *74*, 4171–4185.

6. Sirota, E.B.; Smith, G.S.; Safinya, C.R.; Plano, R.J.; Clark, N.A. X-ray scattering studies of aligned, stacked surfactant membranes. *Science* **1988**, *242*, 1406–1409.
7. Smith, G.S.; Sirota, E.B.; Safinya, C.R.; Plano, R.J.; Clark, N.A. X-ray structural studies of freely suspended ordered hydrated DMPC multimembrane films. *J. Chem. Phys.* **1990**, *92*, doi:10.1063/1.457764.
8. Chiang, H.-T.; Chen-White, V.S.; Pindak, R.; Seul, M. Ordering transitions in thin, freely-suspended phospholipid films. *J. Phys. II* **1995**, *5*, 835–857.
9. Langevin, D.; Monroy, F. Marangoni stresses and surface compression rheology of surfactant solutions. Achievements and problems. *Adv. Colloid Interface Sci.* **2014**, *206*, 141–149.
10. Even, C.; Pieranski, P. On "hearing the shape of drums": An experimental study using vibrating smectic films. *Europhys. Lett.* **1999**, *47*, doi:10.1209/epl/i1999-00420-8.
11. Even, C. Vibrations d'une Membrane Smectique: Rôle de la Forme du Contour. An Experimental Study Using Vibrating Smectic Films. Ph.D. Thesis, University of Paris-Sud, Orsay, France, 29 June 1999. (in French).

New Lyotropic Mixtures with Non-Chiral *N*-Acylamino Acid Surfactants Presenting the Biaxial Nematic Phase Investigated by Laser Conoscopy, Polarized Optical Microscopy and X-ray Diffraction

Erol Akpinar, Dennys Reis, Muhammet Yildirim and Antônio Martins Figueiredo Neto

Abstract: Amino acid-based surfactants were used as the main surfactants to prepare new lyotropic mixtures presenting three nematic phases. One of them is biaxial (N_B), and the two others are uniaxial, discotic (N_D) and calamitic (N_C). These surfactants were the non-chiral molecules, potassium *N*-dodecanoyl-DL-alaninate (DL-KDDA), potassium *N*-dodecanoyl-DL-serinate (DL-KDDS), disodium *N*-dodecanoyl-DL-aspartate (DL-NaDDAs) and potassium *N*-dodecanoyl-glycinate (KDDGly). Measurements of the optical birefringences and X-ray diffraction analysis were used to characterize the nematic phases and phase transitions. Mixtures with DL-KDDS exhibited the largest biaxial phase domain (~9 °C) with respect to the other mixtures in this study. The results obtained with the KDDGly mixture showed that the existence of hydrogen bonding between the head groups of the surfactant molecules seems to hinder the orientation of the micelles under the action of an external magnetic field.

Reprinted from *Materials*. Cite as: Akpinar, E.; Reis, D.; Yildirim, M.; Neto, A.M.F. New Lyotropic Mixtures with Non-Chiral *N*-Acylamino Acid Surfactants Presenting the Biaxial Nematic Phase Investigated by Laser Conoscopy, Polarized Optical Microscopy and X-ray Diffraction. *Materials* **2014**, *7*, 4132–4147.

1. Introduction

One of the most interesting mesophases exhibited by liquid crystals is the biaxial nematic one. Yu and Saupe [1] reported the first experimental evidence of this phase in 1980, exploring the phase diagram of a ternary lyotropic mixture. They showed the existence of two uniaxial (N_D, discotic; and N_C, calamitic) phases and a biaxial (N_B) nematic phase, confirming the theoretical predictions of Freiser [2] and Alben [3]. This fascinating field of research remains active, as evidenced by the interest demonstrated by experimentalists and theoreticians in the last decade [4–8].

The N_B phase has been encountered in several lyotropic mixtures with, at least, a surfactant and a co-surfactant [9]. Mixtures with only one surfactant may show only one of the uniaxial nematic phases.

Lyotropic nematic mixtures doped with chiral molecules give rise to cholesteric lyotropic phases, also named lyocholesterics. Similarly to nematics, three types of lyocholesterics were identified [10–12]: Ch_D, Ch_C and Ch_B, where the subscripts indicate the former nematic phase, which originates the cholesteric ones. To the best of our knowledge, all the lyotropic mixtures presenting the Ch_B phase were obtained by the doping of nematic mixtures with brucine [13] or brucine sulfate heptahydrate [12], *i.e.*, non-amphiphilic chiral molecules. Transitions between these cholesteric phases were investigated theoretically and experimentally [13,14], showing fundamental differences

with respect to the transitions in nematics. It would be interesting to investigate the transitions between the different cholesteric phases in mixtures where the main surfactant is chiral. A strategy to do that is to prepare a mixture with a racemate of the main amphiphilic molecule, *i.e.*, equal amounts of D and L enantiomers, which presents the three nematic phases. After that, changing the relative concentrations of the D and L enantiomers, the three cholesteric phases may be obtained.

Uniaxial nematic phases were obtained from mixtures prepared with some racemates [15,16]; however, the biaxial phase was not encountered in these lyotropic mixtures. We cannot discard the possibility that the N_B phase exists in those mixtures, under proper conditions of temperature and relative concentrations of the components of the mixtures. However, it is important to stress that the choice of the chain length of the co-surfactant is an essential issue to be considered in the preparation of a lyotropic mixture that presents the biaxial nematic phase. Moreover, just the inspection of textures under polarizing microscope is (usually) not enough to fully characterize the nematic phase, since both the N_B and N_C phases show a planar texture in microslides, subjected to an external magnetic field [9]. This fact brings an ambiguity in the complete characterization of the phase and its identification as uniaxial or biaxial. To fully characterize the nematic phase, the tensor order parameter should be measured, as we will discuss in the following.

In this study, we present five new lyotropic mixtures based on *N*-acylamino acid surfactants, which present the N_B phase. Four of them are composed of the racemates, potassium *N*-dodecanoyl-DL-alaninate (DL-KDDA), potassium *N*-dodecanoyl-DL-serinate (DL-KDDS) and disodium *N*-dodecanoyl-DL-aspartate (DL-NaDDAs), as the main amphiphile in each mixture. The fifth *N*-acylamino acid surfactant is the potassium *N*-dodecanoyl-glycinate (KDDGly), which is an achiral molecule. The main experimental techniques used to characterize the nematic phases are X-ray diffraction (XRD), polarized optical microscopy (POM) and laser conoscopy.

2. Results and Discussion

2.1. Nematic Phases of Racemic N-Acylamino Acid Surfactants

The labels and compositions of the samples are given in Table 2, in the Experimental Section.

The uniaxial to biaxial transition temperatures were determined analyzing the temperature dependence of the birefringences (or the symmetric invariants of the order parameter), measured with laser conoscopy and inspecting the characteristic textures in the POM.

The order parameter that has the symmetry of the nematic phase is the optical dielectric tensor, $\overleftrightarrow{\varepsilon}$, a traceless second-rank tensor [2,17]. Its symmetric invariants (σ_i, i = 1, 2, 3) may be written in terms of the optical birefringences. With the birefringences measured in the three nematic phases, the symmetric invariants of the tensor order parameter, σ_2 and σ_3 ($\sigma_1 = 0$), can be calculated [18]:

$$\sigma_2 = \frac{16}{9}\langle n\rangle^2(\Delta n^2 + \Delta n\delta n + \delta n^2)$$

$$\sigma_3 = -\frac{128}{27}\langle n\rangle^2(\Delta n - \delta n)(\Delta n + \delta n/2)(\delta n + \Delta n/2)$$

where $\langle n \rangle$ is the mean index of refraction of the mixture. In the framework of the Landau-de Gennes theory (*i.e.*, mean-field theory), these invariants show a linear dependence with the temperature in the vicinity of the second-order uniaxial to biaxial phase transition.

In our experiments, usually, we started the measurements with the sample in the N_D phase, perfectly oriented with the director parallel to the laser beam. The temperature is then changed step by step to reach the other nematic phases. Figure 1 shows typical results of the conoscopic patterns obtained in our experiments.

Figure 1. Typical conoscopic patterns of the mixture, potassium *N*-dodecanoyl-DL-serinate (DL-KDDS)/Na_2SO_4/1-dodecanol (DDeOH)/water. (**a**) nematic discotic phase (N_D) at 45.0 °C; (**b**) nematic biaxial phase (N_B) near the N_D to N_B transition at 33.7 °C; (**c**) N_B at 31.0 °C; and (**d**) calamitic nematic phase (N_C) at 23.0 °C; (**e**) geometry of the experiment: *P*, *A* and $\vec{H}$ are the directions of the polarizer, analyzer and the applied magnetic field, respectively.

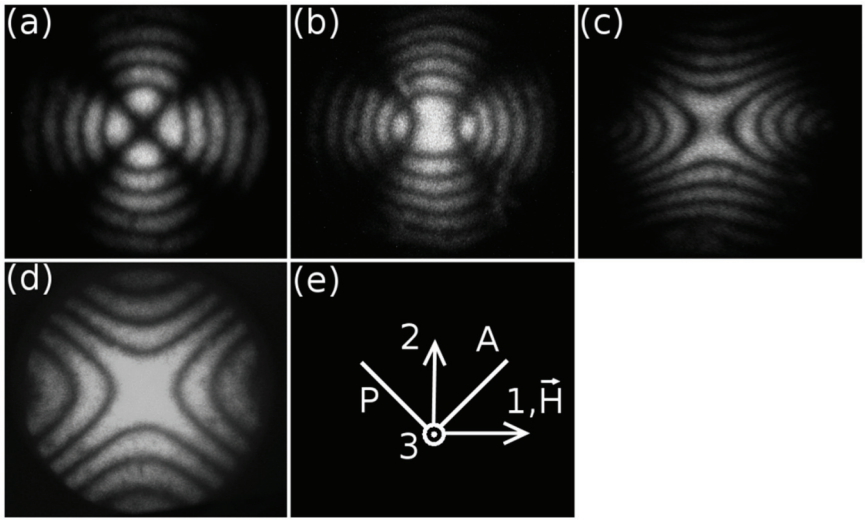

We have checked that the phase sequence as a function of the temperature does not change (within the precision in the measurement of the temperature) for samples stored in a freezer for at least one year. The aspect of the conoscopic fringes is also the same, without noticeable modifications as a function of time. This result assures us that the patterns represent the steady state of the alignment of the sample, subjected to the magnetic field. At this point, it is interesting to discuss in more detail the features of the conoscopic patterns shown in Figure 1. The symmetry of the patterns and the contrast between the fringes and the background assures us that they were produced by well-aligned samples. Unaligned samples could not produce such types of patterns (see, e.g., [19]). Observing only the central part of the pattern (the opening of the Maltese cross), obviously, we cannot differentiate the existence of a biaxial phase from the effect of a uniaxial phase losing its alignment [20]. However, the complete conoscopic patterns of these two situations are completely different. This assures us the existence and alignment of the biaxial phase in our experiments.

The temperature dependence of the birefringences of DL-KDDA, DL-KDDS and DL-NaDDAs are given in Figure 2.

Figure 2. Temperature dependence of the birefringences of the mixtures: (**a**) potassium *N*-dodecanoyl-DL-alaninate (DL-KDDA)/Cs_2SO_4/DDeOH/water; (**b**) DL-KDDS/Na_2SO_4/1-undecanol (UndeOH)/water; (**c**) DL-KDDS/Na_2SO_4/DDeOH/water; and (**d**) disodium *N*-dodecanoyl-DL-aspartate (DL-NaDDAs)/Cs_2SO_4/UndeOH/water. 2P represents a two-phase coexistence region.

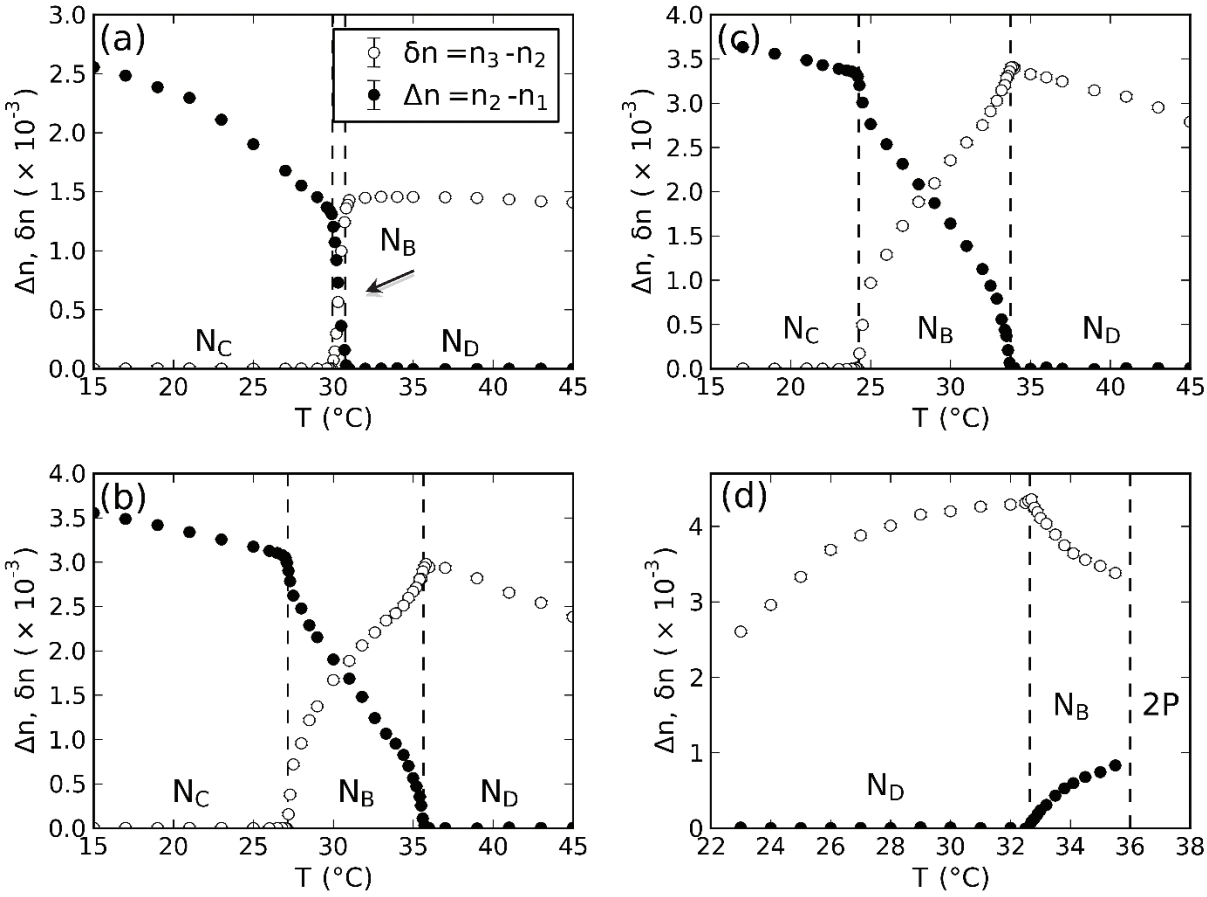

Biaxial nematic domains are present in the phase sequences shown in Figure 2, in between the two uniaxial nematic phases, except in the case of the DL-NaDDAs mixture, where the N_B phase domain ends in a two-phase region at higher temperatures. Interestingly, this last mixture shows the N_D phase domain at lower temperatures, contrary to the other mixtures investigated, where the N_C phase domain occurs at lower temperatures.

With the measured values of the birefringences in the nematic phases, the tensor order-parameter symmetric-invariants may be calculated. Figures 3 and 4 show the temperature dependence of the invariants, σ_2 and σ_3, respectively. The behaviors of $\sigma_{2,3} \times T$ in the vicinity of the uniaxial to biaxial nematic phase transitions are in accordance with the mean-field prediction, *i.e.*, σ_2 and σ_3 show a linear dependence with the temperature. Figure 5 depicts the locations of the nematic phases in the space of the invariants. Solid lines correspond to the uniaxial nematic phases: $\sigma_3 = \pm\sigma_2^{3/2}$, where the + and − signs refer to the N_D and N_C phases, respectively.

Figure 3. Temperature dependence of the tensor order-parameter symmetric-invariant, σ_2, of the mixtures: (**a**) DL-KDDA/Cs_2SO_4/DDeOH/water; (**b**) DL-KDDS/Na_2SO_4/UndeOH/water; (**c**) DL-KDDS/Na_2SO_4/DDeOH/ water; and (**d**) DL-NaDDAs/Cs_2SO_4/UndeOH/water.

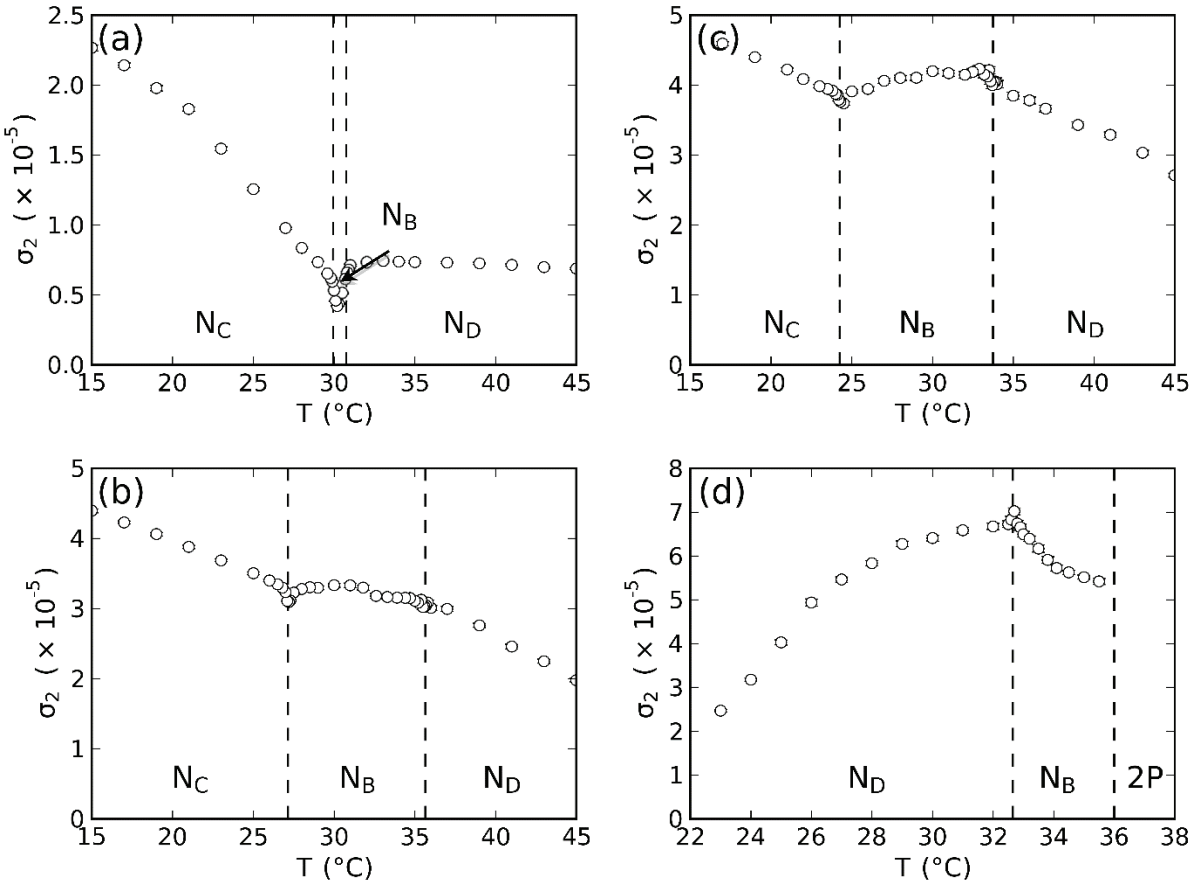

The textures of the nematic phases of these mixtures observed in the POM are the classical ones, already reported in the literature [9]. An interesting question that may be proposed is how the D- and L-enantiomers arrange in the micelles to give rise to a non-chiral nematic phase. However, for their pure L-enantiomers, there is some experimental evidence about their organization in the chiral micelles. Du and co-workers [21] investigated the molecular arrangement of *N*-hexadecanoyl-L-alanine (*N*-HDA) by atomic force spectroscopy. This molecule belongs to the class of *N*-acylamino acids being similar to the amino acid-based surfactant molecules employed by us in this study. This molecule has three additional CH_2 groups in its alkyl chain, with respect to our molecules, and its head group is neutral, e.g., not potassium or sodium salt. They analyzed the formation of the monolayers by chiral *N*-HDA molecules on the silicon and mica surfaces and found that the hydrocarbon chains of *N*-HDA molecules arrange as almost tilted and parallel to each other in the bilayer. They interpreted this molecular arrangement by means of the homochiral effect between chiral carbons in the head groups. A similar result was also reported for monoalkylethylenediamines [22]. It is expected that the head groups of *N*-HDA molecules, L-alanine, form hydrogen bonding among them via neighboring carboxylic acid and amide groups (–C=O···N–H) at the surface of the micelles.

Figure 4. Temperature dependence of the tensor order-parameter symmetric-invariant, σ_3, of the mixtures: (**a**) DL-KDDA/Cs_2SO_4/DDeOH/water; (**b**) DL-KDDS/Na_2SO_4/UndeOH/water; (**c**) DL-KDDS/Na_2SO_4/DDeOH/water; and (**d**) DL-NaDDAs/Cs_2SO_4/UndeOH/water.

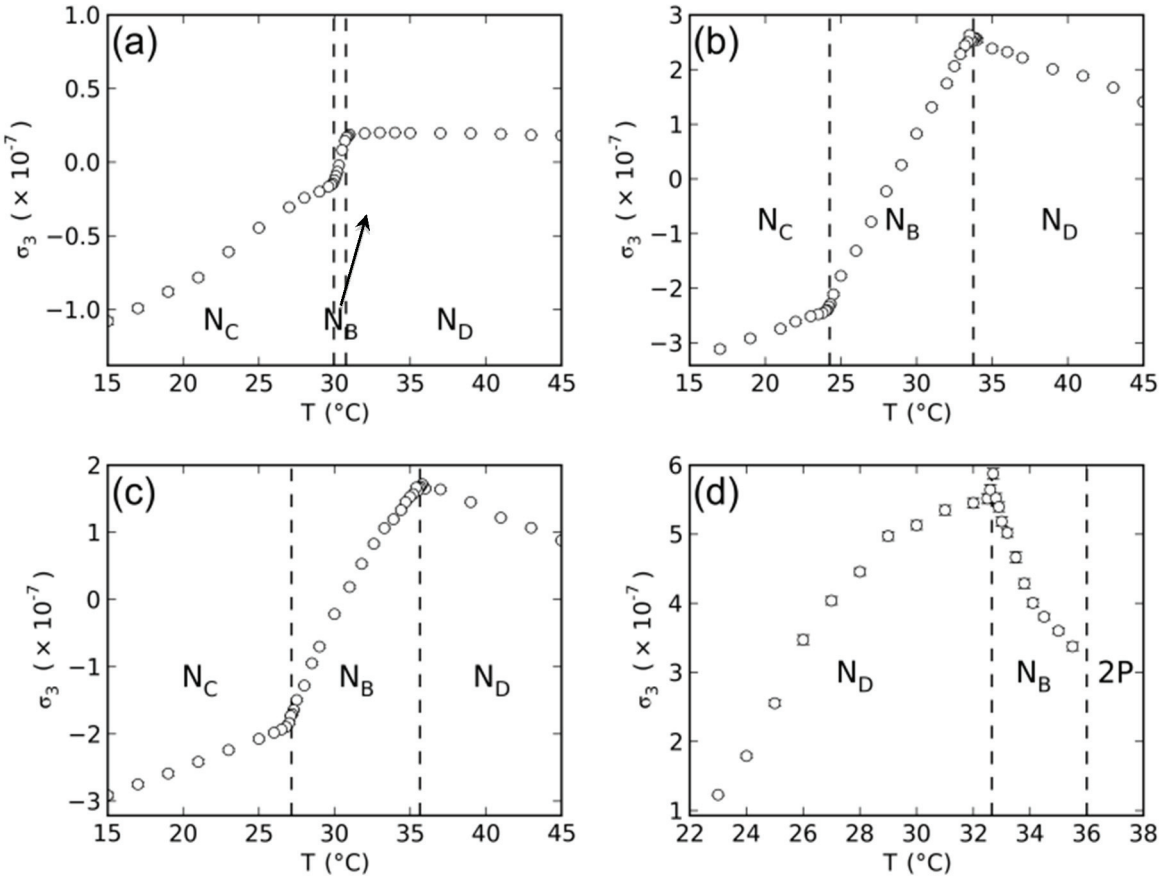

X-ray diffraction experiments performed with these mixtures gave information about the structure and local ordering of the micelles. A difficulty we faced with mixtures where Cs ions were present was the high absorption coefficient of the mixtures for the X-ray wavelength employed in the experiments. In the particular case of Samples 1 and 4, it was not possible to have reliable diffraction patterns in our experimental setup. The data of the different samples are presented in Table 2. s_i, i = 1,3 are the moduli of the scattering vector that correspond to the position of the diffraction bands along the horizontal (1-axis) and vertical (3-axis) of the laboratory frame axes. Thus, the repeating distances along these directions are s_i^{-1}. Typical X-ray patterns are presented in Figure 6. The X-ray scattering at small angles (visible near the beam stopper in Figure 6) will not be analyzed in the present work. Three bands exist in these patterns: two along the 3-axis and one along the 1-axis directions. The outer band along the 3-axis is barely visible in the patterns.

Figure 5. Loci of the nematic phases in the space of the invariants, σ_2 and σ_3, of the mixtures: (**a**) DL-KDDA/Cs_2SO_4/DDeOH/water; (**b**) DL-KDDS/Na_2SO_4/UndeOH/water; (**c**) DL-KDDS/Na_2SO_4/DDeOH/water; and (**d**) DL-NaDDAs/Cs_2SO_4/UndeOH/water.

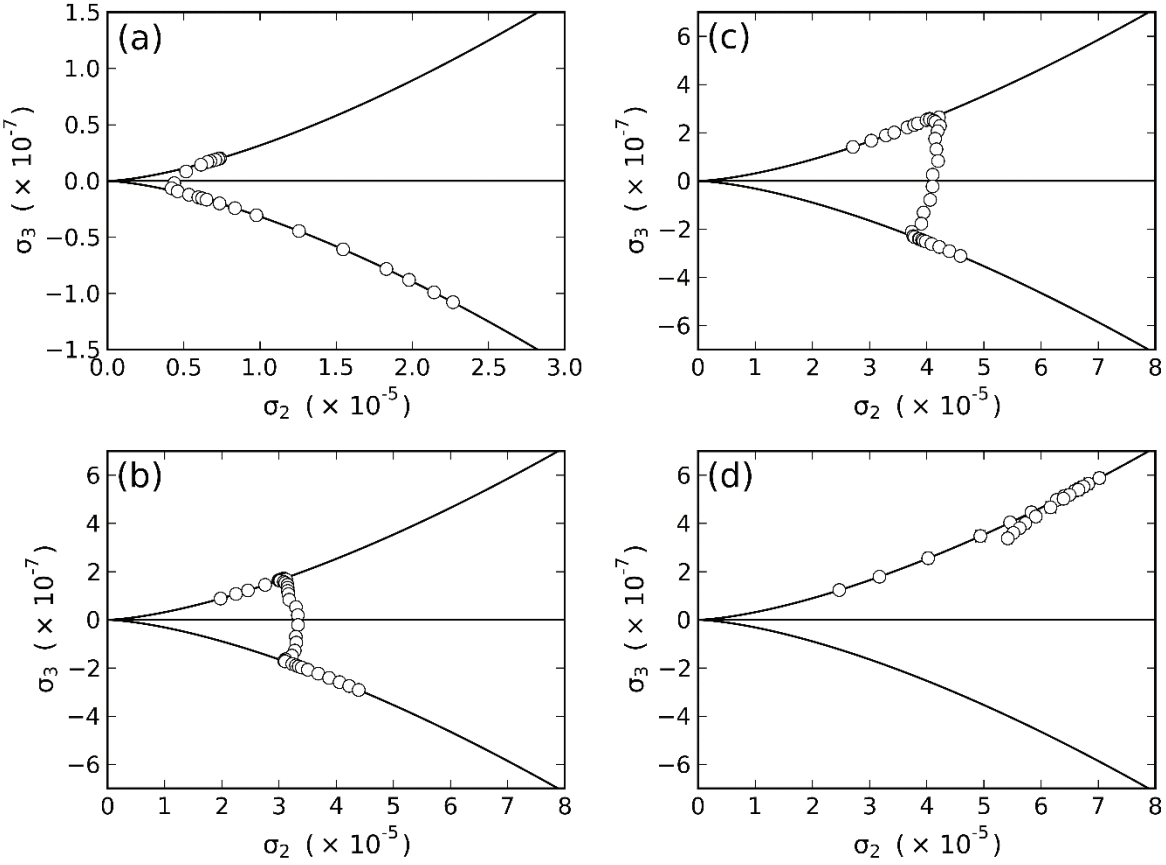

Figure 6. Typical X-ray diffraction patterns of the mixture DL-KDDS/Na_2SO_4/ 1-dodecanol/H_2O: (**a**) N_D phase, $T = 36.0$ °C; (**b**) N_C phase, $T = 24.0$ °C.

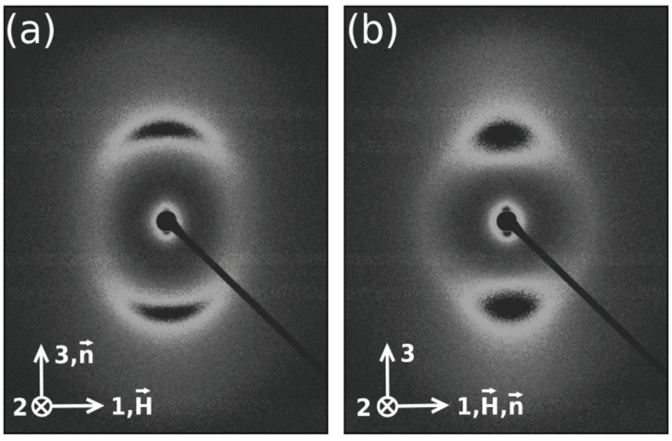

The plot of the diffracted intensity as a function of the modulus of the scattering vector along the 3-axis (Figure 7) reveals its presence. The two bands along the 3-axis are originated from the pseudo-lamellar ordering of the micelles, corresponding to the first and second-order bands, typical of lyotropic nematics with, at least, two amphiphiles [23]. To go further in the analysis of the

diffraction bands, we have to assume a model for the micelles. The model that is consistent with all the results from the different experimental techniques, adequate to describe the micelles in mixtures that present the three nematic phases, is the intrinsically biaxial micelles (IBM) model (see, e.g., [9] for a comprehensive discussion about this model). This model assumes that the micelles have an orthorhombic symmetry in the three nematic phases, and orientational fluctuations of the correlation volumes originate the different symmetries of the nematic phases. The micelles may be sketched as a flattened ellipsoid, with three characteristic dimensions: the smallest one corresponds to the main amphiphilic bilayer, and the two others lie in the flat surface of the ellipsoid. Without additional information about the thickness of the main amphiphilic bilayer of the different mixtures investigated, we have to restrict our analysis to the average volume available per micelle, *i.e.*, the micelle itself and the water that surrounds it. We define a parameter that evaluates the anisotropy of the available volume per micelle as $\Upsilon = s_1^{-1}/s_3^{-1}$. It is interesting to compare the values of Υ obtained in our present experiment with that encountered in the ternary mixture of KL/decanol/water, which is $\Upsilon \sim 2.2$. It is expected that the bigger Υ, the bigger the shape anisotropy of the micelle itself. Thus, the micelles present in Mixtures 2 and 3, in the nematic phases, are expected to be more symmetric (*i.e.*, less anisometric) than those on the KL mixture. This fact is consistent with the maximum values of the birefringences in these racemic mixtures, which are also smaller than those encountered in the KL mixture. Interestingly, the correlation lengths associated with the diffraction bands along Axis 3 of both racemic mixtures are smaller than those of the KL mixture (e.g., $\xi_3 \sim 30$ nm); however, those along Axis 1 are bigger than that of the KL mixture (e.g., $\xi_1 \sim 6$ nm). The order parameters associated with the first-order band along the 3-axis were calculated according to Deutsch calculation [24] and show values consistent with the measurements of the coherence lengths, *i.e.*, the higher ξ, the higher the order parameter.

Figure 7. Diffracted intensity (in logarithmic scale) as a function of the modulus of the scattering vector along the 3-axis. Mixture DL-KDDS/Na_2SO_4/1-dodecanol/H_2O; N_D phase, T = 36.0 °C. The arrow indicates the location of the second-order band.

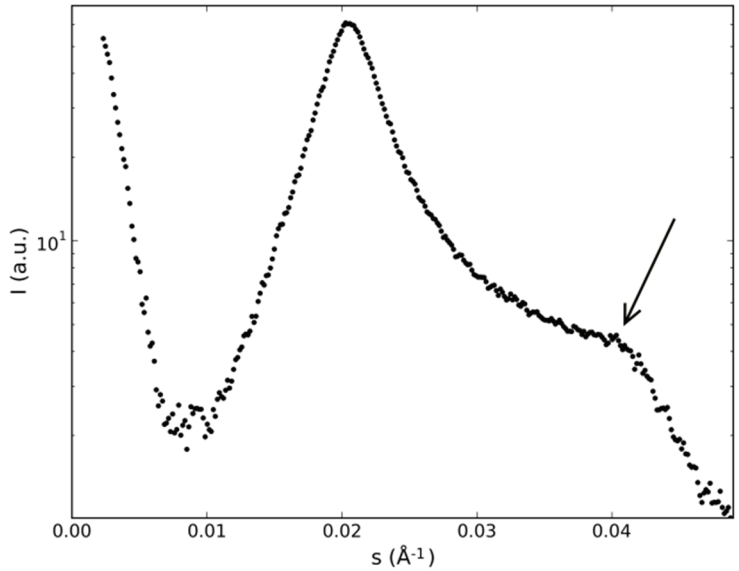

2.2. Nematic Phases of KDDGly/Na_2SO_4/TDeOH/Water

This new mixture presents nematic phases, but exhibited a peculiar behavior with respect to the other racemic *N*-acylamino acid surfactants mixtures in the conoscopy experiment. The N_D phase aligns perfectly in the magnetic field (applying the alignment procedure previously described) only after about four hours. When the temperature is decreased, the center of the conoscopic pattern (the Maltese cross; see, e.g., Figure 1a) splits, indicating the beginning of the N_B phase domain, similar to Figure 1b. Suddenly, all the fringes disappear just after the N_D to N_B transition, indicating a loss of the sample's alignment. The usual orientational procedure employed to align the N_B phase that was shown to be effective in the case of the other mixtures reported here was not enough to orient the biaxial nematic phase in this case. Let us describe, now, the behavior of this mixture placed in a 0.2 mm flat microslide under the POM experiment. In the N_D phase, 1 h after filling the microslide and in the presence of the magnetic field, a characteristic schlieren texture was observed (Figure 8a). After about 5 h, the texture is pseudo-isotropic, with the director perpendicular to the glass surfaces of the microslide and to the magnetic field. Decreasing the temperature, the sample transits to the N_B phase, and the texture reveals defects characteristic of a non-oriented sample (Figure 8b). This result explains to us the disappearance of the conoscopic fringes in the N_D to N_B phase transition, since the sample completely lost its alignment. Decreasing the temperature to about 23 °C, the texture observed is characteristic of the N_C phase (Figure 8c).

To find the temperature of the N_C to N_B phase transition, we kept the sample in the microslide about 72 h at 23.0 °C, in the presence of the magnetic field. A planar texture was obtained with the director aligned parallel to the magnetic field. With the help of a Berek compensator, we measured the optical birefringence in the N_C phase $\Delta n \sim 3 \times 10^{-3}$. Slowly increasing the temperature, when the N_C to N_B transition is achieved ($T = 25.8$ °C), the sample lost its alignment, and the conoscopic fringes do not allow a precise measurement of the birefringence. This behavior is very similar to what we observed at the N_D to N_B transition. This behavior, however, is different from that observed with the racemic mixtures investigated in this work. With those racemic mixtures, when the uniaxial to biaxial phase transition takes place, the two optical axes of the N_B phase lie in the plane perpendicular to the magnetic field, and those, which are not there, are easily replaced in that plane by the orientational procedure described in the Experimental Section. The KDDGly mixture, however, presents a weak coupling with the magnetic field, which avoids the quick orientation of the two optical axes of the N_B phase on that plane. This weak magnetic coupling was also observed in the N_C phase subjected to the magnetic field that took about three days to achieve the planar orientation of the director. Thus, when the sample transits from a uniaxial to the biaxial phase, the two optical axes, in different correlation volumes lie in different planes, giving rise to the defects observed in the textures (see, e.g., Figure 8b).

Let us point out some characteristics of the KDDGly molecule that could help us understand why the nematic phases of this mixture present a weak magnetic coupling. Due to the structure of the KDDGly molecule head group, it is expected that hydrogen bonds exist between neighboring molecules in the micelles [25] (Figure 9).

Figure 8. Textures of *N*-dodecanoyl-glycinate (KDDGly)/Na_2SO_4/1-tridecanol (TDeOH)/water mixture under a magnetic field of 0.3 kG: (**a**) N_D at 40.0 °C after 1 h; (**b**) N_D to N_B phase transition at ~30.1 °C; and (**c**) N_C at 23.00 °C; (**d**) laboratory reference frame. *P*, *A* and $\vec{H}$ are the directions of the polarizer, analyzer and magnetic field, respectively.

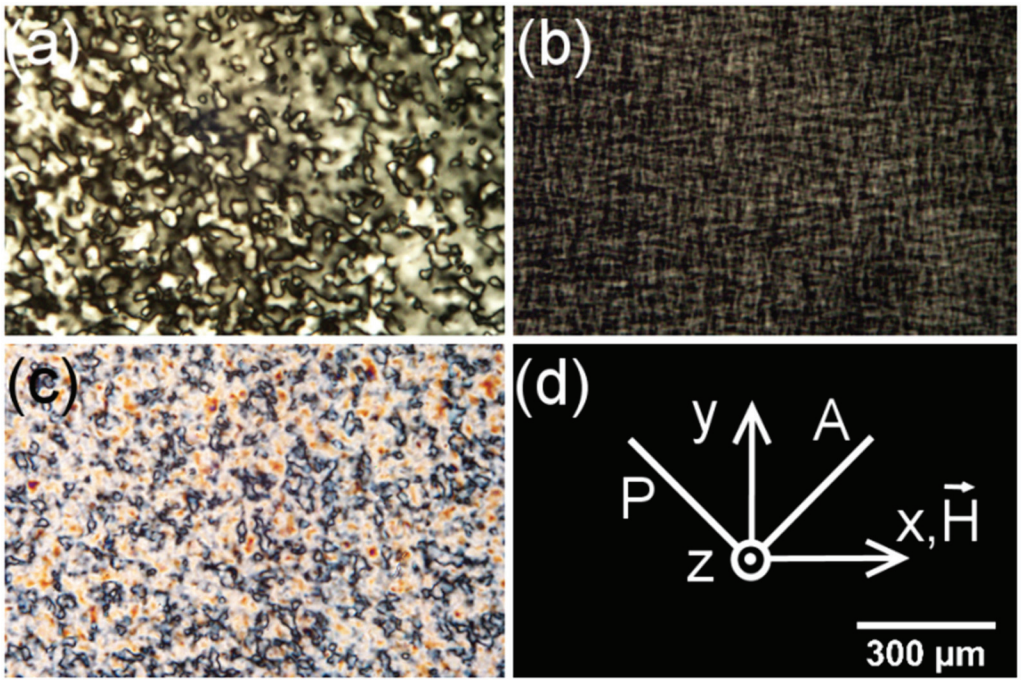

Figure 9. Molecular arrangement of the KDDGly molecules. The hashed bonds between –C=O and –N–H correspond to the hydrogen bonds.

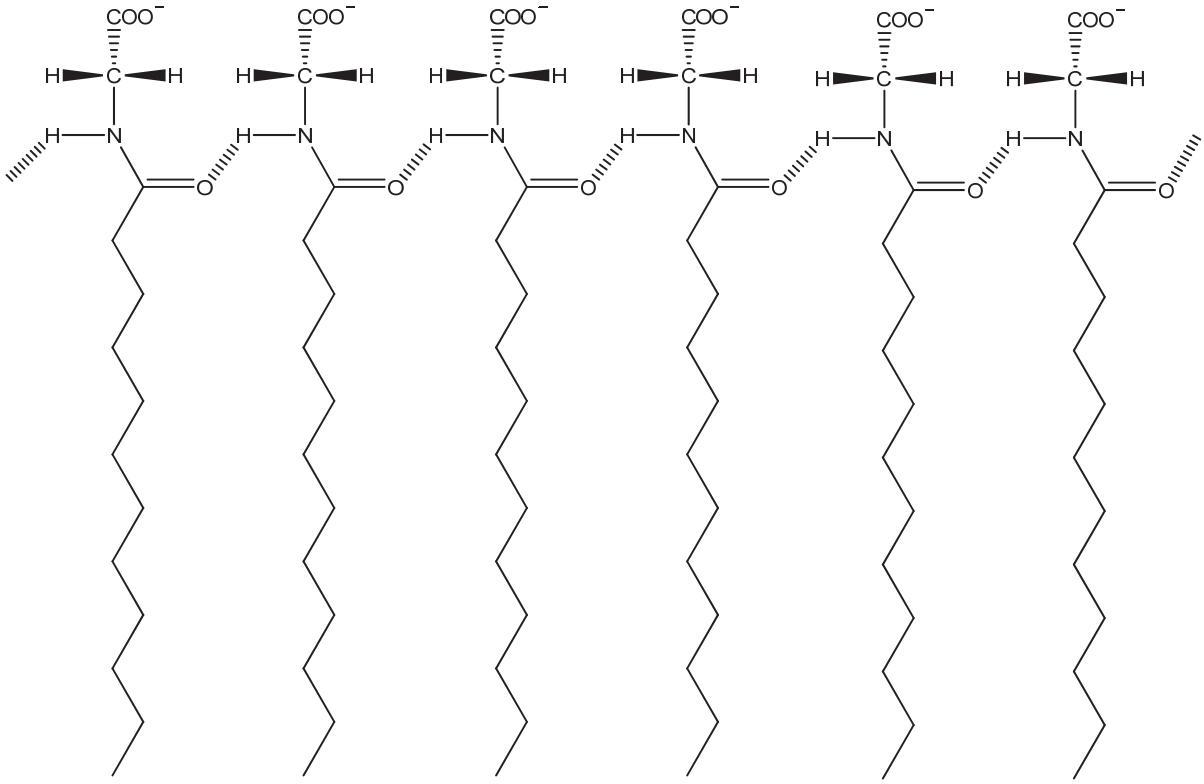

Comparing the molecules KDDGly and KL, the main difference between them is that the KDDGly molecules form hydrogen bonds between them and the KL molecules do not. The different nematic phases of the largely investigated lyotropic mixture, KL/decanol/water [1,9], show an effective magnetic coupling. The orientational procedure employed by us quickly (~minutes) orients the sample. It is known that in micellar systems, there exist a characteristic time for the exchange of amphiphilic molecules between the micelles and the bulk, being of the order of s [26]. When a system composed of anisotropic micelles (as in the case of the lyotropic $\tau \sim 10^{-5}$–10^{-3}s in nematic phases) is subjected to an external magnetic field, the alignment process is complex, having different contributions: (1) a sterical contribution from the micelle-micelle interaction (collective behavior); (2) the coupling of an individual micelle with the magnetic field; and (3) the coupling from each individual amphiphilic molecule (even from the bulk) with the field. The aliphatic chains of the amphiphilic molecules present the anisotropy of the diamagnetic susceptibility of the order of (-10^{-4}) cgs [27]. In the presence of the magnetic field, we expect that the molecular exchange between micelles and the bulk takes the field constraint into account and that the molecules entering in the micelles, as time goes by, be placed in more energetically favored locations in terms of the magnetic coupling between molecules and the field. The existence of hydrogen bonds (typical energy of 10 kcal/mol [28]) between neighboring KDDGly molecules in the micelles could increase this typical time, τ. Coarsely, we could say that micelles with the KDDGly molecules are basic units "more rigid" with respect to those constituted by molecules that do not form hydrogen bonds. In this framework, the KDDGly system would show a lower response to the magnetic field, explaining our difficulty in orienting this sample.

The X-ray diffraction patterns of this mixture also show the pseudo-lamellar ordering, with the first and second-order bands along the 3-axis and a broad band along the 1-axis (see Table 1). The coherence lengths encountered were similar to those of the racemic mixtures. However, the order parameter calculated was smaller, which is consistent with the difficulty in obtaining a well-oriented sample under the action of a magnetic field.

Table 1. X-ray diffraction data. s_i, i = 1,3 represents the moduli of the scattering vector that correspond to the position of the diffraction bands along the horizontal (1-axis) and vertical (3-axis) directions of the laboratory frame axes. OP represents the order parameter, and ξ_i, i = 1,3 represents the correlation length corresponding to each diffraction band. $\Upsilon = s_1^{-1}/s_3^{-1}$ represents the average anisotropy of the available volume per micelle.

Sample	Phase	s_1^{-1} (nm)	s_3^{-1} (nm)	OP	ξ_1 (nm)	ξ_3(nm)	Υ
2	N_C	7.2 ± 0.3	4.9 ± 0.1	0.27	9	19	1.5
3	N_D	6.5 ± 0.3	4.9 ± 0.1	0.43	12	20	1.3
5	N_D	6.8 ± 0.5	5.5 ± 0.1	0.29	11	19	1.2

3. Experimental Section

Dodecanoyl chloride, DL-alanine, DL-serine, DL-aspartic acid, glycine, Na_2SO_4, Cs_2SO_4, undecanol, dodecanol and tridecanol were purchased from Merck (Darmstadt, Germany) for Merck

and for Sigma), Sigma (Missouri, USA), Fluka and Alfa-Aesar with purities >99%. DL-KDDA and DL-KDDS were synthesized via Jungermann's method [29] with a minor revision. After *N*-acylamino acids were prepared by the reaction of dodecanoyl chloride with the corresponding amino acid, they were precipitated from boiling toluene, and the products, *N*-acylamino acids, were filtered off as white solids. In this way, since dodecanoic acid, which may be produced during the amidization reaction, is highly soluble in toluene at room temperature, it can be removed from the products easily. Then, the *N*-acylamino acids were neutralized with ethanolic KOH in ethanol to obtain their potassium salts at room temperature. Since Jungermann's method gave a very low reaction yield (<40%), we applied an alternative method to synthesis DL-NaDDAs and KDDGly given in the literature [30]. All *N*-acylamino acid surfactants were characterized by FTIR spectroscopy. The molecular structures of the surfactant molecules are given in Figure 10.

Figure 10. The molecular structures of *N*-dodecanoylamino acid surfactants: (**a**) KDDGly; (**b**) D-KDDA; (**c**) D-KDDS; and (**d**) D-NaDDAs. For (**b**), (**c**) and (**d**), their mirror images give corresponding L-enantiomers, *i.e.*, L-KDDA, L-KDDS and L-NaDDAs, respectively. DL-racemic mixtures are composed of a 50:50 percent of D- and L-enantiomers.

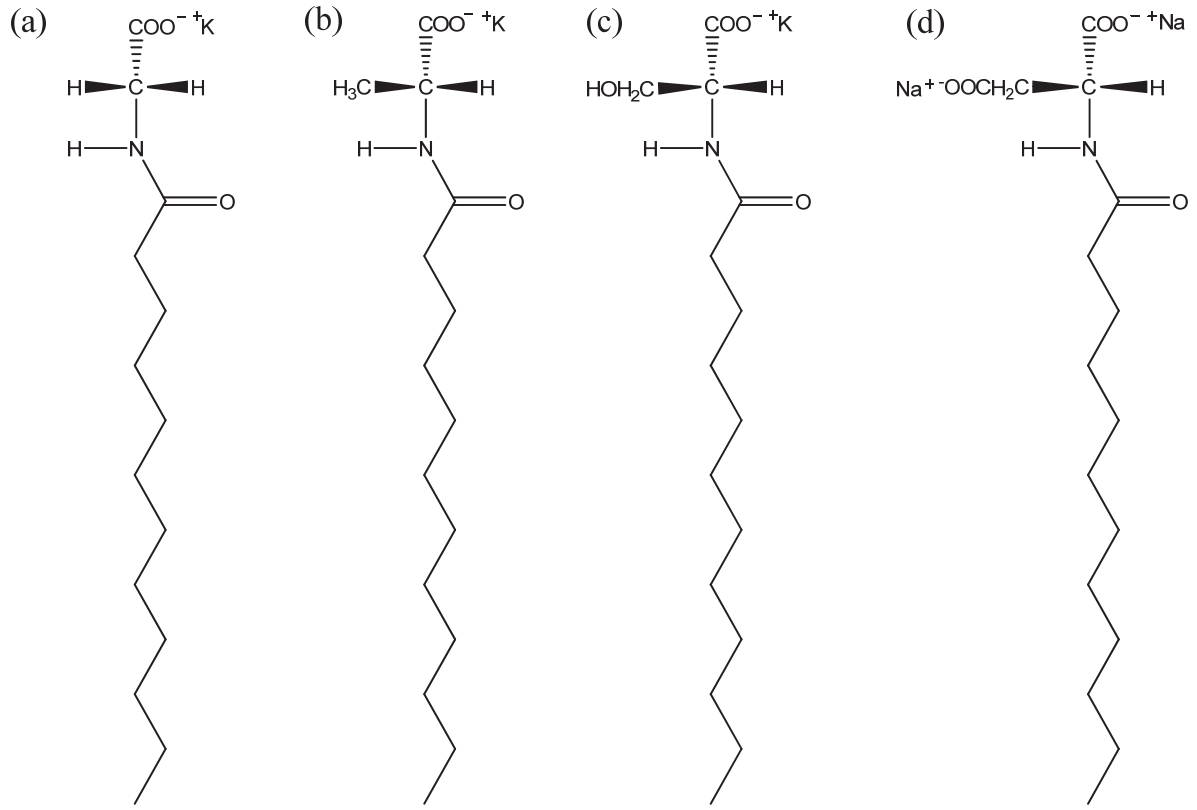

3.1. Sample Preparation

Lyotropic liquid crystalline mixtures were prepared by weighing each constituent in test tubes. Mixtures were subjected to successive agitation in vortex and centrifugation until complete homogenization. Heating was not necessary during the mixture preparation procedure. In the

following, a water-based ferrofluid (Ferrotec) was added to the mixture (about 1 μL of ferrofluid per 1 g of the mixture). It is known that this amount of ferrofluid does not affect the phase transition temperatures and phase sequence of the mixture [9]. The mixtures concentrations are given in Table 2.

Table 2. Compositions of the mixtures investigated. The phase sequences correspond to the observed phases (from left to right, the temperature was increased). UndeOH, DDeOH and TDeOH are the alcohols, 1-undecanol, 1-dodecanol and 1-tridecanol, respectively. X is the mole percent fraction of each constituent. ΔT_{NB} represents the biaxial nematic phase domain.

Sample	Surfactant	X_{surf}	$X_{Cs_2SO_4}$	$X_{Na_2SO_4}$	X_{UndeOH}	X_{DDeOH}	X_{TDeOH}	X_{H_2O}	Phase Sequence	ΔT_{NB} (°C)
1	DL-KDDA	3.33	0.94	–	–	1.08	–	94.64	N_C, N_B, N_D	~1.10
2	DL-KDDS	3.56	–	1.09	0.68	–	–	94.67	N_C, N_B, N_D	~8.60
3	DL-KDDS	3.41	–	1.15	–	0.76	–	94.67	N_C, N_B, N_D	~9.60
4	DL-NaDDAs	3.95	3.05	–	2.05	–	–	90.95	N_D, N_B	~2.85
5	KDDGly	2.74	–	1.00	–	–	0.81	95.45	N_C, N_B, N_D	~4.35

3.2. Laser Conoscopy

Laser conoscopy [18] is a very reliable technique to measure the two birefringences ($\Delta n = n_2 - n_1$ and $\delta n = n_3 - n_2$) in the three nematic phases, N_D, N_B and N_C, as a function of temperature. The subscripts, 1, 2 and 3, refer to the laboratory frame axes with respect to which of the nematic phases are aligned: the two orthogonal Axes 1 and 2 define the horizontal plane, and Axis 3 is perpendicular to this plane and parallel to the laser beam propagation direction. It is possible to precisely measure birefringences of the order of 10^{-3} with this technique, which is the case for lyotropic liquid crystals.

For birefringence measurements via laser conoscopy, lyotropic nematic samples doped with ferrofluid were transferred into a cell made of two optical circular glasses and a ring of glass 2.5 mm-thick (sample thickness set in 2.5 mm). A static magnetic field H = 3.05 kG (Walker Sci. electromagnet), parallel to Axis 1, helps the orientation of the samples. The experimental setup has a HeNe laser (λ = 632.8 nm), a Neocera LTC-21 temperature controller (Neocera, Beltsville, USA), with a precision of 0.001 °C, and a Julabo Refrigerated/Heating water-bath circulator (Julabo, Seelbach, Germany) with a precision of 0.01 °C.

A key point in the laser conoscopy technique is to get high-quality conoscopic patterns, which are obtained with well-aligned samples. For this purpose, samples were rotated about the angle of ±30° several times around Axis 3 in the N_D and N_B phases with an applied external magnetic field (H = 3.05 kG). Then, ongoing from N_D to N_C, passing through N_B, the measurement of the birefringences is performed as a function of temperature. In the case of the N_C phase, the sample is left at rest in the presence of $\vec{H}$ (see, e.g., [9] for details).

3.3. X-ray Diffraction

The microstructure and local ordering of the micelles were investigated by X-ray diffraction using a Xenocs Xeuss system, which consists of a GeniX^{3D} beam delivery system with a Cu anode X-ray

tube (λ = 0.15411 nm), a collimation composed of two scatterless slits and a Pilatus 300K detector (Dectris, Baden, Switzerland). The beam has a square cross-section of 0.8 × 0.8 mm^2. The beam center correction and the sample to detector distance of 72.6 cm were measured with a sample of silver behenate. The sample holder is a small parallelepiped made of copper with inner channels for water circulation, which enables the control of temperature with a precision of 0.1 °C. There is a centered vertical hole parallel to the long face of the parallelepiped to place glass capillary tubes of 1.5 mm in diameter. Perpendicular to this, there is a horizontal small window that allows the passage of the X-ray beam. Besides, two permanent magnets are attached to the sidewalls of the holder. The magnetic field in sample position is of about 1 kG. The samples were oriented in each nematic phase using the same procedure described above for laser conoscopy. The laboratory frame of reference was defined with Axis 3 along the vertical direction parallel to the capillary long axis, Axis 2 in the direction of the X-ray beam and Axis 1 parallel to the magnetic field direction.

Measurements in the N_C and N_D phases have been done for the different lyotropic samples. At a given temperature, the samples were irradiated in the direction perpendicular to the magnetic field direction. The exposure time for each measurement was 15 min. The data analysis was done in the framework proposed in [23], and the order parameter was calculated according the work of Deutsch [24]. The angular and radial integrations were done using the FIT2D software. Water (background) and noise subtractions were done for each integrated datum.

4. Conclusions

Five new lyotropic mixtures were reported presenting the biaxial nematic phase. In particular, four of them have in their composition racemates of *N*-acylamino acid surfactants as the main amphiphile. In three of these mixtures, the two uniaxial and the biaxial nematic phases were identified. The analysis of the optical birefringences and the invariants of the order parameter as a function of the temperature indicate that the uniaxial to biaxial phase transitions are of second order. The mixtures with DL-KDDS were those that presented the largest biaxial phase domain in terms of temperature. Moreover, the bigger the number of carbon atoms on the aliphatic chain of the co-surfactant, the larger the biaxial phase domain. In the case of the mixture with KDDGly, the three nematic phases were also identified. However, the orienting process that combines the presence of a magnetic field and rotations of the sample, extremely efficient in all the other mixtures investigated here, was shown to be not efficient. In the uniaxial phases, the orientation was achieved after a long time, and in the biaxial phase, it was not even completely achieved. Hydrogen bonds between neighboring head group molecules of KDDGly are suggested as being responsible for this weak response of the system to the magnetic field.

Acknowledgments

We thank Abant Izzet Baysal University Directorate of Research Projects Commission (BAP, Grant No. 2012.03.03.529) and The Scientific and Technological Research Council of Turkey (TÜBİTAK, Grant No. 113Z469) for supporting this present study. INCT and NAP on Complex Fluids, FAPESP and CNPq for financial support.

Author Contributions

Erol Akpinar prepared the samples and did the conoscopic and optical experiments. Muhammet Yildirim synthesized and characterized all *N*-acylamino acid surfactants. Dennys Reis performed the X-ray diffraction experiments and did the data analysis. He also assembled the conoscopy setup and wrote the data analysis software for it. Antonio Martins Figueiredo Neto planned the experiments with the new mixtures. All the authors participated in the writing of the manuscript.

Conflicts of Interest

The authors declare no conflict of interest.

References

1. Yu, L.J.; Saupe, A. Observation of a Biaxial Nematic Phase in Potassium Laurate-l-Decanol-Water Mixtures. *Phys. Rev. Lett.* **1980**, *45*, 1000–1003.
2. Freiser, M.J. Ordered States of a Nematic Liquid. *Phys. Rev. Lett.* **1970**, *24*, 1041–1043.
3. Alben, R. Phase Transitions in a Fluid of Biaxial Particles. *Phys. Rev. Lett.* **1973**, *30*, 778–781.
4. Golo, V.L.; Kats, E.I.; Sevenyuk, A.A.; Sinitsyn, D.O. Twisted quasiperiodic textures of biaxial nematic liquid crystals. *Phys. Rev. E* **2013**, *88*, 042504:1–042504:7.
5. Luckhurst, G.R.; Sluckin, T.J. *Biaxial Nematic Liquid Crystals: Theory, Simulation and Experiment*; John Wiley: Chichester, UK, 2014.
6. Lehmann, M.; Görtz, V. *Handbook of Liquid Crystals, 11 Design of Biaxial Nematic Mesogens, Nematic and Chiral Nematic Liquid Crystals. Part III. Discotic, Biaxial and Chiral Nematic Liquid Crystals*; Wiley: Weinheim, Germany, 2014.
7. Tschierske, C.; Photinos, D.J. Biaxial Nematic Phases. *J. Mater. Chem.* **2010**, *20*, 4263–4294.
8. Pickena, S.J.; Dingemansb, T.J.; Madsenc, L.A.; Francescangelid, O.; Samulski, E.T. Uniaxial to biaxial nematic phase transition in a bent-core thermotropic liquid crystal by polarising microscopy. *Liq. Cryst.* **2012**, *39*, 19–23.
9. Figueiredo Neto, A.M.; Salinas, S.R.A. *The Physics of Lyotropic Liquid Crystals: Phase Transitions and Structural Properties*; Oxford University Press: New York, NY, USA, 2005; pp. 190–196, 264–268.
10. Radley, K.; Saupe, A. Cholesteric States of Micellar Solutions. *Mol. Phys.* **1978**, *35*, 1405–1412.
11. Acimis, M.; Reeves, L.W. A Type II Aqueous Cholesteric Lyomesophase. *Can. J. Chem.* **1980**, *58*, 1533–1541.
12. Figueiredo Neto, A.M.; Galerne, Y.; Liébert, L. Cholesterization of a Biaxial Nematic Lyomesophase Studied by X-Ray Diffraction and Optical Microscopy. *J. Phys. Chem.* **1985**, *89*, 3939–3941.
13. Reis, D.; Akpinar, E.; Figueiredo Neto, A.M. Effect of Alkyl Chain Length of Alcohols on Cholesteric Uniaxial to Cholesteric Biaxial Phase Transitions in a Potassium Laurate/Alcohol/Potassium Sulfate/Water/Brucine Lyotropic Mixture: Evidence of a First-Order Phase Transition. *J. Phys. Chem. B* **2013**, *117*, 942–948.

14. Brand, H.R.; Pleiner, H. Cholesteric to Cholesteric Phase Transitions in Liquid Crystals. *J. Phys. Lett.* **1985**, *46*, 711–718.
15. Alcantara, M.R.; de Melo, M.V.M.C.; Paoli, V.R.; Vanin, J.R. New cholesteric and nematic lyotropic mesophases from di-sodium N-lauroyl-aspartate. *Mol. Cryst. Liq. Cryst*. **1983**, *90*, 335–347.
16. Akpinar, E.; Giesselmann, F.; Acimis, M. Effect of micelle size and intermicellar distance on the chirality transfer in the intrinsic lyotropic cholesteric phases. *Liq. Cryst*. **2013**, *40*, 1183–1194.
17. De Gennes, P.G.; Pros, J. *The Physics of Liquid Crystals*; Oxford University Press: Oxford, UK, 1993; pp. 66–99.
18. Galerne, Y.; Marcerou, J.P. Temperature behavior of the order-parameter invariants in the uniaxial and biaxial nematic phases of a lyotropic liquid crystal. *Phys. Rev. Lett.* **1983**, *51*, 2109–2111.
19. Born, M.; Wolf, E. *Principles of Optics*, 6th ed.; Pergamon Press: Oxford, UK, 1980; pp. 678–703.
20. Berejnov, V.; Cabuil, V.; Perzynski, R.; Raikher, Y. Lyotropic System Potassium Laurate/1-Decanol/Water as a Carrier Medium for a Ferronematic Liquid Crystal: Phase Diagram Study. *J. Phys. Chem. B* **1998**, *102*, 7132–7138.
21. Du, X.; Hlady, V. Monolayer formation on silicon and mica surfaces rearranged from *N*-hexadecanoyl-L-alanine supramolecular structures. *J. Phys. Chem. B* **2002**, *106*, 7295–7299.
22. Lu, X.; Zhang, Z.; Liang, Y. Bilayer formation in dilute aqueous solution from monoalkylethylenediamine. *Langmuir* **1996**, *12*, 5501–5503.
23. Figueiredo Neto, A.M.; Galerne, Y.; Levelut, A.M.; Liébert, L. Pseudo-lamellar ordering in uniaxial and biaxial lyotropic nematics: A synchrotron X-ray diffraction experiment. *J. Phys. Lett.* **1985**, *46*, 499–505.
24. Deutsch, M. Orientational order determination in liquid crystals by X-ray diffraction. *Phys. Rev. A* **1991**, *44*, 8264–8270.
25. Bordes, R.; Holmberg, K. Physical chemical characteristics of dicarboxylic amino acid-based surfactants. *Coll. Surf. A* **2011**, *391*, 32–41.
26. Hunter, R.J. *Foundations of Colloid Science*, 5th ed.; Oxford Science Publications: New York, NY, USA, 1993.
27. Trew, V.C.G. The Diamagnetic Susceptibility of some Alkyl Benzenes and Higher Aliphatic Hydrocarbons. *Trans. Faraday Soc.* **1953**, *49*, 604–611.
28. Wendler, K.; Thar, J.; Zahn, S.; Kirchner, B. Estimating the Hydrogen Bond Energy. *J. Phys. Chem. A* **2010**, *114*, 9529–9536.
29. Jungermann, E.; Gerecht, J.F.; Krems, I.J. The preparation of long chain N-acylamino acids. *J. Am. Chem. Soc*. **1956**, *78*, 172–174.
30. Varaşteanu, D.; Piscureanu, A.; Chican, I.E.; Corobea, M.C. Aspects regarding the synthesis and surface properties of some glycine based surfactants. *U.P.B. Sci. Bull. B* **2011**, *73*, 147–154.

Part IV: Synthesis and Characterization

Novel Discotic Boroxines: Synthesis and Mesomorphic Properties

Tobias Wöhrle, Angelika Baro and Sabine Laschat

Abstract: A new synthetic approach to highly substituted triphenylboroxines **11** is described. Their mesomorphic properties were investigated by differential scanning calorimetry (DSC), polarizing optical microscopy (POM) and X-ray diffraction (SAXS, WAXS). The tris(3,4,5-trialkyloxy)phenyl functionalized derivatives **11b–e** showed broad mesophases for a minimum alkyl chain length of C9. The phase widths ranged from 110 K to 77 K near room temperature, thus decreasing with enhanced alkyl chain lengths. Textures observed under POM indicated a columnar hexagonal (Col_h) mesophase symmetry that was confirmed by X-ray diffraction experiments.

Reprinted from *Materials*. Cite as: Wöhrle, T.; Baro, A.; Laschat, S. Novel Discotic Boroxines: Synthesis and Mesomorphic Properties. Materials **2014**, *7*, 4045–4056.

1. Introduction

The discovery of stable liquid crystalline phases formed by disk-shaped molecules with long alkyl chains in their periphery is generally dated to the seminal work of Chandrasekar published in 1977 [1]. Since then discotic liquid crystals have attracted the attention of many research groups worldwide [2–4]. Due to the one dimensional charge and ion transport in the columnar mesophase, the ability of liquid crystals (LCs) to self-heal structural defects by thermal annealing and the ease of processing via spin coating, drop casting and other solution processing methods highly useful applications [5–7] could berealized such as organic solar cells [8], organic field effect transistors [3] and organic light emitting diodes [9].

From a molecular perspective, several scaffolds have turned out to be successful candidates for the nanosegregation, which ultimately led into the formation of columnar mesophases. Besides tri- and hexasubstituted benzenes, in particular triphenylenes [10], perylenes [11], hexa-*peri*-hexabenzocoronenes [12,13], porphyrins [14,15], phthalocyanines [15], quinoxalines and other aza analogues of polycyclic aromatic hydrocarbons were used as mesogenic subunits. However, not only disk-shaped mesogens, but also non-conventional [16] and supramolecular and hydrogen bonded liquid crystals [17] can self-assemble into columnar aggregates. While a variety of LC materials containing heterocyclic 6-membered rings have been synthesized [18], e.g., triazines such as **1** [19–21] or cyclotriphosphazenes such as **2** [22,23] (Figure 1), surprisingly little is known about liquid crystalline boroxines, the cyclic trimers of organoboronic acids. Aryl boronic acids are valuable reagents for a number of metal-catalyzed reactions, the most prominent one thereof is certainly the Suzuki-Miyaura cross-coupling reaction [24–28]. Furthermore, boroxines may serve as useful building blocks for flame retardants, lithium ion battery materials and covalent organic frameworks [29,30]. The only example considering mesomorphism was a report by Preece and

coworkers who studied a series of tris(alkoxyphenyl)boroxines **3**, which, however, did not reveal any mesophases (Figure 1) [31].

Figure 1. Chemical structure of liquid crystals (LC) materials containing a heterocyclic six-membered ring as core unit.

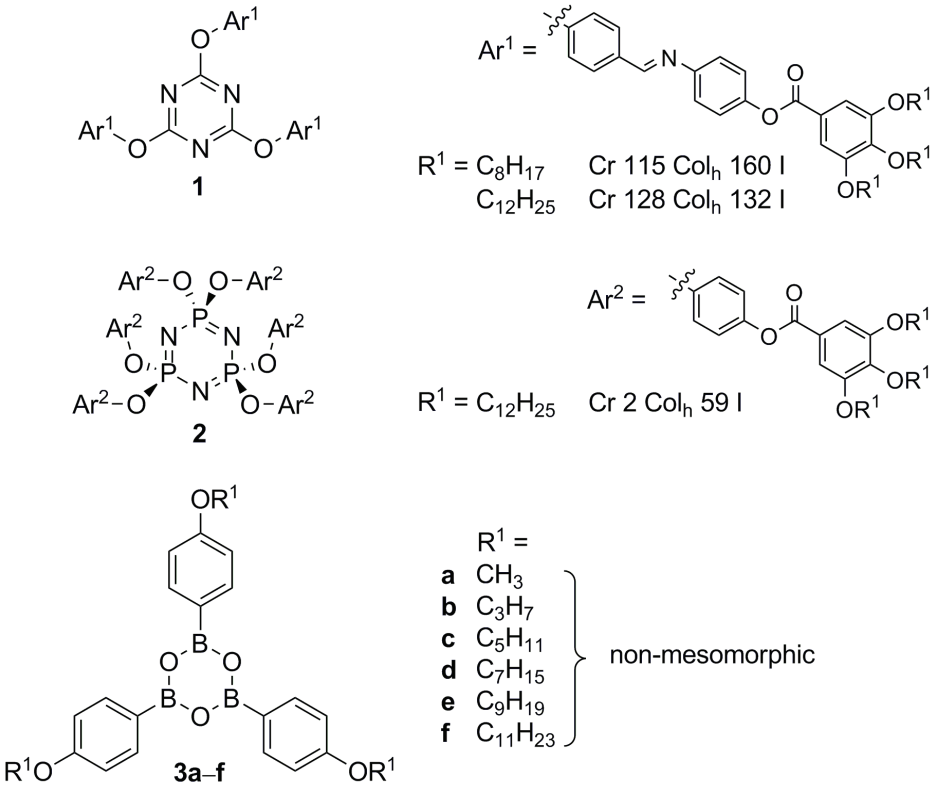

Based on this precedence we anticipated that the attachment of additional alkoxy groups at the aryl rings should favor nanosegregation and thus induce mesophase formation. The results towards this goal are reported below.

2. Results and Discussion

2.1. Synthesis of Boroxines

First, we intended to attach alkyloxy groups with chains lengths of C12-C18 at the phenyl rings in boroxine **3** following known procedures [32–35]. However, only **3g** ($R^1 = C_{12}H_{25}$) could be isolated in 30% yield, whereas boroxines with alkyl chain lengths >12 were not obtained as a problem of poor solubility of the precursor boronic acid (for details see Supplementary Information). Derivative **3g** did not show mesomorphic properties.

Following our envisioned strategy, 4-bromo-1,2-dialkoxybenzenes **4** [36,37] were lithiated with *n*-BuLi, THF at −78 °C, followed by treatment with $B(OMe)_3$ and then directly hydrolyzed by addition of aqueous HCl to the mixture. No trace of the boronic acids was detected, but the boroxines **5** were isolated (Scheme 1). Their yields decreased considerably with increasing chain lengths from 51% for **5a** to 7% for **5d** due to purification problems. Column chromatography led to decomposition,

thus leaving recrystallization as only method to purify **5**. With increasing chain length the solubility of dialkoxybromides **4**, boronic acids **6** and boroxines **5** was more and more alike. Therefore, the crude product of **5e** with two $C_{16}H_{33}$ groups at the phenyl ring was found as an inseparable mixture of those three and no pure product could be obtained.

Scheme 1. Synthesis of boroxines **5** starting from the respective dialkoxy- bromobenzenes **4**. Boronic acid **6c** was prepared for comparison and assignment of ^{1}H NMR and IR data (see Supplementary Information).

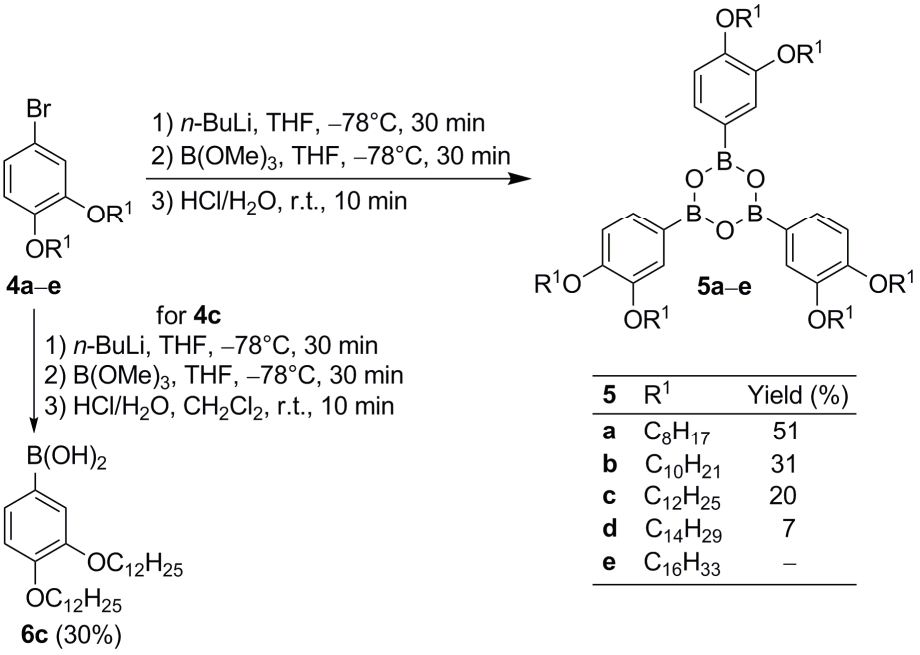

5	R^1	Yield (%)
a	C_8H_{17}	51
b	$C_{10}H_{21}$	31
c	$C_{12}H_{25}$	20
d	$C_{14}H_{29}$	7
e	$C_{16}H_{33}$	–

The synthesis of tris(3,4,5-trialkoxyphenyl)boroxines **11** commenced with the 5-bromo-1,3,4-trialkoxybenzenes **7** [38–41]. Their conversion into the boronic acids according to the method described in Scheme 1 turned out to be problematic, because inseparable mixtures of boronic acids and boroxines were obtained. This was also true, when the initial bromo-lithium exchange was replaced by formation of a Grignard species instead. Therefore, an alternative method was applied (Scheme 2).

Bromides **7** were treated with *n*-BuLi, followed by addition of isopropoxypinacolborolane [42] to yield the corresponding pinacolborolanes **8** [38] which were directly treated with bisethanolamine in *i*-PrOH. The resulting diethanolamine complexes **9** precipitated from the solution and after filtration, they were hydrolyzed without further purification with HCl in THF giving a mixture of boroxines **11** and boronic acids **10**. Refluxing this mixture with pyridine in Et_2O [43] followed by hydrolysis with HCl in Et_2O provided the desired free boroxines **11** quantitatively. Noteworthy, this strategy did not need purification at any step. Only pinacolborolanes **8** were deprotected to complexes **9** which precipitated in analytically pure form (shown for **9e** in the Supplementary Information). The subsequent two reaction steps proceeded in quantitative yield without any impurities. The overall yields of **11** starting from **7** were in the range of 20%–40%. The solid products **11** were air-stable, however, storage in solvents containing traces of water led to slow decomposition to the corresponding boronic acids **10**.

Scheme 2. Synthesis of boroxines **11a–e** bearing three 3,4,5-trialkoxyphenyl substituents. For comparison, diethanolamine complex **9e** was isolated. Its ^{1}H and ^{13}C NMR spectra are given together with characteristic IR bands for distinction of **10** and **11** (Table S2 in the Supplementary Information).

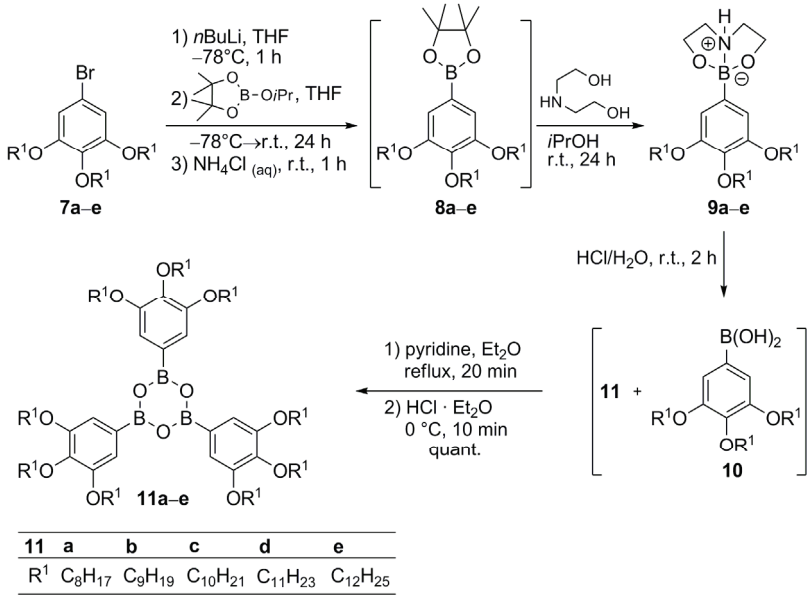

2.2. Mesomorphic Properties of Boroxines

The liquid crystalline properties of compounds **5** and **11** were studied by differential scanning calorimetry (DSC), polarizing optical microscopy (POM) and X-ray diffraction (XRD: wide-angle X-ray scattering (WAXS), small-angle X-ray scattering (SAXS)).

All compounds **5a–d** bearing three 3,4-dialkoxyphenyl substituents did not show any mesomorphism. In contrast, boroxines **11** with additional alkoxy group turned out to be mesogenic with exception of derivative **11a** with C8 alkyloxy side chains. The results obtained from DSC measurements are summarized in Table 1 and Figure 2.

Table 1. Phase transitions of the mesogenic boroxines **11a–e**. [a,b].

Compound	Phase	T_m [°C] (ΔH [kJ·mol^{-1}])	Phase	T_c [°C] (ΔH [kJ·mol^{-1}])	Phase	Cycles
11a	Cr	24	–	–	I	2nd heating
11b	Cr	25 (65.5)	Col_h	135 [c] (3.4)	I	2nd heating
11b	Cr	7 (25.2)	Col_h	129 [c] (1.3)	I	2nd cooling
11c	Cr	30 (84.3)	Col_h	130 [c] (7.7)	I	2nd heating
11c	Cr	22 (73.4)	Col_h	127 [c] (4.4)	I	2nd cooling
11d	Cr	42 (116.4)	Col_h	128 [c] (2.3)	I	2nd heating
11d	Cr	24 (72.7)	Col_h	126 (2.5)	I	2nd cooling
11e	Cr	49 (123.9)	Col_h	126 [c] (5.6)	I	2nd heating
11e	Cr	33 (86.1)	Col_h	123 (3.3)	I	2nd cooling

[a] The following phases were observed: crystalline (Cr), columnar hexagonal (Col_h), isotropic liquid (I); [b] transition temperatures were determined by DSC (heating/cooling rate 5 K·min^{-1}); [c] peak temperature.

Boroxines **11b–e** displayed broad mesophases near room temperature. For boroxine **11b** with C9 alkyloxy side chains a liquid crystalline phase between 25 °C and 135 °C was observed. With increasing chain lengths melting points continuously rose up to 49 °C (**11e**) and clearing points receded to 123 °C resulting in reduced phase widths from 100 K (**11c**) to 77 K (**11e**).

Figure 2. Mesophase stabilities of boroxines **11a–e** upon second heating (heating rate 5 K·min^{-1}). Mesophase widths are given.

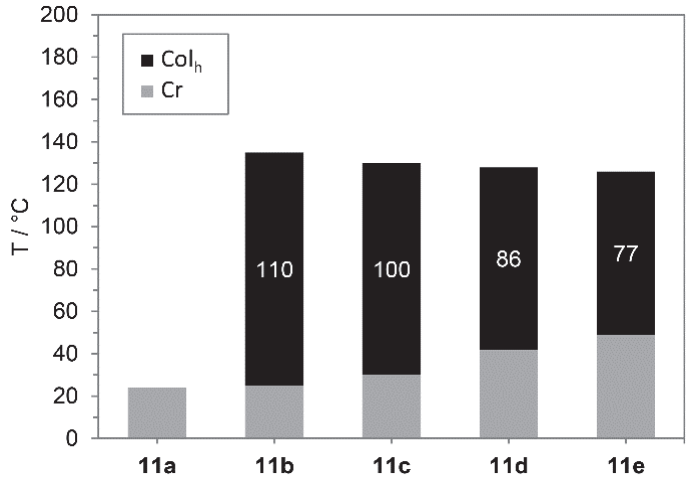

Considering the DSC traces of **11b–11e** identical behaviour of all derivatives during heating and cooling cycle is evident. As example, DSC curves of **11e** are shown in Figure 3 (for further DSC curves see Supplementary Information). Melting points were clearly visible while clearing point peaks were less intensive and very broad. Hence, peak temperatures are given in Table 1. Upon cooling both melting and clearing point displayed a supercooling of phase transitions. Clearing points were slightly affected. Boroxine **11b** shows the largest shift of 6 K from 135 °C upon heating to 129 °C upon cooling. The melting points of **11b** and **11d**, however, were significantly shifted by 18 K from 25 °C (**11b**) and 42 °C (**11d**) to 7 °C and 24 °C, respectively.

Figure 3. DSC curves of **11b** (second heating/cooling cycle, heating/cooling rate 5 K·min^{-1}).

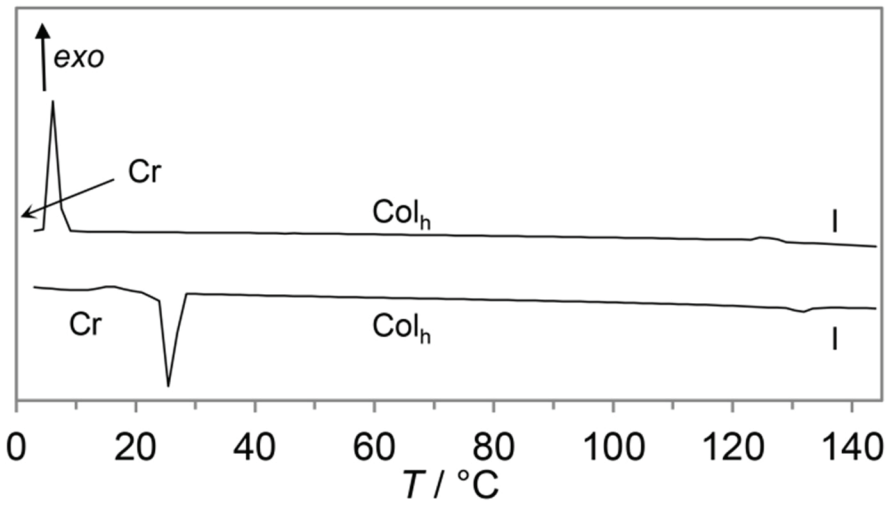

Under the microscope boroxines **11b–11e** behaved similarly. Upon cooling from the isotropic liquid all derivatives formed homeotropic areas with few defects (Figure 4 top).

Figure 4. Textures of **11b–e** as seen between crossed polarizers upon cooling from isotropic liquid (cooling rate 5 K·min^{-1}, magnification ×100). (**top**): standard glass slides, (**bottom**): trimethylchlorosilane-treated glass slides.

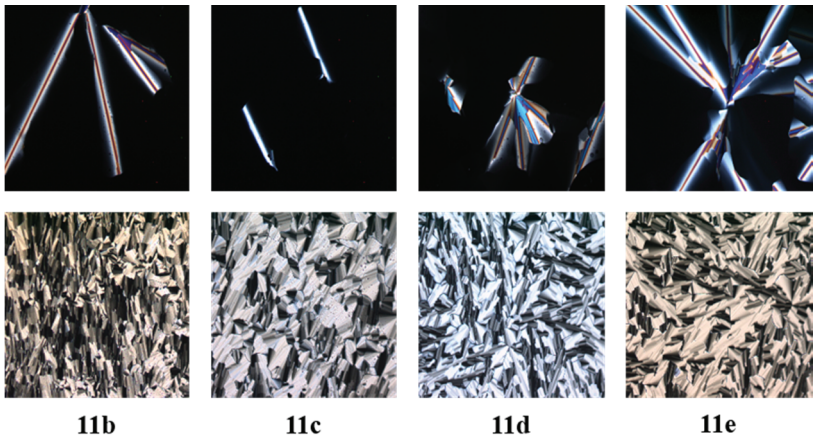

Presumably, the boron atoms coordinate at the oxygen atoms of the glass surface, resulting in aligned mesophases perpendicular to the surface. Therefore, the glass slides were treated with trimethylchlorosilane prior to use. In this way, broken fan-shaped textures being typical for columnar mesophases could be observed for boroxines **11b–11e** under the POM (Figure 4 bottom).

In order to get further insight into the phase geometry, derivatives **11b–e** were investigated by XRD (SAXS and WAXS). Figure 5 shows both the SAXS profile and WAXS pattern exemplarily for boroxine **11e**. In the small-angle region three reflections are visible in a ratio of $1:1/\sqrt{3}:1/2$ which were indexed as (10), (11) and (20) [44]. This diffraction pattern is typical for columnar hexagonal (Col_h) phase geometries. In the wide-angle region a diffuse halo was observed, which is generated through the interaction of the molten-like alkyl chains. In the case of derivatives **11b–d**, however, only the (10) reflection and the diffuse halo were clearly visible in the diffractograms. Due to identical molecule geometry also Col_h mesophases are assumed for **11b–d** (for XRD data see Supplementary Information).

Figure 5. Small-angle X-ray scattering (SAXS) profile of the liquid-crystalline phase of **11e** at 100 °C (Inset: wide-angle X-ray scattering, WAXS).

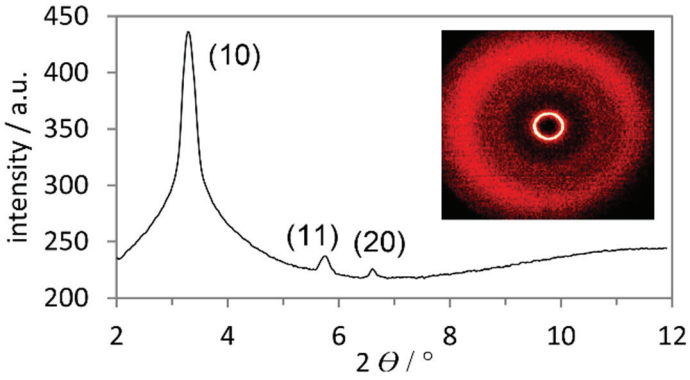

3. Experimental Section

3.1. Materials

All reagents were used as purchased from the suppliers without further purification. Solvents were dried and distilled under nitrogen prior to use and unless otherwise stated all reactions were carried out under nitrogen atmosphere with Schlenk-type glassware.

*3.2. General Procedure for the Synthesis of Tris(3,4,5-Trialkoxyphenyl)boroxines (**11**)*

To a solution of the appropriate **7** (4.225 mmol) in abs. THF (150 mL) at −78 °C was added *n*-BuLi (4.50 mL, 7.2 mmol, 1.6 M in *n*-hexane, Merck KGaA, Darmstadt, Germany) and the reaction mixture was stirred for 1 h. Then isopropyl pinacol borate (1.32 mL, 1.20 g, 6.34 mmol, Sigma-Aldrich, Steinheim, Germany) was added and the reaction mixture stirred for a further 1 h at −78 °C. After warming to room temperature over 24 h, the reaction was terminated by addition of NH_4Cl (50 mL, saturated solution) and stirring for 1 h. The resulting aqueous suspension was extracted with Et_2O (3 × 50 mL). The combined organic layers were washed with H_2O (2 × 100 mL) and brine (80 mL) and dried ($MgSO_4$). The solvent was removed under vacuum and the crude product **8** was directly used for the next step.

The crude appropriate pinacolborolane **8** was dissolved in a minimal amount of isopropanol, diethanolamine (0.85 mL, 0.89 g, 8.45 mmol, calcd for quantitative yield in the previous step, Sigma-Aldrich, Steinheim, Germany) was added, and the mixture was stirred for 24 h at ambient temperature. The suspension was filtered giving the boronic acid diethanolamine complexes **9** as white solids. Those were dissolved in THF (15 mL) and stirred with HCl (7 mL, 2 M) for 2 h at room temperature. The resulting aqueous suspension was extracted with Et_2O (3 × 30 mL). The combined organic layers were washed with H_2O (2 × 500 mL) and brine (50 mL) and dried ($MgSO_4$). The solvent was removed under vacuum giving mixtures of boronic acids **10** and the appropriate boroxines **11** in good overall yield.

The respective mixture of **10** and **11** (0.3 mmol, calcd for the maximum amount of **10**) was dissolved in abs. Et_2O and, together with mol sieves (4 Å) to trap resulting water, heated to reflux. Pyridine (abs., 0.1 mL, 0.095 g, 1.2 mmol) was added and the mixture was stirred for additional 20 min. The solution was then cooled with ice (0 °C) and $HCl{\cdot}Et_2O$ (pH = 1) was added. After 10 min, the precipitate was collected on a glass fritted funnel and the filtrate was fully evaporated *in vacuo* to give the desired boroxines **11** as colorless solids in quantitative yield.

3.2.1. Tris(3,4,5-Trioctyloxyphenyl)boroxine (**11a**)

^{1}H NMR (500 MHz, $CDCl_3$): δ = 0.83–0.95 (m, 27H, CH_3), 1.23–1.43 (m, 72H, CH_2), 1.44–1.56 (m, 18H, $OCH_2CH_2CH_2$), 1.72–1.90 (m, 18H, OCH_2CH_2), 4.01–4.14 (m, 18H, OCH_2), 7.39 (s, 6H, 2-H) ppm. ^{13}C NMR (126 MHz, $CDCl_3$): δ = 14.11, 14.12 (CH_3), 22.70, 22.72, 26.1, 26.2, 29.3, 29.40, 29.46, 29.55, 29.56, 30.39, 31.87, 31.93 (CH_2), 69.2, 73.5 (OCH_2), 113.9 (C-2), 142.7 (C-4), 152.9 (C-3) ppm. FT-IR (ATR): $\tilde{\nu}$ = 2927 (w), 2855 (w), 1574 (w), 1467 (w), 1417 (w), 1333 (s, B-O), 1110 (w), 904 (s), 726 (vs, BX), 649 (s) cm^{-1} (BX denotes the anhydride band [45]).

MS (MALDI-TOF): *m/z* calcd. for $[C_{90}H_{159}B_3O_{12}]^+$ 1465.21, found 1465.04. Anal. calcd. for $C_{90}H_{159}B_3O_{12}$ (1465.68 g·mol^{-1}): C 73.75, H 10.93; found: C 73.39, H 11.02.

3.2.2. Tris(3,4,5-Trinonyloxyphenyl)boroxine (**11b**)

^{1}H NMR (500 MHz, $CDCl_3$): δ = 0.85–0.91 (m, 27H, CH_3), 1.21–1.43 (m, 90H, CH_2), 1.45–1.56 (m, 18H, $OCH_2CH_2CH_2$), 1.73–1.90 (m, 18H, OCH_2CH_2), 4.04–4.13 (m, 18H, OCH_2), 7.39 (s, 6H, 2-H) ppm. ^{13}C NMR (126 MHz, $CDCl_3$): δ = 14.12 14.13 (CH_3), 22.71, 22.72, 26.1, 26.2, 29.3, 29.4, 29.52, 29.55, 29.62, 29.66, 29.7, 30.4, 31.94, 31.97 (CH_2), 69.2, 73.5 (OCH_2), 113.9 (C-2), 142.7 (C-4), 152.9 (C-3) ppm. FT-IR (ATR): $\tilde{\nu}$ = 2958 (w), 2924 (w), 2853 (w), 1575 (w), 1467 (w), 1417 (w), 1334 (s, B-O), 1261 (w), 1213 (w), 1111 (w), 1021 (w), 905 (s), 849 (w), 804 (w), 725 (vs, BX), 649 (w) cm^{-1}. MS (MALDI-TOF): *m/z* calcd. for $[C_{99}H_{177}B_3O_{12}]^+$ 1591.35, found 1591.79. Anal. calcd. for $C_{99}H_{177}B_3O_{12}$ (1591.92 g·mol^{-1}): C 74.70, H 11.21; found: C 74.30, H 11.30.

3.2.3. Tris(3,4,5-Tridecyloxyphenyl)boroxine (**11c**)

^{1}H NMR (500 MHz, $CDCl_3$): δ = 0.82–0.96 (m, 27H, CH_3), 1.17–1.45 (m, 108H, CH_2), 1.45–1.63 (m, 18H, $OCH_2CH_2CH_2$), 1.71–1.93 (m, 18H, OCH_2CH_2), 4.02–4.13 (m, 18H, OCH_2), 7.39 (s, 6H, 2-H) ppm. ^{13}C NMR (126 MHz, $CDCl_3$): δ = 14.1 (CH_3), 22.7, 26.1, 26.2, 29.40, 29.41, 29.51, 29.54, 29.60, 29.65, 29.7, 29.8, 30.38, 31.93, 31.95 (CH_2), 69.22, 73.50 (OCH_2), 113.9 (C-2), 142.7 (C-4), 152.9 (C-3) ppm. FT-IR (ATR): $\tilde{\nu}$ = 2958 (w), 2923 (w), 2853 (w), 1574 (w), 1466 (w), 1417 (w), 1333 (s, B-O), 1261 (w), 1212 (w), 1112 (w), 1014 (w), 905 (s), 801 (w), 723 (vs, BX), 645 (w) cm^{-1}. MS (MALDI-TOF): *m/z* calcd. for $[C_{108}H_{195}B_3O_{12}]^+$ 1717.49, found 1717.89. Anal. calcd. for $C_{108}H_{195}B_3O_{12}$ (1718.16 g·mol^{-1}): C 75.50, H 11.44; found: C 75.25, H 11.46.

3.2.4. Tris(3,4,5-Triundecyloxyphenyl)boroxine (**11d**)

^{1}H NMR (500 MHz, $CDCl_3$): δ = 0.80–0.94 (m, 27H, CH_3), 1.20–1.43 (m, 126H, CH_2), 1.45–1.58 (m, 18H, $OCH_2CH_2CH_2$), 1.70–1.93 (m, 18H, OCH_2CH_2), 4.02–4.13 (m, 18H, OCH_2), 7.39 (s, 6H, 2-C) ppm. ^{13}C NMR (126 MHz, $CDCl_3$): δ = 14.1 (CH_3), 22.7, 26.1, 26.2, 29.4, 29.50, 29.54, 29.6, 29.71, 29.75, 29.76, 30.4, 31.94, 31.96 (CH_2), 69.2, 73.50 (OCH_2), 113.9 (C-2), 142.7 (C-4), 152.9 (C-5) ppm. FT-IR (ATR): $\tilde{\nu}$ = 2958 (w), 2920 (s), 2851 (w), 1575 (w), 1506 (w), 1467 (w), 1419 (s), 1336 (vs, B-O), 1261 (w), 1241 (w), 1212 (w), 1172 (w), 1111 (s), 1021 (w), 845 (w), 802 (w), 721 (s, BX), 667 (w), 648 (w) cm^{-1}. MS (MALDI-TOF): *m/z* calcd. for $[C_{117}H_{213}B_3O_{12}]^+$ 1843.63, found 1843.49. Anal. calcd. for $C_{117}H_{213}B_3O_{12}$ (1844.41 g·mol^{-1}): C 76.19, H 11.64; found: C 76.39, H 11.33.

3.2.5. Tris(3,4,5-Tridodecyloxyphenyl)boroxine (**11e**)

^{1}H NMR (500 MHz, $CDCl_3$): δ = 0.88 (m, 27H, CH_3), 1.17–1.44 (m, 144H, CH_2), 1.45–1.61 (m, 18H, $OCH_2CH_2CH_2$), 1.74–1.90 (m, 18H, OCH_2CH_2), 4.00–4.16 (m, 18H, OCH_2), 7.39 (s, 6H, 2-H) ppm. ^{13}C NMR (126 MHz, $CDCl_3$): δ = 14.12 (CH_3), 22.7, 26.1, 26.2, 29.4, 29.53, 29.55, 29.6, 29.72, 29.77, 29.78, 30.4, 31.9 (CH_2), 69.23, 73.50 (OCH_2), 113.9 (C-2), 142.7 (C-4), 152.9 (C-3) ppm.

FT-IR (ATR): $\tilde{\nu}$ = 2957 (w), 2919 (s), 2850 (s), 1575 (w), 1467 (w), 1419 (s), 1336 (vs, B-O), 1260 (w), 1213 (w), 1113 (s), 1012 (w), 907 (w), 846 (w), 799 (w), 736 (s), 720 (s, BX), 648 (w), 578 (w) cm^{-1}. MS (MALDI-TOF): *m/z* calcd. for $[C_{126}H_{231}B_3O_{12}\text{-}H]^+$ 1969.77, found 1968.80. Anal. calcd. for $C_{126}H_{231}B_3O_{12}$ (1970.65 $g \cdot mol^{-1}$): C 76.80, H 11.82; found: C 77.02, H 11.92.

3.3. Instrumental Analysis

The following instruments were used for characterization of the compounds. NMR: Bruker Avance 500 (^1H, 500 MHz; ^{13}C, 126 MHz) and Bruker Avance 300 (^1H, 300 MHz; ^{13}C, 75 MHz). ^1H and ^{13}C NMR spectra were referenced to tetramethylsilane (TMS, Sigma-Aldrich, Steinheim, Germany) (δ_H = 0.0 ppm, δ_C = 0.0 ppm) as an internal standard. Unless otherwise stated, spectra were recorded at room temperature. Assignment of the resonances was supported by chemical shift calculations and 2D experiments (COSY and HMBC). Elemental analyses: Carlo Erba Strumentazione Elemental Analyzer, Modell 1106. IR: Bruker Vector 22 FT-IR Spectrometer with MKII golden gate single reflection Diamant ATR system. MS (ESI): Bruker Daltonics microTOF-Q spectrometer. Polarizing optical microscopy: Olympus BX50 polarizing microscope combined with a Linkam TP93 central controller. X-ray diffraction (WAXS, SAXS regions): Bruker AXS Nanostar C diffractometer employing Ni-filtered CuKα radiation (λ = 1.5418 Å), standard stationary temperature control unit for temperature programs. Differential scanning calorimetry (DSC): Mettler-Toledo DSC 822e. Flash chromatography was performed on silica gel, grain size 40–63 μm (Fluka) and aluminium sheets precoated with silica gel 60 F254 (Merck) were used for thin layer chromatography.

4. Conclusions

A new and easy approach towards discotic boroxines and study of their mesomorphic properties is reported. Pure boroxines **11** were accessible starting from 5-bromo-1,3,4-trialkoxybenzenes **7** via four-step reaction which did not need purification of intermediates.

Derivatives **5** bearing three dialkyloxyphenyl groups are found to be non-mesomorphic. In contrast, linkage of three trialkyloxyphenyl substituents gave boroxines **11** displaying liquid crystalline behaviour. A minimum of C9 alkyl chain length (**11b**) turned out to be necessary for mesophase formation because **11a** with C8 alkyl chains is non-mesogenic. The phase widths ranged from 77 K (**11e**) to 110 K (**11b**) near room temperature, thus decreasing with enhanced alkyl chain lengths. Under POM, fan-shaped textures typical for columnar mesophases were observed for all boroxines **11b**–**e**. The phase geometry was further supported by X-ray diffraction showing in the small-angle region the typical diffraction pattern of columnar hexagonal mesophases.

Acknowledgments

Generous financial support by the Ministerium für Wissenschaft, Forschung und Kunst des Landes Baden-Württemberg, the Bundesministerium für Bildung und Forschung (shared instrumentation grant No. 01 RI 05177), and the Fonds der Chemischen Industrie is gratefully acknowledged.

Author Contributions

Tobias Wöhrle performed the synthesis and characterization. Tobias Wöhrle, Angelika Baro and Sabine Laschat prepared the manuscript.

Conflicts of Interest

The authors declare no conflict of interest.

References

1. Chandrasekhar, S.; Sadashiva, B.K.; Suresh, K.A. Liquid crystals of disc-like molecules. *Pramana* **1977**, *9*, 471–480.
2. Laschat, S.; Baro, A.; Steinke, N.; Giesselmann, F.; Hägele, C.; Scalia, G.; Judele, R.; Kapatsina, E.; Sauer, S.; Schreivogel, A.; *et al.* Discotic liquid crystals: from tailor-made synthesis to plastic electronics. *Angew. Chem. Int. Ed.* **2007**, *46*, 4832–4887.
3. Bushby, R.J.; Kawata, K. Liquid crystals that affected the world: Discotic liquid crystals. *Liq. Cryst.* **2011**, *38*, 1415–1426.
4. Kumar, S. Design concepts and synthesis of discotic liquid crystals. In *Handbook of Liquid Crystals*, 2nd ed.; Goodby, J.W., Collings, P.J.; Kato, T.K., Tschierske, C., Gleeson, H., Raynes, P., Eds.; Wiley-VCH: Weinheim, Germany, 2014; Volume 4, pp. 467–520.
5. Sergeyev, S.; Pisula, W.; Geerts, Y.H. Discotic liquid crystals: A new generation of organic semiconductors. *Chem. Soc. Rev.* **2007**, *36*, 1902–1929.
6. Woltman, S.J.; Jay, G.D.; Crawford, G.P. Liquid-crystal materials find a new order in biomedical applications. *Nat. Mater.* **2007**, *6*, 929–938.
7. Kaafarani, B.R. Discotic liquid crystals for opto-electronic applications. *Chem. Mater.* **2011**, *23*, 378–396.
8. Kumar, S. Discotic liquid crystals for solar cells. *Curr. Sci.* **2002**, *82*, 256–257.
9. Kopitzke, J.; Wendorff, J.H. Diskotische Flüssigkristalle: Materialien für die Optoelektronik. *Chem. Unserer Zeit* **2000**, *34*, 4–16. (In German)
10. Kumar, S. Recent developments in the chemistry of triphenylene-based discotic liquid crystals. *Liq. Cryst.* **2004**, *31*, 1037–1059.
11. Würthner, F. Perylene bisimide dyes as versatile building blocks for functional supramolecular architectures. *Chem. Commun.* **2004**, 1564–1579.
12. Seyler, H.; Purushothaman, B.; Jones, D.J.; Holmes, A.B.; Wong, W.W.H. Hexa-*peri*-hexabenzocoronene in organic electronics. *Pure Appl. Chem.* **2012**, *84*, 1047–1067.
13. Wu, J.; Pisula, W.; Müllen, K. Graphenes as potential material for electronics. *Chem. Rev.* **2007**, *107*, 718–747.
14. Fox, M.A.; Bard, A.J.; Pan, H.-L.; Liu, C.-Y. Functionalized porphyrin discotic liquid crystals: Photoinduced charge separation and trapping. *J. Chin. Chem. Soc*. **1993**, *40*, 321–327.
15. Eichhorn, H. Mesomorphic phthalocyanines, tetraazaporphyrins, porphyrins and triphenylenes as charge-transporting materials. *J. Porphyr. Phthalocyanines* **2000**, *4*, 88–102.

16. Tschierske, C. Liquid crystal engineering—New complex mesophase structures and their relations to polymer morphologies, nanoscale patterning and crystal engineering. *Chem. Soc. Rev.* **2007**, *36*, 1930–1970.
17. Kato, T.; Yasuda, T.; Kamikawa, Y.; Yoshio, M. Self-assembly of functional columnar liquid crystals. *Chem. Commun.* **2009**, 729–739.
18. Roy, B.; de, N.; Majumdar, K.C. Advances in metal-free heterocycle-based columnar liquid crystals. *Chemistry* **2012**, *18*, 14560–14588.
19. Majumdar, K.C.; De, N.; Roy, B.; Bhaumik, A. Synthesis and mesophase characterisation of a series of new triazine-based disc-shaped molecules. *Liq. Cryst.* **2010**, *37*, 1459–1464.
20. Kohlmeier, A.; Vogel, L.; Janietz, D. Multiple hydrogen bonded mesomorphic complexes between complementary 1,3,5-triazine und pyrimidine derivatives. *Soft Matter* **2013**, *9*, 9476–9486.
21. Castelar, S.; Barberá, J.; Marcos, M.; Romero, P.; Serrano, J.-L.; Golemme, A.; Termine, R. Supramolecular dendrimers based on the self-assembly of carbazole-derived dendrons and triazine rings: Liquid crystals, photophysical and electrochemical properties. *J. Mater. Chem. C* **2013**, *1*, 7321–7332.
22. Barberá, J.; Bardaji, M.; Jiménez, J.; Laguna, A.; Martinez, M.P.; Oriol, L.; Serrano, J.L.; Zaragozano, I. Columnar mesomorphic organizations in cyclotriphosphazenes. *J. Am. Chem. Soc.* **2005**, *127*, 8994–9002.
23. Barberá, J.; Jiménez, J.; Laguna, A.; Oriol, L.; Pérez, S.; Serrano, J.L. Cyclotriphosphazene as a dendritic core for the preparation of columnar supermolecular liquid crystals. *Chem. Mater.* **2006**, *18*, 5437–5445.
24. Coeffard, V.; Moreau, X.; Thomassigny, C.; Greck, C. Übergangsmetallfreie Aminierung von Arylboronsäuren und deren Derivaten. *Angew. Chem.* **2013**, *125*, 5794–5796.
25. Suzuki, A. Cross-coupling reactions of organoboranes: An easy way to construct C–C bonds (Nobel Lecture). *Angew. Chem. Int. Ed.* **2011**, *50*, 6722–6737.
26. Miyaura, N. Metal-catalyzed reactions of organoboronic acids and esters. *Bull. Chem. Soc. Jpn.* **2008**, *81*, 1535–1553.
27. Miyauro, N. Organoboron compounds. *Topics Curr. Chem.* **2002**, *219*, 11–59.
28. Hayashi, T. Rhodium-catalyzed asymmetric 1,4-addition of organoboronic acids and their derivatives to electron deficient olefins. *Synlett* **2001**, 879–887.
29. Tokunaga, Y. Boroxine chemistry: From fundamental studies to applications in supramolecular and synthetic organic chemistry. *Heterocycles* **2013**, *87*, 911–1021.
30. Korich, A.L.; Iovine, P.M. Boroxine chemistry and applications: A perspective. *Dalton Trans.* **2010**, *39*, 1423–1431.
31. Belloni, M.; Manickam, M.; Wang, Z.-H.; Preece, J.A. Toward boronate ester mesogenic structures. *Mol. Cryst. Liq. Cryst.* **2003**, *399*, 93–114.
32. An, P.; Shi, Z.-F.; Dou, W.; Cao, X.-P.; Zhang, H.-L. Synthesis of 1,4-bis[2,2-bis (4-alkoxyphenyl) vinyl]benzenes and side chain modulation of their solid-state emission. *Org. Lett.* **2010**, *12*, 4364–4367.

33. Zou, Y.; Yi, T.; Xiao, S.; Li, F.; Li, C.; Gao, X.; Wu, J.; Yu, M.; Huang, C. Amphiphilic diarylethene as a photoswitchable probe for imaging living cells. *J. Am. Chem. Soc.* **2008**, *130*, 15750–15751.
34. Lindner, N.; Kölbel, M.; Sauer, C.; Diele, S.; Jokiranta, J.; Tschierske, C. Formation of columnar and cubic mesophases by calamitic molecules: novel amphotropic biphenyl derivatives. *J. Phys. Chem. B* **1998**, *102*, 5261–5273.
35. Kwiatkowski, M.; Chattopadhyaya, J. The 9-(4-octadecyloxyphenylxanthen)-9-yl-group. A new acid-labile hydroxyl protective group and its application in the preparative reserve-phase chromatographic separation of oligoribonucleotides. *Acta Chem. Scand. B* **1984**, *38*, 657–671.
36. Artal, M.C.; Toyne, K.J.; Goodby, J.W.; Barberá, J.; Photinos, D.J. Synthesis and mesogenic properties of novel board-like liquid crystals. *J. Mater. Chem.* **2001**, *11*, 2801–2807.
37. Kaller, M.; Tussetschläger, S.; Fischer, P.; Deck, C.; Baro, A.; Giesselmann, F.; Laschat, S. Columnar mesophases controlled by counterions in potassium complexes of dibenzo[18]crown-6 derivatives. *Chem. Eur. J.* **2009**, *15*, 9530–9542.
38. Yasuda, T.; Shimizu, T.; Liu, F.; Ungar, G.; Kato, T. Electro-functional octupolar π-conjugated columnar liquid crystals. *J. Am. Chem. Soc.* **2011**, *133*, 13437–13444.
39. Martinez-Palau, M.; Perea, E.; Lopez-Calahorra, F.; Velasco, D. Synthesis of luminescent N-arylcarbazoles by copper bronze-mediated reaction. *Lett. Org. Chem.* **2004**, *1*, 231–237.
40. Ma, C.-Q.; Pisula, W.; Weber, C.; Feng, X.-L.; Müllen, K.; Bäuerle, P. Dendritic oligothiophenes terminated with tris(alkyloxy)phenylethynyl tails: Synthesis, physical properties, and self-assembly. *Chem. Eur. J.* **2011**, *17*, 1507–1518.
41. Lee, H.; Kim, D.; Lee, H.-K.; Qiu, W.; Oh, N.-K.; Zin, W.-C.; Kim, K. Discotic liquid crystalline materials for potential nonlinear optical applications: synthesis and liquid crystalline behavior of 1,3,5-triphenyl-2,4,6-triazine derivatives containing achiral and chiral alkyl chains at the periphery. *Tetrahedron Lett.* **2004**, *45*, 1019–1022.
42. Jung, M.E.; Tsvetelina, I.; Lazarova, T.I. New Efficient Method for the Total Synthesis of (*S*,*S*)-Isodityrosine from Natural Amino Acids. *J. Org. Chem.* **1999**, *64*, 2976–2977.
43. Beckmann, J.; Dakternieks, D.; Andrew Duthie, A.; Allan, E.K.; Lim, A.E.K.; Tiekink, E.R.T. Ring strain in boroxine rings: computational and experimental considerations. *J. Organomet. Chem.* **2001**, *633*, 149–156.
44. Prasad, S.K.; Rao, D.S.S.; Chandrasekhar, S.; Kumar, S. X-Ray studies on the columnar structures of discotic liquid crystals. *Mol. Cryst. Liq. Cryst.* **2003**, *396*, 121–139.
45. Snyder, H.R.; Konecky, M.S.; Lennarz, W.J. Aryl Boronic Acids. II. Aryl Boronic Anhydrides and their Amine Complexes. *J. Am. Chem. Soc.* **1958**, *80*, 3611–3615.

Structural Rheology of the Smectic Phase

Shuji Fujii , Shigeyuki Komura and Chun-Yi David Lu

Abstract: In this review article, we discuss the rheological properties of the thermotropic smectic liquid crystal 8CB with focal conic domains (FCDs) from the viewpoint of structural rheology. It is known that the unbinding of the dislocation loops in the smectic phase drives the smectic-nematic transition. Here we discuss how the unbinding of the dislocation loops affects the evolution of the FCD size, linear and nonlinear rheological behaviors of the smectic phase. By studying the FCD formation from the perpendicularly oriented smectic layers, we also argue that dislocations play a key role in the structural development in layered systems. Furthermore, similarities in the rheological behavior between the FCDs in the smectic phase and the onion structures in the lyotropic lamellar phase suggest that these systems share a common physical origin for the elasticity.

Reprinted from *Materials*. Cite as: Fujii, s.; Komura, S.; Lu, C.-Y.D. Structural Rheology of the Smectic Phase. *Materials* **2014**, *7*, 189–212.

1. Introduction

Rheology is a fundamental issue in soft matter science. One of the most successful achievements in the rheology of soft matter is the Doi-Edwards model, which describes the viscoelastic response of entangled polymer melts [1]. This model guides further theories and experiments which contribute not only to the industrial application of polymer materials but also to the progress of the basic polymer science. In contrast to the success in the polymer systems, the rheology of soft matter with meso-scale structures is still a developing field. Structured fluids such as foam, emulsions and colloidal systems as well as polymers have been also widely studied for many industrial applications [2–5]. However, the attempt to describe their universal rheological properties has only started using the concept of "soft glassy rheology" [5,6]. Besides these glassy materials, the rheology of surfactant systems which exhibit the gyroid phase with a three-dimensional periodic structure, or the sponge phase with randomly connected bicontinuous interface remains unexplored except for some pioneered studies [7–12]. Their unique viscoelastic responses arise predominantly from deformation of meso-scale internal structures whose rearrangement can be easily induced under deformation or flow.

The rheology of soft matter looks for a fundamental understanding in terms of the micro/meso structures of the systems. Representative examples of "structural rheology" include emulsions, foams, colloidal dispersions, surfactant solutions, and liquid crystals. Molecular systems such as a lubricant confined in a narrow space also exhibit various responses depending on their microstructure [13–15]. Since there are many different structures, to unify the rheology of structured fluids is an attractive yet challenging subject. Furthermore, as the soft structures can also evolve in the flow, a good selection of the structure unit is essential to understand the system. If we can establish a fundamental principle for the "structural rheology", the significance of the soft matter

in the industrial application will increase. In this review, we take defects as the key structures to understand the smectic rheology.

In this review article, we discuss the structural rheology of thermotropic smectic liquid crystal as a typical example [16–19]. Among various soft materials which spontaneously form internal structures such as lamellar, hexagonal, cubic, and gyroid phases [20–23], the simplest one-dimensional periodic structure is the smectic-A phase in thermotropic liquid crystals. The smectic liquid crystals exhibit a solid-like response in the layer perpendicular direction and a fluid-like response within the layers. Although the solid and the fluid-like responses do not mix for the smectic with a perfect alignment, self-organized textures combine these responses and give rise to the viscoelasticity. Even in such simple systems, phenomena such as shear-thinning and the orientation transition of the smectic layer are observed once a flow field is applied [24–29]. In lyotropic lamellar phases, it is known that bilayer membranes form multi-lamellar vesicles (onions) under shear flow [30–34].

As Horn and Kleman [35] pointed out in their pioneering work, smectic rheology is influenced by defects in the bulk. It has been explained that shear-thinning behavior depends on the defect dynamics and/or the defect density [25,36–38]. Although the importance of defects in the smectic rheology is a common understanding, there are relatively few studies that focus on the role of defects either explicitly or systematically [39–42]. Meyer *et al.* and Lu *et al.* [36–38] studied the shear-thinning behavior by considering the dynamics of screw dislocations and dislocation loops. They found that the theoretically predicted shear-thinning behavior $\dot{\gamma} \sim \sigma^m$, where $\dot{\gamma}$ is the shear rate and σ the shear stress, was consistent with the experimental results within a limited range of the shear rate.

The thermotropic smectic liquid crystal 8CB changes from the crystalline phase to the smectic phase at $T = 21.5\,^{\circ}\mathrm{C}$, and further to the nematic phase at $T_{\mathrm{SN}} = 33.4\,^{\circ}\mathrm{C}$. In this review article, using 8CB as a typical example of smectics, we summarize the structural observation, the linear and nonlinear rheological behavior of the smectic-A phase close to (but below) T_{SN}. In the next section, we briefly explain the defects in the smectic liquid crystal phase. The temperature and the shear rate dependences of the defect size are discussed in Section 3. In Section 4, the nonlinear rheology of the smectic phase is investigated from the viewpoint of unbinding of dislocations, and summarize them in a dynamic phase diagram. The physical origin of the elasticity of the smectic phase with defects is suggested in Section 5. In the following section, we explain the dynamics of defect formation induced by a non-equilibrium phase transition in the smectic phase under flow. Finally, we mention the similarities between textural defects in the thermotropic smectic phase and the onion structures in the lyotropic lamellar phase.

In our study, we did not perform any surface treatment of the shear cell. The lack of the surface anchoring may induce the misalignment of the smectic layers and lead to the nucleation of focal conic domains (FCDs). However, in our experiment, reproducible results could be obtained by applying the pre-shear even without any anchoring treatment.

2. Defect Structures in the Smectic Phase

A liquid crystal has fluidity of a liquid and elasticity of a crystal. It also contains defects which locally break the translational symmetry and form reconnected layers [43]. Smectic-A phase

with a layered structure is perturbed by two types of line defects; edge dislocations and screw dislocations which are parallel and perpendicular to the layer surface, respectively. These line defects appear in pairs with opposite signs so that two screw dislocations with opposite signs linked by edge dislocations form a dislocation loop. Since the dislocation loop locally compresses the layer thickness, an increase in the dislocation loop density causes the accumulation of strain energy. Furthermore, FCDs are formed to relax the compression deformation [44,45]. FCDs are visible under an optical microscope and have sizes from a few micrometers to a hundred micrometers.

As shown in Figure 1, there are two types of FCDs which can be distinguished by the sign of the Gaussian curvature of the layers. The first type, FCD-I, has negative Gaussian curvature forming a toroidal shape, and is frequently observed in thermotropic liquid crystals. Whereas the second type, FCD-II, has a concentric sphere like onion structure which is observed only in lyotropic lamellar phases. As presented in Figure 1b, FCD-Is are connected by edge dislocations to form "oily streaks" which are commonly observed both in thermotropic and lyotropic systems [46].

Figure 1. Schematic diagrams of (**a**) two different types of focal conic domains, FCD-I and FCD-II; and (**b**) oily streak structure in which five vertical cross sections of FCD-I are connected by four edge dislocations [45,46]. In the FCDs, the layers are folded into Dupin cyclides with ellipse and hyperbola so that the curved layers remain equidistant. Reproduced by permission of EDP sciences.

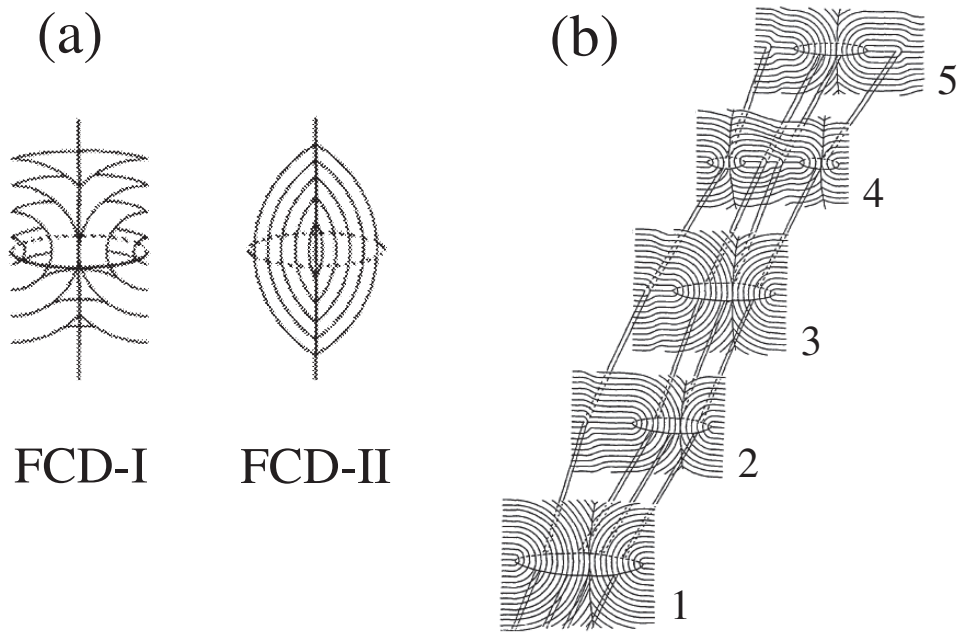

Not only the edge dislocations but also the screw dislocations also affect the FCD structure. In the FCDs, the layers are folded into Dupin cyclides with ellipse and hyperbola which can be identified as disclinations. Kleman *et al.* [47] and Meyer *et al.* [48] experimentally observed that the interaction between FCDs and dislocations creates kinks on disclinations. As a result of this interaction, the screw dislocations will align along the kink. Unbinding of the dislocation loops will thus increase the kink density and may affect the FCD shape.

It has been recognized that formation of dislocation loops plays an important role in the smectic-nematic (SN) transition [49]. Helfrich [50] proposed that an increase in the dislocation loop density destroys the smectic order, and the unbinding of dislocation loops drives the SN-transition. In his model, the stability of dislocation loops is determined by its energy per unit length, *i.e.*, line tension. When the temperature is increased, the line tension decreases and becomes negative above $T = T_{\rm SN}$. This leads to the spontaneous nucleation and proliferation of dislocation loops, and the decay of the smectic order is reflected by the temperature dependence of the layer compression modulus B. Benzekri *et al.* [51,52] showed that B decreases according to a power-law behavior with a critical exponent given by the Nelson-Toner model [53]. Using freeze-fracture transmission electron microscopy technique, Moreau *et al.* [54] showed that dislocation loop size indeed increases in the vicinity of the SN-transition for a lyotropic liquid crystal.

3. FCDs under Shear Flow

As Horn and Kleman presented [35], the FCD density increases by applying a shear flow. Their experimental observations suggest that non-equilibrium textural defects is additionally induced by the shear flow. Hence the smectic structures are strongly affected by the formation of non-equilibrium defects. In this section, we discuss the relation between the proliferation of dislocation loops and the FCD size and the shear rate [16].

Figure 2 shows polarized light microscope images of 8CB in the smectic phase under shear flow. These images were obtained immediately after applying different shear rates for 10 min for various temperatures ranging from the room temperature to $T_{\rm SN}$. The vertical and the depth directions correspond to the flow and the velocity gradient directions, respectively. It can be seen that strings of FCDs along the flow direction fill the space. We also note that the FCD size decreases with increasing the shear rate at each temperature. Under constant shear rate, on the other hand, the FCD size increases as the temperature approaches $T_{\rm SN}$.

To systematically study the effects of the temperature and shear rate on the FCD size, it is necessary to determine the mean diameter L of FCDs. A microscope image taken under the shear rate $\dot{\gamma} = 0.1$ s^{-1} is presented in Figure 3 as an example in order to show how to obtain L. As shown in the figure, the average of L can be estimated by tracing the distinguishable outlines of the FCDs with circles. Some FCDs are not used because their boundary contrast is too low. These FCDs are located either above or below the focus plane. We calculate L as the number average within the focus plane region. Close to the transition temperature $T_{\rm SN}$, one expects that the correlation length of the fluctuation and the dislocation size behave similarly to obey the scaling law in terms of the reduced temperature $t = (T_{\rm SN} - T)/T_{\rm SN}$ [55,56]. From our experiment, we found that L depends on t and $\dot{\gamma}$ as $L \sim \dot{\gamma}^{-0.2}$ (at each temperature) and $L \sim t^{-0.5}$ (at each shear rate), respectively. As presented in Figure 4, the FCD size L can be scaled by the combined variable $\dot{\gamma}^{-0.2}t^{-0.5}$.

Although there is no theory on the shear rate and/or temperature dependence of L, an analogous scaling relation with the same exponent was predicted for the defect spacing which varies as $\sim \dot{\gamma}^{-0.2}$ [36,37]. Moreover, the average dislocation loop size diverges as $\sim t^{-0.5}$ according to the defect model by Helfrich [50]. We remind that dislocation loops are formed by pairs of edge

and screw dislocations, and FCDs are linked by edge dislocations. Since the accumulation of the strain energy due to an increase in the defect density is the driving force for the FCD formation, the agreement of these exponents (0.2 and 0.5) suggests that the proliferation of dislocation loops controls the FCD size. Incidentally, it has been suggested that the non-equilibrium structural transition of lyotropic lamellar phase under shear is governed by the dislocation size [29].

Figure 2. Polarized microscope images of the smectic phase under shear flow at different temperatures (**a**) $T = 33.0$; (**b**) 31.0; (**c**) 29.0; (**d**) 25.0 °C and shear rates $\dot{\gamma} = 0.1, 1, 10, 20, 100, 200$ s^{-1}. The shear flow was applied along the vertical direction of the images which were taken just after the cessation of it. The scale bar corresponds to 100 μm.

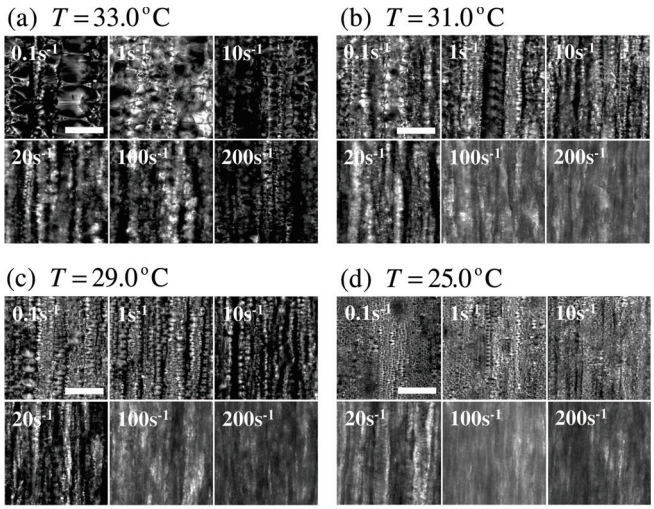

.

Figure 3. Typical microscope image used to estimate the FCD size at $T = 25.0$ °C and $\dot{\gamma} = 0.1$ s^{-1}. The averaged diameter L of FCDs was estimated by tracing each FCD with a red circle as shown in the picture. The scale bar corresponds to 50 μm.

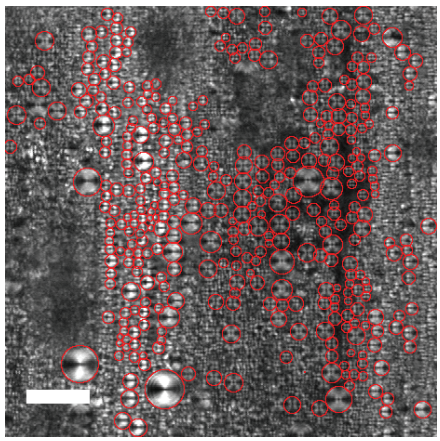

Figure 4. Log-log plot of the FCD size L as a function of the shear rate $\dot{\gamma}$ and the reduced temperature t. Different symbols correspond to different temperatures. The scaling variable is chosen to be $\dot{\gamma}^{-0.2}t^{-0.5}$ so that all the data points fall onto a straight dashed line whose slope is unity.

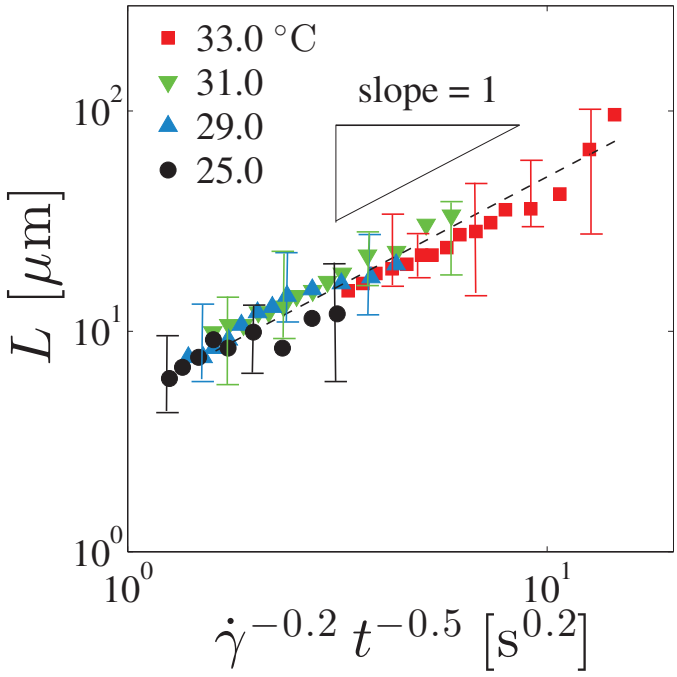

4. Nonlinear Rheology of the Smectic Phase

It is known that the smectic phase exhibits both shear-thinning behavior and yield stress [24–26,28,35]. Although it has been anticipated that such rheological behavior is influenced by defects [41,42], we have further shown in the previous section that these structures are FCDs which originate from dislocation loops. In this section, we discuss how the presence of FCDs are reflected in the rheology of the smectic phase [16].

Figure 5 shows the flow curves in the temperature range from 25.0 °C to 34.0 °C across the SN-transition temperature $T_{\rm SN} = 33.4\,$°C. These flow curves are obtained by measuring the steady-state value of the shear rate $\dot{\gamma}$ when various values of the shear stress σ are applied. Within the power-law behavior $\dot{\gamma} \sim \sigma^m$, $m > 1$ and $m = 1$ correspond to the shear-thinning and the Newtonian behaviors, respectively. Since $m > 1$ for $T < T_{\rm SN}$, the smectic phase exhibits a shear-thinning behavior.

It should be noted that the flow curves are not fully described by a single power-law since the slope in Figure 5 gradually changes as a function of the shear stress. Colby *et al.* [24] also observed a similar behavior of the flow curve. In order to discuss the nonlinear rheological response in more detail, we focus on the flow curve at $T = 25.0\,$°C as a typical example. First we realize that this flow curve reaches to a finite stress value when the shear rate is extrapolated to zero. This means that there is a yield stress $\sigma_{\rm y}$, below which the flow ceases. Previously, Horn and Kleman [35]

or Colby *et al.* [25] reported that the smectic phase shows the yield stress. The flow curves for other temperatures also exhibit yield stress; it decreases at higher temperatures and vanishes at T_{SN}. Furthermore, focusing on the high-shear flow curves near the transition point (e.g., $T = 33.0\,^{\circ}\mathrm{C}$), we see that the rheological behavior changes from shear-thinning to Newtonian at a specific shear stress. The corresponding threshold stress value σ_{t} required to become Newtonian shifts toward the lower value when approaching T_{SN}. In the nematic phase at higher temperatures, only Newtonian behavior is observed.

Figure 5. Log-log plot of the steady-steady shear rate $\dot{\gamma}$ as a function of the applied shear stress σ at different temperatures. The inset shows a typical curve ($T = 33.1\,^{\circ}\mathrm{C}$) divided into three regimes. Regime 0 is fitted by the Herschel-Bulkley model given by Equation (1); Regime I is fitted by the power-law behavior given by Equation (2); and Regime II corresponds to the Newtonian behavior. At the threshold stress σ_{t}, the transition from Regime I to Regime II takes place. The SN-transition temperature T_{SN} is 33.4 °C.

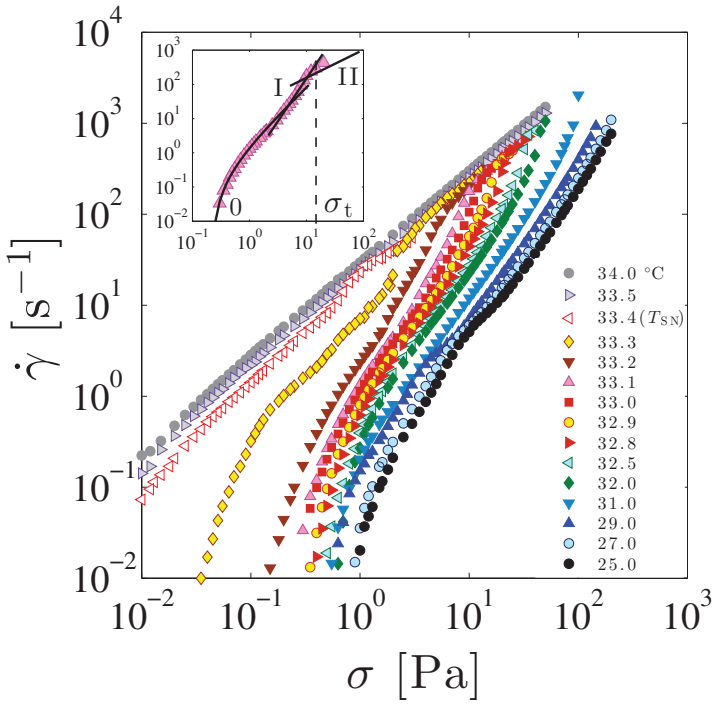

To extract the temperature dependence of the power-law exponent and the yield stress, the flow curve was divided into three regions: shear-thinning region (Regime 0) showing the yield stress, shear-thinning region (Regime I) described by a power-law, and Newtonian region (Regime II). Notice that σ_{t} represents the boundary value between Regime I and Regime II. To estimate the yield stress in Regime 0, we use the empirical Herschel-Bulkley (HB) model

$$\sigma = \sigma_{\mathrm{y}} + A\dot{\gamma}^{n} \tag{1}$$

where A and n are parameters, and $\sigma_{\rm y}$ is the yield stress. This model has been frequently used to describe the non-Newtonian behaviors of yield stress fluids [57–59]. In addition to the HB model for Regime 0, Regime I was fitted with the power-law:

$$\sigma = C\dot{\gamma}^{1/m} \tag{2}$$

Various quantities can be obtained by fitting these equations to the flow curve (see the inset of Figure 5).

The temperature dependence of each parameter is summarized in Figure 6. Whereas $\sigma_{\rm y}$ and A rapidly decrease and vanish at $T_{\rm SN}$, the exponent n does not show a simple temperature dependence. On the other hand, C and m are almost constant up to around $T = 32.0\,^{\circ}$C and show a significant increase as $T_{\rm SN}$ is approached from below. The abrupt increase of C and m near $T_{\rm SN}$ indicates that the enhanced critical fluctuation or the proliferation of dislocation loops significantly affects the shear-thinning behavior. The shear-thinning exponent $m \approx 1.7$ obtained at the low-temperature region coincides with the theoretically predicted exponent $m = 5/3$ by Kleman *et al*. [36,37].

As discussed in the previous section, the growth of dislocation loops causes the increase of the FCD size. Horn and Kleman employed a dimensional argument to relate the yield stress $\sigma_{\rm y}$ and the FCD size L by $\sigma_{\rm y} \sim K/L^2$, where K is the bending modulus of the smectic phase [35]. Notice that the value of K is only weakly dependent on the temperature [60]. According to this relation, we see that a decrease of $\sigma_{\rm y}$ near $T_{\rm SN}$ corresponds to a rapid increase of L. Qualitatively, this temperature dependence of L agrees with the direct observations of FCDs in Figures 2 and 4. Hence we expect that the growth of dislocation loops influences the temperature dependence of $\sigma_{\rm y}$ through the increase of the FCD size. We shall further discuss the elasticity of FCDs in the next section.

Next we discuss the transition from shear-thinning (Regime I) to Newtonian behavior (Regime II) using the dynamic phase diagram. In addition to $\sigma_{\rm t}$ obtained from Figure 5, the temperature dependence of the viscosity η under constant shear stress was measured to construct non-equilibrium phase diagram. The temperature dependence of η measured at shear stress of $\sigma = 10$, 30, 50, and 100 Pa is shown in Figure 7. Several results are found; (i) at low temperatures, η decreases as the temperature increases; (ii) above a certain temperature T_1, η is almost constant; and (iii) at T_2 slightly lower than $T_{\rm SN}$, a peak is observed. The two characteristic temperatures T_1 and T_2 shift toward lower values as the shear stress is increased.

The above results are summarized in the dynamic phase diagram presented in Figure 8. Here we find that the shear stress dependence of T_1 and the temperature dependence of $\sigma_{\rm t}$ are almost identical to each other. Furthermore, both T_1 and T_2 change linearly with respect to σ. The temperature estimated by extrapolating T_1 and T_2 to zero shear stress coincides with $T_{\rm SN}$ at quiescent state, and the phase diagram can be divided into three regimes. Comparing with the flow curves of Figure 5 and the temperature dependence of η in Figure 7, we see that the low-temperature region ($T \leq T_1$) corresponds to the shear-thinning region (Regime I), while the temperature region $T_1 \leq T \leq T_2$ exhibits the Newtonian behavior (Regime II). For convenience, these two regions are denoted by "$\mathrm{SmA_I}$ phase" and "$\mathrm{SmA_{II}}$ phase", respectively.

Figure 6. (**a**) The yield stress σ_{y}, the pre-factor A, the exponent n in Equation (1), and (**b**) the pre-factor C, the shear-thinning exponent m in Equation (2) as a function of the temperature T. These values are obtained by the best fit in Figure 5 for each regime. Vertical dashed line indicates the SN-transition temperature; $T_{\mathrm{SN}} = 33.4\,^{\circ}\mathrm{C}$.

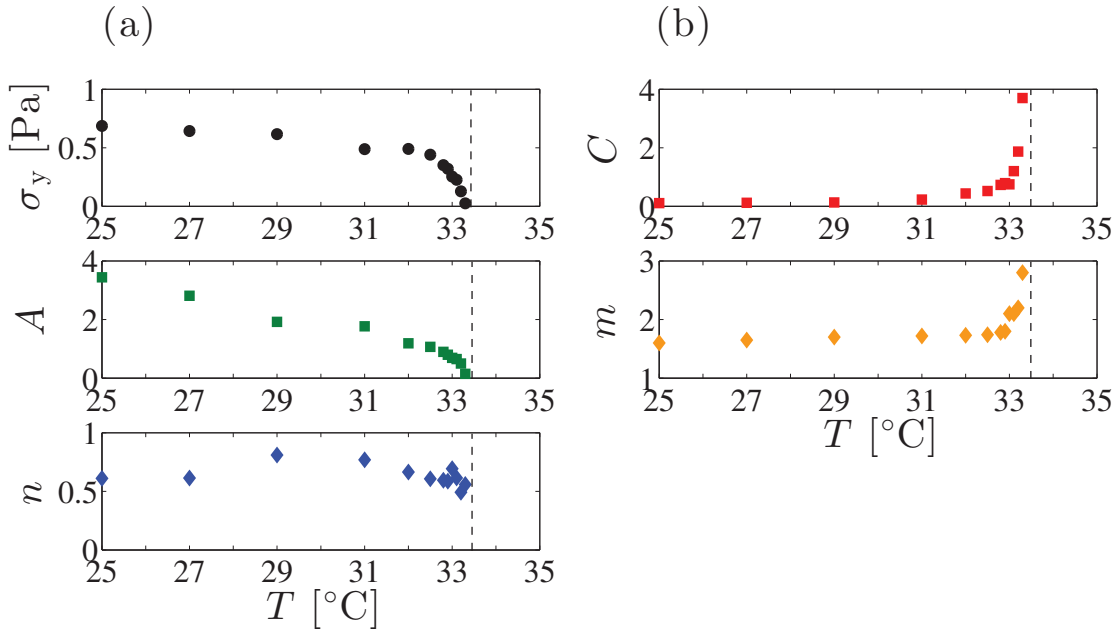

Figure 7. Shear viscosity η as a function of the temperature T obtained at different applied shear stress $\sigma = 10, 30, 50, 100$ Pa. Here $\log \eta$ is shifted by a constant a in order to have a better visibility. Vertical dashed line indicates the SN-transition temperature; $T_{\mathrm{SN}} = 33.4\,^{\circ}\mathrm{C}$.

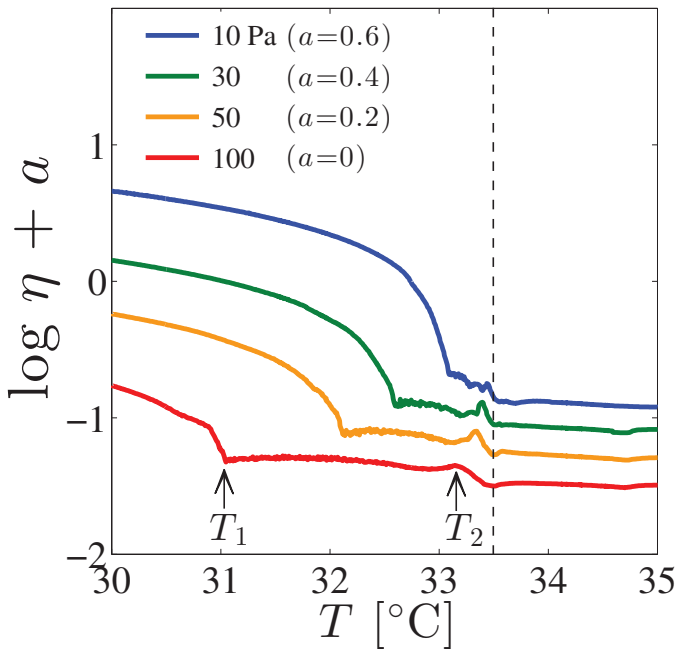

Figure 8. Dynamic phase diagram of 8CB under shear plotted against the temperature T and the applied shear stress σ. The smectic becomes Newtonian above $\sigma_{\rm t}$, whereas T_1 and T_2 are characteristic temperatures identified in Figure 7. The vertical dashed line indicates $T = T_{\rm SN}$. The lines of $\sigma_{\rm t}$ and T_1 coincide with each other. "$\rm SmA_I$" and "$\rm SmA_{II}$" denote the smectic phases in Regime I and II, respectively, while "N" indicates the nematic phase.

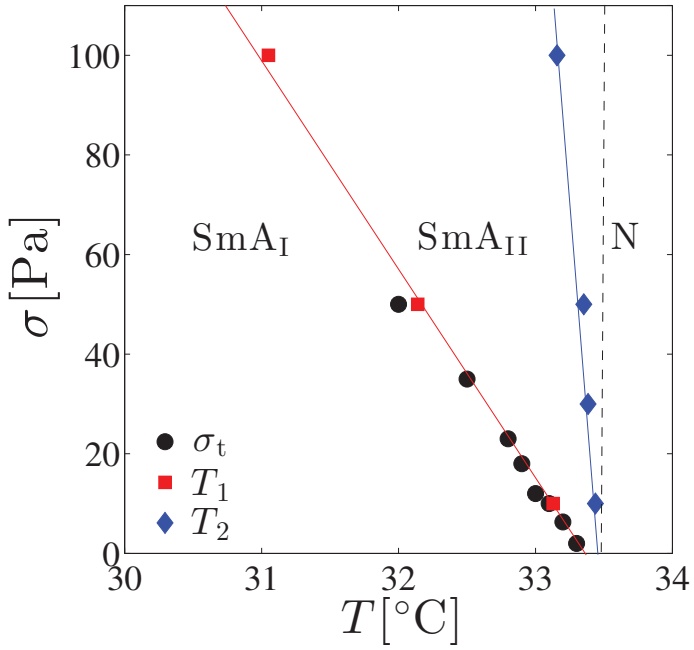

Previously, dynamic orientation diagram of the smectic phase was constructed with the use of rheo-physical methods such as small angle X-ray scattering under shear flow by Safinya *et al.* [27] and Panizza *et al.* [26], or rheo-dielectric measurement by Negita *et al.* [61]. Our dynamic phase diagram qualitatively agrees with their results. Although Safinya *et al.* [27] and Negita *et al.* [61] presented their diagrams as a function of the temperature and the shear rate, we also confirmed that our diagram roughly coincides with them by mapping the shear stress to the shear rate using the flow curves in Figure 5. As shown in Figure 9, it is known that two orientation states are possible in the smectic phase: perpendicular orientation in which the layer normal is perpendicular to both the velocity gradient and flow direction, and parallel orientation in which it is parallel to the velocity gradient direction [62,63].

Since the dynamic phase diagram obtained in Figure 8 and the orientation diagrams based on rheo-physical methods coincide, $\rm SmA_I$ phase is a mixture of the perpendicular and parallel orientations, or a leak structure for which layers are cylindrically rounded [26]. On the other hand, $\rm SmA_{II}$ phase consists of the perpendicular orientation. From this finding, we realize that the rheological behavior and the layer orientation are closely linked to each other. Furthermore, since T_2 coincides with $T_{\rm SN}$ for sufficiently low-shear stress ($\sigma = 10$ Pa), we anticipate that the peak in η reflects the precession motion of the monomers in the SN-transition [27,61]. The shift of T_2 toward

lower temperatures when subjected to high-shear stress implies that the SN-transition is induced by the shear flow. In addition to the proliferation of dislocation loops in thermal equilibrium state, the shear-induced SN-transition is due to the creation of non-equilibrium dislocation loops caused by the shear flow. The shear-induced SN-transition originates from the unbinding of dislocation loops which are created both under equilibrium and out-of-equilibrium conditions. A rich rheological behavior associated with the shear-induced layer orientation has been also found in the lyotropic lamellar phases [64–66].

Figure 9. Schematic diagram of a smectic phase with perpendicular (left) and parallel (right) orientations under shear flow. ∇, $\mathbf{v}$ and $\mathbf{n}$ correspond to the flow gradient, flow and vorticity directions, respectively. The $\mathrm{SmA_I}$ phase consists of both perpendicular and parallel orientations, while only the perpendicular orientation appears in the $\mathrm{SmA_{II}}$ phase.

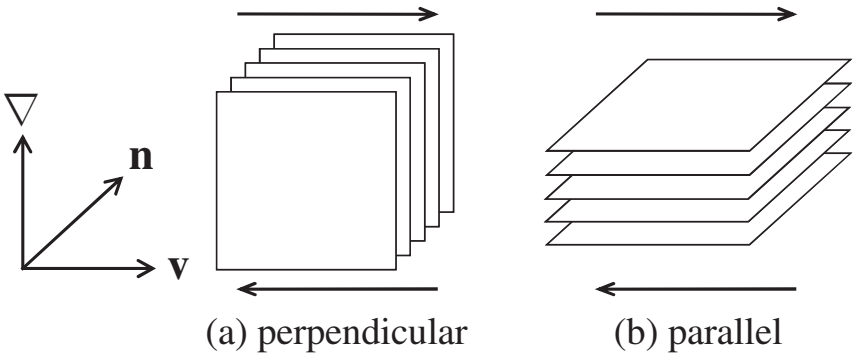

5. Linear Viscoelasticity of the Smectic Phase

In this section, we discuss the influence of FCDs on the linear viscoelasticity of the smectic phase [17]. We also argue the physical origin of the elasticity of the smectic phase with FCDs. As described in the previous section, the dynamical smectic phase changes from the $\mathrm{SmA_I}$ phase to $\mathrm{SmA_{II}}$ phase as a function of the shear stress and temperature. Since the $\mathrm{SmA_{II}}$ phase exhibits only Newtonian behavior, we mainly concentrate on the viscoelasticity of the $\mathrm{SmA_I}$ phase.

In rheological measurements, the shear modulus G can be obtained by the ratio between the shear stress σ and the strain γ as $G = \sigma/\gamma$. On the other hand, σ is given by the product of the viscosity η and the shear rate $\dot{\gamma}$, *i.e.*, $\sigma = \eta\dot{\gamma}$. Viscoelastic materials exhibit both elastic and viscous responses which can be measured by applying oscillating strain with an angular frequency ω and an amplitude of γ_0; $\gamma = \gamma_0 \sin(\omega t)$. The dynamic storage modulus G' and the loss modulus G'' are determined by the following relation:

$$\sigma = \gamma_0[G'(\omega)\sin(\omega t) + G''(\omega)\cos(\omega t)] \tag{3}$$

In our experiment, all of the measurements were performed within the linear viscoelastic region which was confirmed by the strain sweep tests.

Figure 10 shows the frequency dependence of G' and G'' measured after the system is subjected to a given pre-shear stress. For all temperatures, G' is always larger than G''. Moreover, a plateau

region is observed in the low-frequency range, as Colby *et al.* also reported [24]. This solid-like viscoelastic behavior is strongly correlated with the defect density. In fact, Larson *et al.* [28] showed that both G' and G'' decrease when the defects are removed by applying a large amplitude oscillatory shear. Hence the plateau modulus reflects the defect density.

Figure 10. Log-log plot of the dynamic storage modulus G' and loss modulus G'' as a function of the frequency ω at different temperatures. Filled and open symbols correspond to G' and G'', respectively. Different symbols shown in (**d**) represent the applied pre-shear stresses for which the steady states are obtained.

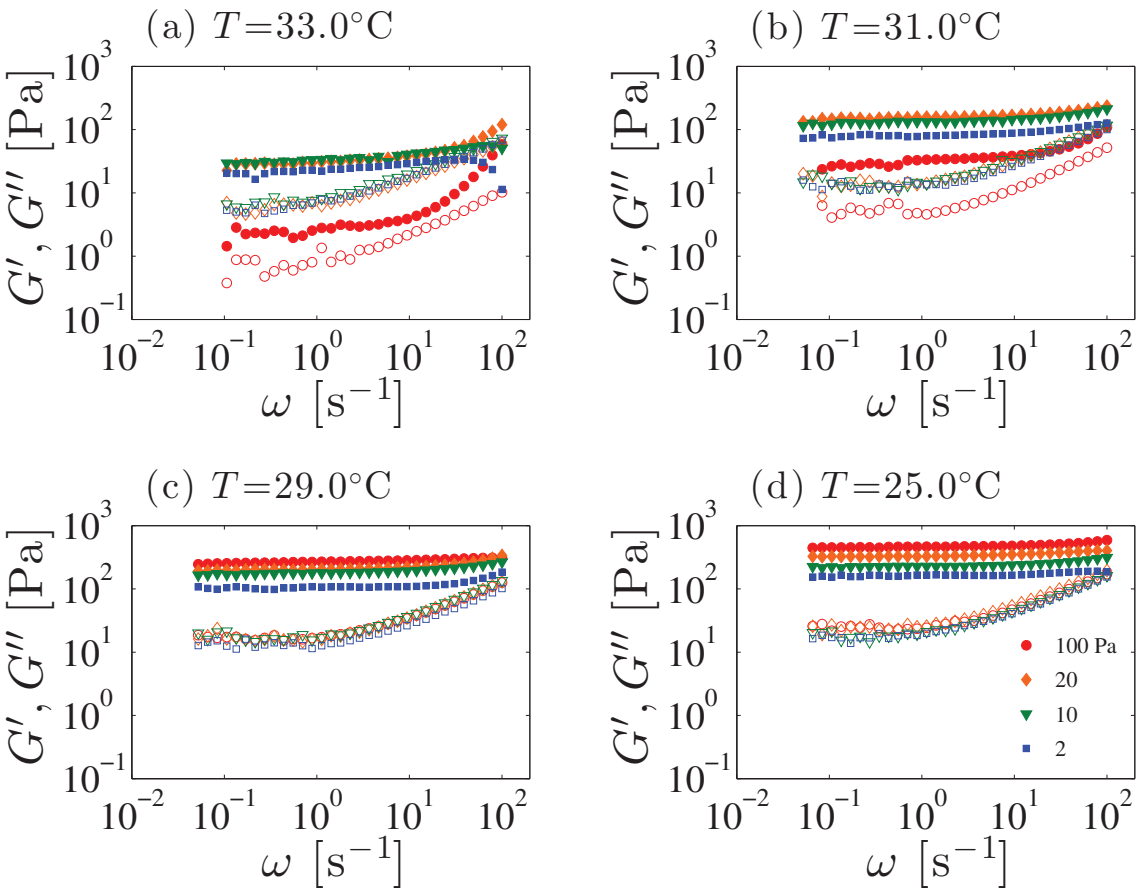

Concerning the pre-shear stress dependence of the plateau value of G' (denoted as G_0) at different temperatures, G_0 becomes larger with increasing the pre-shear stress. However, as the temperature approaches to T_{SN} such as at $T = 33.0\,^{\circ}\mathrm{C}$, it decreases at high pre-shear stress and deviates from a simple scaling suggested in Figure 11. Comparing the pre-shear stress dependence of G_0 to Figures 5 and 8, we notice that the shear stress value where G_0 decreases is located near the boundary between the $\mathrm{SmA_I}$ and the $\mathrm{SmA_{II}}$ phases. Thus, the plateau value of G' reflects the defects associated with orientations of the layers. As discussed before, FCDs fill the $\mathrm{SmA_I}$ phase under shear flow, whereas they are not observed in the $\mathrm{SmA_{II}}$ phase. Hence, FCDs dominate the elasticity of the $\mathrm{SmA_I}$ phase. Once the orientation transition of the smectic layers takes place to become $\mathrm{SmA_{II}}$, the elasticity due to FCDs vanishes.

Figure 11. Log-log plot of the plateau shear modulus G_0 as a function of the shear rate $\dot{\gamma}$ and the reduced temperature t. Different symbols correspond to different temperatures. The scaling variable is chosen as $\dot{\gamma}^{0.2}t^{0.7}$ so that most of the data points fall onto a straight dashed line whose slope is unity.

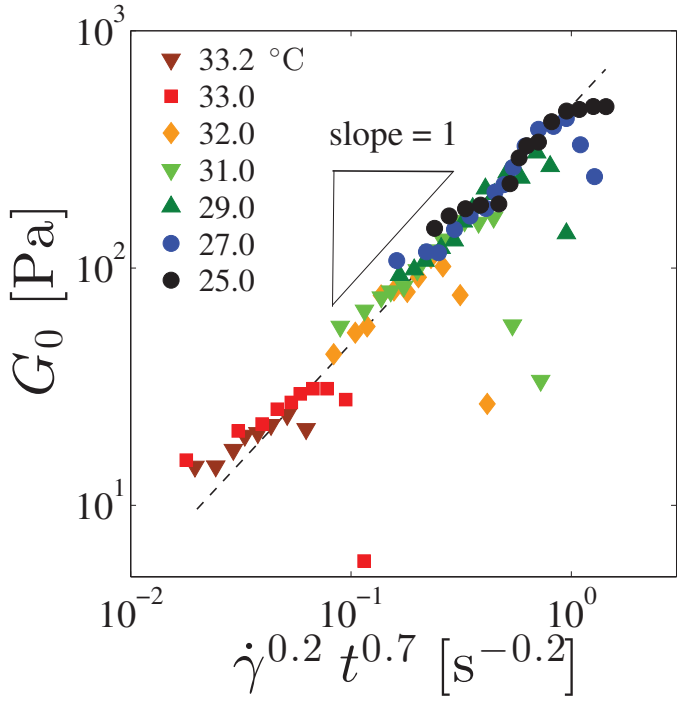

Similar to the temperature dependence of the yield stress, G_0 also decreases as $T_{\rm SN}$ is approached. Since the FCD size L influences the shear modulus G', a similar scaling behavior found in Figure 4 is expected to hold. Here the value of G' at $\omega = 0.1$ s^{-1} was chosen as G_0 which is plotted in Figure 11 as a function of the combined variable of $\dot{\gamma}$ and t. Adopting the result of Figure 5, the measured steady shear rate $\dot{\gamma}$ for each applied pre-shear stress σ can be used for the scaling plot. To obtain the scaling plot for G_0, we first determined the power-law dependence $G_0 \sim \dot{\gamma}^{0.2}$ at each temperature. Then the power-law behavior of G_0 as a function of t with an exponent 0.7 was extracted so that all the data points fall onto a straight line with a slope of unity, *i.e.*, $G_0 \sim \dot{\gamma}^{0.2}t^{0.7}$. Except for the data close to the border between the $\mathrm{SmA_I}$ and $\mathrm{SmA_{II}}$ phases, all G_0 values fall on a straight line. Below, we discuss the physical meaning of these scaling behaviors for G_0 and L.

When comparing the two scaling relations $G_0 \sim \dot{\gamma}^{0.2}t^{0.7}$ and $L \sim \dot{\gamma}^{-0.2}t^{-0.5}$ obtained from independent measurements, it appears that G_0 is almost inversely proportional to L, $G_0 \sim 1/L$, although the temperature exponent is slightly different. In order to satisfy this relation, the proportionality coefficient on the right hand side must have the dimension of surface tension, *i.e.*, energy per unit area. For layered systems such as the smectic phase or the lamellar phase, de Gennes and van der Linden proposed an effective surface tension given by $\gamma_{\rm eff} \simeq \sqrt{KB}$, where K and B are

the bending and the compression moduli, respectively [55,67,68]. Here the numerical pre-factor is dropped. Thus the plateau shear modulus of the smectic phase G_0 should obey the following relation:

$$G_0 = C' \frac{\sqrt{KB}}{L} \tag{4}$$

where C' is the dimensionless proportionality coefficient. In the case of 8CB, it is known that K is almost constant, $K = (5.2 \pm 0.3) \times 10^{-12}$ N [60], whereas B decreases with increasing temperature close to T_{SN}. According to the experimental result of Benzekri *et al.*, the temperature dependence of B is given by $B = (7.5 \times 10^7) \times t^{0.4 \pm 0.03}$ Pa [51,52]. To verify the validity of Equation (4), we compare the value of $G_0 L$ obtained from our experimental result and $\gamma_{\mathrm{eff}} = \sqrt{KB}$ estimated from the literature, *i.e.*, $G_0 L = (4.56 \times 10^{-3}) \times t^{0.2}$ Nm^{-1} and $\sqrt{KB} = (1.97 \times 10^{-2}) \times t^{0.2}$ Nm^{-1}. It is remarkable that both quantities scale as $\sim t^{0.2}$. This result implies that the temperature dependencies of G_0 and L are related through the scaling $B \sim t^{0.4}$.

Based on our experimental result, we conclude that the physical origin of the elasticity in the smectic phase is the effective surface tension $\gamma_{\mathrm{eff}} \simeq \sqrt{KB}$ of the FCDs. An analogous picture also holds for the elasticity of concentrated emulsions [69,70]. Furthermore, a similar relation to Equation (4) has also been observed for the onion phase in surfactant solutions which can be identified with FCD-II [71,72]. The proportionality coefficient C' for the onion phase is about $C' \approx 0.4$ – 1.2, which is fairly close to $C' = 0.456/1.97 \approx 0.23$ obtained for the FCDs. The relatively small value of C' for 8CB may be due to the polydispersity of the FCD size. We mentioned before that FCD-I can be observed not only in the thermotropic smectic phase but also in the lyotropic lamellar phase, while FCD-II appears only in the lyotropic systems. Formation of these textures depend both on the bending and the Gaussian moduli. As shown in Figure 1, the main geometrical difference between FCD-I with toroidal shape and FCD-II with spherical shape is the sign of the Gaussian curvature. Therefore, the energy cost for the deformation of FCDs, as determined by $\sqrt{KB}$, dominates the elasticity in these two systems in spite of the geometrical difference. We expect that the origin of elasticity is a universal feature that is common to different layered systems.

Equation (4) for the elastic modulus G_0 is different from the relation for the yield stress $\sigma_{\mathrm{y}} \sim K/L^2$ predicted by Horn and Kleman [35]. It should be noted, however, that G_0 in our case was measured within a linear regime, whereas the non-linear effect cannot be ignored in the estimation of yield stress. Generally, the shear modulus and the yield stress are not proportional to each other.

6. FCD Formation Induced by Shear Quench

In the previous sections, we mentioned that the FCDs induced by the unbinding of dislocations influence the viscoelasticity of the smectic phase. In this section, we explain our results in the non-equilibrium FCD formation when the system is subjected to shear stress-quench from high to low values [18]. Some studies on the FCD formation behavior under shear have been also reported [73,74].

Microscope images in Figure 12a,b show the time sequences of snap shots after quenching the system from $\sigma = 85$ to 0.1 Pa at $T = 33.0\,^{\circ}$C, and from $\sigma = 85$ to 1.5 Pa at $T = 31.0\,^{\circ}$C, respectively.

Comparing with the dynamic phase diagram in Figure 8, one sees that conditions of the stress-quench in (a) correspond to the FCD formation starting from the SmA_{II} phase, while (b) is the FCD growth inside the SmA_{I} phase. The brightness in the image represents the birefringence intensity.

Figure 12. Time sequence of polarized images after quenching the system at (**a**) $T = 33.0\,^{\circ}$C and (**b**) $T = 31.0\,^{\circ}$C. Shear stress was quenched (**a**) from $\sigma = 85$ Pa to 0.1 Pa, and (**b**) from $\sigma = 85$ Pa to 1.5 Pa, respectively. The horizontal direction is the flow direction. The FCDs are moving under the shear flow, and these images were picked out from the movies. The size of each image is 150 μm $\times$ 200 μm. The brightness of the image reflects the birefringence intensity. The scale bars correspond to 50 μm.

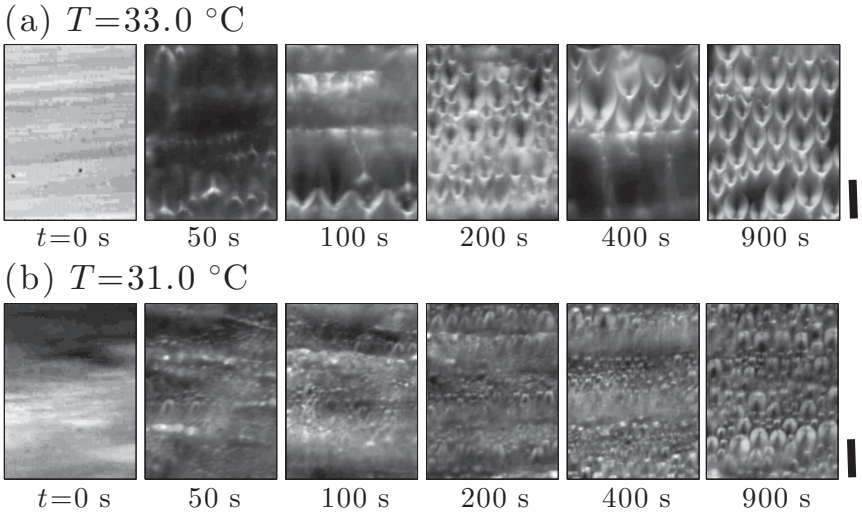

The microscope image at $t = 0$ s in Figure 12a is considerably bright because of the perpendicular orientation of the smectic layers [16,26,27]. After the stress-quench, the birefringence intensity quickly decays within a few seconds. Such a relaxation of the birefringence is caused by a flip of smectic layers from the perpendicular orientation to the parallel one. After the relaxation, a parabolic pattern appears around $t = 50$ s, showing the appearance of FCDs whose number density increases as a function of time. At $t = 0$ s in Figure 12b, on the other hand, the birefringence intensity is inhomogeneous. In later times, we see parabolic patterns as well as circular objects which are also FCDs with smaller sizes. There is a distribution of the FCD size, and the population of larger sizes increases with time. Around $t = 900$ s in both cases, there are large FCDs aligned along the flow direction.

Figure 13 shows the measured shear rate $\dot{\gamma}$ as a function of time t for stress-quenches at the same temperatures as in Figure 12. In Figure 13a for $T = 33.0\,^{\circ}$C, open symbols correspond to the stress-quench within the SmA_{II} phase, while closed symbols indicate the stress-quench from the SmA_{II} phase to the SmA_{I} phase. As drawn in the graph, the initial decay of $\dot{\gamma}$ can be fitted by a single exponential function which is called the first mode. On the other hand, when the system undergoes a non-equilibrium transition from the SmA_{II} to SmA_{I} phases, the shear rate exhibits a second decay mode as observed in Figure 13. In comparison with the microscope observations, we

notice that the second mode appears when the formation of FCDs starts. As the terminal stress is decreased, the fraction of the second mode gradually increases.

Figure 13. Log-log plot of the measured shear rate $\dot{\gamma}$ as a function of the elapsed time t after the stress-quench from $\sigma = 85$ Pa to $60, 40, 20, 10, 7, 5, 3, 2, 1.5, 1$ Pa (from upper to bottom) for (**a**) $T = 33.0\,^{\circ}$C and (**b**) $T = 31.0\,^{\circ}$C, respectively. Open and closed symbols correspond to the shear quench within the $\mathrm{SmA_{II}}$ phase and those from the $\mathrm{SmA_{II}}$ to the $\mathrm{SmA_{I}}$ phases, respectively. Data for (**b**) correspond to the stress-quench only within the $\mathrm{SmA_{I}}$ phase. Solid curves are the fits using a single exponential function with a characteristic time (first mode).

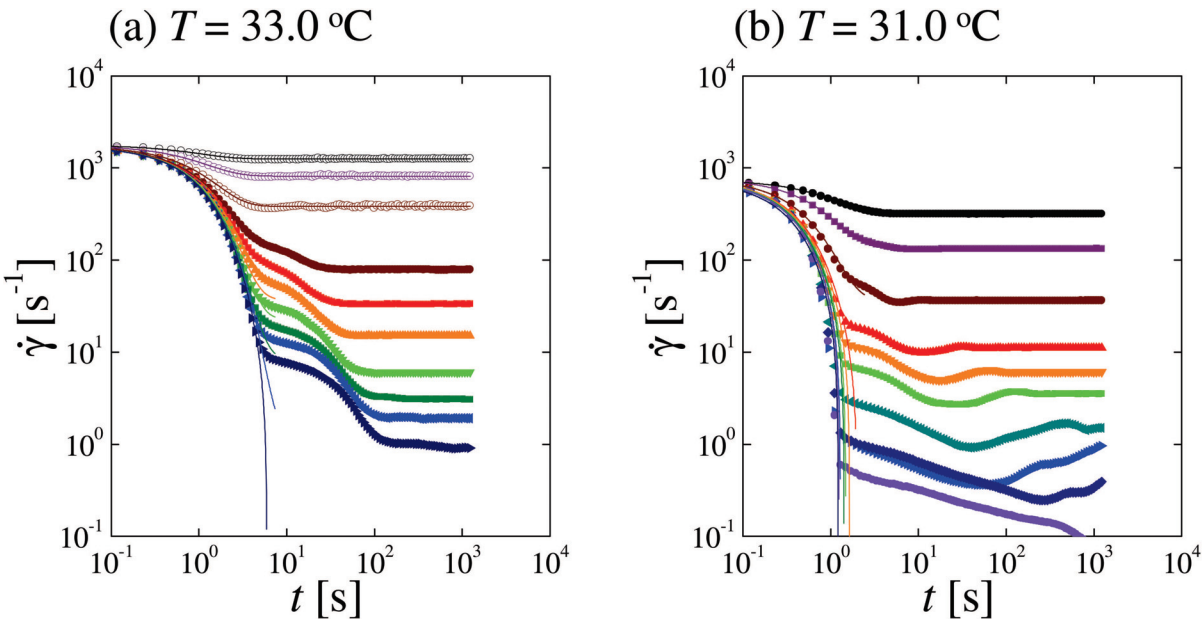

The obtained relaxation time for the first mode shows a slowing down at T_{SN}. Since the smectic layers in the $\mathrm{SmA_{II}}$ phase consist of a perpendicular orientation, the relaxation of the layer orientation accompanies a creation of edge dislocations before the FCD formation. It is known that the dislocations exhibit climb motion under shear stress [75,76]. The characteristic time for the climb motion of edge dislocation under stress is described by

$$\tau_{\mathrm{climb}} \sim \frac{d}{B\alpha b} \tag{5}$$

where d is the sample thickness, α the angle of the cone-plate shear cell, and b the mobility of the edge dislocation. Using typical values $d \approx 10$ μm, $B \approx 10^6$ Pa, $\alpha = 0.017$ rad, and $b \approx 10^{-8}$ m^{2}s/kg, we obtain $\tau_{\mathrm{climb}} \simeq 0.1$ s, which roughly corresponds to the experimentally observed first mode. Hence the first relaxation can be attributed to the climb motion of edge dislocation, and the slowing down close to T_{SN} suggests that the climb motion is affected by the unbinding of the dislocation. Moreover, a similar slowing down is observed for the second mode. The validity of Equation (5) can be further checked by systematically changing d and α.

When the system is quenched within the $\mathrm{SmA_{I}}$ phase at $T = 31.0\,^{\circ}$C as shown in Figure 13b, the shear rate shows anomalous behavior depending on the stress-quench depth. As the quench depth

is increased, the two decay modes are observed similar to those for $T = 33.0\,^{\circ}\mathrm{C}$. However, there is a distinct third mode in which the shear rate increases (rather than decreases) after the double relaxation. Since this third mode corresponds to the time region when the alignment of FCDs takes place, it can be attributed to the formation of oily streaks. The third mode becomes slower when the temperature is decreased. Notice that oily streaks consist of FCDs connected by edge dislocations as depicted in Figure 1b. Hence the alignment of FCDs is affected by the dislocation unbinding [46]. Slowing down of these characteristic times in the vicinity of the SN-transition indicates that the dislocation unbinding dominates not only the SN-transition but also the dynamics of textural defects.

Here we shall qualitatively discuss the eccentricity of FCDs under shear flow. In Figure 12, elliptic FCDs can be seen with minor axis aligned along the flow direction. The eccentricity of the FCDs is caused by the shear since the FCDs at quiescent state are mostly circles as shown in Figure 3. When the shear stress is quenched, the layers will first disassemble along the velocity gradient direction, and may reconnect with the slightly tilted state to accommodate FCDs with the large Burger vectors [18]. Asymmetry of the FCDs along the vorticity direction would reflect the tilted layers in the FCDs. Moreover, the dynamic coupling between the dislocation loops and the shear flow may induce the distortion of the FCDs since the dislocation loops can adapt to the applied shear stress [38]. Kleman *et al.* [47] and Meyer *et al.* [48] indeed pointed out that the interaction of the FCDs with dislocations causes the distortion of the FCD shape. Detailed analysis on the eccentricity would clarify how the dislocation loops attribute to the FCD structure.

Finally, it is interesting to point out the similarity between the FCD (FCD-I) formation from the perpendicularly oriented layers and the onion (FCD-II) formation from the planar lamellae with parallel orientation. In our experiment, the double decay modes in the shear rate at fixed shear stress indicate that the viscosity increases with two steps. Such a behavior is also observed in the shear-induced onion formation at fixed shear rate [31,32]. Especially, the creation of dislocations prior to the FCD formation coincidences with the previous observation in the lyotropic system in which the increase of the defect density is essential for the onion formation [33]. Hence the proliferation of the dislocations plays an important role in the structural development from the planar layers for both thermotropic and lyotropic cases. A qualitatively similar time evolution of the viscosity in these systems suggests that the structural development dominated by defects is an universal mechanism in the layered systems.

7. Conclusions and Outlook

In this review article, we have discussed that the following properties are closely related to the unbinding of the dislocation loops; (i) scaling behavior of the FCD size; (ii) temperature dependence of the yield stress; (iii) shear-induced SN-transition; (iv) physical origin of elasticity; and (v) FCD formation from the $\mathrm{SmA_{II}}$ phase. In particular, we have clarified the physical origin of the elasticity by comparing the scaling relations for the FCD size and the shear modulus. This result indicates that the defects significantly affect the smectic rheology. Furthermore, the similarity in the rheological properties between FCDs and onions is a noteworthy consequence.

It should be noted that the origin of the nonlinear rheological behavior still remains to be clarified. Both the yield stress and the plateau shear modulus, commonly used to characterize the elasticity, depend on the FCD size. The shear modulus originates from the effective surface tension, whereas the source of the yield stress is poorly understood. Nonetheless, the estimated yield stress using an empirical relation $\sigma_{\rm y} \sim K/L^2$ with $L \approx 10$ –10^2 μm roughly coincides with our experimental observation in Figure 6. More detailed study will shed light on the yield stress in the smectic phase. By the same token, the shear-induced onion formation in lyotropic systems is strongly concerned with interactions of defects such as dislocations and oily streaks [30,33]. Understanding the origin of the nonlinearity in the smectic phase with defects will also lead to the elucidation of the shear-induced structural transition.

We expect that the concept of structural rheology is applicable not only to the smectic phase but also to other structured fluids [2,3,5,77–79]. One of the most interesting systems, which could be tackled by a similar concept, is the rheology of the blue phase in cholesteric nematic liquid crystals. In this phase, the interaction between disclinations generates the yield stress, and anomalous rheological behavior is expected depending on the type of disclination networks [80,81]. Especially, shear-induced breakup and reconnection of the disclination network may induce a new non-equilibrium structure, as observed under electric field [82]. Soft glassy nature of the amorphous blue phase due to the disordered disclination network is also an interesting issue related to the defect-mediated rheology. Melting of the amorphous blue phase due to shear can be explained by the proliferation of disclinations as in the lyotropic hexagonal phase [23].

Thanks to the development in visualization technology and microrheology method, better understanding of the stress response due to meso-scale structures has become possible in recent years [22,83–87]. Simultaneous measurements of the viscoelasticity and image acquisition will give us a time resolved spatial information under shear [77–79,88]. These technological developments are expected to contribute to the fundamental science of non-equilibrium soft matter in the future.

Acknowledgments

We thank Y. Ishii for useful discussion, and T. Takahashi, H. Orihara, M. Imai, and Anton Paar Co. Ltd. for the use of their rheometer and the microscopy devices. This work was mainly supported by Grant-in-Aid for Scientific Research (B) grant No. 25287107 from MEXT of Japan. Shigeyuki Komura would like to further acknowledge support from the Grant-in-Aid for Scientific Research on Innovative Areas “Fluctuation & Structure” (grant No. 25103010), Grant-in-Aid for Scientific Research (C) grant No. 24540439 from the MEXT of Japan, and the JSPS Core-to-Core Program “International research network for non-equilibrium dynamics of soft matter”.

Author Contributions

Shuji Fujii performed the experiments. Shigeyuki Komura gave the concept on the structural rheology. Chun-Yi David Lu gave pertinent comments on the data analysis and interpretations. Shuji

Fujii and Shigeyuki Komura wrote the manuscript. All the authors discussed the results and analysis and commented on the manuscript.

Conflicts of Interest

The authors declare no conflict of interest.

References

1. Doi, M.; Edwards, S.F. *The Theory of Polymer Dynamics*; Clarendon Press: Oxford, UK, 1986.
2. Cohen-Addad, S.; Pitois, O.; Höhler, R. Flow in foams and flowing foams. *Annu. Rev. Fluid Mech.* **2013**, *45*, 241–267.
3. Lespiat, R.; Cohen-Addad, S.; Höhler, R. Jamming and flow of randomly close packed spherical bubbles: An analogy with granular materials. *Phys. Rev. Lett.* **2011**, *106*, 148320, doi:10.1103/PhysRevLett.106.148302.
4. Besseling, R.; Isa, L.; Weeks, E.R.; Poon, W.C.K. Quantitative imaging of colloidal flows. *Adv. Colloid Int. Sci.* **2009**, *146*, 1–17.
5. Mason, T.G. New fundamental concepts in emulsion rheology. *Curr. Opin. Colloid Int. Sci.* **1999**, *4*, 231–238.
6. Sollich, P.; Lequeux, F.; Hebraud, P.; Cates, M.E. Rheology of soft glassy materials. *Phys. Rev. Lett.* **1997**, *78*, 2020–2023.
7. Yamamoto, J.; Tanaka, H. Shear effects on layer undulation fluctuations of a hyper-swollen lamellar phase. *Phys. Rev. Lett.* **1995**, *74*, 932–935.
8. Tamate, R.; Yamada, K.; Vinals, J.; Ohta, T. Structural rheology of microphase separated diblock copolymers. *J. Phys. Soc. Jpn.* **2008**, *77*, 034802:1–034802:6.
9. Eskimergen, R.; Mortensen, K.; Vigild, M.E. Shear instability of a gyroid diblock copolymer. *Macromolecules* **2005**, *38*, 1286–1291.
10. Fredrickson G.H.; Bates, F.S. Dynamics of block copolymers: Theory and experiments. *Annu. Rev. Mater. Sci.* **1996**, *26*, 501–550.
11. Diat, O.; Roux, D. Effect of shear on dilute sponge phase. *Langmuir* **1995**, *11*, 1392–1395.
12. Porcar, L.; Hamilton, W.A.; Butler, P.D. Scaling of shear-induced transformations in membrane phases. *Phys. Rev. Lett.* **2002**, *89*, 168301, doi:10.1103/PhysRevLett.89.168301.
13. Cui, C.T.; Cummings, H.D.; Cochran, H.D. Molecular simulation of the transition from liquid like to solid like behavior in complex fluids confined to nanoscale gaps. *J. Chem. Phys.* **2001**, *114*, 7189, doi:10.1063/1.1359736.
14. Jabbarzadeh, A.; Harrowell, P.; Tanner, R.I. Crystal bridges, tetra tic order, and elusive equilibria: The role of structure in lubrication films. *J. Phys. Chem. B* **2007**, *111*, 11354–11365.
15. Jabbarzadeh, A.; Tanner R.I. Thin lubricant films confined between crystalline surfaces: Gold *versus* mica. *Tribol. Intern.* **2011**, *44*, 711–719.

16. Fujii, S.; Ishii, Y.; Komura, S.; Lu, C.-Y.D. Smectic rheology close to the smectic-nematic transition. *EPL* **2010**, *90*, 64001, doi:10.1209/0295-5075/90/64001.
17. Fujii, S.; Komura, S.; Ishii, Y.; Lu, C.-Y.D. Elasticity of smectic liquid crystals with focal conic domains. *J. Phys.: Condens. Matter* **2011**, *23*, 235105, doi:10.1088/0953-8984/23/23/235105.
18. Fujii, S.; Komura, S.; Lu, C.-Y.D. Structural rheology of focal conic domains: Stress-quench experiment. *Soft Matter* **2014**, *10*, 5289–5295.
19. Fujii, S. Structural rheology of smectic liquid crystalline phase. *J. Soc. Rheol. Jpn.* **2012**, *40*, 229–237. (In Japanese)
20. Jones, J.L.; McLeish, T.C.B. Rheological response of surfactant cubic phases. *Langmuir* **1995**, *11*, 785–792.
21. Radiman, S.; Toprakcioglu, C.; McLeish, T.C.B. Rheological study of ternary cubic phases. *Langmuir* **1994**, *10*, 61–67.
22. Mohammad, M.A.; Mezzenga, R. Particle tracking microrheology of lyotropic liquid crystals. *Langmuir* **2011**, *27*, 6171–6178.
23. Ramos, L.; Molino, F. Shear melting of a hexagonal columnar crystal by proliferation of dislocations. *Phys. Rev. Lett.* **2004**, *92*, 018301, doi:10.1103/PhysRevLett.92.018301.
24. Colby, R.H.; Ober, C.K.; Gillmor, J.R.; Connelly, R.W.; Duong, T.; Galli, G.; Laus, M. Smectic rheology. *Rheol. Acta* **1997**, *36*, 498–504.
25. Colby, R.H.; Nentwich, L.M.; Clingman, S.R.; Ober, C.K. Defect-mediated creep of structured materials. *Europhys. Lett.* **2001**, *54*, 269, doi:10.1209/epl/i2001-00305-x.
26. Panizza, P.; Archambault, P.; Roux, R. Effects of shear on the smectic-A phase of thermotropic liquid crystals. *J. Phys. II France* **1995**, *5*, 303–311.
27. Safinya, C.R.; Sirota, E.B.; Plano, R.J. Nematic to smectic-A phase transition under shear flow: A nonequilibrium synchrotron x-ray study. *Phys. Rev. Lett.* **1991**, *66*, 1986–1989.
28. Larson, R.G.; Wineyl, K.I.; Patel, S.S.; Watanabe, H.; Bruinsma, R. The rheology of layered liquids: Lamellar block copolymers and smectic liquid crystals. *Rheol. Acta* **1993**, *32*, 245–253.
29. Dhez, O.; Nallet, F.; Diat, O. Influence of screw dislocations on the orientation of a sheared lamellar phase. *Europhsy. Lett.* **2001**, *55*, 821–826.
30. Diat, O.; Roux, D.; Nallet, F. Effect of shear on a lyotropic lamellar phase. *J. Phys. II France* **1993**, *3*, 1427–1452.
31. Nettesheim, F.; Zipfel, J.; Olsson, U.; Renth, F.; Lindner, P.; Richtering, W. Pathway of the shear-induced transition between planar lamellae and multilamellar vesicles as studied by time-resolved scattering techniques. *Langmuir* **2003**, *19*, 3603–3618.
32. Fujii, S.; Koschoreck, S.; Lindner, P.; Richtering, W. Influence of a triblock copolymer on phase behavior and shear-induced topologies of a surfactant lamellar phase. *Langmuir* **2009**, *25*, 5476–5483.
33. Fujii, S.; Mitsumasu, D.; Isono, Y.; Richtering, W. Shear-induced onion formation of polymer-grafted lamellar phase. *Soft Matter* **2012**, *8*, 5381–5390.

34. Kosaka, Y.; Ito, M.; Kawabata, Y.; Kato, T. Lamellar-to-onion transition with increasing temperature under shear flow in a nonionic surfactant/water system. *Langmuir* **2010**, *26*, 3835–3842.
35. Horn, R.G.; Kleman, M. Observation on shear-induced textures and rheology of a smectic-A phase. *Ann. Phys.* **1978**, *3*, 229–234.
36. Meyer, C.; Asnacios, S.; Bourgaux, C.; Kleman, M. Rheology of lyotropic and thermotropic lamellar phases. *Rheol. Acta* **2000**, *39*, 223–233.
37. Meyer, C.; Asnacios, S.; Kleman, M. Universal properties of lamellar systems under weak shear. *Eur. Phys. J. E* **2001**, *6*, 245–254.
38. Lu, C.-Y.D.; Chen, P.; Ishii, Y.; Komura, S.; Kato, T. Non-linear rheology of lamellar liquid crystals. *Eur. Phys. J. E* **2008**, *25*, 91–102.
39. Basappa, G.; Suneel; Kumaran, V.; Nott, P.R.; Ramaswamy, S.; Naik, V.M.; Rout, D. Structure and rheology of the defect-gel states of pure and particle-dispersed lyotropic lamellar phases. *Eur. Phys. J. B* **1999**, *12*, 269–276.
40. Ramos, L.; Zapotocky, M.; Lubensky, T.C.; Weitz, D.A. Rheology of defect networks in cholesteric liquid crystals. *Phys. Rev. E* **2002**, *66*, 031711, doi:10.1103/PhysRevE.66.031711.
41. Medronho, B.; Migule, M.G.; Olsson, U. Viscoelasticity of a nonionic lamellar phase. *Langmuir* **2007**, *23*, 5270–5274.
42. Medronho, B.; Rodrigues, M.; Migule, M.G.; Olsson, U.; Schmidt, C. Shear-induced defect formation in a nonionic lamellar phase. *Langmuir* **2010**, *26*, 1477–1481.
43. Kleman, M.; Lavrentovich, O.D. *Soft Matter Physics: An Introduction*; Springer: Berlin/Heidelberg, Germany, 2002.
44. Williams, C.E.; Kleman, M. Dislocations, grain boundaries and focal conics in smectic-A. *J.Phys.* **1975**, *36*, C1:315–C1:320.
45. Boltenhagen, P.; Kleman, M.; Lavrentovich, O.D. Freeze-fracture observations in the L_α phase of a swollen surfactant in the vicinity of the L_3 and the L_1 phase transitions *J. Phys. II France* **1994**, *4*, 1439–1448.
46. Boltenhagen, P.; Lavrentovich, O.D.; Kleman, M. Oily streaks and focal conic domains in L_α lyotropic liquid crystals. *J. Phys. II France* **1991**, *1*, 1233–1252.
47. Kleman, M.; Meyer, C.; Nastishin, Y.A. Imperfections in focal conic domains: The role of dislocations. *Philos. Mag.* **2006** *86*, 4439–4458.
48. Meyer, C.; Nastishin, Y.; Kleman, M. Kinked focal conic domains in a SmA. *Mol. Cryst. Liq. Cryst.* **2007** *477*, 43/[537]–53/[547].
49. Holyst, R. Dislocations in lamellar and liquid crystal films: Equilibrium location, edge profiles, and phase transitions. *Phys. Rev. Lett.* **1994**, *26*, 4097–4100.
50. Helfrich, W. Defect model of the smectic-A-nematic phase transition. *J. Phys.* **1978**, *39*, 1199–1208.
51. Benzekri, M.; Marcerou, J.P.; Nguyen, H.T.; Rouillon, J.C. Critical behavior of the layer compressional elastic constant B at the smectic-A-nematic phase transition. *Phys. Rev. B* **1990**, *41*, 9032–9037.

52. Benzekri, M.; Claverie, T.; Marcerou, J.P.; Rouillon, J.C. Nonvanishing of the layer compressional elastic constant at the smectic-A-to-nematic phase transition: A consequence of Landau-Peierls instability? *Phys. Rev. Lett.* **1992**, *68*, 2480–2483.
53. Nelson, D.R.; Torner, J. Bond-orientational order, dislocation loops, and melting of solids and smectic-A liquid crystals. *Phys. Rev. B* **1981**, *24*, 363–387.
54. Moreau, P.; Navailles, L.; Giermanska-Kahn, J.; Mondain-Monval, O.; Nallet, F.; Roux, D. Dislocation-loop-mediated smectic melting. *EPL* **2006**, *73*, 49–54.
55. De Gennes, P.G.; Prost, J. *The Physics of Liquid Crystals*; Clarendon Press: London, UK, 1993.
56. Davidov, D.; Safinya, C.R.; Kaplan, M.; Dana, S.S.; Schaetzing, R.; Birgeneau, R.J.; Litster, J.D. High-resolution x-ray and light-scattering study of critical behavior associated with the nematic-smectic-A transition in 4-cyano-4'-octylbiphenyl *Phys. Rev. B* **1979**, *19*, 1657–1663.
57. Herschel, W.H.; Bulkley, B. Measurement of consistency as applied to rubber-benzene solution. *Proc. Am. Assoc. Test Mater.* **1926**, *26*, 621–633.
58. Moller, P.C.F.; Mewis, J.; Bonn, D. Yield stress and thixotropy: On the difficulty of measuring yield stresses in practice. *Soft Matter* **2006**, *2*, 274–283.
59. Moller, P.; Fall, A.; Chikkadi, V.; Derks, D.; Bonn, D. An attempt to categorize yield stress fluid behavior. *Philos. Trans. R. Soc. A* **2009**, *367*, 5139–5155.
60. Zywocinski, A.; Picano, F.; Oswald, P.; Geminard, J.C. Edge dislocation in a vertical smectic-A film: Line tension *versus* temperature and film thickness near the nematic phase. *Phys. Rev. E* **2000**, *62*, 8133–8140.
61. Negita, K.; Kaneko, H. Rheodielectric study on shear-induced structural change in the smectic-A phase of 4-n-octyl-4'-cyanobiphenyl (8CB). *Phys. Rev. E* **2009**, *80*, 011705, doi:10.1103/PhysRevE.80.011705.
62. Bruinsma, R.; Rabin, Y. Shear-flow enhancement and suppression of fluctuations in smectic liquid crystals. *Phys. Rev. Lett.* **1992**, *45*, 994–1008.
63. Goulian, M.; Milner, S.T. Shear alignment and instability of smectic phases. *Phys. Rev. Lett.* **1995**, *74*, 1775–1778.
64. Ramaswamy, S. Shear-induced collapse of the dilute lamellar phase. *Phys. Rev. Lett.* **1992**, *69*, 112–115.
65. Porcar, L.; Warr, G.G.; Hamilton, W.A.; Butler, P.D. Shear-induced collapse in a lyotropic lamellar phase. *Phys. Rev. Lett.* **2005**, *95*, 078302, doi:10.1103/PhysRevLett.95.078302.
66. Berghausen, J.; Zipfel, J.; Lindner, P.; Richtering, W. Shear-induced orientations in a lyotropic defective lamellar phase. *Europhys. Lett.* **1998**, *43*, 683–689.
67. van der Linden, E.; Droege, J.H.M. Deformability of lamellar droplets. *Physica A* **1993**, *193*, 439–447.
68. van der Linden, E.; Hogervorst, W.T.; Lekkerkerker, H.N.W. Relation between the size of lamellar droplets in onion phases and their effective surface tension. *Langmuir* **1996**, *12*, 3127–3130.

69. Princen, H.M.; Kiss, A.D. Rheology of foams and highly concentrated emulsions: III. Static shear modulus. *J. Colloid Interface Sci.* **1986**, *112*, 427–437.
70. Princen, H.M.; Kiss, A.D. Rheology of foams and highly concentrated emulsions: IV. An experimental study of the shear viscosity and yield stress of concentrated emulsions. *J. Colloid Interface Sci.* **1989**, *128*, 176–187.
71. Panizza, P.; Roux, D.; Vuillaume, V.; Lu, C.-Y.D.; Cates, M. Viscoelasticity of the onion phase. *Langmuir* **1996**, *12*, 248–252.
72. Leng, J.; Nallet, F.; Roux, D. Anomalous elasticity of an ordered lamellar liquid foam. *Eur. Phys. J. E* **2001**, *4*, 337–342.
73. Chatterjee, S.; Anna, S.L. Formation and ordering of topological defect arrays produced by dilatational strain and shear flow in smectic-A liquid crystals. *Phys. Rev. E* **2012**, *85*, 011701, doi:10.1103/PhysRevE.85.011701.
74. Chatterjee, S.; Anna, S.L. Interaction of toroidal focal conic defects with shear flow. *Soft Matter* **2012**, *8*, 2698–2705.
75. Oswald, P.; Kleman, M. Experimental evidence for helical instability of screw dislocation lines in a smectic-A phase. *J. Phys. Lett. (France)* **1984**, *45*, L319–L328.
76. Oswald, P.; Kleman, M. Lubrication theory of smectic-A phases. *J. Phys. Lett. (France)* **1982**, *43*, L411–L415.
77. Aida, K.; Na, Y.H.; Nagaya, T.; Orihara, H. Droplet coalescence process under electric fields in an immiscible polymer blend. *Phys. Rev. E* **2010**, *82*, 031805, doi:10.1103/PhysRevE.82.031805.
78. Aida, K.; Na, Y.H.; Nagaya, T.; Orihara, H. Storage shear modulus of columnar structure formed in an immiscible polymer blend under electric fields. *Phys. Rev. E* **2009**, *80*, 041807:1–041807:5.
79. Orihara, H.; Takikawa, Y. Brownian motion in shear flow: Direct observation of anomalous diffusion. *Phys. Rev. E* **2011**, *84*, 061120:1–061120:5.
80. Henrich, O.; Stratford, K.; Cates, M.; Marenduzzo, D. Structure of blue phase III of cholesteric liquid crystals. *Phys. Rev. Lett.* **2011**, *106*, 107801:1–107801:4.
81. Henrich, O.; Stratford, K.; Coveney, P.V.; Cates, M.; Marenduzzo, D. Rheology of cubic blue phases. *Soft Matter* **2013**, *9*, 10243–10256.
82. Kitzerow, H.-S.; Crooker, P.P.; Heppke, G. Line shapes of filed-induced blue-phase III selective reflections. *Phys. Rev. Lett.* **1991**, *67*, 2151–2154.
83. Mason, T.G.; Weitz, D.A. Optical measurement of frequency-dependent linear viscoelastic moduli of complex fluids. *Phys. Rev. Lett.* **1995**, *74*, 1250–1253.
84. Crocker, J.C.; Valentine, M.T.; Weeks, E.; Gisler, T.; Kaplan, P.D.; Yodh, A.G.; Weitz, D.A. Two-point microrheology of inhomogeneous soft materials. *Phys. Rev. Lett.* **2000**, *85*, 888–891.
85. Sonn-Segev, A.; Groswasser, A.B.; Diamant, H.; Roichman, Y. Response of a compilex fluid at intermediate distances. *Phys. Rev. Lett.* **2014**, *112*, 088301:1–088301:5.

86. Kimura, Y.; Mizuno, D. Microrheology of a swollen lyotropic lamellar phase. *Mol. Cryst. Liq. Cryst.* **2007**, *478*, 759–769.
87. Yamamoto, N.; Ichikawa, M.; Kimura, Y. Local mechanical properties of a hyperswollen lyotropic lamellar phase. *Phys. Rev. E* **2010**, *82*, 021506, doi:10.1103/PhysRevE.82.021506.
88. Dutta, S.K.; Mbi, A.; Arevalo, R.C.; Blair, D.L. Development of a confocal rheometer for soft and biological materials. *Rev. Sci. Instrum.* **2013**, *84*, 063702:1–063702:7.

The Design and Investigation of Nanocomposites Containing Dimeric Nematogens and Liquid Crystal Gold Nanoparticles with Plasmonic Properties Showing a Nematic-Nematic Phase Transition (N_u-N_x/N_{tb})

Maria-Gabriela Tamba, Chih Hao Yu, Bai Jia Tang, Christopher Welch, Alexandra Kohlmeier, Christopher P. Schubert and Georg H. Mehl

Abstract: The construction of liquid crystal compositions consisting of the dimeric liquid crystal, **CB_C9_CB** (cyanobiphenyl dimer = 1",9"-bis(4-cyanobiphenyl-4'-yl)nonane), and the range of nematic systems is explored. The materials include a laterally functionalized monomer, which was used to construct a phase diagram with **CB_C9_CB**, as well as one laterally linked dimer liquid crystal material and two liquid crystal gold nanoparticle (LC-Au-NPs) systems. For the Au-NP-LCs, the NP diameters were varied between ~3.3 nm and 10 nm. Stable mixtures that exhibit a nematic-nematic phase transition are reported and were investigated by POM (polarizing optical microscopy), DSC (differential scanning calorimetry) and X-ray diffraction studies.

Reprinted from *Materials*. Cite as: Tamba, M.; Yu, C.H.; Tang, B.J.; Welch, C.; Kohlmeier, A.; Schubert, C.P.; Mehl, G.H. The Design and Investigation of Nanocomposites Containing Dimeric Nematogens and Liquid Crystal Gold Nanoparticles with Plasmonic Properties Showing a Nematic-Nematic Phase Transition (N_u-N_x/N_{tb}). *Materials* **2014**, *7*, 3494–3511.

1. Introduction

The investigation of materials that show nematic-nematic transitions has increased considerably over the last few years since the first report on such a phase behaviour in dimeric liquid crystals [1]. This is due to the scientific novelty of a new nematic phase, different in organisation to that of the classical uniaxial nematic (Nu) phase. Additionally, there is considerable interest in the structure of this low temperature nematic phase, as its mode of assembly is not yet fully understood. Hence, it has been identified, rather cautiously, as N_x, as a twist-bent nematic phase, N_{tb}, or as a heliconical nematic phase [2–10]. These issues of phase assignment still need to be clarified, but they raise the more general question of whether a number of different thermotropic nematic phases, positioned below the classical N phase, do exist in organic or inorganic materials [11–13]. Beyond the interest in the fundamental issues of phase structure, the observation that the low temperature nematic phase in dimers, which in this contribution is termed N_x, simply because its structure has not yet been fully clarified, is characterized by the spontaneous formation of chiral domains. This is of technological relevance, as this property can, in principle, be used to either stabilize or to enhance chirality in already chiral systems, such as TGB (twist grain boundary) arrays, blue phases or to induce chirality in plasmonic metal nanoparticle systems [14]. Here, chirality promises a wide range of novel optical effects [15,16]. Moreover, these LC nanoparticle (NPs) systems are potentially extremely interesting for LC applications, as it has been shown that nanoparticles dispersed in liquid crystals can result in enhanced switching behaviour. It has been reported that electro-optical switching in the microsecond

regime is possible in the N_x phase [9]. The first step to realize such advantageous properties is to explore the miscibility of metal nanoparticles in dimeric systems forming the N_x phase. This is the subject matter of this report. Here, we report the first miscibility study of gold nanoparticles (Au-NPs) in dimers with a nematic-nematic phase transition.

Though a number of NP systems have been functionalized with LC groups in order to enhance their solubility in liquid crystals, the number of calamitic nematogenic systems is very low, and the number of those that exhibit LC behaviour is very small indeed, as discussed in recent reviews [16–19].

2. Results and Discussion

As a starting point for the miscibility studies, the dimer, **CB_C9_CB** (cyanobiphenyl dimer), shown in Figure 1, was used, as the structure of the N_x phase in this material has been investigated intensively [1,7–10,20]. As LC-Au-NP systems, LC nanoparticle materials reported earlier were used [21–24]. As the LC-Au-NP materials to be investigated employ laterally connected mesogenic groups, different from those that have been shown to exhibit N_x phase behaviour, the design of the N_x phase forming composites was approached in a systematic study. In the first step, mixtures with a laterally functionalized nematogen, the liquid crystal, 4′-undecyloxybiphenyl-4-yl-4-octyloxy-2-(pent-4-en-1-yloxy) benzoate (**1**), shown in Figure 1, were performed in order to evaluate the limit of the phase stability in the N_x phase in such a mesogenic system. For that, a full phase diagram was constructed. A laterally functionalized mesogen was selected, due to the tendency of these systems to show nematic phase behaviour. In the second step, specific compositions of **CB_C9_CB** with a dimeric system containing siloxane groups (**2**) were prepared to gain additional knowledge in order to optimize the composition range for the mixtures with the LC-NPs. In the final step, compositions were prepared with LC gold particles. Here, liquid crystal Au-NPs were used, which have been reported earlier, using structures, very close to those of the laterally connected mesogen investigated initially. Two systems were explored.

In the first system, the particle size is as about 3.3 nm (Material **3**), and in the second material, the particle diameter is about 10 nm (Material **4**). The chemical structures of the investigated systems are shown in Figure 1.

The addition of the corresponding liquid crystal, **1 (**4′-undecyl oxybiphenyl-4-yl 4-octyloxy-2-(pent-4-en-1-yloxy) benzoate), which has a positive dielectric anisotropy, Δε, to the dimer, **CB_C9_CB**, allows the construction of phase diagrams. Though the structures of **1** have been discussed earlier as a precursor for mesomorphic silsesquioxanes and carbosilazane dendrimers, detailed LC properties have not yet been discussed [25,26]. Compound **1** exhibits an enantiotropic nematic phase; typical defect textures are shown in Figure 2.

Figure 1. Chemical structures of the materials investigated. **CB_C9_CB**, cyanobiphenyl dimer.

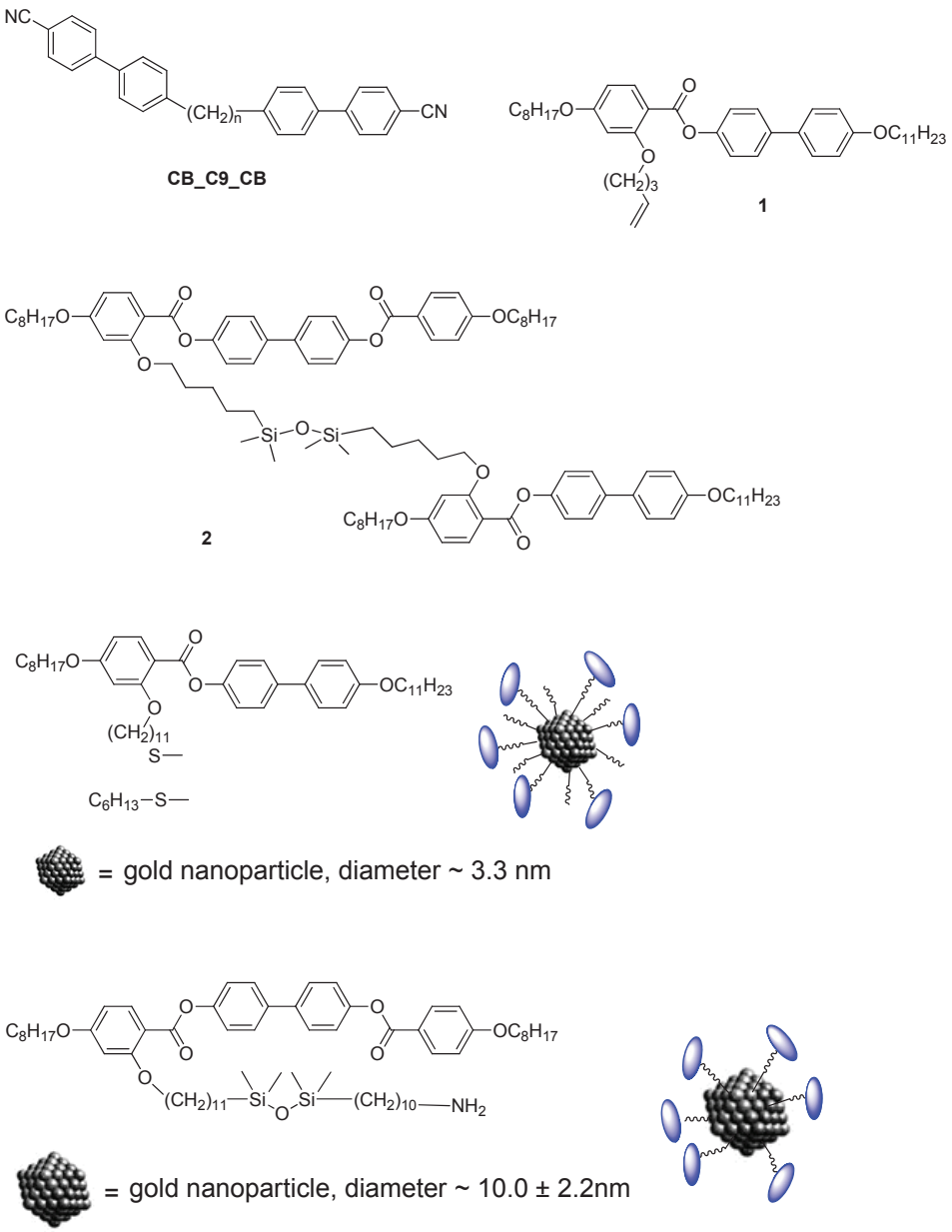

Figure 2. Textures of the nematic phase of **1** between untreated glasses observed between crossed polarizers. (**a**) N phase at 25 °C; (b) N phase at 50 °C.

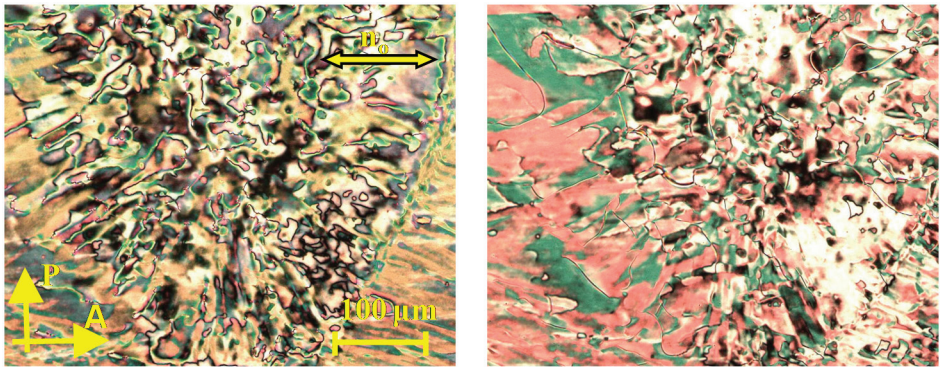

(**a**) (**b**)

DSC measurements were conducted at varying heating and cooling rates on samples of Compound **1**. The transition temperatures and the corresponding enthalpy values of Compound **1** taken from the heating and cooling DSC scan (10 K/min, see Figure 3) are given below.

Figure 3. DSC studies (10 K/min) of Compound **1**; values are taken from the first heating and cooling scans. Cr 54.5 (71.14) N 73.3 (2.39) Iso (°C); Iso 71.8 (−2.59) N 2.06 (−1.84) X −24.6 (−6.78) Cr (°C); the numbers in brackets are the transition enthalpies in $J \cdot g^{-1}$.

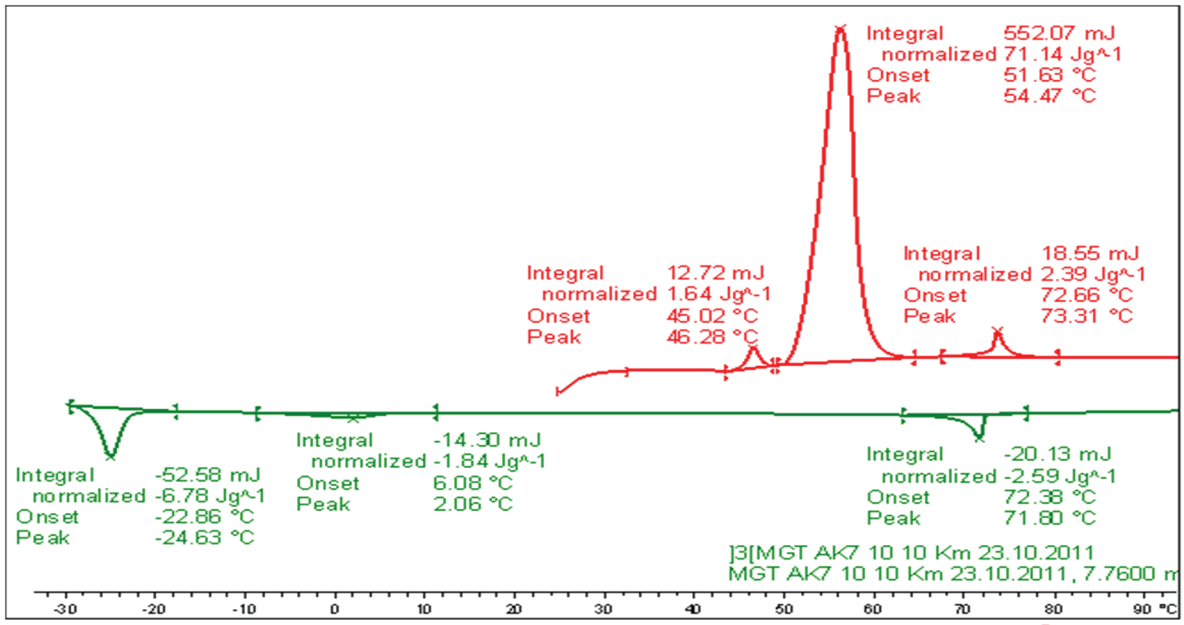

A systematic investigation of the binary mixtures (w/w) of Material **1** with positive dielectric anisotropy with the cyanobiphenyl dimer, **CB_C9_CB** (5%–50% (w/w)), was carried out. All binary mixtures exhibit liquid crystalline behaviour. The mesophase types and the transition temperatures for these mixtures are given in Table 1. All compounds exhibit nematic phases. The mesophases of the mixtures were characterized by their optical textures, calorimetric studies and by X-ray investigations. No additional layer-structured mesophases are induced in the mixed phase region of this binary systems, *i.e.*, only nematic phases could be found. Remarkably, for the system, **CB_C9_CB**, more than 40% (w/w) of **1** can be added before the N_X phase is lost (see Figure 4). However, it is noted that the N_x phase stability is strongly reduced upon adding **1**, *i.e.*, for the system with 30% (w/w) of **1** in **CB_C9_CB** (**MGTP201**), a reduction of the transition temperature of the high-temperature N phase to the low-temperature N_x phase of about 54 °C could be found. In other words, the nematic N_X phase transition occurs on cooling at 62.1 °C. Moreover, the stability of the enantiotropic (that is thermodynamically stable) N_x phase is lost upon adding between 5% (w/w) to 10% (w/w) of the monomeric Compound **1**.

Table 1. Transition temperatures of the binary mixtures (w/w) of **1** with dimer **CB_C9_CB**, taken from the first DSC heating and cooling scans (10 K·min^{-1}). Cr = Crystallie; N = Nematic; Nx = Nematic (x or tb); Iso = isotropic liquid.

Binary Mixtures	1 % (w/w)	CB_C9_CB % (w/w)	Transition Temperatures (°C)
CB_C9_CB	0	100	Cr 85.2 N_x 107.3 N 124.2 Iso; Iso 122.4 N 104.9 N_x 40.5 Cr
MGTP205	5	95	Cr 69.9 N_X 95.8 N 112.8 Iso; Iso 111.3 N 92.9 N_X 35.3 Cr
MGTP204	10	90	Cr 85.8 N 108.5 Iso; Iso 107.2 N 86.7 N_X 31.1 Cr
MGTP200	15	85	Cr 83.7 N 105.2 Iso; Iso 104.5 N 77.8 N_X 31.1 Cr
MGTP206	20	80	Cr 85.2 N 101.1 Iso; Iso 97.2 N 72.7 N_X 35.3 Cr
MGTP207	25	75	Cr 84.7 N 96.1 Iso; Iso 90.9 N 70.0 N_X 29.9 Cr
MGTP201	30	70	Cr 69.6 N 90.9 Iso; Iso 86.5 N 62.1 N_X 34.2 Cr
MGTP202	40	60	Cr 68.4 N 83.8 Iso; Iso 80.3 N 51.4 N_X 34.3 Cr
MGTP203	50	50	Cr 66.5 N 78.7 Iso; Iso 74.6 N 31.7 Cr
1	100	0	Cr 54.5 N 73.3 Iso; Iso 71.8 N 2.06 X −24.6 Cr

Figure 4. Transition temperatures of the binary mixtures of dimer **CB_C9_CB** in **1**, taken from the first DSC heating and cooling scans (10 K·min^{-1}); the phase diagram of the transition temperatures of these mixtures, taken from the first DSC (**a**) heating scans (10 K·min^{-1}) and (**b**) cooling scans (10 K·min^{-1}).

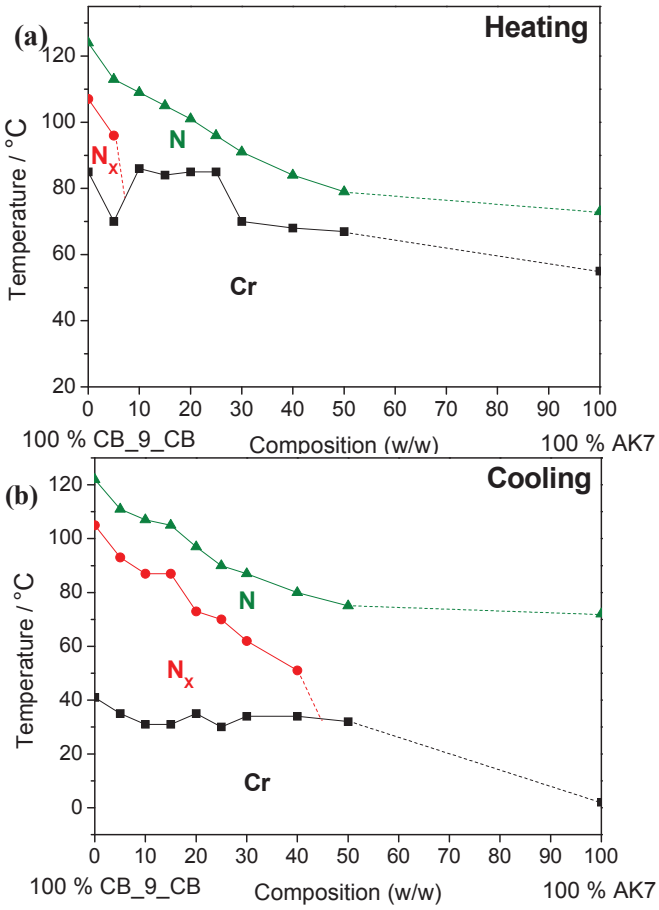

As a representative example the mesophase behaviour of the binary mixture, **MGTP201**, with 30% (w/w) **1** in **CB_C9_CB** will be described in more detail. The POM studies and the calorimetric investigations evidenced the existence of an N–N_x phase sequence with textural and structural features similar to the pure cyanobiphenyl dimer, **CB_C9_CB**.

The high-temperature phase could be easily identified as a nematic phase by its characteristic texture. At the phase transition to the NX phase, a fine structured rope texture or fan-like texture develops, as shown in Figure 5a,b. The sheared texture contains non-specific features with homeotropically oriented regions and some oily streaks, as shown in Figure 5c.

Figure 5. Textures of the **MGTP201** (30% (w/w) **1** in 70% **CB_C9_CB**) between untreated glasses observed in the same region on cooling between crossed polarizers: (**a**) schlieren texture in the high-temperature nematic N phase at 85 °C; (**b**) fan-like texture accompanied by rope texture developing in the low-temperature N_x phase at 48 °C and (**c**) sheared texture of the low-temperature N_x phase at 48 °C.

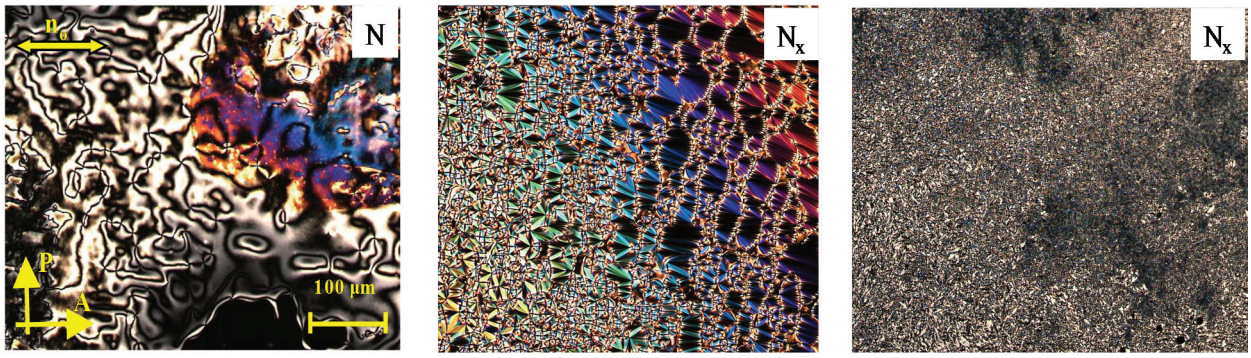

(**a**) (**b**) (**c**)

DSC measurements were conducted at different heating and cooling rates on samples of the binary mixture, **MGTP201**, consisting of a mixture of 30% (w/w) **1** in **CB_C9_CB**. The transition temperatures and the corresponding enthalpy values of the compound **MGTP201** taken from the heating and cooling DSC scans recorded at 10 K/min (see Figure 6) are given below.

X-ray measurements were performed whilst applying a magnetic field of about 0.5 T to orient samples of the composition, **MGTP201**. The results confirm the presence of two nematic phases. The X-ray patterns in the high-temperature nematic state show the known features of the XRD patterns of the nematic phases of the pure cyanobiphenyl dimer, *i.e.*, diffuse crescent-like scattering on the meridian in the small angle region, parallel to the orienting magnetic field, and diffuse crescent-like scattering on the equator in the wide angle region. The diffractograms collected at 77 °C are shown in Figure 7a,b. Similar to the pure cyanobiphenyl dimer, this pattern does not change significantly at the phase transition to the low-temperature N_x phase recorded at 50 °C and shown in Figure 7c,d. There is no indication of a transition to a smectic phase, even though the textural features, such as the fan-shaped texture and or polygonal textures, would suggest, initially, the formation of a smectic-like structure.

It is noted that an addition of 15%–20% (w/w) of **1** to **CB_C9_CB** results in a decrease of the isotropisation temperature by ~20–24 °C, when compared to pure **CB_C9_CB**.

Based on these successful miscibility studies with a monomer, the work was extended to the dimeric system, **2**, which is characterized by a very wide nematic range and by having features, such as the central siloxane group, that are present in one of the to be investigated LC gold nanoparticle systems. Compound **2** is a dimeric non-symmetric system, whose synthesis has been reported earlier [27]. Material **2** exhibits a wide enantiotropic nematic phase; a typical POM texture is shown in Figure 8. The nematic phase stability of **2** ranges on heating form −8.8 to 107.6 °C. The material was synthesized according to a reported method, and the results of the investigations of the LC phase behaviour are shown below [27].

Figure 6. DSC studies (10 K/min) of the binary mixture, **MGTP201** (30% (w/w) **1** in 70% (w/w) **CB_C9_CB**); the values are taken from the second heating and cooling scans. Cr 69.6 (33.05) N 90.9 (1.46) Iso; Iso 86.5 (−2.54) N 62.1 N_x (−1.86) 34.2 (−23.73) Cr (°C); the numbers in brackets are the transition enthalpies in $J \cdot g^{-1}$.

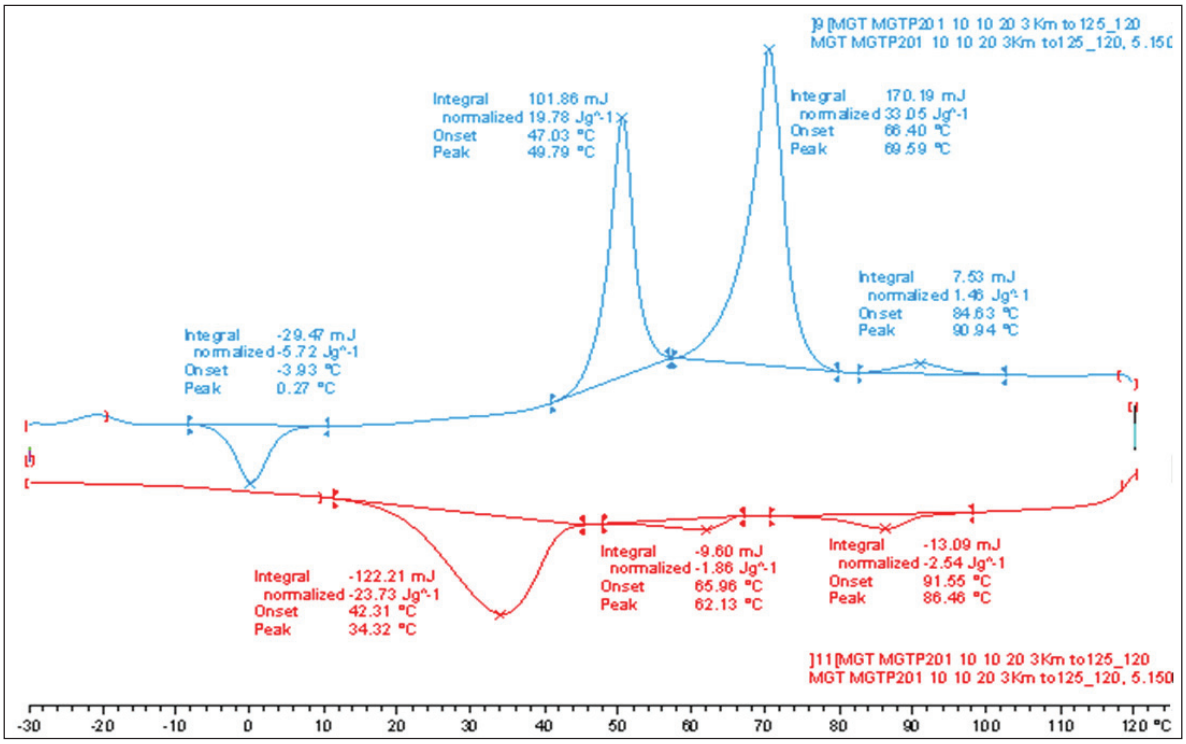

Figure 7. XRD patterns of an aligned sample of the mixture, **MGTP201**, in the magnetic field on cooling. (**a**,**b**) XRD patterns of the nematic phase at 77 °C: (**a**) original pattern; (**b**) the same XRD pattern, but the intensity of the isotropic liquid is subtracted; (**c**,**d**) XRD patterns of the N_x at 50 °C: (**c**) original pattern; (**d**) the same XRD pattern, but the intensity of the isotropic liquid is subtracted.

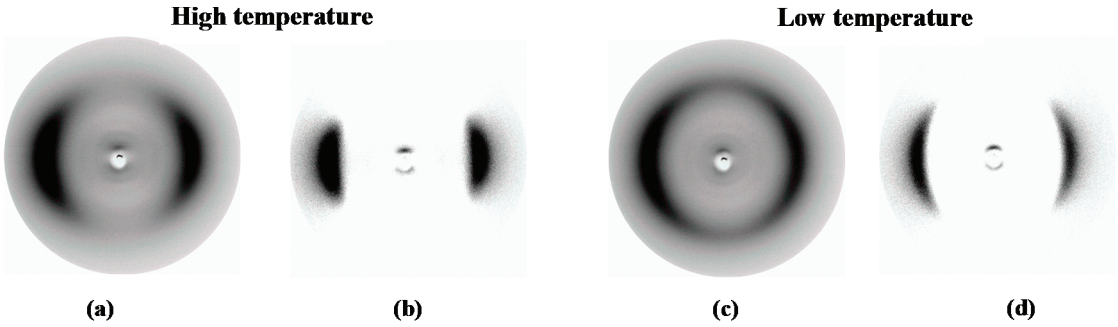

Figure 8. Textures of the nematic phase of **2** between untreated glasses observed between crossed polarizers.

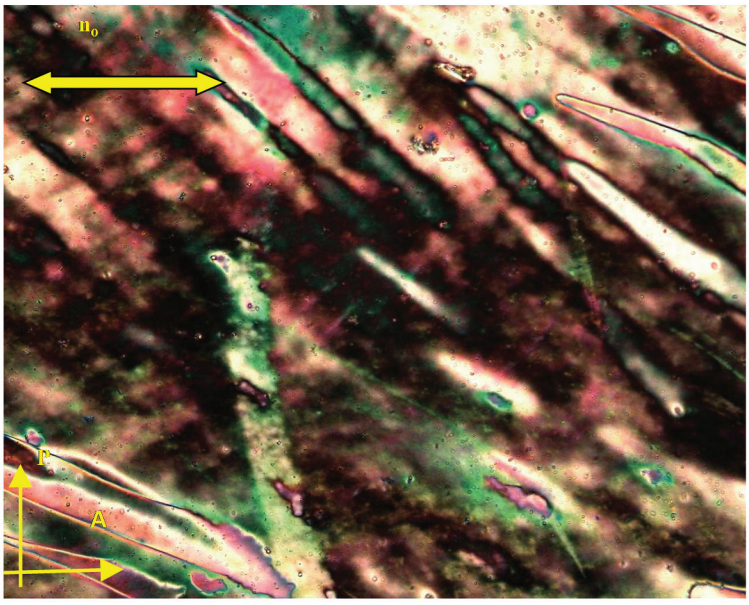

DSC measurements were conducted with different heating and cooling rates on samples of Compound **2**. The transition temperatures and the corresponding enthalpy values of Compound **2** taken from the heating and cooling DSC scans recorded at 10 K/min, shown in Figure 9, are given below.

An investigation of the selected composition of the binary mixtures (w/w) of Material **2** with a positive dielectric anisotropy with the cyanobiphenyl dimer, **CB_C9_CB**, at concentrations of 15% and 25% (w/w) evidenced that all of the compositions exhibit a nematic phase behaviour. The mesophase types and transition temperatures for these mixtures are given in Table 2. The mesophases of the mixtures were characterized by their optical defect textures, calorimetric studies and by X-ray investigations. No additional layer- structured mesophases are induced in the mixed phase region of this binary systems, *i.e.*, only nematic phases could be found.

It is noted that the recorded systems show monotropic N_x phase behaviour; or in other words, the N_x phase is a meta-stable phase, which can be obtained upon cooling from the nematic (N) phase. As a representative example of the mesophase behaviour, the results for the binary mixture, **MGTP208**, with 15% (w/w) **2** in **CB_C9_CB** will be described in more detail. The POM studies and the calorimetric investigations evidenced the existence of an N–N_x phase sequence with textural and structural features similar to the pure cyanobiphenyl dimer, **CB_C9_CB**. The high-temperature phase could be easily identified as a nematic phase by its characteristic texture; a typical schlieren texture is shown in Figure 10a. At the phase transition to the N_X phase, a fan-shaped texture develops. This is shown in Figure 10b. The sheared texture, shown in Figure 10c, contains non-specific features and some oily streaks.

Figure 9. DSC studies (10 K/min) of Compound **2**, the first heating and cooling scan. The values are taken from the second heating and cooling scans. The transitions are: N 107.6 (2.22) Iso (°C); Iso 106.2 (−2.03) N −14.0 Tg (°C); the numbers in brackets are the transition enthalpies in $J \cdot g^{-1}$.

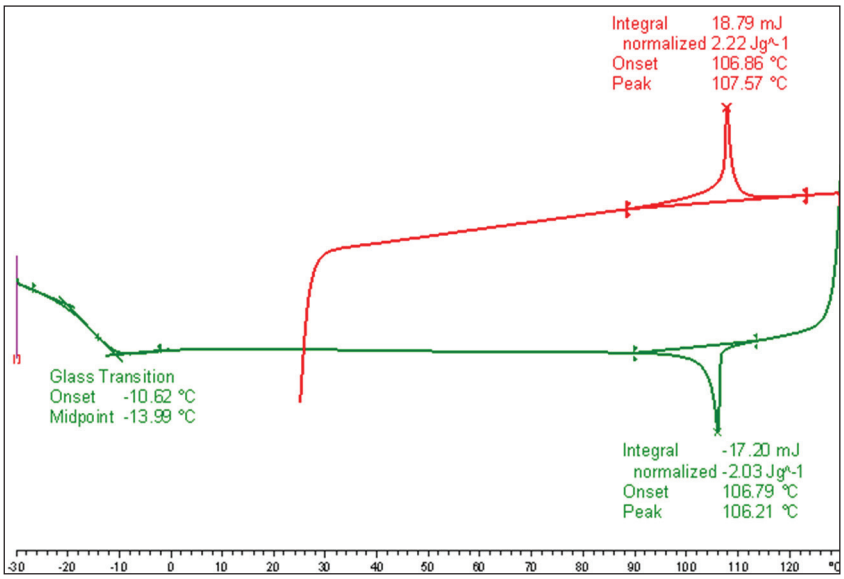

Table 2. Transition temperatures of the binary mixtures (w/w) of **2** with the dimer, **CB_C9_CB**, taken from the first DSC heating and cooling scans (10 $K \cdot min^{-1}$).

Binary mixtures	2 % (w/w)	CB_C9_CB % (w/w)	Transitions temperatures (°C)
CB_C9_CB	0	100	Cr 85.2 N_x 107.3 N 124.2 Iso; Iso 122.4 N 104.9 N_x 40.5 Cr
MGTP208	15	85	Cr 86.7 N 112.0 Iso; Iso 110.3 N 88.1 N_X 41.4 Cr
MGTP209	25	75	Cr 86.7 N 108.8 Iso; Iso 106.4 N 83.7 N_X 41.2 Cr
2[a]	100	0	Tg −8.8 N 107.6 Iso; Iso 106.3 N −14 Tg

[a] Values for the heating scan are taken from the second heating scan.

Figure 10. Textures of the **MGTP208** (15% (w/w) **2** in 85% (w/w) **CB_C9_CB**) between untreated glass slides, observed in the same region upon cooling between crossed polarizers: (**a**) schlieren texture in the high-temperature nematic N phase at 100 °C; (**b**) fan-like texture of the low-temperature N_x phase at 70 °C and (**c**) sheared texture of the low-temperature N_x phase at 70 °C.

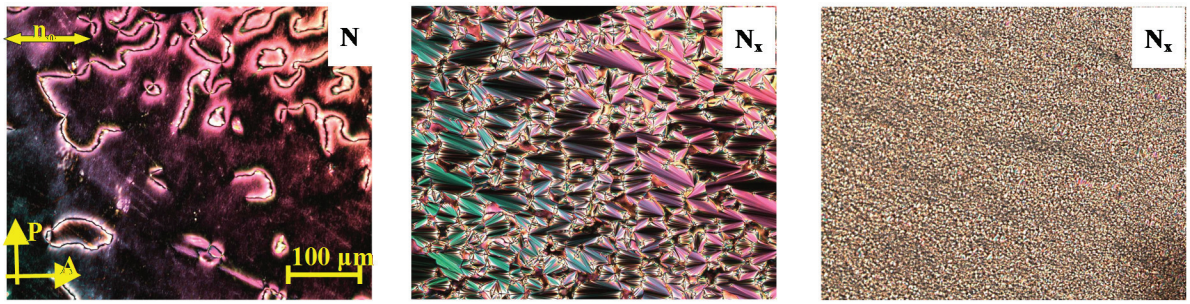

(**a**) (**b**) (**c**)

DSC measurements were conducted at different heating and cooling rates of samples of the binary mixture, **MGTP208**. The transition temperatures and the corresponding enthalpy values of the binary mixture, **MGTP208**, taken from the heating and cooling DSC scan collected at 10 K/min, are shown in Figure 11 below. The lowering of the isotropisation temperature of the composition of ~12 °C, when compared to pure **CB_C9_CB** is lower than found for the comparable mixture with the monomeric system, **1**.

Figure 11. DSC studies (10 K/min) of the binary mixture, **MGTP208** (15% (w/w) **2** in 85% **CB_C9_CB**); the values are taken from the first heating and cooling scans. Cr 86.7 (49.74) N 112.0 (1.96) Iso (°C); Iso 110.3 (−2.22) N 88.1(−2.35) N_x 41.4 (−41.44) Cr (°C); the numbers in brackets are the transition enthalpies in $J \cdot g^{-1}$.

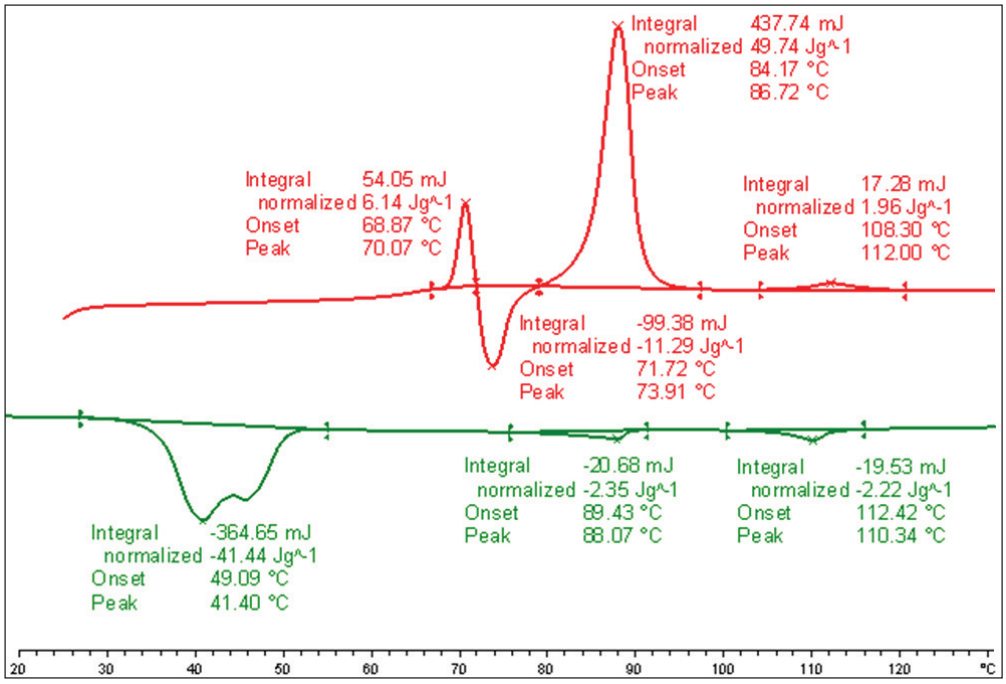

X-ray measurements were performed whilst applying a magnetic field of about 0.5 T applied to orient the samples of the composition, **MGTP208.** The results confirm the presence of two nematic phases. The X-ray patterns in the high-temperature nematic state show the known features of the XRD patterns of the nematic phase of the pure cyanobiphenyl dimer, *i.e.*, diffuse crescent-like scattering on the meridian in the small angle region (parallel to the orienting magnetic field) and diffuse crescent-like scattering on the equator in the wide-angle region. A diffractogram of the composition, **MGTP208**, recorded at 97 °C is shown in Figure 12a,b. Similar to the pure cyanobiphenyl dimer, this pattern does not change significantly at the phase transition to the low-temperature N_X phase. The diffractogram recorded at 70 °C is shown in Figure 12c,d. There is no indication of a transition to a smectic phase, even though the textural features, such as a fan-shaped texture and/or polygonal textures, occur.

Based on the results on the monomeric and dimeric systems, the miscibility of **CB_C9_CB** with liquid crystal gold nanoparticles was explored. These initial experiments suggested that a concentration of ~15% of the gold nanoparticle system in **CB_C9_CB** might still allow for N_x phase formation. As the initial LC gold nanoparticle system, Material **3** was selected. For **3**, the gold particles have a diameter of ~3.3 nm; the chemical synthesis, liquid crystal phase behaviour and plasmonic properties have been reported elsewhere [22]. The results for the mixture, **MGTP212** (15% **3** in 85% **CB_C9_CB** w/w) will be described. The POM studies and the calorimetric investigations evidenced the existence of the phase sequence, N–N_x, with textural and structural features similar to the pure cyanobiphenyl dimer, **CB_C9_CB**. The high-temperature phase could be easily identified as a nematic phase by its characteristic texture. At the phase transition to the N_x phase, a fine structured fan-shaped texture develops, as shown in Figure 13a,b. The sheared texture contains non-specific features, a small-scale fan-shaped texture and homeotropically oriented regions and some oily streaks, shown in Figure 13c.

Figure 12. XRD patterns of an aligned sample of mixture **MGTP208** in the magnetic field upon cooling. (**a**,**b**) XRD patterns of the nematic phase at 97 °C: (**a**) original pattern; (**b**) the same XRD pattern, but the intensity of the isotropic liquid is subtracted. (**c**,**d**) XRD patterns of the N_x at 70 °C: (**c**) original pattern; (**d**) the same XRD pattern, but the intensity of the isotropic liquid is subtracted.

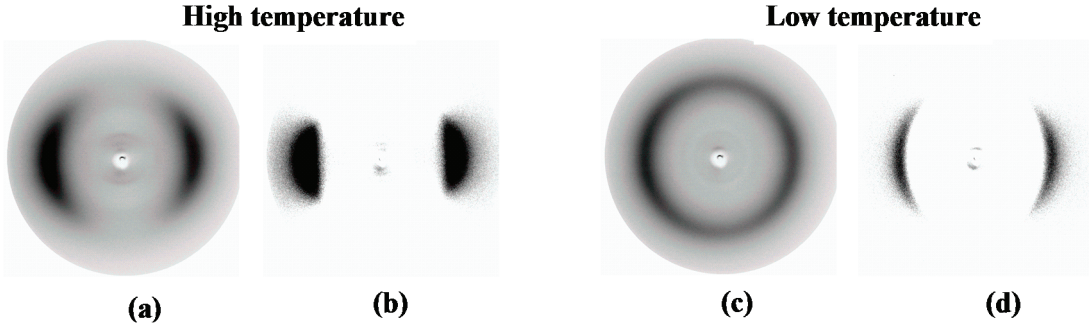

Figure 13. Textures of the binary mixture, **MGTP212** (15% (w/w) **3** in 85% **CB_C9_CB**), at $U = 0$ V between untreated glasses observed in the same region upon cooling between crossed polarizers: (**a**) schlieren texture in the high-temperature nematic N phase at 113 °C; (**b**) fan-like texture of the low-temperature N_x phase at 100 °C and (**c**) sheared texture of the low-temperature N_x phase at 84 °C.

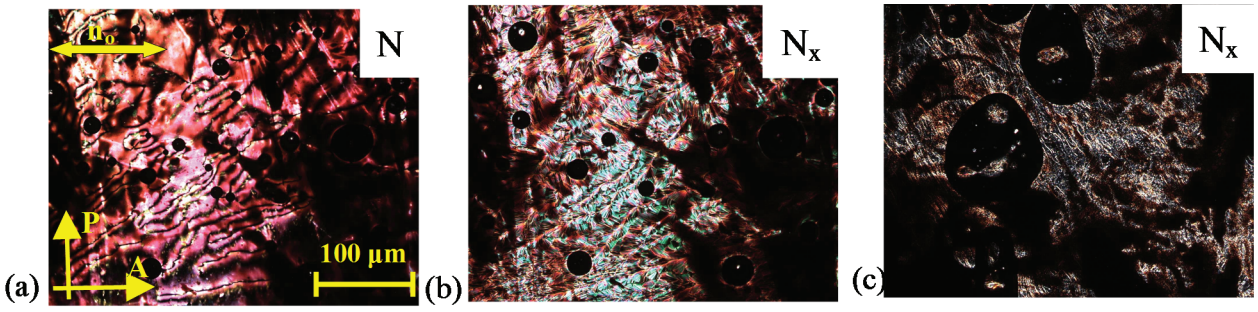

DSC measurements were conducted at different heating and cooling rates of samples of the binary mixture, **MGTP212 (**15% **(**w/w) **3** in 85% **CB_C9_CB**). The transition temperatures and the corresponding enthalpy values of the binary mixture, **MGTP212**, taken from heating and cooling DSC scans (10 K/min) are shown in Figure 14. A crucial feature is that only a very small reduction of the isotropisation temperature occurs, when compared to pure **CB_C9_CB** and the stabilisation of the N_x phase formation, which is enantiotropic in this system can be observed.

X-ray measurements were performed whilst applying a magnetic field of about 0.5 T to orient the samples of the binary mixture, **MGTP212** (15% (w/w) **3** in 85% **CB_C9_CB**). The results confirm the presence of two nematic phases. The X-ray patterns in the high-temperature nematic state show the known features of the XRD patterns of the nematic phases of the pure cyanobiphenyl based dimers, *i.e.*, diffuse crescent-like scattering on the meridian in the small angle region (parallel to the orienting magnetic field) and diffuse crescent-like scattering on the equator in the wide-angle region collected at 112 °C and shown in Figure 15a. Similar to the dimer containing cyanobiphenyl units, this pattern does not change significantly at the phase transition to the low-temperature NX phase. A representative diffraction pattern, collected at 80 °C, is shown in Figure 15b. Small angle intensities occur. θ-scans of the diffraction pattern in the N and N_x and the isotropic phases are shown in Figure 15c. As the small angle intensities persist in the isotropic phase, they are attributed to the average distance of the gold nanoparticles dispersed in the mixture. The distribution of the wide-angle scattering along χ in the N and N_x phases (plotted are the recorded intensities *vs.* χ (15°–25° 2θ)) is shown Figure 15d for data recorded at 112 °C and 80 °C. To enhance the visibility of the signal, the raw data was divided by the data collected in the isotropic phase at 135 °C. It is noticeable that the macroscopic orientation in the N_x phase is much larger than in the N phase, where there is hardly any increased orientation when compared to the isotropic phase. Beyond the small angle intensity, attributed to the gold nanoparticles, there is no indication of a transition to a smectic phase, even though the POM textural features, such as the fan-shaped texture, could suggest such a smectic-like structure formation.

Figure 14. DSC studies (10 K/min) of the **MGTP212**; the values are taken from the first heating and cooling scans. Cr 85.6 (49.05) Nx 105.7 (1.19) N 122.2 (2.90) Iso (°C); Iso 121.2 (−3.02) N 105.5 (−1.47) Nx 30.3 (−21.38) Cr; the numbers in brackets are the transition enthalpies in $J \cdot g^{-1}$.

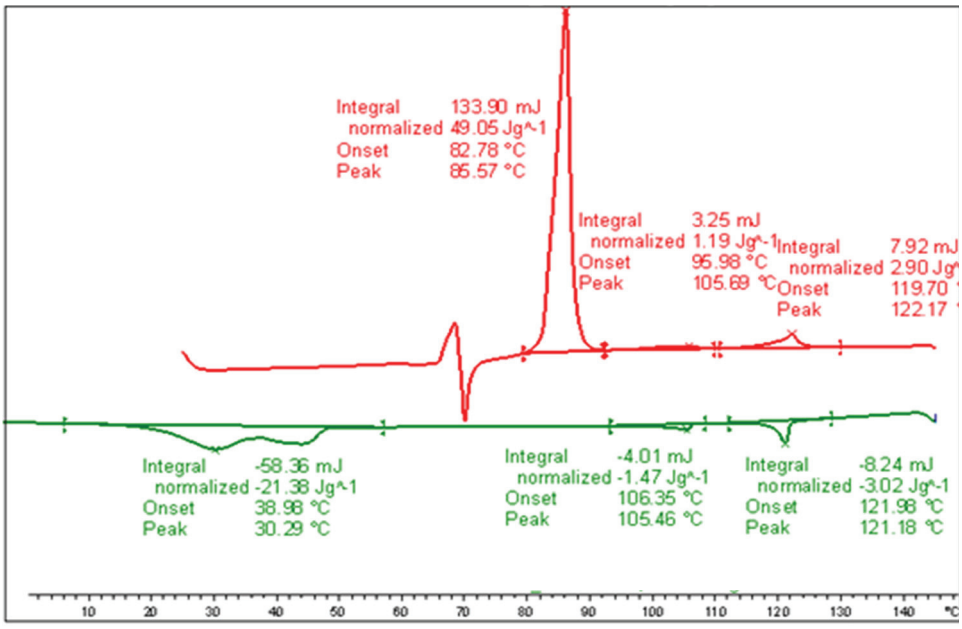

Based on these results, the investigations were extended to the gold nanoparticle system, **4**, where the synthesis and the liquid crystal properties have been reported elsewhere [24]. The NP system, **4**, is characterized by particle diameters of ~10 nm; the LC groups are attached by an amino group to the gold nanoparticles; the spacer linking LC groups and nanoparticles contain a siloxane group, introduced in order to lower the glass transition temperatures and the viscosity of the system. Based on the previous results and for systematic reasons, a high concentration of **CB_C9_CB** in the mixture was targeted. The results of the investigation of the mixture, **MGTP211** (15% **4** in **CB_C9_CB** w/w), will be described. The POM studies and the calorimetric investigations evidenced the existence of an N–N_x phase sequence with textural and structural features similar to the pure cyanobiphenyl dimer, **CB_C9_CB**. The high-temperature phase could be easily identified as a nematic phase by its characteristic texture. At the phase transition to the Nx phase, a fine structured fan-shaped texture develops, shown in Figure 16a,b. The sheared texture contains a non-specific features, a small-scale fan-shaped texture and homeotropically oriented regions and some oily streaks, shown in Figure 16c.

Figure 15. XRD patterns of an aligned sample of the mixture **MGTP212** in a magnetic field upon cooling: (**a**) N phase at 112 °C (the insert subtracted intensities were recorded in the isotropic phase); (**b**) N_x at 80 °C (the insert subtracted intensities of the isotropic phase); (**c**) θ-scan of the diffraction pattern in the N and N_x phases; SAXS: d = 0.470 nm (112 °C), d = 0.453 nm (80 °C); (**d**) distribution of the wide-angle scattering along χ in the N and N_x phases; intensity *vs*. χ (15°–25° 2θ).

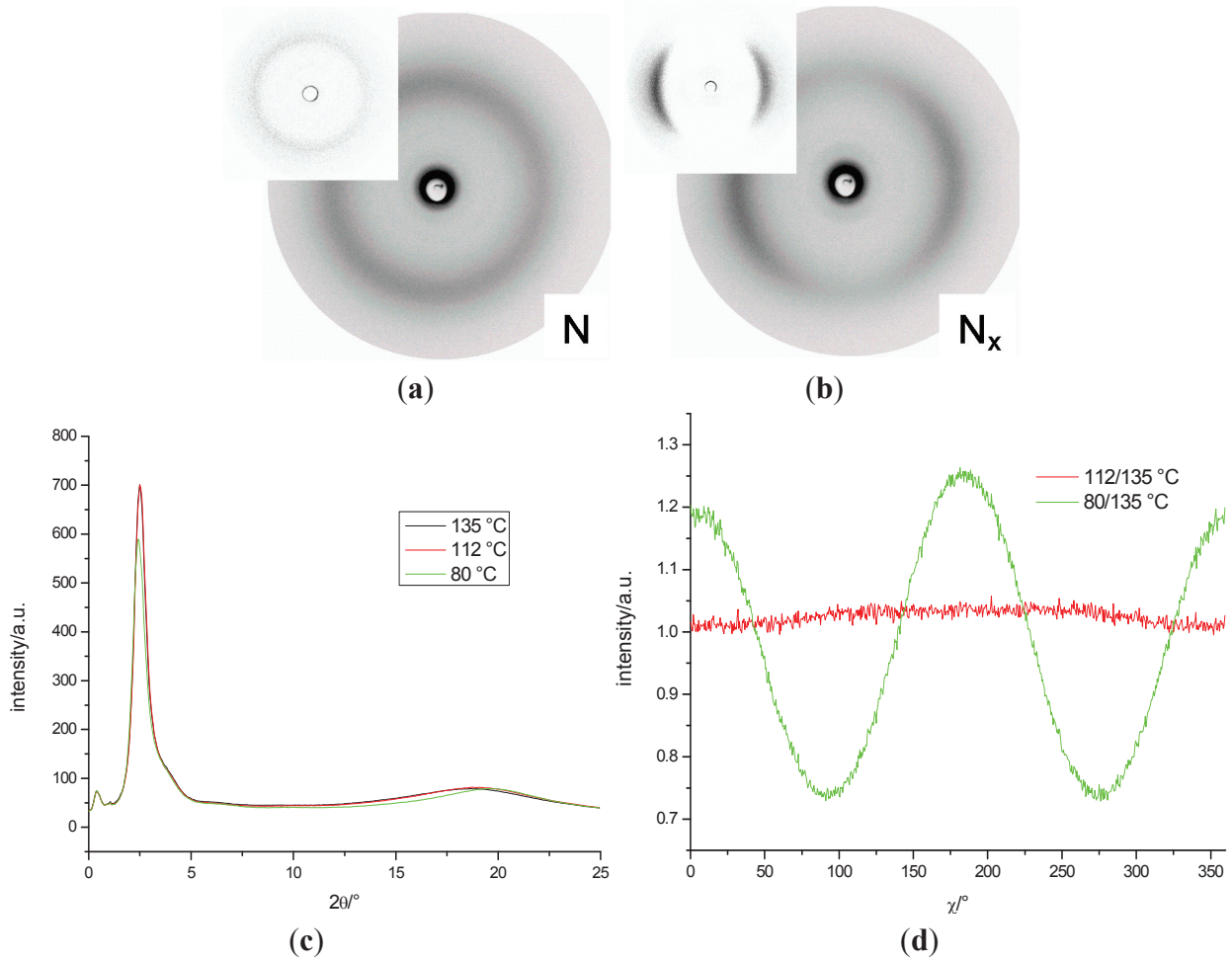

DSC measurements were conducted at varying heating and cooling rates of the samples of the binary mixture, **MGTP211** (15% (w/w) **4** in 85% (w/w) **CB_C9_CB**). The transition temperatures and the corresponding enthalpy values taken from the heating and cooling DSC scans (10 K/min) are shown in Figure 17. The surprising result is that the N_x phase formation has been stabilized; the composition with a 15% (w/w) addition of **4** forms an enantiotropic N_x phase, stable upon heating up to 104.7 °C.

Figure 16. Textures of the binary mixture, **MGTP211** (15% (w/w) **4** in 85% **CB_C9_CB**), between untreated glasses observed in the same region upon cooling between crossed polarizers: (**a**) schlieren texture in the high-temperature nematic N phase at 113 °C; (**b**) fan-like texture of the low-temperature N_x phase at 100 °C; and (**c**) sheared texture of the low-temperature N_x phase at 84 °C.

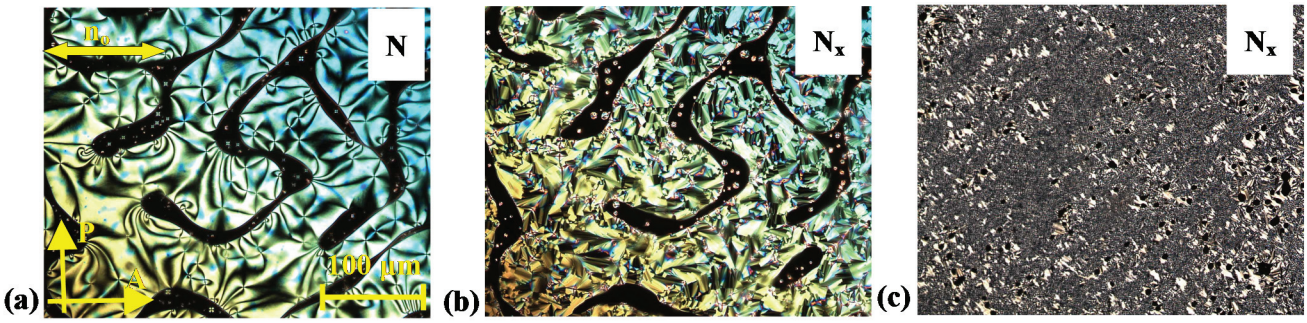

Figure 17. DSC studies (10 K/min) of the mixture, **MGTP211**; the values are taken from the first heating and cooling scans. Heating: Cr 85.4 (29.3) Nx 104.7 (1.42) N 121.2 (2.20) Iso. Numbers in brackets, transition enthalpies $J \cdot g^{-1}$. Cooling: Iso 114.2 (−2.29) N 102.7 (−1.63) N_x 47.1 (−39.96) Cr; the numbers in brackets are the transition enthalpies in $J \cdot g^{-1}$.

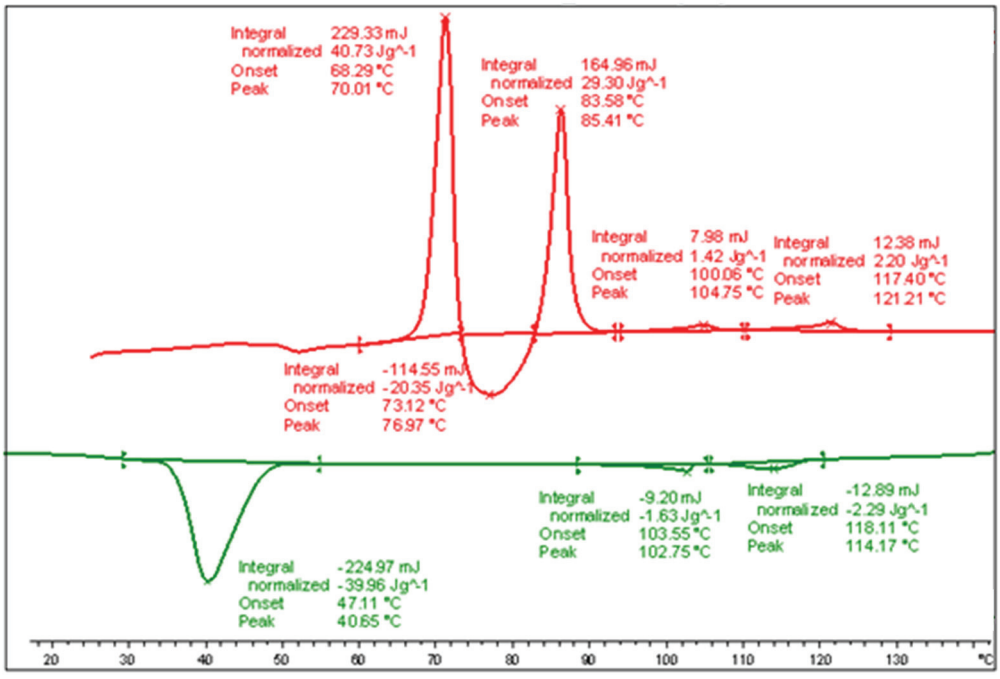

X-ray measurements were performed whilst applying a magnetic field of about 0.5 T on oriented samples of the binary mixture, **MGTP211**. The results show that the composition can be aligned by a relatively weak magnetic field. The results confirm the presence of two nematic phases. The X-ray patterns in the high-temperature nematic state show the known features of the XRD patterns of the nematic phases of the pure cyanobiphenyl or terphenyl dimers, *i.e.*, diffuse crescent-like scattering on the meridian in the small angle region (parallel to the orienting magnetic field) and diffuse crescent-like scattering on the equator in the wide-angle region, shown in Figure 18a; the data were

recorded at 108 °C. Similar to a pure dimer containing cyanobiphenyl units, this pattern does not change significantly at the phase transition to the low-temperature N_X phase; an example is in Figure 18b of the data recorded at 80 °C. Figure 18c shows the distribution of the wide-angle scattering along χ in the N phase at 108 °C and N_x phases at 80 °C (plot: recorded intensity *vs.* χ (15°–25° 2θ); the values are divided by the data recorded in the isotropic phase at 135 °C, for better contrast). Though there seems to be some sharpening of the intensities at ~90°, parallel to the external magnetic field, at 80 °C, when compared to the nematic phase, overall, the differences are minimal. The θ-scan of the diffraction patterns in the N and N_x phases at 108 and 80 °C show no strong small angle intensities; the data is very similar to the pure **CB_C9_CB**.

Figure 18. XRD patterns of an aligned sample of the mixtures, **MGTP211**, in a magnetic field (vertical) on cooling: (**a**) N phase at 108 °C; (**b**) N_x at 80 °C; (**c**) distribution of the wide-angle scattering along χ in the N and N_x phases; intensity *vs.* χ (15°–25° 2θ); (**d**) θ-scan of the diffraction pattern in the N and N_x phases; SAXS: d = 1.29 nm (108 °C), d = 1.29 nm (80 °C).

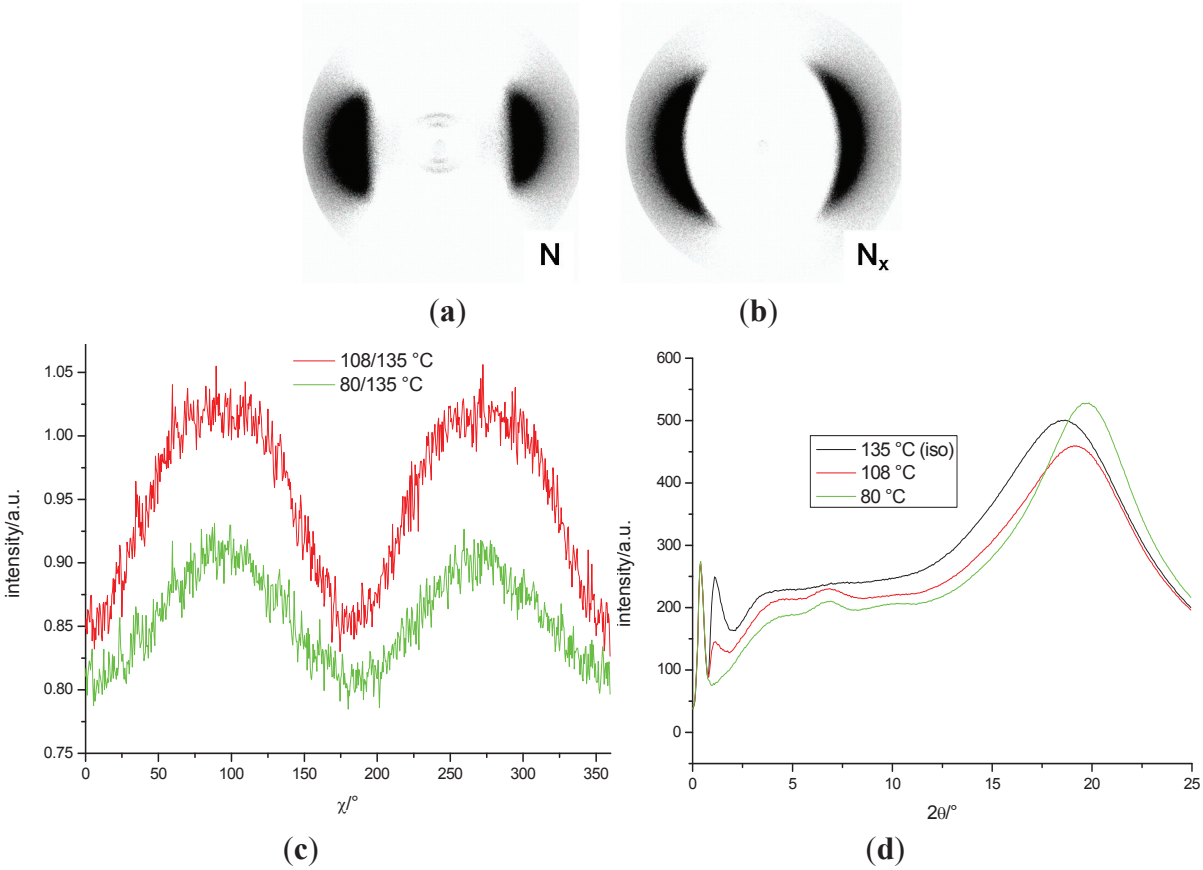

The absence of the reflections for average distances of the large gold particles is attributed to their size. They are anticipated to be at smaller angles than what can be recorded with the equipment available. There is no indication of a transition to a smectic phase, even though the textural features, such as the fan-shaped texture and polygonal textures, could suggest a smectic-like structure, indicative of the limited use of the analysis of optical defect textures for the identification of the N_x phase formation.

3. Experimental Section

The synthesis of the materials has been reported elsewhere. X-ray diffraction experiments were performed on an MAR345 diffractometer with a 2D image plate detector (CuKα radiation, graphite monochromator, λ = 1.54 Å) (MAR Research, Hamburg, Germany). The samples were heated in the presence of a magnetic field using a home-built capillary furnace. Phase transitions were determined using a Mettler DSC822e stage (Mettler Toledo Intl. Inc. Switzerland) DSC with STARe software calibrated with indium in a nitrogen atmosphere calibrated against an indium standard (156.6 °C; 28.45 $J \cdot g^{-1}$; reported transition temperatures are the peak of the endotherm). Polarising microscopy studies were carried out using an Olympus BX51 polarising microscope (Olympus Corp., Tokyo, Japan). The microscope was equipped with a Mettler-Toledo FP900 heating stage (Mettler Toledo Intl. Inc., Greifensee, Switzerland).

4. Conclusions

In a systematic study, the dimer system, **CB_C9_CB**, was mixed with a laterally functionalized monomer, a structurally related laterally connected dimer system and LC nanoparticles, where the diameter of the gold particles was varied between ~3.3 and ~10 nm. In all the investigated materials, a nematic-nematic phase transition could be introduced, though at varying concentrations of the components. The compositions were characterised by POM, DSC and XRD investigations. The results show that it is possible to construct stable liquid crystal nanocomposites with materials having a metallic plasmonic response. It was found that, surprisingly, the N_x phase formation was not destabilized in mixtures with liquid crystalline gold nanoparticles; however, destabilization of the N_x phase formation occurred when mixing with a conventional laterally functionalized nematic monomer and a structurally related dimer. These results open up investigations of systems that combine the advantageous properties of nematic-nematic systems with those that have the properties of metallic nanoparticles.

Acknowledgements

The work was carried out through funding by the Engineering and Physical Sciences Research Council (EPSRC) grants EP/J004480/1 and EP/G030006/1 and the EU FP7 contracts, 216025 and 228455. Mass spectroscopic analysis of the organic materials by the national mass spectrometry facility in Swansea is acknowledged.

Author Contributions

Maria-Gabriela Tamba carried out the miscibility studies and the LC characterisation of the materials investigated. Chih Hao Yu, Bai Jia Tang, Christopher P. Schubert and Christopher Welch were responsible for the synthesis of the NP-LCs. Alexandra Kohlmeier, Christopher Welch and Maria-Gabriela Tamba were responsible for the synthesis of the liquid crystals. Georg H. Mehl directed the research and wrote the manuscript with input from Maria-Gabriela Tamba.

Conflicts of Interest

The authors declare no conflict of interest.

References

1. Panov, V.; Nagaraj, M.; Vij, J.K.; Panarin, Y.P.; Kohlmeier, A.; Tamba, M.G.; Lewis, R.A.; Mehl, G.H. Spontaneous periodic deformations in nonchiral planar-aligned bimesogens with a nematic-nematic transition and a negative elastic constant. *Phys Rev. Lett.* **2010**, *105*, 167801, doi:10.1103/PhysRevLett.105.167801.
2. Chen, D.; Porada, J.H.; Hooper, J.B.; Klittnick, A.; Shen, Y.; Tuchband, M.R.; Korblova, E.; Bedrov, D.; Walba, D.M.; Clark, N.A.; *et al.* Chiral heliconical ground state of nanoscale pitch in a nematic liquid crystal of achiral molecular dimmers. *Proc. Natl. Acad. Sci. USA* **2013**, *110*, 15931–15936.
3. Cestari, M.; Diez-Berart, S.; Dunmur, D.A.; Ferrarini, A.; de la Fuente, M.R.; Jackson, D.J.B.; Lopez, D.O.; Luckhurst, G.R.; Perez-Jubindo, M.A.; Richardson, R.M.; *et al.* Phase behavior and properties of the liquid-crystal dimer 1",7"-bis(4-cyanobiphenyl-4'-yl) heptane: A twist-bend nematic liquid crystal. *Phys. Rev. E* **2011**, *84*, 031704, doi:10.1103/PhysRevE.84.031704.
4. Beguin, L.; Emsley, J.W.; Lelli, M.; Lesage, A.; Luckhurst, G.R.; Timimi, B.A.; Zimmermann, H. The chirality of a twist-bend nematic phase identified by NMR spectroscopy. *J. Phys. Chem. B* **2012**, *116*, 7940–7951.
5. Meyer, C.; Luckhurst, G.R.; Dozov, I. Flexoelectrically driven electroclinic effect in the twist-bend nematic phase of achiral molecules with bent shapes. *Phys. Rev. Lett.* **2013**, *111*, 067801, doi:10.1103/PhysRevLett.111.067801.
6. Borshch, V.; Kim, Y.-K.; Xiang, J.; Gao, M.; Jákli, A.; Panov, V.P.; Vij, J.K.; Imrie, C.T.; Tamba, M.G.; Mehl, G.H.; Lavrentovich, O.D. Nematic twist-bend phase with nanoscale modulation of molecular orientation. *Nat. Commun.* **2013**, *4*, 2635, doi:10.1038/ncomms3635.
7. Burnell, E.; Kohlmeier, A.; Tamba, M.G.; Mehl, G.H.; Dong, R. Solute NMR study of a bimesogenic liquid crystal with two nematic phases. *Chem. Phys. Lett*. **2012**, *552*, 44–48.
8. Tripathi, C.S.P.; Losada-Perez, P.; Leys, J.; Kohlmeier, A.; Tamba, M.-G.; Mehl, G.H.; Glorieux, C. The nematic-nematic phase transition in a liquid crystal dimer CBC9CB and mixtures with 5CB: A high-resolution adiabatic scanning calorimetric study. *Phys. Rev. E* **2011**, *84*, 041707, doi:10.1103/PhysRevE.84.041707.
9. Panov, V.P.; Balachandran, R.; Nagaraj, M.; Vij, J.K.; Tamba, M.G.; Kohlmeier, A.; Mehl, G.H. Microsecond linear optical response in the unusual nematic phase of achiral. *Appl. Phys. Lett.* **2011**, *99*, 261903, doi:10.1063/1.3671996.
10. Hoffmann, A.; Vanakaras, A.G.; Kohlmeier, A.; Mehl, G.H.; Photinos, D.J. On the structure of the Nx phase of symmetric dimmers. **2014**, arXiv:1401.5445v1.
11. Keith, C.; Lehmann, A.; Baumeister, U.; Prehm, M.; Tschierske, C. Nematic phases of bent-core mesogens. *Soft Matter* **2010**, *6*, 1704–1721.

12. Zep, A.; Aya, S.; Aihara, K.; Ema, K.; Pociecha, D.; Madrak, K.; Bernatowicz, P.; Takezoe, H.; Gorecka, E. Multiple nematic phases observed in chiral mesogenic dimmers. *J. Mater. Chem. C* **2013**, *1*, 46–49.
13. Tschierske, C.; Photinos, D.J. Biaxial nematic phases. *J. Mater. Chem.* **2010**, *20*, 4263–4294.
14. Sharma, A.; Worden, M.; Hegmann, T. Nanoparticle-Promoted thermal stabilization of room temperature cholesteric blue phase mixtures. *Ferroeletrics* **2012**, *431*, 154–163.
15. Pendry, J.B. A chiral route to negative refraction. *Science* **2004**, *306*, 1353–1355.
16. Menzel, C.; Helgert, C.; Rockstuhl, C.; Kley, E.B.; Pertsch, A.T.T.; Leder, F. Asymmetric transmission of linearly polarized light at optical metamaterials. *Phys. Rev. Lett.* **2010**, *104*, 253902, doi:10.1103/PhysRevLett.104.253902.
17. Donnio, B. Liquid-Crystalline metallodendrimers. *Inorg. Chim. Acta* **2014**, *409*, 53–57.
18. Nealon, G.L.; Greget, R.; Dominguez, C.; Nagy, Z.T.; Guillon, D.; Gallani, J.J.; Donnio, B. Liquid-Crystalline nanoparticles: Hybrid design and mesophase structures. *Beilstein J. Org. Chem*. **2012**, *8*, 349–370.
19. Stamatoiu, O.; Mizaei, J.; Feng, X.; Hegmann, T. Liquid crystals: Materials design and self assembly. In *Topics in Current Chemistry*; Tschierkse, C., Ed.; Springer Verlag: Berlin, Germany, 2012; Volume 318, pp. 331–393.
20. Balachandran, R.; Panov, P.; Vij, J.K.; Kocot, A.; Tamba, M.G.; Mehl, G.H. Elastic properties of bimesogenic liquid crystals. *Liq. Cryst.* **2013**, *40*, 681–688.
21. Cseh, L.; Mehl, G.H. The design and the investigation of room temperature thermotropic nematic gold nanoparticles. *J. Am. Chem. Soc.* **2006**, *128*, 13377–133786.
22. Zeng, X.; Cseh, L.; Fowler, A.; MacDonald, J.E.; Mehl, G.H.; Ungar, G. 3-D ordered gold strings by coating nanoparticles with mesogens. *Adv. Mater.* **2009**, *21*, 1746–1750.
23. Dintinger, J.; Tang, B.J.; Zeng, X.; Liu, F.; Kienzler, T.; Mehl, G.H.; Ungar, G.; Rockstuhl, C.; Scharf, T. A self organized anisotropic liquid crystal-plasmonic metamaterial. *Adv. Mater.* **2013**, *25*, 1999–2004.
24. Yu, C.H.; Schubert, C.; Tang, B.J.; Welch, C.; Tamba, M.G.; Mehl, G.H. Design, synthesis and characterisation of mesogenic amine capped nematic gold nanoparticles with surface enhanced plasmonic resonances. *J. Am. Chem. Soc.* **2012**, *134*, 5076–5079.
25. Elsäßer, R.; Mehl, G.H.; Goodby, J.W.; Veith, M. Novel nematic dendrimers based on carbosilazane cores. *Angew. Chem. Int. Ed*. **2001**, *40*, 2688–2690.
26. Elsäßer, R.; Mehl, G.H.; Goodby, J.W.; Photinos, D.J. Nematic silsesquixanes—Towards nanocrystals dispersed in a nematic liquid crystal matrix. *Chem. Commun*. **2000**, 851–852.
27. Diez, S.; Dunmur, D.A.; de la Fuente, M.R.; Karahaliou, P.K.; Mehl, G.H.; Meyer, T.; Jubindo, M.A.P.; Photinos, D.J. Dielectric studies of a laterally-linked siloxane ester dimer. *Liq. Cryst.* **2003**, *30*, 1021–1030.

Part V: Applications of Liquid Crystals

Emerging Applications of Liquid Crystals Based on Nanotechnology

Jung Inn Sohn, Woong-Ki Hong, Su Seok Choi, Harry J. Coles, Mark E. Welland, Seung Nam Cha and Jong Min Kim

Abstract: Diverse functionalities of liquid crystals (LCs) offer enormous opportunities for their potential use in advanced mobile and smart displays, as well as novel non-display applications. Here, we present snapshots of the research carried out on emerging applications of LCs ranging from electronics to holography and self-powered systems. In addition, we will show our recent results focused on the development of new LC applications, such as programmable transistors, a transparent and active-type two-dimensional optical array and self-powered display systems based on LCs, and will briefly discuss their novel concepts and basic operating principles. Our research will give insights not only into comprehensively understanding technical and scientific applications of LCs, but also developing new discoveries of other LC-based devices.

Reprinted from *Materials*. Cite as: Sohn, J.I.; Hong, W.-K.; Choi, S.S.; Coles, H.J.; Welland, M.E.; Cha, S.N.; Kim, J.M. Emerging Applications of Liquid Crystals Based on Nanotechnology. *Materials* **2014**, *7*, 2044–2061.

1. Introduction

Liquid crystals (LCs), first discovered in 1888 by an Austrian botanist, Frederick Reinitzer, continue to attract intense research interest because of their orientational order, the existence of strong dipoles and easily polarizable groups, the rigidness of the long axis, anisotropic features in the structural, optical, electrical and magnetic properties, as well as their easy response to electric, magnetic and surface forces [1–5].

Much effort has been devoted to the great scientific and technological developments and achievements for advanced photonic devices and high-performance display applications of LCs, as well as for creating novel device concepts and new LC applications. As a result, LCs will be able to become ubiquitous in diverse applications, ranging from displays to electronics, sensors, lasers and optical computing in our daily life [2,6].

To date, besides the familiar displays being the most common applications of LC technology, numerous studies on LCs have been performed to provide unparalleled opportunities to facilitate the basic understanding of the science and to develop new non-display applications. In this regard, especially, ferroelectric LCs that possess a variety of advantages, such as a permanent electric polarization, high flexibility and fast response time, have attracted considerable attention in recent years as the basis for noble field effect transistors (FETs), memory cells and optical switching device applications [5,7]. In particular, among FET-based non-volatile memory devices, the ferroelectric FET, an important type of memory cells without a storage capacitor, is significantly attractive for

memory and switch applications, because of the wide range of its interesting features, including small cell size, non-destructive read-out, low-power consumption, good retention and fast response time [8–15]. Another example of emerging applications based on LCs is holography, which is an ideal technology to realize three-dimensional (3D) dynamic images by changing the refractive index [16,17]. However, unfortunately, photo-refractive materials and photo-chromic materials require high external voltages and long response times, respectively, to modulate the refractive index [18–22]. To avoid such difficulties, arrays of carbon nanotubes (CNTs)/nanofibers were introduced to locally modulate the refractive index of the LC medium at low operation voltages [23–25]. Recently, we also developed a transparent, active-type 2D optical array that operates at low voltage using a graphene/CNT hybrid structure instead of using opaque metals [16]. In addition to demonstrating proof-of-principle concepts for individual single LC device applications, it is also possible to achieve technological advances and revolution into a rapidly growing multidisciplinary field involving displays, electronics and energy harvesting to integrate displays into a self-powered system [26,27]. Recent developments in piezoelectric power generators harvesting energy steadily from ambient mechanical vibrations without regard to time, place or any external conditions, present innovative and emerging research topics [26,28–32]. Among various piezoelectric materials and structures, a ZnO nanowire has been intensively studied as one of the most attractive materials. In particular, recent advance in the ZnO nanowire-based piezoelectric power generators exhibited highly promising piezoelectric performance for a self-powered source, due to its dimensionality and piezoelectric semiconducting properties containing non-toxicity, eco-friendliness and geometrical versatility [28,30,33].

In this paper, we aim to present and review snapshots of our recent research carried out on emerging applications of LCs, particularly focusing on the development of new applications based on a combination of LCs and functional nanomaterials, such as, ZnO nanowires, CNTs and graphene. In addition, we will briefly discuss novel device concepts and basic principles of programmable transistors, a transparent and active-type 2D optical array and multifunctional hybrid systems based on LCs. These explorations will give insights not only in comprehensively understanding the technical and scientific applications of LCs, but also developing new discoveries of other LC-based devices.

2. Results and Discussion

2.1. Programmable Transistors Based on Ferroelectric Liquid Crystals

The intrinsic memory functionality of ferroelectric FETs based on a semiconducting channel and ferroelectric materials arises from the modulation of the charge carrier concentration in the channel, which defines two different conductance states, by switching the polarization of the ferroelectrics electrically, as shown in Figure 1. When a positive gate pulse is applied, the polarization of ferroelectrics is rearranged in the direction of the ferroelectric-semiconductor interface, resulting in the build-up of positive charges on the semiconducting surface. Subsequently, this leads to the accumulation of electrons and, thus, a high conductance state, corresponding to the ON state (Figure 1a) [7,12]. Conversely, when a negative gate pulse is applied, the negative polarization leads to the depletion of electrons and results in a low conductance state, that is, the OFF state (Figure 1b). Accordingly, to

create novel functionality in FETs using ferroelectric materials as a new approach for the fabrication of programmable ferroelectric transistors, serving as a hybrid cell for memory, switch and display applications [34–37], we must first demonstrate ferroelectric LC-induced conductance modulation and hysteresis behaviour in a FET.

Figure 1. Schematic views of ferroelectric liquid crystal (LC)-coated ZnO nanowire field effect transistors (FETs) exhibiting charge accumulation and depletion in the channel. (**a**) The ON memory state; (**b**) the OFF memory state. PVP, poly(4-vinylphenol).

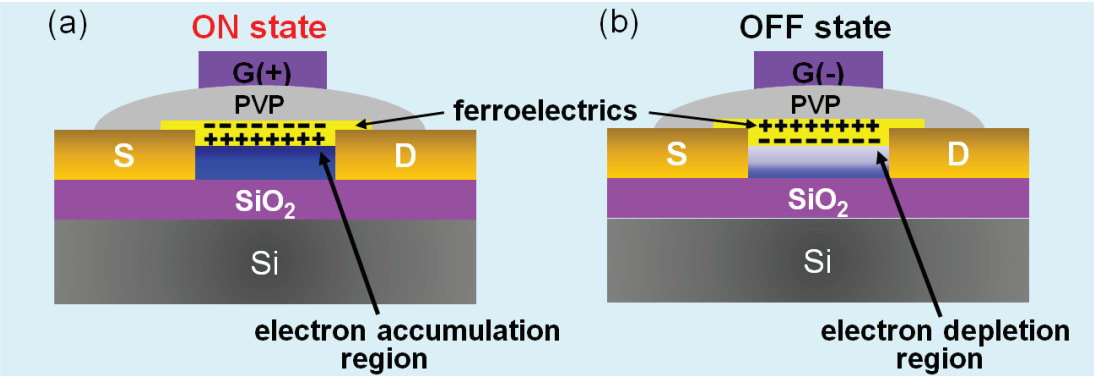

In order to address whether the ferroelectric polarization of LCs can affect the electrical transport in FETs, we performed output (source-drain current *versus* voltage, I_{DS}-V_{DS}) and transfer (source-drain current *versus* gate voltage, I_{DS}-V_G) measurements with a conventional back-gate FET device structure (the inset of Figure 2b) [7]. Figure 2a,b shows the representative data of the output characteristics and transfer characteristics of a back-gate ZnO nanowire FET without a ferroelectric LC layer, respectively. The output curves exhibit well-defined linear regimes at low biases and saturation regimes at high biases, showing the typical pinch-off characteristics of n-type semiconductor FETs [7,11,12,38]. It was observed that the back-gate nanowire FET exhibited negligible hysteresis, being caused by uncontrolled chemical species adsorbed on the ZnO nanowire when exposed to ambient air [7,12], before coating ferroelectric LCs, as shown in Figure 2b. Figure 2c,d shows the electrical properties of the ferroelectric LC-coated nanowire FET with a back-gate structure. Noticeably, we observed that the electrical performance of ZnO nanowire FETs is significantly improved after coating a ferroelectric layer. Here, note that we performed electrical measurements with the same device before and after the coating of ferroelectric LCs in order to circumvent size and morphology effects, such as the channel length and nanowire diameter. Thus, the main reasons causing the conductance enhancement of the nanowire FET with a ferroelectric LC layer can be due to the polarization effect, as well as the suppression of chemisorption effects of oxygen and/or water molecules at the ZnO surface [7,39]. It was also observed that the FET (Figure 2d) exhibits a clockwise hysteresis behaviour obtained with a double sweep of the gate voltage from −10 to 20 V at variable drain voltages (V_{DS} = 0.1 and 1 V). Here, an interesting finding is that the hysteresis width of the nanowire FET considerably increases after coating a ferroelectric LC layer compared with that of the conventional nanowire FETs without a ferroelectric LC layer (Figure 2b). These results indicate that the channel conductance and threshold voltages of ZnO nanowire FETs

are strongly dependent on the channel charge density of the ZnO nanowires, which can be effectively modulated by the polarization of ferroelectric LCs.

To further verify the origin of the large hysteresis and modulation of the channel conductance in the nanowire FET device, we fabricated a top-gate nanowire FET (the inset of Figure 3), which is an attractive configuration to allow the favourable polarization of the ferroelectric layer, inducing a more effective field effect on the nanowire channel [7,12]. As expected, we observed that, unlike the hysteresis behaviour of the back-gate nanowire FET with a ferroelectric LC layer, the top-gate nanowire FET with the ferroelectric LC layer exhibits a counter-clockwise hysteresis loop, as shown in Figure 3. That is, in contrast to a back-gate configuration causing the opposite polarization states, as the gate voltage was swept from a negative (positive) value, a negative (positive) polarization of the ferroelectric LC was induced on the nanowire surface. This implies that hysteresis behaviours associated with threshold voltage shifts and channel conductance are strongly dependent on the sign of polarization charges induced in the ZnO nanowire channel according to voltage sweep directions. This is consistent with the results of previous studies on ferroelectric memory transistors [12,40].

Figure 2. (**a**) Output characteristics (I_{DS}-V_{DS}) and (**b**) transfer characteristics (I_{DS}-V_G) of a back-gate ZnO nanowire FET without a ferroelectric LC layer. The inset shows a schematic view of a ZnO nanowire FET with a back-gate configuration; (**c**) output characteristics and (**d**) hysteretic behaviours of the ferroelectric LC-coated ZnO nanowire FET. Reprinted with permission from [7]. Copyright 2013, American Institute Physics.

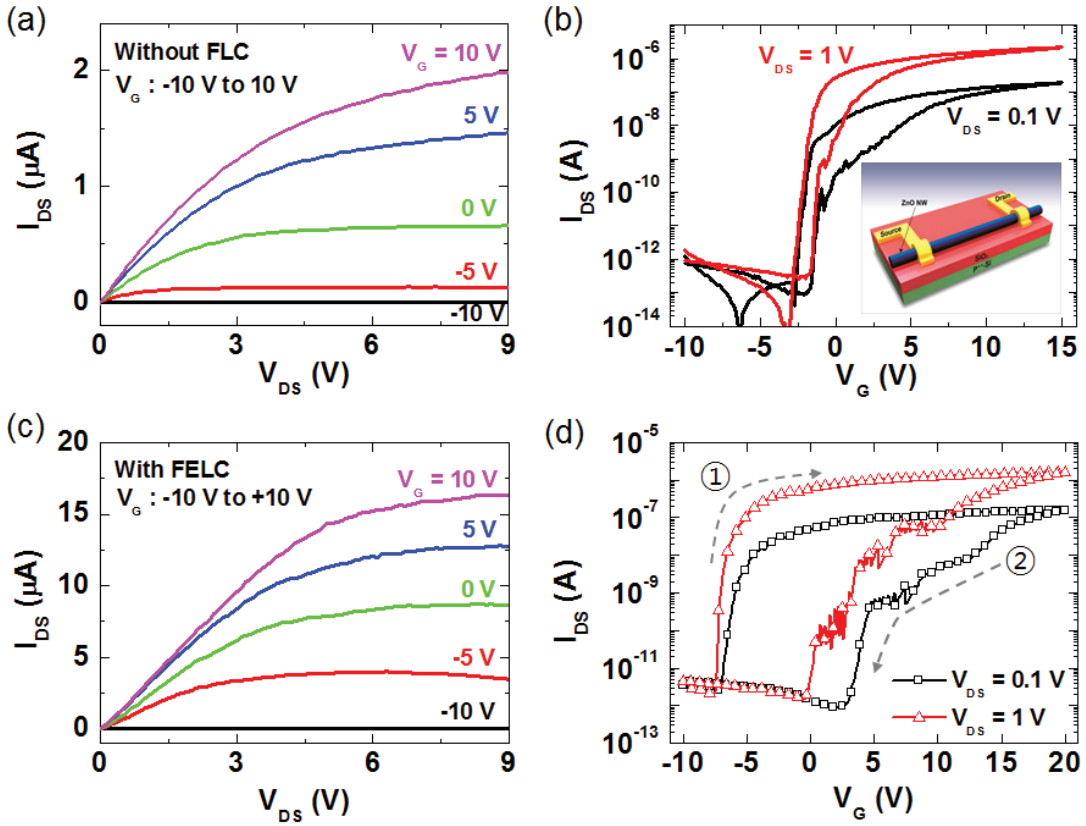

Figure 3. Hysteretic behaviour of a top-gate ZnO nanowire FET with a ferroelectric LC layer.

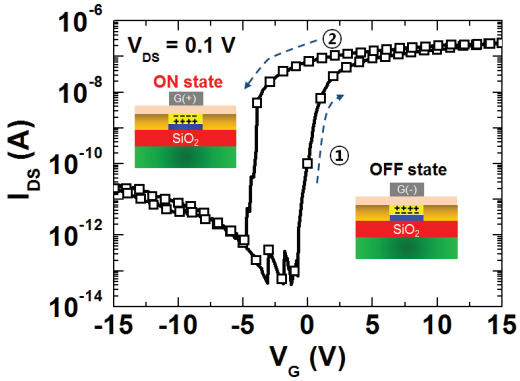

To demonstrate the practical memory properties of ferroelectric LC-coated nanowire FETs, we investigated the switchability and retention time of a device with a top-gate structure [7]. Figure 4a shows the reversible, reproducible ON and OFF switching characteristics of a memory device. Two different conductance states, defined as the ON (high conductance) and the OFF (low conductance) states of a memory, were measured at the read gate voltage (V_G = 0 V) after the application of a writing and an erasing gate voltage pulse of 15 and −15 V, respectively.

Figure 4. (**a**) Reversible, reproducible ON and OFF switching characteristics of a top-gate nanowire FET with a ferroelectric LC layer; (**b**) retention times for the ON and OFF states of ferroelectric LC-coated FETs measured after the application of a writing pulse (+15 V) and an erasing pulse (−15 V). Reprinted with permission from [7]. Copyright 2013, American Institute Physics.

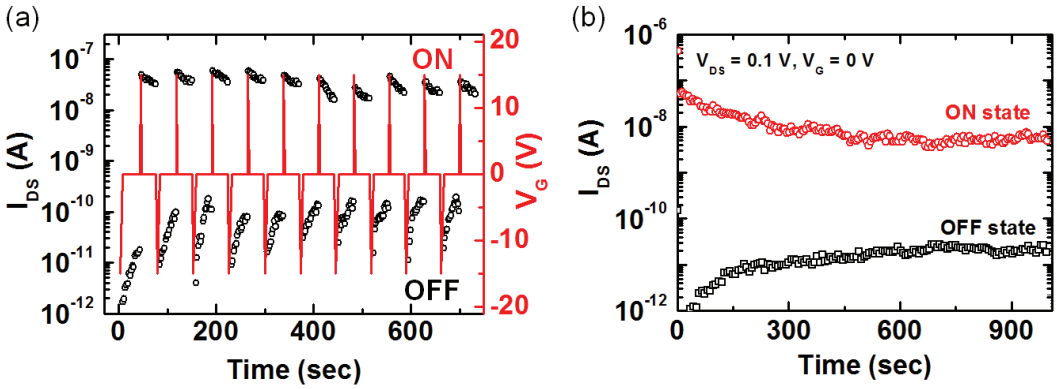

Figure 4b shows the retention characteristics of the ferroelectric LC-coated nanowire FET-based memory measured at V_{DS} = 0.1 V and V_G = 0 V after a device was switched to the ON and OFF states using writing and erasing gate voltage pulses, respectively. We find that the ON and OFF states were retained over 10^3 s. Although the retention times of our memory device based on ferroelectric LCs are still short and need to be further improved for data storage device applications, it is noteworthy that we demonstrate proof-of-principle concepts, showing the feasibility of creating a new hybrid system with switch, memory and display functions. Additionally, we believe that the observed memory effects originate from the reversible switching between two polarization states, which are effectively reoriented according to the polarity sign of applied gate voltages and, thus,

resulting in the accumulation or depletion of the channel electrons in the ZnO nanowire, as illustrated in Figure 1. This study will provide great potentials for use of LCs in a hybrid system with switch, memory and display functions.

2.2. Future Three-Dimensional Holography Based on Liquid Crystals

To avoid the requirements of high external voltages to modulate the refractive index of LCs, a combination of a graphene/carbon nanotube (CNT) hybrid structure, such as a transparent active-type 2D optical array, and LCs, as the medium inducing various refractive index changes, can be considered as a viable strategy. An array of CNT pixels was fabricated on the patterned catalysts to modulate the refractive index in a desired location by using chemical vapour deposition, as shown in Figure 5a,c [16]. A strong local field can be generated by geometrically sharp CNTs with a large field enhancement factor, which locally modulates the refractive index of the LC medium at low operation voltages [23–25]. In addition, instead of using opaque metals, graphene with 96% transmittance per layer was used as the transparent electrodes for the transmissive mode for optical devices. Here, note that the height distribution of the CNT forests is important for obtaining uniform diffraction patterns. This distribution was measured using an optical surface profiler. Figure 5b shows that CNTs were uniformly distributed on each pixel with an average height of 1 ± 0.2 μm.

Figure 5. (**a**) Fabrication schematics of graphene/vertically aligned carbon nanotube (CNT) hybrid structure on quartz; (**b**) a 3D image of CNT heights obtained from optical surface profiler; (**c**) scanning electron microscopy (SEM) images of graphene/vertically aligned CNTs on quartz substrates. The inset shows a digital photographic image of our optical element. Reprinted with permission from [16]. Copyright 2011, John Wiley and Sons. VACNT, vertically aligned CNT.

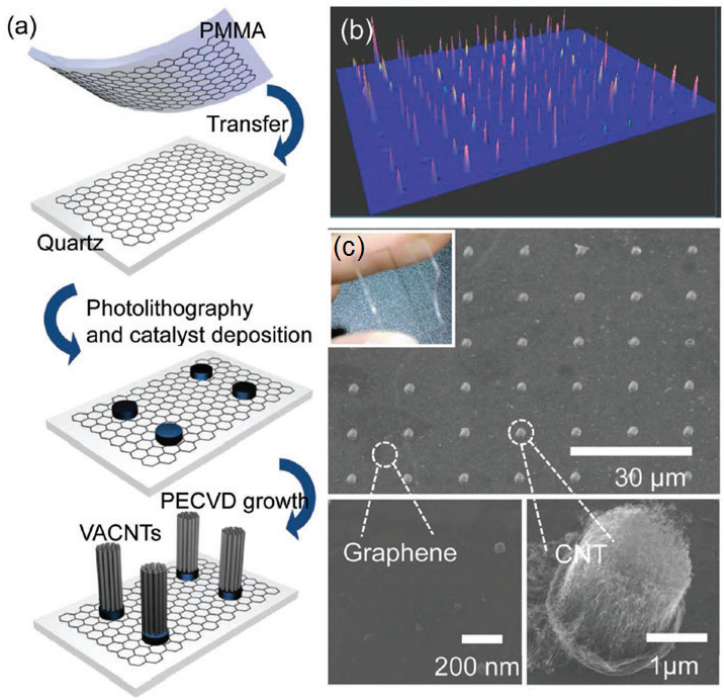

Figure 6 shows the diffraction pattern through the graphene/vertically aligned CNTs (VACNTs) hybrid structure as a function of the applied voltage from zero to 6 V [16]. We used a He-Ne Laser with a 633 nm wavelength to generate diffraction patterns from the graphene/VACNT hybrid structure on a quartz substrate, as shown in Figure 6a.

The LC director was aligned randomly in the graphene plane and aligned homogeneously parallel to the upper electrode, whose anchoring was invoked by the rubbing polyimide. Thus, the light can be transmitted partially from the graphene region, whereas CNTs absorb light and emit light again like an antenna, which act as a slit to generate a spherical wave. A series of light transmitted through 2D slits behaves like a 2D Young's slit, creating a planar interference pattern. LC molecules near the CNTs can be aligned parallel to the long axis of a CNT [41,42], and in particular, those located at the tip of CNTs can be aligned more strongly parallel to the field direction, because the field is strongly enhanced by the sharp CNT tip [43]. The path difference of light from slits can be modulated by the degree of alignment of LC molecules in each slit, being varied by an external electric field. Thus, each pixel acts as a circular slit, and hence, a 2D diffraction pattern from periodically arranged 2D CNT pixels (15 μm space in the current study) was observed, as shown in Figure 6c. As the voltage increases to 2 V, a strong local field enhanced by the CNT tips changes the LC director nearby to modify the local refractive index. Therefore, Δn in the local area increased the change in light intensity of the diffraction pattern, as shown in Figure 6d [23–25,44]. At a voltage higher than 6 V, all the LC directors were aligned along the field direction; therefore, Δn ~ 0, invoking no diffraction pattern changes and, thus, resulting in reducing the light intensity (Figure 6e).

Figure 6. (**a**) Schematic of the measurement for diffraction patterns; (**b**) schematic illustration for the structure of the fabricated optical device. LCs are aligned by the applied electric fields between two electrodes with the spacing of 20 μm. Digital photographic images of diffraction patterns at (**c**) 0 V, (**d**) 2 V, and (**e**) over 6 V, respectively. Reprinted with permission from [16]. Copyright 2011, John Wiley and Sons. ITO, indium-tin-oxide.

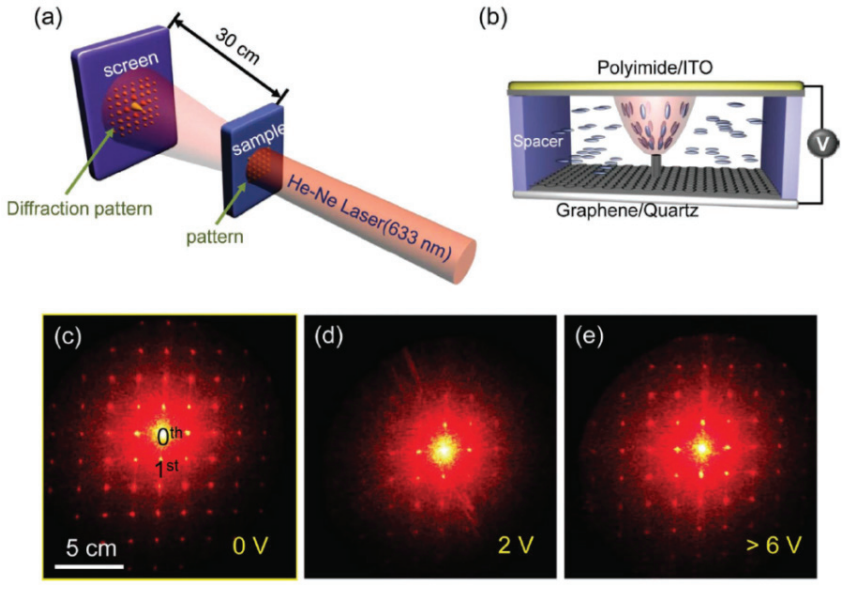

We measured the detailed light intensity changes at the first order spot as a function of voltages for different tip morphologies [16]. As the voltage increases, more LC molecules were aligned along the field, inducing larger Δn near the tip. Thus, this resulted in the increase in the intensity of the first order until a maximum value was reached. After a maximum value of the intensity, the alignment of LC molecules no longer occurs, and therefore, Δn decreases, reducing the intensity of the diffracted first order light. A similar trend was also observed independent of the tip morphology and type of CNTs. We also observed that the peak voltage was reduced when the single-walled CNTs were aligned better, due to a more efficient alignment of LC molecules near the CNTs. The maximum diffraction intensity was observed around 2–3 V. As expected, a higher peak voltage was required for multi-walled CNTs due to their poor alignment and/or smaller field enhancement factor [41]. It is further noted that the degree of alignment of the CNTs plays an important role in improving the diffraction light intensity. We believe that our current approach for the development of transparent optical elements could be beneficial for realizing future 3D holography.

2.3. Self-Powered Liquid Crystal Displays

In addition to innovative and conceptual approaches to future LC applications, practical and multidisciplinary applications via the convergence of displays and energy generation technology have also attracted considerable attention. There is no doubt that the mobile information technology is one of the most important key features describing current society. In particular, display technology represented by LC displays in mobile devices is an essential, commonly used component for the information exchanges.

One of the most important issues in mobile devices is sustainable energy supply. Although the battery technology has been continuously improved, so far, it has always been required to realize sustainable cord-free, *i.e.*, self-powered devices. For this reason, various energy harvesting technologies have been actively studied, especially, and piezoelectric nano-energy harvesting has been considered as a promising technology, which is accelerated with the development of nanotechnology.

The energy harvesting functionality of piezoelectric ZnO nanowires arises from the modulation of the piezoelectric polarization when the mechanical force is applied on the nanowire, which induces the relative displacement of the Zn cations with respect to the O anions along the strain direction [33]. This piezoelectric effect produces ionic charges distributed along the nanowire and, hence, results in the piezoelectric field, which drives electrons to flow in an external circuit to balance the piezoelectric potential generated across the two ends of a nanowire. Consequently, the negative piezoelectric potential developed on the compressed top side of a nanowire by mechanical stress leads to the accumulation of electrons on the bottom side (the middle of Figure 7), whereas when the external force is released, the accumulated electrons on the bottom side flow back to the top side (the right of Figure 7) through the external circuit in order to balance the difference in Fermi levels at the two sides [26].

Figure 7. Operation principle of a piezoelectric energy harvester fabricated with ZnO nanowires. Reprinted with permission from [26]. Copyright 2013, Royal Society of Chemistry.

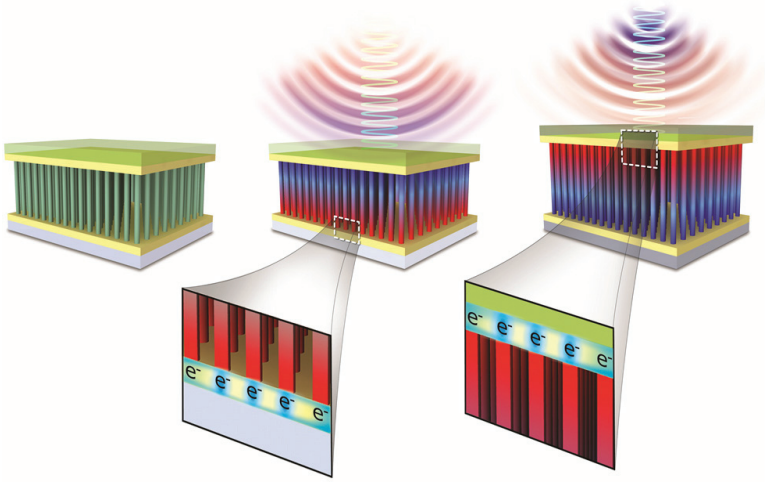

LCs, basically, are operated by voltages, which are favourable power consumption characteristics to the piezoelectric energy harvester without the need for a high current supply. In this regard, Wang's group at the Georgia Institute of Technology reported that a piezoelectric nano-generator can generate enough energy to drive a small LC display (Figure 8) [45]. They demonstrated that the harvesting performance is enhanced by using conical ZnO nanowires. Due to the geometrical shape, the nanowires are assembled with a unipolar feature, which is probably the key for producing a macroscopic piezoelectric potential in the direction normal to the substrate. This harvester produced output voltage up to 2 V (an equivalent open circuit voltage of 3.3 V) with a few hundreds of nano amperes of output current, which can drive a small LCD panel.

For sustainable piezoelectric energy harvesting to drive integrated devices, such as LC displays, it is important to target the proper mechanical energy sources. Sound is one of the most common and abundant mechanical energies in our daily life. However, due to the rarefaction nature of the air, the media of sonic waves, it is difficult to harvest the mechanical energy of sound. Since the first sonic-driven piezoelectric energy generator was reported by using of ZnO nanowires in 2008 [30], various efforts have been continued to improve the performance of sound energy harvesters. As a result, recently, it has been reported that enhanced sound energy harvesters can produce enough output power to operate a polymer-dispersed LC (PDLC) light shutter [27,46,47].

Recently, we successfully demonstrated operating PDLC light shutters using sonic-driven piezoelectric energy generators, as shown in Figure 9 [27]. It has been well known that the free electrons in an as-grown ZnO nanowire significantly screen piezoelectrically generated charges, resulting in decreasing the output piezopotential [26]. Therefore, to enhance the output characteristics, we introduced p-type counter dopants, such as P and Ag, to eliminate the free carrier screening effect by decreasing free electrons in the ZnO nanowire, because as-grown ZnO nanowires are naturally n-type semiconducting with superior conductivity due to oxygen deficiencies [26]. The doping process was carried out at low temperature compatible with glass substrate-based processes by using all solution processes based on a spin-on-dopant method [27]. Here, it is important to note that the low

temperature process is crucial for the hybrid system to integrate energy harvesters into displays, because most of all the display components are fabricated based on glass or plastic substrates.

Figure 8. (**a**) A schematic image of the fabricated energy harvester using ZnO conical nanowires (CNWs) and (**b**) a model showing the setup for measuring the energy conversion. The polystyrene substrate used to hold the nanogenerator at its upper side, where the force, F, is applied. The CNWs are under compressive strain during the deformation; (**c**) the model used for calculating the potential distribution across the top and bottom electrodes of the harvester with the presence of a pair of CNWs; (**d**) the measured output voltage; (**e**) a snap shot of an LC display driven by the harvester. Reprinted with permission from [45]. Copyright 2010, American Chemical Society.

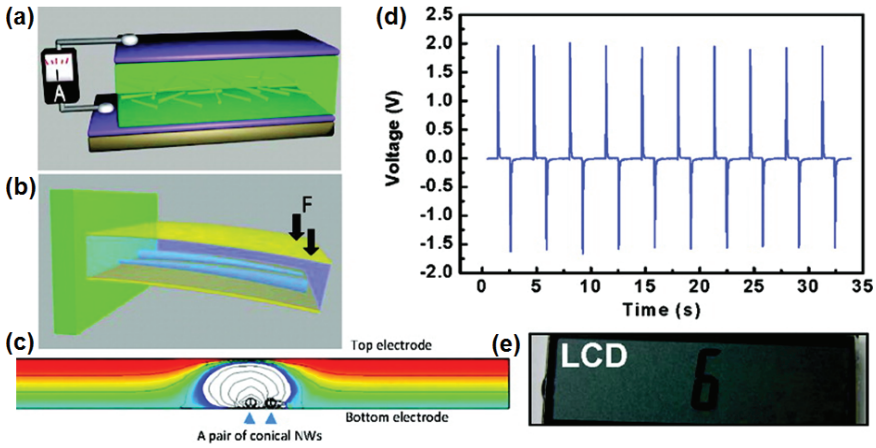

Figure 9. (**a**) SEM images of p-type ZnO:P nanorods on a glass substrate; (**b**) the piezoelectric output potential measured from sound-driven piezoelectric nanogenerators (SPNGs) consisting of ITO-coated flexible polyethylene terephthalate (PET) as a top electrode and ZnO nanorods before and after P-doping; (**c**) a polymer-dispersed LC (PDLC) device (4 cm × 5 cm) switched on (**left**) by an SPNG and (**right**) before being switched on using an SPNG, respectively. Reprinted with permission from [27]. Copyright 2014, Royal Society of Chemistry.

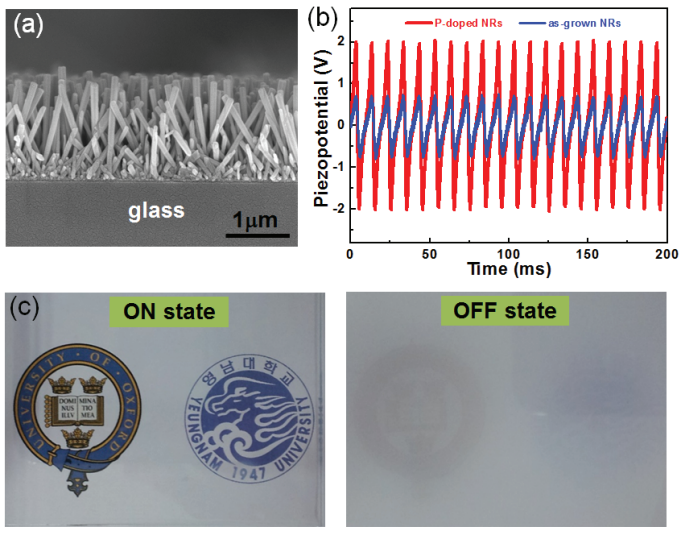

Furthermore, in order to address the issues related to the mechanical impedance of the substrate, we investigated various substrates toward an optimized harvesting system, as external mechanical energy sources are generally transferred into piezo-structures through the substrate. In this regards, textile with favourable form factors is one of the promising substrates for an effective harvester, due to its wide degree of freedom in shapes with flexible and stretchable characteristics, as well as higher efficiency in coupling external sonic waves into its own vibrational motion (Figure 10). Figure 10a shows the vibrational amplitudes of three different substrates, Si, flexible polyethersulfone (PES), and textile measured under the same input sonic power of 100 dB at 100 Hz using a laser optical vibrometer. The vibrational amplitudes were 30, 960 and 2250 μm for Si, flexible PES and textile substrates, respectively. With the optimized structures based on a textile substrate, the high output voltage and current of the harvester (8 V and 2.5 μA from 10 cm^2) were generated as shown in Figure 10c. In addition, to demonstrate the capability of directly driving a practical display device, reflective mode display (PDLC display) panels (9 cm × 3 cm) were driven by the textile nanogenerator (Figure 10d) [46].

Figure 10. (**a**) Large-area SEM images of ZnO nanowires grown on a textile substrate; (**b**) comparison of the vibration amplitude of the Si, flexible PES and textile substrates that were vibrated by a sonic wave; (**c**) output voltage and current from the large-area textile harvester (10 cm^2) at 100 dB and 100 Hz; (**d**) a PDLC display panel operated by the sound-driven textile harvester. Reprinted with permission from [46]. Copyright 2012, Royal Society of Chemistry.

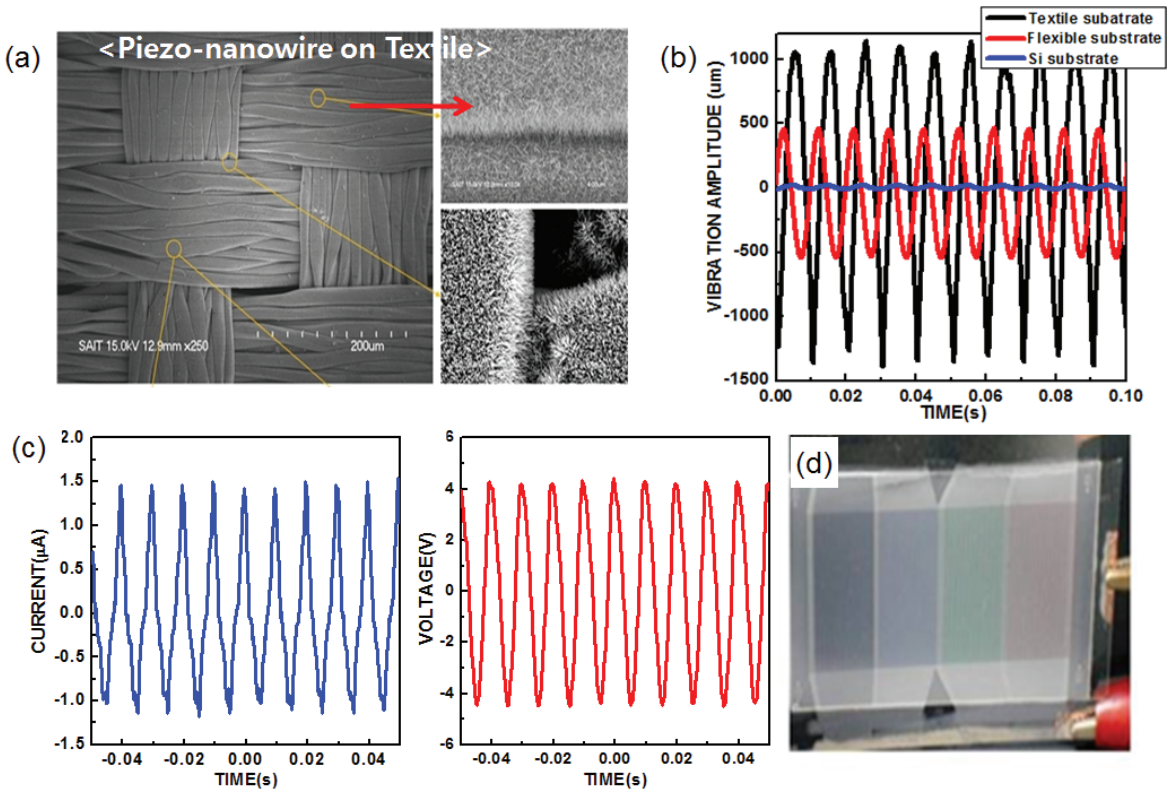

It is also expected that the combination of carrier controlled ZnO nanowires and textile substrates would be one of the viable ways to generate higher output power. To this end, we directly synthesized

Ag-doped ZnO nanowires by using a hydrothermal synthesis method fabricated under 90 °C without introducing any high temperature post-annealing processes. The Ag-doped nanogenerators made based on 10 cm^2 of a polyester textile substrate generated a power of 0.5 μW under a sound input of 80 dB, 100 Hz, which is nearly 2.9 times higher than that of a nanogenerator with un-doped ZnO nanowires, and successfully operated PDLC light shutters (Figure 11) [47]. These findings imply that our doping approach at low temperature provides opportunities for the potential use of textile nanogenerators with high performance as self-powered devices.

Grid-free displays, especially powered by an energy harvester, will be the basis serving as a key component for future mobile devices, and our study on the piezoelectric energy generator integrated with LC displays will provide great potential for realizing grid-free display systems.

Figure 11. (**a**) Schematic diagram of device operation for the ZnO nanowire-based nanogenerator grown on the flexible polyester; (**b**) piezoelectric potential and (**c**) piezoelectric current measured from Ag-doped ZnO nanowires (red line) and un-doped ZnO nanowires, respectively, (black line) on polyester substrates using sound waves; (**d**) OFF-state of the PDLC device; (**e**) ON-state of the PDLC device after generating sound waves. Reprinted with permission from [47]. Copyright 2013 Royal Society of Chemistry.

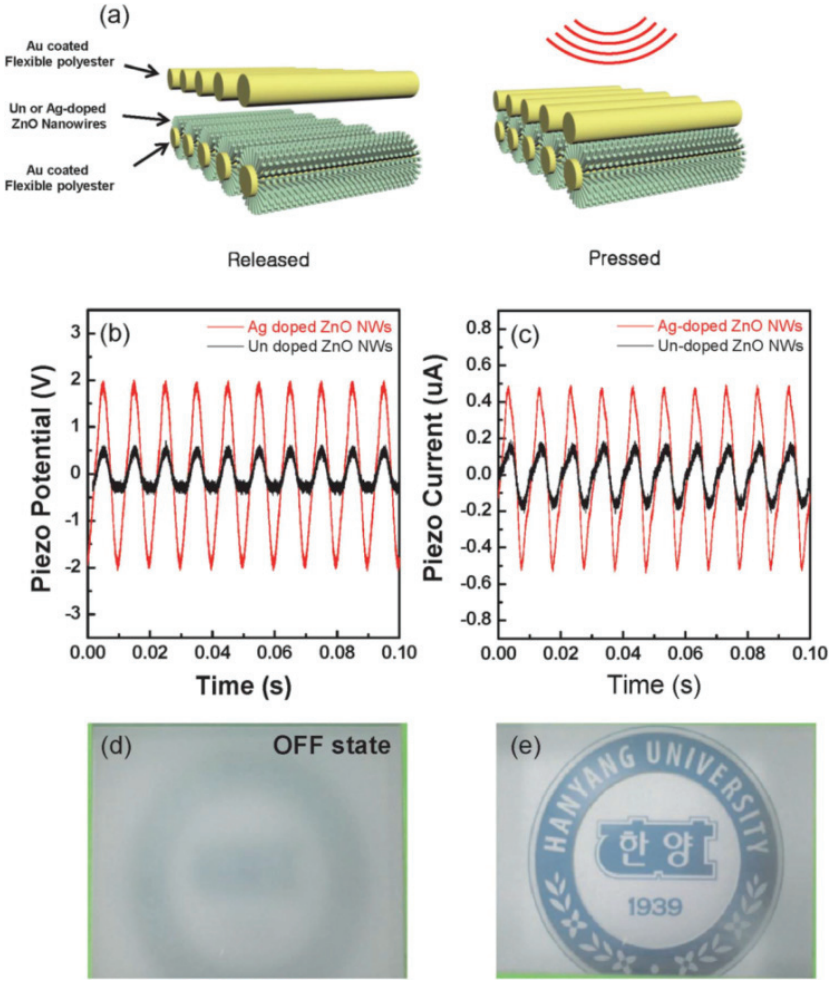

3. Experimental Section

Growth of ZnO nanowire arrays: ZnO nanowires were grown on a-plane sapphire substrates with Au catalysts by a vapour transport method. ZnO powder and graphite powder were mixed in a weight ratio of 1:1, and then, the mixed powders were ground together. A layer of Au thin film (~3 nm) was deposited on the sapphire substrate using electron-beam evaporation. The source materials and substrates were placed in an alumina boat, which was loaded at the centre of an alumina reaction tube located in a high-temperature tube furnace. The ZnO nanowires were then grown on the substrates at a temperature of 930 °C for 20 min under a flow of Ar (23 sccm [standard cubic centimeters per minute]).

Fabrication of nanowire FETs: To fabricate ZnO nanowire FET devices, ZnO nanowires were first dispersed by sonication in isopropyl alcohol and then transferred onto a silicon substrate by dropping a liquid suspension of ZnO nanowires from a pipette. A 100 nm-thick silicon oxide layer was employed as a gate oxide layer on a heavily doped p-type silicon substrate used as a global back gate. Source and drain electrode patterns were defined by conventional photolithography followed by electron beam evaporation of Ti (80 nm)/Au (40 nm) electrodes on a nanowire and lift off processes. The separation of source and drain electrodes was ~3 μm. The ferroelectric LC was simply spin-coated at 4000 rpm onto the ZnO nanowire channel by using a solution-based spin-coating method. For the top-gate nanowire FETs, cross-linked poly(4-vinylphenol) (PVP) (acting as a dielectric layer) was coated on the prepared substrate with source and drain electrodes, followed by a curing step. The cross-linked PVP dielectric layer was prepared by mixing PVP (10 wt% of solvent) with additive poly(melamine-co-formaldehyde) methylated (5 wt% of solvent) in propylene glycol monomethyl ether acetate (PGMEA). Top-gate electrodes were made by depositing a 50 nm-thick Au layer on the PVP layer using the electron beam evaporator.

Graphene/VACNT hybrid structure: Graphene was synthesized on a Cu foil (75 μm) using a thermal chemical vapour deposition (CVD) method and transferred onto the quartz substrate. The reaction chamber was heated to 1000 °C and then CH_4 (5 sccm), Ar (1000 sccm) and H_2 (200 sccm) gases were introduced into the reaction chamber for 2 min. After coating PMMA film on a graphene/Cu substrate, the Cu film was removed by submerging the film into Cu etchant (CE-100, TRANSENE Company, Danvers, MA, USA). The graphene/PMMA film was then transferred onto a quartz substrate. This process was repeated to obtain several layers of graphene. Conventional photolithography was used to make dot arrays with a ~1 μm dot size and ~15 μm spacing between dots. 10 nm Al and 1 nm Fe layers were deposited as catalysts for CNT growth. Vertically aligned CNTs were synthesized by remote plasma-enhanced CVD with Ar (200 sccm), H_2 (200 sccm) and C_2H_4 (75 sccm) gases at 750 °C for 5 min.

Optical cell assembly: The graphene/VACNTs hybrid structure was covered with the top ITO glass electrode separated by a 20-μm spacer. ITO glass was coated with polyimide and rubbed for horizontal alignment of the liquid crystal. A nematic liquid crystal with positive dielectric anisotropy (Merck, Darmstadt, Germany, ZLI 4792) was injected into the cell.

Polymer dispersed liquid crystal: PDLC composite materials consisting of a nematic LC TL203 (Merck, the ordinary refractive index no = 1.529) and a monomer PN393 (Merck, the polymer

refractive index np = 1.499) with weight ratio of 78:22 has been made by applying a UV-polymerization-induced phase separation method. The intensity of the UV light for curing the monomers was 20 mJ/cm^2, and indium-tin-oxide (ITO)-coated glass was used as the device substrates.

4. Conclusions

We present recent research snapshots of LCs that are focused on developing new LC applications. We recently demonstrated emerging applications of LCs ranging from electronics to holography and self-powered systems. Moreover, we describe novel concepts and operating principles of new memory and transparent and active-type 2D optical array devices based on LCs. Finally, we show self-powered display systems integrated with piezoelectric nanogenerators as one of the key technologies for future grid-free displays. This review will give insights not only into understanding the basic technical and scientific applications behind LCs, but also into developing new discoveries of the practically use of other LC-based devices.

Acknowledgments

The research leading to these results has received funding from the European Community's Seventh Framework Programme (FP7/2007-2013) under grant agreement no. 216777, Project "Nanocomputing Building blocks with Acquired Behaviour (NABAB)". This work was also supported by Korea Institute of Energy Technology Evaluation and Planning (KETEP) under grant No. 20128510010080 and 20138520030800. W.-K. Hong acknowledges the financial support from the National Research Foundation of Korea (NRF) grant funded by the Korean Government (No. NRF-2013K2A1C1076556) and the Korea Basic Science Institute (KBSI) (No. T43516).

Author Contribution

J. I. Sohn and W.-K. Hong, S. S. Choi and S. Cha conducted the part of experiments described in the article. H. J. Coles, M. E. Welland and J. M. Kim contributed to the scientific discussion and the structure of the article. The article was written and edited by J. I. Sohn and S. Cha.

Conflicts of Interest

The authors declare no conflict of interest.

References

1. Reinitzer, F. Beiträge zur kenntniss des cholesterins. *Monatsh. Chem.* **1888**, *9*, 421–441 (in German Language).
2. Yang, D.-K.; Wu, S.-T. *Fundamentals of Liquid Crystal Devices*; John Wiley & Sons: New York, NY, USA, 2006.
3. De Gennes, P.G.; Prost, J. *The Physics of Liquid Crystals*, 2nd paperback ed.; Clarendon Press: Oxford, UK, 1995.
4. Stephen, M.J.; Straley. Physics of liquid crystals. *Rev. Mod. Phys.* **1974**, *46*, 617–704.

5. Goodby, J.W. *Ferroelectric Liquid Crystals: Principles, Properties and Applicatio*ns; Gordon and Breach Science Publishers: London, UK, 1992; Volume 7.
6. Coles, H.; Morris, S. Liquid-crystal lasers. *Nat. Photon.* **2010**, *4*, 676–685.
7. Hong, W.-K.; Sohn, J.I.; Cha, S.; Kim, J.M.; Park, J.-B.; Choi, S.S.; Coles, H.J.; Welland, M.E. Programmable ZnO nanowire transistors using switchable polarization of ferroelectric liquid crystal. *Appl. Phys. Lett.* **2013**, *102*, 053504:1–053504:4.
8. Naber, R.C.G.; Tanase, C.; Blom, P.W.M.; Gelinck, G.H.; Marsman, A.W.; Touwslager, F.J.; Setayesh, S.; de Leeuw, D.M. High-performance solution-processed polymer ferroelectric field-effect transistors. *Nat. Mater.* **2005**, *4*, 243–248.
9. Mathews, S.; Ramesh, R.; Venkatesan, T.; Benedetto, J. Ferroelectric field effect transistor based on epitaxial perovskite. *Science* **1997**, *276*, 238–240.
10. Hoffman, J.; Reiner, J.W.; Walker, F.J.; Han, J.P.; Ahn, C.H.; Ma, T.P. Ferroelectric field effect transistors for memory applications. *Adv. Mater.* **2010**, *22*, 2957–2961.
11. Hong, W.-K.; Jo, G.; Sohn, J.I.; Park, W.; Choe, M.; Wang, G.; Kahng, Y.H.; Welland, M.E.; Lee, T. Tuning of the electronic characteristics of ZnO nanowire field effect transistors by proton irradiation. *ACS Nano* **2010**, *4*, 811–818.
12. Sohn, J.I.; Choi, S.S.; Morris, S.; Bendall, J.S.; Coles, H.J.; Hong, W.-K.; Jo, G.; Lee, T.; Welland, M.E. Novel nonvolatile memory with multibit storage based on a ZnO nanowire transistor. *Nano Lett.* **2010**, *10*, 4316–4320.
13. Fu, W.; Xu, Z.; Bai, X.; Gu, C.; Wang, E. Intrinsic memory function of carbon nanotube-based ferroelectric field-effect transistor. *Nano Lett.* **2009**, *9*, 921–925.
14. Zheng, Y.; Ni, G.-X.; Toh, C.-T.; Zeng, M.-G.; Chen, S.-T.; Yao, K.; Özyilmaz, B. Gate-controlled nonvolatile graphene-ferroelectric memory. *Appl. Phys. Lett.* **2009**, *94*, 163505.
15. Lee, H.S.; Min, S.-W.; Park, M.K.; Lee, Y.T.; Jeon, P.J.; Kim, J.H.; Ryu, S.; Im, S. MoS_2 nanosheets for top-gate nonvolatile memory transistor channel. *Small* **2012**, *8*, 3111–3115.
16. Kim, U.J.; Lee, I.H.; Bae, J.J.; Lee, S.; Han, G.H.; Chae, S.J.; Gunes, F.; Choi, J.H.; Baik, C.W.; Kim, S.I.; *et al*. Graphene/carbon nanotube hybrid-based transparent 2D optical array. *Adv. Mater.* **2011**, *23*, 3809–3814.
17. Butt, H.; Montelongo, Y.; Butler, T.; Rajesekharan, R.; Dai, Q.; Shiva-Reddy, S.G.; Wilkinson, T.D.; Amaratunga, A.J. Carbon nanotube based high resolution holograms. *Adv. Mater.* **2012**, *24*, OP331–OP336.
18. Ostroverkhova, O.; Moerner, W.E. Organic photorefractives: Mechanisms, materials, and applications. *Chem. Rev.* **2004**, *104*, 3267–3314.
19. Tay, S.; Blanche, P.-A.; Voorakaranam, R.; Tunc, A.V.; Lin, W.; Rokutanda, S.; Gu, T.; Flores, D.; Wang, P.; Li, G.; *et al*. An updatable holographic three-dimensional disply. *Nature* **2008**, *451*, 694–698.
20. Blanche, P.-A.; Bablumian, A.; Voorakaranam, R.; Christenson, C.; Lin, W.; Gu, T.; Flores, D.; Wang, P.; Hsieh, W.-Y.; Kathaperumal, M.; *et al*. Holographic three-dimensional telepresence using large-area photorefractive polymer. *Nature* **2010**, *468*, 80–83.
21. Talarico, M.; Golemme, A. Optical control of orientational bistability in photorefractive liquid crystals. *Nat. Mater.* **2006**, *5*, 185–188.

22. Lee, S.; Jeong, Y.-C.; Heo, Y.; Kim, S.I.; Choi, Y.-S.; Park, J.-K. Holographic photopolymers of organic/inorganic hybrid interpenetrating networks for reduced volume shrinkage. *J. Mater. Chem.* **2009**, *19*, 1105–1114.
23. Wilkinson, T.D.; Wang, X.; Teo, K.B.K.; Milne, W.I. Spare multiwall carbon nanotube electrode arrays for liquid-crystal photonic devices. *Adv. Mater.* **2008**, *20*, 363–366.
24. Rajasekharan-Unnithan, R.; Butt, H.; Wilkinson, T.D. Optical phase modulation using a hybrid carbon nanotube-liquid-crystal nanophotonic device. *Opt. Lett.* **2009**, *34*, 1237–1239.
25. Rajasekharan, R.; Bay, C.; Dai, Q.; Freeman, J.; Wilkinson, T.D. Electrically reconfigurable nanophotonic hybrid grating lens array. *Appl. Phys. Lett.* **2010**, *96*, 233108.
26. Sohn, J.I.; Cha, S.N.; Song, B.G.; Lee, S.; Kim, S.M.; Ku, J.; Kim, H.J.; Park, Y.J.; Choi, B.L.; Wang, Z.L.; *et al*. Engineering of efficiency limiting free carriers and an interfacial energy barrier for an enhancing piezoelectric generation. *Energy Environ. Sci.* **2013**, *6*, 97–104.
27. Sohn, J.I.; Jung, Y.-I.; Baek, S.-H.; Cha, S.; Jang, J.E.; Cho, C.-H.; Kim, J.H.; Kim, J.M.; Park, I.-K. A low temperature process for phosphorous doped ZnO nanorods via a combination of hydrothermal and spin-on dopant methods. *Nanoscale* **2014**, *21*, 2046–2051.
28. Wang, Z.L.; Song, J.H. Piezoelectric nanogenerators based on zinc oxide nanowire arrays. *Science* **2006**, *312*, 242–246.
29. Hu, Y.; Zhang, Y.; Xu, C.; Lin, L.; Snyder, R.L.; Wang, Z.L. Self-powered system with wireless data transmission. *Nano Lett.* **2011**, *11*, 2572–2577.
30. Cha, S.N.; Seo, J.-S.; Kim, S.M.; Kim, H.J.; Park, Y.J.; Kim, S.-W.; Kim, J.M. Sound-driven piezoelectric nanowire-based nanogenerators. *Adv. Mater.* **2010**, *22*, 4726–4730.
31. Cha, S.; Kim, S.M.; Kim, H.; Ku, J.; Sohn, J.I.; Park, Y.J.; Song, B.G.; Jung, M.H.; Lee, E.K.; Choi, B.L.; *et al*. Porous PVDF as effective sonic wave driven nanogenerators. *Nano Lett.* **2011**, *11*, 5142–5147.
32. Johnson, J.C.; Knutsen, K.P.; Yan, H.; Law, M.; Zhang, Y.; Yang, P.; Saykally, R.J. Ultrafast carrier dynamics in single ZnO nanowire and nanoribbon lasers. *Nano Lett.* **2004**, *4*, 197–204.
33. Wang, Z. ZnO nanowire and nanobelt platform for nanotechnology. *Mater. Sci. Eng.* **2009**, *64*, 33–71.
34. Miyajima, D.; Araoka, F.; Takezoe, H.; Kim, J.; Kato, K.; Takata, M.; Aida, T. Ferroelectric columnar liquid crystal featuring confiend polar groups within core-shell architecture. *Science* **2012**, *336*, 209–213.
35. Miyajima, D.; Araoka, F.; Takezoe, H.; Kim, J.; Kato, K.; Takata, M.; Aida, T. Columnar liquid crystal with a spontaneous polarization along the columnar axis. *J. Am. Chem. Soc.* **2010**, *132*, 8530–8531.
36. Choi, S.S.; Morris, S.M.; Huck, W.T.S.; Coles, H.J. Electrically tuneable liquid crystal photonic bandgaps. *Adv. Mater.* **2009**, *21*, 3915–3918.
37. Choi, S.S.; Morris, S.M.; Coles, H.J.; Huck, W.T.S. Wavelength tuning the photonic band gap in chiral nematic liquid crystals using electrically commanded surface. *Appl. Phys. Lett.* **2007**, *91*, 231110.

38. Hong, W.-K.; Sohn, J.I.; Hwang, D.-K.; Kwon, S.-S.; Jo, G.; Song, S.; Kim, S.-M.; Ko, H.-J.; Park, S.-J.; Welland, M.E.; *et al*. Tunable electronic transport characteristics of surface-architecture controlled ZnO nanowire field effect transistors. *Nano Lett.* **2008**, *8*, 950–956.
39. Hong, W.-K.; Kim, B.-J.; Kim, T.-W.; Jo, G.; Song, S.; Kwon, S.-S.; Yoon, A.; Stach, E.A.; Lee, T. Electrical properties of ZnO nanowire field effect transistors by surface passivation. *Colloids Surf.* **2008**, *313–314*, 378–382.
40. Noh, S.H.; Choi, W.; Oh, M.S.; Hwang, D.K.; Lee, K.; Im, S.; Jang S.; Kim, E. ZnO-based nonvolatile memory thin-film transistors with polymer dielectric/ferroelectric double gate insulators. *Appl. Phys. Lett.* **2007**, *90*, 253504.
41. Jeong, S.J.; Park, K.A.; Jeong, S.H.; Jeong, H.J.; An, K.H.; Nah, C.W.; Pribat, D.; Lee, S.H.; Lee, Y.H. Electroactive superelongation of carbon nanotube aggregates in liquid crystal medium. *Nano Lett.* **2007**, *7*, 2178–2182.
42. Jeon, S.Y.; Park, K.A.; Baik, I.-S.; Jeong, S.J.; Jeong, S.H.; An, K.H.; Lee, S.H.; Lee, Y.H. Dynamic response of carbon nanotubes dispersed in nematic liquid crystal. *Nano* **2007**, *2*, 41–49.
43. Jeong, H.J.; Choi, H.K.; Kim, G.Y.; Song, Y.I.; Tong, Y.; Lim, S.C.; Lee, Y.H. Fabrication of efficient field emitters with thin multiwalled carbon nanotubes using spray method. *Carbon* **2006**, *44*, 2689–2693.
44. Dai, Q.; Rajasekharan, R.; Butt, H.; Won, K.; Wang, X.; Wilkinson, T.D.; Amaragtunga, G. Transparent liquid-crystal-based microlens array using vertically aligned carbon nanofiber electrodes on quartz substrates. *Nanotechnology* **2011**, *22*, doi:10.1088/0957-4484/22/11/115201.
45. Hu, Y.; Zhang, Y.; Xu, C.; Zhu, G.; Wang, Z. High-output nanogenerator by rational unipolar assembly of conical nanowires and its application for driving a small liquid crystal display. *Nano Lett.* **2010**, *10*, 5025–5031.
46. Kim, H.; Kim, S.M.; Son, H.; Kim, H.; Park, B.; Ku, J.; Sohn, J.I.; Im, K.; Jang, J.E.; Park, J.-J.; *et al*. Enhancement of piezoelectricity via electrostatic effects on a textile platform. *Energy Environ. Sci.* **2012**, *5*, 8932–8936.
47. Lee, S.; Lee, J.; Ko, W.; Cha, S.; Sohn, J.; Kim, J.; Park, J.; Park, Y.; Hong, J. Solution-processed Ag-doped ZnO nanowires grown on flexible polyester for wearable nanogenerator applications. *Nanoscale* **2013**, *5*, 9609–9614.

Liquid-Crystal-Enabled Active Plasmonics: A Review

Guangyuan Si, Yanhui Zhao, Eunice Sok Ping Leong and Yan Jun Liu

Abstract: Liquid crystals are a promising candidate for development of active plasmonics due to their large birefringence, low driving threshold, and versatile driving methods. We review recent progress on the interdisciplinary research field of liquid crystal based plasmonics. The research scope of this field is to build the next generation of reconfigurable plasmonic devices by combining liquid crystals with plasmonic nanostructures. Various active plasmonic devices, such as switches, modulators, color filters, absorbers, have been demonstrated. This review is structured to cover active plasmonic devices from two aspects: functionalities and driven methods. We hope this review would provide basic knowledge for a new researcher to get familiar with the field, and serve as a reference for experienced researchers to keep up the current research trends.

Reprinted from *Materials*. Cite as: Si, G.; Zhao, Y.; Leong, E.S.P.; Liu, Y.J. Liquid-Crystal-Enabled Active Plasmonics: A Review. *Materials* **2014**, 7, 1296–1317.

1. Introduction

Plasmonics [1–13], the study of the interaction between electromagnetic field and free electrons in a metal, has drawn increasing attention recently due to its huge potential for solving many eminent issues encountered by our world. Up to now, exciting plasmonic applications, for instance, super-resolution imaging [14–19], optical cloaking [20–23], and energy harvesting [24–29], have been reported. Many other potential applications are under development. All these developments are attributed to the advanced nanofabrication techniques. Top-down nanofabrication techniques such as electron beam lithography [30–33] and focus ion beam milling [34–40] allow the accurate fabrication of structures at nanoscale with desirable trade-off on the high equipment expenses, as well as the considerably long time during sample preparation. Bottom-up techniques like self-assembly [41–43] can easily achieve regular patterns at a large scale at a rather low cost, but are not preferred for the cases that require accurate positioning and alignment with nanometer precision. Despite their strengths and weaknesses, both top-down and bottom-up techniques make their unique contributions to plasmonics by providing various nanostructures for plasmonic applications for different purposes. One major drawback of such plasmonic devices is that the fabricated nanostructures serve as passive devices providing consistent outputs given the same inputs, which greatly limits their application because of the additional investments required in fabricating another similar device with little change in the sample design. Thus, the new research field of active plasmonics emerges, which deals with reconfigurable function after the devices are fabricated, with the help of active mediums responsive to certain stimulus. Many active mediums have been used to build active plasmonic devices, including liquid crystals [44–59], molecular machines [60,61], elastic polymers [62–64], and chemical oxidation/reduction [65–67]. Among all the mentioned active mediums, liquid crystal stands out from all the rest because of its large birefringence on refractive index, low threshold on transition among different states, and versatile driven methods to cause the transitions. As a truly

unique gift from nature, liquid crystals possess the smallest elastic constants and the largest birefringence among all known materials. In addition, their large birefringence spans the entire visible-infrared spectrum and beyond, which was first reported by Wu [68] in 1986. By virtue of their organic nature, they can be chemically synthesized and processed on a very large scale; they are also compatible with almost all technologically important optoelectronic materials. The alignment of liquid crystals can be easily controlled by many means, such as electricity, light, and acoustic waves, thus making them an excellent candidate for the development of active nanophotonics.

By integrating liquid crystals with plasmonic nanostructures, active plasmonic materials and devices with enhanced performance have been demonstrated. In this review, we summarize the recent research *progress* and achievements in liquid crystal based plasmonics. We hope the contents covered in this review can serve as a tutorial introduction to readers with little background in either plasmonics or liquid crystals. We also hope experienced researchers can further expand their knowledge of the given topic and be inspired to take this field to new horizons.

2. Plasmonics and Liquid Crystal Basics

2.1. Surface Plasmons

Surface plasmons are a special kind of light formed by collective electron oscillations at the interface of a noble metal and dielectric. They can only propagate at the metal/dielectric interface and decay exponentially away from the interface. Surface plasmons exhibit different properties as their counterparts with the same frequencies, like much larger wave vectors, very short wavelengths, and limited propagating length with the dumping loss while propagating inside the metal. They also fit into Maxwell equations, and the wave vector supported by different combinations of metal and dielectric interfaces can be calculated by solving the equation as shown below:

$$k_{sp} = k_0 \sqrt{\frac{\varepsilon_m \varepsilon_d}{\varepsilon_m + \varepsilon_d}} \quad (1)$$

where k_{sp} represents the wave vector of surface plasmons and k_0 is the wave vector of the incident light in vacuum. ε_m and ε_d are dielectric constants of metal and dielectric, respectively. From the equation above, it is clear that direct conversion from propagating electromagnetic waves into surface plasmons is impossible due to the mismatch of their wave vectors. There are many different ways to solve this problem and the most commonly used ones are Kretschmann/Otto configurations and gratings, as illustrated in Figure 1.

The Kretschmann configuration consists of a prism with high refractive index attaching to a glass slide with refractive index matching to oil; the other side of the glass slide is covered with a thin layer of gold film. There are two metal/dielectric interfaces found in this system as air/gold and glass/gold interfaces. According to Equation (1), the two different interfaces support different surface plasmon modes. Incident light from the prism side cannot excite surface plasmons on both interfaces; however, with the help of a large refractive index from the prism side, it is possible that the leakage horizontal wave vectors from the incident light on the prism side will match the surface plasmon wave vector on the air side, validating the relation of:

$$n_p k_0 \sin\theta = k_0 \sqrt{\frac{\varepsilon_m \varepsilon_{air}}{\varepsilon_m + \varepsilon_{air}}} = k_{sp,air} \quad (2)$$

where n_p is the refractive index of the prism; ε_{air} is the dielectric constant of air and θ represents the incident angle from the prism side. One alternative way is to use gratings, where the grating constant provides the missing momentum components from the incident light to surface plasmons. In order to do so, the period of the gratings should be at the close range of the incident wavelength. The equation describing this process can be expressed as:

$$k_{sp} = n_i k_0 \sin\theta \pm m\Lambda \quad (3)$$

$\Lambda = 2\pi/d$ is the grating constant (d is the period of grating). n_i is the refractive index of incident plane; θ is the incident angle and m is integer. Both methods are well investigated and have found their wide applications in plasmonic-related research with many other excitation methods being developed. Sometimes they can be combined together to maximize the system performance. The excitation conditions have to be strictly followed to allow surface plasmons to be excited; while a less strict method requiring irregular sharp edges can also excite surface plasmons through the strong scattering caused by the wave vector match; however, the exciting efficiency is quite low since only a small amount of wave vectors can match with surface plasmon wave vectors during the exciting process.

Figure 1. (**a**) Kretschmann configuration for surface plasmon excitation. The matching of wave vectors between surface plasmons and the incident light is achieved with the help of a prism with high refractive index and (**b**) the large surface plasmon wave vectors can also be obtained with the help of a grating. The grating provides additional wave vector components that can assist the conversion from incident light into surface plasmon waves.

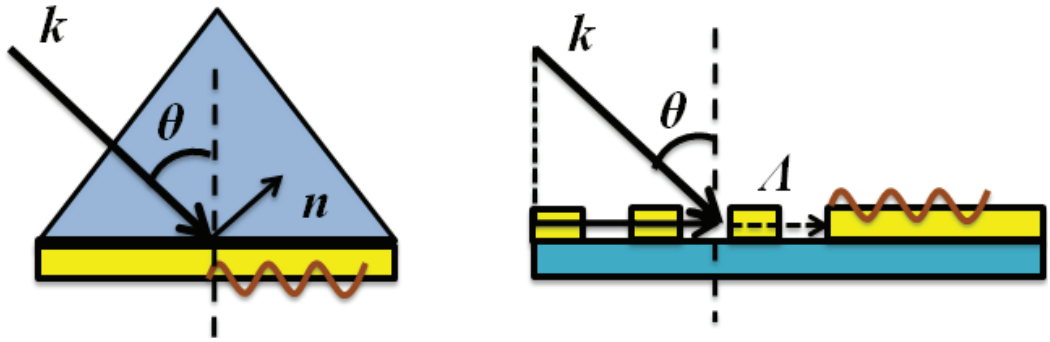

(**a**) (**b**)

Plasmonics is the further extension of surface plasmons, with its focus on the light-matter interaction occurring at nanoscales along with different nanoparticles and nanostructures. At this scale, light can not only be confined at the metal/dielectric interface, but also can be squeezed, tightly focused/confined, and manipulated at will with the assistance from various nanostructures. Its huge potential in various applications such as energy, biomedicine, metamaterials and photonic/quantum computing has been explored and revealed from time to time.

2.2. Liquid Crystals

Liquid crystals have attracted a lot of attention due to the unique electro-optical and thermo-optical properties and have been used in numerous applications [69,70], such as liquid crystal displays for televisions, projectors, watches, cellphones, spatial light modulators for adaptive optics in real time optical imaging, optical switches and attenuators for telecommunications, and optical phase arrays for beam steering, *etc*. The research on liquid crystal materials and devices is of special importance not only to the quality of our daily life but also to the development of the human society.

Figure 2. Phases of liquid crystals: (**a**) nematic phase; (**b**) smectic phase and (**c**) cholesteric phase.

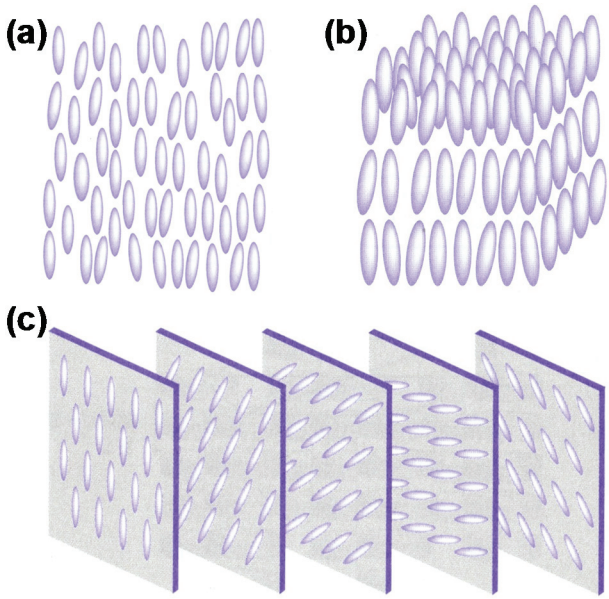

Generally speaking, there are three phases of thermotropic liquid crystals, known as the nematic phase, smectic phase, and cholesteric phase. Figure 2a illustrates the nematic phase in which only long range orientational order of the molecular axis exists. Figure 2b shows the smectic phase in which one-dimensional translational order as well as orientational order exists. Figure 2c illustrates the cholesteric phase of a liquid crystal by viewing the distribution of molecules at several planes that are perpendicular to the helical axis. The cholesteric phase is actually a nematic type of liquid crystal except that it is composed of chiral molecules. As a consequence, the structure acquires a spontaneous twist in line with a helical axis normal to the director. The twist can be right-handed or left-handed depending on the molecular chirality. Under proper treatment, a slab of nematic liquid crystal can be obtained with a uniform alignment of the director. Such a sample exhibits uniaxial optical symmetry with two principal refractive indices n_o and n_e. The ordinary refractive index n_o is for light with electric field polarization perpendicular to the director and the extraordinary refractive index n_e is for light with electric field polarization parallel to the director. The birefringence (or optical anisotropy) is defined as $\Delta n = n_e - n_o$. If $n_o < n_e$, liquid crystal is of positive birefringence, whereas if $n_o > n_e$, it is of negative birefringence. In classical dielectric theory, the macroscopic refractive index is related to the molecular polarizability at optical frequencies. The existence of the

optical anisotropy is mainly due to the anisotropic molecular structures. In the optical regime, $\varepsilon_{\parallel} = \varepsilon_0 n_e^2$ and $\varepsilon_{\perp} = \varepsilon_0 n_o^2$, thus $\Delta\varepsilon = \varepsilon_0 (n_e^2 - n_o^2)$. For most liquid crystals, the ordinary refractive index is around 1.5. The optical anisotropy plays an essential role in changing the polarization state of light in liquid crystals.

For light propagating in the liquid crystal with an incident angle θ relative to the optical axis, shown as Figure 3, two eigen refractive indices are seen by the light with two modes of propagation. One mode with its polarization direction perpendicular to the plane formed by the wave vector and the optic axis is called ordinary wave, which sees a refractive index of n_o (independent of the incident angle θ). The other one with its polarization direction parallel to the plane formed by the wave vector and the optic axis is called extraordinary wave, which sees an effective refractive index (dependent of the incident angle θ). The effective refractive index seen by the light can be written as:

$$n_{\text{eff}}(\theta) = \left[\frac{\cos^2 \theta}{n_o^2} + \frac{\sin^2 \theta}{n_e^2} \right]^{-\frac{1}{2}} \tag{4}$$

Similarly, the optical anisotropy is also a function of temperature and approximately linearly proportional to the order parameter *S*. A general trend of the refractive index is plotted in Figure 4 as a function of temperature [71]. As we can see, the optical anisotropy decreases as the temperature increases and vanishes in the isotropic phase.

Figure 3. Light propagation in uniaxial mediums.

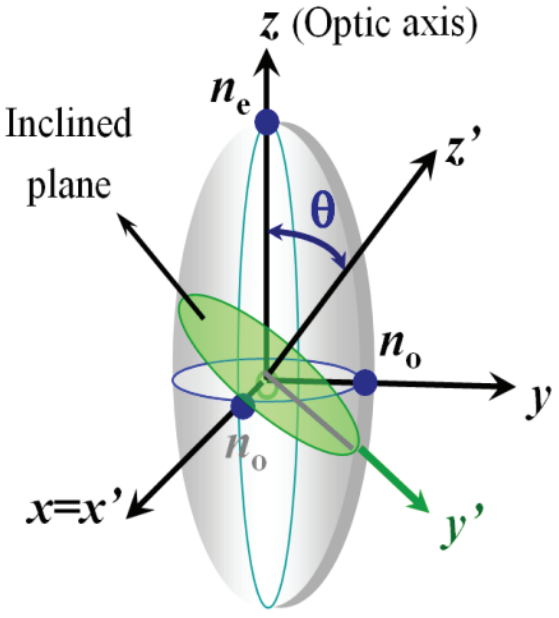

By combining liquid crystals with plasmonics, a new research category of liquid crystal based plasmonics as a branch of active plasmonics is eminent and starts to draw increasing attention from researchers all over the world. Here, we summarize recent research progresses and achievements of the liquid crystal plasmonics to share our thoughts about the field, and hopefully inspire talented researchers who are interested in pursuing excellence in this research area.

Figure 4. Temperature-dependent refractive indices of 5CB at λ = 546, 589 and 633 nm. Squares, circles, and triangles are experimental data for refractive indices measured at λ = 546, 589 and 633 nm, respectively. Figure 4 is adapted from reference [71].

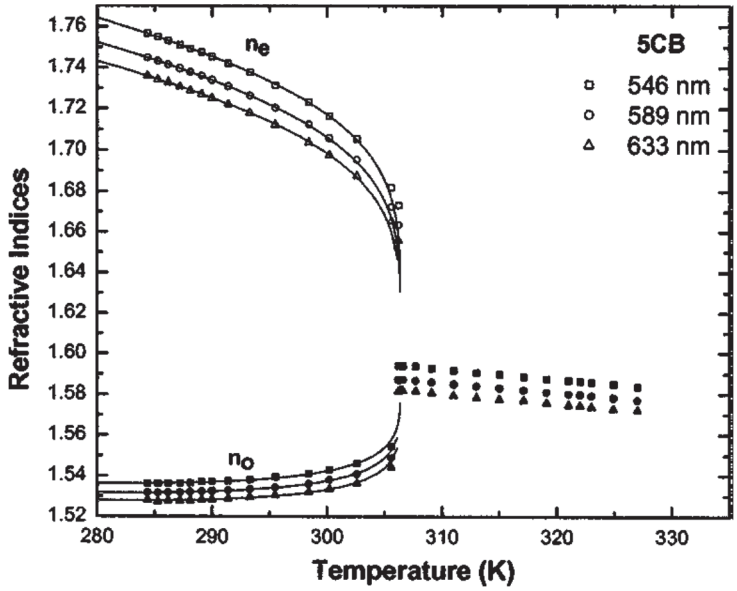

3. Active Plasmonic Devices Based on Liquid Crystals

The birefringence of liquid crystal is demonstrated as a difference in refractive index, making it an ideal active medium for active plasmonic devices for different applications, such as plasmonic switches [50–54], active plasmonic color filters [30,35,39] and plasmonic waveguides [72]. While the concept of applying liquid crystal to plasmonic nanostructure is straightforward, there are various ways to pump or drive the liquid crystal to achieve a noticeable refractive index change. In the following, representative liquid crystal based active plasmonic devices will be categorized and discussed according to the driving methods.

3.1. Electric-Field-Driven Method

Electric fields have very strong impacts on rod shape of liquid crystal molecules. When the liquid crystal molecules are subject to an electric field, one end of a molecule has positive charges, while the other end is negatively charged, forming an electric dipole. As a result, the director of the liquid crystal molecules will be re-oriented along the direction of an external electric field. Therefore, electric field is the most commonly used method to drive the liquid crystal devices. Utilizing this characteristic of the liquid crystal, efforts have been made to combine liquid crystals with periodically nanostructured metal films to develop electronically controlled transmission, reflection, and absorption of the plasmonic structures, concerning their applications on switches, filters, and modulators. One example is given by Dickson *et al*. [55], who have demonstrated precise control over surface plasmon dispersion and transmission of gold nanohole arrays using liquid crystals. A schematic of the experimental setup is shown in Figure 5a. A liquid crystal layer with the thickness controlled by the spacers is sandwiched between a conductive indium-tin-oxide (ITO) glass substrate and a gold film with nanohole arrays milled by using a focused ion beam. White light impinging

from the ITO side of the sample will pass through the liquid crystal layer and then reach the nanostructures to excite different surface plasmon polariton modes. Upon applying voltages, electric fields are built up across the ITO substrate and the gold film, and the liquid crystal molecules tend to realign along the electric field direction. As a result, effective refractive index at the interface of gold/liquid crystal is changed and subsequently results in a variation on the surface plasmon dispersion relation; thus, changing the excitation conditions of certain plasmon modes. This change is phenomenally reflected as a transmission modulation from the spectrum and provides us an active control of surface plasmon modes. De Sio *et al.* [57] also reported that a carrier accumulation layer in the proximity of the ITO substrate can be formed under the external electric field, hence modifying the effective refractive index around the metallic nanostructures and affecting their plasmonic resonances subsequently. To achieve an additional degree of control freedom, dual-frequency liquid crystal (DFLC) therefore is much preferred in designing an active plasmonic device, because it responds to the applied voltages with different frequencies. DFLC can change its sign of dielectric anisotropy from positive to negative, or negative to positive, upon the frequency change of the applied electric fields [73,74]. Complementary gold nanodisk and nanohole arrays have been demonstrated using electron-beam lithography followed by lift-off process, which are promising carriers to build plasmonic devices, as shown in Figures 5b,c. By overlaying a DFLC layer on these nanodisk and nanohole structures, reversible tuning of plasmonic resonances and transmission have been demonstrated. In these hybrid systems, homeotropic alignment of DFLC was set at the initial state by using a self-assembly alignment layer of hexadecyl trimethyl ammonium bromide (HTAB). When the frequency of the applied electric field is lower than the crossover frequency of DFLC, and all the liquid crystal molecules will keep the homeotropic alignment, *i.e.*, perpendicular to the substrate, which is independent of applied voltages. Once the applied frequency exceeds the crossover frequency, the liquid crystal molecules tend to prefer the homogeneous alignment, *i.e.*, parallel to the substrate, which is dependent on applied voltages. As a result, the switching/tuning effect with various transmissions can be easily obtained by varying applied voltages. Another example of tuning nanorod plasmons using liquid crystal is given by Khatua and co-workers [58]. With the applied external voltage as low as 4 V, complete modulation of the polarized scattering intensities of individual gold nanorods can be simply achieved. Note that the demonstrated strategy can be readily translated to other antenna architectures with more complex designs and various plasmonic elements for the electrical manipulation of light in structures with nanoscale dimensions.

Recently, a plasmonic Fano switch has also been demonstrated with a more specific design [75]. The device consists of a specifically designed cluster of gold nanoparticles fabricated using electron-beam lithography. The cluster comprises a large hemi-circular disc surrounded by seven smaller nanodiscs as shown in Figure 6a. Interactions between LSPRs of the individual nanoparticles within a cluster lead to a so-called Fano resonance, which is a result of near-field coupling between collective “bright” and “dark” plasmon modes of the cluster. By breaking the symmetry of the nanoparticle cluster through the hemi-circular centre disc, the Fano resonance is polarization-dependent and can only be observed for one polarization of the incident light. As a result, no Fano resonance appears in the light spectrum, for incident light that is polarized at 90° to this direction. The nanoparticle clusters are incorporated into liquid crystals in which the molecules at the device

interface can be rotated in plane by 90° when an AC voltage of about 6 V is applied. The field creates a twist in the overall alignment direction of the crystals, which leads to a phase transition from "homogenous nematic" (voltage off) to "twisted nematic" (voltage on). Due to the birefringence of the liquid crystal, the voltage-induced phase transition causes an orthogonal rotation of the scattered light from the plasmonic clusters as it travels through the device. This results in switching between the optical response with and without the Fano resonance, as shown in Figure 6b.

Figure 5. (**a**) Schematic and experimental setup of a plasmonic switch consisting of nanostructures and liquid crystals. Electric field is generated by applying voltages across the gold film and bottom ITO glass, switching effect at the wavelength of 670 nm is shown in the inset; (**b**) SEM image of nanohole array and the working mechanism of DFLC. The scale bar indicates one period length of 300 nm; (**c**) SEM image of gold nanorods of another design of plasmonic switch using DFLC. The inset extinction spectrum shows the plasmonic resonance change under different voltage and frequency combinations. Figure 5**a**–**c** is adapted from reference [55], reference [47] and reference [50], respectively.

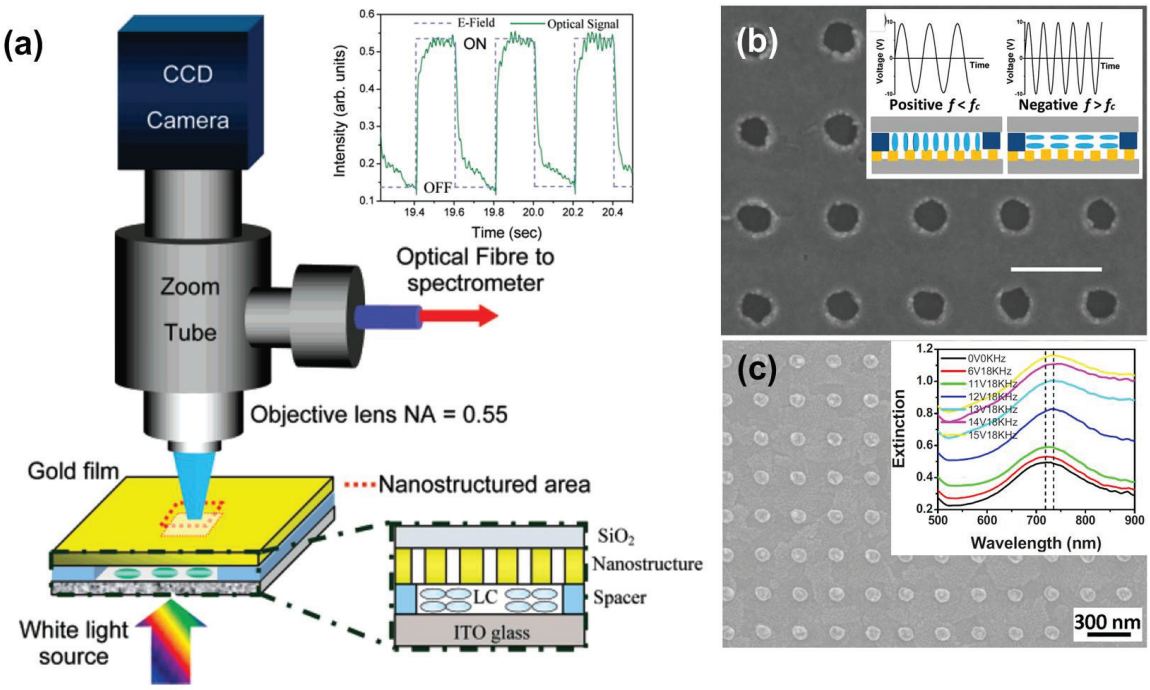

3.2. Light-Driven Method

All-optical tuning method has been widely applied in liquid crystal based optical elements like spatial light modulator, filter, reflector, *etc.*; and it has many advantages such as non-contact tuning, low power consumption, and friendly integration, making it an exciting concept to be applied on light driven liquid crystal based devices. As compared to the electrical tuning method, light driven method requires: (1) no conductive ITO substrates; (2) low power consumptions and (3) large operation windows covering UV to mid-IR. Azobenzene and its derivatives are a widely used guest in a liquid crystal host. They have a trans-cis reversible isomerization dynamic behavior upon

exposure to a UV or visible light beam. The isomerization will disrupt the local order of surrounding liquid crystal molecules in the mixture, resulting in realignment of those liquid crystal molecules to exhibit a refractive index change. Such an index change has been utilized for dynamic control of many photonic devices, such as switchable gratings [51,76–79] and photonic crystals [80,81]. It is also straightforward for dynamic control of surface plasmons [52,82,83]. One example of a light-driven plasmonic switch has been demonstrated by Hsiao *et al.* [52] with a light responsive liquid mixture consisting of nematic liquid crystals and an azobenzene derivative. 4-butyl-4'-methyl-azobenzene (BMAB) is used to induce the switching effect. Figure 7a shows the spectral changes of BMAB under UV exposure that reflects its trans-cis isomerization process. Figure 7b shows the extinction spectra of a photoresponsive liquid crystal/gold nanodisk array (see the inset of Figure 7b) cell at normal incidence of a probing beam before (solid curve) and after (dashed curve) the light pump (λ = 420 nm, I = 20 mW) at the incident angle of 45°. One can observe a 30 nm blue-shift of the extinction peak. Figure 7c shows the spectral changes of extinction in another azo dye (methyl red) doped grating integrated with the same gold nanodisk array [83]. The switching effect before and after the light pump is shown in Figure 7d with both switching "ON" and "OFF" time less than 4 seconds, which is the typical response time for the azobenzene and its derivatives under the continuous light pump. However, under the pulsed laser pump, the response time of azobenzene doped liquid crystals could reach nanoseconds since the photoisomerization of azobenzene from trans-state to cis-state could undergo the pathway of either π–π^* rotation or n–π^* inversion with different response speeds [84].

Figure 6. (**a**) SEM image of the octamer structure (top), which shows Fano-like and non-Fano like spectra with polarization at 0° and 90° (bottom); (**b**) the scattering spectra of the octamer structure in the V_{on} and V_{off} states measured at a detection: the homogenous nematic phase in the V_{off} state (top) and the twisted nematic phase in the V_{on} state (bottom). All figures are adapted from reference [75].

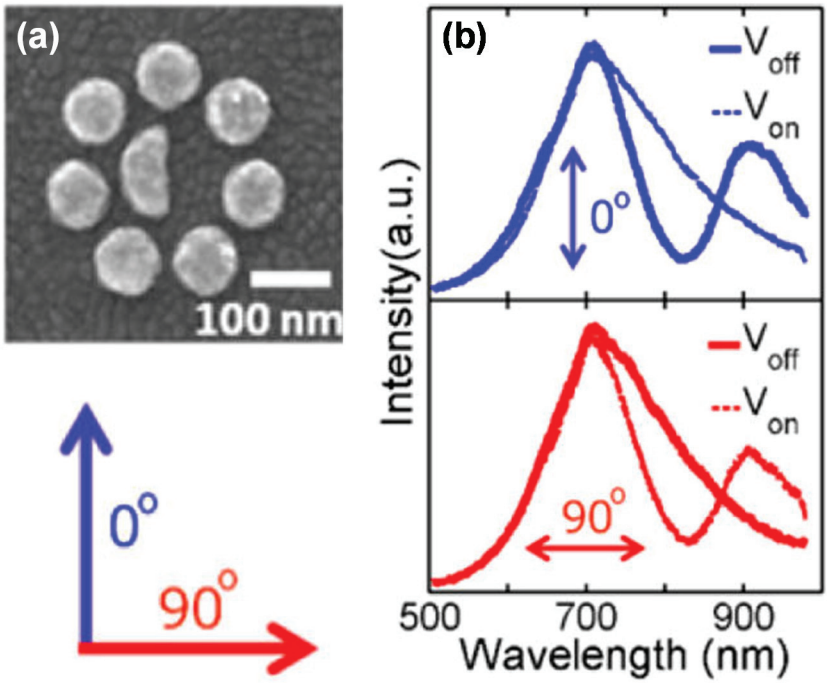

Figure 7. (**a**) The spectral changes of BMAB under UV exposure that reflects its trans-cis isomerization process; (**b**) extinction spectra (normal incidence) of a photoresponsive liquid crystal/gold nanodisk array cell before (solid curve) and after (dashed curve) the application of a 20 mW pump light (λ = 420 nm) at an incident angle of 45°. Thirty nm blue-shift of the extinction peak can be observed. The alignment of liquid crystal molecules is achieved mechanically using photo-responsive azobenzene. (**c**) The spectral changes of extinction in another azo dye (methyl red) doped grating integrated with the same gold nanodisk array and (**d**) switching effect and time of holographic polymer-dispersed liquid crystals gratings upon laser excitation. Figure 7a,b is adapted from references [39,52], respectively. Figure 7c,d is adapted from reference [83].

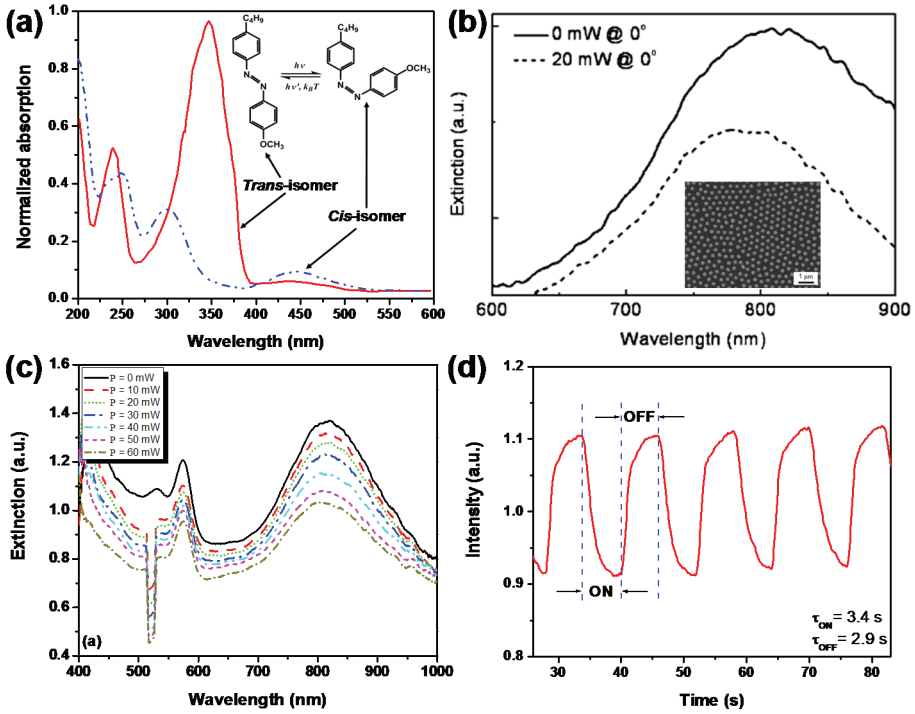

Based on the same working mechanism, we have also demonstrated light-driven plasmonic color filters with high optical transmission and narrow bandwidth by overlaying a layer of photoresponsive liquid crystals on gold annular aperture arrays (AAAs). The schematic of the light-driven plasmonic color filters and experimental setup is shown in Figure 8a. The enlarged Part I in Figure 8a shows the fabricated square pattern of gold AAAs using focused ion beam lithography. The inner and outer radii of each individual aperture are labeled as r_{in} and r_{out}, respectively. The magnified Part II in Figure 8a shows the working mechanism of the optical driving process: a reversible nematic–isotropic phase transition induced by the trans-cis photoisomerization of the photochromic liquid crystals. The gold AAAs with various aperture sizes and periods have been reported to generate different colors in the visible range. The addition of photoreponsive liquid crystals will then make the transmission of color filters optically tunable. The photosensitive liquid crystal mixture has similar composition as other mixtures discussed above. With its large birefringence Δn = 0.225 (at the wavelength of 589 nm, n_o = 1.521, n_e = 1.746), it offers major intensity modulation of the transmitted color through the plasmonic color filter shown in Figure 8b, where the intensity of each

individual color generated from plasmonic structures can be further tuned, as confirmed by both simulations and experiments in the reported work [39]. Therefore, any color could be achieved through the composition of three tunable primary red, green and blue color filters. This all-optical tuning behavior is highly reversible and reproducible, making such a kind of color filter promising in all-optical information processing and displays. Another useful device is plasmonic absorbers, which can exhibit extraordinary absorption efficiency of more than 90% at designated wavelength bands by engineering nanostructures with different shapes and sizes. Inclusion of birefringent nematic liquid crystals in their makeup can make the absorption bands electrically or optically tuned or modulated, hence providing additional freedom to control the absorption bands. Zhao *et al*. have experimentally demonstrated a light-driven plasmonic absorber based on a nematic liquid crystal host doped with an azo dye [45]. Figure 8c shows the schematic of light-driven reconfigurable plasmonic absorber. A cladding layer of liquid crystals mixed with azo dyes is added on top of the plasmonic absorber. The use of azo dye is to effectively absorb the light energy and transfer the absorbed energy to heat up the liquid crystal environment. The liquid crystal used here is thermo-sensitive type with transition temperature of 35 degrees (5CB). Liquid crystal will transform from a nematic to isotropic state after heating up, along with a gradual refractive index change from 1.61 to 1.56 with the increase of temperature. The refractive index change modifies the frequency selected surfaces as well as the resonance frequency of the resonant cells formed by top gold nanostructures, and a bottom gold layer. A noticeable shift of the absorption dips of around 25 nm has been confirmed in Figure 8d. Note that the photosensitive liquid crystals with an azo group in their mesogenic structure exhibit a higher solubility compared to non-mesogenic azo-dyes [85–87]. Furthermore, the orientational order of liquid crystals still remains high in the presence of mesogenic azo dopants and their photoisomerization effect on the host liquid crystal is stronger than that of non-mesogenic dopants.

3.3. Surface Acoustic Wave (SAW)-Driven Method

Although liquid crystal driven by surface acoustic waves (SAWs) is loosely connected to the scope of this review paper, we put it here as an insight into prospective integration of liquid crystal with micro- and nano-technologies. SAWs are sound waves propagating along the surface of a piezoelectric substrate. Its low power consumption and intactness from the driven medium make it an effective approach to re-align the liquid crystal molecules. Liu *et al.* [49] have demonstrated a SAW-driven light shutter based on polymer-dispersed-liquid-crystal (PDLC). A schematic of the designed light shutter is shown in Figure 9a. It consists of a PDLC film layer and two inter-digital transducers (IDTs) on a piezoelectric substrate. The PDLC film consists of liquid crystal droplets randomly distributed in a polymer matrix. Before applying SAW, the PDLC film exhibits strong scattering due to the refractive index mismatch between the polymer matrix and liquid crystal droplets, thus demonstrating a non-transparent state. When a radio frequency signal is applied to IDT, SAW is excited and then propagates along the surface. When the propagating SAW encounters the PDLCs, a longitudinal wave is induced and leaks into the PDLCs. The longitudinal wave will cause the liquid crystal molecules to realign to eliminate the refractive index mismatch, *i.e.*, their ordinary refractive index matches with that of the polymer. As a result, the PDLC film becomes completely

transparent. The acoustic wave induced streaming inside the liquid crystal rich regions as well as the temperature change caused by the attenuation of this longitudinal wave are believed to be key factors to reorient the alignment of liquid crystal molecules. Figure 9b shows the experimental results marking the "ON" and "OFF" states of the SAW-driven shutter. The word "PDLC" can be clearly observed by turning 'ON' the shutter, and the film is opaque when the shutter is "OFF". We believe that such a SAW-driven liquid crystal mechanism will be applicable to the plasmonic devices as well. Our research on SAW-driven plasmonic devices incorporated liquid crystals is currently on-going.

Figure 8. (**a**) Light driven plasmonic color filter tuned by liquid crystals. The nanostructure used is a new type AAA that can generate different colors by changing the sizes and periods of AAA. One example of AAA is given in the inset; (**b**) different colors generated using plasmonic color filters. By pumping the liquid crystal mixtures to realign the liquid crystal molecule orientation, intensity modulation on the ultra-small color filter can be achieved and demonstrated in the reported work.; (**c**) one representative case of reconfigurable plasmonic absorber using liquid crystal. The small and big nanodisk arrays in the inset are designed to produce two absorption maximums to improve the performance of the plasmonic absorbers and (**d**) light sensitive liquid crystal mixture is used to tune the absorption dips in real time. Experimental results confirm a tuning range around 25 nm in the near infrared range. Figure 8a,b is adapted from reference [39] while Figure 8c,d is adapted from reference [45].

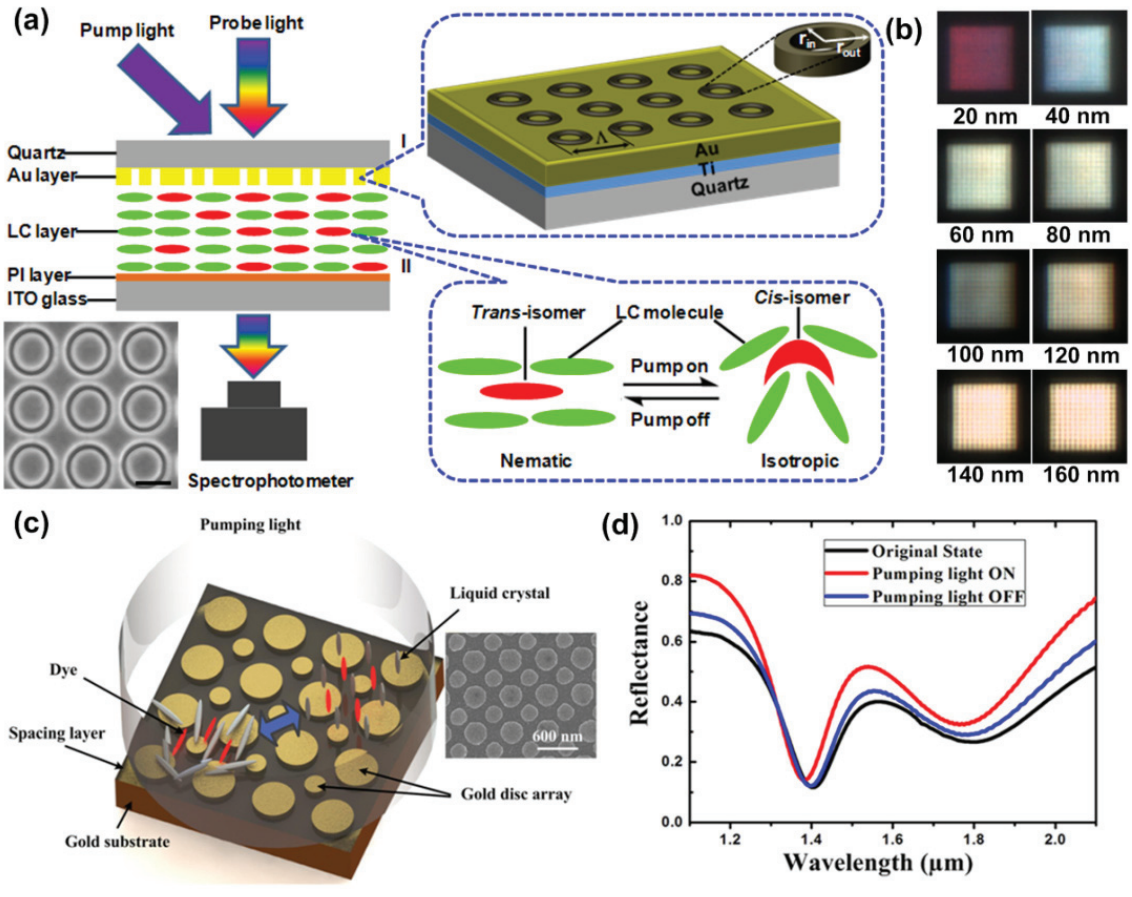

Figure 9. (**a**) Light shutter based on acoustic modulation of PDLC. The shutter effect is caused by realignment of liquid crystal molecules; (**b**) experimental demonstration of acoustic driven light shutter. Letters of "PDLC" beneath the PDLC film can be clearly observed after SAW applied. Transmission changes before and after SAW applied is shown. Response time can be estimated. All figures are adapted from reference [49].

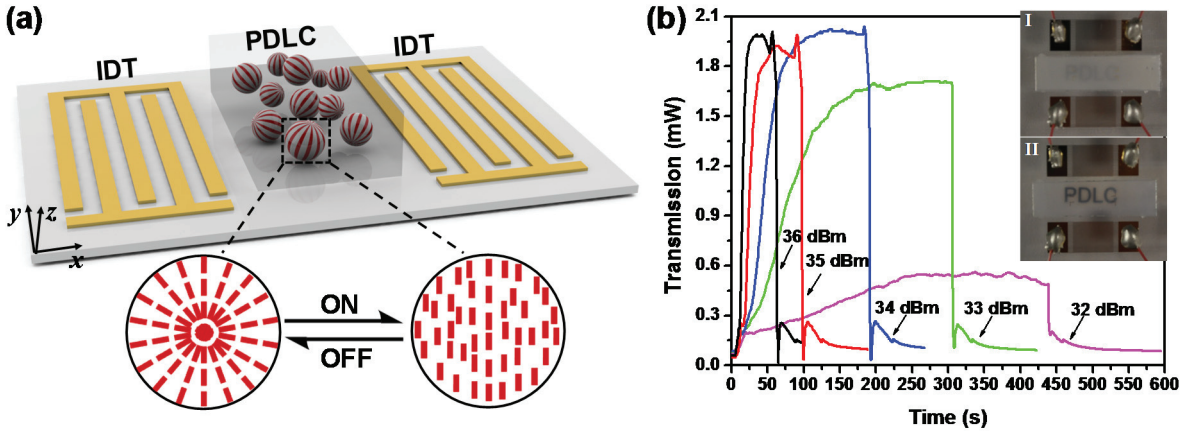

3.4. Heat-Driven Method

Temperature also plays an important role in affecting the liquid crystal refractive indices. As the temperature increases, the extraordinary refractive index, n_e, behaves differently from the ordinary refractive index, n_o. The derivative of n_e (*i.e.*, $\partial n_e/\partial T$) is always negative. However, $\partial n_o/\partial T$ changes from negative to positive as the temperature exceeds the crossover temperature [88,89]. For many liquid crystals, the temperature-dependent refractive indices can be accurately controlled, hence providing another effective means to develop active plasmonics. As previously discussed in Figure 4, we can clearly observe that the optical anisotropy decreases as the temperature increases and finally disappears (*i.e.*, $n_e = n_o$) at the isotropic phase regardless of wavelength. Based on this mechanism, Altug group has demonstrated the thermal tuning of SPPs using liquid crystals [90], as shown in Figure 10. Varying the temperature within the nematic phase from 15 to 33 °C, they demonstrated a refractive index change as large as ≈0.0317, thus enabling a tuning of plasmonic wavelength as large as ≈19 nm. The ability to control the order of liquid crystal molecules from nematic to isotropic phase provides an efficient way of spectral tuning. At the phase transition temperature, more than 12 nm shift has been achieved via changing the temperature by only ≈1 °C corresponding to a refractive index change of ≈0.02. It has been known that plasmonic nanoparticles can induce a photo-thermal heating effect, which depends on the geometries of the nanoparticles strongly and has been extensively investigated [91–94]. It is expected that with the involvement of liquid crystals, such a photo-thermal heating effect will also affect the effective refractive index of the liquid crystals and hence tune the plasmonic resonances as well.

Figure 10. (**a**) Schematic view of the experimental setup containing a liquid crystal cell thermally controlled by a heat bath, white light incident source collected by an objective lens and a spectrometer collecting the plasmonic response for different temperature values and (**b**) zoomed schematic of the liquid crystal cell between the upper CaF_2 window and the plasmonic chip. This figure is adapted from reference [90].

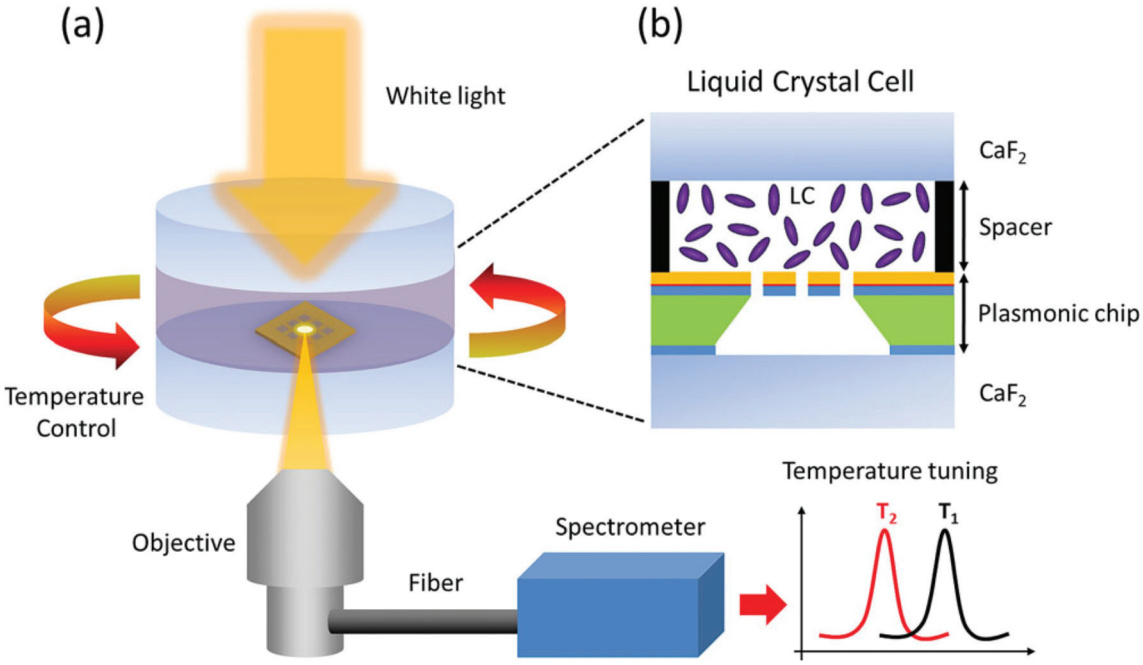

4. Summary and Outlooks

In summary, we have reviewed the recent research *progress* and achievements in liquid crystal based plasmonics. Different driving methods of the liquid crystal based plasmonic devices have been categorized and discussed. The versatile driving methods of the liquid crystals provide enormous freedom in the design and implementation of the plasmonic devices. Although tremendous efforts have been focused on the development of liquid crystal based active plasmonic devices in recent years, many challenges still remain before they can be efficiently used in practice. In the below, we provide a more specific description of these challenges as well as future demands.

4.1. Current Challenges

Currently, most liquid crystal based plasmonic devices are fabricated by mechanically assembling liquid crystals on passive plasmonic nanostructures on a substrate. However, large-area uniform liquid crystal alignment on the nanostructures is still a big challenge given the fact that only the liquid crystal molecular layer that is near (generally < 100 nm) to the plasmonic nanostructures affects the plasmonic signals. In order to achieve large-area uniform liquid crystal alignment in plasmonic devices, one possible way is to co-self-assemble liquid crystals and plasmonic nanoparticles [95–98]. Based on the co-self-assembly method, uniform areas up to 100 μm^2 have been achieved, which is promising for device development.

4.2. Future Demands

4.2.1. Fast Response Liquid Crystals

High speed is always demanding for active plasmonic devices, especially for future development of nanophotonic circuitry/chips with multiple functions assembled. Currently, most liquid crystal based plasmonic devices have a millisecond scale response using the electric-field-driven method. To have a faster speed, one could choose some special liquid crystals, such as ferroelectric liquid crystals, which in general have microsecond response time. In confining the liquid crystal in a polymer matrix, it will also help increase the response speed. For example, millisecond response time has been achieved in a polymer-dispersed liquid crystal (PDLC) system, in which microscale liquid crystal droplets are randomly confined in a polymer matrix [99,100]. While in a holographic polymer-dispersed liquid crystal (HPDLC) system, in which nanoscale liquid crystal droplets are periodically confined in a polymer matrix, microsecond response time has been demonstrated [101–103]. More recently, polymer network liquid crystal (PNLC) [104] and polymer-stabilized blue phase liquid crystal (BPLC) [105] have received much attention since both systems can achieve sub-millisecond response time.

4.2.2. Large Birefringence Liquid Crystals

Currently, liquid crystals employed in most reported work have the birefringence of 0.1–0.2. Although such a birefringence has already given detectable changes in terms of peak shift or intensity, there is much room for further improvement. To achieve more pronounced changes, liquid crystals possessing larger birefringence are highly desired. Thus far, liquid crystals with large birefringence of >0.4 [106–108] and even >0.7 [109] have been reported, respectively. We believe that much enhanced performance, such as large peak shift and intensity modulation, will be achieved by integrating the large birefringent liquid crystal into plasmonic nanostructures, hence beneficial to the development of active plasmonics.

4.2.3. Multi-Function or Multi-Control Integration

At the current stage, a single function of liquid crystal based plasmonic devices has been demonstrated in terms of proof-of-concepts. Looking ahead, it will be great that a single device could do multiple functions. Liquid crystal enabled plasmonic devices look promising for achieving multiple functions. In addition, multi-mode controls of liquid crystals will also lend a convenient hand and allow us to choose their functions freely under certain circumstances. For example, azo-dye-doped liquid crystals or azobenzene liquid crystals can respond to not only electric fields but also light [110], which gives us more freedom to control them.

Acknowledgments

Guangyuan Si thanks the Natural Science Foundation of Hebei Province (Grant No. A2013501049), Science and Technology Research Funds for Higher Education of Hebei Province

(Grant No. ZD20132011), Fundamental Research Funds for the Central Universities (Grant No. N120323002), and the Science and Technology Foundation of Liaoning Province (Grant No. 20131031). Eunice Sok Ping Leong and Yan Jun Liu also thank the funding support from Joint Council Office (JCO) of the Agency for Science, Technology and Research (A*STAR) under the grant No. 12302FG012.

Conflicts of Interest

The authors declare no conflict of interest.

References

1. Barnes, W.L.; Dereux, A.; Ebbesen, T.W. Surface plasmon subwavelength optics. *Nature* **2003**, *424*, 824–830.
2. Ebbesen, T.W.; Lezec, H.J.; Ghaemi, H.F.; Thio, T.; Wolff, P.A. Extraordinary optical transmission through sub-wavelength hole arrays. *Nature* **1998**, *391*, 667–669.
3. Bozhevolnyi, S.I. *Plasmonic Nanoguides and Circuits*; Pan Stanford Publishing Pte. Ltd.: Singapore, 2009.
4. Degiron, A.; Smith, D.R. *Surface Plasmon Nanophotonics*; Brongersma, M.L., Kik, P.G., Eds.; Springer: Berlin, Germany, 2007; pp. 55–71.
5. Garcia-Vidal, F.J.; Martin-Moreno, L.; Pendry, J.B. Surfaces with holes in them: New plasmonic metamaterials. *J. Opt. A Pure Appl. Opt.* **2005**, *7*, S97–S101.
6. Cai, W.; Shalaev, V. *Optical Metamaterials*; Springer: Berlin, Germany, 2010.
7. Smith, S.J.; Purcell, E.M. Visible light from localized surface charges moving across a grating. *Phys. Rev.* **1953**, *92*, 1069–1070.
8. Veselago, V.G. The electrodynamics of substances with simulataneous negative values of ε and μ. *Usp. Fiz. Nauk* **1967**, *92*, 517–526.
9. Zayats, A.V.; Smolyaninov, I.I.; Maradudin, A.A. Nano-optics of surface plasmon-polaritons. *Phys. Rep*. **2005**, *408*, 131–314.
10. Smolyaninova, V.N.; Smolyaninov, I.I.; Kildishev, A.V.; Shalaev, V.M. Broadband transformation optics devices. *Materials* **2010**, *3*, 4793–4810.
11. Dutta, N.; Mirza, I.O.; Shi, S.; Prather, D.W. Fabrication of large area fishnet optical metamaterial structures operational at near-IR wavelengths. *Materials* **2010**, *3*, 5283–5292.
12. Alu, A.; Engheta, N. Emission enhancement in a plasmonic waveguide at cut-off. *Materials* **2011**, *4*, 141–152.
13. Si, L.; Jiang, T.; Chang, K.; Chen, T.; Lv, X.; Ran, L.; Xin, H. Active microwave metamaterials incorporating ideal gain devices. *Materials* **2011**, *4*, 73–83.
14. Pendry, J.B. Negative refraction makes a perfect lens. *Phys. Rev. Lett*. **2000**, *85*, 3966–3969.
15. Fang, N.; Lee, H.; Sun, C.; Zhang, X. Sub-diffraction-limited optical imaging with a silver superlens. *Science* **2005**, *308*, 534–537.
16. Pendry, J.B.; Smith, D.R. The quest for the superlens. *Sci. Am.* **2006**, *295*, 60–67.

17. Vincenti, M.A.; D'Orazio, A.; Cappeddu, M.G.; Akozbek, N.; Bloemer, M.J.; Scalora, M. Semiconductor-based superlens for subwavelength resolution below the diffraction limit at extreme ultraviolet frequencies. *J. Appl. Phys.* **2009**, *105*, 103103:1–103103:6.
18. Liu, Z.; Durant, S.; Lee, H.; Pikus, Y.; Fang, N.; Xiong, Y.; Sun, C.; Zhang, X. Far-field optical superlens. *Nano Lett.* **2007**, *7*, 403–408.
19. Liu, Z.; Durant, S.; Lee, H.; Pikus, Y.; Xiong, Y.; Sun, C.; Zhang, X. Experimental studies of far-field superlens for sub-diffractional optical imaging. *Opt. Express* **2007**, *15*, 6947–6954.
20. Schurig, D.; Mock, J.J.; Justice, B.J.; Cummer, S.A.; Pendry, J.B.; Starr, A.F.; Smith, D.R. Metamaterial electromagnetic cloak at microwave frequencies. *Science* **2006**, *314*, 977–980.
21. Pendry, J.B.; Schurig, D.; Smith, D.R. Controlling electromagnetic fields. *Science* **2006**, *312*, 1780–1782.
22. Jacob, Z.; Narimanov, E.E. Semiclassical description of non magnetic cloaking. *Opt. Express* **2008**, *16*, 4597–4604.
23. Smolyaninov, I.I.; Smolyaninova, V.N.; Kildishev, A.V.; Shalaev, V.M. Anisotropic metamaterials emulated by tapered waveguides: application to optical cloaking. *Phys. Rev. Lett.* **2009**, *102*, 213901:1–213901:5.
24. Zhu, G.; Lin, Z.; Jing, Q.; Bai, P.; Pan, C.; Yang, Y.; Zhou, Y.; Wang, Z.L. Toward large-scale energy harvesting by a nanoparticle-enhanced triboelectric nanogenerator. *Nano Lett.* **2013**, *13*, 847–853.
25. Walter, M.J.; Borys, N.J.; van Schooten, K.J.; Lupton, J.M. Light-harvesting action spectroscopy of single conjugated polymer nanowires. *Nano Lett.* **2008**, *8*, 3330–3335.
26. Aubry, A.; Lei, D.Y.; Fernandez-Dominguez, A.I.; Sonnefraud, Y.; Maier, S.A.; Pendry, J.B. Plasmonic light-harvesting devices over the whole visible spectrum. *Nano Lett.* **2010**, *10*, 2574–2579.
27. Andreussi, O.; Biancardi, A.; Corni, S.; Mennucci, B. Plasmon-controlled light-harvesting: Design rules for biohybrid devices via multiscale modeling. *Nano Lett.* **2013**, *13*, 4475–4484.
28. Kim, I.; Bender, S.L.; Hranisavljevic, J.; Utschig, L.M.; Huang, L.; Wiederrecht, G.P.; Tiede, D.M. Metal nanoparticle plasmon-enhanced light-harvesting in a photosystem I thin film. *Nano Lett.* **2011**, *11*, 3091–3098.
29. Dang, X.; Qi, J.; Klug, M.T.; Chen, P.; Yun, D.S.; Fang, N.X.; Hammond, P.T.; Belcher, A.M. Tunable localized surface plasmon-enabled broadband light-harvesting enhancement for high-efficiency panchromatic dye-sensitized solar cells. *Nano Lett.* **2013**, *13*, 637–642.
30. Si, G.Y.; Zhao, Y.H.; Lv, J.; Lu, M.; Wang, F.; Liu, H.; Xiang, N.; Huang, T.J.; Danner, A.J.; Teng, J.; *et al.* Reflective plasmonic color filters based on lithographically patterned silver nanorod arrays. *Nanoscale* **2013**, *5*, 6243–6248.
31. Huang, W.; Qian, W.; Jain, P.K.; El-Sayed, M.A. The effect of plasmon field on the coherent lattice phonon oscillation in electron-beam fabricated gold nanoparticle pairs. *Nano Lett.* **2007**, *7*, 3227–3234.
32. Sun, S.; Leggett, G.J. Matching the resolution of electron beam lithography by scanning near-field photolithography. *Nano Lett.* **2004**, *4*, 1381–1384.

33. Atay, T.; Song, J.; Nurmikko, A.V. Strongly interacting plasmon nanoparticle pairs: From dipole−dipole interaction to conductively coupled regime. *Nano Lett.* **2004**, *4*, 1627–1631.
34. Si, G.Y.; Zhao, Y.H.; Lv, J.; Wang, F.; Liu, H.; Teng, J.; Liu, Y.J. Direct and accurate patterning of plasmonic nanostructures with ultrasmall gaps. *Nanoscale* **2013**, *5*, 4309–4313.
35. Si, G.Y.; Zhao, Y.H.; Liu, H.; Teo, S.L.; Zhang, M.S.; Huang, T.J.; Danner A.J.; Teng, J.H. Annular aperture array based color filter. *Appl. Phys. Lett.* **2011**, *99*, 033105:1–033105:3.
36. Jiang, X.; Gu, Q.; Wang, F.; Lv, J.; Ma, Z.; Si, G. Fabrication of coaxial plasmonic crystals by focused ion beam milling and electron-beam lithography. *Mater. Lett.* **2013**, *100*, 192–194.
37. Si, G.; Danner, A.J.; Teo, S.L.; Teo, E.J.; Teng, J.; Bettiol, A.A. Photonic crystal structures with ultrahigh aspect ratio in lithium niobate fabricated by focused ion beam milling. *J. Vac. Sci. Technol. B* **2011**, *29*, 021205:1–021205:5.
38. Si, G.; Teo, E.J.; Bettiol, A.A.; Teng, J.; Danner, A.J. Suspended slab and photonic crystal waveguides in lithium niobate. *J. Vac. Sci. Technol. B* **2010**, *28*, 316–320.
39. Liu, Y.J.; Si, G.Y.; Leong, E.S.P.; Xiang, N.; Danner, A.J.; Teng, J.H. Light-driven plasmonic color filters by overlaying photoresponsive liquid crystals on gold annular aperture arrays. *Adv. Mater.* **2012**, *24*, OP131–OP135.
40. Liu, Y.J.; Si, G.Y.; Leong, E.S.P.; Wang, B; Danner, A.J.; Yuan, X.C.; Teng, J.H. Optically tunable plasmonic color filters. *Appl. Phys. A* **2012**, 107, 49–54.
41. He, J.; Huang, X.; Li, Y.; Liu, Y.; Babu, T.; Aronova, M.A.; Wang, S.; Lu, Z.; Chen, X.; Nie, Z. Self-assembly of amphiphilic plasmonic micelle-like nanoparticles in selective solvents. *J. Am. Chem. Soc.* **2013**, *135*, 7974–7984.
42. Gandra, N.; Abbas, A.; Tian, L.; Singamaneni, S. Plasmonic planet-satellite analogues: Hierarchical self-assembly of gold nanostructures. *Nano Lett.* **2012**, *12*, 2645–2651.
43. Li, X.; Cole, R.M.; Milhano, C.A.; Bartlett, P.N.; Soares, B.F.; Baumberg, J.J.; de Groot, C.H. The fabrication of plasmonic Au nanovoid trench arrays by guided self-assembly. *Nanotechnology* **2009**, *20*, doi:10.1088/0957-4484/20/28/285309.
44. Khoo, I.C. Nonlinear optics of liquid crystalline materials. *Phys. Rep.* **2009**, *471*, 221–267.
45. Zhao, Y.; Hao, Q.; Ma, Y.; Lu, M.; Zhang, B.; Lapsley, M.; Khoo, I.C.; Huang, T.J. Light-driven tunable dual-band plasmonic absorber using liquid-crystal-coated asymmetric nanodisk array. *Appl. Phy. Lett.* **2012**, *100*, 053119:1–053119:4.
46. Smalley, J.S.T.; Zhao, Y.; Nawaz, A.A.; Hao, Q.; Ma, Y.; Khoo, I.C.; Huang, T.J. High contrast modulation of plasmonic signals using nanoscale dual-frequency liquid crystals. *Opt. Express* **2011**, *19*, 15265–15274.
47. Hao, Q.; Zhao, Y.; Juluri, B.K.; Kiraly, B.; Liou, J.; Khoo, I.C.; Huang, T.J. Frequency-addressed tunable transmission in optically thin metallic nanohole arrays with dual-frequency liquid crystals. *J. Appl. Phys.* **2011**, *109*, 084340:1–084340:4.
48. Liu, Y.J.; Leong, E.S.P.; Wang, B.; Teng, J.H. Optical transmission enhancement and tuning by overlaying liquid crystals on a gold film with patterned nanoholes. *Plasmonics* **2011**, *6*, 659–664.
49. Liu, Y.J.; Ding, X.; Lin, S.S.; Shi, J.; Chiang, I.; Huang, T.J. Surface acoustic wave driven light shutters using polymer-dispersed liquid crystals. *Adv. Mater.* **2011**, *23*, 1656–1659.

50. Liu, Y.J.; Hao, Q.; Smalley, J.S.T.; Liou, J.; Khoo, I.C.; Huang, T.J. A frequency-addressed plasmonic switch based on dual-frequency liquid crystal. *Appl. Phy. Lett.* **2010**, *97*, 091101:1–091101:3.
51. Liu, Y.J.; Zheng, Y.B.; Shi, J.; Huang, H.; Walker, T.R.; Huang, T.J. Optically switchable gratings based on azo-dye-doped, polymer-dispersed liquid crystals. *Opt. Lett.* **2009**, *34*, 2351–2353.
52. Hsiao, V.K.S.; Zheng, Y.B.; Juluri, B.K.; Huang, T.J. Light-driven plasmonic switches based on Au nanodisk arrays and photoresponsive liquid crystals. *Adv. Mater.* **2008**, *20*, 3528–3532.
53. Chu, K.C.; Chao, C.Y.; Chen, Y.F.; Wu, Y.C.; Chen, C.C. Electrically controlled surface plasmon resonance frequency of gold nanorods. *Appl. Phys. Lett.* **2006**, *89*, 103107:1–103107:3.
54. Zografopoulos, D.C.; Beccherelli, R. Long-range plasmonic directional coupler switches controlled by nematicliquid crystals. *Opt. Express* **2013**, *21*, 8240–8250.
55. Dickson, W.; Wurtz, G.A.; Evans, P.R.; Pollard, R.J.; Zayats, A.V. Electronically controlled surface plasmon dispersion and optical transmission through metallic hole arrays using liquid crystal. *Nano Lett.* **2008**, *8*, 281–286.
56. Kossyrev, P.A.; Yin, A.; Cloutier, S.G.; Cardimona, D.A.; Huang, D.; Alsing, P.M.; Xu, J.M. Electric field tuning of plasmonic response of nanodot array in liquid crystal matrix. *Nano Lett.* **2005**, *5*, 1978–1981.
57. De Sio, L.;Cunningham, A.; Verrina, V.; Tone, C.M.; Caputo, R.; Burgi, T.; Umeton, C. Double active control of the plasmonic resonance of a gold nanoparticle array. *Nanoscale* **2012**, *4*, 7619–7623.
58. Khatua, S.; Chang, W.S.; Swanglap, P.; Olson, J.; Link, S. Active modulation of nanorod plasmons. *Nano Lett.* **2011**, *11*, 3797–3802.
59. Vivekchand, S.R.C.; Engel, C.J.; Lubin, S.M.; Blaber, M.G.; Zhou, W.; Suh, J.Y.; Schatz, G.C.; Odom, T.W. Liquid plasmonics: Manipulating surface plasmon polaritons via phase transitions. *Nano Lett.* **2012**, *12*, 4324–4328.
60. Zheng, Y.; Yang, Y.; Jensen, L.; Fang, L.; Juluri, B.K.; Flood, A.H.; Weiss, P.S.; Stoddart, J.F.; Huang, T.J. Active molecular plasmonics: Controlling plasmon resonances with molecular switches. *Nano Lett.* **2009**, *9*, 819–825.
61. Zheng, Y.; Hao, Q.; Wang, Y.; Kiraly, B.; Chiang, I.; Huang, T.J. Light-driven artificial molucular machines. *J. Nanophoton.* **2010**, *4*, 042501:1–042501:35.
62. Geandier, G.; Renault, P.; Bourhis, E.L.; Goudeau, P.; Faurie, D.; Bourlot, C.; Djemia, P.; Castelnau, O.; Cherif S.M. Elastic-strain distribution in metallic film-polymer substrate composites. *Appl. Phy. Lett.* **2010**, *96*, doi:10.1063/1.3293450.
63. Yang, J.; You, J.; Chen, C.; Hsu, W.; Tan, H.; Zhang, X.W.; Hong, Z,; Yang, Y. Plasmonic polymer tandem solar cell. *ACS Nano* **2011**, *5*, 6210–6217.
64. Chah, S.; Noolandi, J.; Zare, R.N. Undulatory delamination of thin polymer films on gold surfaces. *J. Phys. Chem. B* **2005**, *109*, 19416–19421.
65. Novo, C.; Funston, A.M.; Mulvaney, P. Direct observation of chemical reactions on single gold nanocrystals using surface plasmon spectroscopy. *Nat. Nanotechnol.* **2008**, *3*, 598–602.

66. Lioubimov, V.; Kolomenskii, A.; Mershin, A.; Nanopoulos, D.V.; Schuessler, H.A. Effect of varying electric potential on surface-plasmon resonance sensing. *Appl. Opt.* **2004**, *43*, 3426–3432.
67. Ung, T.; Liz-Marzan, L.M.; Mulvaney, P. Controlled method for silica coating of silver colloids. Influence of coating on the rate of chemical reactions. *Langmuir* **1998**, *14*, 3740–3748.
68. Wu, S.T. Birefringence dispersions of liquid crystals. *Phys. Rev. A* **1986**, *33*, 1270–1274.
69. Yang, D.K.; Wu, S.T. *Fundamentals of Liquid Crystal Devices*; John Wiley & Sons Inc: Hoboken, NJ, USA, 2006.
70. Khoo, I.-C. *Liquid Crystals*, 2nd ed.; John Wiley & Sons Inc: Hoboken, NJ, USA, 2007.
71. Li, J.; Gauza, S.; Wu, S. Temperature effect on liquid crystal refractive indices. *J. Appl. Phys.* **2004**, *96*, 19–24.
72. Zografopoulos, D.C.; Beccherelli, R. Liquid-crystal-tunable metal–insulator–metal plasmonic waveguides and Bragg resonators. *J. Opt.* **2013**, *15*, doi:10.1088/2040-8978/15/5/055009.
73. Schadt, M. Dual-frequency addressing of field effects. *Mol. Cryst. Liquid Cryst.* **1982**, *89*, 77–92.
74. Xianyu, H.; Wu, S.T.; Lin, C.L. Dual frequency liquid crystals: A review. *Liquid Cryst.* **2009**, *36*, 717–726.
75. Chang, W.; Lassiter, J.B.; Swanglap, P.; Sobhani, H.; Khatua, S.; Nordlander, P.; Halas, N.J.; Link, S. A plasmonic Fano switch. *Nano. Lett.* **2012**, *12*, 4977–4982.
76. Liu, Y.J.; Dai, H.T.; Sun, X.W. Holographic fabrication of azo-dye-functionalized photonic structures. *J. Mater. Chem.* **2011**, *21*, 2982–2986.
77. Liu, Y.J.; Su, Y.-C.; Hsu, Y.-J.; Hsiao, V.K.S. Light-induced spectral shifting generated from azo-dye doped holographic 2D gratings. *J. Mater. Chem.* **2012**, *22*, 14191–14195.
78. De Sio, L.; Tedesco, A.; Tabirian, N.; Umeton, C. Optically controlled holographic beam splitter. *Appl. Phys. Lett.* **2010**, *97*, 183507:1–183507:3.
79. De Sio, L.; Serak, S.; Tabirian, N.; Umeton, C. Mesogenic versus non-mesogenic azo dye confined in a soft-matter template for realization of optically switchable diffraction gratings. *J. Mater. Chem.* **2011**, *21*, 6811–6814.
80. Liu, Y.J.; Cai, Z.Y.; Leong, E.S.P.; Zhao, X.S.; Teng, J.H. Optically switchable photonic crystals based on inverse opals partially infiltrated by photoresponsive liquid crystals. *J. Mater. Chem.* **2012**, *22*, 7609–7613.
81. Liu, Y.J.; Dai, H.T.; Leong, E.S.P.; Teng, J.H.; Sun, X.W. Azo-dye-doped absorbing photonic crystals with purely imaginary refractive index contrast and all-optically switchable diffraction properties. *Opt. Mater. Express* **2012**, *2*, 55–61.
82. De Sio, L.; Klein, G.; Serak, S.; Tabiryan, N.; Cunningham, A.; Tone, C.M.; Ciuchi, F.; Bürgi, T.; Umeton, C.; Bunning, T. All-optical control of localized plasmonic resonance realized by photoalignment of liquid crystals. ***J. Mater. Chem. C*** **2013**, ***1***, 7483–7487.
83. Liu, Y.J.; Zheng, Y.B.; Liou, J.; Chiang, I.-K.; Khoo, I.C.; Huang, T.J. All-optical modulation of localized surface plasmon coupling in a hybrid system composed of photo-switchable gratings and Au nanodisk arrays. *J. Phys. Chem. C* **2011**, *115*, 7717–7722.

84. Tamai, N.; Miyasaka, H. Ultrafast dynamics of photochromic systems. *Chem. Rev.* **2000**, *100*, 1875–1890.
85. De Sio, L.; Ricciardi, L.; Serak, S.; La Deda, M.; Tabiryan, N.; Umeton, C. Photo-sensitive liquid crystals for optically controlled diffraction gratings. *J. Mater. Chem.* **2012**, *22*, 6669–6673.
86. Hrozhyk, U.A.; Serak, S.V.; Tabiryan, N.V.; Hoke, L.; Steeves, D.M.; Kimball, B.R. Azobenzene liquid crystalline materials for efficient optical switching with pulsed and/or continuous wave laser beams. *Opt. Express* **2010**, *18*, 8697–8704.
87. Hrozhyk, U.A.; Serak, S.V.; Tabiryan, N.V.; Hoke, L.; Steeves, D.M.; Kimball, B.; Kedziora, G. Systematic study of absorption spectra of donor–acceptor azobenzene mesogenic structures. *Mol. Cryst. Liquid Cryst.* **2008**, *489*, 257–272.
88. Li, J.; Gauzia, S.; Wu, S.T. High temperature-gradient refractive index liquid crystals. *Opt. Express* **2004**, *12*, 2002–2010.
89. Li, J.; Wen, C.H.; Gauza, S.; Lu, R.; Wu, S.T. Refractive indices of liquid crystals for display applications. *J. Display Technol.* **2005**, *1*, 51–61.
90. Cetin, A.E.; Mertiri, A.; Huang, M.; Erramilli, S.; Altug, H. Thermal tuning of surface plasmon polaritons using liquid crystals. *Adv. Opt. Mater.* **2013**, *1*, 915–920.
91. Bardhan, R.; Lal, S.; Joshi, A.; Halas, N.J. Theranostic nanoshells: From probe design to imaging and treatment of cancer. *Acc. Chem. Res.* **2011**, *44*, 936–946.
92. De Sio, L.; Placido, T.; Serak, S.; Comparelli, R.; Tamborra, M.; Tabiryan, N.; Curri, M.L.; Bartolino, R.; Umeton, C.; Bunning, T. Nano-localized heating source for photonics and plasmonics. *Adv. Opt. Mater.* **2013**, *1*, 899–904.
93. Richardson, H.H.; Hickman, Z.N.; Gocorov, A.O.; Thomas, A.C.; Zhang, W.; Kordesch, M.E. Thermooptical properties of gold nanoparticles embedded in ice: Characterization of heat generation and melting. *Nano Lett.* **2006**, *6*, 783–788.
94. Wilson, O.M.; Hu, X.; Cahill, D.G.; Braun, P.V. Colloidal metal particles as probes of nanoscale thermal transport in fluids. *Phys. Rev. B* **2002**, *66*, 224301:1–224301:6.
95. Khatua, S.; Manna, P.; Chang, W.-S.; Tcherniak, A.; Friedlander, E.; Zubarev, E.R.; Link, S. Plasmonic nanoparticles-liquid crystal composites. *J. Phys. Chem. C* **2010**, *114*, 7251–7257.
96. Liu, Q.K.; Cui, Y.X.; Gardner, D.; Li, X.; He, S.L.; Smalyukh, I.I. Self-alignment of plasmonic gold nanorods in reconfigurable anisotropic fluids for tunable bulk metamaterial applications. *Nano Lett.* **2010**, *10*, 1347–1353.
97. Umadevi, S.; Feng, X.; Hegmann, T. Large area self-assembly of nematic liquid-crystal-functionalized gold nanorods. *Adv. Funct. Mater.* **2013**, *23*, 1393–1403.
98. Milette, J.; Cowling, S.J.; Toader, V.; Lavigne, C.; Saez, I.M.; Bruce Lennox, R.; Goodby, J.W.; Reven, L. Reversible long range network formation in gold nanoparticle-nematic liquid crystal composites. *Soft Matter* **2012**, *8*, 173–179.
99. Wu, B.-G.; Erdmann, J.H.; Doane, J.W. Response times and voltages for PDLC light shutters. *Liq. Cryst.* **1989**, *5*, 1453–1465.
100. Liu, Y.J.; Sun, X.W. Electrically switchable computer-generated hologram recorded in polymer-dispersed liquid crystals. *Appl. Phys. Lett.* **2007**, *90*, 191118:1–191118:3.

101. Tondiglia, V.P.; Natarajan, L.V.; Sutherland, R.L.; Bunning, T.J.; Adams, W.W. Volume holographic image storage and electro-optical readout in a polymer-dispersed liquid-crystal film. *Opt. Lett.* **1995**, *20*, 1325–1327.
102. Liu, Y.J.; Sun, X.W.; Liu, J.H.; Dai, H.T.; Xu, K.S. A polarization insensitive 2 × 2 optical switch fabricated by liquid cystal-polymer composite. *Appl. Phys. Lett.* **2005**, *86*, 041115:1–041115:3.
103. Liu, Y.J.; Sun, X.W.; Dai, H.T.; Liu, J.H.; Xu, K.S. Effect of surfactant on the electro-optical properties of holographic polymer dispersed liquid crystal Bragg gratings. *Opt. Mater.* **2005**, *27*, 1451–1455.
104. Sun, J.; Wu, S.T. Recent advances in polymer network liquid crystal spatial light modulators. *J. Polym. Sci. Part B Polym. Phys.* **2014**, *52*, 183–192.
105. Yan, J.; Rao, L.; Jiao, M.; Li, Y.; Cheng, H.C.; Wu, S.T. Polymer-stabilized optically isotropic liquid crystals for next-generation display and photonics applications. *J. Mater. Chem.* **2011**, *21*, 7870–7877.
106. Gauza, S.; Wang, H.; Wen, C.H.; Wu, S.T.; Seed, A.J.; Dabrowski, R. High birefringence isothiocyanato tolane liquid crystals. *Jpn. J. Appl. Phys.* **2003**, *42*, 3463–3466.
107. Dabrowski, R.; Kula, P.; Herman, J. High birefringence liquid crystals. *Crystals* **2013**, *3*, 443–482.
108. Arakawa, Y.; Kang, S.; Nakajima, S.; Sakajiri, K.; Cho, Y.; Kawauchi, S.; Watanabe, J.; Konishi, G. Diphenyltriacetylenes: Novel nematic liquid crystal materials and analysis of their nematic phase-transition and birefringence behaviours. *J. Mater. Chem. C* **2013**, *1*, 8094–8102.
109. Gauza, S.; Wen, C.H.; Wu, S.T.; Janarthanan, N.; Hsu, C.S. Super high birefringence isothiocyanato biphenyl-bistolane liquid crystals. *Jpn. J. Appl. Phys.* **2004**, *43*, 7634–7638.
110. De Sio, L.; Umeton, C. Dual-mode control of light by two-dimensional periodic structures realized in liquid-crystalline composite materials. *Opt. Lett.* **2010**, *35*, 2759–2761.

Improving the Pass-Band Return Loss in Liquid Crystal Dual-Mode Bandpass Filters by Microstrip Patch Reshaping

Javier Torrecilla, Virginia Urruchi, José Manuel Sánchez-Pena, Noureddine Bennis, Alejandro García and Daniel Segovia

Abstract: In this paper, the design and experimental characterization of a tunable microstrip bandpass filter based on liquid crystal technology are presented. A reshaped microstrip dual-mode filter structure has been used in order to improve the device performance. Specifically, the aim is to increase the pass-band return loss of the filter by narrowing the filter bandwidth. Simulations confirm the improvement of using this new structure, achieving a pass-band return loss increase of 1.5 dB at least. Because of the anisotropic properties of LC molecules, a filter central frequency shift from 4.688 GHz to 5.045 GHz, which means a relative tuning range of 7.3%, is measured when an external AC voltage from 0 V_{rms} to 15 V_{rms} is applied to the device.

Reprinted from *Materials*. Cite as: Torrecilla, J.; Urruchi, V.; Sánchez-Pena, J.M.; Bennis, N.; García, A.; Segovia, D. Improving the Pass-Band Return Loss in Liquid Crystal Dual-Mode Bandpass Filters by Microstrip Patch Reshaping. *Materials* **2014**, *7*, 4524–4535.

1. Introduction

During the last two decades, liquid crystals (LC) have become a promising approach for the design of tunable devices at microwave frequencies. The anisotropy of the molecules of these materials allows LC electrical properties to depend on their molecules orientation, which can be changed by applying an external electric field. Concretely, the LC permittivity can be varied between two extreme values, $\varepsilon_{r\perp}$ and $\varepsilon_{r\parallel}$, as a function of the applied voltage. This is the reason which permits LC-based devices to be voltage-controlled. Some examples of tunable devices based on LC technology at microwave frequencies in the bibliography are capacitors [1], antennas [2], filters [3], *etc*.

Moreover, the advantages of using LC in size, cost or power consumption [4] compared to other studied technologies for designing tunable microwave devices, make these materials very suitable for this purpose. For example, varactor diodes need high voltages, up to 30 V, in order to achieve large tuning ranges for frequencies higher than 1 GHz [5], while devices based on ferrite technology [6] require a magnetic field for tuning, which leads to problems in terms of size and power consumption. Therefore, the improvement of the existing LC-based prototypes and the development of new LC tunable devices at these frequencies are interesting challenges to be faced in the immediate future.

Filters are very important devices at microwave telecommunication systems, for example, in satellite communications, due to their ability of selecting (bandpass filters) or rejecting (bandstop or notch filters) bands of frequencies. Furthermore, the demand on the development of tunable filters has increased during the last years. In this work, a tunable LC-based band-pass filter with microstrip geometry is presented. A reshaping of a dual-mode square patch geometry reported in previous works has been proposed as the microstrip filter. This new patch structure is expected to improve the filter

performance, increasing the pass-band return loss. A high return loss is desirable in a filter frequency response because it involves a lower pass-band filter insertion loss variation. The design, manufacture and experimental results of the device are detailed in this paper.

2. Liquid Crystal Bandpass Filter Design

Since dual-mode technology for bandpass filters was introduced by Wolff in 1972 [7], these filters have been widely used in microstrip technology because of their advantages, specifically in size reduction. This is a critical issue in LC-based devices, since a size reduction involves a decrease of the amount of used LC and, thus, a lower manufacturing cost. Dual-mode operation consists of a resonant circuit where two electromagnetic degenerated modes are excited due to the presence of some kind of perturbation in the microstrip structure. Therefore, a two-pole filter can be obtained with a single resonator, which implies a significant size reduction. For implementing dual-mode filters in microstrip technology, different topologies have been used, such as square-loops [8] or T-shaped stubs [9].

The topology shown in Figure 1a is a dual-mode filter structure developed by S. Li *et al*. [10] achieving a good performance [11]. It consists of a microstrip metallic square patch with a central square notch and two perpendicular feed lines for exciting the two degenerated modes. In this work, a reshaping of the patch of this structure has been proposed. The modification consists of making a square cut of size k etched on the patch, as it is shown in Figure 1b. This new microstrip patch is expected to improve the passband return loss (S_{11} parameter) and to narrow the filter bandwidth.

Figure 1. Geometry of a microstrip square patch resonator with a central square notch (dual-mode). (**a**) Without any additional cut; (**b**) With a square cut on a specific corner.

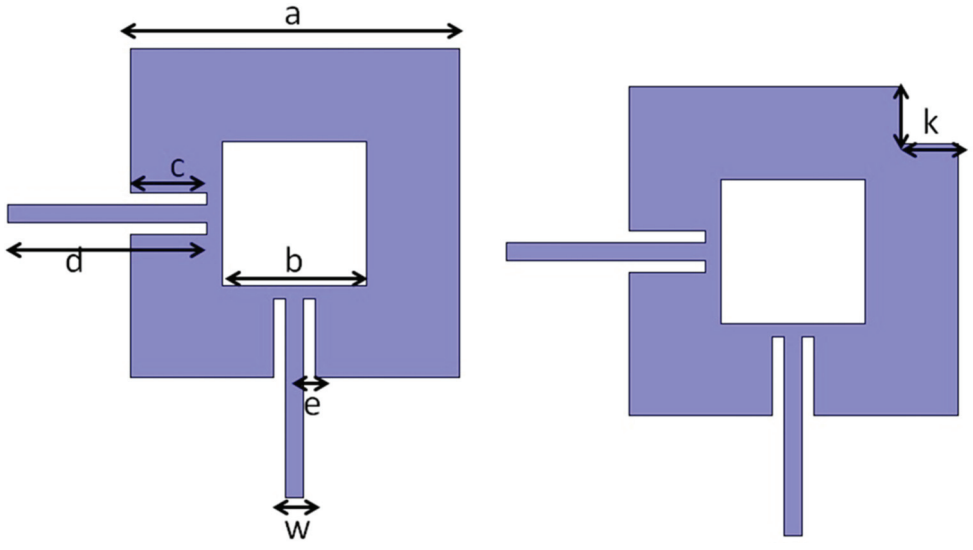

(**a**) (**b**)

The value of the filter central frequency (f_c) for the structure presented in Figure 1 is a function of the structure dimensions and the effective permittivity (ε_{eff}). It is especially sensible to variations in the *b* dimension, while filter bandwidth depends on the *a*, *c* and *e* dimensions [10]. Thus, for fixed dimensions of the structure, f_c can be varied as ε_{eff} is modified. In addition, permittivity depends on

the substrate materials of the device, so a suitable choice of the substrate materials has been the strategy to achieve the device tunability. In this work, LC is used as the dielectric substrate of the microstrip line in the device. As LC permittivity changes between two extreme values, $\varepsilon_{r\perp}$ and $\varepsilon_{r\parallel}$, by applying voltage, the filter central frequency is also voltage-controlled. Therefore, the use of LC as dielectric substrate is the reason which allows the filter to be tunable.

LC is a fluid material, so it needs to be confined in a cavity inside the device which will be afterwards sealed. For this reason, the filter is implemented by using an inverted-microstrip structure, as shown in Figure 2. This structure has been already reported in other LC-based devices [12]. The LC cavity is designed of 0.25-mm thick and delimited by the spacers; the dielectric material Taconic TLX-08 ($\varepsilon_r = 2.55$) is employed for them. This material is also used as the substrate that supports the microstrip line with 0.8-mm thick.

Before the fabrication of the device and the filling with the LC, several electromagnetic simulations by using the software Ansoft HFSS have been run for optimizing the filter dimensions. Initially, the LC cavity has been considered to be empty in the simulations, that is, $\varepsilon_r = 1$. As it is recalled in Section 3, LC permittivity extreme values are unknown at microwave frequencies. The dimensions of the patch have been chosen by comparing the spectral response of the filter with a conventional dual-mode patch (Figure 1a) and with the new patch with a square cut (Figure 1b). The results of the patch dimensions for the topology presented in Figure 1a is solved for a filter central frequency nearby 7.5 GHz considering empty the LC cavity. These values are summarized in Table 1. The microstrip line width (w) has been designed of 0.65 mm in order to obtain input impedance (Z_{in}) close to 50 Ω.

Figure 2. An inverted-microstrip structure for a LC bandpass filter. The detail of the parts of the filter is shown. Note that figure is not drawn to scale.

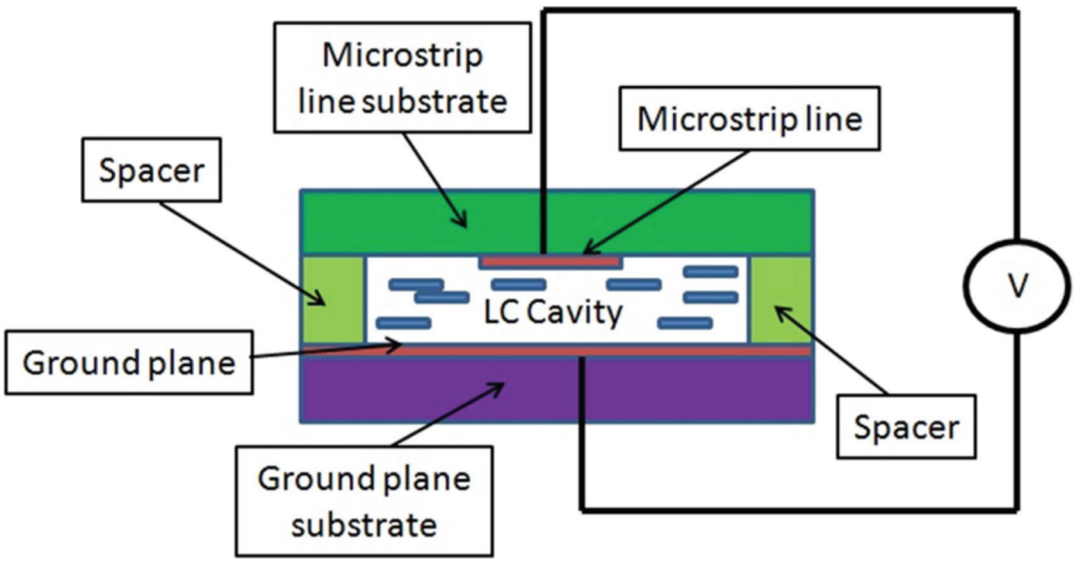

Table 1. Results for the dimensions of the conventional dual-mode patch. Some concerned parameters are: bandwidth (BW), central frequency (f_c) and input impedance (Z_{in}).

Dimension	Value	Comments
a	11.6	Changes in BW
b	5	Changes in f_c
c	2.8	Changes in BW
d	10	Changes in BW
e	0.5	Changes in BW
w	0.65	Changes in Z_{in}

Once the dimensions have been fixed, a square cut with side k is made in the conventional microstrip square patch. The new dual-mode structure (Figure 1b) is simulated for several values of k. With k = 2 mm a significant band-pass return loss improvement is achieved. Figure 3 shows a comparison between the filter frequency response (parameters S_{21} and S_{11}) obtained in simulation for the new dual-mode patch and for the conventional one. Table 2 summarizes the performance of both structures.

Figure 3. S-parameters obtained in simulation for both filters with a conventional dual-mode patch and with the new dual-mode one with a square cut.

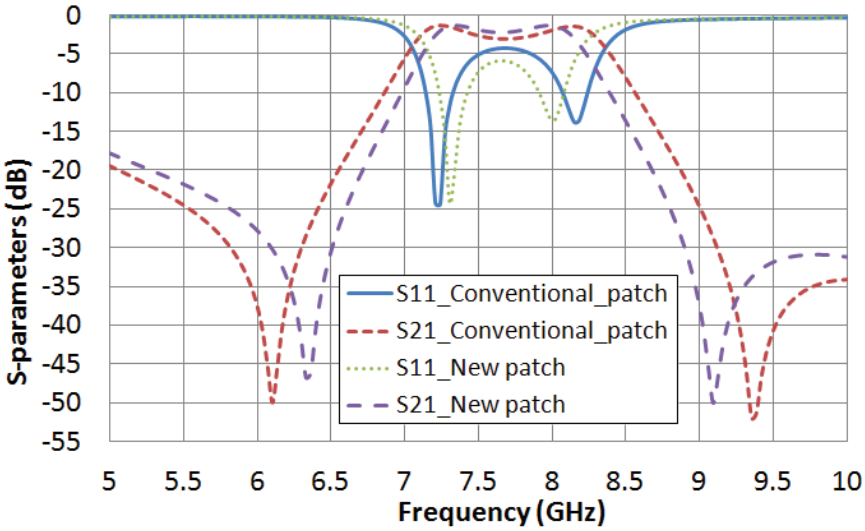

Table 2. Comparison between the performances of both dual-mode filters.

Structure	Central Frequency (f_c)	Bandwidth (BW)	Return Loss (RL)
With a conventional patch	7.69 GHz	1320 MHz	4.3 dB
With a new patch	7.665 GHz	1050 MHz	5.8 dB

The results for the empty filters suggest that the patch with the new shape improves the pass-band return loss (RL) and narrows the filter bandwidth of the filter. A filter bandwidth reduction of 20.5% is achieved, which leads to obtain a pass-band return loss increase of 1.5 dB.

3. Manufacturing of the Device

Once the viability and improvements of the new dual-mode structure have been confirmed with the simulations in an empty device, the device is manufactured and built over an inverted-microstrip structure (Figure 2). As it was described previously, Taconic TLX-08 (Taconic Europe, Ry, Denmark) is used for the spacers and for the microstrip line support. FR4 ($\varepsilon_r = 4.4$) is used as the substrate which supports the ground plane and it is not expected to affect the filter behavior.

The manufactured device (Figure 4) is filled with the nematic LC Merck MDA-98-1602 (Merck, Darmstadt, Germany), whose properties are, initially unknown at microwave frequencies. It is important to take account that LC are materials employed, specially, for the design of tunable electrooptical devices, so they are not usually tested at microwave frequencies. In the manufacturing process, LC molecules are aligned parallel to the microstrip line by rubbing a thin film of polyimide which acts as an alignment layer. In these conditions, when no voltage is applied, the LC permittivity is minimum, $\varepsilon_{r\perp}$. As voltage is applied, the molecules rotate and, at a saturation voltage value, LC molecules are oriented nearly perpendicular to the microstrip line; at this point, LC permittivity reaches its maximum value, ε_{rl}. The tunability of the filter central frequency is achieved; the LC permittivity increases, while the filter central frequency decreases, as voltage is applied.

Figure 4. Manufactured LC bandpass filter.

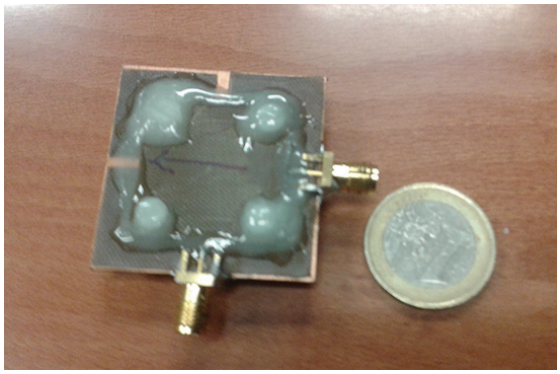

4. Experimental Results and Discussion

The device S-parameters are measured by using an Agilent 8703B network analyzer (Agilent Technologies, Santa Clara, CA, USA). A sinusoidal AC signal of 1 kHz is used as the voltage for switching the LC. In order to superimpose the LC driving voltage with the microwave signal, a bias-T device is connected between the port 1 of the analyzer and the filter input.

The filter is measured for several values of external LC driving voltage between 0 V_{rms} and 15 V_{rms}. Figures 5 and 6 graph the frequency dependence of S_{21} and S_{11} parameters, respectively, for different values of applied voltage. In the absence of applied voltage, the filter central frequency reaches its maximum value, 5.045 GHz. As it was expected, this value is clearly below the obtained in simulation when the LC cavity was considered to be empty (7.665 GHz), because LC permittivity is supposed to be greater than 1. As an increasing voltage is applied, the LC permittivity increases, so the filter central frequency decreases. When the LC driving voltage reaches the saturation value (15 V_{rms}), the filter central frequency is minimum, 4.688 GHz, because of the fact that the LC

permittivity is maximum, ε_l. The tunability of the filter central frequency as a function of the LC driving voltage is shown in Figure 7.

Figure 5. LC driving voltage dependence of the S_{21} parameter for the new bandpass filter.

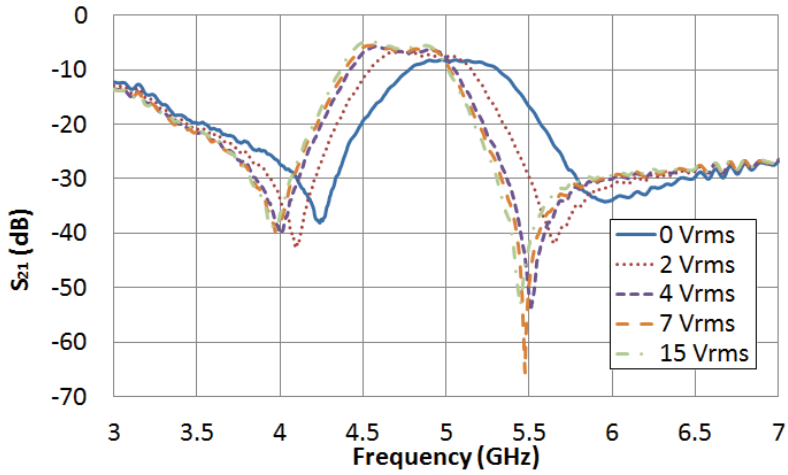

Figure 6. LC driving voltage dependence of the S_{11} parameter for the new bandpass filter.

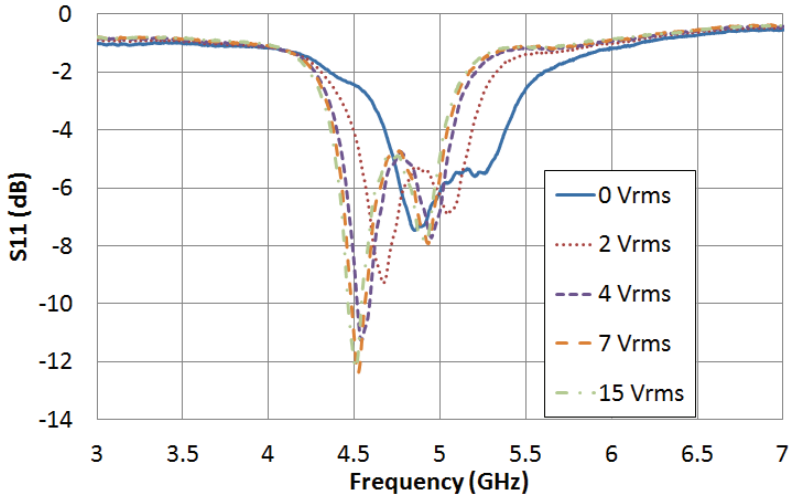

Figure 7. Tunability of the filter central frequency as a function of the LC driving voltage.

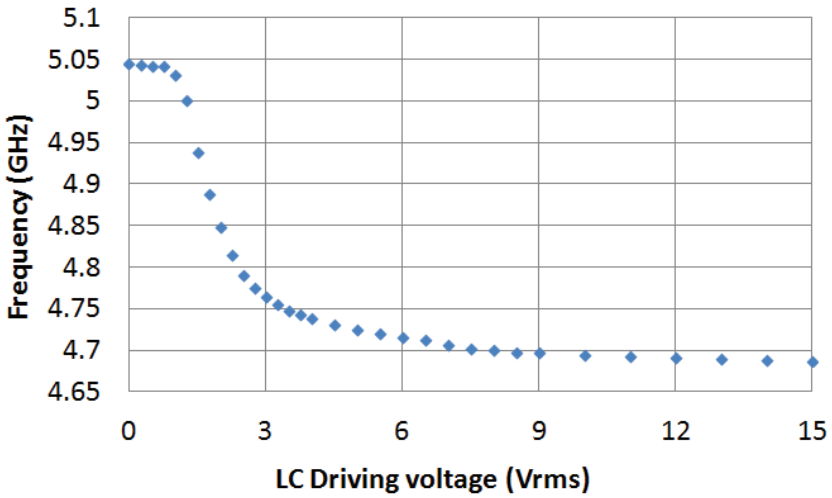

A filter central frequency tuning range of 357 MHz is achieved, which means a tuning relative range of 7.3%. Comparison between liquid crystal filters is not an easy task because multiple criteria, for comparing performance of the filters, are available: central frequency, filter bandwidth, number of poles, topology, *etc*. However, not at all comparable between them. Tunable bandpass filters of Table 3 share some characteristics that are comparable between them, independently of the specific structure, configuration and dimensions. Therefore, the new filter we have proposed, with a compact and non-complex structure, has similar performance, in terms of relative tuning range, than filters with the same number of poles [13,14]. But, the performance could be improved even further if high dielectric anisotropy liquid crystals were used [15]. Of course, by increasing the number of poles of the filter [3], leads to higher performance but also to higher filter complexity.

Table 3. Filter performance compared to other LC-based bandpass filters.

LC-based filter	Centroal Frequency (f_0)	Relative Tuning Range	Number of Poles	Comments
Presented work	5 GHz	7.3%	2	Dual-mode filter structure. Merck MDA-98-1602 as used LC
Goelden *et al*. [3]	20 GHz	10%	3	3-pole microstrip filter. A highly anisotropic LC is used
Bernigaud *et al*. [13]	5 GHz	6%	2	DBR filter structure. Merck BL037 as used LC
Missaoui *et al*. [14]	5 GHz	4.8%	2	2-pole DBR structure. Merck LC K15 is used

The filter bandwidth gets narrower as an increasing voltage is applied, while the relative bandwidth, defined as the ratio between the bandwidth and the central frequency, remains constant. The pass-band return loss of the filter slightly gets worse as an increasing voltage is applied. Table 4 shows a summary of the measurements.

Table 4. Summary of the experimental measurements of the spectral response for the new LC bandpass filter.

LC Drive Voltage	LC Dielectric Constant (ε)	Central Frequency (f_c)	Bandwidth (BW)	Relative Bandwidth (BW/f_c)	Return Loss (RL)
0 V_{rms}	$\varepsilon_{r\perp}$	5.045 GHz	636 MHz	0.126	5.4 dB
15 V_{rms}	ε_{rl}	4.688 GHz	568 MHz	0.122	4.9 dB

The variation of the frequency as a function of the applied voltage shown in Figure 7 suggests that the LC director $\hat{n}$, which is the vector that represents the local average orientation of LC molecules in the LC bulk, has an average tilt angle which changes as voltage is applied. For low values of voltage, tilt angle is close to 0°, while it is nearby 90° for high values of voltage. This average tilt angle presents a quasi-linear dependence for intermediate values of the applied voltage, while it tends to saturation for extreme values.

A complementary analysis of the spectral response performance, comparing the simulations and the measurements, has been carried out this time for the filter filled with the LC. Due to LC features

are initially unknown at microwave frequencies, an iterative process is programed for fitting both experimental and simulated responses. The routine considers several values for LC permittivity and loss tangent, and keeps the device dimensions invariant. As a result, the software protocol gives rise to a preliminary estimation of the dielectric properties of the LC. Therefore, the extreme values of permittivities, $\varepsilon_{r\perp}$ and ε_{rl}, and LC loss tangent, tan $\delta_{\perp}$ and tan δ_{l}, are inferred. As it is shown in Figure 8, a fairly good agreement between the measured filter frequency response (when no voltage is applied) and the simulated response (with $\varepsilon_r = 2.62$ and tan $\delta = 0.05$) is achieved. In the same way, the measured frequency response by applying the saturation voltage value (15 V_{rms}) and the simulation response, considering $\varepsilon_r = 3.06$ and tan $\delta = 0.02$, are also in reasonable agreement (Figure 9).

Figure 8. Comparison between the measured frequency response when no voltage is applied and the simulated considering when $\varepsilon_r = 2.62$ and tan $\delta = 0.05$.

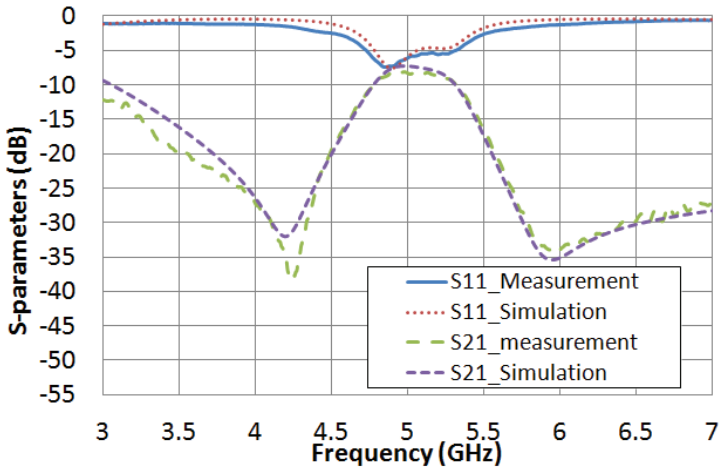

Therefore, in a preliminary estimation, it can be inferred that the dielectric properties for the used LC at 5 GHz are the shown in Table 5.

Figure 9. Comparison between the measured frequency response when 15 V_{rms} are applied and the simulated considering when $\varepsilon_r = 3.06$ and tan $\delta = 0.02$.

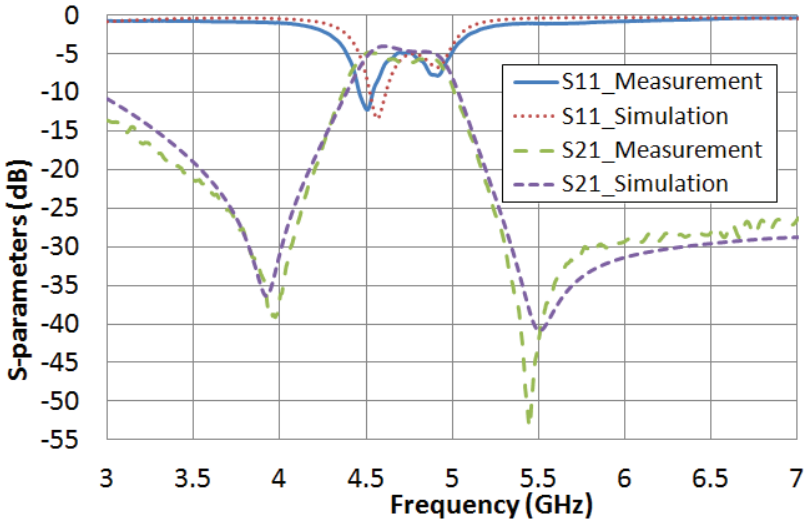

Table 5. Preliminary estimation of the dielectric properties extreme values for the LC Merck MDA-98-1602.

Applied LC drive voltage	Estimated LC permittivity (ε)	Estimated LC Loss Tangent (tan δ)
0 V_{rms}	$\varepsilon_{r\perp} = 2.62$	$\tan\delta_{\perp} = 0.05$
15 V_{rms}	$\varepsilon_{r\parallel} = 3.06$	$\tan\delta_{\parallel} = 0.02$

Let us note that LC loss tangent estimated values are high. This may be the reason why the filter exhibits high insertion loss, as it is shown in Figure 5.

With these estimated values, a comparison between the microstrip conventional square patch and the new patch, supposing the cavity filled with LC, can be obtained in simulation for the extreme values of LC permittivity and loss tangent. Figure 10 shows the frequency response of both structures considering $\varepsilon_{r\perp} = 2.62$ and $\tan\delta_{\perp} = 0.05$. In Table 6, the performances of the new square patch structure and the conventional one are summarized. A filter bandwidth narrowing of 14.7% and a pass-band return loss increase of 1.5 dB, which means an increase of 30.6%, are achieved by using the new patch. In the same way, Figure 11 and Table 7 present a comparison between both structures when $\varepsilon_{r\parallel} = 3.06$ and $\tan\delta_{\parallel} = 0.02$ are considered, obtaining a filter narrowing of 17.8% and a pass-band return loss improvement of 1.9 dB, which means an improvement of 38.8%.

Table 6. Comparison between the performance of both dual-mode filters considering $\varepsilon_{r\perp} = 2.62$ and $\tan\delta_{\perp} = 0.05$.

Structure	Central Frequency (f_c)	Bandwidth (BW)	Return Loss (RL)
With a conventional patch	5.037 GHz	737 MHz	3.4 dB
With a new patch	5.039 GHz	629 MHz	4.9 dB

Figure 10. S-parameters obtained in simulation for both structures considering $\varepsilon_{r\perp} = 2.62$ and $\tan\delta_{\perp} = 0.05$.

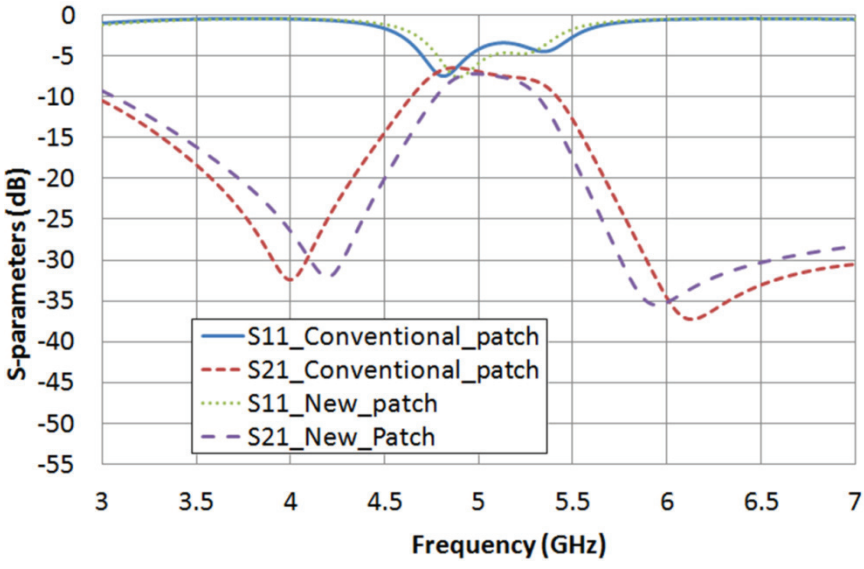

Figure 11. S-parameters obtained in simulation for both structures considering $\varepsilon_{r\parallel} = 3.06$ and $\tan \delta_{\parallel} = 0.02$.

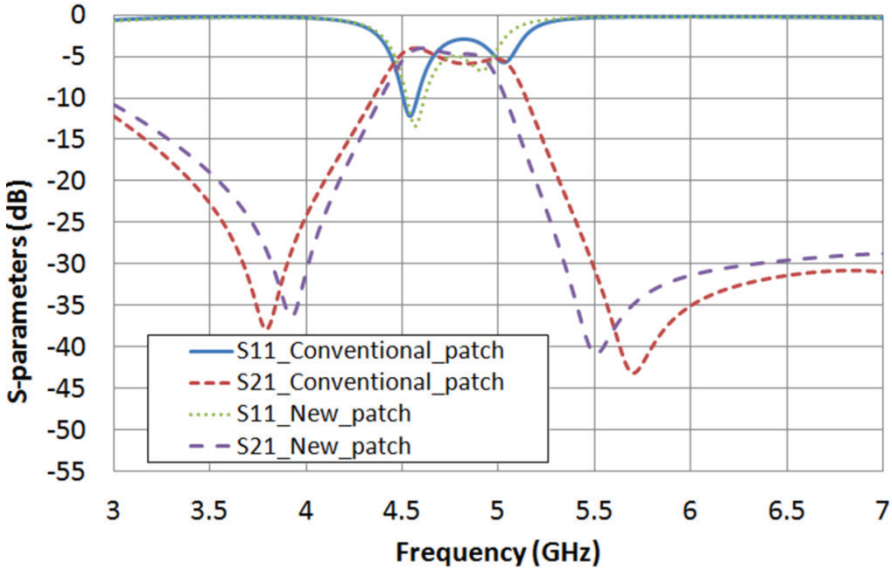

Table 7. Comparison between the performance of both dual-mode filters considering $\varepsilon_{r\parallel} = 3.06$ and $\tan \delta_{\parallel} = 0.02$.

Structure	Central Frequency (f_c)	Bandwidth (BW)	Return Loss (RL)
With a conventional patch	4.723 GHz	661 MHz	3 dB
With a new patch	4.671 GHz	543 MHz	4.9 dB

5. Conclusions

In this work, a tunable LC-based bandpass filter using dual-mode microstrip technology has been designed and experimentally measured. A reshaping of a square patch dual-mode geometry has been proposed as the microstrip filter. This new structure is expected to achieve a significant pass-band return loss improvement.

Because of LC molecules dielectric anisotropy, a filter central frequency variation from 4.688 GHz to 5.045 GHz is experimentally obtained, which means a relative tuning range of 7.3%. The experimental results have led to a preliminary estimation of the LC permittivity and loss tangent, whose values were initially unknown at microwave frequencies, obtaining $\varepsilon_{r\perp} = 2.62$ and $\varepsilon_{r\parallel} = 3.06$ for the LC permittivity and $\tan \delta_{\perp} = 0.05$ and $\tan \delta_{\parallel} = 0.02$. Simulations have been run supposing these estimated values, confirming the improvements of using the new dual-mode structure.

Acknowledgments

Authors acknowledge Grupo de Fotónica Aplicada (Universidad Politécnica de Madrid, Spain) for the use of their facilities for the manufacture of the device. Authors thank funding support from the Spanish Ministerio de Economía y Competitividad (grant No. TEC2009-13991-C02-01) and Comunidad de Madrid (grant No. FACTOTEM2 S2009/ESP/1781).

Author Contributions

Javier Torrecilla and Alejandro García devised the device configuration, carried out numerical simulations and measurements, analyzed data and wrote the manuscript. Virginia Urruchi and Noureddine Bennis analyzed data, participated in the manufacturing process of the device and wrote the manuscript. José Manuel Sánchez-Pena and Daniel Segovia supervised the study, edited the manuscript and contributed to discuss the results and to the scientific revision of the article.

Conflicts of Interest

The authors declare no conflict of interest.

References

28. Yeh, J.A.; Chang, C.A.; Cheng, C.; Huang, J.; Hsu, S.S.H. Microwave characteristics of liquid-crystal tunable capacitors. *IEEE Electron*. *Device Lett*. **2005**, *7*, 451–453.
29. Missaoui, S.; Kaddour, M. Liquid crystal-reconfigurable conformal monopole antennas structures for microwave applications. *J*. *Eng*. *Technol*. *Res*. **2012**, *3*, 57–64.
30. Goelden, F.; Gaebler, A.; Karabey, O.; Goebel, M.; Manabe, A.; Jakoby, R. Tunable band-pass filter based on liquid crystal. In Proceedings of the 5th German Microwave Conference, Berlin, Germany, 15–17 March 2010.
31. Collings, P.J.; Hird, M. *Introduction to Liquid Crystals Chemistry and Physics*, 1st Ed.; Taylor & Francis: London, UK, 1997; pp. 505–538.
32. Xiang, Q.; Feng, Q.; Huang, X.; Jia, D. A novel tri-mode bandwidth tunable filter with harmonic suppression. *Progr*. *Electromagnet*. *Res*. *C* **2013**, *34*, 183–184.
33. Yang, G.; Xing, X.; Daigle, A.; Liu, M.; Obi, O.; Naishadham, K.; Sun, N. Tunable miniaturized patch antennas with self-biased multilayer magnetic films. *IEEE Trans*. *Antennas Propag*. **2009**, *7*, 2190–2193.
34. Wolff, I. Microstrip bandpass filter using degenerate modes of a microstrip ring resonator. *Electron*. *Lett*. **1972**, *6*, 302–303.
35. Cheong, P.; Lv, T.; Choi, W.; Tam, K. A compact microstrip square-loop dual-mode balun-bandpass filter with simultaneous spurious response suppression and differential performance improvement. *IEEE Microw*. *Wirel*. **2011**, *2*, 77–79.
36. Zhu, L.; Tan, B.C.; Kuek, S.J. A compact ultra-wideband (UWB) bandpass filter using microstrip t-shaped stub. In Proceedings of the International Conference of Computational Problem Solving, Chengdu, China, 21–23 October 2011; pp. 382–384.
37. Li, S.; Cai, H.; Wu, W.; Li, Y.; Wang, Z. New dual-mode microstrip bandpass filter with a square notch. In Proceedings of the IEEE International Conference on Communication Technology, Nanjing, China, 11–14 November 2010.
38. Torrecilla, J.; Marcos, C.; Urruchi, V.; Sánchez-Pena, J.M. Tunable dual-mode bandpass filter based on liquid crystal technology. In Proceedings of the 43rd European Microwave Conference, Nürnberg, Germany, 6–10 October 2013.

39. Torrecilla, J.; Ávila-Navarro, E.; Marcos, C.; Urruchi, V.; Sánchez-Pena, J.M.; Arias, J.; Sánchez-López, M.M. Microwave tunable notch filter based on liquid crystal using spiral spurline structure. *Microw. Opt. Technol. Lett.* **2013**, *10*, 2420–2423.
40. Bernigaud, J.F.; Martin, N.; Laurent, P.; Quendo, C.; Tanne, G.; Della, B.; Huret, F.; Gelin, P. Liquid crystal tunable filter based on DBR topology. In Proceedings of the 36th European Microwave Conference, Manchester, UK, 10–15 September 2006.
41. Missaoui, S.; Kaddour, M. Liquid crystal-based reconfigurable tunable filter with DBR topology. *ISRN Mater. Sci.* **2011**, *2011*, 784615:1–784615:5.
42. Dabrowski, R.; Kula, P.; Herman, J. High birefringence liquid crystals. *Crystals* **2013**, *3*, 443–482.

Liquid Crystal Lensacons, Logarithmic and Linear Axicons

José Francisco Algorri, Virginia Urruchi, Braulio García-Cámara and José Manuel Sánchez-Pena

Abstract: Until now, several attempts have been made to obtain axicons by using liquid crystals. Previous results had always a considerable deviation from the linear response and the resulting aperture is square. In addition, classical fabrications methods are expensive and only produce fixed phase profiles. In this study, a novel structure to obtain tunable axicons with a perfect conical shape and a circular aperture is proposed and theoretically studied. The proposed optical device is based on nematic liquid crystal and phase shifted electrical signals. A simulation program consisted of Finite Elements Method to solve the voltage distribution combined with the Frank-Oseen equation to solve the molecular position of the nematic liquid crystal is employed. This device is totally reconfigurable by using low voltage signals. The focus depth and the position of this one can be controlled electrically.

Reprinted from *Materials*. Cite as: Algorri, J.F.; Urruchi, V.; García-Cámara, B.; Sánchez-Pena, J.M. Liquid Crystal Lensacons, Logarithmic and Linear Axicons. *Materials* **2014**, *7*, 2593–2604.

1. Introduction

The term axicon was first proposed by Mcleod in 1954 (from Greek: "axis image") [1]. In the referred work, a glass cone was first studied to image a point source into a line focus. The main advantage over traditional optical lenses is that axicons produce a field distribution that is proportional to the zero order Bessel function (J_0). In the near field, these beams are characterized by a bright central part surrounded by concentric rings of decreasing intensity. The energy density in the central part of the Bessel beam is high and the focus depth (distance of the preservation) is greater than for Gaussian beams [2]. For this reason, they are also known as non-diffracting Bessel beam (Gaussian beams are broadened and blurred by the diffraction). With the development of optical manufacturing and processing technologies, this type of optical lenses is now commercially available. Despite the usually high fabrication costs, the applications have grown exponentially. First applications were focused on precision alignment for large telescopes [3] and laser machining [4]. After this, negative and positive axicons were used to change the diameter of the Bessel beam ring for ablating corneal material for corneal surgery [5]. In 1992, a scanning optical system based on axicons was proposed [6]; in such a way that now almost every supermarket bar code reader uses axicons. Medical applications have also benefited from the use of axicons, for example: optical coherence tomography [7,8], tissue characterization [9], biophotonics [10,11], among others. Other important applications are optical tweezers [12], atom optics [13], *etc.*

The great number of applications has created an increasing interest in the fabrication of these optical elements. Classical manufacturing methods, using diamond turning from solid materials such as BK7 glass or fused silica, cause them to be expensive. Gradient index (GRIN) axicon has been demonstrated in [14], but the profile has a round axicon tip. Computer-generated holographic optical

elements have been also proposed [15] but may require accuracies of nanometers. To overlay these problems, Fresnel axicons were proposed in ref. [16], but they still have the problem of a fixed phase profile.

The parameters defining an axicon are the propagation distance, z_{max}, the ring spacing, $\Delta\rho$, and the size of the beam core, r_0. All of these terms proportionally depend on the effective cone angle. This is the main reason of axicons are catalogued by this latter parameter. When the effective cone angle of an axicon can be changed, a total control over the resulting Bessel beam is achieved. However, the variation of the effective cone angle of an axicon is a difficult task. Some systems to make tunable axicons are the fluidic axicon [17] or liquid crystal spatial light modulators (LC-SLM) [18]. Fluidic axicons have a tunable range limited by the refraction index of the fabrication materials. In contrast, the main problems of LC-SLM are the price and the characteristic structure, based on pixels surrounded by opaque areas, causing losses of light efficiency. The pixel resolution causes limitations in the effective cone angle too; the aliasing limits this one to few miliradians [17]. Some works have been researching new ways to create tunable axicons with LC. For example, the generation of axicons with several millimeters of diameter, based on modal control technique, has been proposed in ref. [19]. This technique uses a high resistivity layer to distribute the voltage continuously. In a previous study, we have proposed and demonstrated a structure based on several electrodes and modal control technique to generate an array of four optical elements. This structure can produce four axicons of several millimeters with a high range of tunability [20]. The results obtained have always shown a considerable deviation from the linear response and the resulting aperture is square.

In this study, a structure to obtain tunable axicons with a reconfigurable shape, perfect circular aperture and a high range of tunability, is proposed and theoretically studied. The proposed optical device is based on nematic LC and phase shifted electrical signals. The specific patterned electrode produces a circular aperture. It also reduces the typical phase deviation produced in the edges of the active area when a modal technique is used. A simulation program consisted of Finite Elements Method (FEM) to solve the voltage distribution combined with the Frank-Oseen equation to solve the molecular position of the nematic LC is employed. This device is totally reconfigurable by using low voltage signals. Lensacons, logarithmic axicons and even another type of this kind of optical elements known as fractional axicons, which is a new concept proposed recently in ref. [21], can be obtained. The amplitude of the optical phase shift, as well as the position of this one, can be controlled electrically. This device could contribute to developing new applications and to reduce the fabrication costs of the actual devices.

2. Structure and Theoretical Basis

The proposed device comprises two tin-doped indium oxide (ITO) coated glasses separated by spacers of 50 μm. The resulting cavity has to be filled with a MDA 98-1602 nematic LC. The appropriate values of the LC have been obtained from the datasheet issued from the manufacturer (Merck Ltd., Kanagawa, Japan). The design of the electrode pattern at the top and bottom substrate consists of two circular sections of ITO electrodes (Figure 1a). A high resistivity layer covering the ITO electrodes is required. Several materials can be employed, depending on the necessary sheet

resistance (R_{sq}), for instance, Titanium Oxide (TiO_2), PEDOT, thin films of ITO or Nickel, *etc.* The resistivity of these materials ranges from 0.1 to 10 MΩ/sq. The necessary resistance is inversely proportional to the voltage frequency and directly proportional to the thickness. In this case, a resistivity of 1 MΩ/sq, 1 kHz of voltage frequency and 50 μm of thickness are used in the simulations. A lower R_{sq} does not produce any remarkable change, but the power consumption would be higher. Although the thickness is not a critical parameter, the lower the thickness, the lower the optical phase shift, keeping the same phase profile. Substrates are arranged such that their circular areas match with each other. The resulting area is 40 mm^2. The diameter can be increased if the R_{sq} is proportionally decreased. A scheme of the proposed structure, comprising these layers, is shown in Figure 1b. An alignment layer is also deposited over the high resistivity layer (e.g., polyimide). The LC molecules have an elongated shape that causes different molecular polarizabilities between the long and short axis. The effective refractive index depends on the angle between the long axis of the molecules and the linear polarization of the incident light. For this reason, a homogeneous alignment layer, with the same direction as the polarized light, is necessary. After a rubbing process, microgrooves are created in this layer. The main aligning mechanism is based on shear stress induced on the alignment layer [22] and intermolecular interactions between LC and polyimide [23].

The resulting active area is determined by the space between the circular ends of the electrodes. U_1 and U_2 correspond to the voltage distribution in each high-resistivity layer. It is important to mention that the separation distance of 0.4 mm is essential to create perfect axicons and reduce the typical phase deviation produced in the edges of the active area. This specific value is proposed after several optimization tests. If the diameter is increased, this dimension should also be increased in the same proportion. The functionality of this space is established in the next section. The voltage distribution in the active area, which is formed by the two high resistivity layers ($U_1 - U_2$), results in a second-order two-dimensional coupled partial differential equation (PDE) system.

$$\begin{cases} \nabla_s U_1^2 = R_{sq1}\left(G - j\omega C\right)\cdot\left(U_1 - U_2\right) \\ \nabla_s U_2^2 = R_{sq2}\left(G - j\omega C\right)\cdot\left(U_2 - U_1\right) \end{cases} \tag{1}$$

where G and C are distributed conductance and capacitance, respectively, per unit area. R_{sq1} and R_{sq2} are the sheet resistance of the two high resistivity layers. The solution of this system was experimentally validated in [20]. The solver considers all the possible boundary conditions (Dirichlet and Neumann), mainly determined by the applied voltages. The Frank-Oseen equation in combination with the electrical energy is employed to determine the LC molecular position Equation (2):

$$K_{11}\left(\nabla\vec{n}\right)^2 + K_{22}\left(\vec{n}\cdot\nabla\times\vec{n} + \frac{2\pi}{\xi}\right)^2 + K_{33}\left|\vec{n}\times\nabla\times\vec{n}\right|^2 - \frac{1}{2}\vec{D}\cdot\vec{E} \tag{2}$$

where $\vec{n}$ (n_x, n_y, n_z) represent the average local orientation of molecules, K_{ii} are the elastic deformation constants and $\vec{D}$ is the displacement vector and $\vec{E}$ the electric field. The ξ is the pitch of a chiral helicoidal dopant (only for twist purposes). In this case, it is infinite because we use a nematic LC that is just a cholesteric of infinite pitch. As this molecular position also affects the voltage distribution, an iterative process is necessary to determine both the final voltage and

molecular position. This molecular distribution generates a gradient in the refraction index which distribution is proportional to the voltage. In our previous work, we demonstrated how the application of complex signals in this type of systems can generate interesting optical modulations. The proposed device in this study goes one step further improving the structure to create axicons with a perfect conical shape, and avoiding the typical defects in the active area edges. Among the structural parameters, the circular patterned and the optimized space between them, are key factors. Moreover, the use of this device to create a new type of optical element, known as fractional axicon, is also theoretically demonstrated.

Figure 1. Scheme of the proposed structure. (**a**) Top view and (**b**) 3D diagram of the substrates arrangement. Note drawings are not to scale.

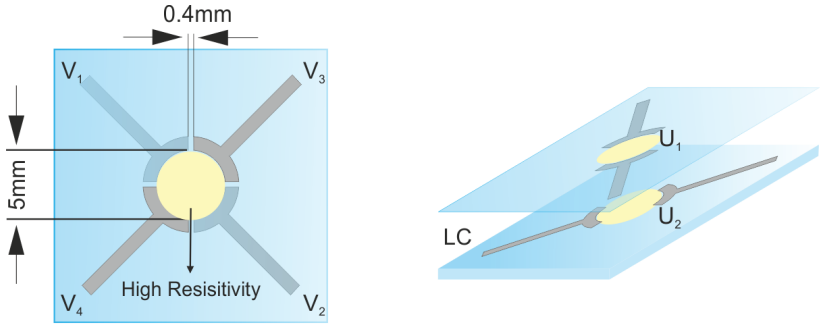

3. Results and Discussion

The simulation program uses the following input parameters about the device structure and the nematic LC features: thickness = 50 µm, K_{11} = 13.6 pN, K_{33} = 15.7 pN, γ_1 = 203 mPas, Δn = 0.2666 (n_e = 1.7779, n_o = 1.5113), $\Delta\varepsilon$ = 16.2 (ε_e = 1.7779, ε_o = 1.5113) and R_{sq1} = R_{sq2} = 1 MΩ/sq, 5° as pretilt angle. The configuration of the device is basically focused on creating three kinds of optical elements: an axicon with a perfect conical shape, which depth of focus and position should be tunable, a lensacon and fractional axicon with the same properties. The driving scheme consists of the application of four electrical signals, with the same frequency (2 kHz) but four different electrical phase shifts (V_1 = 0°, V_2 = 180°, V_3 = 90°, V_4 = 270°) on each electrode. The only configurable parameter is the amplitude of the signals. Additionally, there is necessary an extra signal with different frequency (1 kHz) and variable amplitude (V_0). The electrical phase shift of this signal will be zero and it could be connected to the electrodes by means of an operational amplifier in adder configuration [19]. It creates an offset value in the voltage distribution and eliminate the characteristic zero crossing when phase shifted signals are applied to a modal device.

As commented above, the proposed devices based on modal control technique have always square aperture. In this study, we proposed the use of circular electrodes to avoid this problem. Despite this, there is an undesirable effect produced by the modal control configuration; a voltage gradient along the electrodes. It has been observed that the use of little separation distances between electrodes can reduce this effect producing a small gradient voltage at these gaps, but reducing the voltage gradient along the electrodes. The functionality of the proposed spaces is shown in Figure 2.

Figure 2. Voltage and optical phase shift distribution in the *XZ* plane, and interference pattern for (**a**) a structure without spaces and (**b**) the proposed structure.

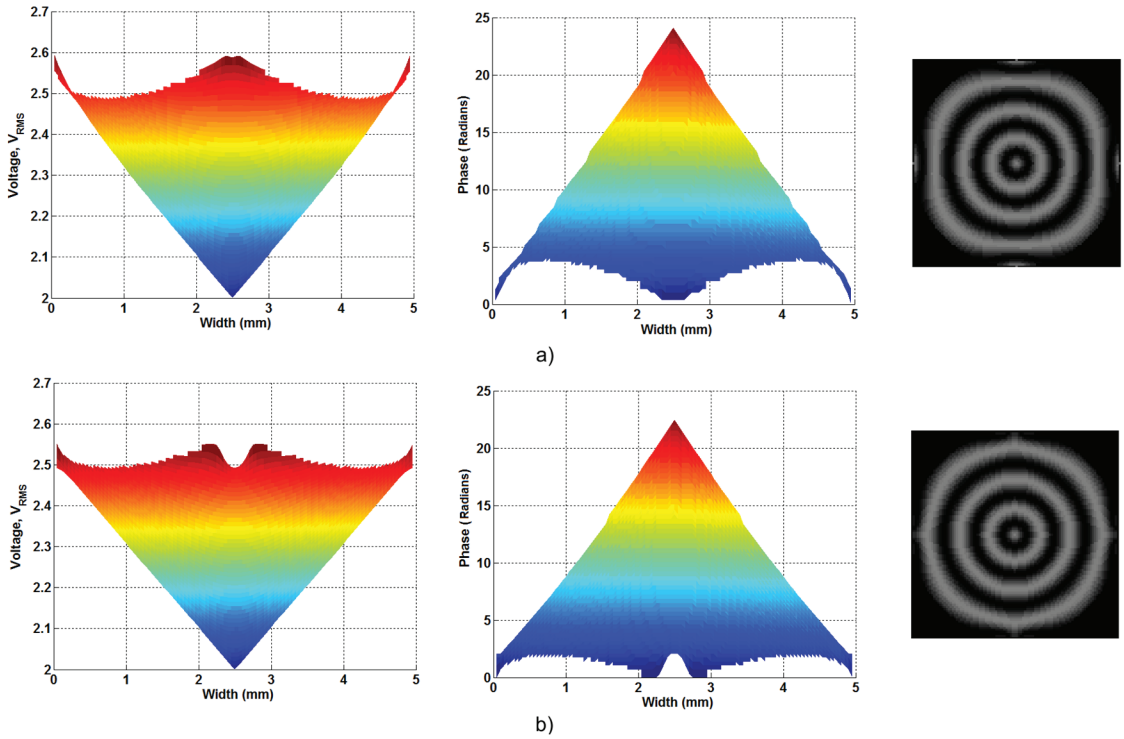

The use of these spaces solves considerable the problem at the edges of the active area. In the interference pattern, the structure without spaces provoke a semi-square rings in the outer zone of the active area. However, the voltage decreasing produced by the spaces make a considerable lower gradient and the interference pattern reveals a circular ring, even in the outer zone of the active area.

In the following sections three different studies have been taken into account. The first one generates linear axicons and reveals how they are totally reconfigurable in terms of optical phase shift amplitude. This is a clear advantage over commercial axicons that typically produce a fixed phase shift. In Section 3.2 the generation of lenascons and fractional axicons is demonstrated. Finally, the application of this device in optical trapping applications (with a focus movable in *x*-*y* focal plane) is shown. In combination with the optical phase shift tunability, the position of the optical trap along the z-axis could also be changed.

3.1. The Linear Axicon

A linear axicon is the optical element that produces an optical phase shift with the shape of a perfect cone. Figure 3 shows the voltage distribution and the resulting optical phase shift, of the proposed structure, with the following voltages: $V_1 = V_2 = V_3 = V_4 = 1\ V_{rms}$ and $V_0 = 1.3\ V_{rms}$. In this figure, the resulting voltage distribution of Equation (1) has a linear shape.

Figure 3. (**a**) Voltage and (**b**) optical phase shift distribution, in three dimensions, of the proposed structure.

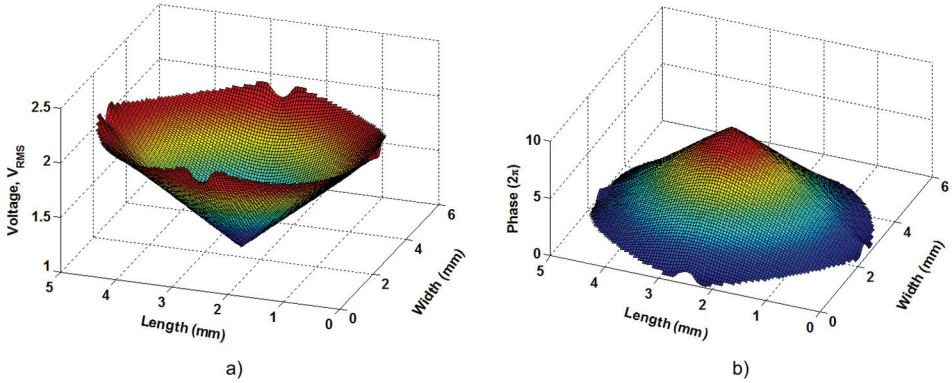

However, the LC birefringence, which is determined by the molecular position as a function of voltage, is a non-linear curve. There is a quasi-linear range after the threshold voltage (when the molecules start to move) and before the saturation voltage (when the molecules start to reach the perpendicular position). When a 10% margin from these two limits is used, a linear range can be obtained. Two molecular distributions are shown in Figure 4. Only one plane is selected to clearly see the molecules. Figure 4a uses an offset voltage of 1.3 V_{rms} and $V_1 = V_2 = V_3 = V_4 = 0.1\ V_{\text{rms}}$. In contrast, in Figure 4b the molecules are completely oriented and the axicon is formed with the following voltages: $V_1 = V_2 = V_3 = V_4 = 1\ V_{\text{rms}}$ and $V_0 = 1.3\ V_{\text{rms}}$.

Figure 4. Molecular distribution (*XZ* plane) for (**a**) a low voltage applied to the electrodes (0.1 V_{rms}); (**b**) and a higher voltage (1.3 V_{rms}).

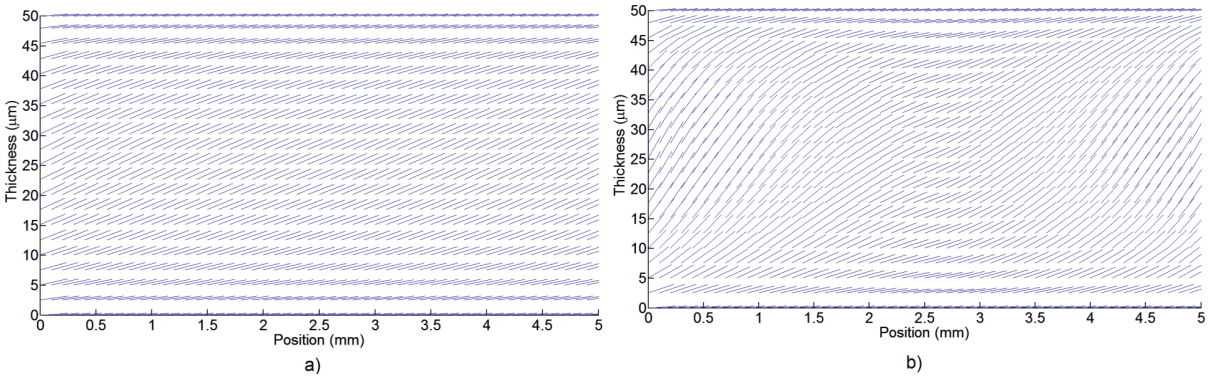

It is not straightforward to obtain clear conclusion from these kinds of figures, for the following reason: only one plane is considered and the number of molecules has been reduced. When the light passes through the device the effective refractive index caused by each molecule generates a phase shift between substrates. This is estimated by integration of the molecular effective refractive index over the thickness.

As can be observed, the voltage distribution produces a linear response in the optical phase shift. For this are necessary small voltage gradients. Despite this, a wide range of tunability can be achieved, as it is shown in Figure 5; only the cone profiles in the *XZ* plane are depicted. The applied voltages are $V_1 = V_2 = V_3 = V_4 = V_x \cdot V_{\text{rms}}$ and a fixed offset voltage $V_0 = 1.3\ V_{\text{rms}}$.

Figure 5. Phase shift profile in the *XZ* plane for several voltages applied to the electrodes.

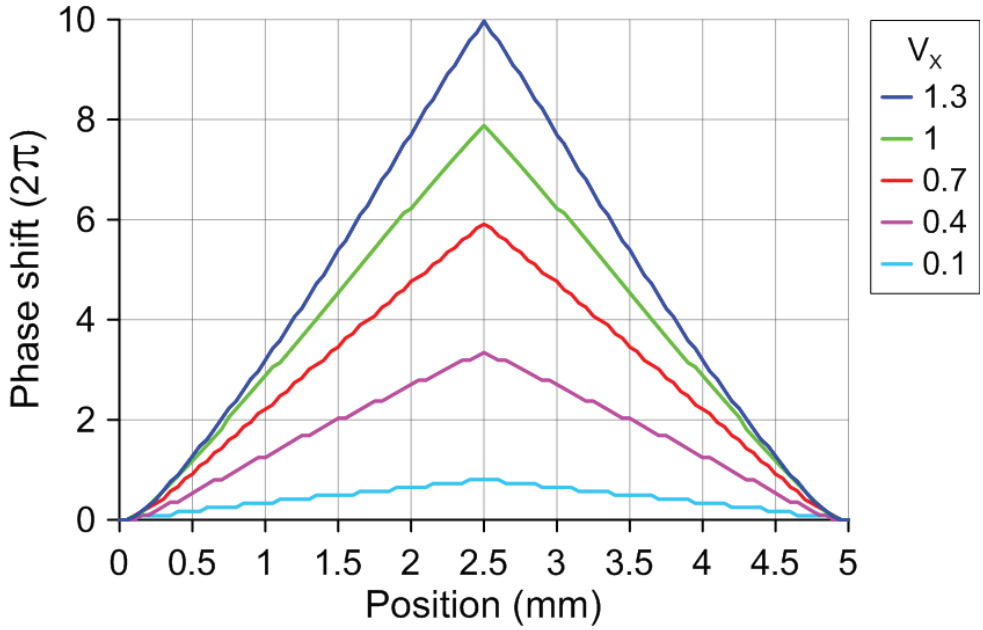

Due to the high birefringence of MDA-98-1602 the optical phase shift is very high. With a slight variation of 1.2 V_{rms}, the optical phase shift is tunable from 1.6π radians to 22π radians. In addition, this optical phase shift can be translated to an effective cone angle. Thus, the characteristic parameters could be changed in a broad range.

3.2. The Lensacon and Logarithmic Axicon

The non-linear response of the LC birefringence has two characteristic curves. The first one is produced when the electrical energy overcomes the forces that hold the molecules in place, and the molecules start to move. The other one, which has an inverse curvature, is produced when the molecules start to reach the perpendicular position. Taking advantage of these zones, the generation of lensacons [24] and logarithmic axicons [25,26], by using LC is proposed and theoretically demonstrated for the first time. These optical elements are axicons in which their profile phase has a little curvature. In order to create the lensacon, the offset voltage (V_0) has to be smaller than the threshold voltage. In contrast, a voltage smaller to the saturation voltage is required to create logarithmic axicons. Figure 6a shows the phase profile of lensacons, for which the applied voltages are $V_1 = V_2 = V_3 = V_4 = V_x \cdot V_{rms}$ and the offset voltage is $V_0 = 0.8\ V_{rms}$. On the other hand, considering a $V_0 = 2.3\ V_{rms}$ and $V_x = 2.5\ V_{rms}$ a logarithmic axicon is observed in Figure 6b. Its molecular distribution is shown in Figure 7.

Changing the voltage of V_1, V_2, V_3 and V_4 (all equal to V_x), these phase profiles could also be tuned. In Figure 6a a tunable lensacon is shown. The optical phase shift can be easily tunable from 0.8π radians to 12π radians, with only a small variation of 0.8 V_{rms}.

Figure 6. Phase shift profile in the *XZ* plane, for (**a**) lensacons; and (**b**) logarithmic axicons.

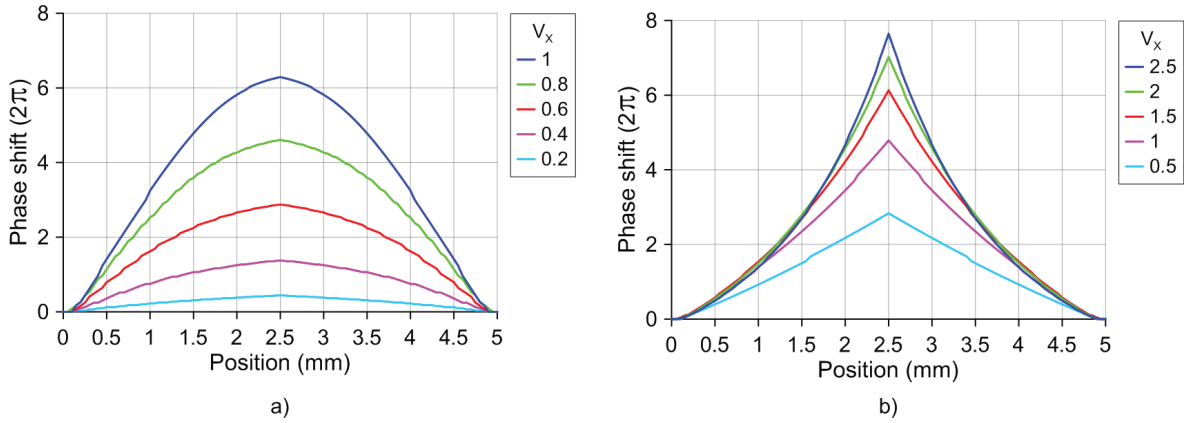

Figure 7. Phase shift profile in the *XZ* plane, for (**a**) lensacons and (**b**) logarithmic axicons.

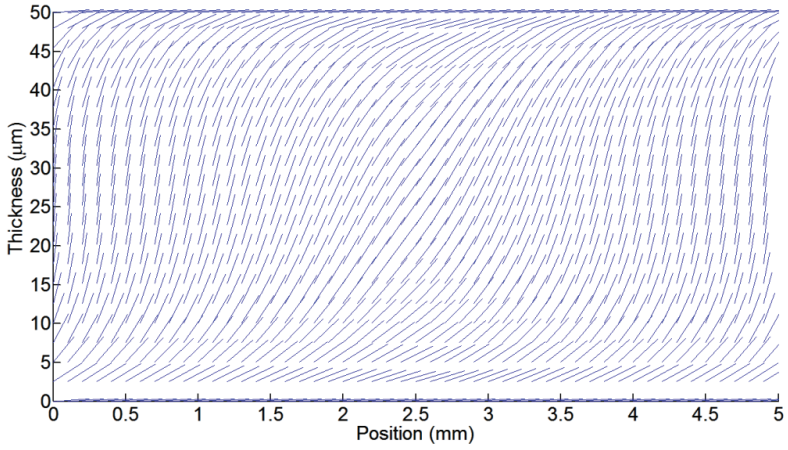

The resulting effect in the case of the logarithmic axicon is a control over the curvature itself. This effect was recently proposed by using diffractive optical elements. This new optical element was called "fractional axicon" (it has a fractional power dependence on the radial coordinate) [21]. In Figure 6b the generation of this optical element simply by low voltage electrical signals is demonstrated.

3.3. Moving Focus

The application of optical tweezers based on modal LC devices has considerably reduced functionality over holographic optical traps (HOTs) or the generalized phase contrast (GPC) systems. This is mainly because they can only be used for single or double traps [27]. Despite this, LC devices have a reduced complexity and in consequence they are low-cost and more compact. Other advantages are the analog control (increasing the accuracy) and a larger light efficiency. The proposed device has reduced RMS deviation from the perfect profile. In combination with the experiment proposed in the previous section, the position of the optical trap along the *z*-axis will also be controllable. In order to move the focus in the *x*-*y* plane, a gradient between electrodes is needed.

The above figures illustrate how the position of the focus can be easily moved in the *x*-*y* plane. The first image correspond to the same cone as Figure 3 (in *XY* plane) where the applied voltages

were $V_1 = V_2 = V_3 = V_4 = 1.3\ V_{rms}$ and $V_0 = 1.3\ V_{rms}$. Then the voltage is increased only in two electrodes (while the others remains at 1.3 V_{rms}), as is described in Figure 8. Each pair of voltages move the focus position in one direction, right (V_1, V_4), left (V_2, V_3), up (V_2, V_4), and down (V_1, V_3). In order to change the position of the optical trap along the z-axis, a change in the total voltage (V_x) is required, as was established in the previous section.

Figure 8. Optical phase shift in the *XY* plane several voltages applied to the electrodes.

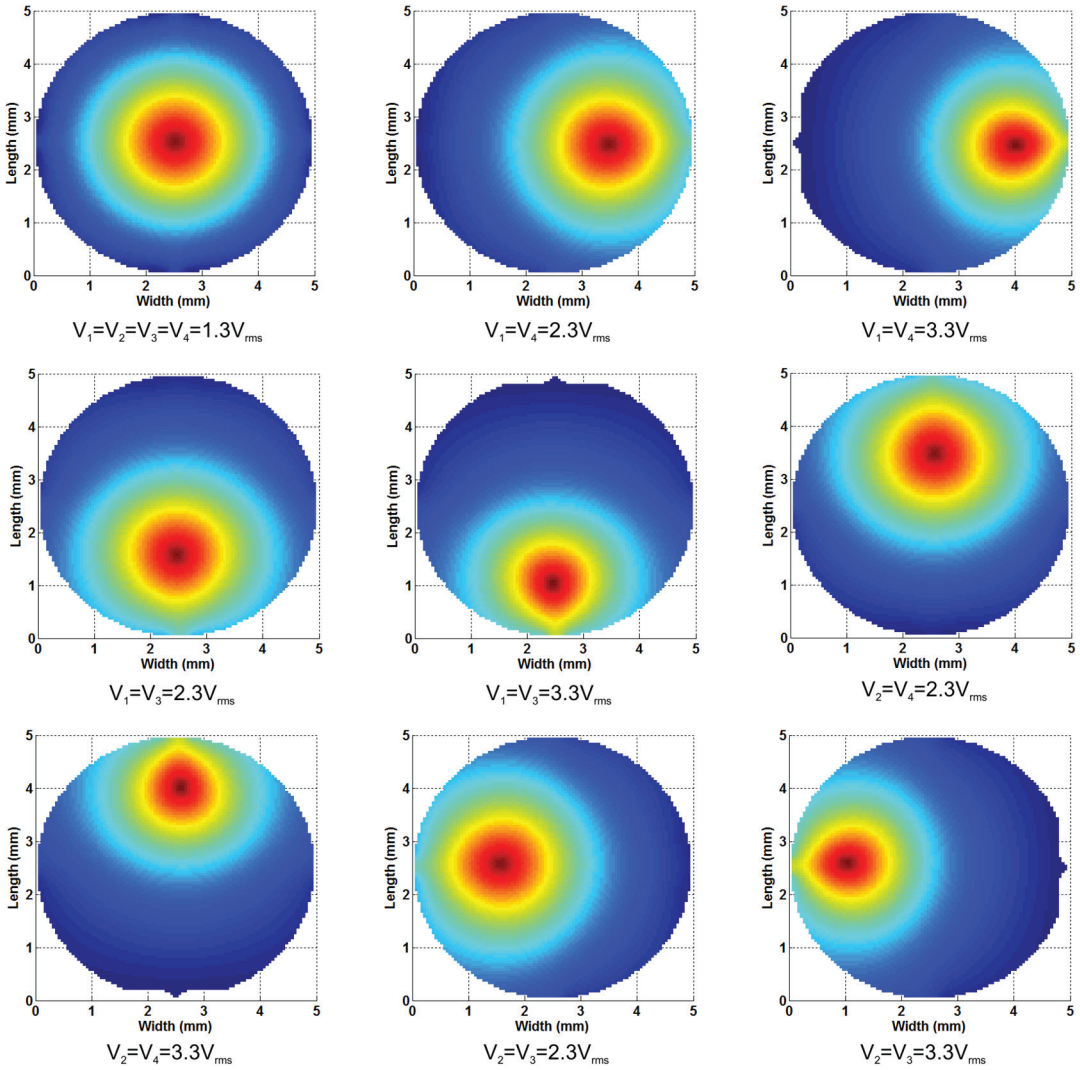

The focusing speed of the proposed device is directly related to the rising and decay time of the LC molecules [28],

$$t_{decay} = \frac{\gamma_1}{K_{11}}\left(\frac{d}{\pi}\right)^2 \quad t_{rise} = \frac{\gamma_1 d^2 / K_{11}\pi^2}{(V/V_{th})^2 - 1} \tag{3}$$

As can be seen these relations are cuadratically proportional to the device thickness. In this case and considering a V_{th} = 1.2 V_{rms}, the decay time will be 3.78 s (switch off the device). If the voltage is increased to 2.3 V_{rms}, for example, the time necessary for the molecules to reach the new position will be 1.41 s.

4. Conclusions

In summary, modal LC axicons offer a simple and low cost solution for the tunable generation of Bessel beams. These ones have several advantages over other reported methods: analog control, high tunability, moving focus in the *x*-*y* plane and high light efficiency. Unlike other reported LC axicons, the proposed device has a circular aperture that creates perfect cone profiles. The inclusion of some little spaces in the patterned electrode reduces undesirable effects in the edges of the active area (reduced aberrations). For the first time, the generation of perfect axicons, lensacons, logarithm axicons and fractional axicons, by the same structure (totally reconfigurable by low voltages), have been proposed and theoretically demonstrated. We conclude that the simulation tool is essential to design this type of devices because some critical parameters as thickness, resistivity of the deposited layer, frequency and amplitude of the voltage control, can be known before the device fabrication. This device could contribute to developing new applications and to reducing the fabrication costs of the actual devices.

Acknowledgments

This work was supported in part by the Ministerio de Ciencia e Innovación of Spain (grant No. TEC2009-13991-C02-01) and the Comunidad de Madrid (grant No. FACTOTEM2 S2009/ESP-1781).

Author Contributions

José Francisco Algorri designed and performed the simulation program, designed a test-bench simulation, analyzed data and wrote the manuscript; Virginia Urruchi and Braulio Garcia-Cámara, analyzed data and wrote the manuscript; José Manuel Sánchez-Pena supervised the project, and edited the manuscript.

Conflicts of Interest

The authors declare no conflict of interest.

References

1. Mcleod, J.H. The Axicon: A New Type of Optical Element. *J. Opt. Soc. Am.* **1954**, *44*, 592–592.
2. Durnin, J.; Miceli, J.J.; Eberly, J.H. Diffraction-free beams. *Phys. Rev. Lett.* **1987**, *58*, 1499–1501.
3. Mcleod, J.H. Axicons and their uses. *J. Opt. Soc. Am.* **1960**, *50*, 166–169.
4. Rioux, M.; Tremblay, R.; Belanguer, P.A. Linear, annular, and radial focusing with axicons and applications to laser machining. *Appl. Opt.* **1978**, *17*, 1532–1536.
5. Ren, Q.; Birngruber, R. Axicon: A new laser beam delivery system for corneal surgery. *IEEE J. Quantum Electron.* **1990**, *26*, 2305–2308.
6. Arimoto, R.; Saloma, C.; Tanaka, T.; Kawata, S. Imaging properties of axicon in a scanning optical system. *Appl. Opt.* **1992**, *31*, 6653–6657.

7. Leitgeb, R.A.; Villiger, M.; Bachmann, A.H.; Steinmann, L.; Lasser, T. Extended focus depth for Fourier domain optical coherence microscopy. *Opt. Lett.* **2006**, *31*, 2450–2452.
8. Lee, K.-S.; Rolland, J.P. Bessel beam spectral-domain high-resolution optical coherence tomography with micro-optic axicon providing extended focusing range. *Opt. Lett.* **2008**, *33*, 1696–1698.
9. Lu, J.; Greenleaf, J.F. Diffraction-Limited Beams and Their Applications for Ultrasonic Imaging and Tissue Characterization. In Proceedings of the New Developments in Ultrasonic Transducers and Transducer Systems, San Diego, CA, USA, 19 July 1992.
10. Tsampoula, X.; Garcés-Chávez, V.; Comrie, M.; Stevenson, D.J.; Agate, B.; Brown, C.T.A.; Gunn-Moore, F.; Dholakia, K. Femtosecond cellular transfection using a non-diffracting light beam. *Appl. Phys. Lett.* **2007**, *91*, 053902:1–053902:3.
11. Cizmar, T.; Kollarov, V.; Tsampoula, X.; Gunn-Moore, F.; Sibbett, W.; Bouchal, Z.; Dholakia, K. Generation of multiple Bessel beams for a biophotonics workstation. *Opt. Express* **2008**, *16*, 14024–14035.
12. Cheong, W.C.; Ahluwalia, B.P.S.; Yuan, X.-C.; Zhang, L.-S.; Wang, H.; Niu, H.B.; Peng, X. Fabrication of efficient microaxicon by direct electron-beam lithography for long nondiffracting distance of Bessel beams for optical manipulation. *Appl. Phys. Lett.* **2005**, *87*, 024104:1–024104:3.
13. Arlt, J.; Hitomi, T.; Dholakia, K. Atom guiding along Laguerre-Gaussian and Bessel light beams. *Appl. Phys. B* **2000**, *71*, 549–554.
14. Fischer, D.; Harkrider, C.; Moore, D. Design and Manufacture of a Gradient-Index Axicon. *Appl. Opt.* **2000**, *39*, 2687–2694.
15. Davidson, N.; Friesem, A.; Hasman, E. Holographic axilens: High resolution and long focal depth. *Opt. Lett.* **1991**, *16*, 523–525.
16. Gourley, K.; Golub, I.; Chebbi, B. Demonstration of a Fresnel axicon. *Appl. Opt.* **2011**, *50*, 303–306.
17. Milne, G.; Jeffries, G.D.M.; Chiu, D.T. Tunable generation of Bessel beams with a fluidic axicon. *Appl. Phys. Lett.* **2008**, *92*, 261101:1–261101:3.
18. Chattrapiban, N.; Rogers, E.; Cofield, D.; Hill, W.; Roy, R. Generation of nondiffracting Bessel beams by use of a spatial light modulator. *Opt. Lett.* **2003**, *28*, 2183–2185.
19. Kirby, A.; Hands, P.; Love, G. Liquid crystal multi-mode lenses and axicons based on electronic phase shift control. *Opt. Express* **2007**, *15*, 13496–13501.
20. Algorri, J.; Love, G.; Urruchi, V. Modal liquid crystal array of optical elements. *Opt. Express* **2013**, *21*, 24809–24818.
21. Khonina, S.N.; Ustinov, A.V.; Volotovsky, S.G. Fractional Axicon as a New Type of Diffractive Optical Element with Conical Focal Region. *Precis. Instrum. Mechanology* **2013**, *2*, 132–143.
22. Geary, J.M.; Goodby, J.W.; Kmetz, A.R.; Patel, J.S.J. The mechanism of polymer alignment of liquid-crystal materials. *Appl. Phys.* **1987**, *62*, 4100–4108.
23. Chung, D.-H.; Takanishi, Y.; Ishikawa, K.; Takezoe, H.; Park, B.; Jung, Y.; Hwang, H.-K.; Lee, S.; Han, K.-J.; Jang, S.-H. Alignment Mechanism of Nematic Liquid Crystal on Rubbed

Polymer Surface Studied by Subsequent Processes of Rubbing and Photoalignment. *Jpn. J. Appl. Phys.* **2000**, *39*, L185–L187.

24. Koronkevich, V.P.; Mikhaltsova, I.A.; Churin, E.G.; Yurlov, Y.I. Lensacon. *Appl. Opt.* **1995**, *34*, 5761–5772.
25. Sochacki, J.; Jaroszewicz, Z.; Staroiski, L.R.; Kolodziejczyk, A. Annular-aperture logarithmic axicon. *J. Opt. Soc. Am. A* **1993**, *10*, 1765–1768.
26. Golub, I.; Chebbi, B.; Shaw, D.; Nowacki, D. Characterization of a refractive logarithmic axicon. *Opt. Lett.* **2010**, *35*, 2828–2830.
27. Hands, P.; Tatarkova, S.; Kirby, A.; Love, G. Modal liquid crystal devices in optical tweezing: 3D control and oscillating potential wells. *Opt. Express* **2006**, *14*, 4525–4537.
28. Yeh, P.; Gu, C. *Optics of Liquid Crystal Displays*, 2nd ed.; John Wiley & Sons: New Jersey, NJ, USA, 2008.

Passive Temperature Stabilization of Silicon Photonic Devices Using Liquid Crystals

Joanna Ptasinski, Iam-Choon Khoo and Yeshaiahu Fainman

Abstract: In this work we explore the negative thermo-optic properties of liquid crystal claddings for passive temperature stabilization of silicon photonic integrated circuits. Photonic circuits are playing an increasing role in communications and computing, but they suffer from temperature dependent performance variation. Most existing techniques aimed at compensation of thermal effects rely on power hungry Joule heating. We show that integrating a liquid crystal cladding helps to minimize the effects of a temperature dependent drift. The advantage of liquid crystals lies in their high negative thermo-optic coefficients in addition to low absorption at the infrared wavelengths.

Reprinted from *Materials*. Cite as: Ptasinski, J.; Khoo, I.-C.; Fainman, Y. Passive Temperature Stabilization of Silicon Photonic Devices Using Liquid Crystals. *Materials* **2014**, 7, 2229–2241.

1. Introduction

Silicon photonic devices and circuits offer a rapidly growing and promising technology for high-speed signal transmission systems with data rates of 100 Gbps, which far exceed the capabilities of copper cabling. Such devices are suited for data centers and high performance computing applications where standard copper based Ethernet networking is inadequate. Photonics based systems offer the advantage of reduced energy consumption in addition to the ability to pack a larger number of communication channels into a smaller space [1]. In the next few years, large numbers of silicon photonic products will come to market and there will be an increase in the number of complex silicon photonic systems developed in academia [2]. As silicon photonic chips mature, the technology is likely to be increasingly used in processing tasks such as interconnecting multiple cores within processor chips to boost access to shared cache and busses. Eventually, silicon photonics may be involved in actual processing, augmenting or replacing a chip's semiconductor transistors with optical equivalents with greater computing performance [3]. The field of silicon photonics is expressly well positioned at this time as paths for commercialization are now widely accessible, the costs and risks associated with prototyping products have dropped, and adopting the same silicon processing tools that the semiconductor industry uses to fabricate Complementary Metal–Oxide–Semiconductor (CMOS) transistors opens access to an immense infrastructure for yield improvement, metrology and process control [2]. Conversely, as optics penetrates deeper into the chip temperature stability becomes more important due to silicon's high thermo-optic coefficient (1.86×10^{-4}/°C) accompanied by an appreciable modification of the refractive index in the presence of rising temperature and resulting in performance deterioration of photonic devices and systems [4,5]. Correspondingly, at power densities of 100 W/cm^2 in modern microelectronic Very Large Scale Integration (VLSI) chips, the problem of heat dissipation is a major challenge even with the most advanced packaging technologies. Local temperature stabilization becomes impossible with thousands of devices with varying temperature profiles across a single chip [6].

There has been a tremendous amount of research on the suppression of temperature sensitivity in silicon based chipscale devices and a common approach consists of using external heaters or thermoelectric coolers. A related scheme focuses on the use of direct local heating of the silicon device by alternating the bias current, or using silicon itself as a resistive material for heating [4,7]. However, as these approaches are active, they increase power consumption and account for the largest share in a power budget of state-of-the-art silicon photonics [4], in addition to demanding a large device foot-print and cost. Passive thermal stabilization techniques rely on the use of a negative thermo-optic coefficient (TOC) material to offset silicon's high positive TOC [5,6], tailoring the degree of optical confinement in silicon waveguides [7], or a careful design of the device geometry [4,8,9]. Materials used for thermal stabilization consist of polymers, such as acrylates demonstrated by Ye *et al.* [10], where a temperature dependent peak resonance wavelength shift of a racetrack resonator was reduced 8.3 times. However, the demonstration was geometry specific and performed over a very small temperature range. Other research consisted of working with Polymethyl methacrylate, a common lithography resist, or ExguideTM LFR-372 (ChemOptics Inc., Daejeon, Korea) over a wider temperature range with similar findings [5,8,11]. A drawback to polymers is that they are vulnerable to temperature degradation, chemical instability, ultraviolet (UV) aging, and poor mechanical characteristics [12,13]. Alternative methods which rely on engineering of the device geometry to lower the temperature sensitivity of the entire waveguiding system require additional space on the chip, are sensitive to fabrication tolerances and assume that the temperature compensating devices are located in the same thermal hotspot [7,12].

Here we explore a passive thermal stabilization scheme for resonant photonic devices using liquid crystal (LC) claddings. Liquid crystals' relatively low viscosity (the viscosity of E7 is 40 cps at 20°C [14]) makes it possible to backfill them into chambers made during the fabrication process in a manner similar to microfluidic devices [15–17]. The main allure of liquid crystal claddings lies in their large negative thermo-optic coefficients and low absorption at the infrared and visible wavelengths, which translates into lower insertion losses. The thermo-optic coefficient dn/dT in nematics is extraordinarily large, ranking among the largest of all known materials [18]. The rod-like nematic liquid crystals exhibit optical birefringence: ordinary refractive index n_o for light polarized perpendicular to the liquid crystal and extraordinary refractive index n_e for light polarized parallel to the liquid crystal [19]. LC crystalline properties become apparent when the liquid crystal is contained in thin flat cells. The alignment of the liquid crystal axis in such cells is essentially controlled by the cell walls whose surfaces are treated in a variety of ways to achieve various director axis alignments [20]. Homeotropic alignment (where the LC long axis is perpendicular to the surface) is typically achieved by treating the cell walls with a surfactant such as hexadecyl-trimethyl-ammoniumbromide (HTAB) and planar alignment is most easily achieved by rubbing unidirectionally with a lens tissue; LCs then align their long axis along the rubbed direction [20]. As a material, LCs are low cost, easy to use (including the possibility of filling various volumes), offer high damage threshold to laser radiation, and overcome roughness and stress induced scattering loss and polarization dependence [21,22]. Moreover, LC molecular design provides leeway in modifying their structure and properties [18–22].

We use ring resonators, which are highly sensitive to changes in the refractive index to characterize the thermo-optic properties of liquid crystals. A ring resonator consists of a closed loop waveguide commonly in the shape of a ring or a racetrack. Coupling to and from the device is achieved by placing bus waveguides within a close proximity of the ring, allowing for evanescent modes to overlap and allow coupling [23]. The ring behaves as an interferometer and shows a resonance for light whose phase change after each full trip around the ring is an integer multiple of 2π, where the difference between the vacuum wavelengths corresponding to two resonant conditions is referred to as the free spectral range (FSR) [23,24]. A resonant wavelength change is observed in response to an effective index change for the resonant mode and the amount of the resonant wavelength shift is influenced by the length of the ring perimeter [23], where the resonant wavelength is described by:

$$\lambda_{\text{res}} = \frac{L \cdot n_{eff}}{m} \tag{1}$$

here L is the ring perimeter, n_{eff} is the effective index of the mode, and m is an integer.

Figure 1. Simulation showing a resonance shift due to rising temperature for a ring resonator clad in silicon dioxide.

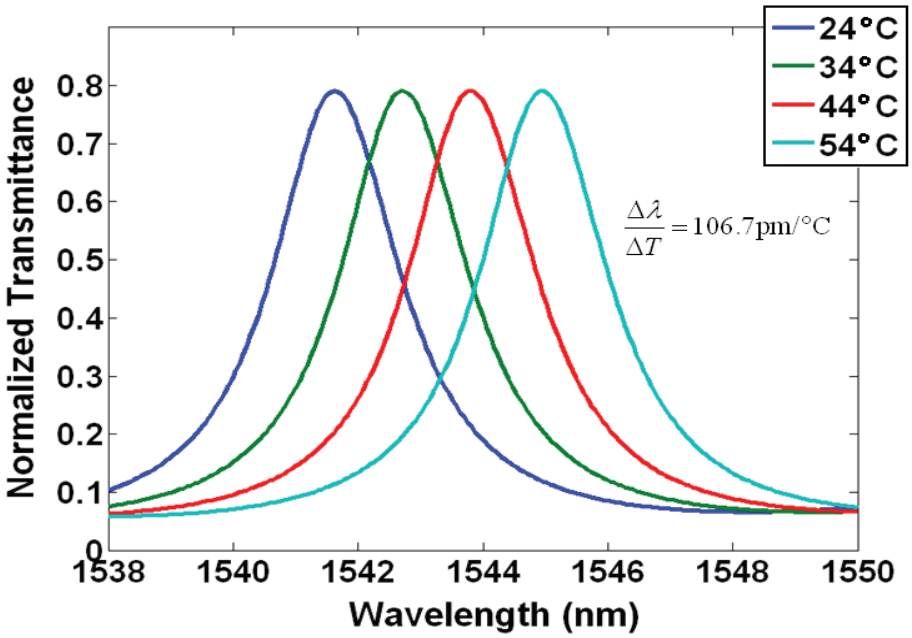

Figure 1 depicts a 2D finite-element simulation in COMSOL Multiphysics (Palo Alto, CA, USA) showing the projected fundamental TE like mode resonance shift due to rising temperature for a silicon ring clad in SiO_2. Silicon photonic waveguides commonly consist of a silicon core and silica claddings, because the large refractive index contrast between the core and cladding allows for total internal reflection with a very large incident angle [24–26]. Typically, the TE like mode is more frequently used than the TM like mode due to its low bending loss, stronger confinement in the waveguide core, and minimal leakage into the silicon substrate beneath the buried oxide (BOX) layer. In this simulation, the ring was 500 nm wide, 250 nm tall, and with a perimeter of 62.2 µm. The effective index method was used in defining the effective mode indices and propagation constants of our ring resonator. The high TOC of silicon ($\Delta n_{\text{Si}}/\Delta T = 1.86 \times 10^{-4}$/°C) together with the TOC of

SiO_2 ($\Delta n_{SiO2}/\Delta T = 1 \times 10^{-5}$/°C) resulted in a 3.2 nm resonance shift for a 30 °C change in temperature, from 1541.7 nm to 1544.9 nm, which translates to $\Delta\lambda/\Delta T$ = 106.7 pm/°C.

In modern dense wavelength division multiplexing (DWDM) systems with channel spacing of <1 nm, a difference of $\Delta\lambda/\Delta T$ = 106.7 pm/°C will greatly influence channel location and crosstalk [27].

2. Results and Discussion

2.1. Liquid Crystal Materials

Liquid crystals used in the experiment consisted of 5CB (Sigma Aldrich, St. Louis, MO, USA), E7 (Merck, Hunterdon County, NJ, USA), Lixon ZSM-5970 (Chisso Corp., Minamata, Japan), and MDA-05-2968 (Merck). Table 1 depicts some of the common characteristics of these liquid crystal mixtures.

Table 1. Room temperature properties of liquid crystals used in the experiment.

Liquid Crystal Mixture	Clearing Point	Optical Anisotropy			
		Δn	n_e	n_o	$<n>$
5CB (@22 °C, 589 nm)	35 °C	0.191	1.725	1.534	1.598
E7 (@20 °C, 589 nm)	58 °C	0.226	1.747	1.521	1.597
Lixon (@25 °C, 589 nm)	123 °C	0.109	1.596	1.487	1.523
MDA-05-2968 (@20 °C, 589 nm)	109.5 °C	0.2685	1.781	1.5125	1.602

2.2. Results

Ring resonator samples consisting of 9.9 μm radius, 500 nm width, 250 nm height, 100 nm gap between the ring and bus waveguide were characterized. A measurement was performed on a sample clad in air, which resulted in an 87.5 pm/°C resonance shift and it served as the baseline. Subsequent measurements were completed with liquid crystal claddings listed in Table 1. It should be noted that the samples did not rely on an alignment layer in order to achieve a specific liquid crystal orientation and the liquid crystals were assumed to be randomly oriented exhibiting an average refractive index $<n>$. The experimental results are shown in Table 2 and Figure 2, where Table 2 provides a summary of the observed resonance shift per degree Celsius, while Figure 2 tracks the resonant wavelength change as a function of increasing temperature. MDA-05-2968 LC produced a peak wavelength shift of 58 pm/°C, while the best response was attained with 5CB (40 pm/°C) and it is further detailed in Figure 3, where the measured resonance is shown at each temperature increment. Samples clad in E7 and Lixon presented a thermal drift of 56.3 pm/°C and 52.3 pm/°C, respectively.

Table 2. Summary of results appearing in Figure 2.

Liquid Crystal Cladding	Resonance shift/°C	Measured Temperature Range
5CB	40 pm	24 – 32 °C
E7	56.3 pm	24 – 56 °C
MDA-05-2968	58 pm	24 – 74 °C
Lixon	52.3 pm	24 – 46 °C

Figure 2. Measured ring resonator samples clad in liquid crystal (LC) mixtures.

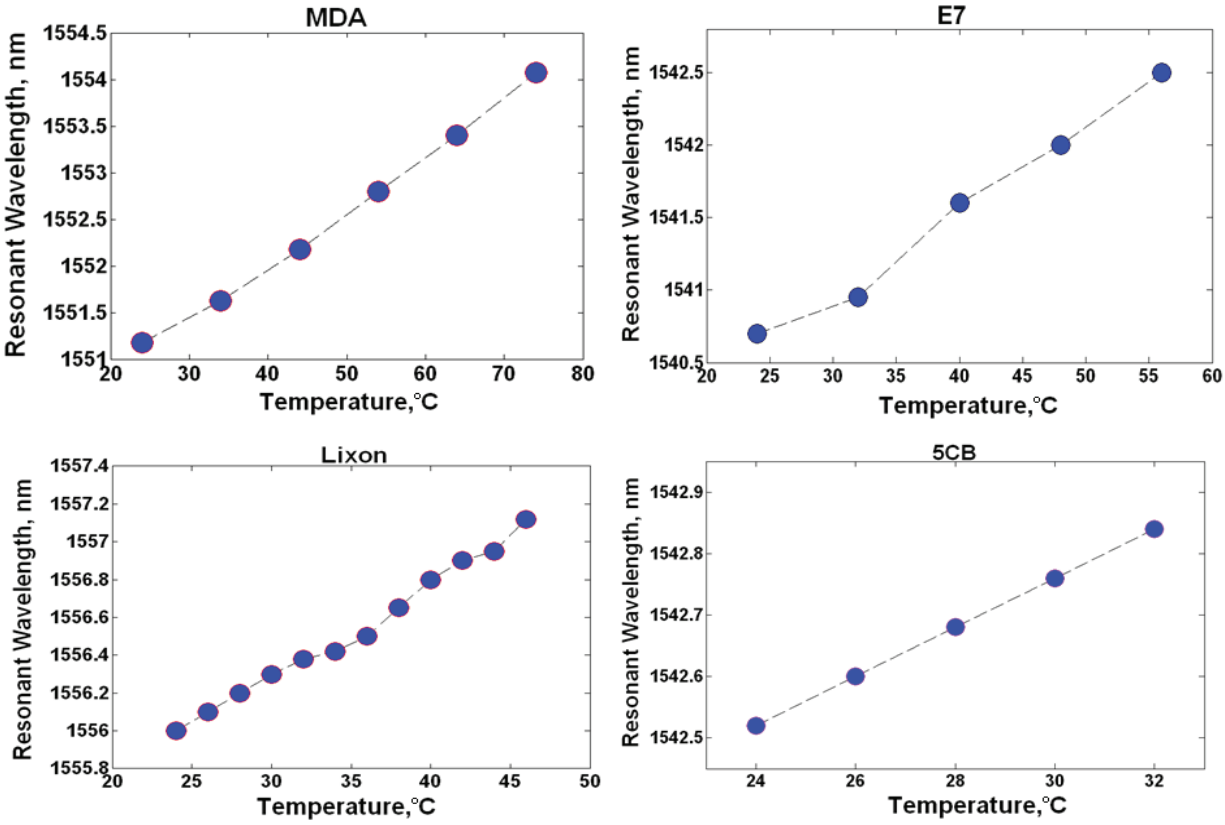

Figure 3. Peak wavelength shift for 5CB clad resonator. The thermal drift is 40 pm/°C.

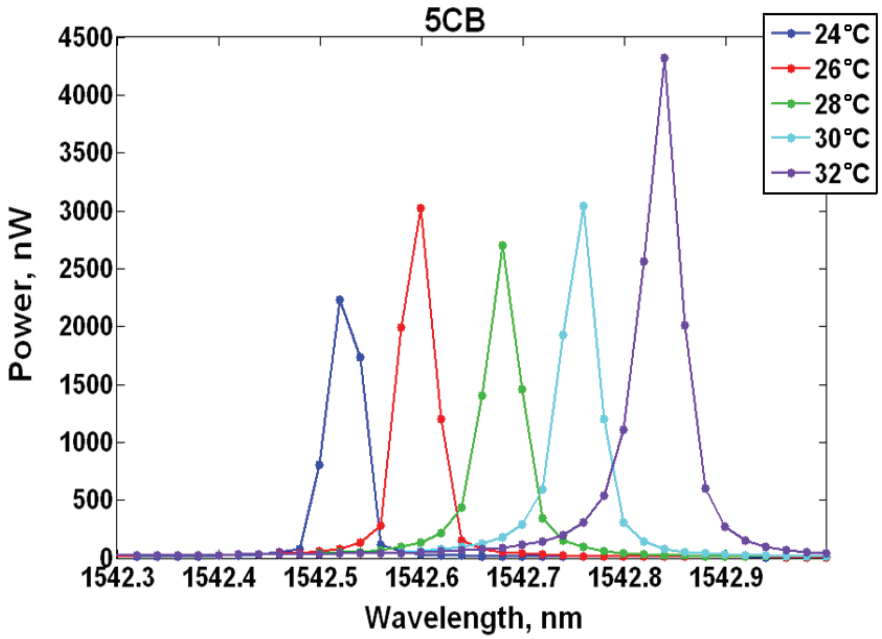

It can be seen in Figure 2 that the resonant wavelength shift of LC clad ring resonators is linear. This is to be expected, as the average LC index decreases linearly as temperature rises in both the anisotropic and isotropic phase [28,29].

The measured resonance shifts were used in calculating the thermo-optic coefficients of the liquid crystal mixtures at 1550 nm. First, the measured air-clad ring resonator response served to validate a COMSOL Multiphysics model. The measured resonance shift of an air clad resonator was 87.5 pm/°C, which strongly agrees with the COMSOL simulation resonance shift of 87.5 pm/°C, and it gives us confidence in our model. The measured and the simulated results for an air cladding are depicted in Figure 4. Experimentally observed liquid crystal cladding resonance shifts were used to obtain the change in the silicon waveguide mode effective indices using Equation (1). The effective mode indices then served to calculate the thermo-optic coefficient of the LC mixtures using our COMSOL model. Table 3 contains a summary of the results. 5CB provides the greatest negative average refractive index <n> TOC of $\Delta n_{5CB}/\Delta T = -8.7 \times 10^{-4}$/°C at 1550 nm. Lixon possesses the next best TOC of $\Delta n_{Lixon}/\Delta T = -7.2 \times 10^{-4}$/°C; followed by E7 $\Delta n_{E7}/\Delta T = -6.7 \times 10^{-4}$/°C, and MDA $\Delta n_{MDA}/\Delta T = -6.5 \times 10^{-4}$/°C. In relation to literature, our estimated TOC value of E7 ($\Delta n_{E7}/\Delta T = -6.7 \times 10^{-4}$/°C) is slightly greater than the average temperature dependent refractive index <n> value reported ($\Delta n/\Delta T = -5.24 \times 10^{-4}$/°C) [30]. This inconsistency is due to some of the E7 molecules being initially aligned in the n_e state as compared to a completely random <n> state. LC molecules in the n_e orientation will undergo a considerably larger refractive index change as a function of temperature in comparison to those randomly aligned [29,30]. It is not until the isotropic state that the LC $\Delta n/\Delta T$ fully equalizes [29].

Figure 4. (**A**) Measured resonance shift in air of a ring resonator; (**B**) Simulated shift of a ring resonator clad in air as a function of rising temperature.

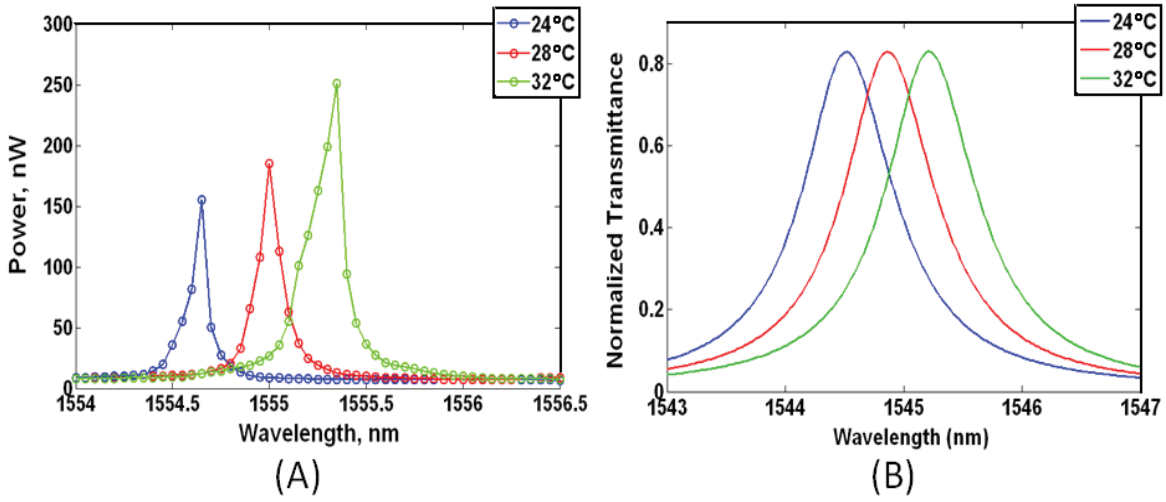

Table 3. Change in the effective index as a function of a 30 °C increase in temperature and the corresponding thermo-optic coefficient of the liquid crystal mixture at 1550 nm.

Liquid Crystal Cladding	Effective Index Shift for a 30 °C rise in Temperature	LC $\Delta n/\Delta T$
5CB	$\Delta n_{eff} = -0.0021$	−0.00087/°C
E7	$\Delta n_{eff} = -0.0029$	−0.00067/°C
Lixon	$\Delta n_{eff} = -0.0027$	−0.00072/°C
MDA-05-2968	$\Delta n_{eff} = -0.0030$	−0.00065/°C

While liquid crystals aid in minimizing temperature associated effects, complete athermal response cannot be achieved without modifying the device geometry. The amount of thermal stabilization is directly related to the extent of the optical mode overlap with liquid crystals, or any other negative TOC material. For instance, the mode of narrower waveguides will sense more of the liquid crystal cladding due to a larger portion of it being present outside of the silicon core region. An example of this appears in Figure 5, which depicts the amount of TE like mode power density that extends outside of the waveguide core as a function of waveguide width. For a 500 nm wide, 250 nm tall silicon waveguide surrounded by $n = 1.53$ index cladding, a 26% mode overlap with the cladding region is achieved. A 300 nm wide waveguide will result in a 58% cladding overlap. It should be noted that, besides device geometry, the exact cladding material's refractive index and surface roughness also come into play in mode confinement and propagation loss. Thus, while a narrower waveguide allows for increased interaction with the liquid crystal cladding, it also results in enhanced losses arising from a larger portion of the optical mode interacting with the sidewall surface roughness of the silicon core [31]. These interface imperfections originate during the fabrication process from line edge corrugations of the electron beam resist, pattern transfer, or from the etching process itself [32]. The roughness of core–cladding interfaces results in transmission loss that scales with the square of the roughness amplitude [32], which is the main reason why we chose waveguides of 500 nm width for our experiment as compared to narrower ones.

Figure 5. Silicon rectangular waveguide core width and the corresponding TE-like mode power density that extends into the cladding region. The waveguide height was kept constant at 250 nm. The cladding region refractive index was $n = 1.53$.

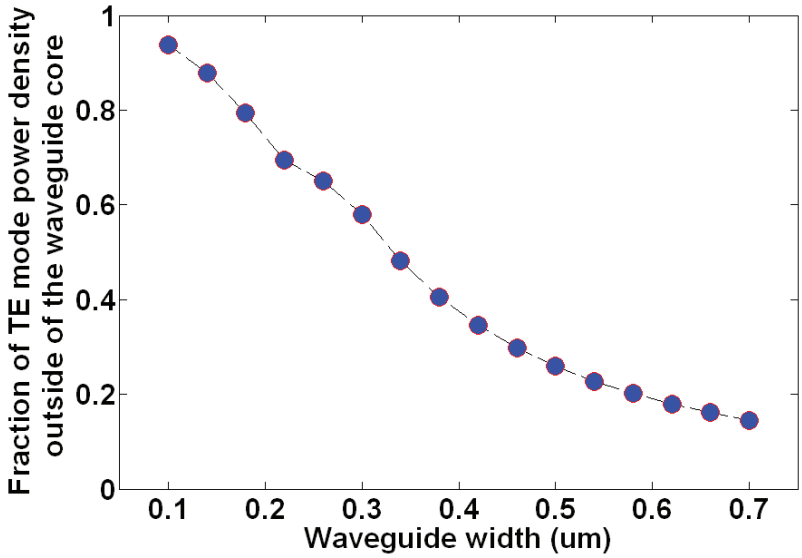

In our measurements, 5CB, which possesses the lowest clearing point temperature (T_{ni} = 35°C), boasted the largest negative TOC. 5CB is applicable to achieving predictable operation of silicon-based wavelength-division multiplexing (WDM) devices located on typical high performance multicore chips which may endure ±10 °C temperature variations [9]. Due to 5CB's flash point of 113 °C [33], Lixon with its clearing point temperature of T_{ni} = 123 °C, may be better suited for applications in which the microprocessor die hot spot thermal range fluctuates between 70–120 °C [34].

3. Experimental

3.1. Sample Fabrication and Preparation

Samples were fabricated using a 680 μm thick silicon on insulator (SOI) wafer composed of a silicon handle, a 3 μm BOX layer and 250nm of silicon placed on top of the BOX. The 3 μm SiO_2 layer aids in preventing the evanescent field of the optical mode from penetrating the silicon substrate below. Dow Corning (Midland, MI, USA) FOX-16 electron beam (e-beam) resist was diluted in Methyl isobutyl ketone (MIBK), one part FOX-16 to two parts MIBK (by weight), and spun at 4000 rpm resulting in a 180 nm thick coat [20]. The samples were patterned with a Vistec (Toronto, Canada) EBPG 5200 e-beam system using a dosage of 5120 μC/cm^2 and developed in Tetramethylammonium hydroxide (TMAH) for 1 min. Dry etch of silicon was performed using Oxford Plasmalab 100 RIE/ICP (Oxford Instruments, Abingdon, Oxfordshire, UK) with a mixture of 25 sccm of SF_6 and 50 sccm of C_4F_8 at a temperature of 15 °C, and with a reactive-ion etching (RIE) power of 30 W and inductively coupled plasma (ICP) power of 1200 W. The resulting silicon waveguides were covered by a 1800 nm layer of SiO_2 cladding deposited via Oxford Plasmalab 80 Plus plasma-enhanced chemical vapor deposition (PECVD) at 350 °C using a mixture of 5% SiH_4 and 95% N_2 at 117 sccm with 710 sccm of N_2O at a deposition rate of 72 nm/min. The PECVD chamber pressure was 1000 mT and the RF power was 20 W at 13.56 MHz. Window areas positioned over resonator rings were patterned with Shipley S1805 photoresist (Shipley Company, Marlborough, MA, USA), exposed in a Hybrid Technology Group (HTG) Mask Aligner and etched in a CMOS grade buffered oxide solution (BOE) consisting of 33.5% NH_4, 7% HF, and 59.5% H_2O, for a duration of 195 s. The remaining S1805 photoresist was removed with Shipley Microposit Remover 1165 (Shipley Company, Marlborough, MA, USA). The fabrication process is portrayed in Figure 6 and scanning electron microscope (SEM) images of the fabricated samples appear in Figure 7. Figure 7A depicts a silicon ring resonator of 9.9 μm radius and 500 nm width. Figure 7B shows the ring resonator sample clad in SiO_2 and with a window etched over the ring to accommodate the LC cladding. Placement of the liquid crystal cladding was carried out in a clean room environment and preceded by a sample cleaning step using oxygen plasma. The oxygen plasma step aids in the removal of organic contaminants and it promotes adhesion and bonding to other surfaces.

3.2. Experimental Setup

Our experimental setup consisted of an Agilent 8163B telecom-grade tunable laser (Santa Clara, CA, USA) (1470–1570 nm range) connected to a polarization scrambler and fiber coupled to the on-chip waveguide. An Oven Industries 5C7-195 Benchtop Temperature Controller (Mechanicsburg, PA, USA) linked to a thermo-electric module assisted in the heating and cooling of the LC mixture. The thermoelectric module was embedded inside of a sample mount and the sample mount was placed on a three axis mechanical stage allowing for precise alignment with the input beam and imaging optics. A thermocouple fastened to the sample stage monitored the temperature to within 0.1 °C precision. The transmission spectrum was imaged in free space onto a Newport 2931-C power

meter (Newport Corporation, Irvine, CA, USA). Control of the telecom source and the power meter was automated. The optical setup is illustrated in Figure 8.

Figure 6. Fabrication process steps.

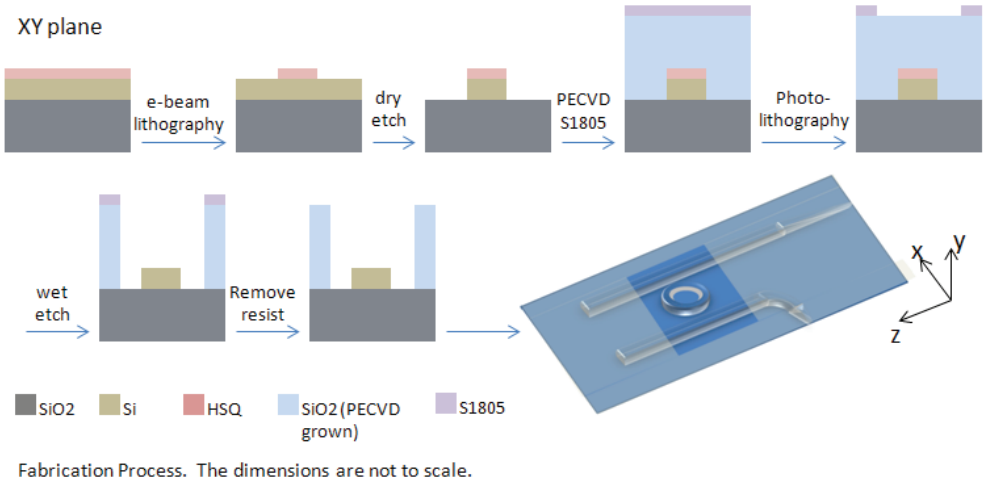

Figure 7. Fabricated ring resonator samples. (**A**) Close up of the ring resonator structure; (**B**) Ring resonator with a window etched in SiO_2 for liquid crystals.

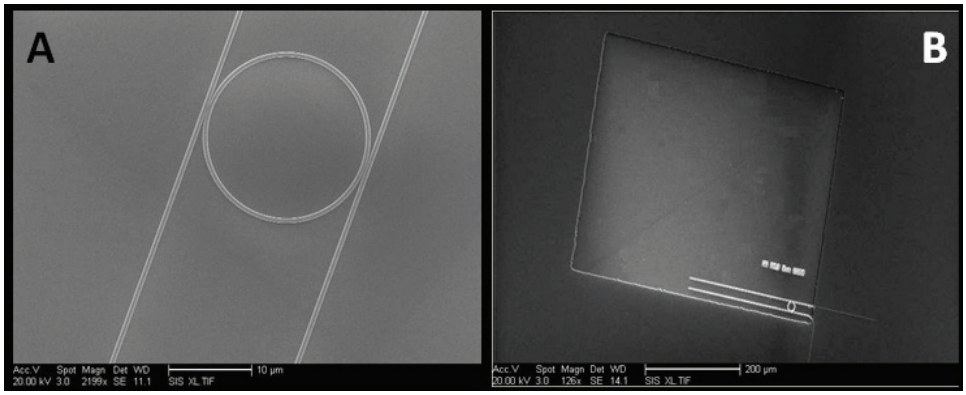

Figure 8. Optical setup.

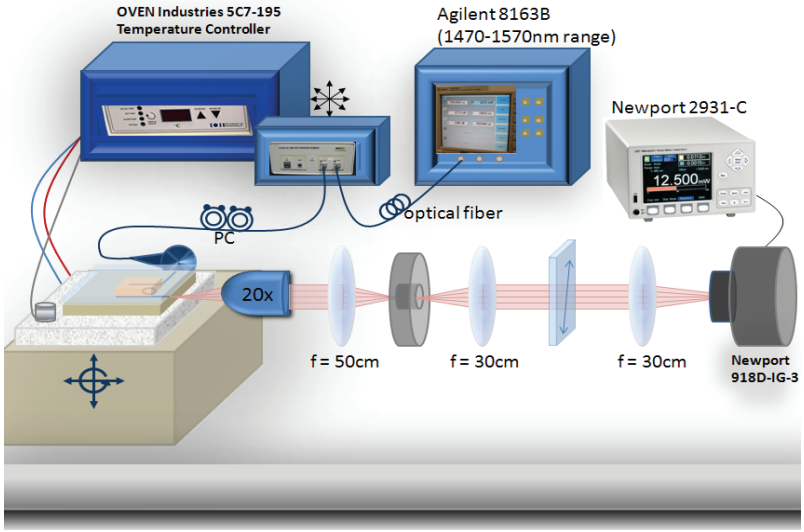

4. Conclusions

In summary, we have explored the use of liquid crystals for passive temperature stabilization of silicon photonic devices. Liquid crystals possess high negative thermo-optic coefficients and their refractive index decreases linearly as temperature rises in both the anisotropic and isotropic phase. Using ring resonators clad in liquid crystals, we show that thermal drift can be mediated, although a full athermal response requires alteration of the silicon device geometry. The amount of thermal stabilization is directly related to the extent of the optical mode overlap with liquid crystals, or any other negative TOC material. The advantage of liquid crystals lies in their high negative thermo-optic coefficients in addition to low absorption at the infrared wavelengths.

Acknowledgments

This work was supported and funded by the Space and Naval Warfare Systems Center Pacific (SSC PAC) Naval Innovative Science and Engineering (NISE) Program, the Defense Advanced Research Projects Agency, the Air Force Office of Scientific Research, Office of Naval Research Multidisciplinary University Research Initiative (MURI), the National Science Foundation (NSF) Center for Integrated Access Networks, and the Cymer Corporation. We thank Kim Sung for the Lixon LC, and Maribel Montero for electron beam exposure.

Author Contributions

Joanna Ptasinski designed and performed the experiments, analyzed data and wrote the manuscript; Iam-Choon Khoo supervised the project, designed experiments and edited the manuscript; Yeshaiahu Fainman supervised the project, designed experiments and edited the manuscript.

Conflicts of Interest

The authors declare no conflicts of interest.

References

1. Glick, M.; Rumley, S.; Dongaonkar, G.; Li, Q.; Bergman, K.; Dutt, R. Silicon Photonic Interconnection Networks for Data Centers. In Proceedings of the 2013 IEEE Photonics Society Summer Topical Meeting Series, Waikoloa, HI, USA, 8–10 July 2013.
2. Streshinsky, M.; Ding, R.; Liu, Y.; Novack, A.; Galland, C.; Lim, A.E.-J.; Lo, P.G.-Q.; Baehr-Jones, T.; Hochberg, M. The road to affordable, large-scale silicon photonics. *Opt. Photonics News* **2013**, *24*, 32–39.
3. Bigelow, S.J. Understanding Silicon Photonics Technology. Available online: http://searchdatacenter.techtarget.com/feature/Understanding-silicon-photonics-technology (accessed on 11 March 2014).
4. Guha, B.; Gondarenko, A.; Lipson, M. Minimizing temperature sensitivity of silicon Mach-Zehnder interferometers. *Opt. Express* **2010**, *18*, 1879–1887.

5. Milosevic, M.M.; Garders, F.Y.; Thomson, D.J.; Mashanovich, G.Z. Temperature Insensitive Racetrack Resonators for Near Infrared Applications. In Proceedings of the Optical Fiber Communication Conference, Los Angeles, CA, USA, 4–8 March 2012.
6. Ye, W.N.; Michel, J.; Kimerling, L.C.; Eldada, L. Polymer-cladded athermal high-index-contrast waveguides. *SPIE Proc.* **2008**, *6897*, doi:10.1117/12.789478.
7. Guha, B.; Kyotoku, B.B.C.; Lipson, M. CMOS-compatible athermal silicon microring resonators. *Opt. Express* **2010**, *18*, 3487–3493.
8. Teng, J.; Dumon, P.; Bogaerts, W.; Zhang, H.; Jian, X.; Han, X.; Zhao, M.; Morthier, G.; Baets, R. Athermal Silicon-on-insulator ring resonators by overlaying a polymer cladding on narrowed waveguides. *Opt. Express* **2009**, *17*, 14627–14633.
9. Zhou, L.; Kashiwagi, K.; Okamoto, K.; Scott, R.P.; Fontaine, N.K.; Ding, D.; Akella, V.; Yoo, S.J.B. Towards athermal optically-interconnected computing system using slotted silicon microring resonators and RF-photonic comb generation. *Appl. Phys. A* **2009**, *95*, 1101–1109.
10. Ye, W.N.; Sun, R.; Michel, J.; Eldada, L.; Pant, D.; Kimerling, L.C. Thermo-Optical Compensation in High-Index-Contrast Waveguides. In Proceedings of the 2008 5th IEEE International Conference on Group IV Photonics, Cardiff, UK, 17–19 September 2008; pp. 401–403.
11. Milosevic, M.M.; Emerson, N.G.; Gardes, F.Y.; Chen, X.; Adikaari, A.A.D.T.; Mashanovich, G.Z. Athermal waveguides for optical communication wavelengths. *Opt. Lett.* **2011**, *36*, 4659–4661.
12. Padmaraju, K.; Bergman, K. Resolving the thermal challenges for silicon microring resonator devices. *Nanophotonics* **2013**, doi:10.1515/nanoph-2013-0013.
13. Raghunathan, V.; Izuhara, T.; Michel, J.; Kimerling, L. Stability of polymer-dielectric bi-layers for athermal silicon photonics. *Opt. Express* **2012**, *20*, 16059–16066.
14. Bahadur, B.; Liquid Crystal Displays. In *Molecular Crystals and Liquid Crystals*, 1st ed.; Brown, G.H., Gray, G.W., Labes, M.M., Dienes, G.J., Eds.; Taylor & Francis: Abingdon, UK, 1984.
15. Burckel, D.B.; Samora, S.; Wiwia, M.; Wendta, J.R. Development of CMOS-Compatible Membrane Projection Lithography. In *Metamaterials: Fundamentals and Applications VI (Proceedings of SPIE)*; SPIE Press: Bellingham, WA, USA, 2013.
16. Iliescu, C.; Taylor, H.; Avram, M.; Mia, J.; Franssila, S. A practical guide for the fabrication of microfluidic devices using glass and silicon. *Biomicrofluidics* **2012**, *6*, doi:org/10.1063/1.3689939.
17. Frienda, J.; Yeo, L. Fabrication of microfluidic devices using polydimethylsiloxane. *Biomicrofluidics* **2010**, *4*, doi:org/10.1063/1.3259624.
18. Khoo, I.C.; Normandin, R. The mechanism and dynamics of transient thermal grating diffraction in nematic liquid crystal films. *IEEE J. Quantum Electron.* **1985**, *21*, 329–335.
19. Li, Q. *Liquid Crystals beyond Displays: Chemistry, Physics, and Applications*, 1st ed.; John Wiley & Sons: Hoboken, NJ, USA, 2012.
20. Khoo, I.C. *Liquid Crystals*, 2nd ed.; John Wiley & Sons: Hoboken, NJ, USA, 2007.
21. Jacobs, S.D.; Cerqua, K.A.; Marshall, K.L.; Schmid, A.; Guardalben, M.J.; Slerrett, K.J. Liquid-crystal laser optics: Design, fabrication and performance. *J. Opt. Soc. Am. B* **1988**, *5*, 1962–1979.

22. Demus, D.; Goodby, J.W.; Gray, G.W.; Spiess, H.W.; Vill, V. *Handbook of Liquid Crystals: Volume 2B, Low Molecular Weight Liquid Crystals II*; John Wiley & Sons: Hoboken, NJ, USA, 2011.
23. Ptasinski, J.; Kim, S.W.; Pang, L.; Khoo, I.C.; Fainman, Y. Optical tuning of silicon photonic structures with nematic liquid crystal claddings. *Opt. Lett.* **2013**, *38*, 2008–2010.
24. Yamada, K. Silicon Photonic Wire Waveguides: Fundamentals and Applications. In *Silicon Photonics II*; Springer: Berlin, Germany, 2011.
25. Reed, G.T.; Knights, A.P. *Silicon Photonics: An Introduction*, 1st ed.; John Wiley & Sons: Hoboken, NJ, USA, 2004; pp. 127–132.
26. Reed, G.T. *Silicon Photonics*, 1st ed.; John Wiley & Sons: Hoboken, NJ, USA, 2008; pp. 259–263.
27. Yamaguchi, Y.; Takahashi, Y.; Toda, H.; Kuri, T.; Kitayama, K. Multi-Channel Crosstalk in a 25-GHz Spaced DWDM Millimeter-Wave-Band Radio-over-Fiber System. In Proceedings of the MWP/APMP 2008 International Topical Meeting on Microwave Photonics, Gold Coast, Queensland, Australia, 9 September–3 October 2008.
28. Domanski, A.W.; Budaszewski, D.; Sierakowski, M.; Wolinski, T.R. Depolarization of partially coherent light in liquid crystals. *Opto Electron. Rev.* **2006**, *14*, 305–310.
29. Li, J.; Gauza, S.; Wu, S.-T. Temperature effect on liquid crystal refractive indices. *J. Appl. Phys.* **2004**, *96*, 19–24.
30. Li, J.; Wu, S.-T.; Brugioni, S.; Meucci, R.; Faetti, S. Infrared refractive indices of liquid crystals. *J. Appl. Phys.* **2005**, *97*, doi:org/10.1063/1.1877815.
31. Yap, K.P.; Delage, A.; Lapointe, J.; Lamontagne, B.; Schmid, J.H.; Waldron, P.; Syrett, B.A.; Janz, S. Correlation of scattering loss, sidewall roughness and waveguide width in silicon-on-insulator (SOI) ridge waveguides. *J. Light. Technol.* **2009**, *27*, 3999–4008.
32. Sparacin, D.K.; Spector, S.J.; Kimerling, L.C. Silicon waveguide sidewall smoothing by wet chemical oxidation. *J. Light. Technol.* **2005**, *23*, 2455–2461.
33. Sigma-Aldrich Co. LLC., MSDS 5CB Liquid Crystal. Available online: http://www.sigmaaldrich.com/catalog/product/aldrich/328510?lang=en&region=US (accessed on 12 March 2014).
34. Borkar, S.; Karnik, T.; Narendra, S.; Tschanz, J.; Keshavarzi, A.; De, V. Parameter Variations and Impact on Circuits and Microarchitecture. In Proceedings of the IEEE Proceedings on Design Automation Conference, Anaheim, CA, USA, 2–6 June 2003.

MDPI AG
Klybeckstrasse 64
4057 Basel, Switzerland
Tel. +41 61 683 77 34
Fax +41 61 302 89 18
http://www.mdpi.com/

Materials Editorial Office
E-mail: materials@mdpi.com
http://www.mdpi.com/journal/materials

MDPI • Basel • Beijing • Wuhan
ISBN 978-3-906980-86-7
www.mdpi.com